Conformational Transitions of the Ras Protein Involved in Macromolecular Interactions and Modulated by Small Compounds. A Biophysical Approach Using NMR and X-Ray Crystallography at Ambient and High Pressures

DISSERTATION ZUR ERLANGUNG DES DOKTORGRADES DER NATURWISSENSCHAFTEN (DR. RER. NAT.) DER FAKULTÄT FÜR BIOLOGIE UND VORKLINISCHE MEDIZIN DER UNIVERSITÄT REGENSBURG

Vorgelegt von Pedro Lopes

aus Marinhas, Esposende. Portugal

2018

Das Promotionsgesuch wurde eingereicht am:

Die Arbeit wurde angeleitet von:
Prof Dr. Dr. Hans Robert Kalbitzer

Unterschrift

_____

- This page was deliberately left blank -

Table of Contents

2. Methods

3. results

Acknowledgments

First and foremost I would like to thank the Bayerischen Forschungsstiftung for their complete financial support and to Prof. Dr. Dr. Hans Robert Kalbitzer for accepting me in his group, for sharing his ideas, scientific knowledge and for his overall contribution as main supervisor of the entire project.

I would like to thank to Dr. Michael Spoerner, without whom this work would have been impossible to perform. His insightful ideas, ^{31}P NMR expertise and broad knowledge on the Ras field were always detrimental for the project's well being.

Many thanks to Prof. Dr. Werner Kremer, for all the suggestions, advices and concerns not only with the scientific side but also with the human side, not only with me but with all members of the group.

My deepest gratitude to Dr. Sunilkumar P. Narayanan for helping me with his incredible scientific expertise, particularly for all the teachings in the field of high pressure NMR. More importantly, thank you for your friendship and for guiding me through the ways of life and science.

My deepest gratitude to the high pressure crystallography team that I had the pleasure to work with: Dr's. Nathalie Colloc´h, Eric Girard, Anne-Claire Dhaussy and Prof. Dr. Thierry Prangé. Your brightness, insightful ideas and seemingly endless wisdom caused my scientific interests to irrevocably entwine with the field of X-ray crystallography. Your expertise and extraordinary technical skills are to me the prototype of what great scientists and the scientific method should always be.

The warmest thank you to Dr. Malte Andrasch for sharing with me his extensive and remarkable knowledge in the fields of protein biochemistry and biophysics. More importantly, thank you for your positive and vibrant energy during many dark moments. Thank you still for your ongoing help and concern towards the future.

I am grateful to Sabine Laberer for her help in the scope of molecular biology techniques, particularly with DNA technologies. Similarly, I would like to thank Sabine Ruppel, to whom I owe all the expertise I acquired in the field of protein biochemistry and purification techniques. Thank you for your constant effort to teach me, even through the barriers imposed by communicating in a different language.

My deepest thank you to Dominique Quetting, for her help with the expression and purification of difficult proteins and for the permanent concern in providing the most organised and efficient laboratorial environment. Above all, thank you for your friendship, for all the laughs, relaxing coffees together with Sunil and the nice moments we spent looking for furniture.

I want to show my gratitude to Dr. Markus Bech Erlach for his help and know-how with the processing and interpretation of NMR spectra and contagious positive attitude.
From many students that I had the pleasure to meet and work with side-by-side, I leave here my heartfelt thank you to all: Beatta Zablocka, Gani, Margarita Neun, Maria Watzlowik, Silvia Planck, Linda Stabi, Martin Winter, Simon Nimmermehr, Andy, Mathias Karl, Marcell Kaljanac. Thank you, for your eagerness to learn the ways of science, for your questions and for your teachings. Above all, thank you for the awesome moments and stories we shared and for introducing me to the subtle details of another culture and lifestyle.
I am grateful to Claudia Kiesewetter and Marcus Hoering for their prompted availability to help me with the translation of the summary of this thesis. Thank you Claudia for your brightness and lovely friendship and Marcus for all the good laughs and memorable stories.
I am ever so grateful to my brother João Miguel for always being a positive influence in my life and to my parents Manuel Lopes and Maria Celina for their support and concern with my well-being.
I leave here a word of appreciation to all the musicians that accompanied me for the long hours and lonely nights spent at the biochemistry and NMR laboratories. Among many, I am especially grateful to Sirs Mark Knopfler, David Gilmour and Gary Moore for the legacy they gave to all of us. Their music was countless times the only motivation to carry on and it will always be a source of inspiration through my entire life.
Last but by no means least, I leave here my heartfelt deepest gratitude to the most important person of all: my Carina! Thank you for your constant tender and care, for your patience and for helping me more times than I can remember. As you know so well my dear, writing this book has been an exercise of sustained suffering through which I persisted only because of your relentless support and dedication. It came to realisation only because of you and therefore it is dedicated to you!

Summary

The guanine binding nucleotide protein Ras is a small GTPase that controls central regulatory processes such as cell differentiation, proliferation and apoptosis by alternating between an active, GTP-bound, and an inactive, GDP-bound state. Both, the intrinsic hydrolysis of GTP and the exchange reaction from GDP to GTP are very slow. Two classes of regulatory proteins called GAP's and GEF's are necessary to accelerate these two respective reactions. Active Ras interacts also with another class of proteins generally called effectors. Using ^{31}P NMR spectroscopy two conformational states that interconvert in the millisecond time scale could be directly observed. They are named state 1(T) and state 2(T) (T or D, depending whether if Tri- or Di-phosphate is bound) and correspond to the GEF and to the effector recognition states, respectively. Their nature is influenced by specific mutations and by the type of bound nucleotide. It was verified that specific somatic mutations render Ras a very potent oncogene. As consequence, the protein becomes insensitive to inactivation by GAP's and therefore locked in the active state, leading ultimately to uncontrolled cellular proliferation. Approximately 30% of all human tumours are estimated to harbour mutations in one of the three isoforms (H, K and NRas) at positions 12, 13 or 61, with KRas being the most preponderant one. Due to its key role in malignant transformation, efforts have been made over the years to develop effective inhibitors against a seemingly undruggable protein.

In the framework of this thesis, it was demonstrated that KRas^{WT} shows an almost identical behaviour to HRas^{WT} in terms of their intrinsic equilibria. Their ^{31}P NMR spectra is dominated by two conformational states with an equilibrium constant, K_{12}, of 2.0 measured at the γ-phosphate of bound GppNHp. The ability to modulate the equilibrium was further addressed by elucidating the mode of action of Zn^{2+}-cyclen. It was shown that this compound can selectively recognise and stabilise state 1(T), disrupting the affinity of both isoforms towards effectors such as Raf-RBD. Titration experiments showed a cooperative binding at two different sites with a Hill coefficient of 2 and an apparent dissociation constant of 9.9 mM for both isoforms.

The inhibition of the oncogenic KRas^{G12D} by a library of 15 different small compounds was further investigated. ^{31}P NMR showed that at least two of them (#755 and #757) led to a significant stabilisation of state 1(T), with more than 70% decrease in the equilibrium constant. A 75% decrease in the affinity of the Ras-Raf complex in the presence of 300 μM of each drug was obtained from ITC measurements. The screening showed that the compounds initially developed for inhibition of Ras bound to GDP are also able to inhibit

Ras in the triphosphate-bound form and are good candidates for further lead optimisation.

High pressure (HP) ^{31}P NMR was conducted in the isolated GppNHp molecule and in several Ras proteins. For all of them, the pressure-dependence of the chemical shifts revealed to be non-linear as given by the obtained positive values of the second order pressure coefficients, B_2. A direct shift of the conformational equilibrium from state 2(T) towards state 1(T), given by the decrease in the equilibrium constant from 1.7 at 0.1 MPa to 0.24 at 250 MPa was observed for Ras^{WT}. Additional transitions were detected involving the GAP binding and the nucleotide-free states, named 3(T) and 1(0), respectively.

State 3(T) was identified by ^{31}P NMR upon titration of Ras with NF1 and assigned to the resonance line at δ= -3.00 ppm in the spectrum of Ras^{WT}•Mg^{2+}•GppNHp. At equimolar concentrations saturation was achieved for the γ-phosphate but not for the β-phosphate, supporting the existence of conformational differences in the local environment of this phosphate group upon formation of the protein complex.

Using site-directed mutagenesis and ^{31}P NMR spectroscopy, it was verified that several point mutants (H27E, S39L, E3V and D33K) led to a pronounced modification of the conformational equilibrium. The highest effect was observed for Ras^{D33K}•Mg^{2+}•GppNHp that is almost completely shifted towards state 2(T) as given by the increase of the equilibrium constant from 1.7 to 11.3. The mutation is located in the effector-loop region of Ras involved in the interaction with different proteins. A 30-fold decreased affinity towards Raf-RBD (K_D= 10.4 μM) comparatively to Ras^{WT} (K_D= 0.42 μM) and an impaired affinity towards NF1 was observed. The increase of the equilibrium constant from 1.7 to 2.0 in the case of Ras^{E3V} represents a good example of a typical conformational modulation by an allosteric mechanism, as the mutation is located in a distal site relative to the bound nucleotide.

The crystal structures of Ras^{WT} and Ras^{D33K} were solved for the first time under high pressure. Analysis of the unit cell compressibility revealed the existence of a transition zone for Ras^{WT} between 200 and 270 MPa. A decrease of the main-chain temperature factors from 20 Å^2 at 0.1 MPa to 13.5 Å^2 at 650 MPa, together with the increase in the average rmsd values, gave an insight for the possible stabilisation of non-native conformations at high pressures. Ras^{D33K}, on the other hand, is less sensitive to pressure, with the transition zone occurring around 500 MPa and significant rearrangements at 880 MPa. Typical pressure-induced modifications involved the helix α_2 as part of switch 2, the loop λ_7, helix α_1 at the beginning of switch 1.

Zusammenfassung

Das Guaninnukleotid-bindende Ras Protein ist eine kleine GTPase, die durch den Wechsel zwischen dem aktiven, GTP-gebundenen Zustand und dem inaktiven, GDP-gebundenen Zustand verschiedene regulatorische Prozesse in der Zelle kontrolliert, wie z.B. Zelldifferenzierung, Zellproliferation und Apoptose. Sowohl die intrinsische Hydrolyse von GTP als auch die Austauschreaktion von GDP zu GTP sind sehr langsam. Um diese Reaktionen zu beschleunigen wird die Hilfe der zwei regulatorischen Proteinklassen GAP's und GEF's benötigt. Außerdem interagiert Ras in seinem aktiven Zustand mit einer weiteren Proteinklasse, den sogenannten Effektoren. Mit Hilfe der ^{31}P-NMR-Spektroskopie können die zwei Konformationen, deren Umwandlung nur Millisekunden benötigt, direkt detektiert werden. Die beiden Zustände werden als 1(T) und 2(T) bezeichnet (T bzw. D, je nachdem ob Tri- oder Diphosphat gebunden ist) und entsprechen jeweils dem GEF und dem Effektor-erkennenden Zustand. Beeinflusst werden sie durch spezifische Mutationen und durch die gebundene Nukleotidform. Außerdem ist bekannt, dass spezifische somatische Mutationen Ras zu einem potenten Onkogen machen. Als Folge daraus wird das Protein unempfindlich gegen die Inaktivierung durch GAP's und verbleibt im aktiven Zustand, der zu einer unkontrollierten Zellteilung führt. In 30% aller menschlichen Tumore liegen Mutationen in einer der drei Ras Isoformen (H, K und NRas) in den Positionen 12, 13 oder 61 vor, von denen KRas am häufigsten betroffen ist. Wegen seiner Schlüsselfunktion bei der Tumorbildung wurden im Laufe der letzten Jahre viele Versuche unternommen, um effektive Inhibitoren gegen das scheinbar unbehandelbare Protein zu finden.

Im Rahmen dieser Arbeit konnte nachgewiesen werden, dass KRas^{WT} und HRas^{WT} ein nahezu identisches Verhalten in Bezug auf ihre intrinsischen Gleichgewichte besitzen. Ihre ^{31}P-NMR-Spektren werden von zwei konformationellen Zuständen dominiert, die eine Gleichgewichtskonstante K_{12} von 2.0 besitzen, die am γ-Phosphat des gebundenen GppNHp bestimmt wurde. Die Möglichkeit dieses Gleichgewicht zu beeinflussen wurde durch den Wirkungsmechanismus von Zn^{2+}-Cyclen verdeutlicht. Es konnte gezeigt werden, dass diese Komponente selektiv den Zustand 1(T) stabilisiert und die Affinität beider Isoformen gegenüber den Effektoren (z.B. Raf-RBD) stört. Titrationsexperimente haben eine kooperative Bindung an zwei verschiedenen Seiten mit einem Hill-Koeffizienten von 2 und einer Dissoziationskonstanten von 9.9 mM für beide Isoformen ergeben.

Die Inhibition von onkogenem KRas^{G12D} durch 15 verschiedene kleine Substanzen wurde weiter untersucht und es konnte mit Hilfe der ^{31}P-NMR-Spektroskopie gezeigt werden, dass mindestens zwei dieser Komponenten (#755 und #757) zu einer signifikanten Stabilisierung

des Zustands 1(T), mit einer Verkleinerung der Gleichgewichtskonstanten von mehr als 70%, führen. Mittels ITC Messungen konnte eine 75%ige Abnahme der Affinität des Ras-Raf Komplexes in der Anwesenheit von 300 μM der entsprechenden Komponente bestimmt werden. Die Experimente zeigten, dass die Komponenten, die ursprünglich für die Inhibition des GDP-gebundenen Ras entwickelt wurden, auch Ras in seiner Triphosphat-gebundenen Form inhibieren können und dementsprechend optimale Kandidaten für eine weitere Optimierung wären.

Das isolierte GppNHp Molekül sowie verschiedene Ras Proteine wurden mittels Hochdruck ^{31}P-NMR-Spektroskopie untersucht. In allen Fällen konnte eine nicht lineare Abhängigkeit der chemischen Verschiebung anhand der positiven Werte des Druckkoeffizienten zweiter Ordnung (B_2) gezeigt werden. Für Ras^{WT} konnte eine direkte Verschiebung des koformationellen Gleichgewichts von Zustand 2(T) zu Zustand 1(T) anhand der Abnahme der Gleichgewichtskonstanten von 1.7 bei 0.1 MPa zu 0.24 bei 250 MPa beobachtet werden. Außerdem wurden zwei zusätzliche Übergänge detektiert, die Zustand 3(T) und 1(0) benannt wurden. Dabei handelt es sich um den GAP-bindenden Zustand und um den Nukleotid freien Zustand.

Der Zustand 3(T) wurde mittels Titrationsexperiment und ^{31}P-NMR-Spektroskopie identifiziert, bei dem NF1 zu Ras titriert wurde und die Resonanzlinie bei δ= -3.00 ppm dem Spektrum von Ras^{WT}•Mg^{2+}•GppNHp zugeordnet wurde. Bei equimolarer Konzentration wurde eine Sättigung für das γ-Phosphat, aber nicht für das β-Phosphat, erzielt. Diese Tatsache unterstützt die Existenz der konformationellen Unterschiede in der lokalen Umgebung dieser Phosphat Gruppe bei der Bildung des Proteinkomplexes.

Mit Hilfe von ortsspezifischer Mutagenese und der ^{31}P-NMR-Spektroskopie konnte nachgewiesen werden, dass einige Punktmutationen (H27E, S39L, E3V und D33K) zu einer starken Modifikation des konformationellen Gleichgewichts führen. Der stärkste Effekt wurde bei Ras^{D33K}•Mg^{2+}•GppNHp beobachtet. Hier erfolgt eine nahezu komplette Verschiebung hin zu Zustand 2(T), wie anhand der Zunahme der Gleichgewichtskonstanten von 1.7 zu 11.3 zu erkennen ist. Die Mutation befindet sich an der Effektor-Schleifen Region von Ras, die in die Interaktion mit verschiedenen Proteinen involviert ist. Eine 30-fache Abnahme der Affinität zu Raf-RBD (K_D= 10.4 μM) im Vergleich mit Ras^{WT} (K_D= 0.42 μM) und eine gestörte Affinität zu NF1 konnte beobachtet werden. Die Zunahme der Gleichgewichtskonstanten von 1.7 zu 2.0 von Ras^{E3V} stellt ein gutes Beispiel einer typischen konformationellen Änderung durch einen allosterischen Mechanismus dar, da sich die Mutation auf der entfernten Seite des Nukleotid Bindungszentrums befindet.

Die Kristallstrukturen von Ras^{WT} und Ras^{D33K} wurden erstmals unter Hochdruck ermittelt. Die Analyse der Kompressibilität der Einheitszelle zeigte die Existenz einer Übergangszone für Ras^{WT} zwischen 200 und 270 MPa. Durch die Abnahme der Hauptketten Temperatur Faktoren von 20 $Å^2$ bei 0.1 MPa zu 13.5 $Å^2$ bei 650 MPa, zusammen mit der Zunahme der Durchschnittwerte von rmsd, konnte ein Einblick in die mögliche Stabilisierung von nicht nativen Konformationen bei Hochdruck erhalten werden. Auf der anderen Seite ist Ras^{D33K} weniger sensitiv zu Druck und besitzt seine Übergangszone bei etwa 500 MPa und signifikante Änderungen treten ab 880 MPa auf. Typische Druck induzierte Modifikationen involvieren die Helix α_2 als Teil des Switch 2, die Schleife λ_7 und die Helix α_1 am Anfang des Switch 1.

- This page was deliberately left blank -

1. Introduction

“No human investigation can be called true science
without passing through mathematical tests”
Leonardo Da Vinci

1.1 Ras as a Molecular Switch

This thesis deals with the Ras protein, a prototype member of a large superfamily called guanine nucleotide binding proteins (GNBP's or G proteins, for short) that act as molecular switches by cycling between an 'on' (active) and an 'off' (inactive) state, thus controlling diverse regulatory processes of capital importance in the living cells. Ras was identified in 1964 when Jennifer Harvey observed that a preparation of murine leukaemia virus (MLV) induced rat sarcomas in newborn mice [1]. Within the next three years, an additional retrovirus containing a new Ras gene, homologous to the first one, was further discovered by Werner Kirsten [2]. Ten years later, a third gene was identified in human Neuroblastoma cells [3]. The three homologue proteins codified by the three genes were thereafter named as H, K and NRas. Their complex structural dynamics and profound biochemical importance has been unveiled slowly but steadily for more than half a century, up to the present day. Since the last decade there has been an uprising interest by the scientific community in the chemistry of Ras (particularly KRas) due to its involvement in tumour formation and progression, triggered by an impaired function of the molecular switch mechanism that originates the permanent activation of the protein. A renewed scientific endeavour is taking place at the moment, in an attempt to find truly effective Ras inhibitors capable of drugging a seemingly undruggable protein [4].

The GNBP superfamily can be grouped by sequence homology into five major subgroups. Incidentally the subgroups also define a more or less similar biological function. The Ras family is a branch that contains the Ras protein itself, together with the three isoforms and is involved in cell proliferation, gene expression, differentiation and apoptosis; the Rho (Ras homologous) controls the dynamics of the cytoskeleton; the Rab (Ras in the brain) and Arf (ADP ribosylation factor) families regulate the vesicular transport and the Ran (Ras in the nucleolus) determines the direction of the nucleocytoplasmic transport and regulates the mitotic spindle organization [5]. Altogether they are the masters of the signalling transduction pathways, controlling virtually all molecular events by which any chemical or physical stimuli is relayed into the nucleus and culminates with an appropriate cellular response (e.g. transcription of specific genes). All members have the ability to bind the small nucleotides guanosine di-phosphate (GDP) and guanosine tri-phosphate (GTP) with high selectivity and affinity (in order of 10 pM), being the binding process strongly dependent of Mg^{2+}, which is their natural co-factor.

With exception of Ran, all G proteins are posttranslationally modified by addition of lipids either at their N-terminus by acetylation (myristoylation) or at their C-terminus by prenylation

and palmitoylation [6]. Prenylation takes place by addition of farnesyl or geranyl-geranyl lipidic groups via a stable thioether linkage, catalysed by the enzyme farnesyltransferase. Palmitoylation takes place through the formation of a reversible thioester linkage and is used to dynamically regulate membrane localization. These modifications serve as important components of their membrane targeting motifs and promote membrane binding. GNBP's can be also regulated by non-lipidic modifications such as phosphorylation, nitrosylation, mono- and di-ubiquitination, acetylation and oxidation, all of which alter the protein localization and/or interaction with regulatory molecules. An in-depth coverage of these topics can be found in excellent recent reviews [7-9].

The human Ras superfamily contains 167 proteins, of which 39 belong to the Ras sub-family and comprise a total of 940 structures deposited in the protein data bank (pdb), as of October 2017, either in uncomplexed forms or bound to any regulatory protein or small ligand.

1.1.1 Structural and Biochemical Considerations

The first crystal structure of Ras was solved in 1988 independently by Sung-Hou Kim [10] and Alfred Wittinghofer [11] with a 2.1 and 2.6 Å resolution, respectively. In the next year, the latter group published a refined structure with a resolution of 1.35 Å that became a representative model of the protein and a starting point for many theoretical and experimental structural studies in the years to come (pdb: 5p21) [12]. All Ras members share the same structural fold, so-called "G domain", containing the catalytic machinery comprised of 6 β-strands (β_1-β_6) flanked by and 5 α-helices (α_1-α_5) and 10 connecting loops (λ_1-λ_{10}, Figure 1.1). The G domain contains five fingerprint regions, named from G1 to G5, all of them located in loops: G1, also called the P-loop (aa 10-17; GxxxxGKS, x= any aliphatic amino acid) is a glycine-rich loop that twines around the negatively charged phosphate groups, binding tightly to them through its main chain positively charged N atoms. Lys16 contacts directly the β- and γ-phosphates and is crucial for nucleotide binding. The OH group of Ser17 contacts the β-phosphate and the Mg^{2+} ion [13]. The region G2, also called switch 1 (switch 1, aa 30-40 in HRas) or "effector region" since is involved in the binding of effectors when in the GTP state, is one of the regions that changes conformation upon nucleotide exchange. It contains a Thr35 that is totally conserved in all members of the superfamily and crucial for sensing the presence of the γ-phosphate of GTP, establishing a polar contact with it via its NH main chain. The same amino acid also binds the Mg^{2+} ion via its OH side chain [14]. The region G3, also called switch 2 (switch 2, aa 59-70 in HRas) has no conserved sequence besides a small loop at its beginning called the

DxxG motif (aa 57-60) in which Gly60 forms a main chain H-bond with the γ-phosphate. Another important residue in switch 2 is Gln61 that plays a crucial role in the stimulation of GTP hydrolysis (section 1.1.4) [15]. G4 is the N/TKxD motif (aa 116-119), where the Asp119 contacts the nitrogen atoms from the base with a bifurcated H-bond and Asn116 contacts the C=O group from the purine ring, thus conferring specificity for the guanidinium base. Lys117 stacks along the plane of the base [16]. G5, also called SAK (aa 145-147), is a weakly conserved motif in which the backbone NH groups interact with the C=O moiety from the guanine base. These five structural elements of the G domain are depicted in Figure 1.2, along with key molecular contacts to the nucleotide.

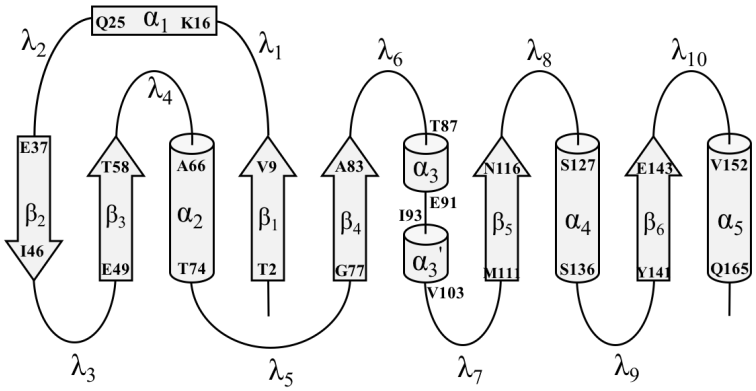

Figure 1.1. Topology of the G domain. The diagram represents the order of secondary structure. Helices are shown as cylinders and marked as α_1-α_5 (helix α_3 is slightly distorted) and the β-sheets are shown as arrows and marked as β_1-β_6. Loops are labelled λ_1-λ_{10}. The amino acids flanking the beginning and the end of each element of secondary structure are indicated.

The three Ras isoforms (H, K and NRas) share more than 90% identity across the catalytic domain but differ considerably in the last 25 residues, having less than 15% similarity. These residues constitute the C-terminal part of the protein and are called the hypervariable region (HVR). They are necessary for interaction with the membrane and play a fundamental role in signalling processes. For technical reasons, most of the biochemical studies were performed over the years with truncated variants of Ras, comprising only the catalytic domain (aa 1-166, 18 kDa). It was demonstrated that the first 166 residues are necessary and sufficient for the biochemical properties of the protein [15, 17]. In fact, to the present date, there are no crystal structures of the full-length (aa 1-189, 21 kDa) *wild type* Ras deposited in pdb. The only available structure was obtained in 2012 for the mutant KRas4b^{G12D}•Mg^{2+}•GDP [18]. FL Ras undergoes crystallization as easy as the truncated variant but attempts to retrieve diffraction data from HVR fail consistently due to the lack of electron density, which portends the high flexibility of this region. In recent years, however, the scientific interest in FL Ras instead of the truncated variant gained much more attention, especially after the discovery that the HVR is capable of acting on the catalytic domain, modulating its action and being largely responsible for the biological differences across the three isoforms [19-21].

Ras is intrinsically capable of hydrolysing the GTP nucleotide by transferring electrons to a water molecule strategically placed in the catalytic centre that promotes the nucleophilic attack of the γ-phosphate (Figure 1.2). The averaged half-life for this process is ca. 25 min. (Table 3.14). Very often the natural nucleotides need to be replaced by more stable, non-hydrolysable ones, especially when performing long term experiments of several hours or days, common in NMR spectroscopy. A frequently used analogue is GppNHp, being structurally identical to GTP except for the oxygen atom that mediates the β- and γ-phosphates that becomes replaced by an NH group. Other analogues include GTPγS and $GppCH_2p$ [22]. Detailed analysis revealed that both GTP and GppNHp bind Ras in the same manner with only slight differences in the bridging NH group, indicating that small local changes can still lead to drastic differences in the dynamics of the catalytic site [23].

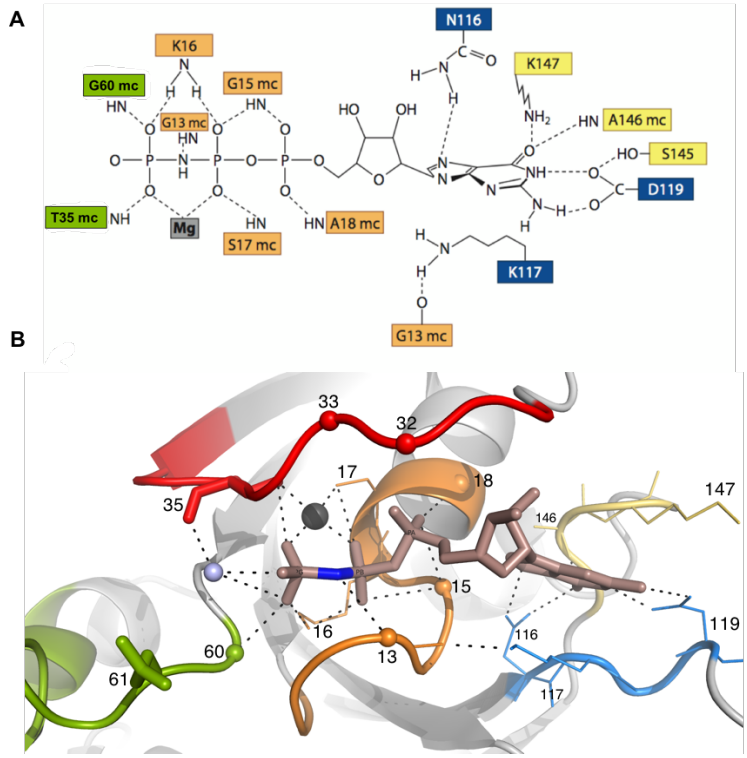

Figure 1.2. HRas•Mg^{2+}•GppNHp as the prototype of the G domain: structural details of the catalytic centre. **A.** Schematics of the interaction between selected residues and **B.** their representation in the crystal structure (pdb: 5p21). switch 1 and switch 2 are coloured in red and green, respectively, the P-loop is coloured in orange and the G4 and G5 motifs are coloured in blue and yellow, respectively. The position of important residues is indicated by small spheres (centred at their α-carbon) or explicitly by lines. Q61 is implicated in the hydrolysis of the γ-phosphate by interacting transiently with a nearby catalytic water (shown as a light blue sphere). Thr32, whose side chain (not represented) can bind transiently to the γ-phosphate is also indicated. Its neighbor, Asp33, is a very important residue in the scope of the work developed in this thesis. The Mg^{2+} ion is shown as a black sphere. The detail of the amide group of the non-hydrolysable GppNHp nucleotide is shown in blue colour. The nitrogen atom establishes a polar contact with Gly13 from the P-loop. This interaction is absent in the case of the natural nucleotide GTP.

The switch mechanism between the active and the inactive states is accompanied by prominent structural changes in the switch 1 and switch 2 regions: in GppNHp-bound HRas, the γ-phosphate forms two H-bonds with Gly60 from switch 2 and Thr35 from switch 1. The Mg^{2+} ion is bidentately coordinated by the non-bridging oxygen atoms of β- and γ-phosphates, Thr35, Ser17 (from the P-loop) and two H_2O molecules [24-26]. Quantum mechanical (QM) calculations showed that Mg^{2+} provides a temporary storage for electrons

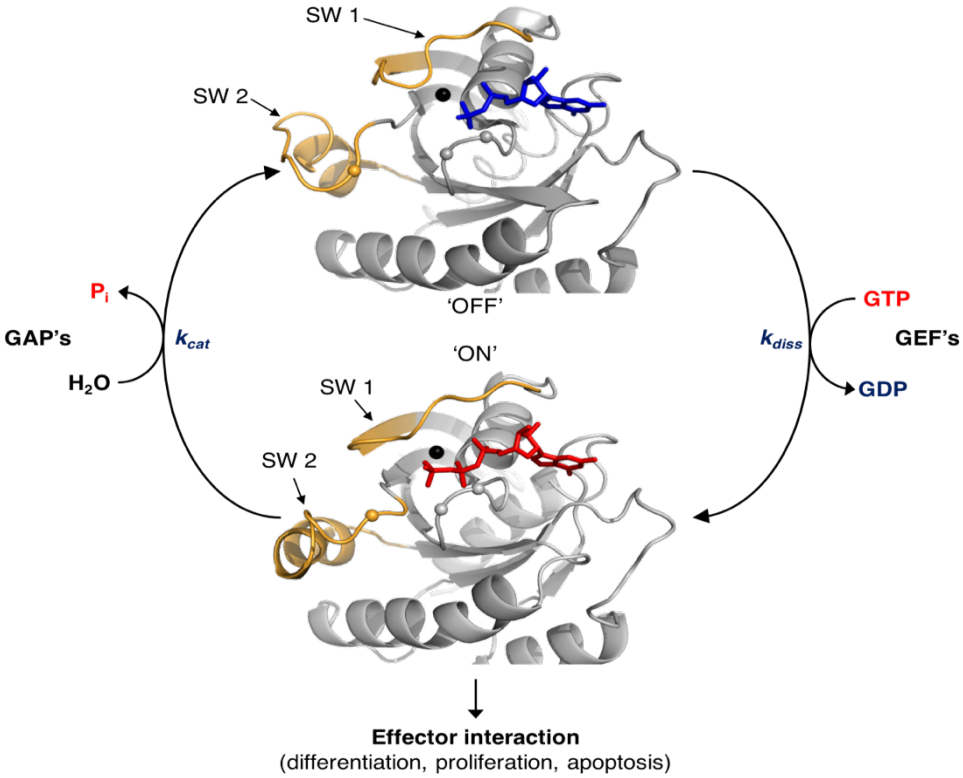

Figure 1.3. The switch mechanism in three dimensions. The Ras protein is in a continuous cycle of activation/ inactivation defined by the permanent exchange between GTP and GDP nucleotides. The crystal structures of the inactive, GDP-bound (blue colour), and active, GTP-bound, (red colour) HRas protein are shown (pdb: 1q21 and 5p21, respectively). The flexible switch 1 and switch 2 regions are coloured in orange and the coordinated Mg^{2+} ion is shown as a black sphere. The two common mutation sites in cancer (G12 and G13) lie close to the nucleotide and are represented as grey spheres. The totally conserved Q61 is shown as an orange sphere and can be used here to visually understand the movement of the switch regions as the protein cycles between GDP and GTP. The activation mechanism is catalysed by GEF's and the intrinsically slow hydrolysis of GTP is catalysed by GAP's. In the active form, Ras interacts with effectors to trigger downstream signaling events.

taken from the triphosphate and that after release of the γ-phosphate it returns them back to GDP, contributing for the process of hydrolysis [27].

Upon GTP hydrolysis, the β-phosphate has no direct interactions with Thr35 and Gly60; coupled with the loss of coordination between the Mg^{2+} ion and Thr35. These alterations promote an extensive remodelling of switch 1 and switch 2, both adopting now a more 'relaxed' or open conformation and effectively moving away from the nucleotide, as shown in Figure 1.3. At the same time the helix α_2 (aa 66-74, Figure 1.1) undergoes a large rotation together with the unwind of one of its helical turns. This open conformation contributes afterwards for the dissociation of GDP, perpetuating the cycle. Another important difference upon nucleotide exchange is Tyr32 located in switch 1: in GppNHp-bound Ras, Tyr32 is set upwards, pointing to the solvent, whereas in the GDP-bound Ras undergoes a large flip and shifts towards the interaction site. The root mean square deviation (rmsd) between the whole catalytic domains of GppNHp and GDP-bound HRas is 1.58 Å for the backbone

atoms. If the switch regions are excluded, the rmsd is only 0.66 Å [28, 29].

Ras is an incomplete enzyme: its intrinsic rate of GTP hydrolysis (also called GTPase activity) is too slow for many cellular processes and needs to be catalysed by a group of proteins called GTPase activating proteins (GAP's). Similarly, the release of GDP is also intrinsically very slow and needs to be catalysed by guanine nucleotide exchange factors (GEF's) [30, 31].

Ras is capable of initiating more than 10 different signalling cascades (Figure 1.4) that control cell differentiation, proliferation or apoptosis by transducing extracellular ligand-mediated stimuli to the nucleolus. The general mechanism for transduction can be described as follows: upon recognition of the external stimuli, different receptors (tyrosine kinases, RTK's, G-protein-coupled receptors, etc.) hetero-dimerize and auto-phosphorylate each other. In the case of the common RTK receptor, additional adaptor proteins called Grb2 or Shc bind to one of its domains called SH2. The binding promotes the recruitment of GEF's to the membrane, which, in turn, will activate the Ras protein by stimulating the exchange of GDP to GTP. Active Ras can now interact with its multiple downstream targets generally called effectors (from more than 10 known effectors of Ras, the most representative ones within the framework of this thesis, are Raf-RBD, Ral-GDS, PI3K and Byr2 [32, 33]). Each effector will activate specific kinase proteins that will start a series of kinase chain reactions through which the signal is relayed down, reaching the cellular nucleus and culminating with the transcription of genes that will confer an appropriate response to the original stimuli. One of the most common signalling cascades of Ras is the

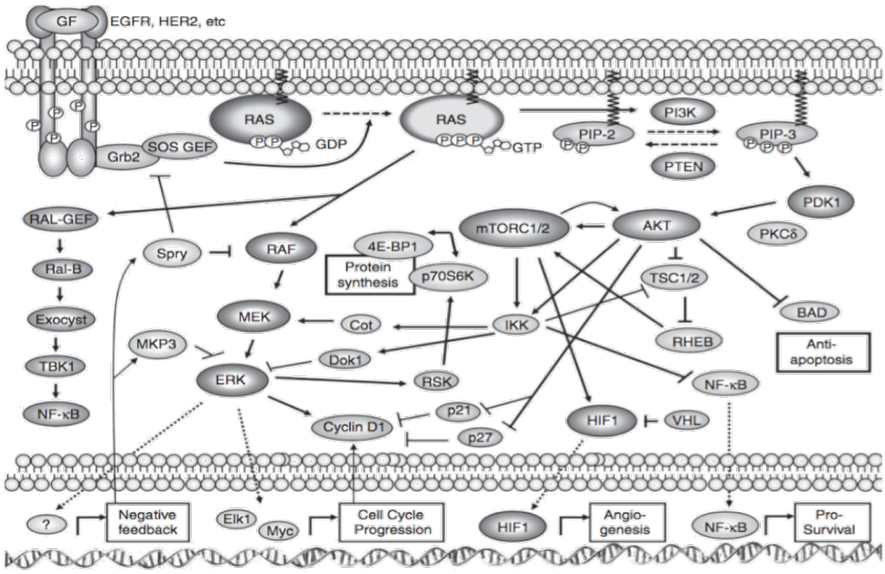

Figure 1.4. Schematics of the main Ras signaling pathways. From more than 10 known signaling cascades under direct control of Ras, the MAPK (Ras/Raf/MEK/ERK) is the best understood. For sake of simplicity the full names for the abbreviations in the scheme are not given here. The reader is submitted to the original review [34] from where this scheme was adapted.

mitogen-activated protein kinase (MAPK) pathway that uses the protein Raf as effector and two different MAP kinases: MEK and ERK.

Phosphorylated ERK translocates to the nucleus and triggers gene transcription [34]. The signalling cascade is eventually inactivated by negative feedback from the nucleus after gene transcription, which leads to the hydrolysis of γ-phosphate of GTP-bound Ras, catalysed by GAP's, as the protein returns to the original (inactive) GDP-bound state [35].

1.1.2 Interaction with GEF's: the 'Switch On' Reaction

The direct consequence of the picomolar affinity between Ras and GDP/GTP is that nucleotide dissociation is not compatible with the time scale of most cellular processes. The activation of Ras needs to be catalysed by GEF's, a large class of multidomain enzymes capable of accelerating the exchange reaction by 3 to 4 orders of magnitude [36, 37]. The GEF-catalysed reaction is an intricate multistep process whose kinetics have been described in detail only for the HRas•Cdc25 complex. The affinity of binding between the two proteins (K_D) was found to be 4.6 nM and the maximal acceleration by Cdc25 of the rate of nucleotide dissociation was estimated to be more than 10^5-fold [36]. In general, Ras has a similar affinity for both, GDP and GTP, and GEF's do not favour the re-binding of either nucleotide. The direction of the reaction is dictated instead by the concentrations of the free nucleotides in the cell at a given time. Since normally the GTP concentration is 10-fold higher than GDP, the resulting product of the catalytic reaction is Ras loaded with GTP [38].

GEF's can be grouped in two different classes. The first one comprises the RasGEF's which are activated by second messengers like Ca^{2+}, calmodulin or diacylglycerol [39]. The second class is represented by the son-of-sevenless (SOS). Human SOS1 is a very large multiprotein of ~1330 residues (152.4 kDa) containing at least 4 different domains, from which the catalytic domain (aa 551-1050, abbreviated as SOS^{cat}, 36 kDa) is the one involved in Ras binding and catalysis [40, 41]. SOS^{cat} comprises the Ras exchanger motif (Rem, aa 551-750), the Cdc25 motif (aa 751-1050) and a C-terminal region (aa 1051-1333) that provides a docking site for the adaptor protein Grb2 (Figure 1.4) [42]. Previous investigations have shown that the Rem motif is responsible for the stability of the whole catalytic domain and that the Cdc25 motif is necessary and sufficient for nucleotide exchange [36, 43]. The first crystal structure of the nucleotide free HRas•SOS^{cat} complex was solved in 1998 [44] and shows Ras bonded to the Cdc25 motif, with no direct contacts to Rem (Figure 1.5A). The primary contact regions are the P-loop, helix α_1 and the switch regions. The most significant conformational change in HRas is due to the insertion of an

helical hairpin composed of helices α_H and α_I from Cdc25 that penetrates through the catalytic pocket and projects switch 1 away from the nucleotide binding site (Figure 1.5B). The hairpin introduces in the nucleotide binding site a hydrophobic side chain (Leu938), which blocks magnesium binding by interacting with Ser17 from Ras, and an acidic side chain (Glu942), which overlaps with the site where the α-phosphate of the nucleotide would otherwise be bound. At the same time, switch 2 is held very tightly by SOS and constitutes the heart of the interface between the two proteins. A cluster of three residues with hydrophobic side chains from Ras, Tyr64, Met67 and Tyr71, is buried into the hydrophobic core of SOS. Surrounding this hydrophobic triad is an array of polar interactions between the two proteins making almost all side chains of switch 2 coordinated to SOS (for example, Ala59 occupies the previous position of Mg^{2+} ion and the Glu62 side chain interacts with both, the NH group from Gly60 and the side chain of Lys16). As consequence, the conformation of switch 2 is very well defined in the complex, contrary to the typical poorly ordered conformation in the nucleotide-bound forms of Ras. In summary, switch 1 is pushed away from its normal position whereas switch 2 is pulled towards the nucleotide binding site [31, 44]. From these structural insights, the mechanism of nucleotide association/ dissociation was proposed to be as follows: in the dissociation process, the phosphate moieties of GDP are released first after binding of SOS, and then the base and ribose moieties are released. In contrast, the association process takes place by binding first the base and the ribose moieties of GTP and only then the phosphate groups. Significant conformational changes of the switch regions are thought to occur to rebuild the

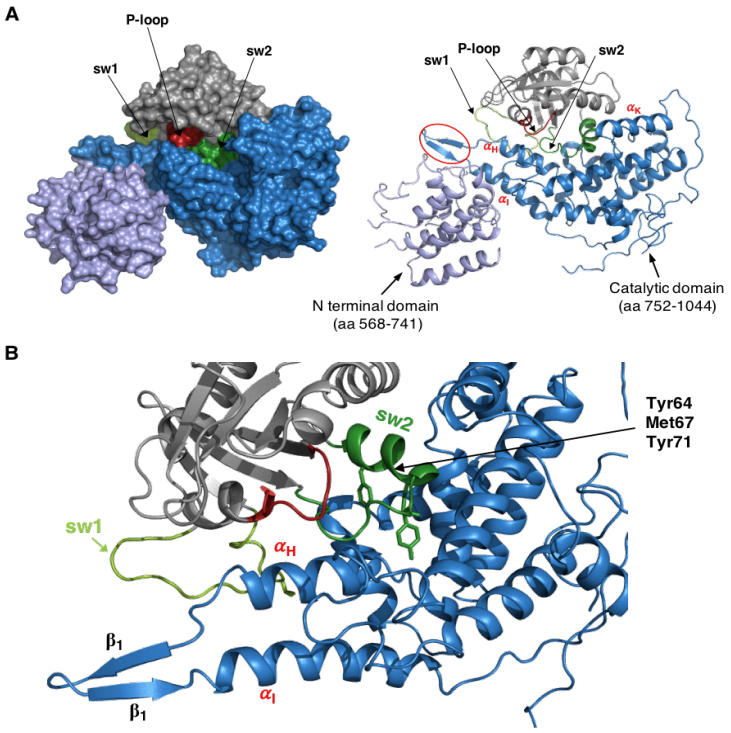

Figure 1.5. Structural insights on the Ras•SOS complex (pdb: 1bkd). **A.** Surface and cartoon representation of nucleotide free Ras (coloured in grey) bound to the catalytic domain of SOS (coloured in blue). The Rem, N-terminal motif (coloured in light purple) is also shown. The hairpin formed by the helixes α_H and α_I from SOS is indicated. **B.** Details of the binding interface between the two proteins. Switch 2 is 'clamped' by SOS through interaction with hydrophobic residues and switch 1 is projected away from the vicinity of the nucleotide upon insertion of the helical hairpin. Adapted from [44].

binding sites for the phosphate and Mg^{2+} and subsequently to displace SOS [31, 37].
It is worth mention that a new binding site of Ras to SOS^{cat} was found in 2003. This site is located between the Rem and the Cdc25 motifs and is in a distal position relative to the binding site on the Cdc25 motif [45]. Interestingly, the solved crystal structure is of a ternary complex HRas•GppNHp•SOS^{cat}:Ras(nucleotide-free) (pdb: 1nvw), where the nucleotide-bound Ras is located in the newly discovered distal site and the nucleotide-free Ras is located at the 'usual' place, at the Cdc25 domain. The implications of a second biding site are thought to be related to a mechanism of feedback activation of SOS: the binding at the distal site has a profound influence in the conformation of the Rem motif, resulting in its rotation by about 10° relative to Cdc25. In turn, this rotation echoes the interactions between the helical hairpin and switch 1 of nucleotide-free Ras in the active site [45, 46].

1.1.3 Interaction with Effectors

In the active state, GTP-bound Ras relays signals to the downstream targets by direct association with different proteins generally called "effectors". There are more than 10 different known families of effectors capable of interacting with the Ras subfamily alone and many more that bind to other GTPases [47-49]. All known effectors differ in their function and surprisingly show no homology in their structure despite having a common region of ~100 amino acids usually named 'Ras binding domain' (RBD) that was found to be necessary and sufficient for Ras recognition. RBD binds preferentially Ras-GTP with typical dissociation constants between 0.01 and 3 μM [48, 50, 51] in contrast with Ras-GDP, whose apparent K_D values are in the upper μM range, corresponding to an averaged 1000-fold decreased affinity [52]. The most representative and well-studied effector of Ras is the Raf protein (from rapid accelerated fibrosarcoma), expressed in all mammals as three paralogues (ARaf, BRaf and CRaf. CRaf is sometimes called Raf1 and is the variant used in the work presented in this thesis) [35]. Raf is a 72 kDa serine-threonine kinase involved in the signalling of the MAPK pathway composed of three conserved main regions (Figure 1.6): the RBD located in its N-terminal segment (aa 55-132, 9.4 kDa), presenting a ubiquitin-like architecture ($\beta\beta\alpha\beta\beta\alpha\beta$), followed by a C-kinase homologous (C1 or CRD) domain (aa 133-184), which is a specialized zinc finger, rich in cysteines and stabilized by two zinc ions. Both domains (RBD and CRD) act as a single unit to negatively regulate the activity of the protein [53]. They are labelled together as belonging to the CR1 region (conserved region 1). Between this auto inhibitory CR1 region and the catalytic domain (CR3) there is a hinge region, named CR2 (aa 185-349), whose sequence is rich in serine amino acids despite being poorly conserved across related Raf genes. CR2 acts as a natural hinge between the

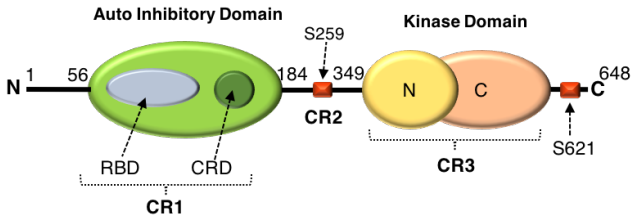

Figure 1.6. General architecture of effector proteins representing the auto inhibitory domain (CR1), where Ras binds at the RBD site, the hinge region (CR2), and the kinase, catalytic, domain (CR3).

rigid auto inhibitory (CR1) and catalytic (CR3) domains enabling complex movements and profound conformational rearrangements within the molecule [54]. This hinge contains a small island of amino acids that are responsible for recognition of a protein named 14-3-3 when a critical Ser259 (in CRaf) becomes phosphorylated. The C-terminal part of Raf, labelled as CR3 (aa 350-648), holds the kinase domain and is responsible for its catalytic activity [55]. In many biophysical investigations it is a common procedure to express the RBD domain of Raf alone and use it in subsequent kinetic and/or thermodynamic Ras-binding experiments. The RBD's of different effectors share very little homology: comparative studies show that no particular sequence pattern is recognizable between Raf, AF6, Ral-GDS or Ral-GEF, which envisages the idea that the C1 domain is a structural module that appears to have been "shuffled around" in the course of evolution [56, 57]. Rather interestingly, their non-similarity constitutes the basis for the description of Ras as a master switch of the cell, capable of adapting its surface and interacting with a such wide conformational variety of effectors [58]. Despite of the observed differences, the topology of RBD is identical for many effectors [59]. The first structural insights for the interaction between Ras and Raf were discovered in 1996 by Nassar and co-workers, who solved a 2.0 Å crystal structure of the complex between the HRas homologue Rap1A bound to GppNHp and Raf-RBD (pdb: 1gua) [60]. Rap1A is highly homologous to Ras with more than 57% similarity and shares the same effector interface. The complex revealed that Raf-RBD interacts mainly with switch 1, in good agreement with previous experiments indicating that specific mutations in HRas switch 1 (Y32F, P34S/G T35V, E37A and D38A/N, among others) significantly impaired the association to Raf-RBD [61, 62]. The binding interface is thus formed by the antiparallel co-alignment of RBD β_2 and Rap1A β_2 within the switch 1 region. Detailed analysis showed that the crucial contacts stem from strong/weak salt bridges formed between $Rap1A^{E31}$-Raf^{K84}, $Rap1A^{D33}$-$Raf^{K84/R73}$, $Rap1A^{E37}$-$Raf^{R59/R67}$ and $Rap1A^{D38}$-Raf^{R89}. Subsequent molecular dynamics (MD) investigations using a model structure of $HRas^{D33A}$•Mg^{2+}•GTP•Raf-RBD showed that Asp33 establishes one of the strongest salt bridges at the interaction surface and that a mutation at this position severely impairs the binding between the two proteins [63].

The first crystal structure of $HRas^{WT}$•Mg^{2+}•GppNHp bound to Raf-RBD was solved only in

2015 (pdb: 4g0n) [64] and shows the same general features observed for the Rap1A-Raf complex at the binding interface involving switch 1. However, this new structure shows evidence that other regions of Ras are also involved. Particularly, it was found that Gln61, located at switch 2 has a global impact on the conformational dynamics of both Ras and Raf during complex formation. This residue interacts with a bridging water (w189), which in turn interacts with the side chain of Tyr32, the γ-phosphate and the catalytic water (w175). More importantly, the same residue was found to be connected to Leu101 and Lys109, both located in Raf at a distal position relative to Gln61. MD simulations have shown that the connection is through a long-range communication pathway, already previously identified in the Raps-Raf-RBD complex [65, 66] that foretells the occurrence of an allosteric mechanism for the Ras-Raf interaction. These findings are also in agreement with experimental evidence presented in 2010 by our group for the involvement of Gln61 in the complex formation [67].

The Ras-Raf complex is highly dynamic, exhibiting both fast association and dissociation [68]. The association is a two step mechanism governed by an hyperbolic dependence of the observed rate constants on increasing concentrations of Raf [69]. The binding initiates with a formation of a loosely bound encounter complex that rapidly isomerises into a tightly bound complex. An overall affinity of 0.05 μM, a k_{on}= 35.5 μM^{-1} s^{-1} and a k_{off}= 1.7 s^{-1} was derived for the effector in complex with Ras^{WT}•Mg^{2+}•GppNHp [51]. Due to the fact that the Ras-Raf interface is formed by electrostatic interactions, it was proposed that the formation of the initial low-affinity complex is mainly driven by electrostatics and allows Ras to discriminate binding partners very quickly [70], before isomerizing to the higher affinity complex.

The determination of the crystal structure of full-length Raf proteins has failed so far due to the heterogeneity of the purified Raf proteins caused by phosphorylation at numerous regulatory sites [71]. The special structure of the multidomain complex is, up to the present day, a matter of speculation. Frequent Raf phosphorylation can also happen during the expression of the recombinant protein in bacterial systems. For such reason, a ^{31}P NMR spectra of Raf alone is normally recorded before any ^{31}P NMR titration experiments involving Ras or other GTPases.

1.1.4 Interaction with GAP's: the 'Switch Off' Reaction

Ras is not a GTPase on its own right. The experimentally measured rate of hydrolysis (defined as k_{cat}) is $4.7x10^{-4}$ s^{-1} at 310 K [31]. GTPase activating proteins, or GAP's, effectively accelerate this reaction by at least 5 orders of magnitude, with a k_{cat}= 19 s^{-1} measured at 298 K [72]. Both, the intrinsic and the GAP-accelerated hydrolysis, are complex phosphoryl-transfer reactions still not very well understood. At the basis of the mechanism is the transfer of the γ-phosphoryl group to a water molecule responsible for the nucleophilic attack. During the process the electrophilicity of the γ-phosphate is enhanced by the Mg^{2+} ion that acts as a Lewis acid, leading to a decrease in the dipole-moment of the P-O bond. The overall mechanism is very much like a typical S_N2 reaction at a carbon: the nucleophilic water approaches the electrophilic centre from the backside position, opposite to the leaving group. As the pair approaches, the geometry at the phosphate centre changes from tetrahedral to trigonal bipyramidal at the transition state. As the P_γ-O-P_β bond gets longer, the geometry around the leaving group returns to its original tetrahedral state, but now with an inverted stereochemical configuration [73-75]. The matter of disagreement is about the nature of the phosphoryl transfer, which might be associative involving a metaphosphate-like PO_3^{2-}, where bond breaking of the β,γ-anhydride linkage takes place when the nucleophile approaches, or dissociative, where bond making to the nucleophile takes place before bond breaking (Figure 1.7A) [76, 77]. The difference between the intrinsic hydrolysis and the GAP-assisted one is in the substrate used to activate the catalytic water molecule involved in the nucleophilic attack: the intrinsic reaction relies in a substrate-assisted mechanism, in which the γ-phosphate itself acts as a base and activates the nucleophilic water (w189), which in turn donates a proton to the O3 atom of the γ-phosphate. This primary protonation changes the electrostatic environment and promotes a ~1.5 Å movement of the catalytic water (w175) coordinated to Gln61 towards the γ-phosphorous atom. In the new position, this water can form an H-bond with the primary hydroxyl ion and exchange a proton with it, thus regenerating the original w189, or could contact directly the γ-phosphorous atom, forming a secondary hydroxyl ion. In either case the result is the formation of the transition state and concomitant hydrolysis of the γ-phosphate (Figure 1.7B, left side) [23, 72, 78]. The influence of GAP in this process has been a matter of discussion for a long time. One assumption is that GAP is confined to the catalysis of a rate-limiting isomerization step in Ras, which becomes activated only through its action but Ras is, on itself, an efficient GTPase [79]. A second assumption is that GAP is directly involved in the hydrolysis process, providing crucial residues and stabilizing the transition state.

The true role of GAP is still unknown but it was glimpsed in the 90ies by the use of metal-fluorides such as AlF_3 [80, 81], or more recently, MgF_3^- [82], both capable of mimicking the transition state of the phosphor-transfer reaction. A representative structure for the Ras-GAP interaction is the one solved for HRas•Mg^{2+}•GDP•AlF_3•GAP-334 in 1997 by Alfred Wittinghofer and his team (pdb: 1wq1) [83] and seems to indicate that GAP has an active role in the process by providing a crucial positive charge through the insertion of an arginine side chain (Arg789), often called 'arginine finger' into the catalytic site of Ras, thus neutralizing the developing negative charges during the transition state (Figure 1.7B, right side) [84-86]. Arg789 coordinates to the O3 atom of γ-phosphate and to the β,γ-bridging oxygen. Its carbonyl oxygen is H-bonded to the side chain NH of Ras Gln61, which also forms H-bonds to the attacking water (w175) along with Thr35. The engagement of Arg789 stabilizes the intrinsically mobile switch 2 region and works like a 'trigger of a gun' by acting on Gln61, positioning it correctly in space and allowing it to extract an hydrogen atom from the catalytic water, which can in turn, act as the nucleophilic substrate for the hydrolytic reaction [87]. Additional biochemical studies showed that the interplay between Arg789 and Gln61 is crucial, as mutants of Gln61 show severely impaired GAP-mediated hydrolysis [88, 89]. It is worth mention that the complete mechanism is far from being fully understood. In fact,

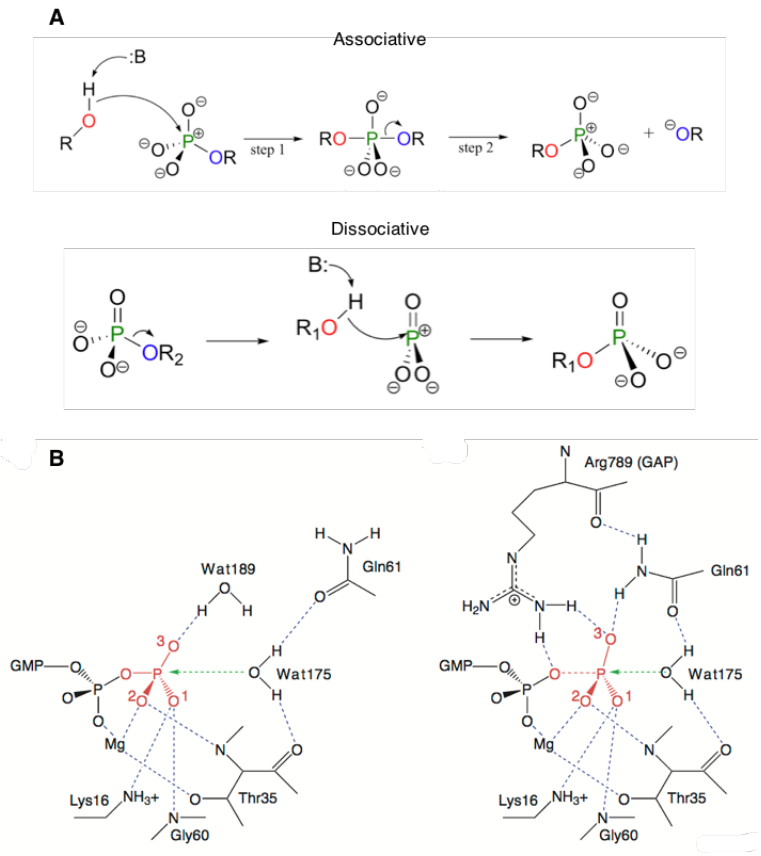

Figure 1.7. Molecular mechanism of the phosphoryl transfer reaction. **A.** There are two possible reaction paths through which the phosphoryl transfer reaction can happen, depending if the nucleophile attacks before (associative) or after (dissociative) P-O bond breaking **B.** Comparison of Ras catalytic environment for the intrinsic (left) and GAP-activated (right) GTP hydrolysis. In the first case, w189 makes two H-bonds, one with the O3 of γ-phosphate and another with w175, the latter being held in place by Gln61 and Thr35. The second case represents the proposed transition sate for the complex Ras•Mg^{2+}•GDP•AlF_3•GAP-334. No H_2O molecule equivalent to w189 is described in this structure (pdb: 1wq1). Instead, Arg789 acts as an arginine finger that 'pulls the trigger' in the reaction by forming two H-bonds, one with the O3 atom from γ-phosphate and another with the bridging O atom between β- and γ-phosphates. Adapted from [23].

many Ras-like proteins lack the arginine finger during the GAP-assisted reaction. RanGAP's use a tyrosine instead, and RapGAP's use a tandem switch 1 Tyr and an Asn from GAP [90, 91].

1.1.5 Differential Dynamics of the Switch Mechanism

The multitude of crystal structures of the G domain tend to confer a misleading picture that the switch regions are preponderantly fixed in space, either in a "closed" conformation, as in GTP-bound Ras or when bound to effectors, or in an "open" conformation, as in GDP-bound Ras, that disfavours effector binding. However, this is an inadequate or at least an incomplete picture of the overall dynamics. In fact, 3D NMR spectroscopy has shown that the switch regions of HRas•Mg^{2+}•GDP are disordered and fluctuate in the nanosecond time scale (Figure 1.8A) [92]. The topology of the fold of the solution structure (pdb: 1crp) is identical to the crystal structure (pdb: 4q21 [30]), but the segments comprising switch 2 are highly flexible (contrary to switch 1 that seems to be moderately restrained), suggesting the presence of multiple conformations especially in switch 2 which provide an unprecedented insight into the activation of the GTPase activity by GAP's: when GAP binds to Ras, the mobility of switch 2 is restricted and the catalytically active conformation becomes stabilized. In its absence, the population of the active conformation is much lower due to the continuous conformational fluctuations, hence the slower intrinsic GTP hydrolysis [28, 93]. Attempts have been made to determine the solution structure of *wild type* GppNHp-bound Ras but due to chemical exchange broadening processes, most of the P-loop and switch regions are undetectable [94]. However, solution structures of the mutant Ras^{T35S}•Mg^{2+}•GppNHp in which the slow conformational exchange is eradicated have been recently obtained and show that contrary to GDP-bound Ras, switch 1 displays a wide range of conformational variety in contrast with the moderate changes of the switch 2 and P-loop (Figure 1.8B) [95]. The dynamics of Ras^{T35S}•GppNHp are therefore fundamentally different from Ras^{WT}•GDP,

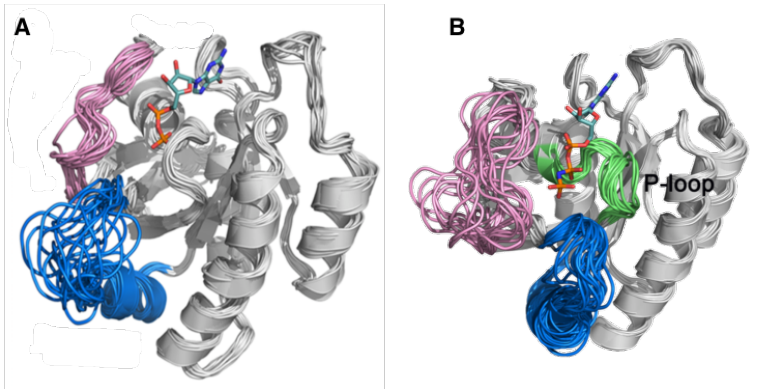

Figure 1.8. Dynamics of the switch regions. **A.** Cartoon representation of the backbone superposition of the first 20 lowest-energy NMR structures of GDP-bound HRas (pdb: 1crp). switch 1 and switch 2 are coloured in pink and blue, respectively. **B.** Similar representation for the NMR structure of $HRas^{T35S}$•Mg^{2+}•GppNHp (pdb: 2lcf). Note the different mobility of switch 1 between the two structures. Adapted from [28].

an observation that could not be easily done if considering only the 'static' crystal structures [96]. Frequently, the switch regions are also found to be disordered in the crystal (i.e. they do not show appreciable electron density). In some cases, where well-defined electron density can be found, they often pack against neighbouring molecules. Such situation prompts a careful examination of the structure: if a specific conformation of an intrinsically disordered region is stabilized just because of packing forces, it should be regarded as a crystallization artefact and not as a true structural feature. This effect is evidenced for example by comparing two available structures of Ras•GDP: in the first one (pdb: 4q21, [30]) there are extensive contacts with the neighbouring molecules and both switch regions are well defined. In the second one (pdb: 1ioz, [97]) switch 2 is located next to a wide solvent channel and shows no density. The difference makes evident that crystallization conditions and the crystal environment have an influence on the study of mobile regions. The equilibrium between the different states of the switch conformations in the GTP form is a delicate balance, fine-tuned to transiently stabilize the active Ras sufficiently to allow activation of downstream effectors without switching it off again via intrinsic GTP hydrolysis, while allowing stabilization of the switch regions into the catalytically competent conformation by the GAP proteins [98, 99].

1.1.6 Consequences of Ras Mutations

Specific point-mutations at one of three amino acid positions, Gly12, Gly13 and Gln61, are able to turn Ras into a potent oncogenic protein, rendering it a driving force in the initiation and proliferation of a significant set of human cancers [100]. A survey from the COSMIC database shows that mutated Ras is present in more than 30% of all human tumours [101, 102], with an incidence level of more than 95% in pancreas carcinomas [103], 65% in colon cancer [104], 46% in endometrial carcinomas, among many others [105]. The structural mechanisms that potentiate oncogenic activity are well known. Glycine is the smallest amino acid. Introducing any other side chain (even the small valine) in the confined catalytic space leads to a steric clash with both Gln61 from Ras and the arginine finger from GAP, disturbing the necessary spatial molecular arrangements for the GAP-assisted hydrolysis [83]. This steric hindrance renders the G12 mutants insensitive to GAP, resulting in an impaired GTP hydrolysis. The protein becomes then permanently locked in the active, GTP-bound state, relaying permanent signals its downstream targets that culminate with the permanent activation of specific signalling cascades such as MAPK, sustaining permanent proliferation and differentiation [102]. The most frequently mutated isoform is KRas (86%), followed by NRas (11%) and HRas (3%). The preponderance of KRas and the necessity to

develop of isoform specific inhibitors is one of the reasons that led to the revival of the field in the recent years [21, 106]. The most prevalent mutations at position 12 are G12D (36%), G12V (23%), G12C (14%), G13D (7%) and Q61H (0.6%) [107]. Nevertheless, it was shown that except for proline, any amino acid substitution at position 12 renders Ras oncogenic [100, 108]. It is notwithstanding that any G12 mutation is in general tolerated in the ground state of the Ras-GAP complex, meaning that the binding to GAP can still take place with equal or only slightly decreased affinity compared to Ras^{WT}. However, the transition state cannot be formed due to the above mentioned steric hindrances [109].

1.1.7 Partial Loss-of-Function Mutants

All Ras-driven cancers are a consequence of the constitutive activation of this protein. For such reason the oncogenic mutants are also sometimes called 'gain-of-function'. However not all Ras mutations are gain-of-function. Particular relevance is given in this thesis to the so-called 'partial-loss-of-function' mutants, which are capable of interacting only with a specific subset of known Ras effectors [61, 110]. A common example is Ras^{T35S}: Thr35 is a totally conserved residue in switch 1 (Figure 1.2) involved in the coordination to the Mg^{2+} ion and to the γ-phosphate. Mutation to serine or alanine impairs the association of Ras with the effectors Byr and RalGDS but not with Raf. The basis for such selection lies on the fact that Thr35 interacts with the residue Lys52 of both RalGDS and Byr2 but it does not interact with Raf [111, 112]. Another example is Ras^{E37G} (binds to RalGDS but not to Raf, [113]) and the double mutant $Ras^{G12V/T35S}$. These differences are a preposition for the key role that specific residues play in effector selectivity when Ras is constrained by a preferred interaction site with respect to the membrane. Kinetic and stopped-flow analysis showed that the interaction of Ras^{T35S} with Raf-RBD still follows a two-step mechanism, like the *wild type* protein. However, the affinity to Raf is lowered more than 60-fold [51]. On the other hand, similar experiments done with Ras^{T35A} showed that Raf association is a one step mechanism and has a linear dependence on the concentration of Raf. The mutant can still bind and form the weak complex but isomerization to the high affinity complex is impossible.

1.1.8 Probing the Bound Nucleotide: ^{31}P NMR Spectroscopy

The main instrumental method used within the work conducted in this thesis is ^{31}P NMR spectroscopy. Phosphorous-31 is an active nucleus with a spin quantum number of I=1/2 and a natural abundance of 100%. ^{31}P NMR is in general a very attractive tool for the study of GNBP's or any other biological molecular system containing phosphate groups. The conformational modifications during the operation of the Ras molecular switch are

accompanied by structural changes of the regions directly involved in nucleotide binding, which can be followed and quantified by modifications observed in the ^{31}P NMR spectra such as chemical shift values, linewidths or relaxation characteristics. The peak areas can be used as a direct measure of the relative populations of conformational states. The major drawbacks of the method, however, are the high amount of protein needed (in the 0.5-1.5 mM range) and the rather long acquisition times due to the low magnetic susceptibility of this nucleus (only 6.64% of ^{1}H) [114, 115].

^{31}P NMR performed on Ras bound either to its natural nucleotide, GTP, or to non-hydrolysable ones such as GppNHp at 310 K originates very simple spectra containing three single lines labelled as α, β and γ, one for each phosphate group. However, at 278 K the situation is different: two distinct conformational sates (named as 1 and 2) represented by different chemical shifts are obtained. These conformational states are actually only defined when any guanosine triphosphate is bound (T) and may be different when guanosine diphosphate is bound (D). To this respect, they are written within the conventions of this thesis as states 1(T) and 2(T) or 1(D) and 2(D), whenever the nucleotide ligand is concerned [67]. These states are in a dynamic equilibrium with exchange rates in the millisecond time scale at low temperature. The relative population of 2(T) over 1(T) varies among different Ras isoforms and mutants as it will be demonstrated in this thesis. For HRas^{WT}(1-189)•Mg^{2+}•GppNHp state 2(T) was found to be 1.9 times more populated than sate 1(T) [51, 116, 117]. At high temperatures (310 K), the exchange process obeys to the fast condition and the two split signals of each phosphate coalesce into one, whose chemical shift value is located at the population averaged position. The coexistence of the two conformational states was also revealed by solid-state ^{31}P NMR performed on Ras crystals [118, 119] and precipitated Ras [120]. Figure 1.9 shows a typical ^{31}P NMR spectrum of HRas^{WT}(1-189)•Mg^{2+}•GppNHp (spectrum a). Upon addition of Raf-RBD (spectrum d), s

tate 1(T) disappears and state 2(T) becomes stabilised. For such reason this state is also described as the effector binding state (i.e. it corresponds to the population of Ras whose conformation is

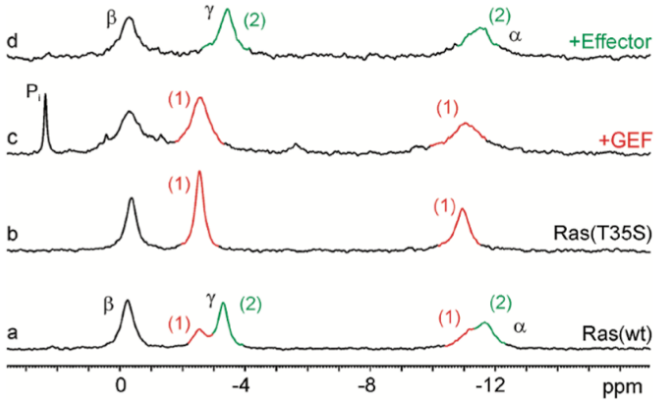

Figure 1.9. ^{31}P NMR spectroscopy on HRas•Mg^{2+}•GppNHp proteins. The spectrum of Ras *wild type* is shown (a), together with the state 1(T) mutant Ras^{T35S} (b). The protein complexes of Ras^{WT}•SOS^{cat} and Ras^{WT}•Raf-RBD are shown in (c) and (d), respectively. Taken from [125].

selectively recognised by effectors) [117, 121, 122]. In contrast, state 1(T) shows more than 20-fold lower affinity towards effectors, as shown by ^{31}P NMR, calorimetric and fluorescence-based studies [123, 124]. Additional experiments demonstrated that it is selectively recognized by GEF proteins, as revealed by strong line broadening of its resonance line upon titration with SOS (spectrum c). For this reason, state 1(T) is sometimes referred as the weak effector-binding or the GEF interacting state [125].

1.2 Drugging an Undruggable Protein

The frequency of Ras mutations in three of the four most lethal cancers (lung, colon and pancreatic) has spurred an intense interest in developing inhibitors in the form of small molecules capable of acting directly or indirectly in the oncogenic protein and quell its permanent activation. This necessity was further increased in the 90ies when it was discovered that alongside with its involvement in cancer, some KRas mutations in the human germinative line can cause severe developmental diseases generally named Rasophathies [126] and that result from direct Ras point mutations in different locations (some common positions are 12, 13, 61, 14, 22, 26, 34,50, 58, 60, 152, 153, 156, all being gain-of-function) [127], leading to conditions known as *Noonan syndrome* (NS) [128], *Costello syndrome* (CS) [129], cardio-facio-cutaneous syndrome (CFC) [130], among others [131, 132].

A tremendous effort was indeed devoted to the endeavour of finding effective inhibitors over the last half century, with some ups, downs, and many frustrations along the way, dictated by the fact this globular protein has no direct or obvious pockets where small molecules can bind. For a long time Ras was considered to be undruggable [133]. However, since 2012 a renaissance on the topic is taking place and the scientific research has never been as active as nowadays, either at academic institutions or pharmaceutical companies. A very concise description of the most common strategies used to turn off the aberrant molecular switch will be presented in the following section. For an in-depth coverage of this topic the reader is referred to a variety of recent and excellent review publications [17, 133-137].

1.2.1 General Strategies

Inhibitors of posttranslational modifications

As stated in section 1.1, these modifications are crucial for the intracellular trafficking and attachment of Ras to the plasma membrane. The search of compounds that block its lipidation at the C-terminus, catalysed by farnesyl transferase, was intensively pursued in

the last century through the creation of specific inhibitors for this enzyme (generally called FTI's). Three of the most potent ones were *Lonafarnib* [138], *Tipifarnib* [139] and *Salirasib* [140]. All have shown to be effective in HRas-driven cancer models in the pre-clinical setting but ultimately failed in advanced human clinical trials against KRas and showed a serious toxicity to normal tissues [141, 142]. The scientific interest for this approach was further decreased in 1995 when it was found that cancer cells have mechanisms to bypass lipidation on KRas and NRas, contributing to acquired resistance to this class of drugs [143].

Inhibitors for the interaction with GEF's

Several inhibitors of GDP-to-GTP exchange GEF-catalysed reaction have been reported. A peptide based on the α_H helix of SOS1 was found to bind Ras in a cleft near the switch regions with a K_D= 158 μM. Although not very potent, further optimization of the helical peptide is currently underway [144].

In 2012 two independent groups reported several KRas4b binders that were discovered using fragment-based screening by NMR and have a similar mode of action [18, 145]: they bind close to the α_2 helix and β_1 sheet in a pocket that is not readily observed in the ligand-free structure of the protein. The pocket seems to be formed only upon binding of the compounds by the movement of Tyr71 and Met67 out of the way, creating a primary and a secondary binding cleft. All compounds tested bind to $KRas^{G12D}$•Mg^{2+}•GDP with K_D values in the low hundred μM range, and although not very potent, they revealed to be promising candidates for further lead optimization. ^{31}P NMR spectroscopic studies were conducted in the framework of this thesis with some of these drugs and are presented in detail in section 3.2 of the results.

Inhibitors for the interaction with effectors

The direct inhibition of the interaction with effectors is a widely used strategy to prevent aberrant signalling in oncogenic Ras. Within this group it is worth mentioning the nonsteroidal anti-inflammatory drug called *Sulindac sulphide* and derivatives [146] which were found to bind Ras at the Raf binding site and have a median inhibitory concentration (IC) of 30 μM [147, 148]. Due to the fact that both switch regions are not visible in [^{1}H-^{15}N]-HSQC NMR experiments, the exact binding place of this class of drugs is unknown but thought to be close to switch 1 [147]. ^{31}P NMR titration studies involving this drug are presented in section 3.2.12 of the results.

1.2.2 Recent Breakthroughs

A major breakthrough in the direct targeting of mutated Ras was achieved five years ago when for the first time, small inhibitors that bind specifically and irreversibly to $KRas^{G12C}$ were developed [149]. These compounds rely on the mutated cysteine residue for selective binding and allosterically alter the preference of $KRas^{G12C}$ to favour GDP over GTP, impairing at the same time the binding to Raf-RBD. The feat was achieved by attaching different electrophiles to the β-phosphate of GTP that can covalently bind to Cys12 [150]. Further structural investigations by X-ray crystallography and affinity measurements showed that upon binding of the drug, the switch regions assume an open, inactive conformation, which is incompatible with effector binding [151]. The compounds are especially relevant in the treatment of lung cancer as the G12C mutation is the most prevalent one, occurring in 7% of these tumours [101]. At the same time, they provide a useful conceptual framework to develop other compounds that could selectively target other common Ras mutations such as G12D and G12V.

Another emerging area, although not in the scope of direct Ras inhibition, is the development of ERK and Raf dimer inhibitors. The dimerization of ERK, triggered by the activation of the MAPK pathway, is necessary for its extracellular function. Based on this observation, in 2015 a water-soluble small compound named DEL-22379 was identified to be capable of blocking the dimerization process and consequently to inhibit growth and induced-apoptosis in cultured Ras mutant cancer cell lines [152]. At the same time, it was discovered that dimerization of Raf is also required for normal Ras-dependent Raf activation. On this basis a small peptide named *Vemurafenib* was developed and shown to be efficient in the inhibition of Raf dimers [153]. Although this drug has limited efficacy against tumours that possess constitutive Ras-independent, Raf-activating dimers [154], it already has received FDA approval and shows a promising future.

1.2.3 Allosteric Inhibition: the Case of Zn^{2+}-cyclen

^{31}P NMR spectroscopic investigations revealed the existence of a dynamic equilibrium between at least two different conformational states in Ras•Mg^{2+}•GppNHp named 1(T) and 2(T), as mentioned in section 1.1.7. Based on these findings it was hypothesised that the use of small compounds capable of shifting the equilibrium towards state 1(T) would represent a novel approach in the antitumoural therapy against Ras. This hypothesises was tested using the small drug Zn^{2+}-cyclen, developed at our department and found to be capable of recognizing and selectively stabilising state 1(T), impairing therefore Ras-Raf association [155, 156]. Structural NMR experiments revealed that the compound binds in

two different locations in the surface of the protein, one at the nucleotide binding site, near the γ-phosphate and the other at the distal position, close to the C-terminus, interacting directly with His166. X-ray crystallography was also performed for the protein-drug complex $HRas^{WT}$•Mg^{2+}•GppNHp•Zn^{2+}-cyclen and allowed its direct visualization bound at His166 (Figure 1.10) but not at the second binding site, close to the nucleotide. Analysis of the crystal packing showed that the proteins in the unit cell were in contact by means of the effector loops, lying face-to-face next to each other. The concentration of Zn^{2+}-cyclen used (25mM) was too low to overcome the crystal forces that held the effector loop shut [157, 158]. Due to its ability to selectively recognise and bind a specific conformational state, Zn^{2+}-cyclen can be viewed as a parental drug and a lead compound that can be used for the development of novel allosteric Ras inhibitors, capable of selectively recognising rare conformational and functional states of the protein.

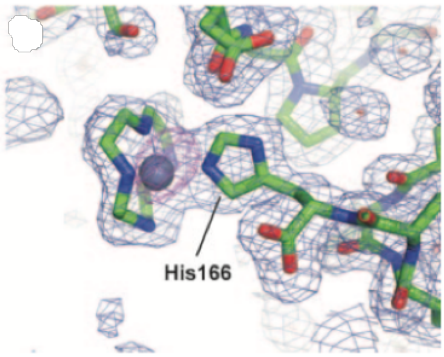

Figure 1.10. Electron density map showing the coordination of Zn^{2+}-cyclen at the C-terminus of Ras^{WT} (pdb: 3l8y). Adapted from [157].

1.3 High Pressure Technologies in the Study of Protein Conformation and Dynamics

Proteins exist in solution in a dynamic equilibrium as an *ensemble* of conformers; they are multiconformational entities designed by natural selection not just for the ground or native sate but also for higher energy, non-native states involved in function, folding and unfolding events. Multiple conformations are universal rather than exceptional [159].

The conformational landscape of a protein can be represented by the folding funnel model (Figure 1.11A) [160] upon which the protein energy landscape can also be drawn [161] and allows one to correlate conformation with function: the lowest energy state is depicted as a global minimum and folding intermediates as local minima that can widely differ in depth and shape. High energy intermediates populate the walls of the funnel. From this picture it can be reasoned that all functional states of a protein need to be sterically possible and have to coexist in solution, that is, the minimum number of folding intermediates is given by the number of its functional states (however not all folding intermediates need to be necessarily correlated to function) [125]. A similar reasoning arises by generalization of the Wyman-Changeux theory for cooperative binding [162]. Despite from the fact that NMR can be able to detect signals from the conformational *ensemble* in solution, the reality is that it

reports a single structure, close to the one in the crystal [163] and neglects minor conformers either because the fluctuation is too rapid (>10^3 s^{-1}) or slow but rare. One way to populate and consequently detect these low-lying intermediate and excited states is by varying physico-chemical parameters such as pH, concentration of a denaturant, temperature, etc. However, the drawback is that it cannot be generally assured that conformers under extreme conditions represent the same intrinsic conformers in the absence of chemical perturbants [164, 165]. The alternative to this approach is to apply pressure. Indeed, pressure leads to a shift of the population distribution based on the simple ground that it favours a smaller volume for the system, as a direct consequence of the *Le Châtelier* principle (i.e. it favours "excited" states, with lower free energy of stabilisation at normal pressure). The effective volume of a protein in solution is given by the partial molar volume that includes the volume of hydration water as it is inseparable from the volume of the protein alone [166]. There are two ways through which the partial molar volume can fluctuate when subjected to pressure (Figure 1.11B): one is within the same *subensemble* of conformers (the case where the high-energy conformers are far distant) and leads to a general compression of the system, where the population shifts towards the lower-volume microscopic state but within the same *subensemble*. The second case (generally more interesting for identification of rare states in proteins) is a shift of the conformational equilibrium from the native *subensemble* (N) to a different, energetically higher *subensemble* (I), both differing in their topology of folding and function [163, 167].

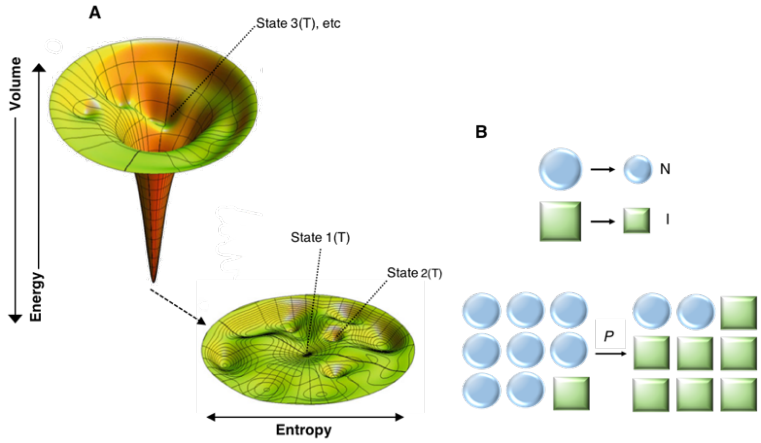

Figure 1.11. Physics of high pressure applied to biomolecules. **A.** Functional states of Ras and their relationship with the folding funnel. The free energy of the microstates is plotted for the two components of the conformational space. The native, lowest energy conformers corresponding to states 1(T) and 2(T) lie at the bottom of the funnel (the enlarged view of the bottom is depicted) and high energy states such as 3(T) populate its walls. **B.** Representation of the two possible ways through which a molecular system can attain a lower effective volume: by general compression within the same *subensemble* of conformer N or I (top) and/or by a shift of the equilibrium from N to I, in favour of the *subensemble* I with lower volume (bottom). Adapted from [160].

1.3.1 ^{31}P HP NMR to Study Nucleotide-bound Ras Proteins

Pioneering work was done in our department over the years in the field of HP NMR to study protein structure, conformation and dynamics. Some examples include the β-amyloid fibril tangles [168], the HPr protein [169], the human prion proteins [170] and the Ras protein [125, 171]. As shown by ^{31}P NMR (section 1.1.7), HRas^{WT}•Mg^{2+}•GppNHp exists in a dynamic equilibrium between at least two conformational *subensembles* denoted as states 1(T) and 2(T). Using HP, it could be demonstrated that this equilibrium can be shifted towards state 1(T) in a reversible manner (Figure 1.12A): at 200 MPa the relative population of state 2(T) over 1(T) at the γ-phosphate decreases from 1.9 to 0.44 at 278 K. The difference in the specific partial molar volume, ΔV, for the transition was found to be 17.2 mL mol^{-1} [125]. From the instrumental point of view, high hydrostatic pressure can be transmitted to the sample inserted in the NMR spectrometer in two ways: either automatically using a commercially available piston compressor [172] or manually, using an in-house built high pressure line. Technical aspects prevent ^{31}P HP NMR of being performed automatically, therefore for the time being, this nucleus can only be recorded using the manually operated pressure line whose main components are depicted in Figure 1.12B and include a water reservoir, a piston with a manually operating lever, a bourdon manometer and at least two valves that can be used to open and close different parts of the circuit. The protein sample is inserted in an especial NMR tube made of ceramic, capable

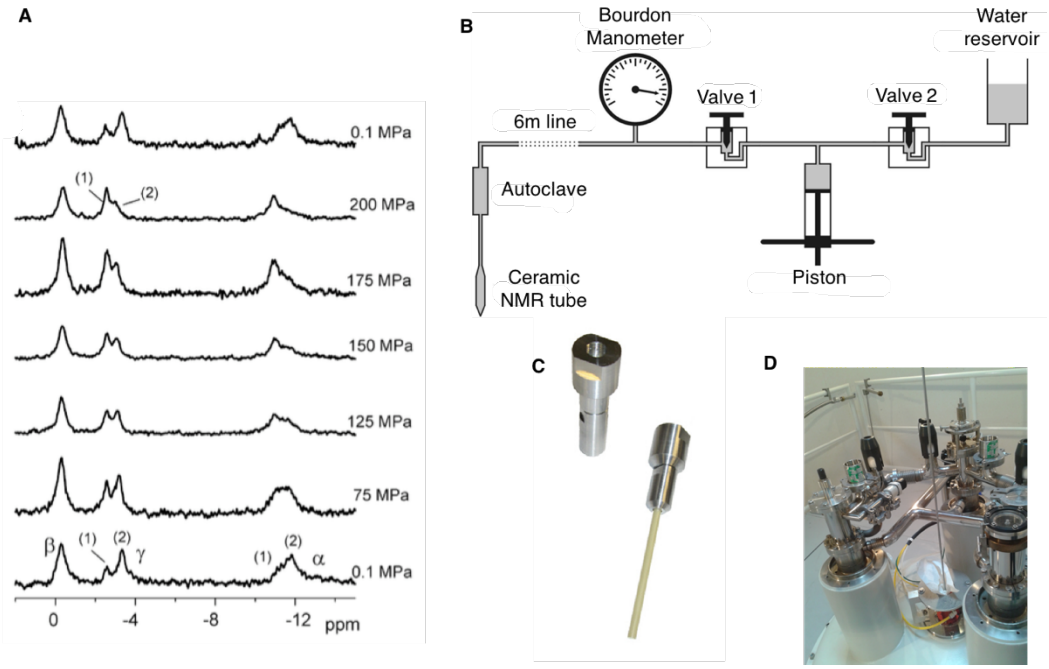

Figure 1.12. ^{31}P HP NMR spectroscopy. **A.** ^{31}P HP series of HRas^{WT}(1-189)•Mg^{2+}•GppNHp at 278 K, pH 7.4. The conformational transition from state 2(T) into state 1(T) can be observed at the γ-phosphate by following the evolution of the relative integrals along the pressure series. **B.** Schematics of the in-house built manually operated HP line. **C.** Photograph of the autoclave and the HP ceramic NMR tube that is connected at the end of the line. **D.** Photograph of the HP line inserted through the magnet bore of an 800 MHz spectrometer. Adapted from [125].

of withstanding very high pressures (up to 300 MPa, Figure 1.12C) and then mounted in an autoclave which is a small piece of alloy specifically engineered to close the circuit and to connect the ceramic tube to the HP line. The end of the line is inserted into the spectrometer as shown in Figure 1.12D and pressure is applied by rotating the lever of the piston.

1.3.2 Rare Interaction States Detected by [^{1}H-^{15}N]-HSQC HP NMR Spectroscopy

Subsequent automated HP NMR investigations using heteronuclear [^{1}H-^{15}N]-HSQC experiments were conducted on HRas^{WT} bound to GppNHp [171] and allowed the identification of additional rare states from which a more accurate picture of the conformational landscape could be drawn: the Ras switch mechanism envisages at least three states, corresponding to complexes with GEF's (state 1(T)), effectors (state 2(T)) and GAP's (state 3(T)), which could all be identified by fitting the ^{1}H and ^{15}N pressure-induced chemical shifts and cross peak volume changes (i.e. distances between components) for each amino acid with a second order Taylor expansion. From the fitting routine a fourth state came out, corresponding to the nucleotide-free Ras (represented as 1(0)). This additional state can be envisaged as the one that 'closes' the cycle. In parallel, the pressure-dependent chemical shifts were fitted with a thermodynamic model, allowing the determination of ΔG and ΔV values for the transition between any two conformational states at a given temperature. By gathering the values obtained for each amino acid and grouping them in specific numeric intervals with appropriate margins of

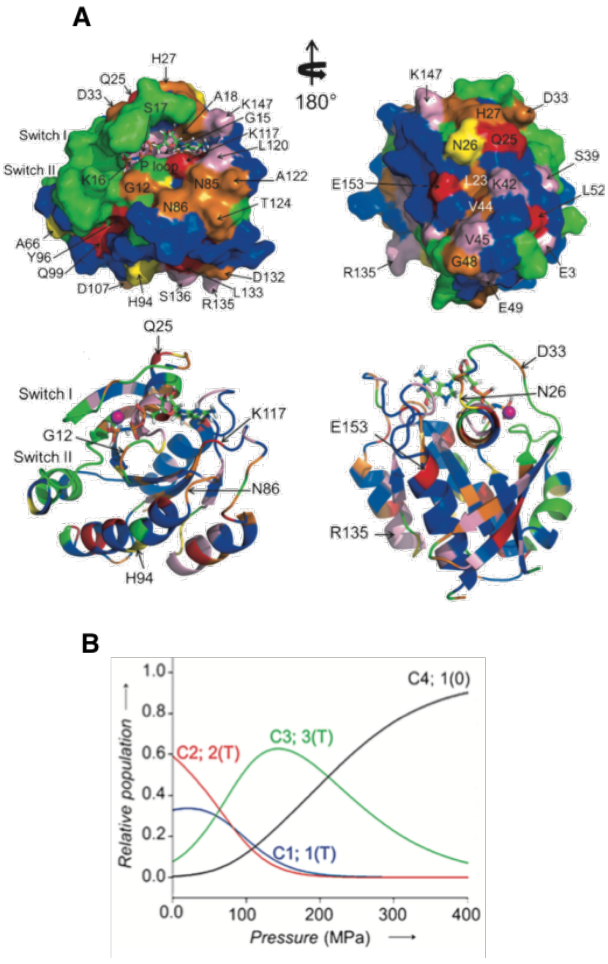

Figure 1.13. Pressure dependence of the conformational transitions. **A.** amino acids sensing different transitions are colour-coded in the crystal structure of Ras (2-to-1, 2-to-3, 2-to-0 are depicted in yellow, orange and pink, respectively. Residues sensing more than one transition at the same time are coloured in red. Residues that could not be detected are in green and residues showing no pressure response are in blue). B. Calculated thermodynamic model for the relative evolution of the population of states 1 to 4 with pressure. Taken from [171].

error, it was possible to identify the residues that are involved in (or 'sensing') a specific conformational transition. They were colour coded in the surface of the crystal structure as shown in Figure 1.13A and reveal important information about the dynamics of the 'hidden' conformations. For example, all the orange residues are involved in the transition from the ground state 2(T) to the excited state 3(T), whose population is very low at ambient pressure (0.1 MPa), as indicated by the diagram in Figure 1.13B. This information constitutes the basis of the mutational analysis on Ras performed in this thesis and presented in section 3.4 of the results: the main idea is that the substitution of an amino acid involved in a particular transition (e.g. 2(T)-to-3(T)) could shift of the conformational equilibrium towards the lowest populated state (3(T) in the present example), allowing its direct observation at ambient pressure in the newly created Ras-mutant. Within this framework, the information retrieved from HP guides the search for specific residues on the protein that are prone to be involved in some kind of interaction with an otherwise undetectable, high-energy state. This represents a novel method to detect conformational *ensembles* that are often the true functional states of a protein and the ones involved in a specific disease or anomaly, instead of the native one(s) commonly detected. As in the case of Ras, the development of drugs that could directly bind at its surface and promote a shift of the equilibria towards a non-native, low populated state, such as 3(T) (the GAP recognising state), would promote an immediate increase of the GTPase activity of the protein and therefore lead to its deactivation in Ras-driven cancer cells. The feasibility of this methodology has already been shown with the mode of action of Zn^{2+}-cyclen, capable of selectively binding and recognising state 1(T) [157].

1.3.3 High Pressure Macromolecular Crystallography (HPMX)

Nowadays HP is used together not only with NMR but with almost all spectroscopic techniques available, with the aim to understand the properties of matter and chemical reactions. Its relationship with crystallography is also not new: the field has been very active for many years in the study of the earth and materials science [173]. However, the situation is different regarding biosciences. HPMX of proteins is still a technically challenging and complex task that requires a great level of expertise. In Europe, it can be performed in very few beamline facilities (Figure 1.14A) and its application was initially confined to the study of deep sea organisms until very recently [174, 175].

HPMX can be performed either at cryo-temperature or at room temperature (RT). This distinction has implications in the physico-chemical state for the protein. In the scope of this thesis, the attention will be centred in the second case. RT HPMX can be performed using

two techniques: the first one is based on a beryllium pressure cell [176] and the second one is based in the diamond anvil cell (DAC, Figure 1.14B) [177, 178]. The development of the DAC was a feat of technical engineering, pioneered by Roger Fourne, Eric Girard and other experts in the field, which contributed to the routine collection of macromolecular crystals in the recent years [179-181], showing that HPMX is a full-fledged technique [182, 183]. During the DAC-based data collection, the crystal impregnated with mother liquor is kept in between the culets of the two diamonds that constitute the DAC and pressure is transmitted and constantly maintained using an inert gas (typically He). Its major drawback lies in the cell geometry that imposes constrains on the data collection. The aperture of the cell limits the rotation angle that can be scanned to a maximum of 85º. However, this constrain can be compensated by the use of very bright X-ray sources (30-40 keV) that contribute to increase the accessible reciprocal space and at the same time to reduce the absorption of the diamond windows [184, 185].

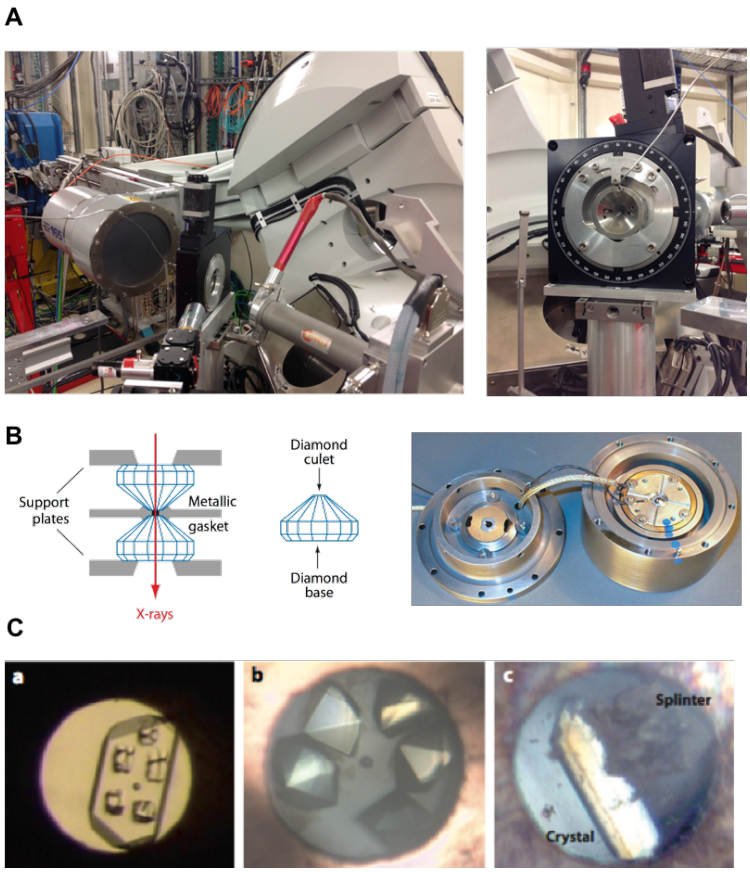

Figure 1.14. Instrumentation for HPMX. The technique requires especial diffractometers engineered to accommodate the high pressure cell. **A.** view of the 6-axis diffractometer located at the Crystal beamline in Soleil synchrotron, Paris. The DAC is mounted in the metallic block at the centre. The X-ray source (coming from the right side) needs to be perfectly aligned with the rotation axis. A close-up of the DAC mounted in the goniometer is shown in the right photograph. **B.** Components of the DAC evidencing the two diamond faces and a metallic gasket positioned in between the diamond culets. **C.** Lysozyme protein crystals: a) multiple impacts of the X-ray beam into a single crystal by translating the DAC by 50 μm every 10º. b) as alternative, multiple crystals can be loaded into the compression chamber. c) tiny diamond splinter introduced in the compression chamber to modify the orientation of the protein crystal with respect to the culets of the diamond. Adapted from [177, 178].

It is worth mention that in the scope of HPMX, protein crystals should not be considered as rigid systems. On the contrary, they are biphasic entities in which a solid phase, the protein, coexists with a solvent phase made of channels that run across the crystal and represent a total of 30-80% of its volume. The channels communicate with the surrounding liquid in

which the crystal is grown and ensure that a true hydrostatic pressure is applied to the protein. Most of the crystals are grown in low symmetry space groups, in monoclinic or orthorhombic, lattices that difficult the generation of high completeness data. Furthermore, the low aperture of the DAC poses additional difficulties in the application of the rotation method. The problem can sometimes be solved by merging diffraction data from several crystals and/or by introducing a tiny, X-ray transparent, diamond splinter (from a broken anvil) within the sample cavity to change the orientation of the crystal with respect to the diamond culets (Figure 1.14C).

Despite the large amount of crystallographic studies, HPMX has never been reported on Ras. In an attempt to shed light into the unanswered question of why most ambient pressure Ras crystals reveal only the "closed" conformation of the switch regions instead the observed equilibrium between the "opened" and "closed" *subensembles*, (roughly corresponding to states 1(T) and 2(T)), as detected by liquid and solid-state ^{31}P NMR, HPMX on Ras^{WT} was conducted in the framework of this thesis.

1.4 Research Goals of this Thesis

The focus of this thesis can be comprehensively divided into five main topics.

• Due to the increasingly interest by the scientific community on the dynamics and inhibition of the full-length KRas isoform, a primary concern was to address the conformational equilibria of this protein by means of ^{31}P NMR and compare it directly with the wealth of experimental data obtained for HRas. The primary intent of the study was to understand if some of the structural and biochemical properties of HRas can indeed be transferred to KRas. In the follow-up of these investigations, a series of experiments were devised for both isoforms in order to gain insight into the perturbation of Ras-effector interaction by a typical state 1(T) inhibitor such as Zn^{2+}-cyclen.

• In the sequence of the gathered results, a systematic investigation on the inhibition of the oncogenic KRas^{G12D}•Mg^{2+}•GppNHp protein by a series of 15 different compounds was pursued. Their effect on the conformational equilibria of the protein was investigated by ^{31}P NMR and their ability to disrupt the Ras-Raf complex formation was inspected by ITC. The main intent of the study was to shed some light into the mode of action of these drugs, to score them according to their ability to modulate the conformational dynamics of the protein and to demonstrate the usefulness of ^{31}P NMR as a screening method that can be applicable to all GNBP's.

• The investigation of the conformational dynamics of proteins by pressure perturbation is a central topic at our department. Given our expertise and recent new instrumentation available, a series of HP ^{31}P NMR investigations were envisaged by starting first with the study of the pressure effects on the isolated GppNHp nucleotide, in the absence and in the presence of the Mg^{2+} ion, and following up to similar studies on Ras^{WT} and the mutants T35S, G12V and D33K. Two main goals were set in this extensive study: the first was to obtain a framework for the correction of the intrinsic pressure effects arising from the nucleotide alone (that would be given by the HP measurements on the isolated GppNHp) from the true effects arising from the conformational modification of the nucleotide-bound protein under pressure. The second goal was to investigate how different Ras proteins respond under pressure in terms of their equilibrium dynamics measured at the nucleotide level.

• Taking together the present HP data and the past, 2D [^{1}H-^{15}N]-HSQC HP NMR investigations established by our group, specific amino acids on the surface of Ras were selected and chosen to perform site directed mutagenesis with the expectation that the mutation could shift the conformational equilibria in the same direction as the one observed from the HP investigations. A total of seven mutants were created *de novo* for the purpose. Their conformational equilibria was screened by ^{31}P NMR for the GDP-, GppNHp- and GTP-bound nucleotides and their biochemical properties were analysed by ITC for their affinity to bind the effector Raf-RBD and by HPLC for their intrinsic GTPase activity. The mutants showing more drastic modifications comparatively to Ras^{WT} were further investigated by a variety of methods including ^{31}P NMR titrations, 2D [^{1}H-^{15}N]-HSQC NMR, T_1 relaxation time measurements, nanoDSF and HP ^{31}P NMR. The ultimate goal of the proposed task was to give a proof-of-concept for the use of HP as a screening method for rare states and to find novel potential allosteric binding sites that could be targeted in the future by state-specific Ras inhibitors.

• The last chapter of this thesis deals with a topic of great scientific endeavour: HPMX. The motivation to perform HP crystallography on Ras arose in the first place as an attempt to complement the HP NMR data and, secondarily, to try to solve an apparently contradictory scientific mystery: the observation that Ras exists in solution as an equilibrium between two conformational states, 1(T) and 2(T), which are equally detected when Ras crystals are subjected to solid state ^{31}P NMR but not detected when the very same crystals are used in conventional X-ray crystallography.

2. Methods

“The strongest arguments prove nothing so
long as the conclusions are not verified by experience.
Experimental science is the queen of sciences and the goal of all speculation”
Karl Popper

2.1 Material

2.1.1 Plasmids

pTac

This vector was provided by Dr. Kühlmann from Max Planck Institute of Molecular Physiology, Dortmund, and it was used for the expression in LB media of all Ras proteins (WT and mutants). The expression was induced by the presence of isopropyl-β-D-thiogalactopyranoside (IPTG), which binds the lac repressor, thus allowing the transcription by the RNA polymerase. IPTG itself is not metabolized by the bacterial system.

pGEX4T1 (GE Healthcare®)

This vector carries an N-terminal glutathione S-transferase (GST) and a sequence encoding ampicillin resistance. The 26 kDa GST-tag was used for purification by affinity chromatography and accounts for increasing further the solubility of the expressed protein during the purification. The vector was used in the expression of the catalytic domains of the effector protein Raf-RBD and the GAP protein Neurofibromatin 1 (NF1-333). The constructs were provided by S. Wohlgemuth and P. Stege from the Max Planck Institute of Molecular Physiology, Dortmund.

pET14b (Novagene®)

This vector includes a T7lac promoter, ampicilin resistance and an additional N-terminal six histidine tag (His_6-tag) that allows the efficient purification of the recombinant protein by affinity chromatography, being the tag cleavable with thrombin. The vector was used in the expression of the GEF protein, Son-of-Sevenless (SOS).

2.1.2 Oligonucleotides

The nucleotide sequences listed below correspond to the primers designed to perform site directed mutagenesis on $HRas^{WT}$(1-166). They were manufactured either at Metabion AG (Planegg) or Mycrosynth AG (Lindau) in the desired quantities and degrees of purity.

Table 2.1. Primers used in site-directed-mutagenesis to obtain the respective mutants.

Mutation	Primer sequence 5'- 3'	Mutant Name
C79G_T81G_antisense	GGTCGTATTCGTCCACAAACTCGTTCTGGATCAGCTGGATG	H27E
C79G_T81G	CATCCAGCTGATCCAGAACGAGTTTGTGGACGAATACGACC	
G97A_C99G_antisense	GGAATCCTCTATAGTGGGCTTGTATTCGTCCACAAAATGGTT	D33K
G97A_C99G	AACCATTTTGTGGACGAATACAAGCCCACTATAGAGGATTCC	
C78G_antisense	GTATTCGTCCACAAAATGCTTCTGGATCAGCTGGATG	N26K
C78G	CATCCAGCTGATCCAGAAGCATTTTGTGGACGAATAC	
C280G_antisense	TGCTCCCTGTACTGGTCGATGTCCTCAAAAGAC	H94D
C280G	GTCTTTTGAGGACATCGACCAGTACAGGGAGCA	

G196A_antisense	TGGTCCCGCATGGTGCTGTACTCCTCC	A66T
G196A	GGAGGAGTACAGCACCATGCGGGACCA	
C116T_C117A_antisense	ACCTGCTTCCGGTATAAATCCTCTATAGTGGGGTCGTATTCG	S39L
C116T_C117A	CGAATACGACCCCACTATAGAGGATTTATACCGGAAGCAGGT	
A29T_antisense	CCAACAACAACAAGCTTGTATACTGTCATAGAATTCTGTTTCC	E3V
A29T	GGAAACAGAATTCTATGACAGTATACAAGCTTGTTGTTGTTGG	

2.1.3 Bacterial Strains Used for DNA Cloning and Amplification

These strains inhibit the Lac/Tac promoter by the action of the LacI^{q-} gene, preventing any unwanted expression of the target gene from the transformed plasmids. They were used to achieve high level multiplication of plasmids during the production of the transgenic protein constructs.

E. coli TG1 (Lucigen)

Genotype: F'[traD36 lacIq Δ(lacZ)M15 proA+B+] glnV (supE) thi-1 Δ(mcrB-hsdSM)5 (rK mK McrB-) thi Δ(lac-proAB).

One Shot® TOP10 Chemically Competent *E. coli* (Invitrogen)

Genotype: F$^-$ mcrA Δ(mrr-hsdRMS-mcrBC) ϕ80lacZΔM15 ΔlacX74 recA1 araD139 Δ(ara-leu)7697 galU galK rpsL (StrR) endA1 nupG λ-.

DH5α™-T1® Chemically Competent *E. coli* (Thermo Fisher), as part of the SDM kit

Genotype: F- ϕ80lacZΔM15 Δ(lacZYA-argF)U169 recA1 endA1 hsdR17(rk-, mk+) phoA supE44 thi-1 gyrA96 relA1 tonA (confers resistance to phage T1).

2.1.4 Bacterial Strains used for Protein Expression

These strains were used with the purpose of obtaining the highest possible yields of the desired constructs upon expression. They are specific protease deficient to avoid degradation of the target recombinant proteins.

E. coli BL21 (Novagen)

Genotype: F- ompT hsdSB (RB- MB) gal dcm

The strain has no LacI^{q-} gene, so that the induction by IPTG is only possible due to the properties of the transformed plasmid. Otherwise there would be a basal/permanent expression of the target construct, which can become a problem in some cases.

E. coli BL21 (DE3) pLysS (Novagen)

Genotype: F- ompT hsdSB (RB- MB) gal dcm (DE3) pLysS (CAMR)

As BL21, but with an additional DE3 element which codes for a T7-RNA polymerase and a lac repressor. This allows a IPTG inducible expression if the transformed plasmid contains a T7 promoter. Additionally, the strain is resistant to chloramphenicol and contains a pLys

sequence that codifies the T7 lysozyme, capable of inhibiting the T7 RNA polymerase, leading to an even stronger control of basal expression and a more stringent induction by IPTG

E. coli CK600K (Stratagene)

Genotype: McrA-, sup E44, thi-1, thr-1, leuB6, lacY1, tonA21

2.1.5 Media and Antibiotics

2.1.5.1 Lysogeny Broth (LB)

LB is a rich medium that contains all the nutritional requirements for *E. coli* to support a high cell density and maintaining growth in the logarithmic phase for an extended period, resulting in good yields of plasmidic DNA and heterologous protein expression. Tryptone and yeast extract are the sources of carbon, nitrogen, vitamins, minerals and amino acids essential for growth.

Composition:

- 10.0 g bacto-tryptone
- 10.0 g NaCl
- 5.0 g yeast extract
- NaOH 0.1 g (pH 7.0)

Dissolved in 1.0 L Millipore H_2O and autoclaved. The medium can be stored at 4 ºC for two weeks or longer (if antibiotic is added). For bacterial platting, LB/Agar was prepared by adding 15 g/L of bacteriological grade agar to the aforementioned medium. If the medium had to be used immediately after autoclaving, care was taken to let it cool down to a temperature suitable for addition of antibiotics without causing any degradation to them.

2.1.5.2 Terrific Broth (TB)

TB was mainly used for the overexpression of SOS. This medium contains slightly more bacto-tryptone and 5 times more yeast extract than LB, providing large quantities of growth factors and nucleic acid precursors. Glycerol was used as an additional source of carbohydrates, having the advantage of not being metabolized into acetic acid, as it happens with glucose (which, in some expression systems, also acts as a repressor). The presence of phosphate buffer allows a better control of the physiological pH during the exponential growth.

Composition of the TB buffer:

- 12.0 g bacto-tryptone
- 24.0 g yeast extract
- 4.0 mL glycerine

Dissolved in 900 mL of Millipore H_2O and autoclaved.

Separately, a phosphate buffer was prepared by dissolving 164.32 g of K_2HPO_4 and 23.13

g KH_2PO_4 in 1.0 L of Millipore H_2O and autoclaved. It Is important to not autoclave the TB buffer with the phosphate buffer added to it. Therefore, both components were autoclaved separately and mixed afterwards at room temperature. This prevents the precipitation of the phosphates, that undergo exothermic dissolution, by ionic metals (brought in trace quantities from the yeast extract or tryptone) at high temperatures [186].
The final medium was prepared by adding 100 mL of the phosphate buffer to 900 mL of the aforementioned TB buffer, to yield 1.0 L of TB medium ready to use.

2.1.5.3 New Minimal Medium (NMM)

NMM contains the minimum of nutrients that support the proliferation of cells and colony growth. All amino acids, nutrients and complex molecules need to be built *de novo* by the cellular machinery [187]. This is the medium of choice to express uniformly ^{15}N and/or ^{13}C-labeled proteins needed to perform heteronuclear multidimensional NMR experiments.
In the scope of this thesis, Ras^{WT} and selected mutants were uniformly labelled with $^{15}NH_4Cl$ with the aim to investigate their conformation and dynamics by 2D [^1H-^{15}N]-HSQC NMR. Below are described the details of the procedure:

A – Preparation of minimal medium

MM contains a Carbon source which is typically glucose (or sometimes a less energy rich sugar such as succinate) and different salts that provide essential elements (e.g. Mg, N, P, S) and allow protein and nucleic acid synthesis by the bacteria.
Composition:

- 7.5 g Na_2HPO_4
- 3.0 g KH_2PO_4
- 0.5 g NaCl
- 0.25 g $MgSO_4$ x $7H_2O$
- 0.014 g $CaCl_2$ x $2H_2O$

Dissolved in 1.0 L of Millipore H_2O and autoclaved. This medium can be stored for long term usage at 4 ºC. Sodium phosphate dibasic and nitrogen dihydrogenophosphate act as a source of Na, K and P and are simultaneously buffers for maintaining the pH during the bacterial growth.

B – Preparation of a micronutrient stock solution (SL6)

This solution contains all the micronutrients needed for cell growth dissolved in 1.0 L of Millipore H_2O and autoclaved. The solution can be stored in the dark at 4 ºC for long term usage.
Composition:

- 100 mg $ZnSO_4$ x$7H_2O$
- 30 mg $MnCl_2$
- 10 mg $CuCl_2$ x $2H_2O$
- 20 mg NiCl x $2H_2O$

- 300 mg HBO_3
- 30 mg Na_2MoO_4
- 200 mg $CoCl_2$ x $6H_2O$

C – Preparation of the Iron sulphate/EDTA solution (SL4)

This solution needs to be freshly prepared and used shortly after.

Composition:

- 500 mg EDTA
- 200 mg $FeSO_4$ x $7H_2O$

Dissolved in a total volume of 90 mL of previously autoclaved H_2O.

For a better dissolution and to avoid the occurrence of slight precipitation, the two chemicals were dissolved separately and only then mixed together. The final solution is light green coloured, typical of aqueous ferrous sulphate (green vitriol). As the oxidative process takes place over time, formation of ferric sulphate will give rise to a deep yellow/green colour. At such point, the solution should not be used any longer and a freshly one should be prepared.

D – Preparation of a SL6/SL4 mixture (SL mix)

In this procedure 1.0 mL of the micronutrient (SL6) solution was added to 0.9 mL of the SL4 solution. The mixture was filled in up to a final volume of 10 mL using previously autoclaved H_2O.

E – Adding the SL mix to the minimal medium and the N and C sources

Final composition:

- 900 mL minimal medium
- 10 mL SL mix
- 4.0 g Glucose

Filled up to a final volume of 1.0 L with previously autoclaved H_2O.

NMM was ready to use after filtration. The amount of glucose and ammonium sulphate can be adjusted accordingly to the growth demands of the bacterial strain. A minute amount of thiamine, taken in the tip of a spatula was added to the medium prior to filtration. The active form of this vitamin, thiamine pyrophosphatase, is a cofactor of enzymes involved in the synthesis of three amino acids: valine, isoleucine and leucine. Its addition to the medium is not essential but it can help to enhance the bacterial growth, especially in the case strains such as DH5α, which are knocked out for thiamine synthesis (genotype: thy-) [188, 189].

2.1.6 Chemicals

All pro analysis grade chemicals were purchased from the following companies: Fluka (Neu-Ulm), Merck (Darmstadt), Roche (Mannheim), Novabiochem (Läufelingen, Switzerland), Roth (Karlsruhe), Pharma-Waldorf (Düsseldorf), Sigma (Deisenhofen), Serva (Heidleberg)

and QIAGEN. They were always analysed and used accordingly to their respective safety datasheets. Metal(II)-cyclens were synthesized by the Organic Chemistry Department (chair Prof. B. König) at Regensburg University.

2.1.7 Expendable Materials and Common Solutions

Table 2.2. List of the enzymes used.

Enzyme	Provider
Alkaline Phosphatase	Boehringer/Roche
DNaseI	Boehringer/Roche
Lysozyme	Sigma
Thrombin	Sigma
Immobilized Alkaline Phosphatase	MoBiTec
Taq DNA Polymerase	Fermentas, Quiagen, NEB
Pierce™ protease inhibitor	ThermoFisher

Table 2.3. List of protein and DNA ladders used.

Standard	Provider
PageRuler Unstained Protein Ladder	Thermo Scientific/Fermentas
PageRuler Unstained Protein Ladder Low Range	Thermo Scientific/Fermentas
Page Ruler Prestained Protein Ladder (10-180 kDa)	Thermo Scientific/Fermentas
1 kb/ 100 bp DNA Ladder	New England Biolabs (NEB)

Table 2.4. Commonly used buffer solutions.

Buffer B	50 mM Tris/HCl pH 7.5; 5 mM EDTA; 5 mM DTE; 1mM PMSF	Cell Lysis Ras
Buffer C	32 mM Tris/HCl pH 7.5; 10 mM $MgCl_2$; 1mM DTE	IEX Ras
Buffer D	64 mM Tris/HCl pH 7.5; 10 mM $MgCl_2$; 400 mM NaCl; 2 mM DTE; 0.1 mM GDP	SEC Ras
Buffer E	50 mM Tris/HCl pH 7.5; 2 mM DTE	Nuc. Exchange
Buffer F	40 mM Tris/HCl pH 7.5; 10 mM $MgCl_2$; 2mM DTE	Storage Buff Ras

Table 2.5. List of commonly used expendable materials.

Material	Supplier
Bradford reagent Rotiquant™	Roth
Cuvettes UV/Vis, macro, semi-micro and micro	Carl Roth
NMR tubes:	
• 3 and 5 mm	Norell Inc.
• 5, 8 and 10 mm	Shigemi Co LTD
Vivaspin ultrafiltration units	Vivascience
Filter unities Steritop™ 0.22 μM	Millipore
Eppendorf cups 0.5, 1.5 and 2.0 mL	VWR
Falcon tubes 15/50 mL (16000g)	VWR
Vivaspin® 20 concentrators (various sizes)	Sartorious

2.1.8 Main Instrumentation

Table 2.6. Most often used chromatography columns.

Column Materials	Supplier
Hiload™ 26/10 Q-Sepharose™ Fast-Flow	Amersham Pharmacia
Hiload™ 26/600 Superdex™ 200 prep. grade	GE Healthcare
Hiload™ 16/60 Superdex™ 75 prep. grade	GE Healthcare
Superdex 75 10/300 GL	GE Healthcare
Glutathione Sepharose™ Fast Flow 4	GE Healthcare
Pierce Glutathione Spin Columns (3 ml)	ThermoScientific
Ni Sepharose™ Superflow/Fast Flow 6	GE Healthcare
Sephadex™ G25 NAP10/ NAP15/ PD10	Amersham Biosciences
Nucleosil 100 C18 precolumn	Beckman Coulter
ODS hypersil C18 column	Beckman Coulter

Table 2.7. Main instrumentation used in this thesis.

Instrument	Supplier
Incubator EB 53	Juan
Electrophoretic chambers	GE Healthcare
pH-Meter Φ 32, Φ 340	Beckman Coulter
Thermocycler Mastercycler Personal	Eppendorf
Sonifier 250/450	Branson
Ultrasonic machine (cell lysis)	Branson
Water system Purelab® Ultra, Elga	Millipore
J-6B, Avanti J-20, Avanti J-25	Beckman Coulter
Biofuge Pico, mini Spin	Hereaus Instruments
Analytical Balance	CP64, Sartorius PM 600 Mettler
Beckman HPLC System Gold® 125 Solvent Module	Beckman Coulter
Beckman HPLC 166 Detector	Beckman Coulter
AKTA™ FPLC system, UPC 900, Frac 900	Amersham Pharmacia
water systems	Purelab Ultra, Elga Millipore
UV/Vis spectrophotometer LambdaBIO+	PerkinElmer
Microcal PEAQ-ITC	Malvern Instruments
Monolith NT.115 Series	Nanotemper Techologies
2.0 KBar NMR Ceramic Cell	Daedalus Innovations LLC
2.5 KBar NMR Ceramic Cell	Daedalus Innovations LLC
NMR Spectrometers	
500 MHz Avance with QXI or ^{31}P broadband probe	Bruker Corporation
600 MHz Avance with Prodigy probe	Bruker Corporation
800 MHz Avance with TCI-Cryoprobe	Bruker Corporation
Beamline ID09	ESRF synchrotron. Grenoble, France
Beamline ID27	ESRF synchrotron. Grenoble, France
“Crystal” Beamline	Soleil synchrotron. Paris, France
HP “ELMA” DAC cell	Almax
HP “ELSA” DAC cell	Almax

2.1.9 Software

Table 2.8. Most commonly used software.

Software	Manufacturer/URL	Description
Gold Chromatography V1.7	Beckman	HPLC control and evaluation
UNICORN Control system	Amersham Biosciences	ÄKTA-FPLC control and evaluation
Topspin 3.2	Bruker	NMR acquisition, processing and evaluation
AUREMOL2.4.1beta	Uni-Regensburg/ Kalbitzer	NMR processing and evaluation
MestReNova 10.0	Mestrelab Research	NMR processing and evaluation
GENtle	http://gentle.magnusmanske.de	DNA and protein sequence analysis
PyMol	https://www.pymol.org/	Protein visualization and structure analysis
Chimera 1.9	http://www.cgl.ucsf.edu/chi- mera/	Protein visualization
Microcal Origin 6.0	http://www.originlab.de/	NMR Data analysis and statistics
Origin 10	http://www.originlab.de/	NMR Data analysis and statistics
Microsoft Office	Microsoft	Word processor and data analysis
CorelDraw 16	Corel corporation	Image editor
Microcal PEAQ ITC	Malvern Instruments	ITC analysis software
Online tools/Databanks	**Manufacturer/URL**	**Description**
ExPASy Bioinformatic portal	http://www.expasy.org/	Proteomics tool (very useful)
PDB Databank	http://www.wwpdb.org/	Repository of X-Ray, NMR structures
Uniprot	http://www.uniprot.org/	Protein databank
BLAST	https://blast.ncbi.nlm.nih.gov/Blast.cgi	Basic Local Alignment Search Tool (very usefull)

2.2 Methods

2.2.1 Molecular Biology

2.2.1.1 Preparation of Chemically Competent Cells

E. coli can incorporate exogenous circular DNA molecules, commonly referred as plasmids. One can take advantage of this feature and build specific plasmids containing genetic information for desired proteins or parts of proteins. These can be introduced in bacterial cells in a process called *transformation*. The transformed bacteria are called *competent* and can transcribe the genetic information contained in the plasmid into proteins. Some natural prokaryotes are genetically determined to be naturally transformable (e.g. *Bacillus subtilis*). By contrast, many bacteria are poorly transformable, if at all, under natural circumstances. *E. coli* falls in such category [190]. However, if *E. coli* cells are treated with high concentrations of Ca^{2+} and then chilled, they become adequately competent, increasing their ability to intake double stranded DNA. Inducing artificial competence is always a mildly efficient process, yielding very few (approx. 10^6) transformants per μg of plasmidic DNA [191]. This technique also makes it possible to transcribe genetic information from other organisms into *E.coli*, a concept that allows, for example, the study of human proteins like Ras, without the need of dealing with human material [191].

All material (flasks, pipette tips, etc.) were autoclaved and the conditions kept as sterile as

possible. The handling of the medium and bacterial growth was done in the absence of antibiotics throughout the whole procedure. As result, especial care was taken to avoid contaminations. Vortexing or hard shaking of the samples was also avoided to minimize cell death.

Day 1

With the help of a toothpick, the frozen *E. coli* strains (BL21 and BL21DE3) from a -80 ºC glycerol stock were directly plated in LB/Agar. The bacteria were allowed to grow overnight at 37 ºC.

Day 2

Upon inspection, an individual (isolated) colony was picked and streaked again in a new LB/agar plate. The culture grew overnight once more (this process can be repeated a third time, if desired, to ensure that the final population on the plate arises from a truly, isolated colony, characterized by a single genotype).

Day 3

A 5 mL LB culture was prepared by picking an isolated colony with a toothpick from the double (or tripled) streaked plate. The culture was grown overnight at 37 ºC, 220 rpm.

Day 4

The overnight grown culture was diluted with 100 mL of LB medium. The corresponding OD_{600} was 0.02. The cells were allowed to grow in the same conditions as before (37 ºC, 220rpm), until the OD_{600} reached a value of 0.4-0.5 (ca. 3 h). The growth stage of the bacteria has a significant impact for its ability to take up DNA: in the log phase, they are metabolically more active and prone to perform efficient DNA repair as compared with their activity in the stationary phase. As a result, it is preferred to use bacteria in a log phase.

- At OD_{600}= 0.4-0.5 the bacterial growth was stopped by keeping the cultures on ice with gentle stirring for ca. 15 min.
- The cell culture was centrifuged 6-8 min. at 4 ºC, 4000 rpm. The supernatant was discarded and the pellet re-suspended in transformation buffer 1 (TFB1).

10x TFB1 composition:

- 1.176 g KOH
- 4.8 g RbCl
- 0.588 g $CaCl_2$
- 4.0 g $MnCl_2$

The pH was adjusted to 5.8 with 1.0 M HCl, in a final volume of 40.0 mL. Because of the small amount of powder to be weighted, this buffer was prepared in a 10x concentration stock solution, that can be stored for long periods of time. The buffer was diluted to 1x before adding it to the cells. The resuspension of the pellet is a time-consuming process and should be done slowly to avoid cell lysis.

- The re-suspended cells were left shacking on ice ca. 15 min. After the elapse of this time, they were centrifuged again at 4000 rpm, 6-8 min, 4 ºC.
- The supernatant was discarded and the pellet was re-dissolved in TBF2.

5x TFB2 composition:

- 1.1 g $CaCl_2$
- 0.121 g RuCl
- 0.21 g MOPS

The pH was adjusted to 6.5 with 0.1 M NaOH in a final volume of 20.0 mL.

The presence of $CaCl_2$ accounts for the neutralization of the negative charges at the cell surface and therefore to avoid electrostatic repulsion between the cell wall and the DNA phosphate groups. At the same time the hypotonic transformation buffer solutions lead to cell swelling and to the expulsion of some membranar proteins. Rb^{2+} and Mn^{2+} are reported to have a complementary and enhanced effect as compared to the one of $CaCl_2$ [192]. All the components components become embedded in the cell wall and in the membrane, creating “holes” through which the exogenous plasmids can enter the cell.

- The re-suspended cells were aliquoted in previously cooled Eppendorfs (100 μl), flash frozen with liquid N_2 and stored at -80 ºC.

2.2.1.2 Bacterial Transformation by Heat-Shock

In this process the exogenous genetic material is taken up by the competent cells by altering their membranar fluidity upon a 0ºC-42ºC-0ºC heat shock sequence. The membrane becomes momentaneously more fluid when exposed for a short time to a high temperature, allowing the entrance of genetic material. The enclosed $RbCl_2$ and $MnCl_2$ salts detached from the cell wall and plasma membrane it, leaving the artificially created open “pores”, through which the plasmids can access the cytoplasm [190]. The detailed methodology is presented below.

- An aliquot of the previously prepared competent cells was thawed on ice, the desired plasmid was added (50-200 ng, corresponding to 2-10 μl) and mixed by inverting the Eppendorf cup up and down (care was taken to not abruptly shake the mixture. Polystyrene reaction tubes are to be avoided since DNA can adhere to their surface, reducing the transformation efficiency). The mixture was incubated on ice for ca. 20 min. and subjected to heat shock for about 30-60 seconds at 42 ºC (the exact time depends on the characteristics of the bacterial strain used and should be optimized. The water bath should be brought to the correct temperature before initiating the experiment). After the heat step, the membrane was regenerated by placing the cells on ice for 2-8 min. Following heat

shock, the transformed *E. coli* were cultured in antibiotic free liquid medium for a short period to allow expression of antibiotic resistance genes from the recently acquired plasmid. Typically, 100 µl competent cells were incubated in 1.0 mL SOC medium and allowed to grow at 37 ºC, 500 rpm for 1 hour. Rich media containing glucose and $MgCl_2$, like SOC, is recommended in order to maximize the transformation efficiency [192]. Afterwards the cells were platted on LB/agar containing Ampicillin 1mg/mL (the plates were pre-warmed at 37 ºC and free of condensation). Typically, 50-100 µl of *E. coli* grown in SOC medium were platted for BL21 and BL21DE3, as the process was generally very efficient. In other situations, and when different bacterial strains were used, the quantity of cells platted was optimized to produce a sufficient (but not too numerous) number of individual, distinct colonies. When necessary, the cells cultured with SOC were pelleted by centrifugation for 5 minutes at 600-800 rpm and re-suspended in a smaller volume.

2.2.1.3 Plasmid Isolation and DNA Sequencing

Plasmids from transformed *E. coli* were isolated in order to evaluate their degree of contamination and to scrutinize the correct DNA sequence of newly created Ras mutants. The isolation was carried out using a standard, miniprep kit protocol from Promega™. The methodology used strictly follows the protocol presented by the manufacturer of the kit and it will not be discussed in detail here. The reader is submitted to the respective online miniprep quick protocol [193]. The concentration of the isolated plasmids was typically in the range of 20-100 ng/µl. When needed, larger amounts were also isolated (up to 600 ng/µl) using the midiprep kit from the same manufacturer [194].

All the isolated plasmids were sequenced at SeqLab GmbH (Göttingen). The minimum amount required was 10 µl (150-350 ng). The sequencing of small constructs (up to 1000 bp) was performed by the standard Sanger method employing dideoxynucleotides, using a 5'-3' (sense direction) primer located prior to the open reading frame (ORF) of the inserted sequence. Constructs bigger than 1000 bp were stepwise sequenced, using different overlapping primers.

2.2.1.4 Expression of Unlabelled Ras

Overexpression of wild type and mutants of H, K and NRas, either their truncated (1-166) or full length (1-188/189) forms was accomplished according to Tucker *et al.* [195], using either the 6K600K, BL21 or the BL21DE3 strains transformed with the pTac vector containing a codifying region for antibiotic resistance to ampicillin. The 6K600K strain contains an additional plasmid, accounting for resistance to kanamycin. Experimentally, ampicillin was substituted in our laboratory by carbenicilin. The latter is a carboxyl based

analogue of the former (which has an amine group instead). The basis of the selective growth inhibition is the same: both antibiotics become hydrolysed and therefore inactive by β-lactamase, an enzyme expressed from the plasmid-borne *bla* gene, which is involved in the synthesis and crosslinking of the peptidoglycan wall. However, β-lactamase is secreted by the bacteria into the medium during their exponential growth and the resulting build-up of extracellular β-lactamase can inactivate ampicillin present in the culture medium, thus removing the induced selective pressure on the population. This affects liquid cultures because there is always a portion of the population that is not transformed with the plasmid and also agar platted cultures, as the ampicillin degradation leads to the appearance of satellite colonies: very small groups of cells that have not incorporated the plasmid and therefore can grow around a larger transformed colony. As the β-lactamase is released by the main colony in its vicinity, more ampicillin is degraded by it and the satellite colonies tend to strive. Carbenicilin, on the other hand, is not easily degraded by β-lactamase, thus being a better choice as antibiotic [196].

Following is presented the methodology used for the expression of Ras proteins:

• From a -80 ºC glycerol stock containing the frozen bacteria, 200 mL LB containing 50 mg/mL of the appropriate antibiotic (carbenicilin and kanamycin in case of 6K600K and carbenicilin alone in the case of BL21/ BL21DE3) were inoculated. This so-called pre-culture was grown overnight, typically at 35-37 ºC (*E. coli* 6K600K) or 30 ºC (*E. coli* BL21/BL21DE3), with a constant aeration and shaking velocity of 180 rpm. The detailed methodology on the preparation of LB medium is described in section 2.1.5.1.

• In the second day, the overnight pre-culture was used to inoculate 10.0 L of previously autoclaved LB medium containing 50 mg/mL of the appropriate antibiotics. For a better handling of the volumes, the 10 L were always divided in 4 flasks of 2.5 L each. The cultures were grown at constant aeration and speed, 180 rpm, 37 ºC. The OD_{600} was monitored by optical photometry at specific time intervals. When the culture reached the exponential growth phase (comprised by a OD_{600} value between 0.6-0.8 units), protein expression was initiated by induction with 1.0 mM or 0.3 mM, depending on the *E. coli* strain used (6K600K or BL21/BL21DE3, respectively) of the non-hydrolysable lactose analogue, IPTG. This sugar binds to the lac repressor and promotes a conformational modification that hinders its ability to regulate (repress) the promoter. This leads ultimately to the expression of the Ras gene that is under control of the promoter sequence [190]. The induced culture was allowed to grow overnight at 37 ºC (6K600K) or 30 ºC (BL21/BL21DE3), with a constant speed of 180 rpm.

• In the third day, the culture now in the log phase, was harvested by centrifugation during 40-45 min, at 4 ºC, 4000 g. In order to better handle the 10 L volumes, the centrifugation process was performed 3 times in fractions of 4 L each. The supernatant was discarded and the bacterial pellet was directly stored at -20ºC until further use.

The studies comprising the mutational analysis of HRas(1-166) (see results section 3.4.2) led to the *de novo* creation of several Ras mutant constructs using *E. coli* BL21. For each individual construct, the optimal expression conditions related to expression time, IPTG concentration of the induction, type of medium, temperature, aeration, and, if necessary, the construct *per se* were optimized as best as possible.

2.2.1.5 Expression of ^{15}N labelled Ras

Due to the economic costs involved in the expression of labelled proteins (arising fundamentally from the high prices of ^{15}N and ^{13}C isotopes), all the HRas(1-166) constructed mutants were optimized beforehand for the best possible expression yields. The advantage of performing isotopic labelling lies in overcoming the ambiguity of resonance overlaps in NMR, allowing an unambiguous assignment of the spectra, which would be impossible otherwise for most proteins with a size beyond 10 kDa. Structural studies of large proteins (>30 kDa) require triple-labelling $^{2}H/^{13}C/^{15}N$ for the use of TROSY techniques [197]. In such cases, bacteria must grow in D_2O, usually causing a significant reduction on the protein yield. The strategy taken on the present work to optimize the cell growth of ^{15}N enriched Ras focused primarily on increasing the cell density of the bacterial expression, without manipulating the expression vector [198]. This was accomplished by selecting high-expressing colonies and optimizing growth temperatures and times. Parameters such as O_2 levels, pH and nutrients were disregarded because they can be much better controlled using a fermenter. By contrast, they are more difficult to control using a regular incubator shaker, as the one used during this work. For this purpose, *wild type* Ras and selected mutants were overexpressed in NMM – a “bare bones food” – containing a single source of enriched ^{15}N, added in the form of $^{15}NH_4Cl$. The details regarding its preparation are discussed in section 2.1.5.3. During the optimization process, the expression strategy is determined by simulating a “isotope marked” expression in which the composition of the media is the same, except for the isotope sources, which are the non-labelled ones, ^{14}N-ammonium chloride and ^{12}C-glucose.

In the case of truncated Ras^{WT} and mutants such as D33K, H27E, T35S, the optimized methodology is similar to the one used for the expression of the bacteria in LB (section 2.1.5.1). However, the expression of some variants such as the full length *wild type* KRas

isoform, have been more difficult to obtain in the amounts required for NMR spectroscopy, despite the very good expression yields obtained in rich LB media. A very thorough optimization study of the expression conditions for this protein in NMM is presently an ongoing project at our department.

The typical methodology used for expression of ^{15}N-labelled truncated HRas is as follows:

• From a -80 ºC glycerol stock containing the frozen bacteria, 100 mL of LB containing 50 mg/mL of carbenicilin were inoculated. The pre-culture was grown overnight at 30 ºC with constant aeration and shaking at 200 rpm.

• In the second day, the overnight pre-culture was used to inoculate 5 L of sterile NMM containing 50 mg/mL of carbenicilin. For a better handling, the volume was divided as 2x2.5 L in two Erlenmeyer flasks of 5 L maximum capacity. The culture was grown at 30 ºC, 200 rpm. After reaching an OD_{600} of 0.8-1.0, protein expression was initiated by induction with 0.28 mM IPTG.

Typically, the bacterial growth time is much longer in NMM as compared to the same expression in LB. For example, the time necessary to reach an OD of 0.8 is around 3 hours in LB and 7 hours in NMM. After induction, the cultures were grown overnight at 30 ºC, 200 rpm. For some Ras mutants (D33K, H27E) expression tests determined the best growth temperature to be 25-28 ºC.

• At the third day the cells where harvested by centrifugation during 40-45 min, at 4 ºC, 4000 g. The supernatant was discarded and the bacterial pellet was directly stored at -20 ºC until further use. Cell lysis and the purification of the ^{15}N labeled Ras proteins was accomplished according to the same principle described for the unlabelled proteins (see section 2.2.2.1).

2.2.1.6 Expression of the Effector Protein Raf-RBD

The catalytic domain of Raf-RBD (amino acids 51-131) was expressed in *E. coli* BL21(DE3) as a GST fusion protein using a pGex-4T1 vector. The expression strategy follows the methodology described in section 2.2.1.4 with minor modifications. Briefly, 200 mL of an overnight grown pre-culture, containing 50 mg/mL of carbenicilin were used to inoculate 10 L of LB media containing also 50 mg/mL of carbenicilin. The culture was grown at 37 ºC, 180 rpm, until an OD_{600} of 0.6-0.8 was reached. At this point the growth was slowed down and protein expression initiated by induction of 0.3 mM IPTG. Overnight incubation at 30 ºC was followed by centrifugation of the culture media. The bacterial pellet was frozen and stored at -20 ºC for further use. The cells were lysed and the protein purified by GST-tag affinity chromatography (section 2.2.2.2.2).

2.2.1.7 Expression of the GAP Protein Neurofibromatin 1 (NF1)

The GAP protein NF1 (aa 1198-1531, 35 kDa), a negative regulator of Ras in signal transduction, was expressed as a GST-fusion protein in *E. coli*. BL1DE3. The methodology closely follows the one applied to the expression of Raf-RBD. Inoculation volumes, incubation times and antibiotic concentrations are identical. The purification was accomplished by GST-tag affinity chromatography (section 2.2.2.2.2).

2.2.1.8 Expression of the GEF Protein $SOS^{cat(W729E)}$

The ubiquitous SOS1 was expressed in *E. coli* BL21DE3 in the form of a Histidine tag fusion protein using the pProEx HTb vector. Only the catalytic domain was engineered into the expression vector (aa 566-1049, 55 kDa). The expression was carried in TB medium (section 2.1.5.2).

- A 100 mL pre-culture was prepared by mixing 10.0 mL TB Buffer with 90.0 mL of autoclaved TB medium, containing 50 mg/mL of carbenicilin. The medium was inoculated with the transformed bacteria and the culture was allowed to grow overnight at 30 ºC, 200 rpm.
- 4.5 L of TB medium were autoclaved, followed by the addition of 500 mL of TB buffer, while stirring under sterile conditions (using the laminar flow chamber). To the final medium, 50 mg/mL of carbenicilin were added and the overnight grown pre-culture was used for inoculation. The 5 L volume was divided in 2x2.5 L in two Erlenmeyer's of 5 L maximum capacity. Protein expression was initiated at an OD_{600} of 0.5 by induction with 0.3 mM IPTG. The culture grew overnight at room temperature with constant aeration and speed of 200 rpm.
- Upon overnight incubation, the cells were pelleted by centrifugation at 4 ºC, 4000 rpm and the bacteria stored at -20 ºC until further usage. After cell lysis, the protein was purified by Ni-NTA affinity chromatography described in section 2.2.2.3.2.

2.2.1.9 Polymerase Chain Reaction (PCR)

PCR was mainly used in the scope of this thesis to amplify the DNA sequence of newly created Ras mutants through site directed mutagenesis (section 2.2.1.11). The details of the amplification process (temperature, number of cycles, etc.) were followed according to the instructions provided in the Geneart® Site-Directed Mutagenesis Kit [199]. The reader is referred to the online website of the manufacturer (TermoFisher®) for additional information. A brief description is present below:

• For a single PCR reaction, a pair of oligonucleotides containing the desired point mutation in the middle of the sequence were used as primers (see Table 2.1). They were mixed with 20-25 ng of plasmidic DNA from Ras^{WT} and the deoxyribonucleotides (dATP, dCTP, dGTP dTTP) were added alongside with the thermostable DNA polymerase provided with the kit. These four components were gently mixed and brought to a thermocycler. The general PCR setup is described in Figure 2.1. The denaturation of the double helix was carried out for 2 minutes at 94 ºC, followed by the annealing of the primers to the single stranded DNA at 57ºC for 30 seconds. The synthesis of new DNA took place at 68ºC for 2.5 min. The full cycle was repeated 20 times. The PCR reaction proved to be very effective in most cases. The newly amplified DNA was tested by Agarose gel electrophoresis, purified if necessary, and used directly in the next stages of the site-directed mutagenesis protocol.

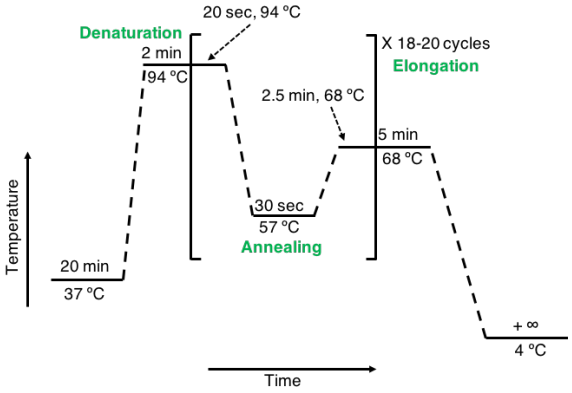

Figure 2.1. Overview of the PCR reaction used for the creation of Ras mutants. Times and temperatures used for each step were optimized accordingly to the size of the amplified plasmid and led generally to good amplification yields. The axes are not up to scale.

2.2.1.10 Agarose Gel Electrophoresis

DNA electrophoresis was routinely carried to assess the quality of PCR products and the purity of isolated plasmids. In this technique, nucleic acids are separated by their molecular mass when subjected to a directional electric field. Their negative charge (due to the phosphate groups of the DNA backbone) promotes their migration from the cathode (negatively charged) to the anode (positively charged). The migration occurs in a polymer matrix made of agarose. The presence of the gel meshwork hinders the progress of the DNA, and small or compact molecules migrate more rapidly than large molecules. The higher the concentration of the gel, the larger molecules are hindered. Consequently, gels of different concentrations are used to separate molecules of different sizes. Ethidium bromide (EtBr), 0.5 μg/μl, is added to the gel for the revelation of the DNA bands. Later in our laboratory it was replaced by Midori green because it is not as health threatening as the first one. Both compounds are dyes that can bind to the DNA fragments and fluoresce with an orange colour under ultraviolet light. The excitation of EtBr can be done directly at 366 nm and indirectly at 254 nm. For Midori green, the excitation occurs at 490 nm. The medium through which the electric current is conducted is either based on a Tris-borate-EDTA (TBE)

or on a Tris-acetate-EDTA (TAE) buffer. Both present their own advantages and disadvantages. TAE is preferred when the DNA is to be used in subsequent enzymatic reactions such as cloning experiments and it is a better conductor of electricity than TBE, being ideal in long runs and in the separation of large fragments. Borat salts from TBE are often inhibitors of many enzymes, which makes this buffer inappropriate if the DNA is to be used in enzymatic reactions.

• 1% Agarose w/v was prepared by mixing 1.0 g of the powder with 100 mL TBE buffer. Upon microwave heating until complete dissolution, the hot liquid was carefully poured in an appropriate chamber and left at 4 ºC for faster solidification. TBE was normally prepared in a 10x stock solution and diluted before usage to 1x (final 1x concentration: 89 mM Tris-base pH 7.6, 89 mM Boric acid and 2 mM EDTA). TAE was rarely used (final 1x concentration: 40 mM Tris/HCl pH 7.6, 20 mM acetic acid, 2 mM EDTA). The DNA samples were mixed with a DNA loading buffer, previously prepared as a 6x stock solution (30% w/v glycerol, 0.25% w/v bromophenol blue and 0.25% xylene cyanol FF). The mixture was properly loaded into the electrophoretic chamber and the gel was run at a constant voltage (100 V for TAE and 200 V for TBE), for approximately 30-40 min.

2.2.1.11 Site-Directed Mutagenesis (SDM)

In vitro site-directed mutagenesis is an invaluable method for glimpsing the complex relationships between protein structure and function, for studying gene expression elements, and for carrying out vector modifications. From the different approaches available to perform this technique, the one chosen in the present work relies on the PCR amplification using the double primer method [200]: for each mutant, two complementary primers (30-45 nucleotides) were designed in such a way that they contained the desired mutated codon in the middle of their sequence (Table 2.1). These primers were directly mixed with the pTac vector containing the codifying sequence for $HRas^{WT}$(1-166) and with all the other necessary elements for the reaction, provided by the Geneart® Site-Directed Mutagenesis kit, from Invitrogen® [199]. These included DNTP's, the *taq* polymerase, DNA methylase and its cofactor S-adenosyl methionine (SAM). All the components were directly used and the protocol provided by the manufacturer was strictly followed. The reaction yields were generally good and no additional purification steps were required at the end. The mutated plasmids were used after the reaction to transform the highly competent DH5α™-TTR-*E. coli* cells, also provided in the same kit. Upon bacterial growth the plasmids were isolated and tested for the mutation through DNA sequencing using the Sanger method.

2.2.2 Protein Biochemistry

2.2.2.1 Purification of Ras Proteins

Due to the different isoforms and Ras mutants that were studied in the scope of this thesis, it is impossible to provide a detailed purification methodology for each one. Nevertheless, most of the methodologies employed are common to all of them, with the exceptions on details such as concentrations, temperature, salt gradients used, etc., which were sometimes fine-tuned according to the characteristics of a specific mutant or changed more drastically from truncated to full length Ras proteins.

2.2.2.1.1 Cell Lysis

All Ras proteins were expressed, secreted and folded into the bacterial cytoplasm. Because they are not directly secreted into the surrounding medium, *E. coli* must be subjected to disruption of their wall and membrane as a means to retrieve them. Some proteins however are expressed as a form of inclusion bodies and therefore not secreted directly into the cytoplasm or to the exogenous media. Although not being the case with Ras, the reader is referred to the possibility of occurrence of this situation. In such cases, a purification in denaturing conditions can retrieve the proteins from the inclusion bodies, provided that they are able to re-fold into their native conformation [201].

In the case of Ras, cell lysis was accomplished by employing firstly a chemical disruption strategy, followed by a mechanical disruption one:

• Using a 500 mL beaker, the frozen bacterial pellet from a 10 L LB culture was dissolved in 200 mL of lysis buffer at room temperature, with constant stirring. The lysis buffer (buffer B, Table 2.4), is prepared by mixing 32 mM Tris/HCl pH 7.5, 5.0 mM Ethylenediaminetetracetic acid (EDTA), 2.0 mM Dithioerythritol (DTE) and 1.0 mM phenylmethane sulfonyl fluoride (PMSF).

EDTA is capable of chelating metal ions with a +2-charge making them unavailable as co-factors of some proteases and DNAses, leading to a reduction of the catalytic activity of those enzymes. PMSF is a serine protease inhibitor. This compound is very unstable in aqueous solutions, having a half-life of 110 min. at pH 7 and 25 ºC. Its activity is therefore rapidly reversible. For more demanding cell lysates, the reader is referred to the alternative AEBSF, an isomer with irreversible inhibitory activity. (Both compounds are neurotoxins and should be handled with care) [202]. DTE is a sulphur containing sugar from the corresponding saccharide erythrose, capable of reducing disulphide bonds of proteins and, more generally, to prevent intramolecular and intermolecular disulphide bonds from forming between cysteine residues [203]. DTT, an epimer of DTE with a slightly higher reducing

potential, can also be used with the same practicality. As a general rule, DTE was added to all the intermediate and final storage buffers (typically in a 0.2 mM concentration).

• After resuspension of the bacterial cells, the beaker was placed at 4 ºC with constant stirring and the chemical lysis process was initiated by adding lysozyme, 1.0 mg/mL. This enzyme catalysis the hydrolysis of 1,4-β-linkages between N-acetylmuramic acid (NAM) and N-acetyl-D-glucosamide (NAG) that comprise the peptidoglycan, leading to the disruption of the bacterial wall [204]. For the next steps of the lysis, ca. 15-20 minutes were waited before the addition of the next component to the cell suspension.

• After the elapse of the above-mentioned time, 8.0 mL of 6% Na-deoxycholic acid were added to the 200 mL lysate. Deoxycholate is an anionic detergent that helps in the denaturation and solubilisation of highly hydrophobic molecules and membranar proteins. Its effect leads to a further disruption of the cell wall [205]. The suspension should have a viscous appearance at this stage.

• In a last step, 20.0 mg per 100 mL of cell suspension of DNAse were added. This enzyme catalysis the hydrolytic cleavage of phosphodiester linkages in the DNA backbone, thus degrading the nucleic acids [206]. It was sometimes necessary to add a small amount of Mg to the cell suspension, normally in the form of $MgCl_2$ (from 2 to 10 μM), because the active DNAse requires Mg^{2+} as co-factor. The cell lysate should have a fluidic, water-like, behaviour by the end of this step. Whenever presented still with appreciable viscosity, some steps of the chemical lysis were repeated (e.g. adding extra lysozyme and/or Na-deoxycholate).

Perhaps because in most of the cases, mechanical and chemical lysis are redundant processes, it is common practice when working with cell lysates, to use only one of them and, generally, one will suffice for the intended purposes. Nevertheless, in the present work a short mechanical disruption was always applied to the cells, to ensure complete effectiveness:

• The beaker containing the suspension was brought on ice to an ultrasonic pulse device. This method induces strong pressure changes and shear forces which lead to further destruction of the cellular structure. Temporary heat spots on the sample are created in the process, which can be harmful for the stability of the overexpressed protein. To prevent that, the disruption was accomplished by keeping the cells all the time on ice and by applying short pulse bursts (typically 5 pulses of 10 seconds each).

• Following the mechanical disruption, the bacterial fragments were separated by centrifugation from the lysate containing the soluble cellular proteins. The process was

carried out at 4 ºC and at 50000-60000 g for ca. 1 hour. The clear, deep yellow supernatant was brought to a clean Erlenmeyer and used immediately in the next purification step.
The lysis of the cells containing uniformly ^{15}N-labelled overexpressed Ras followed the exact same methodology.

2.2.2.1.2 Protein Precipitation with $(NH_4)_2SO_4$

Cell lysates of overexpressed FL Ras proteins (aa 1-188/189) from a single 10 L cell culture were typically subjected to $(NH_4)_2SO_4$ precipitation to capture Ras at an early stage of the process. This method was not applied to truncated Ras variants (aa 1-166) since, from experimental evidence, they are not prone to precipitate as easily as the FL ones.
The solubility of globular proteins is normally increased upon addition of salt (< 0.15 M), an effect termed salting in [207]. However, at higher salt concentrations, the protein stability decreases leading to precipitation. This is commonly referred as salting out [208]. Salts that reduce the solubility of proteins also tend to enhance the stability of the native conformation, as opposed to salting-in ions which are usually denaturants. The mechanism of salting-out is based on preferential solvation due to exclusion of the co-solvent (salt) from the layer of water closely associated with the surface of the protein (hydration layer), which plays a critical role in maintaining solubility and the correctly folded native conformation. There are three main protein-water interactions: ion hydration between charged side chains (e.g., Asp, Glu, Lys), H-bonding between polar groups and water (e.g., Ser, Thr, Tyr, and the main chain of all residues), and hydrophobic hydration (Val, Ile, Leu, Phe). In hydrophobic hydration, the configurational freedom of water molecules is reduced in the proximity of non-polar residues. This ordering of water molecules results in a loss of entropy and is thus energetically unfavourable. When salt is added to the solution, the surface tension of the water increases, resulting in increased hydrophobic interaction between protein and water. The protein responds to this situation by decreasing its surface area in an attempt to minimize contact with the solvent—as manifested by folding (the folded conformation is more compact than the unfolded one) and then self-association leading to precipitation. Both folding and precipitation free up bound water, increasing the entropy of the system and making these processes energetically favourable [208]. The increase in surface tension of water by salt follows the Hofmeister series [209]. As an approximation, those salts that favour salting-out raise the surface tension of water the highest. As $(NH_4)_2SO_4$ has much a higher solubility than any of the phosphate salts, it is the reagent of choice for salting-out. The methodology is described as follows:

• After purification by IEX chromatography, the fractions containing Ras were identified by SDS-PAGE and pooled together into a clean Erlenmeyer flask. Typically, their combined volume was 400-500 mL.

• The amount of $(NH_4)_2SO_4$ necessary to induce precipitation in a 3-3.5 M salt solution was calculated (ca. 200-250 g for a 500 mL volume) and added to the pooled fractions in a stepwise manner, with an waiting time of 15-20 min. between the next addition, (2-3 spoons each time). The entire process took place with continuous slow stirring, at 4 ºC.

• HRas(1-189) precipitated at its maximum for a salt concentration of 3.1 M. When this value was reached, the solution was completely slurry and further addition of salt had no effect on the extent of precipitation (care was taken to not overcome too much this this value, as the opposite effect – an increase in solubility – can sometimes happen).

• The slurry was centrifuged at 4 ºC, 20000 g, for ca. 40-50 min. The supernatant was decanted and stored for further analysis by SDS-PAGE and the precipitated protein fraction was slowly re-dissolved in the smallest possible volume of buffer D (typically 15-18 mL, Table 2.4) and immediately used in the next purification step.

2.2.2.1.3 Ion Exchange Chromatography (IEX)

IEX is based on the electrostatic attraction between proteins in solution and charged groups of the ion exchanger (a matrix with acidic or basic functional groups). The strength of such interaction depends on the charge of these two partners, the dielectric constant of the medium (*D*) and the competition from other ions for the charged groups of the ion exchanger and protein. When the concentration of the competing ions is low, the proteins adsorb to the ion exchanger. When it is high, the proteins are desorbed. The most common variation of such interplay is the adsorption of target proteins from a buffer of low ionic strength, followed by desorption with a buffer of high ionic strength. At higher concentrations of competing ions, the proteins with the weakest interaction will be displaced first. There is no general rule as to what salt concentration is needed to displace a protein with a certain net charge from an ion exchanger. However, most proteins are eluted at salt concentration lower than 1.0 M [210].

The physical mechanism behind protein binding to charged surfaces is not completely understood and can be tentatively explained according to different models: In the simplest approach, called the stoichiometric model of Boardman and Partridge [211], a number of charged groups bind to the same number of oppositely charged groups of an ion exchanger. In this process counter ions are released from both. This model assumes that one group on the protein interacts with just one group in the ion exchanger.

In chromatography, substances alternate between being bound to the stationary phase and moving in the mobile phase. The stationary phase in IEX is a column and the mobile phase a buffer. A substance that spends more time in the stationary phase moves slower. Substances that do not bind to the adsorbent are constantly in the mobile phase. They pass through un-retarded and are, strictly speaking, not submitted to chromatography. This happens when the ionic strength is so high that it eliminates the electrostatic attraction to the ion exchanger and with molecules with no charge or a charge of the same sign as the ion exchanger [210]. Other factors other than the net charge can influence IEX such as the charge distribution on the protein surface, the nature of the particular ions on the solvent (according to the Hofmeister series [209]) and non-electrostatic interactions with the ion exchanger (hydrophobic interactions, H-bonding), the temperature and the presence of additives such as organic solvents as for example acetonitrile (ACN) and methanol (MeOH) leading to an increase of electrostatic interactions.

Ion exchangers consist of a matrix with either acidic or basic groups on the attached ligand. The matrices can be roughly divided into hydrophilic and hydrophobic. Hydrophilic ones are best suited for protein chromatography, since the interaction due to hydrophobic forces is weak and proteins are often irreversibly adsorbed (or denatured in the process of desorption) to hydrophobic matrices, such as polystyrene. Typical hydrophilic matrixes used in IEX separation of proteins are agarose or sepharose. The latter was used in the present work and is based on chains of agarose, arranged in bundles and with different degrees of cross-linking to give a range of rigid, macroporous matrices with good capacity and low nonspecific adsorption.

The functional groups substituted onto a chromatographic matrix determine the charge of an IEX medium: basic ion exchangers are called anion exchangers and contain positive groups. Acidic ion exchangers are called cation exchangers and contain negative groups. Ras has a negative surface net charge at pH 7.5 and therefore binds to anion exchangers. A strong anion exchanger was chosen for Ras purification: the quaternary ammonium (Q), based on 90 μm agarose beads, with the $–CH_2N^+\text{-}(CH_3)_3$ functional group. Another group, DEAE sepharose, ($\text{-}CH_2\text{-}CH_2\text{-}N^+\text{-}(CH_2\text{-}CH_3)_2$), is an example of a weak anion exchanger. Similarly, weak (carboxymethyl - CM) or strong (sulphopropyl - SP) cation exchangers are available, among many others. The reader is advised to consult an updated online list provided by manufacturers [212].

It is worth mention that despite the ion exchangers being usually classified as weak or strong, the name refers to the pK_a values of their functional groups, and indicates nothing regarding their ability to bind proteins. At pH values far from the pK_a protein binding can be

equally strong to either a weak or a strong ion exchanger. Strong ion exchangers show no variation in ion exchange capacity with change in pH, remaining fully charged over a broad pH range. A direct advantage of a strong exchanger lies in the sample loading (binding) capacity, which is maintained at high or low pH since there is no loss of charge from the ion exchanger. Also, the interaction mechanism is simple, as there are no intermediate forms of charge interaction. Most proteins have a pI within the range 5.5 to 7.5 and can be separated on either strong or weak ion exchangers. An advantage of a weak ion exchanger, such as DEAE (anionic) or CM (cationic) is that they can offer a different selectivity (i.e. the ability of the system to separate peaks, the distance between two peaks) compared to strong ion exchangers. A disadvantage arises from the fact that weak ion exchangers can take up or loose protons with changing pH, their ion exchange capacity varies with pH.

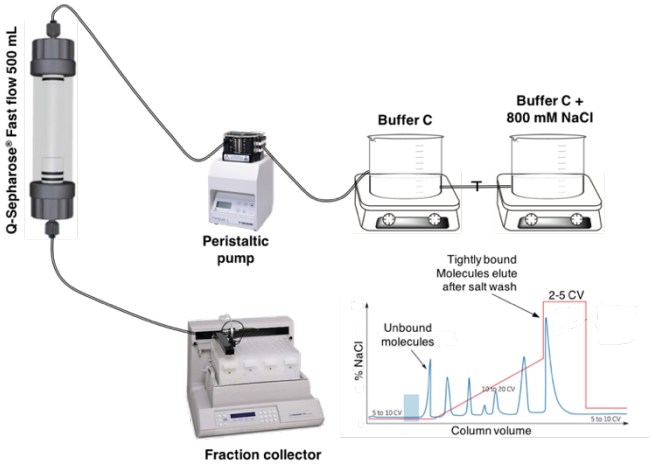

Figure 2.2. Schematics of the experimental setup mounted for the purification of Ras proteins from a 10 L cell culture. After loading the 500 mL Q-sepharose column and washing the unbound molecules, a linear salt gradient was applied to it with aid of a peristaltic pump and at constant stirring: to the low ionic strength buffer C (left container) a high ionic strength buffer C + 800 mM NaCl (right container) was gradually mixed. The elution proceeded overnight using a fraction collector. The red line on the chromatogram indicates the percentage of NaCl during the overall process. The shaded area represents the sample injection volume. The chromatogram does not correspond to a real Ras purification, since the present setup has no detector for absorbance measurement at 280 nm. Adapted from gehealthcare.com

Normally, the concentration of buffer salts during protein adsorption is low (10–50 mM). Proteins adsorbed at a salt concentration too far below desorption concentration can be difficult to desorb and some denaturation can occur. A suitable adsorption concentration can be determined by simple test tube experiments (1-1.5 mL of ion exchanger were equilibrated with the starting buffer and mixed for 1-2 min. with the sample equilibrated in the same buffer. After centrifugation the supernatant was assayed for the protein to determine the level of binding). The residence time on the column can also affect elution. Proteins adsorbed to a column for prolonged periods may be more difficult to elute than proteins desorbed shortly after adsorption.

Below is presented the methodology employed in the purification of Ras proteins:

• After cell lysis, overexpressed protein was purified using Q-Sepharose® Fast Flow™ from GE Healthcare. Two columns of different dimensions were used, depending on the volume of cell lysate: FL Ras was generally expressed in 10 L cell culture batches. The

corresponding 300-380 mL cell lysates were loaded into a 500 mL column (herein defined as column A). Truncated Ras proteins were generally expressed in 5 L batches and the corresponding 150-180 mL cell lysates were loaded into a 280 mL column (herein defined as column B). Both columns were previously equilibrated with 3-5 column volumes (CV) of buffer C (32 mM Tris/HCl pH 7.5, 10 mM $MgCl_2$, 2 mM DTE).

Column B was mounted on a AKTA-FPLC system. The development of the method was done from scratch in this case (from the building of the column to the details of the run) and care was taken to make the process as automated as possible. Column A, due to its bigger dimensions, could not be mounted on AKTA. In such case, the purification was handled by 'manually' setting up a chromatographic separation system inside a 4 ºC refrigerated room. The schematics of the setup are presented in Figure 2.2.

- The clear cell lysate was loaded at low flow rates (ca. 1.5-2.0 mL/min.) to increase the residence time and to avoid high backpressure (especially in column B). Unbound material, including neutral or positively charged molecules was washed with 2-4 CV of buffer C.
- The elution of Ras proceeded by two different methods, according with the type of column used. In both cases a salt gradient elution was done by using Buffer C in the presence of 800 mM NaCl. Column A was eluted with a linear salt gradient mostly due to the limitation of the available experimental setup (Figure 2.2) and column B was eluted using a step gradient profile, previously optimized. Often, a small-scale test tube experiment was performed for a specific Ras mutant and the steps of the gradient were slightly adjusted if necessary. Figure 2.3 shows the step gradient used in the purification of truncated $HRas^{D33K}$ as general example. The eluted fractions were collected overnight with a fixed volume of 18-20 mL (column A) and 12 mL (column B).
- The collected fractions were analysed by SDS-PAGE and immediately used in the next purification step.
- After elution both exchangers contained some material bound (often denatured or precipitated proteins). They were regenerated by extensively running a 2.0 M NaCl solution at low flow rates during 2-3 CV, followed by a thorough washing with 5-10 CV of ultrapure H_2O. Periodically (every 5 runs or so), the columns were further cleaned with NaOH 0.5-1.0 M at room temperature, followed by water and 50% ethanol (EtOH) to remove lipoproteins and lipids. Blank runs, in which only buffers, but

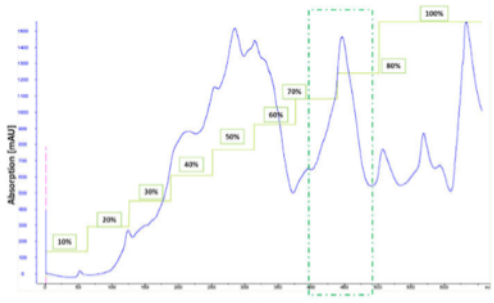

Figure 2.3. Representative Ras elution profile from IEX using a NaCl step gradient with volume fractionation. The peak surrounded by the dashed lines corresponds to the elution of Ras^{D33K}.

no sample, are applied to the columns were also performed periodically (every 10 runs) to determine the presence of the contaminants after a cleaning protocol

• Finally, the columns were transferred to 20% EtOH for storage to avoid stagnation and to minimize chance of microbial growth. After a long period (more than 5 weeks), they were opened on the top and recirculation or agitation of the resin was performed with the aid of a glass rod.

2.2.2.1.4 Size Exclusion Chromatography (SEC)

Gel filtration, also called size exclusion chromatography is a method that separates molecules according to their differences in size, as they pass through a matrix packed in a column. Unlike ion exchange or affinity chromatography, molecules do not bind to the matrix so buffer composition does not directly affect the resolution (degree of separation between peaks). In addition to separate molecules by size, SEC has proven to be a valuable tool for a variety of applications, especially to determine the molecular mass of macromolecules, despite the diversity of available methods (mass spectroscopy, dynamic light scattering, analytical centrifugation, etc.) due to its versatility and ease of establishment in a modern laboratory by integration with an AKTA system (Figure 2.4). It can also be used for desalting a reaction mixture, purification of a monomer from a multimer, and to study protein-protein interactions. SEC can be used in *group separation mode* to remove small molecules from a group of larger molecules and as simple solution for buffer exchange or in *fractionation mode*, to separate multiple components on a sample based on their Mw. Different factors affect the resolution in SEC (i.e. the degree of separation between peaks): sample volume, sample-to-column volume ratio, column dimensions, particle size, packing density, pore size of the particles, flow rate and viscosity of the sample and buffer. The sample volume is expressed in terms of percentage of the total column volume (packed bed). Generally, the application of a sample volume between 0.5-4% of the packed bed is recommended for peak fractionation. The capacity of the SEC separation can be increased by concentrating

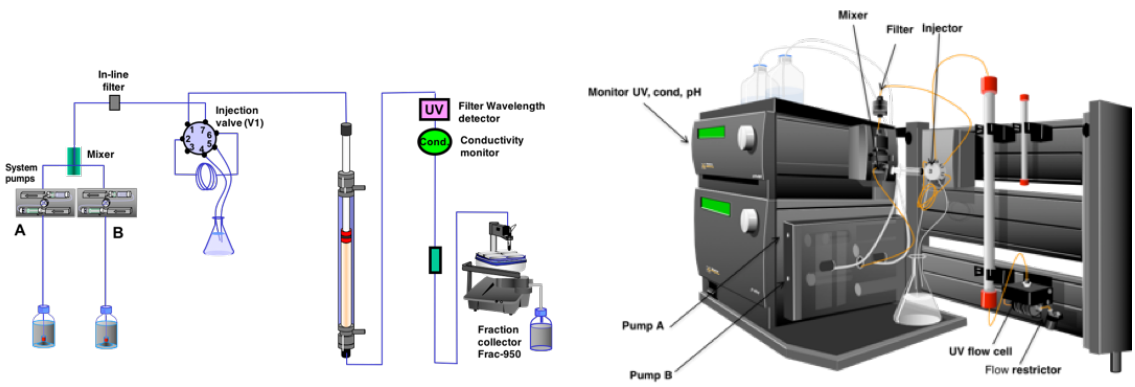

Figure 2.4. General schematics of the AKTA FPLC system. Adapted from "GE imagination at work".

the samples to be injected, although concentrations above 70 mg/mL are not recommended. The height of the packed bed increases both, resolution and the time of the run. However, a common problem of increasing bed height is the build up of back pressure due to the tightly packed media.

The materials presently used for SEC are based on silica, hydrophilized vinyl polymers, or highly crosslinked agarose with bead sizes typically between 5 and 50 mm. The selectivity of the medium depends solely on its pore size distribution. For the present work, the medium of choice was Superdex™, a highly cross-linked porous agarose to which dextran was covalently bound. Depending on the sample volume, two SEC columns of different bed heights were used for Ras purification: 120 mL Hiload Superdex 26/60 75 PG, with a separation range between 3-70 kDa at a flow rate of 1.5 mL/min. and a 300 mL Hiload Superdex 26/600 200 PG with a separation range between 10-600 kDa at a flow rate of 2.2 mL/min.

Following ion exchange chromatography (section 2.2.2.1.3), the fractions containing the Ras protein were pooled and concentrated by ultracentrifugation or subjected to $(NH_4)_2SO_4$ precipitation.

- typically, ca. 5 mL of concentrated sample were manually injected (by using an adequate loop) into a superdex 26/60, previously equilibrated with buffer D (40 mM Tris/HCl pH 7.4, 10 mM $MgCl_2$, 400 mM NaCl, 2 mM DTE, 0.1 mM GDP, Table 2.4). A safety upper pressure limit on the AKTA pump system was set to 0.4 MPa and the isocratic elution initiated with the same buffer. 3.0 mL fractions were collected after 0.2 CV, until a total length of 1.4 CV. This process was repeated 4 or 5 times for the complete purification of the 20-25 mL of the initial protein mixture.
- Typical SEC chromatograms led to the straightforward identification of the Ras proteins, in single, narrow peaks. The fractions underlying the peak area were pooled and concentrated up to a final value of 3.6 mg/mL (2.0 mM). When the identification of Ras by simple evaluation of the chromatogram was ambiguous, a final SDS-PAGE was performed.
- The pure, concentrated Ras proteins dissolved in buffer D were shock frozen in liquid N_2 and stored at -80ºC in 500-600μl aliquots until further use.
- The SEC columns were cleaned according to the same protocol used for IEX (section 2.2.2.1.3). In cases of severe contamination the flow was reversed and the cleaning procedure applied.

2.2.2.2 Purification of Raf-RBD and NF1

Raf-RBD and NF1 333 were both expressed as GST-fusion proteins in *E. coli* BL21DE3. The purification methodology used follows the same principles for both proteins

2.2.2.2.1 Cell Lysis

- The frozen cell pellet from a 10 L cell culture was re-suspended in 200 mL of lysis buffer (50mM Tris/HCl pH 7.5, 250 mM NaCl, 5 mM EDTA, 1mM PMSF, 5mM DTE). NaCl is an important stabiliser of both proteins. During the lysis, its concentration was gradually increased overtime, from 250 mM up to 300 mM.
- The cell pellet was left stirring at room temperature for ca. 15 min. until complete dissolution. The mixture was then kept at 4 ºC with constant, slow stirring. The chemical and mechanical cell lysis was carried out as described elsewhere (section 2.2.2.1.1).
- After lysis, the cell fragments were sedimented by centrifugation at 4 ºC, 25000g for ca. 30 min. The yellow coloured supernatant was decanted from the bacterial precipitate and brought immediately to a 25 mL glutathione sepharose column.

2.2.2.2.2 Affinity Chromatography: GST Fusion Purification

Glutathione-S-transferase (GST) fusion proteins are purified by affinity chromatography using glutathione (GSH) immobilized to a matrix such as sepharose. The binding of a GST-tagged protein to the GSH ligand is reversible, and the protein can be eluted under mild, non-denaturing conditions by the addition of reduced GSH to the elution buffer. This technique provides a mild purification process that does not affect a protein's native structure and function. Figure 2.5 shows a schematic representation of the terminal structure of GSH sepharose.

One of the most important parameters affecting the binding of the GST protein to the solid matrix is the flow rate at which the protein loading is performed. The binding kinetics between GSH and GST is slow, thus it is important to keep a low flow rate (normally lower than 1mL/min.). Washing and elution can be performed at a slightly higher flow rates to save time (2-3 mL/min. using GST sepharose™). The yield of the fusion protein in pure samples can be estimated by A_{280}, giving that the concentration of the GST tag is approximately 0.5 mg/mL for 1 unit of absorbance.

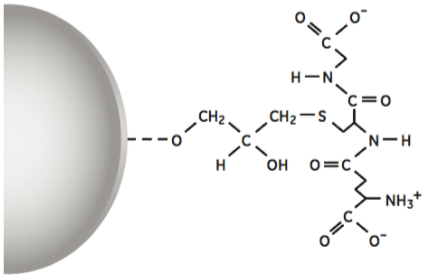

Figure 2.5. Terminal structure of Glutathione Sepharose. Glutathione is specifically and stably coupled to Sepharose by reaction of the SH-group with oxirane groups obtained by epoxy-activation of the Sepharose matrix. The structure of glutathione is complementary to the binding site of glutathione S-transferase. Adapted from GE.healthcare.

The methodology used for the two proteins is presented bellow:

• The corresponding cell lysate was loaded into a 25 mL GSH sepharose® fast flow™ column, previously equilibrated with 3-4 CV of 50 mM Tris/HCl pH 7.5, 250 mM NaCl and 5mM DTE. The sample was loaded at a flow rate of 0.8 mL/min. with the help of a peristaltic pump. The entire process took place inside of a 4 ºC room. Due to the big volume involved (150-200 mL), the AKTA system was not used for the loading of the lysate into the column.

• After protein loading, unbound material was removed by equilibration with the same buffer during 5 CV at 0.8 mL/min.

• The cleavage of either Raf-RBD or NF1 from the GSH column was done by the addition of 10U of thrombin per 2 mg of fusion protein (estimated by A_{280} - thrombin has a specific activity higher than 7500 U per mg of protein. 1U of this protease will digest more than 90% of 100 μg of a test fusion protein in 16h at 22ºC). Cleaving of the fusion protein was allowed to proceed 'on the column', overnight at a very slow rate (0.3 mL/min.). The circuit was closed by connecting the top end to the bottom end of the column. The continuous re-circulation of the mobile phase through the system was ensured by a peristaltic pump.

• Following up next day, the closed circuit was opened and the final protein (Raf-RBD or NF1), now cleaved from GST, was immediately collected into 3 or 4 fractions of 25 mL each, using the same buffer as above.

• The GST bound protein was removed from the column by washing with 6M guanidine hydrochloride (GdmCl), 4-5 CV, followed by 5-10 CV of ultrapure H_2O.

• Oxidized GSH sepharose was restored by equilibrating the column with a 30 mM reduced GSH solution in 100 mM Tris/HCl pH 7.5, for at least 2 CV. (Note that reduced GSH is acidic. The pH was properly adjusted with NaOH during the preparation of this solution). Finally, excess of GSH was removed by equilibration with ultrapure H_2O, rendering the column ready to be re-used. For long term storage, the column was equilibrated with 20% EtOH.

• All the fractions (equilibration, protein loading, elution, column recovery) were stored during the entire process and analysed by SDS-PAGE.

In the final polishing step, both Raf and NF1 were further subjected to SEC chromatography to separate them from thrombin and other possible impurities. The pure protein fractions were aliquoted in 200 μl fractions, shock frozen in liquid N_2 and stored at -80 ºC. Raf-RBD is very stable and was stored in high concentrations, up to 6.5 mg/mL (7 mM). However, NF1 has a rapid degradation time. In fact, NF1 cannot withstand room temperatures and the purification process needs to be accomplished in the shortest time possible to avoid further degradation. Care was taken while concentrating the protein to avoid further losses.

From experimental evidence, the protein cannot be concentrated to higher values than 0.6-0.7 mM (21-24 mg/mL), otherwise precipitation will occur.

2.2.2.3 Purification of $SOS^{cat(W729E)}$

The catalytic domain of SOS^{W729E} was expressed in *E. coli* BL21DE3 in the form of a histidine-tag fusion protein (His-tag).

2.2.2.3.1 Cell Lysis

The pelleted cells from a 5.0L *E. coli* culture were dissolved in 100 mL of 25 mM Tris/HCl pH 7.5, 500 mM NaCl, 20 mM imidazole, 1mM PMSF and 2 mM β-mercaptoethanol. Chemical and mechanical cell disruption was accomplished according to the steps described above for the cell lysis of Ras proteins (section 2.2.2.1.1). By the end of the process, the cell suspension was subjected to centrifugation at 4 ºC, 50000g for approx. 50 min. The clear cell lysate was decanted from the bacterial pellet and loaded immediately in a Ni-NTA affinity column.

2.2.2.3.2 Affinity Chromatography: Histidine-Tag Methodology

Recombinant SOS contains a tag with six histidine residues ($histidine_6$) that feature a high selective affinity for Ni^{2+} and several other metal ions (Zn^{2+}, Co^{2+}) capable of being immobilized on a chromatographic media using chelating ligands. Consequently, a protein containing a His-tag will be selectively bound to metal-ion-charged media such as Ni-Sepharose®, while other cellular proteins will not bind or will bind weakly. Column equilibration, protein loading and elution takes place in a similar way as described above for GST-fusion proteins (section 2.2.2.2.2). The elution step is performed in the presence of imidazole that competes with the recombinant protein for binding to the Ni^{2+} ions. Equilibration and sample buffers are normally complemented with a low concentration of imidazole to reduce the non-specific binding of host cell proteins and the elution can be done as a linear gradient of Imidazole concentration or as a step-gradient. The method of choice should be adjusted beforehand and the final concentration of imidazole to be used is dependent on the characteristics of the recombinant protein. As a general rule, 500 mM imidazole ensures a complete elution of most His-tagged proteins. An alternative is a pH dependent elution that works on the basis that at pH values close to 4.5, the metal ions will be stripped out from the medium. The choice of this alternative depends of course on the tolerance of the protein for low pH values. Chelating agents such as EDTA and EGTA are to be avoided in this chromatographic process as they can strip down the metals from the

column.

The strategy used in SOS purification is described as follows (the complete work was performed in a 4 ºC refrigerated room):

• A 5.0 mL Ni-Sepharose® column connected to a peristaltic pump was equilibrated with the lysis buffer above mentioned (25 mM Tris/HCl pH 7.5, 500 mM NaCl, 20 mM imidazole, 1mM PMSF, 2 mM β-mercaptoethanol), followed by protein loading and removing of unbound material (15-20 CV) with the same buffer at a very low flow rate (0.3-0.5 mL/min.).

• Elution of SOS was accomplished in a single step by preparing a buffer containing 25 mM Tris/HCl pH 7.5, 500 mM NaCl, 2mM β-mercaptoethanol and 500 mM imidazole.

• After elution, the column was regenerated by washing with 10CV of biding buffer.

All the fractions were collected and analysed by SDS-PAGE. Fractions containing SOS were pooled, concentrated and purified by SEC that in this case served two purposes: further purification and polishing from minor contaminants and change the final buffer of the protein, allowing the removal of the high imidazole concentration. Collected fractions from SEC were analysed by SDS-PAGE, pooled, concentrated up to 16 mg/mL (0.3 mM) and aliquoted in 200 μl fractions. The protein was shock frozen in liquid N_2 and stored at -80 ºC. The final storage buffer (after SEC) was 40 mM Tris/HCl pH 7.5, 10 mM $MgCl_2$, 2 mM DTE, 150 mM NaCl.

2.2.2.4 Nucleotide Exchange Reactions

Recombinant Ras is obtained in the GDP-bound form. Although, to study the structure, dynamics and conformational equilibria of other nucleotide-bound forms, a simple but reliable methodology for exchanging the nucleotides was developed. The same methodology and can also be applied to other GNBP's such as Rap and Arf.

2.2.2.4.1 GDP Against GppNHp

There are two different ways to accomplish this task. The first one can be considered the 'classical' method of exchanging the protein and involves an overnight incubation of Ras with alkaline phosphatase (AP). Because both proteins are mixed in a solution, the main disadvantage of this method lies in the difficulty of completely separating both, Ras and AP, by SEC at the end. This was especially problematic for Ras samples that were studied by HP NMR, where sometimes fast hydrolysis of the bound GppNHp was observed and resulting from contamination with AP, even if residually present in the sample.

In an attempt to solve this problem, a second methodology was developed, involving the use of an immobilised AP into a solid matrix.

Exchanging GDP to GppNHp in the 'classical' way.

• Ras has an extremely high affinity for nucleotides ($K_D \sim 10$ pM). This affinity is highly dependent of Mg^{2+} ions and in their absence it decreases by more than 30 times [213]. Thus, in the first step of the process, Mg^{2+} ions were removed from the solution either by several ultracentrifugation steps (using 5.0 mL vivaspin concentrators with an adequate molecular cut-off) or by a small size exclusion chromatography using PD10 columns. In any choosen approach the result was equivalent: Ras-GDP previously stored in buffer D (40 mM Tris/HCl pH 7.5, 10 mM $MgCl_2$, 2 mM DTE, 0.1 mM GDP) was exchanged to buffer E (40 mM Tris/HCl pH 7.5, 2 mM DTE).

• The concentration of the GDP-bound protein now in buffer E was calculated by HPLC (section 2.2.2.6.3) and a 3-fold excess of the non-hydrolysable analogue GppNHp was added, followed by the addition of 200 mM of $(NH_4)_2SO_4$. Finally, 2U of AP per mg of Ras were added. AP catalyses the nucleophilic attack by the water to the phosphate groups, facilitating the dephosphorilation of GDP but not GppNHp. As Ras has a low affinity to the newly formed GMP, a dynamic equilibrium is established in which the nucleotide-free Ras rapidly incorporates the available GppNHp in its binding pocket.

• After overnight incubation with slow shaking at 4 ºC, the completeness of the reaction was verified by HPLC and purification of Ras-GppNHp from by-products (GDP, GMP, guanosine) was done by using either a PD10 or a bigger SEC column connected with the AKTA systems, which allowed the reincorporation of $MgCl_2$ into the final buffer: 40 mM Tris/HCl pH 7.5, 10 mM $MgCl_2$, 2 mM DTE (Buffer F).

• The final concentration of Ras•Mg^{2+}•GppNHp was adjusted by HPLC to the desired value, the exchanged protein shock frozen in liquid N_2 and stored at -80 ºC until further use.

Exchanging GDP to GppNHp using immobilized AP.

This method relied on the use of immobilized AP columns provided by MoBiTec®, which were handled according to the manufacturer's instructions. Ras-GDP proteins were exchanged to buffer E, their concentration measured by HPLC and a 3-fold excess of GppNHp, together with 200 mM of $(NH_4)_2SO_4$ were added, exactly as described above. However, no AP was added. Instead, the 1.5-2.0 mL final solution was brought to the immobilized AP, previously equilibrated in buffer E. Due to the small size of the column, 150 µl of sample were injected each time with the help of a syringe and a small needle. Between each injection a minimum waiting time of 15 min. was held, so that the loaded sample could have enough contact time for the reaction to happen. Elution was simply done by loading the next 150 µl of sample into the column or by pushing air with a syringe (there is no

harmful effect if the column runs dry). The eluted fractions were all collected in the same 1.5-2.0 mL Eppendorf tube and the completeness of the process was evaluated by HPLC. If GDP was still present, the procedure was repeated by passing again the protein through the column. The purification of newly GppNHp-bound Ras and the re-incorporation of Mg^{2+} was done using a PD10 column. The final exchanged protein was stored in buffer F, with the desired concentration.

The immobilized AP method allows the exchanged proteins to be virtually free of AP that could otherwise affect the stability of the bound nucleotide. The process is also faster than the 'classical' way since no overnight incubation is needed.

2.2.2.4.2 GDP Against GTP

Exchanging Ras-GDP to Ras-GTP proceeds in a similar way as the one described above, with the exception that AP cannot be added since it would also hydrolyze GTP. Instead, a great excess of GTP is added, with the expectation to shift the equilibrium towards the Ras-GTP complex:

- After removing Mg^{2+} from the initial buffer D and adding 200 mM of $(NH_4)_2SO_4$, as described above 20 mM EDTA were added (helping further in the chelation of possible residual free Mg^{2+} ions) along with GTP in a 30 to 50-fold excess relative to GDP. The mixture is left for 3-4 hours, slowly shaking, at 4 ºC.
- After the elapse of this time, the free nucleotides were separated from the protein using the same process described above and the GTP-bound/GDP-bound ratio quantified by HPLC. Typical Ras^{WT} proteins have a 70-80% exchange. Oncogenic mutants such has G12D or G12V can achieve 90-95%. It is worth note that, contrary to GppNHp, 100% exchange is never possible in this case.
- The final Ras•Mg^{2+}•GTP was stored in buffer F, at -80 ºC until further use.

2.2.2.5 Polyacrylamide Gel Electrophoresis (SDS-PAGE)

Protein gel electrophoresis was routinely carried to check the success of protein purification. In this technique, proteins become denatured in the presence of sodium dodecylsulfate (SDS), losing their secondary and tertiary structure. SDS is a strong anionic detergent that wraps around the polypeptide backbone when heated at high temperature. The intrinsic charges of the polypeptides become negligible when compared with the negative charges contributed by SDS. The protein-SDS complexes become rod-like structures with a uniform negative charge density and their electrophoretic mobility becomes only a linear function of their molecular masses. In the presence of a directional electric field, small size proteins

move faster than bigger proteins, from the cathode (negatively charged) towards the anode (positively charged). The medium where the electrophoretic movement occurs is a gel made of a polymer matrix called polyacrylamide produced in the laboratory by cross-linking acrylamide with bisacrylamide. This requires a radical initiator and a catalyst to take place in a few minutes instead of several hours. The radical used was normally ammonium persulfate (APS) and the catalyst was Tetramethylethylenediamine (TEMED). The latter reacts with APS and causes the splitting of persulfate ions into sulphate free radicals responsible for initiating the polymerization.

The proteins were loaded firstly into a stacking (or collecting) gel and subsequently separated in a running gel. Typically, the stacking gel has a low concentration of acrylamide and a pH of 6.8 and the running gel a higher concentration of acrylamide (that retards the movement of proteins) and a pH of 8.3. To conduct the current from the cathode to the anode a medium was needed. This medium can be continuous (if the buffer, in the electrophoretic tank and in the gel, is the same) or discontinuous (if the buffer is different). The continuous method was proposed by Lämmli *et al* in 1970 [214] and the discontinuous method was proposed by Schägger *et al* in 1987 [215]. The first is more suitable for the separation of proteins of an average size higher than 30 kDa, while the second is most suitable for best separation of smaller proteins (< 30 kDa). All Ras proteins (truncated and full length) together with Raf-RBD were detected by using the Schägger method. NF1 and SOS were detected by using Lämmeli. The methodology is presented as follows:

- 6.0 μl of a 4-fold concentrated SDS solution (150 mM Tris/HCl pH 6.8, 2% m/v SDS, 20% w/v glycerol) were added to 18.0 μl of protein sample.
- The mixture was incubated for 5 min. at 100 ºC to enhance the denaturation process, followed by centrifugation for 2 min., 10000 rpm at RT. 10 μl of each sample were then directly applied in the top of the stacking gel.
- In the Schägger method, the composition of the buffer used in the gel was 3.0 M Tris/HCl pH 8.4, 0.3% SDS and 0.01% NaN_3. The acrylamide content used on the stacking gel was 5% and in the running gel was 16.5%. The anode buffer (located in the bottom part of the electrophoretic chamber) was 200 mM Tris/HCl pH 8.9 (10x stock solutions were prepared and stored at 4 ºC for routine use) and the cathode buffer (located in the upper part of the chamber) was made by mixing 100 mM Tris/HCl pH 8.9, 100 mM Tricine, 0.1% w/v SDS and 0.01% w/v NaN_3 (similarly, 10x stock solutions were also prepared). For the Lämmeli methodology, the buffer was made of 25 mM Tris-base, 200 mM glycine and 0.1% w/v SDS. The acrylamide content used in the stacking gel was 5% and in the running gel 15%.

• Schägger gels were run at a constant voltage of 100 V for approx. 120-140 min. and Lämmeli gels were run at a constant current of 36 mA for about 50-60 min.

• The Separated proteins by both electrophoretic methods were stained with coomassie solution containing 0.1% w/v of tryphenylmethane brilliant blue G250, 40% v/v methanol and 10% v/v acetic acid. Coomassie binds to proteins through ionic and Van der Waals interactions between the dye sulfonic groups and positive protein amine groups, staining them unspecifically.

• The staining procedure was accomplished by heating the gel for 1-2 min. in a microwave and then shaking it for at least 30 min. at RT. The revealing of the protein bands was accomplished by adding a unstaining solution made upon mixing 20% v/v acetic acid, 10% MeOH v/v and 70% H_2O. The gel was microwaved (1-2 min.) in the presence of this unstaining solution and shaken for at least 30 min.

• In a final step, the revealed gel was transferred to a translucid plastic bag and photographed or digitalized, if necessary.

2.2.2.6 Determination of Protein Concentration

In an attempt to minimize systematic and random errors and, whenever possible, different methods were used to find the most correct concentration for the proteins involved in this project. The obtained values by different methods were always combined and averaged.

2.2.2.6.1 The Bradford Method

The Bradford method is based on the proprieties of coomassie brilliant blue (see also section 2.2.2.5 for details). This dye binds primarily to the negatively charged amino acids of the proteins and changes from a cationic to an anionic state. This is associated with a colorimetric change that can be followed by visible spectroscopy at 595 nm.

• The Bradford assays preformed in this work were all based in a previous calibration curve using BSA. The Roti®-Quant assay kit from Roth® was used in the preparation of the curve. Briefly, a BSA dilution series from 0.5 mg up to 2 mg/mL was set. 1.0μl of each sample was transferred directly into a plastic cuvette and 1.0 mL of Bradford solution was added. Upon gentle mixing by pipetting with up-and-down movements, the mixture was left to rest for ca. 5 min. at 298K and then measured directly at 595 nm (the 'blank' or the 'zero' was previously made by measuring the absorbance of the Bradford solution alone). Using the obtained values, a linear dependence between A_{595} and the mass (in mg or μg) of the protein was plotted. Upon linear fitting in the form of $y=mx+b$ (m being the slop and b being the y-intercept), the protein concentration can be calculated through the equation $C=(Abs_{595}-b)/m$.

The most striking disadvantage of this method is the lack of accuracy by the simple fact that the amino acid composition varies greatly between different proteins. The higher the number of non-polar, reactive side chains, the higher the concentration this method will (inaccurately) deliver.

2.2.2.6.2 UV Absorption at 280 nm Using Nanodrop™

This method is based in the simple fact that proteins that contain tryptophan, tyrosine and, to a small extent, phenylalanine in their primary sequence will strongly absorb light at 280 nm. It relies more in the presence of tryptophan than the others because tryptophan is the amino acid with the highest absorption efficiency at this wavelength. The direct measurement at 280 nm has the advantage of being a very simple and non-destructive process (unlike Bradford). Nowadays, instrumental advances in photometry led to the development of highly accurate and versatile machines such as the Nanodrop™ that allows the determination of protein concentration in less than 30 seconds.

Within the framework of this thesis, all the measurements were performed using Nanodrop™ One (ThermoFisher Scientific) from the department of Biophysics II (chair Prof. Dr. Reinhard Sterner), using the single channel mode by sweeping in a 190-850 nm range. 2.0 μl of protein sample was pipetted directly into the pedestal of the device. The concentration can be obtained from the direct application of the Beer-Lambert law, $A_{280}=c.l.\varepsilon$. When the extinction coefficient, ε, of the protein is rigorously known, this is a method of choice (provided that the protein absorbs strongly at 280 nm). When there is no accurately published literature about ε, its value can be estimated by using an online application such as ExPAsy ProtParam tool [216]. Because ProtParam only considers the linear sequence of the protein and doesn't take into account the structure (which can affect the 'real' extinction coefficient value), the protein was always denatured before measuring its concentration.

2.2.2.6.3 Analytical High Performance Liquid Chromatography (HPLC)

Analytical HPLC was the method of choice in this work to measure the concentration of Ras proteins, to measure their intrinsic GTPase activity and to follow up nucleotide exchange reactions (section 2.2.2.4). Ras concentration was quantified by reverse phase chromatography (RPLC), according to Hoffman *et al* [217]. The system consists of a C18 nucleosil pre-column, a hypersil C18 reversed-phase column and a UV detector, mounted in this respective order. In RPLC, the polarity of the stationary and mobile phases is interchanged in comparison to normal-phase chromatography: the mobile phase (HPLC

buffer: 100 mM K_2HPO_4/KH_2PO_4 pH 6.4, 10 mM tetrabutylammonium (TBA) and 2% up to 8% acetonitrile (ACN)) is polar and the stationary phase (derivatized silica gel, C18 column) is highly hydrophobic. The Ras protein is denatured by the acetonitrile in the mobile phase (HPLC buffer) and by the highly hydrophobic properties of the pre-column, becoming retained on it as it travels through the system. In the denaturation process the bound-nucleotide is released and travels subsequently through the C18 reversed-phase column.
The process of separation of a mixture of different nucleotides happens as follows: the positively charged TBA ions from the HPLC buffer bind to the negatively charged phosphate groups of the nucleotides, neutralizing their charges. Now, the non-polar nucleotide-TBA complexes can interact with the stationary phase, i.e. the C18 reversed-phase column. The order of appearance (retention time) of a mixture upon an isocratic elution can be rationalized in terms of charges and reversed phase interactions: the retention time of increases with increasing number of phosphates - longer non-polar nucleotides can interact better with the stationary phase, travelling slower through the column. As consequence, the different nucleotides are separated according to their increasing order of molecular mass (guanosine, GMP, GDP, GppNHp, GTP).
The elution profile was determined by a UV detector operating at λ= 254 nm, were absorption of the conjugated π-electron ring system of the purine base takes place. A calibration of the complete HPLC system was carried out periodically with a GDP stock solution of known concentration (λ= 254 nm, ε_{254nm}(GDP)= 13700 M^{-1} cm^{-1}). Ras proteins were typically measured by injecting 20 μl of a 1:10 dilution into the chromatographic system. In the isocratic elution method, the concentration of ACN was adjusted in a way that the time interval between the elution of each nucleotide was long enough to allow the proper integration of the peak areas without peak overlapping. Protein concentration was obtained by using directly the values from the integrated areas into the calibration equation.

2.2.3 Nano Differential Scanning Fluorimetry (nanoDSF)

nanoDSF is a modified differential scanning fluorimetry method in which the fluorescence of natural aromatic amino acids of proteins, especially tryptophan and tyrosine, is employed to monitor protein unfolding as the protein is subjected to a temperature gradient. Both, the fluorescence intensity and the fluorescence maximum depend strongly on the close surroundings of the aromatic amino acids [218, 219]. Thus, the ratio of the fluorescence intensity at 350 nm over 330 nm (corresponding to the maximum of emission for the unfolded and folded cases, respectively) can be plotted as a function of time or temperature and used to obtain the melting temperature (T_m) defined as the temperature at which 50%

of the protein population is unfolded and corresponding to the midpoint of the transition from folded to unfolded. By following the shift in fluorescence emission wavelength, an unfolding curve can be generated. Calculation of T_m can be performed using different methods. A commonly used approach is to determine the maximum of the first derivative of the absorbance signal. This method circumvents the subjective determination of baseline levels and also allows for the determination of multiple melting points, e.g. for antibody unfolding or more complex multi-domain proteins. The method works especially well when one or more tryptophan residues are present but can also be employed in the study of proteins that have no tryptophan residues as is in the case of the Ras protein [220].

In the scope of this work the melting temperature of Ras *wild type* was compared with the mutants H27E, D33K, T35A and T35S. All the samples dissolved in buffer F with concentrations ranging between 1.0 and 1.5 mM were loaded into thin capillaries and measured in the Prometheus NT.48 from Nanotemper® Technologies (Munich, Germany), in a temperature range between 20° and 95°C. Before every Melting Scan a Discover Scan of 7 seconds detecting the capillaries that were loaded into the instrument was performed. Data analysis was performed using the NT Melting Control software (Nanotemper®). T_m values were determined by fitting the tryptophan fluorescence emission at the ratio of 350/330nm using a polynomial function in which the maximum slope is indicated by the peak of its first derivative.

2.2.4 Isothermal Titration Calorimetry (ITC)

ITC is used to determine the thermodynamics of (bio)molecular interactions and the kinetics of enzyme-catalysed reactions in solution and is based in the simple principle that any chemical reaction or physical process is accompanied by a change in heat or enthalpy (ΔH) of the system under study, that can be measured and quantified. Distinct molecular interactions have distinct heat signatures that constitute a unique thermodynamic fingerprint for a particular system and can be rationalised to help with the question of *why* two biomolecules can bind to each other.

ITC is one of the oldest methods used in the field of biophysics to prove molecular interactions but still one of the most common due to its robustness. It allows the measurement of virtually any molecule in solution without the need of previous labelling, contrary to other more modern techniques such as microscale thermophoresis (MST), which sometimes requires hydrophobic fluorescence labelling that can cause unspecific binding [221]. The emitted or absolved heat is also measured directly in solution, contrary

to other methods that require immobilisation of one of the partners into a solid matrix to derive binding parameters (e.g. surface plasmon resonance (SPR) and quartz crystal microbalance (QCM)) [222]. Additional advantages of ITC include no molecular mass limitations and no restrictions regarding the optical properties of the sample, since only heat variations are measured. One of its greatest limitations is, however, the large amount of sample needed, despite recent technological advances in miniaturizing the reaction cell of the instrument [223]. A second disadvantage is its low throughput, with an averaged time of 1 hour per experiment.

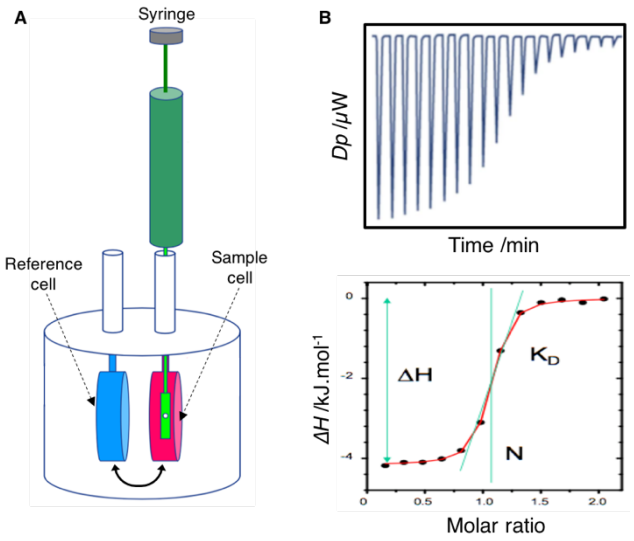

Figure 2.6. ITC as a method to probe molecular interactions. **A.** Representative diagram of a power compensation ITC device showing the syringe (green) used to incrementally add the ligand to the sample located in the cell (red), whose heat variation is constantly monitored and adjusted to a close by reference cell (blue). **B.** The raw heat of the reaction is shown by the spikes that develop from the baseline for each injection (upper graph). Integration of this area over the molar ratio gives the thermogram (lower graph), from which the parameters ΔH, N (binding sites) and K_D can be explicitly calculated. Adapted from [221, 222].

An ITC instrument is a very sensitive device capable of measuring heat effects as small as 0.4 μJ and allows the determination of binding constants between 1.0 nM and 100 μM. The detected heat rates can be as small as 0.4 μJ s^{-1}, permitting for the determination of K_m and k_{cat} values in the range of 10^{-2}-10^{3} μM and 0.05-500 s^{-1}, respectively [224, 225]. The calorimetric experiments conducted in this thesis were performed in a Microcal® PEAQ-ITC (Malvern Instruments Ltd.) calorimeter which is based on the compensation of the thermal effect generated by the addition of ligand (titrant, located in a syringe) to the sample being titrated, located in an adiabatic cell, as shown in Figure 2.6A: close to the sample cell is located a reference cell that is periodically filled with Millipore water. A thermoelectric device measures the temperature difference between the reference and the sample cells as well as between each cell and an adiabatic jacket that isolates the complete chamber. As the reaction is developed (i.e. the titrant is stepwise added to the sample being titrated, a process that is fully automated), the temperature difference between the two cells decreases to zero either by automatically heating the sample cell (if the reaction is endothermic) or by heating the reference cell (if the reaction is exothermic). For each addition, the heating originates a characteristic spike over (endothermic) or under

(exothermic) the baseline. In other words, the generated spikes correspond simply to the power compensation (sometimes called raw heat, measured in μJ s^{-1} or μcal s^{-1}) of the calorimeter that is required to keep the sample cell from changing temperature over the course of the titration. The plot of the raw heat over time is called a thermogram. When designing an ITC experiment it is fundamental to give enough time between each consecutive injection to allow the heat spike to return to the baseline. A typical thermogram of an exothermic reaction is shown in the upper graph of Figure 2.6B. The integration of the individual raw heat over the time for each injection (more specifically, the time needed for the control heat power to return to a baseline level) gives the heat change that can be plotted as a function of the molar ratio of the two interacting partners. The fitted curve of a 1:1 binding model is shown in the bottom graph. In this case the enthalpy is fitted at the heat of 100% binding and the stoichiometry is intuitively denoted by the midpoint of the titration. The slope of the sigmoidal curve is related to the binding constant (K_b and K_D= $1/K_b$) and to the sample concentration for a given system. Considering a general binding of a ligand [L] to a macromolecule [M], K_b is given by:

$$M + L \rightleftharpoons ML \qquad K_b = \frac{[ML]}{[M].[L]} \tag{1}$$

The Gibbs free energy (in kJ mol^{-1}) of binding is given by:

$$\Delta G = -RT \ln K_b = RT \ln K_D \tag{2}$$

Where R is the gas constant given in J^{-1} K^{-1} mol^{-1} and T the absolute temperature, given in K. The entropic contribution, ΔS, is implicitly calculated from the second law of thermodynamics and given in kJ mol^{-1}:

$$\Delta G = \Delta H - T\Delta S \tag{3}$$

A useful parameter is *N* that defines the number of binding sites per macromolecule and is mathematically given by:

$$N = \frac{[L]_b}{[M]_T} = \frac{[ML]}{[M]+[ML]} = \frac{K_b[L]}{1+K_b[L]} \tag{4}$$

In an ITC experiment, the initial heats are larger than the heats for subsequent additions because at the beginning of the titration there is a large excess of empty or unpopulated binding sites which leads to a complete reaction when [L] is added to [M]. The heat produced is linearly dependent of ΔH and non-linearly dependent of K_b. The generic thermogram is modelled by the following equations:

$$\Theta_i = \frac{K_i[L]}{1+K_i[L]} \tag{5}$$

$$[L]_T = [L] + P_T \sum_{i=1}^{j} (n_i \Theta_i) \tag{6}$$

Eqn. (5) is just a particularization of eqn. (4). Θ_i is the is the fraction of site i occupied by ligand; $[L]_T$ is the total ligand concentration, [L] is the free ligand concentration, P_T is the total macromolecule concentration, K_i is the binding constant of process i and n_i is the stoichiometric ratio for the injection i. The total heat produced can be calculated from:

$$Q = P_T V_0 \left(\sum_{i=1}^{j} n_i \Theta_i \Delta H_i \right) \tag{7}$$

$$\Delta Q(k) = Q(k) - Q(k-1) \tag{8}$$

Where V_0 is the initial volume of the sample cell and ΔH_i is the molar enthalpy change for the process i. The differential heat is defined by eqn. (8) where k is the injection number. A non-linear regression algorithm is performed on eqn. (7) to obtain a fit of the experimental data. There are different models that explain the binding process (one-set of sites, two independent sites, sequential sites). All the interactions measured in the present work correspond to a 1:1 binding with the macromolecule having one binding site. In this particular case, the equilibrium constant is given by:

$$K = \frac{\Theta}{(1-\Theta).[L]} \tag{9}$$

All the titration experiments were performed according to the default setting of the device used with a referential power of 10 μcal s^{-1} and a spacing between injections of 150 s or longer, with an injection time of 2 s and a stirring speed of 750 rpm. A total of either 19 or 31 injections of 2 μl each were applied in the determination of the K_D values. For a qualitative, rapid assessment of the binding strength a faster run comprised of 13 injections, 3 μl each, was performed. All the measurements were conducted at 298 K, using 270 μl of Ras (always located in the cell) and 70 μl of the titrant (always located in the syringe).

2.2.5 NMR Spectroscopy

2.2.5.1 Sample Preparation. General Considerations

All NMR measurements involving different Ras isoforms, variants and mutants were performed by dissolving the protein in buffer F (40 mM Tris/HCl pH 7.5, 10 mM $MgCl_2$, 2 mM DTE, 0.2-0.4 mM DSS (2,2-dimethyl- 2-silapentane-5-sulfonate) in 5-10% D_2O, or 20% in the case of HP experiments). For measurements involving the titration of Ras with Raf-RBD, NF1 or SOS1, a minimum of 150 mM and a maximum of 250 mM NaCl, depending on the titrant and general aspect of the mixture, were added prior the titration with the intent to stabilize the protein complexes and to avoid dimerization.

In the NMR investigations performed for GppNHp, the nucleotide was bought from Sigma-Aldrich (Germany) and used directly, without any additional purification. From the white crystalline powder two samples were prepared by dissolving it either in buffer F, which included $MgCl_2$ in one case but not in the other. In order to minimise pH dependent chemical shift changes during the HP experiments, a pH value for the solutions of ca. 2-3 units above the apparent pK_a values of the second deprotonation step of the terminal phosphate. This corresponded to a final pH of 9.0 for the Mg^{2+}•GppNHp sample and 11.5 for GppNHp sample [116, 226]. All NMR measurements performed in this thesis were recorded at either 278 K or 303 K (or both). The temperature of the NMR probehead was always controlled prior to the experiments by using the line separation between methyl and hydroxyl groups of external MeOH as a calibration method [227].

2.2.5.2 Ambient Pressure and HP ^{31}P NMR Data Acquisition

Ambient pressure and HP ^{31}P NMR was recorded either in one of the two spectrometers located at our department: in a Bruker Avance 500 MHz, operating at a ^{31}P frequency of 202.45 MHz and in a Bruker Avance 600 MHz, operating at a ^{31}P frequency of 242.89 MHz. In the first spectrometer either a selective broadband 10 mm ^{31}P probe or a 5 mm QXI probe was used. The protein samples were typically measured in high quality grade 5 mm NMR tubes or in 5/8 mM Shigemi tubes. The second spectrometer was equipped with a Prodigy™ cold probe (Bruker) allowing for the enhanced sensitivity detection of the ^{31}P nucleus. Protons were usually decoupled during data acquisition with a GARP sequence operating at a B_1 field of 830 Hz or 980 Hz, accordingly to the spectrometer used [228]. A 70º-90º pulse and a repetition time of 6-7 s was typically used. A ^{1}H spectrum was recorded for each ^{31}P spectrum.

HP ^{31}P NMR was performed using a home-built online high hydrostatic pressure system which includes a bourdon manometer and a manually operated piston compression (for details see Figure 1.12 and [229]. Pressure was transmitted via a metal-alloy line filled with water to a high pressure ceramic cell connected at the end by an autoclave (Figure 1.12). One of two ceramic cells were used in the multiple experiments, a 200 MPa or a 250 MPa of maximum permissible pressure. Both have an inner diameter of 3 mm and an outer diameter of 5 mm. Recently, a third one was acquired by our department, capable of withstanding a maximum pressure of 300 MPa. A flexible membrane, made of polyethylene terephthalate (PET), was used to separate the water of the pressure line from the buffer of the protein sample. The total volume of both ceramic cells is 320 μl. However, the effective volume where the sample can be recorded is considerably smaller. To reduce the unnecessary volume and therefore economise protein sample, a cylindrical displacement body with a length of ca. 3 cm, made of propylene, was inserted into the ceramic cell. In the process, the protein solution that leaked from the cell was collected, stored and used for other experiments.

2.2.5.3 [^{1}H-^{15}N]-HSQC NMR Acquisition, Processing and Evaluation

2D experiments performed in HRas^{WT}(1-166)•Mg^{2+}•GppNHp (1.1 mM) and HRas^{D33K}(1-166)•Mg^{2+}•GppNHp (1.3 mM). For each protein, a temperature series was recorded ranging from 278 K to 303 K in five-degree step intervals. Prior the experiment both proteins were extensively dialysed against the same buffer. ^{1}H and ^{15}N data collection was performed in a Bruker Avance spectrometer, equipped with a TXI cryoprobe operating at a ^{1}H frequency of 800.12 MHz and a ^{15}N frequency of 81.08 MHz. Each 2D spectrum was recorded as a complex data matrix comprised of 256 or 512x2048 points using a sweep width of 8400 or 9600 Hz in the proton dimension and 2400 Hz or 2800 Hz in the ^{15}N dimension. A recycling delay of 3.4 s was used with 64 scans/FID. Before each 2D experiment, a standard ^{1}H spectrum was recorded. ^{1}H chemical shifts were directly and ^{15}N indirectly referenced to DSS as described elsewhere [230].

All spectra were processed using the Topspin 3.2 program (Bruker Biospin). The assignment of the amide resonances for Ras^{WT}•Mg^{2+}•GppNHp was based on the reported literature [94] and transferred to the presently obtained spectra using the Auremol software [231].

2.2.5.4 ^{31}P (HP) NMR Processing and Evaluation

All ^{31}P NMR spectra were processed using the Topspin® program. Each spectrum was baseline corrected, phase corrected and indirectly referenced to DSS with a Ξ-value of 0.404807356 reported by Maurer and Kalbitzer [232], corresponding to 85% external phosphoric acid contained in a spherical bulb. The FID was filtered with appropriate window functions, depending on the characteristics of the data and the intended purpose of the analysis. Typically, either an exponential multiplication filter (EM) with a line broadening (LB) of 4-15 Hz or a Gaussian multiplication filter (GM) was used. The processed data was subsequently converted to the ASCII format using the MestreC® (v6.1) program and evaluated using the Origin® (v8.9) software. The deconvolution of the spectra was performed by application of a standard non-linear least square routine gradient fit procedure such as the Levenberg-Marquardt (L-M) method [233, 234]. In this process, an initial empirical estimation of the chemical shift position for each resonance line is given and fitted with a Lorentzian line that is then optimized by the algorithm, allowing for the obtention of accurate chemical shift values, peak intensities, areas and half-width linewidths.

^{31}P NMR longitudinal relaxation times (T_1) were determined by an inversion-recovery pulse sequence at 278 K, using a maximum repetition time of 20 s. The obtained integrated areas were plotted and fitted according to the following equation:

$$M_z(t) = M_0 + \left(M_z(0) - M_0 \right)^{-\frac{t}{T_1}} \tag{10}$$

where $M_z(t)$ is the z-magnetization (signal integral) at time t and M_0 is the magnetization in thermal equilibrium [235].

^{31}P NMR studies on the binding of Zn^{2+}-cyclen to HRas and KRas led to the determination of the microscopic dissociation constant, K_D, as well as to the coefficient of cooperativity, n, given by the Hill equation [236, 237]:

$$\delta - \delta_f = (\delta_c - \delta_f)\frac{[L]_f^n}{K_D^n + [L]_f^n} = (\delta_c - \delta_f)\frac{\left([L]_0 - N[Ras]_0 \frac{\delta - \delta_f}{\delta_c - \delta_f} \right)^n}{K_D^n + \left([L]_0 - N[Ras]_0 \frac{\delta - \delta_f}{\delta_c - \delta_f} \right)^n} \tag{11}$$

Where δ_f and δ_c are the chemical shift values of free Ras in state 1(T) and in complex with a ligand, respectively. $[Ras]_0$ and $[L]_0$ correspond to the total concentrations of the protein and the ligand, respectively. $[L]_f$ is the concentration of the free ligand and n is the Hill coefficient [156].

Under equilibrium conditions, if a protein occurs in *N* conformational states, the population difference between two states, 1 and 2, in thermodynamic equilibrium is given by their differences in the Gibbs free energy, $\Delta G_{i,j,}$ given in kJ mol^{-1}:

$$\frac{p_2}{p_1} = K_{12} = e^{\left(-\frac{\Delta G_{12}}{RT}\right)} \tag{12}$$

The equilibrium constant K_{12} is dependent on pressure, P, and absolute temperature, T. Given the universal relation $\Delta G = \Delta G_0 + P\Delta V$, the pressure dependence of the Gibbs free energy for the two states at constant T is given by:

$$\Delta G_{12}(P) = \Delta G_{12}^0 + (P - P_0)\Delta V_{12}^0 + \frac{1}{2}\frac{\partial \Delta V_{12}^0}{\partial P}(P - P_0)^2 \tag{13}$$

Where $\Delta V^0_{12} = \Delta V_{12}(P_0) = V_2(P_0) - V_1(P_0)$ is the difference of the partial molar volumes. The complete quadratic term of this equation is sometimes abbreviated as $\Delta\beta_{12}$ and corresponds to the difference of the partial molar compressibilities. In most cases this term is neglected and the equation can be simply written as:

$$\Delta G_{12}(P) = \Delta G_{12}^0 + (P - P_0)\Delta V_{12}^0 \tag{14}$$

A phenomenological description of the chemical shift pressure-dependence observed for any NMR spectra can be obtained by a model-free approximation of the Taylor expansion to the second order:

$$\delta(P, T_0) = \delta_0(P_0, T_0) + B_1(P_0, T_0)(P - P_0) + B_2(P_0, T_0)(P - P_0)^2 \tag{15}$$

Where δ_0 is the chemical shift at ambient pressure and B_1 and B_2 are the first and second order pressure coefficients, related with a linear (conformational transition within the same ensemble) and non-linear (conformational transition between different ensembles) pressure dependence, respectively. The magnitude of their values depends on the magnitude of the local structural changes induced by pressure. This relationship is not truly quantitative but it can be used at least empirically to evaluate such changes. In some situations, the use of a third order (B_3) Taylor expansion is required for a proper fit of the data. The actual pressure response observed in an NMR spectrum depends on the timescale of the exchange between the different states, characterized by the exchange correlation time, τ_c. If there is an equilibrium between M states i, (i=1, N) of the protein and under a fast

exchange condition ($|\Delta\omega_{ij}|=|\omega_j-\omega_i|<<1/\tau_c$), the observed chemical shift is a combination of the chemical shifts of each state given by the general equation:

$$\delta = \sum_{i=1}^{M} P_i\delta_i = \frac{1}{Z}\sum_{i=1}^{M}\delta_i e^{-\frac{G_i}{RT}} = \frac{\sum_{i=1}^{M}\delta_i e^{-\frac{\Delta G_{1i}}{RT}}}{\sum_{i=1}^{M} e^{-\frac{\Delta G_{1i}}{RT}}} \tag{16}$$

Where Z is the state sum over all possible structural states of M. For a conformational transition between only two states, 1 and 2, the above equation can be greatly simplified:

$$\delta = \frac{1}{1+K_{12}}\delta_1 + \frac{K_{12}}{1+K_{12}}\delta_2 = \frac{\delta_1+\delta_2 e^{-\frac{\Delta G_{12}}{RT}}}{1+e^{-\frac{\Delta G_{12}}{RT}}} \tag{17}$$

Indeed, this was the used equation to fit the pressure-dependent chemical shifts of the ^{31}P NMR lines behaving according to the fast exchange regime.

When the conformational change between states 1 and 2 is slow in the NMR time scale ($|\Delta\omega_{ij}|=|\omega_j-\omega_i|>>1/\tau_c$), the signal areas (in the case of ^{31}P spectra, A) or volumes, V (in the case of [^{1}H-^{15}N]-HSQC spectra) are proportional to their respective concentration and the equilibrium constant K_{12} can be calculated according to:

$$K_{12} = \frac{V_1}{V_2} = e^{-\frac{\Delta G_{12}}{RT}} \tag{18}$$

The relative population p_i of a state i in an N system can be calculated from the equilibrium constant $K_{ij}=[i]/[j]$ as:

$$p_i(P,T_0) = \frac{K_{ij}(P,T_0)}{\sum_{i=1}^{N} K_{ij}(P,T_0)} \tag{19}$$

In terms of ^{31}P NMR, the intrinsic pressure effects arising from the isolated nucleotide were separated from the pressure effects ascribed to the nucleotide-bound Ras for the first time in this thesis. This was achieved by subtracting the variation of the chemical shift values ($\Delta\delta$) measured in the isolated nucleotide to the uncorrected shift values of the Ras protein obtained directly from the experimental spectra [226].

2.2.6 High Pressure Macromolecular Crystallography (HPMX)

Contrary to HP NMR, HPMX is technically more challenging and requires complex instrumental skills. Nevertheless, it is a remarkable technique with a bright future. Its improvement towards a routinely, user friendly methodology, is dependent on technological advances related to the construction of brighter synchrotron radiation sources for faster data acquisition, development of, newer high pressure cells, fully automatic analysis of the diffraction images and new efficient methods for pressure calibration [173].

Conventional, ambient pressure (pamb), X-ray diffraction data was collected for $HRas^{WT}$(1-166) and for $HRas^{D33K}$(1-166). In parallel, a broad crystallographic study involving *wild type* Ras and Ras^{D33K} was performed using state-of-the-art high pressure X-ray techniques.

2.2.6.1 Protein Crystallization

All the proteins studied by HPMX refer to the C-terminal truncated (1-166) and GppNHp-bound HRas used in a concentration between 1-1.5 mM and dissolved in buffer F (40 mM Tris/HCl pH 7.5, 10 mM $MgCl_2$, 2 mM DTE).

Crystallization of Ras^{WT} and Ras^{D33K}

The technique requires the use of large crystals, typically bigger than 200 μm in edge-length. They were produced for the purpose according to the “batch mode” process, using an appropriate crystallization chamber containing 3-spot wells made of glass that were previously siliconized. To each of these spots, typically 15-30 μl of 80 mM Tris/HCl pH 7.5, 20 mM $MgCl_2$, 4 mM DTE and 52-60% PEG-400 were placed at their centre. Afterwards, 30 μl of the protein solution were carefully added in the centre of the previous drop. The two solutions were slowly mixed by gentle pipetting. The chambers were immediately sealed at the top with transparent adhesive tape and placed in a vibration-free zone, in the dark. Nucleation spots were visible under the microscope after ca. 6 h and full crystals were grown after 2-3 days.

Crystallization of Ras^{WT} in complex with Zn^{2+}-cyclen

A series of HP experiments were devised with the intent to understand how the binding of Zn^{2+}-cyclen at the first binding site, near the nucleotide γ-phosphate, is affected upon pressure-induced conformational rearrangements of the switch regions. For the purpose, the previously grown Ras^{WT} crystals were soaked with 10-12 mM of Zn^{2+}-cyclen from a highly concentrated (> 20 mM) stock solution (dissolved in the same buffer used for crystallisation), for at least 10 hours prior data acquisition.

2.2.6.2 Data Collection

Upon committee approval for beam time, X-ray data was collected at the European Synchrotron Radiation Facility (ESRF, Grenoble, France) in the beamlines ID09A and ID27, and at the SOLEIL synchrotron (Saint-Aubain, Paris, France) in the "Crystal" beamline. A total of 4 runs (2 at ESRF, 2 at SOLEIL) were performed, comprising a total of 20 days of synchrotron radiation devoted to the project. The following description on how to acquire HPMX can be used as a practical guide to any of the three different beamlines used. Although, the reader is advised for the existence of specific instrumental and technical details of each beamline that are impossible to cover here in full detail.

• Two identical DAC's (named ELSA and ELMA) of the cylinder-piston type were used (Figure 1.14) [185], one cell being loaded while the other being used for data collection. The first step of sample loading in the DAC was the preparation of a gasket. This is a piece of copper or inconel®, with a typical thickness of 200 μm. The gasket was inserted between the two diamonds, the cap of the DAC was screwed and the gasket was indented by applying a small thrust (achieved by slightly pressurizing the cell with helium gas). Afterwards, the cap was removed and a hole was machined in the gasket by electroerosion with a diameter of exactly 350 μm. The gasket was then placed on the diamond, using the indentation as a guide. A drop of mother liquor (2-3 μl) was deposited in the hole. A crystal was fished out of one of the crystallization drops and gently pushed into the cavity, together with a tiny ruby sphere (Figure 1.14). The drop was deposited just before the deposition of the crystal to reduce evaporation of its most volatile components. The cap of the diamond cell was screwed and a moderate thrust applied to it.

• The slightly pressurized DAC already containing the crystal in its centre was then mounted on the goniometer by attaching it to the χ-cradle set at ω=0. The X-ray beam cross section was typically adjusted to 50x50 μm^2 at ESRF and 20x20 μm^2 at SOLEIL. The pressure was ramped until the desired value by slowly increasing thrust. This was either done by using a manual pressure setup system or an automatic one. Pressure was generated in both cases not by a lever but by a pneumatic mechanism that lets He gas flow into the membrane of the DAC [238]. The pressure inside the DAC cannot be assessed by the applied load because it is difficult to predict the elastic forces and plastic and elastic deformations in its mechanical parts [239]. This determination was performed using the known pressure-dependence of a laser-excited fluorescence from a ruby (R_1 line, λ= 694.2 nm at pamb, the equipment is a commercial product from Betsa®) [182, 240]. The optical system that is used to measure the fluorescence was placed on the X-ray path between the DAC and the detector and can be remotely removed when the pressure adjustment is completed. The

same device, coupled to a CCD camera was also used to image the sample on TV monitors (Figure 1.14).

• The centre of the cavity where the protein crystal was deposited was accurately located in both, the goniometer rotation axis and in the X-ray beam pathway. This was accomplished in two steps: first the cell was scanned in the *y* direction (i.e. perpendicular to the beam in the horizontal plane) at $\pm\omega$ angles. The intensity transmitted through the cavity was monitored by using a photodiode. The centre of the cavity was perfectly placed on the rotation axis when the transmitted signals at $\pm\omega$ were equal. In the second step, the centre of the cavity was placed in the X-ray beam by scanning along *z* (the vertical direction) according to the same principle. Afterwards, the optical system which allows to visualize the crystal and the ruby chip on a TV monitor was switched on. The X-ray position (now located exactly at the centre of the cavity) was marked with a pen by making a dot in the TV monitor. This method was used as a guide-trough for the successive irradiation of a fresh (i.e. non-irradiated) region of the crystal by performing step translations along the *y* and *z* directions, spaced between with each other by a distance slightly greater than the radius of the collimated beam. This process of "walking" on the crystal is a successful strategy to alleviate its rather fast degradation due to the free radical formation (Figure 1.14).

• After centring the crystal, a few frames were recorded. From these frames, information necessary to undertake data collection (lattice type, cell parameters and orientation matrix) was derived. Data collection was performed by the rotation method with the HP cell rotating about the vertical axis.

• Data were collected at a wavelength λ= 0.415 Å in ID09, λ= 0.374 Å in ID27 and λ= 0.510 Å in the Crystal beamlines. The Detectors used were a MarResearch Mar555 flatpanel (ID09), a MarResearch MarCCD165 (ID27) and a Rayonix SX165 (Crystal). The exposure times were 5 s, 30 s and 10 s per frame, respectively, with an oscillation of 1º in all cases.

Crystallographic structures of *wild type* and Ras^{D33K} were previously determined using standard cryo-crystallography. However, since HPMX data are collected at room temperature (RT), reference data sets at ambient pressure in the same sample environment were also collected to minimize potential experimental bias and to provide accurate and meaningful comparisons of high pressure effects.

Diffraction always disappeared anytime the pressure was continuously ramped (i.e. with no waiting time) from 0.1 to ca. 300 MPa. However, when Ras crystals were kept pressurized at 200-300 MPa overnight, diffraction could be generally maintained.

• All data sets were indexed and integrated using *XDS*. The integrated intensities were scaled and merged using *SCALA* and *TRUNCATE* and the structures were solved by molecular replacement (MR) with *MOLREP*. In order to minimize any bias in the areas involved in the transition between states, MR's were performed using a model where the switch 1 (aa 30-41) and switch 2 (aa 60-76) were removed in addition to all heteroatoms and alternate positions. The structure refinements were performed using *REFMAC*. All these programs are part of the CCP4® package. The graphic program *Coot*® was used to visualize $|2F_{obs}–F_{calc}|$ and $|F_{obs}– F_{calc}|$ electron density maps and for manual rebuilding during refinement steps.

Crystal-cell compressibility curves (i.e. unit-cell parameter changes *versus* the pressure) were determined for Ras^{WT} in the absence and in presence of Zn^{2+}-cyclen inhibitor, and for Ras^{D33} alone. All refined crystals belong to the trigonal space-group $P3_221$. The rmsd values and the thermal b-factors were computed using programs from CCP4 package. In the following, rmsd's were always calculated between Cα atoms and average b-factors only for main chain atoms to avoid the alternate positions of the side chains.

- This page was deliberately left blank -

3. Results

"Science is the belief in the ignorance of experts"

R. Feynman

3.1 Dynamics, Equilibrium and Inhibition of Full-Length Ras Studied by ^{31}P NMR

Until recently most biochemical investigations on full length Ras were rare. The work of the past decades was devoted to the truncated variant of 166 amino acids, perhaps because it was easier to handle from the experimental point of view. However, owing the change of paradigm from HRas to KRas, and from studies on the truncated protein to studies on the full length one, a primary concern on our department was to investigate up to which extent the conformational equilibrium detected by ^{31}P NMR for HRas in terms of states 1(T) and 2(T) could be transferred to the KRas protein.

3.1.1 Comparison of the Conformational Equilibrium in HRas^{WT} and KRas4b^{WT}

A great number of studies assessing the equilibrium between states 1(T) and 2(T) has been published for HRas [67, 122, 241, 242] but not as many for KRas. Because the latter is the isoform predominantly mutated is most types of cancer [100, 134], an investigation in terms of equilibria between for the isoforms KRas4b(1-188) and HRas(1-189), was performed herein. Figure 3.1A shows the ^{31}P NMR spectra recorded at 278 K of both proteins bound to Mg^{2+}•GppNHp. The corresponding chemical shift values and linewidths are summarized in Table 3.1. The obtained spectra are very similar: in both cases (and generally for any case within the scope of ^{31}P NMR spectroscopy of Ras proteins) the separation between states 1(T) and 2(T) is the greatest for the γ-phosphate signal. The integration of each resonance signal upon proper deconvolution is directly proportional to the population of the corresponding conformational state at a given pressure and temperature. This can be quantitatively defined by the equilibrium constant which is simply the ratio between the two areas: $K_{12} = A_{state\ 2(T)}/A_{state\ 1(T)}$. For KRas4b, K_{12}= 2.0 and for HRas, K_{12}= 1.9. Both values are determined with an error of ± 0.2 that arises from the fitting procedure of the partially superimposed signals. Qualitatively it can be inferred that under equilibrium conditions at 278 K, the conformational state 2(T) of KRas is ever so slightly more populated as compared with HRas, despite the difference between both being within the limits of the error of the measurement. In terms of chemical shifts, the results show that state 2(T) in KRas is downfield shifted by a $\delta\Delta$ of 0.06 ppm compared with HRas (δ= -3.30 vs -3.24 ppm), a difference that is small but still significant compared with the typical error values of ca. ±0.02 ppm.

Figure 3.1B shows the ^{31}P NMR spectra of the titration of KRas4b^{WT} with the Ras binding domain of the effector Raf kinase. The effects of the titration can be qualitatively interpreted as follows: with increasing amounts of effector new resonance signals close to the ones of state 2(T) arise. At the same time, the integrals corresponding to the state 1(T) decrease

with increasing concentrations of effector. At equimolar concentrations of Ras-Raf, state 1(T) disappears completely. The same observations were previously published for $HRas^{WT}$ [51, 116, 117]. The β-phosphate resonance line becomes broader as the titration proceeds due to the increased molar mass of the complex. This is corroborated by the experimental increase of the linewidth values: at a Ras:Raf ratio of 1:1 the molecular mass of the complex becomes 1.52-fold greater than the one of Ras alone (18 kDa + 9.4 kDa = 29 kDa). The linewidths of the signals representing the conformational state 2(T) become broadened by a factor of 1.5, 1.8 and 1.7 for the α-, β- and γ-phosphate, respectively.

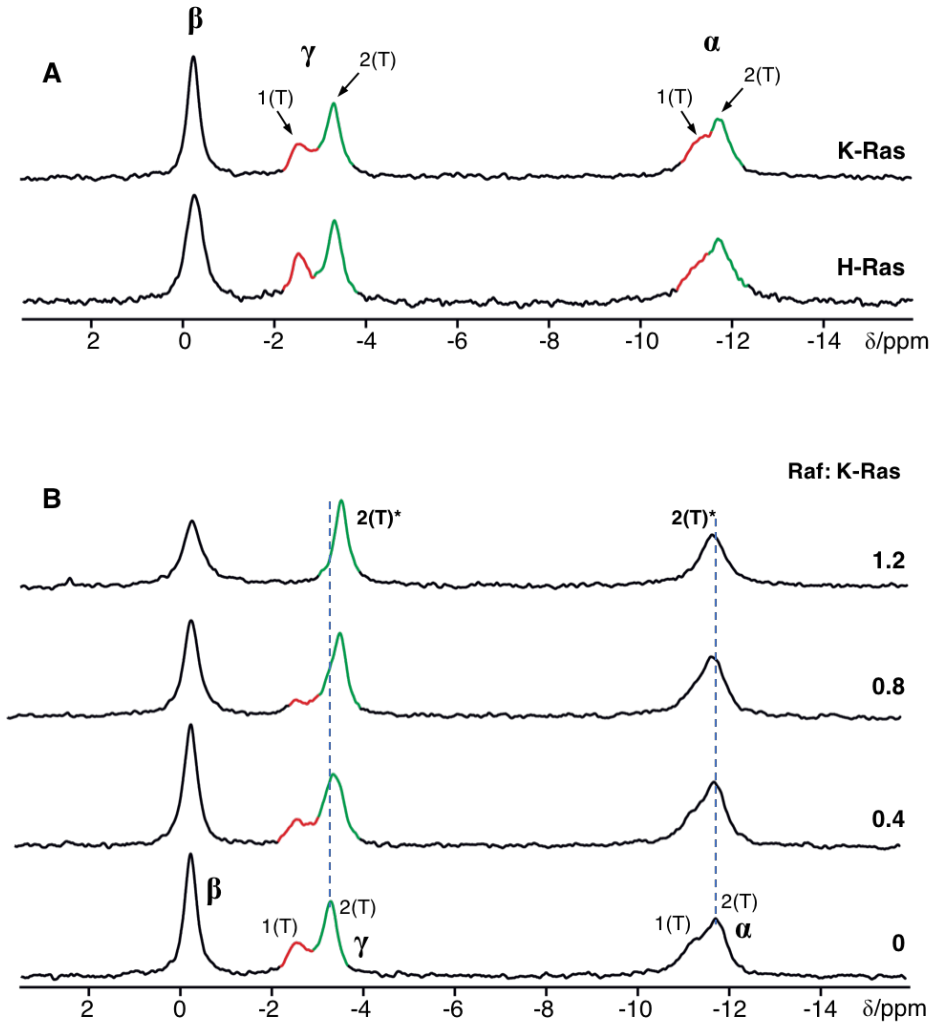

Figure 3.1. Conformational equilibria of human Ras proteins detected by ^{31}P NMR spectroscopy. **A.** ^{31}P NMR spectra of the wild type isoforms $HRas^{WT}$(1-189) and $KRas4b^{WT}$(1-188) complexed with Mg^{2+}•GppNHp. The resonances corresponding to the α, β and γ phosphates are indicated, as well as the conformational states 2(T), coloured green, and 1(T), coloured red, respectively. **B)** Interaction between $KRas4b^{WT}$ and effector protein Raf-RBD. To an initial concentration of 1.3 mM of KRas, increasing amounts of a highly concentrated Raf-RBD solution were added. The molar ratio of Ras to Raf is indicated. The final concentration of Ras is 0.93 mM.

Table 3.1. ^{31}P chemical shift values and linewidths for H and KRas^{WT}(1-188/189)•Mg^{2+}•GppNHp and their titration with the effector Raf-RBD.

protein complex	P:I	α-phosphate		β-phosphate		γ-phosphate		K_{12} [b]
		$\delta_{1(T)}$ [ppm]	$\delta_{2(T)}$ [ppm]	$\delta_{1(T)}$ [ppm]	$\delta_{2(T)}$ [ppm]	$\delta_{1(T)}$ [ppm]	$\delta_{2(T)}$ [ppm]	
FLHRas^{WT}	--	-11.25	-11.71	-0.26	-0.16	-2.54	-3.24	1.9
FLKRas^{WT}	--	-11.27	-11.73	-0.32	-0.21	-2.58	-3.30	2.0
+150 mM NaCl	--	-11.20	-11.74	-0.33	-0.20	-2.57	-3.29	2.0
+ Raf-RBD	**1:0.4**	-11.21	-11.71		-0.24	-2.55	-3.37	4.5
	1:0.8	-11.19	-11.68		-0.23	-2.57	-3.46	6.9
	1:1.2	--	-11.61		-0.27	--	-3.51	--
		$\Delta\nu_{1/2\ 1(T)}$ [Hz]	$\Delta\nu_{1/2\ 2(T)}$ [Hz]	$\Delta\nu_{1/2\ 1(T)/2(T)}$ [a] [Hz]		$\Delta\nu_{1/2\ 1(T)}$ [Hz]	$\Delta\nu_{1/2\ 2(T)}$ [Hz]	--
FLHRas^{WT}	--	136.4	80.5	57.5		94.6	58.5	
FLKRas^{WT}	--	113.0	87.2	54.4		69.0	60.2	
+150 mM NaCl	--	125.6	87.6	46.8		80.2	75.4	
+ Raf-RBD	**1:0.4**	117.2	108.7	54.9		117.2	104.0	
	1:0.8	--	--	64.6		106.6	119.0	
	1:1.2		130.0	89.3			128.3	

All values are fitted from the experimental spectra recorded at 278 K, pH 7.5 with 40 mM Tris/HCl pH 7.5,10 mM $MgCl_2$, 2 mM DTE and 150 mM NaCl.
[a] The given linewidth values for β-phosphate were fitted as a single Lorentzian line.
[b] K_{12} is given by the ratio of the areas of state 2(T) over state 1(T), calculated at the γ-phosphate. The estimated error is ± 0.2. This data is published in ref. [156]. Comparable values are available in the literature in refs. [116,117].

There is a wealth of published data on the binding energetics of Ras-effector interactions measured mainly by ITC and fluorescence techniques that can be taken as reference [243, 244]. But because the binding strength is always dependent on the experimental conditions, the association of Raf-RBD to HRas^{WT} and KRas^{WT} was presently studied by ITC using the same buffer employed for the ^{31}P NMR measurements. The ionic strength is particularly important in this case since the affinity is greatly influenced by the concentration of salt (studies reported a variation from a K_D of 0.010 μM in the absence of NaCl up to 0.35 μM at 125 mM NaCl [245]). The obtained isotherms are presented in Figure 3.2. Raf was placed on the syringe of the calorimeter at a typical concentration of 600 μM and a 12-fold diluted, 50 μM, Ras sample was placed in the cell. The measurements were recorded in duplicate at 298 K by using one of the default methods provided by the instrument manufacturer. All the interaction partners were previously dialyzed against the same buffer ((buffer F: 40 mM Tris/HCl pH 7.5, 10 mM $MgCl_2$, 2 mM DTE) with additionally 150 mM NaCl). The obtained results are shown in two forms: the differential raw power recorded by the instrument, originated after each successive addition of 2.0 μl of Raf to Ras as a function of time is presented in the upper graphs of Figure 3.2 The integration of this heat signature with respect to the Ras:Raf molar ratio over the course of the titration was also plotted (middle graphs). The sigmoidal distribution was fitted with a 1:1 binding model (experimental section

2.2.4, eqn. n°5) and the obtained thermodynamic parameters are presented here as the unchanged output of the fitting routine. From the fitted data, a binding ratio of 0.971 and 1.07 was obtained for $HRas^{WT}$ and $KRas^{WT}$, respectively. The concomitantly obtained K_D values are 0.24 μM (HRas) and 0.72 μM (KRas).

The most interesting finding taken from these measurements is the different affinity of binding measured for both Ras isoforms: the dissociation constant for KRas is 3-fold higher than for HRas, leading to the conclusion that HRas has a greater affinity towards Raf than KRas.

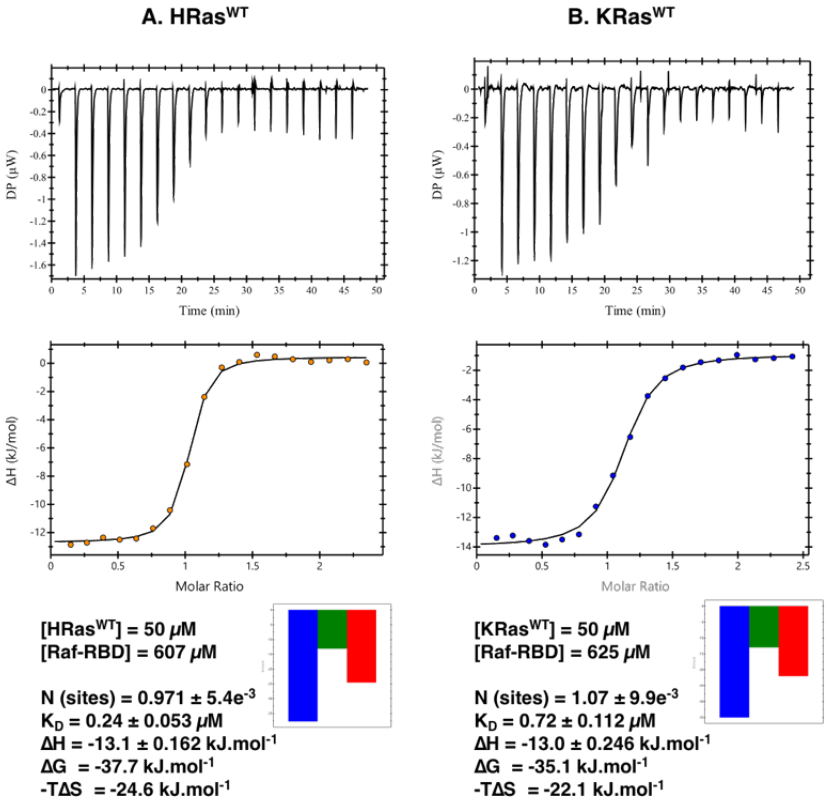

Figure 3.2. Interaction between Ras^{WT}•Mg^{2+}•GppNHp and the effector kinase Raf-RBD studied by ITC. **A.** Measurement performed for $HRas^{WT}$(1-189). **B.** Measurement performed for $KRas^{WT}$(1-188). The upper graphs show raw heat of the reaction with respect to time. The integration of such curve with respect to the molar ratio of Ras:Raf gives the typical sigmoidal curve for the binding process. The experiments were recorded at 298 K. All the proteins were dissolved in the same buffer F with additionally 150 mM NaCl. The signature plots for each interaction are shown alongside with the fitted thermodynamic values. They represent an easy way to understand qualitatively how the reaction is driven (blue: ΔG, green: ΔH, red: -TΔS).

3.1.2 Modulation of the Conformational Equilibrium in KRas4b^{WT} by Zn^{2+}-cyclen

Having in consideration the body of work with metal-cyclens and due to the present results showing the similarities of states 1(T) and 2(T) determined for HRas^{WT} and KRas4b^{WT}, it was hypothesized that wild type KRas4b^{WT} could be modulated by Zn^{2+}-cyclen in a similar way as the one reported for HRas^{WT}. To test if this is the case, a titration of both proteins with this drug was performed. The experiment was already reported in 2005 by our group for HRas^{WT} [155] but it was repeated herein in order to have identical conditions for comparison with KRas. The titration of KRas4b^{WT} was performed for the first time in the framework of this thesis. Meanwhile, both experiments were published in 2014 [156]. Figure 3.3A shows the titrated complexes. In both cases the integrals of the populations corresponding to state 2(T) decrease with increasing concentrations of the inhibitor, whereas the integrals of the populations for state 1(T) increase. At the same time the α- and γ-phosphates shift downfield and the β-phosphate shifts upfield. More specifically it can be observed that the interaction of the ligand with Ras in state 1(T) follows the fast exchange condition in the NMR time-scale because one obtains only one shifting resonance with increasing concentrations of the ligand for this particular signal (red coloured line at the γ-phosphate, Figure 3.3A). Considering the titration of HRas, for example, the chemical shift value for state 1(T) in the ligand free protein is δ= -2.53 ppm and the chemical shift value for the same state when the ligand is bound to the protein (at a ratio of 1:30) is δ= -1.61 ppm (see Table A, appendix section). The chemical shift difference between the free and Zn^{2+}-cyclen bound states is therefore $\Delta\delta$= -1.66+2.52= 0.90 ppm. This corresponds to a $\Delta\nu\approx$ 200 s^{-1}. A similar value can be found also in the case of KRas (Table A, appendix). As consequence, it can be estimated that in the limit, the off-rate between Zn^{2+}-cyclen and both isoforms in state 1(T) needs to be much faster than 200 s^{-1} (i.e. k_{off} >> 200 s^{-1}).

Regarding state 2(T), no significant shift changes are detected in the course of the titration, indicating that the slow exchange condition operates in this case. As for the α-phosphate, a downfield shift of both states is observed during the titration. In the case of β-phosphate, dramatic changes occur: in the Ras proteins alone, both states cannot be separated at the magnetic field used. They are detected as a single resonance line centred at δ= -0.24 ppm for HRas^{WT} and δ= -0.21 ppm for KRas4b^{WT}. However, as the titration proceeds, states 1(T) and 2(T) become clearly separated, with state 1(T) shifting upfield and state 2(T) shifting downfield. At 30 molar equivalents of Zn^{2+}-cyclen (last titration step on Figure 3.3), the separation between them is of $\Delta\delta$= 1.0 ppm for HRas^{WT} and $\Delta\delta$= 0.77 ppm for KRas4b^{WT}, respectively (note that the corresponding $\Delta\delta$ of 1.0 ppm in this case is equal to the one obtained above for state 1(T) at the γ-phosphate).

In an attempt to understand the kinetics of the binding mechanism, the chemical shift change of state 1(T) on the γ-phosphate resonance line induced by the addition of Zn^{2+}-cyclen was plotted as a function of ligand concentration. The result is presented in Figure 3.3B. For both Ras isoforms, very similar results were obtained: the plotted values describe a sigmoidal behaviour that is indicative of a cooperative binding mechanism: upon binding of the first molecules of Zn^{2+}-cyclen, an allosteric modulation of the conformation of the protein is very likely to take place, changing the subsequent affinity of Ras. The data was

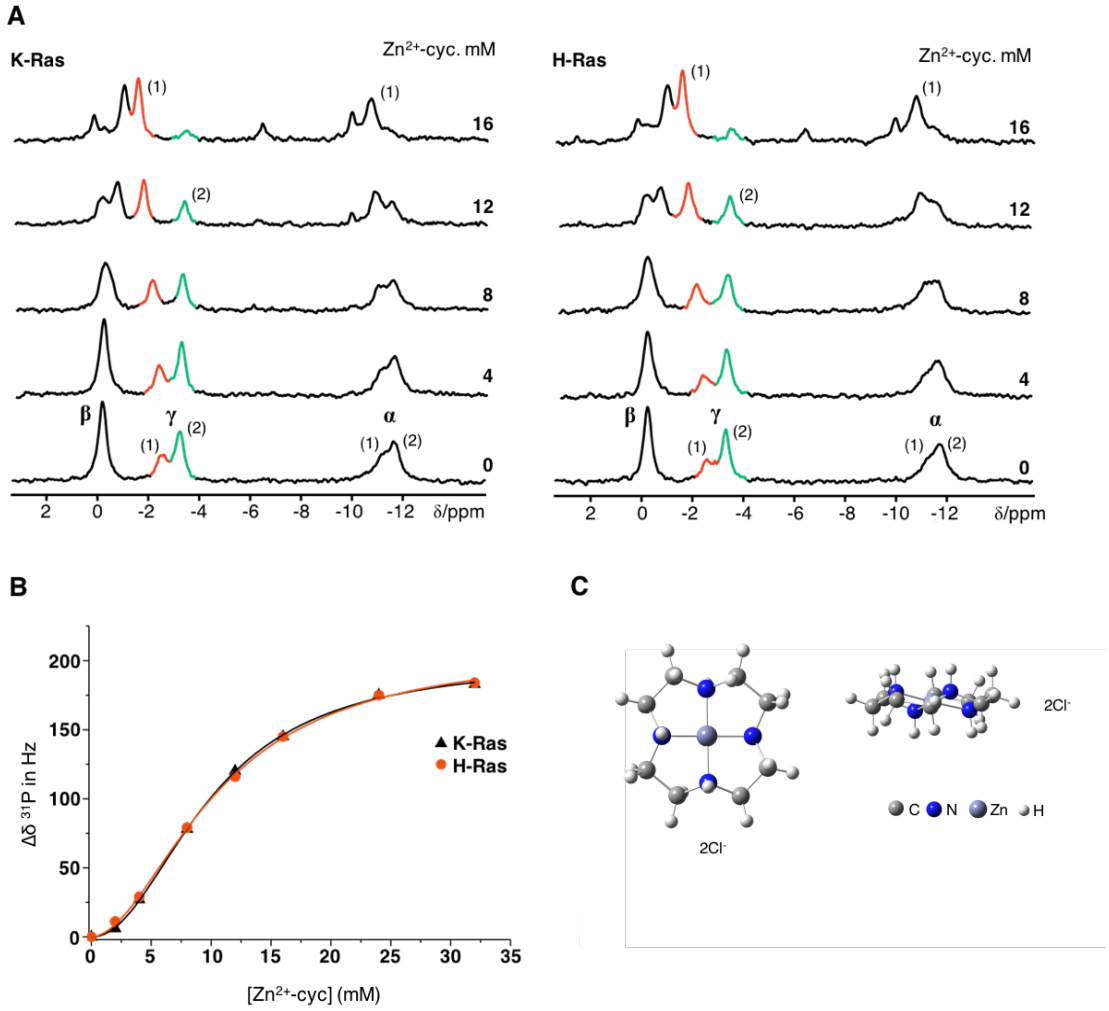

Figure 3.3. Titration of Ras^{WT}•Mg^{2+}•GppNHp with Zn^{2+}-cyclen followed by ^{31}P NMR spectroscopy. **A.** Titration of KRas (left) and HRas (right) with increasing concentrations of Zn^{2+}-cyclen (the concentrations are indicated for each step). Both proteins have the same initial concentration of 1.3 mM. The measurements were carried out at 278 K in 40 mM Tris/HCl pH 7.5; 10 mM $MgCl_2$; 2mM DTE; 150 mM NaCl; 0.1 mM DSS; 5%D_2O. At high concentrations of Zn^{2+}-cyclen (above 12 mM) additional small NMR signals arise at chemical shifts of 0.3, -6.5 and -10 ppm, corresponding to the γ-, β- and α-phosphates, respectively from free Mg^{2+}•GppNHp. No Zn^{2+}-cyclen•Mg^{2+}•GppNHp was detected. **B.** Plot of the obtained chemical shift changes of the γ-phosphate resonance in state 1(T) induced by Zn^{2+}-cyclen as a function of ligand concentration. The sigmoidal pattern of the points was fitted with the Hill equation (eqn. nº11, section 2.2.5.4). The obtained $\Delta\delta_{max}$ value for KRas is 200 ± 3 Hz. The obtained microscopic dissociation constant (K_D) is 9.9 ± 0.2 mM, and the Hill coefficient (n) is 2.0 ± 0.1. The corresponding values obtained for HRas are 200 ± 3 Hz; 10.4 ± 0.3 Hz; 1.9 ± 0.1, respectively. **C.** Optimized structure of Zn^{2+}-cyclen (1,4,7,10-tetraazacyclododecane.Zn^{2+}) complex with chloride counterions. The optimized structure was calculated for the isolated molecule at the DFT/mP1WPW91 level of theory. The detail of the non-planarity of the cyclen ring is shown. Adapted from [156].

fitted with the Hill equation (experimental section 2.2.5.4, eqn. nº11) leading to Hill coefficients of 1.9 ± 0.1 and 2.0 ± 0.1 for $HRas^{WT}$ and $KRas4b^{WT}$, respectively and to an apparent K_D of 9.9 ± 0.1 mM in both cases. The Hill coefficient is a measure of the degree of cooperativity, and normally, a number close to the number of binding sites is characteristic of a large positive cooperativity.

Finally, at high concentrations of Zn^{2+}-cyclen additional small resonance lines are observed in the spectra (this is clearly observed in the last titration step on Figure 3.3A), at δ= 0.3, -6.5 and -10.0 ppm, corresponding to the chemical shift of γ-, β- and α-phosphates, respectively, of the free nucleotide that becomes dissociated from the protein. This is due most likely to the lowered affinity between Ras and the nucleotide as Zn^{2+}-cyclen concentration increases the k_{off} (a factor of 3 was observed at 20 mM Zn^{2+}-cyclen). In the equilibrium (there was no additional nucleotide added to the buffer) this would lead to a small fraction of nucleotide-free Ras that is less stable and tend to precipitate, during the rather time consuming ^{31}P NMR experiments (5 to 6 hours per titration step).

3.1.3 Effect of Raf-RBD Titration on the Displacement of Zn^{2+}-cyclen From $HRas^{WT}$

The displacement of the Ras-Raf interaction by the presence of Zn^{2+}-cyclen is regulated by an allosteric mechanism. Since in such mechanism the two binding sites are cooperative and directly coupled it is possible, in principle, to release Ras-bound Zn^{2+}-cyclen from Ras at high concentrations of effector Raf-RBD. To prove this hypothesis a ^{31}P NMR titration experiment was performed, starting with the $HRas^{WT}$•Mg^{2+}•GppNHp•Zn^{2+}-cyclen protein-drug complex, to which increasing amounts of effector Raf-RBD were added, up to a 1.5-fold excess. The titration steps are presented in Figure 3.4 and the fitted values for chemical shift and linewidths are presented in Table B of the appendix section. Initially the Ras-Zn^{2+}-cyclen complex exists in a conformational state 1(T), with a remaining fraction of state 2(T), showing a small upfield shift. Upon addition of increasing amounts of Raf-RBD the integral of the resonance line corresponding to state 1(T) decreases. It is worth note, however, that its chemical shift and linewidth remains unperturbed (the small deviations presented on table B for these parameters are within the limits of the error of the fitting procedure). At the same time, the signal intensity of state 2(T) increases. The final chemical shift values obtained by line fitting procedures are δ= -11.61, -0.19 and -3.56 ppm for α, β and γ-phosphates, respectively. These values are in close similarity with the ones found for the HRas-Raf complex (Table 3.1). The chemical shift values for Zn^{2+}-cyclen bound state 1(T) are unperturbed over the whole concentration range of the titration experiment.

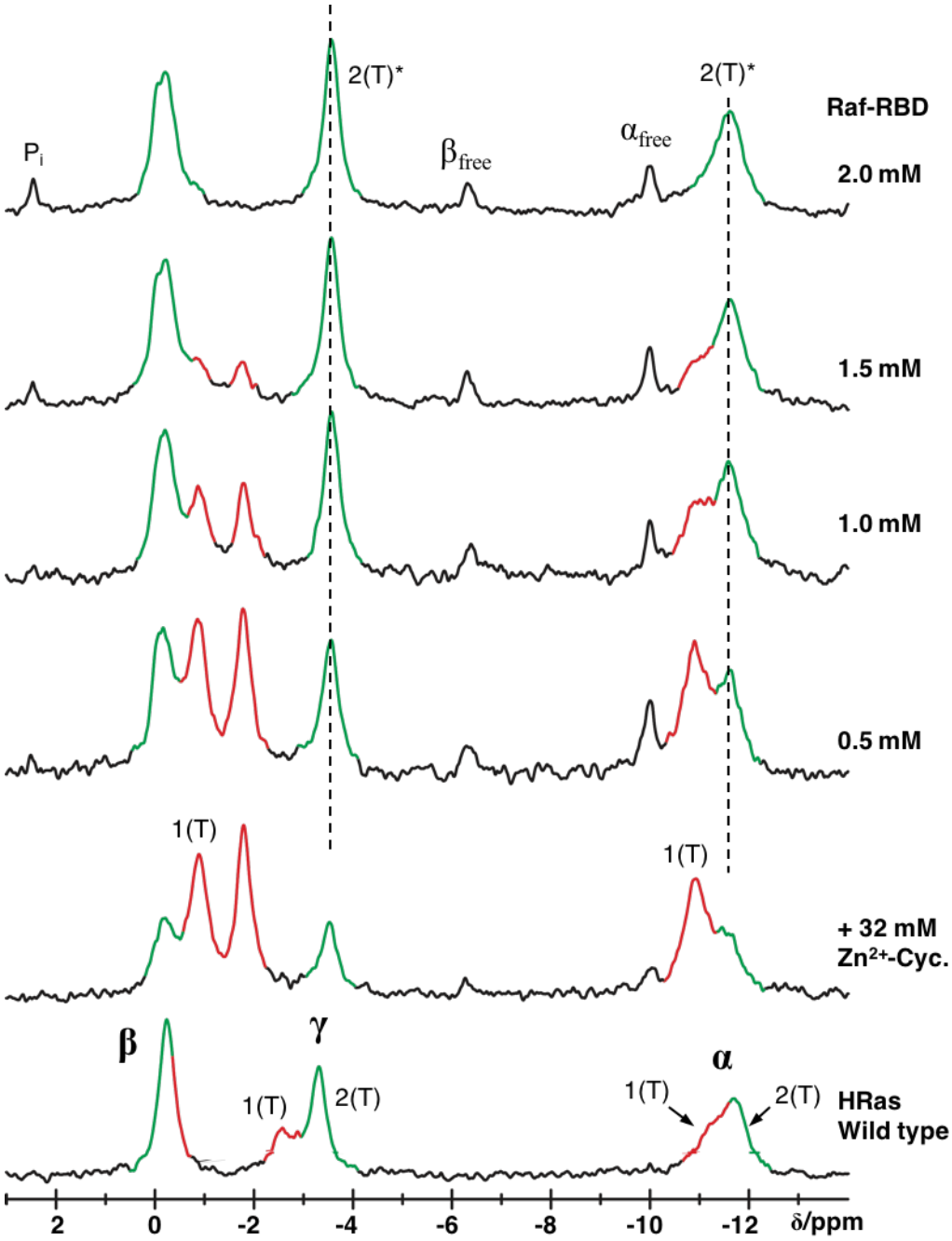

Figure 3.4. Displacement of Zn^{2+}-cyclen from $HRas^{WT}$ upon titration with Raf-RBD followed by ^{31}P NMR spectroscopy. To an initial 1.3 mM Ras protein solution in buffer F (40 mM Tris/HCl pH 7.5; 10 mM $MgCl_2$; 2 mM DTE) with additionally 150 mM NaCl, a great excess of Zn^{2+}-cyclen was added. The concentration of this ligand was kept constant during all the titration steps and equal to 32 mM. The Ras•Zn^{2+}-cyclen complex thereby formed was titrated with increasing amounts of Raf-RBD up to a final concentration of 2.0 mM. The final Ras concentration was 0.8 mM. The dotted lines indicate the chemical shift position corresponding to Ras in the effector-bound conformational state 2(T)*. Additional small signals are visible when Ras becomes saturated with Zn^{2+}-cyclen, corresponding to the γ-, β-, α-phosphate groups of the free nucleotide, located at δ= 0.3, -6.5 and -10.0 ppm, respectively. All the experiments were performed at 278 K and data fitted with an artificial Lorentzian line broadening of 15 Hz. For a better assessment of the evolution of the conformational equilibria during the titration, state 1(T) was coloured red and state 2(T) was coloured green. This data is published in ref [156].

3.1.4 Conformational Equilibria of KRas^{G12D}•GTP and KRas^{G12V}•GTP

The equilibrium of the GTP-bound KRas^{WT}, together with the two oncogenic mutants KRas^{G12D} and KRas^{G12V} was investigated by ^{31}P NMR. The experimental spectra are shown in Figure 3.5 and the fitted chemical shifts and linewidths are listed in Table 3.2. Experimentally, the nucleotide exchange from GDP to GTP is a statistical process solely based in the great excess of the GTP nucleotide that is added to Ras-GDP bound protein (20 to 30-fold). This is the reason why the exchange is typically incomplete and the two resonance lines located at δ= -10.58 and -2.00 ppm, corresponding to the α- and β-phosphates of GDP-bound Ras, are observed in the spectra. For Ras^{WT}, about 74% exchange was obtained. For the oncogenic variants the value is usually higher as they tend to be less prone to release the nucleotide, with a 82% exchange for KRas^{G12D} and, 100%, exchange for KRas^{G12V}. The most striking difference between the three proteins, however, is related with the dynamics observed at the γ-phosphate. In fact, the spectra of KRas^{WT} and KRas^{G12D} shows that state 1(T) is almost non-detectable and lies in the limits of the noise. For both proteins, the equilibrium constant, K_{12}, cannot be determined as only state 2(T) is detectable. On the other hand, state 1(T) can be directly observed in KRas^{G12V} at δ= -6.01 ppm. The corresponding equilibrium constant is K_{12}= 11.60. A similar value is reported elsewhere [123]. From the present data it is also observed a significant downfield shift of state 2(T) in Ras^{G12V} (δ= -7.51 ppm) compared with Ras^{WT} (δ= -7.94 ppm) and Ras^{G12D} (δ= -7.93 ppm). From the calculation of the linewidths (Table 3.2) it is detected a general broadening of the lines in the case of both mutants, as compared to the *wild type*, which can be explained by different time scales of the exchange broadening process between conformational sates on Ras^{WT} as compared to Ras^{G12D} and Ras^{G12V}.

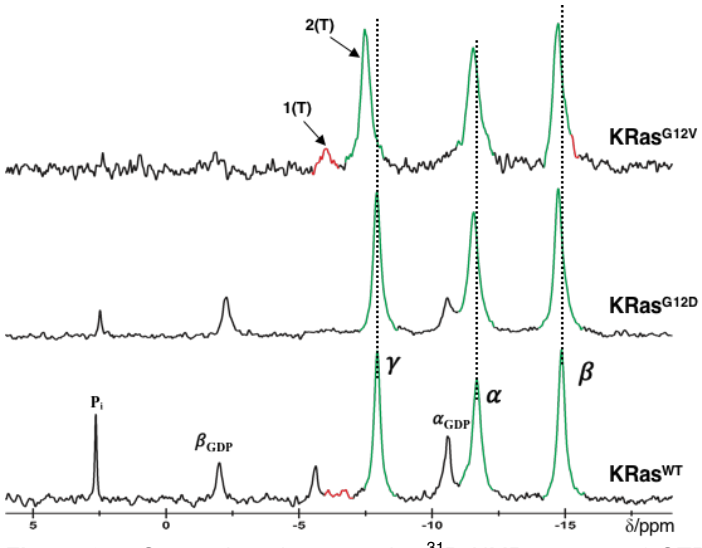

Figure 3.5. Comparison between the ^{31}P NMR spectra of GTP-bound full length KRas^{WT} (bottom), KRas^{G12D} (middle) and KRas^{G12V} (top). The α-, β- and γ-phosphates are indicated, along with the corresponding states 1(T) (red colour) and 2(T) (green colour). The samples were dissolved in buffer F with additionally 0.2 mM DSS and 5% D_2O. Measurements were carried at 278 K at a ^{31}P frequency of 202.456 MHz. The concentration of the three proteins, from the bottom to the top, is 1.5 mM, 2.7 mM and 0.65 mM, respectively. The dashed lines mark the chemical shift position of the *wild type* protein.

Table 3.2. ^{31}P NMR chemical shift values and linewidths of the full length (1-188/189) Mg^{2+}•GTP-bound proteins $KRas^{WT}$, $KRas^{G12D}$ and $KRas^{G12V}$.

Protein	α-phosphate $\delta_{1(T)/2(T)}$ [ppm]	β-phosphate $\delta_{1(T)/2(T)}$ [ppm]	γ-phosphate $\delta_{1(T)}$ [ppm]	γ-phosphate $\delta_{2(T)}$ [ppm]	α_{GDP} δ [ppm]	β_{GDP} δ [ppm]	P_i δ [ppm]
$KRas^{WT}$	-11.68	-14.87	--	-7.94	-10.58	-2.00	2.64
$KRas^{G12D}$	-11.56	-14.76	--	-7.93	-10.59	-2.26	2.48
$KRas^{G12V}$	-11.56	-14.74	-6.01	-7.51	--	--	--
	α-phosphate $\Delta\nu_{1/2\ 1(T)/2(T)}$ [Hz]	**β-phosphate** $\Delta\nu_{1/2\ 1(T)/2(T)}$ [Hz]	**γ-phosphate** $\Delta\nu_{1/2\ 1(T)}$ [Hz]	**γ-phosphate** $\Delta\nu_{1/2\ 2(T)}$ [Hz]	**α_{GDP}** $\Delta\nu_{1/2}$ [Hz]	**β_{GDP}** $\Delta\nu_{1/2}$ [Hz]	**P_i** $\Delta\nu_{1/2}$ [Hz]
$KRas^{WT}$	64.20	45.74	--	40.88	44.67	31.32	2.16
$KRas^{G12D}$	75.20	75.20	--	48.79	63.27	43.35	7.33
$KRas^{G12V}$	98.06	71.74	33.03	63.90	--	--	--

The calculated shift values and linewidths have an error of ±0.001 and ±0.1, respectively. An exponential filter of 15 Hz was applied to the FID and subtracted afterwards from the fitted linewidths.
[a] States 1(T) and 2(T) cannot be separated at the magnetic field used and are therefore represented as single resonance line.

3.1.5 Modulation of the Equilibrium in $KRas^{G12D}$•Mg^{2+}•GppNHp by Zn^{2+}-cyclen

It can be generalized in principle, that the mode of action of state 1(T) inhibitors can be extended from *wild type* Ras to partial-loss-of-function mutants and to oncogenic variants. To test this hypothesis a titration of $KRas^{G12D}$ with Zn^{2+}-cyclen was performed. The results are presented graphically in Figure 3.6 and the fitted shift values and linewidths are given in Table C in the appendix section. The experiment follows the same features reported for $KRas^{WT}$ in section 3.1.2 and leads to the same general result: upon addition of increasing amounts of the drug, state 1(T) is stabilised (its relative area increases) and the population of the conformational state 2(T) decreases. At the same time state 1(T) shifts downfield (the corresponding $\Delta\delta$ is 0.78 ppm, from δ= -2.48 to δ= -1.70 ppm, Table C appendix) and state 2(T) shifts slightly upfield ($\Delta\delta$= -0.08 ppm, from δ= -3.54 to δ= -3.62 ppm). Similar shifts are observed in the case of $KRas^{WT}$ (note that the highest molar ratio of Ras:Zn^{2+}-cyclen is not the same in the two experiments. In the case of $KRas^{WT}$ the last step corresponds to a ratio of 1:30 and in the case of $KRas^{G12D}$ the ratio is only 1:9). In the last titration step (ratio 1:9) of $KRas^{G12D}$, the appearance of sharp resonance lines corresponding to the existence of free nucleotide in solution is again observed for the α_{free} and β_{free}-phosphates at δ= -10.02 ppm and δ= -6.22 ppm, respectively. The chemical shift of the γ_{free}-phosphate (occurring normally at ca. δ= -1.08 ppm) is presently superimposed with state 1(T) and therefore cannot be detected. The presence of inorganic phosphate (P_i) and GMP can also be identified at δ= 3.80 and δ= 2.34 ppm, respectively. It is worth mention that the ^{31}P NMR spectra of both proteins in the absence of the drug (bottom spectra in Figures 3.4 and 3.6)

show also a different equilibria between states 1(T) and 2(T): for $KRas^{WT}$, K_{12}= 1.9 and for $KRas^{G12D}$ K_{12}= 0.7 (measured at the γ-phosphate, Tables A and C in the appendix section, respectively).

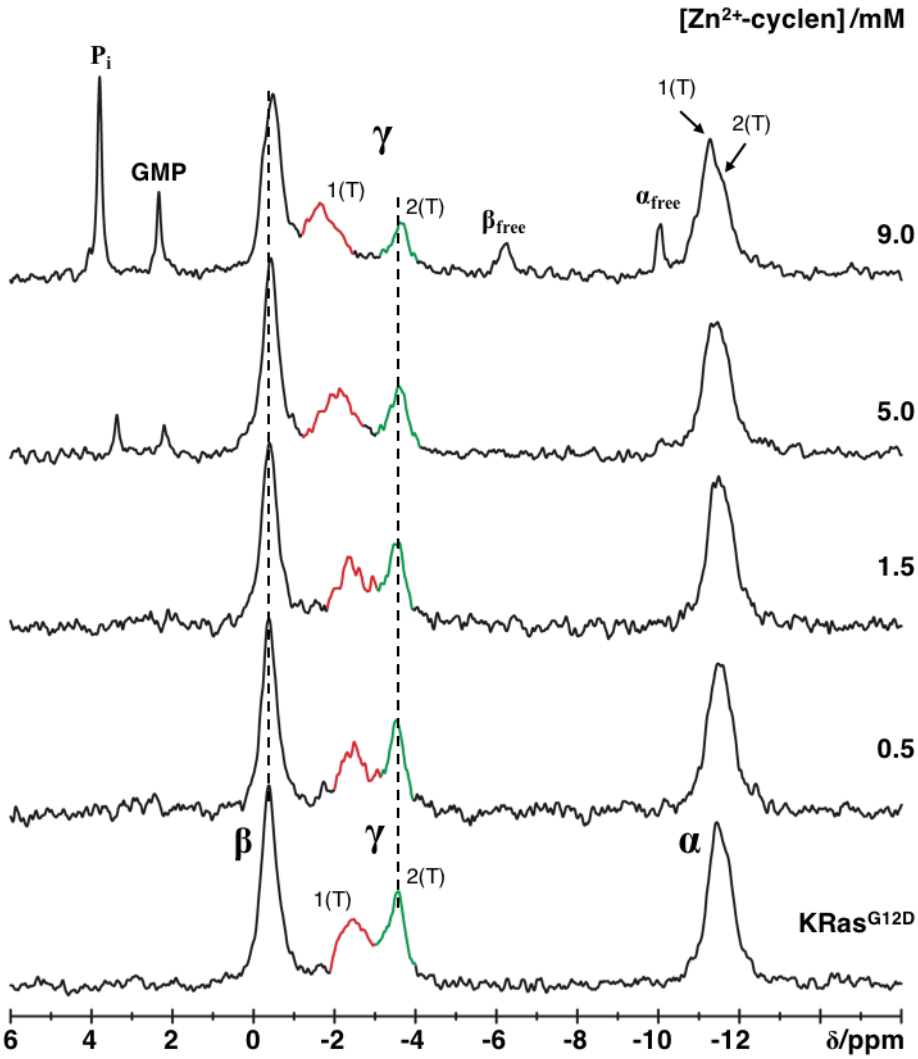

Figure 3.6. Titration of $KRas^{G12D}$(1-188)•Mg^{2+}•GppNHp with Zn^{2+}-cyclen followed by ^{31}P NMR spectroscopy at 278 K. To an initial amount of 1.4 mM of protein dissolved in buffer F (40 mM Tris/HCl pH 7.5; 10 mM $MgCl_2$; 2mM DTE; 0.1 mM DSS; 5% D_2O) with additionally 150 mM NaCl, increasing amounts of Zn^{2+}-cyclen were added (the concentrations are indicated for each step). In the course of the titration, state 2(T) (indicated in green) shifts slightly upfield by a Δδ= -0.08 ppm and state 1(T) (indicated in red) shifts downfield by a Δδ= 0.78 ppm. New additional signals appear in the last steps of the titration, comprising the β- and α-phosphates from the free nucleotide, at δ= -6.22 and δ= -10.02 ppm, respectively. Inorganic phosphate (P_i) is also visible at δ= 3.80 ppm. ^{31}P resonances were recorded in a magnetic field operating at a frequency of 202.456 MHz. An EM window with LB= 15 Hz was used during the processing of the FID.

- This page was deliberately left blank -

3.2 Inhibition of $KRas^{G12D}(1\text{-}188)\bullet Mg^{2+}\bullet GppNHp$ Investigated by ^{31}P NMR and ITC

Direct inhibition of KRas along with the inhibition of Ras-effector and Ras-GEF interactions, are presently topics of very active and intensive research, not only in academia but also at the pharmaceutical industry. ^{31}P NMR was used herein to screen for modifications on the conformational equilibria of oncogenic $KRas^{G12D}(1\text{-}188)$ bound to GppNHp upon interaction with a library of 15 different small drugs. The work reported in this section was performed in collaboration with Boheringer Ingelheim GmbH. The compounds were kindly provided by the R&D department of the company and tested by our group. Some of them were already disclosed to the public domain.

In order to achieve good reproducibility all the $KRas^{G12D}\bullet Mg^{2+}\bullet GppNHp$ samples used were exchanged to the same buffer F (40 mM Tris/HCl pH 7.5; 10 mM $MgCl_2$; 2 mM DTE; 0.2 mM DSS) in 10% D_2O, aliquoted in equal fractions of 1.0 mM each and frozen at -80 ºC. All ^{31}P NMR experiments were performed at 278 K in a magnetic field operating at 202.456 MHz, using a selective ^{31}P 10 mm probe with either 8 or 10 mm Shigemi tubes. For each measurement, 500 μl, 1mM of protein were used. A 70º degree pulse was applied with a total repetition time of 7 seconds. Three spectra with 1600 scans each were recorded, combined and summed up. All the compounds tested were provided by Boheringer as a powder. They were afterwards dissolved in deuterated DMSO with a final concentration of 50 mM. $KRas^{G12D}$ was titrated in two steps: by adding in total 15 μl (first step) followed by 30μl (second step) of the compound stock. This corresponds to a 1.5 mM and 3.0 mM drug concentration, respectively. The $KRas^{G12D}$ concentration was always kept at 1.0 mM.

For all the screened compounds, the equilibrium constant K_{12} was calculated after fitting of the data. An exponential line broadening of 15 Hz was applied to all spectra and subtracted at the end from the fitted linewidth values. Following are presented the obtained results from this study.

3.2.1 Effect of DMSO

Because all compounds were dissolved in perdeuterated DMSO, the influence of this solvent alone in the conformational equilibrium was firstly tested. Ras was dissolved in 6% DMSO, corresponding to the highest concentration used in this work, and the ^{31}P NMR spectra were recorded. The analysis was made for the γ-phosphate to which the states are best separated. The result is presented in Figure 3.7. Addition of DMSO leads to chemical shift changes that cannot be neglected. Both states, 1(T) and 2(T) undergo a upfield shift, with a $\Delta\delta$ of -0.08 ppm for the former and -0.04 ppm for the latter. The α- and β-phosphates, on the other hand, remain unperturbed. DMSO also leads to a general broadening of all spectral lines of ca. 8.0 Hz, except for state 2(T) that remains unaltered. The obtained equilibrium constant decreases from 0.70 to 0.64, corresponding to a 10% difference, which, although small, needs to be accounted in the subsequent titration experiments. All the fitted chemical shift values for all the tested compounds are shown in Table 3.3 at the end of section 3.2. The fitted linewidths are presented in Table 3.4. In all experiments, the α- and β-phosphates were fitted as a single resonance line.

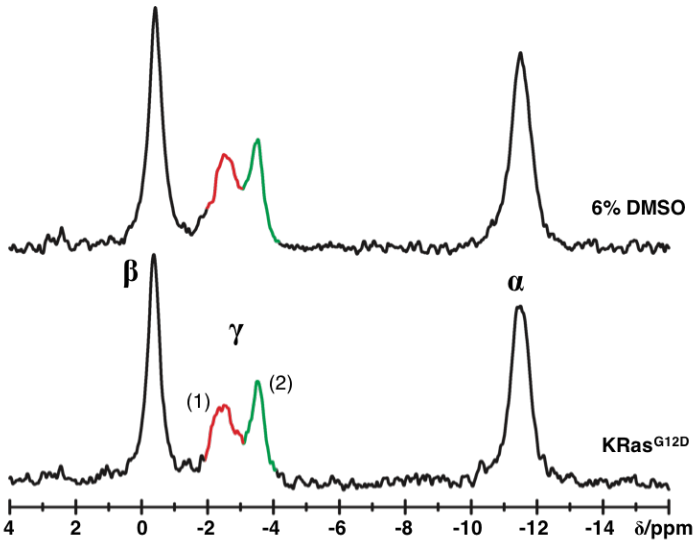

Figure 3.7. Influence of 6% DMSO on the conformational equilibria of KRas^{G12D}•Mg^{2+}•GppNHp.

3.2.2 Compound #16324643

Upon titration with #643, a slight line broadening was observed for state 1(T). At 3.0 mM, K_{12} decreases from 0.64 to 0.57, indicating a shift of the equilibrium towards state 2(T), which is unexpected since in the presence of the drug, the weak effector binding state 1(T) should in principle be favoured. The 11% difference might be not significant due to the spectral noise and the inherent uncertainty of the fitting process.

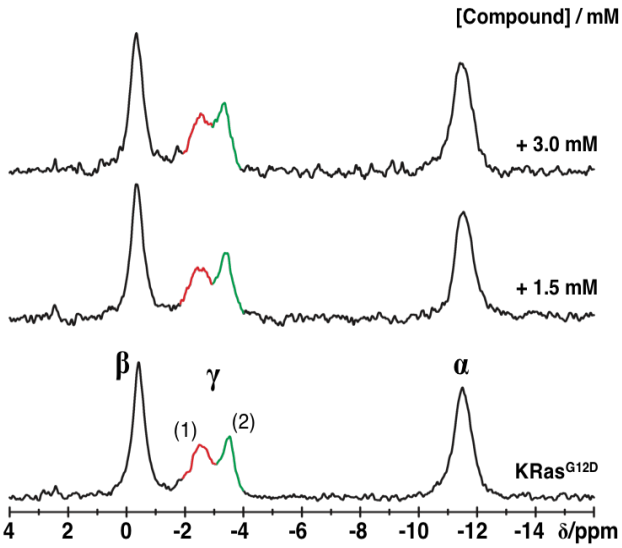

Figure 3.8. Titration of $KRas^{G12D}$•Mg^{2+}•GppNHp with compound #643.

3.2.3 Compound #16328098

Compound #098 promotes a change in the equilibrium constant from 0.64 to 0.72, with state 2(T) being slightly favoured over state 1(T). This corresponds to a small difference of 12% in K_{12} when compared with Ras in 6% DMSO. The fitted chemical shifts and linewidths remain unperturbed.

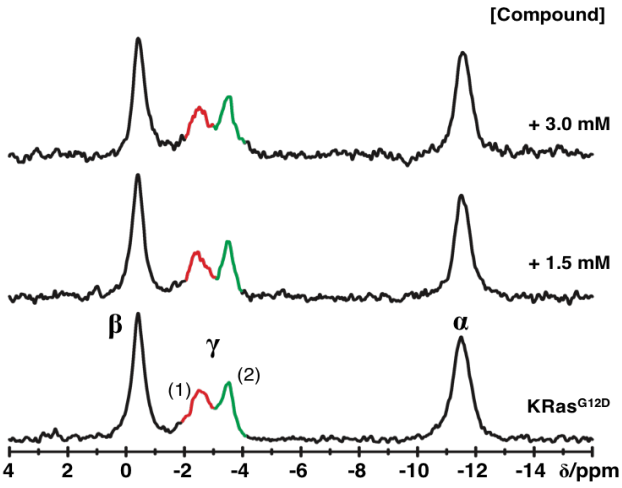

Figure 3.9. Titration of $KRas^{G12D}$•Mg^{2+}•GppNHp with compound #098.

3.2.4 Compound #35127727

This drug was identified as an inhibitor of the SOS-catalysed KRas activation by the Fesik group upon a fragment-based screening using NMR methods [145]. It was determined that the molecule binds directly to $KRas^{G12D}$•Mg^{2+}•GDP but also to H- and $KRas^{WT}$ in a hydrophobic pocket formed by Val7, Leu56 and Tyr71. H-bond contacts are established between the N1 atom of the imidazopyridine ring and the side chain of Ser37 and between indole -NH groups and the side chain of Asp54. Figure 3.10 shows the cartoon and

molecular surface representation of the Ras•#727 complex (pdb: 4epv) and the ^{31}P NMR titration. The equilibrium constant decreases 40% at a 3.0 mM concentration, leading to a pronounced effect in the dynamics of states 1(T) and 2(T). There are significant chemical shift changes observed for β-phosphate that shifts upfield by a $\Delta\delta$= -0.07 ppm and for state 1(T) that shifts downfield by a $\Delta\delta$= 0.08 ppm at a 3.0 mM of the Drug (Table 3.3). A 22 Hz decrease in line broadening is observed for state 1(T) (from $\Delta\nu_{1/2}$=154 to $\Delta\nu_{1/2}$= 138 Hz) and, at the same time, an increase of 38 Hz is observed for state 2(T) (from $\Delta\nu_{1/2}$= 69 to $\Delta\nu_{1/2}$= 106 Hz, Table 3.4).

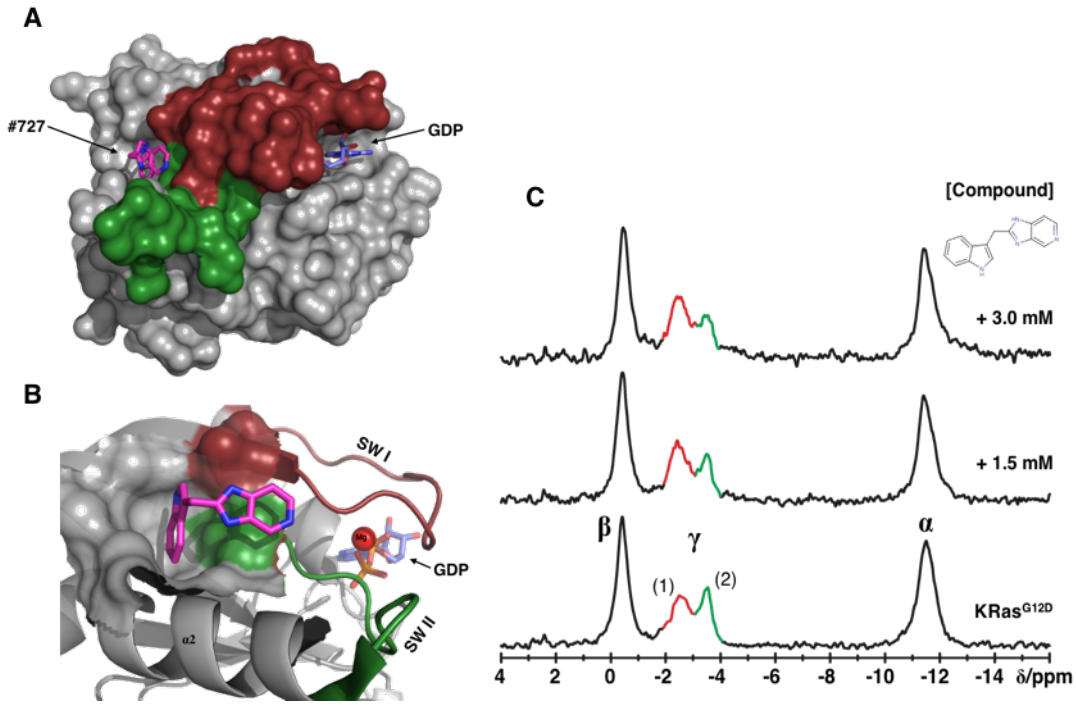

Figure 3.10. A. Surface representation of the crystal structure of KRas•Mg^{2+}•GDP complexed with the compound #727. The switch 1 and switch 2 regions are represented in dark-red and green, respectively. The spatial localization of the small drug relative to the nucleotide position is shown (pdb: 4epv, [145]). **B.** Zoom around the binding site evidencing the hydrophobic region were the compound fits. **C.** Titration of KRas^{G12D}•Mg^{2+}•GppNHp with the drug followed by ^{31}P NMR spectroscopy. The 2D structure of the compound (an indole derivate) is shown.

3.2.5 Compound #35139703

The compound #703 was not completely soluble when mixed with the protein. A slight precipitation was observed in the NMR tube which is reflected by the decrease of intensity on the spectra presented in Figure 3.11 (the spectra was "stretched" vertically – note the difference in the noise level compared with $KRas^{G12D}$ in DMSO). No considerable chemical shift changes are observed except for the α-phosphate that moves upfield by $\Delta\delta$= -0.1 ppm. The difference in the K_{12} values is not meaningful (from 0.64 to 0.68 at a drug concentration of 3.0 mM).

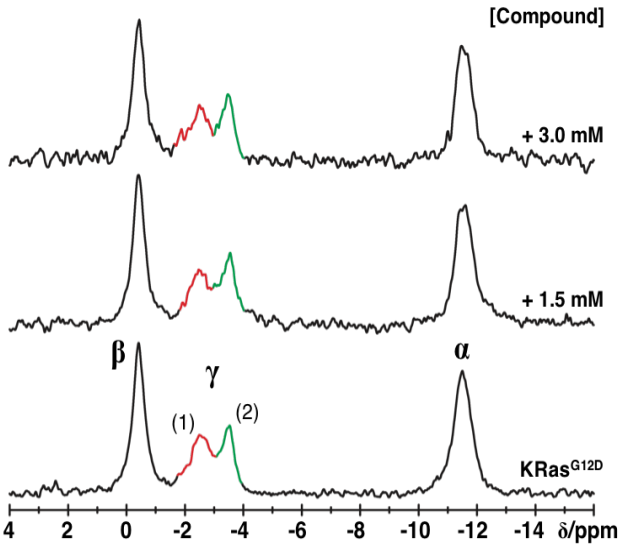

Figure 3.11. Titration of $KRas^{G12D}$•Mg^{2+}•GppNHp with compound #703.

3.2.6 Compound #35141449

Upon addition of the compound #449 to Ras, slight precipitation was observed. The equilibrium constant at 3.0 mM is 0.68, corresponding to an 6% increase compared to Ras alone in 6% DMSO. The difference is within the limits of the error for the measurement and is not significant. An average line broadening of ca. 24 Hz is also observed at 3.0 mM for all the resonance lines, except for the β-phosphate that remains unperturbed.

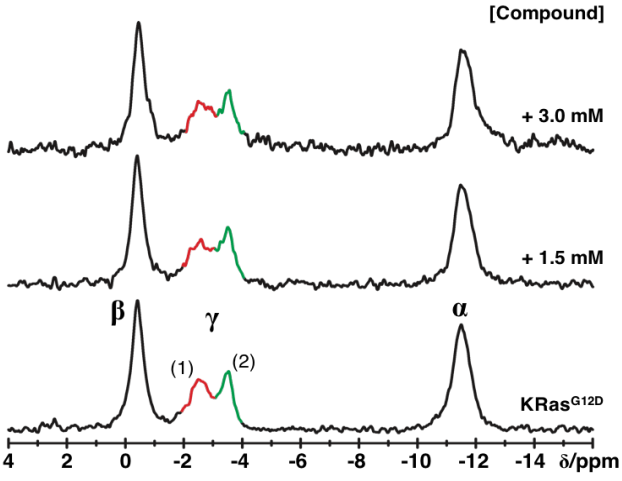

Figure 3.12. Titration of $KRas^{G12D}$•Mg^{2+}•GppNHp with compound #449.

An upfield shift of -0.09 and -0.06 ppm is observed for the α- and β-phosphates, respectively. The γ-phosphate remains unperturbed.

3.2.7 Compound #35145071

This drug is a cyclic peptide obtained by Pei and co-workers through application of the "rapalog" methodology upon screening of a large combinatorial library against $KRas^{G12V}$•Mg^{2+}•GDP [246]. Interaction studies using fluorescence polarization and SPR showed that #071 binds to $KRas^{G12V}$ with high affinity (K_D=0.83 μM) and is also able to disrupt the Ras-Raf interaction with an IC_{50} of 0.2 μM [247].

The ^{31}P NMR titration experiments showed that the addition of this compound to $KRas^{G12D}$ led to protein precipitation in the NMR tube. This is also noticeable by the reduction of the spectral intensity in Figure 3.13B. The equilibrium constant at 1.5 mM is 0.58, which is not significantly different from the K_{12} value for Ras in 6% DMSO (due to the poor spectral quality, the calculation of K_{12} has a greater associated error of ± 0.4). At a drug concentration of 3.0 mM, the resonance lines are broadened almost behind detection and most of the protein became precipitated, rendering impossible the analysis of this titration step. A general increase in the line broadening is observed, especially for state 1(T) ($\Delta\nu_{1/2}$=105 Hz, Table 3.4).

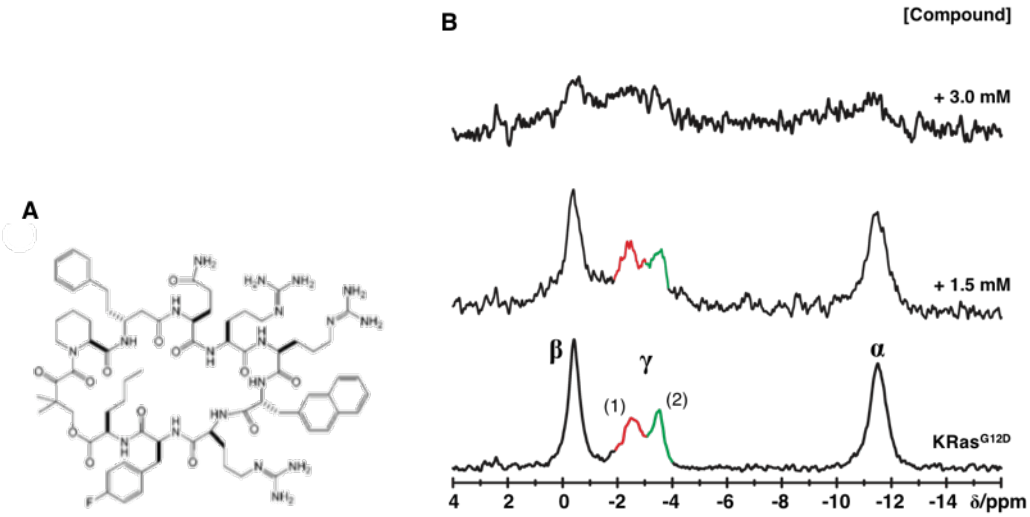

Figure 3.13. A. Representation of the "rapalog" cyclic peptide #071. **B.** Titration of $KRas^{G12D}$•Mg^{2+}•GppNHp with increasing amounts of the compound followed by ^{31}P NMR spectroscopy.

3.2.8 Compound #35117109

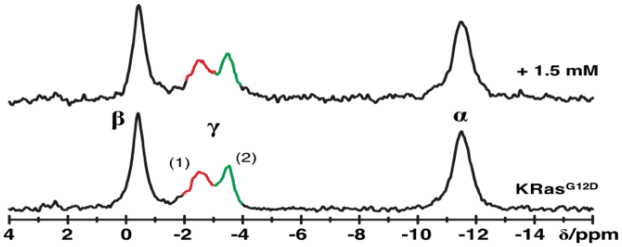

Figure 3.14. Titration of KRas^{G12D}•Mg^{2+}•GppNHp with compound #109.

Contrary to all the compounds tested, where a 50 mM stock solution for each one was prepared prior to the titration, the solubility of compound #109 was very limited. Only a saturated 25 mM solution was prepared in this case. Upon addition of 50 μl to the protein, there were no obvious spectral changes (Figure 3.14). At 1.5 mM of drug, K_{12}= 0.70, corresponding to an increase of 10% compared to the K_{12} of Ras in 6% DMSO, a difference that again is not significant. Also, no significant chemical shift differences from the values obtained for Ras alone in 6% DMSO can be found. The only meaningful effect is an increase of the line broadening for state 2(T) ($\Delta\Delta\nu_{1/2}$= 28 Hz, from $\Delta\nu_{1/2}$= 68 Hz in Ras alone to $\Delta\nu_{1/2}$= 97 Hz in the presence of #109).

3.2.9 Compound #35129755

#755 is an indol derivative with a methylbutanamide group whose synthesis was previously reported by Fesik and co-workers [145]. Its structure is presented in Figure 3.15 (the derivatised functional group is indicated by the red circle) along with the corresponding ^{31}P NMR titration series.

Titration of KRas^{G12D} led to a drastic modification in the conformational equilibria of states 1(T) and 2(T). At 1.5 mM, the equilibrium constant was reduced by 38% and at 3.0 mM it decreased by 70% (from 0.64 to 0.19, Table 3.3). Interestingly, no appreciable line broadening of the signals or significant chemical shift changes are observed during the course of the experiment. There is no information in the literature regarding structural details of the binding mechanism to Ras, neither affinity or kinetic data. From the ^{31}P NMR results

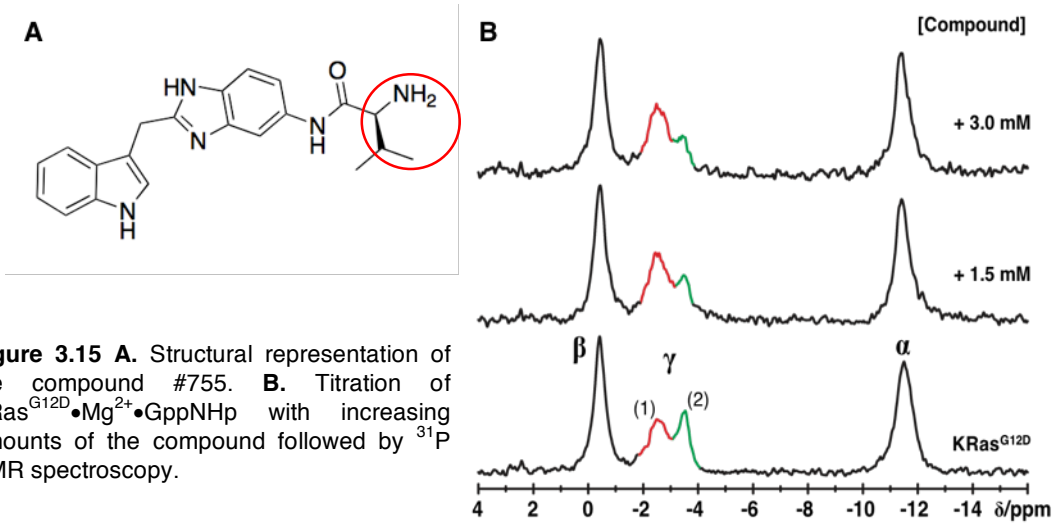

Figure 3.15 A. Structural representation of the compound #755. **B.** Titration of KRas^{G12D}•Mg^{2+}•GppNHp with increasing amounts of the compound followed by ^{31}P NMR spectroscopy.

it seems nevertheless that this small molecule is able to greatly modify the equilibrium population by stabilising state 1(T). In light of these results it was decided to test it further by measuring its ability to disrupt the Ras-Raf complex formation by ITC, with the expectation to retrieve thermodynamic and affinity data. Since in the course of the NMR titration the population of state 2(T) decreases through the shift of equilibrium towards state 1(T), one can hypothesize that the affinity of $KRas^{G12D}$ to Raf should decrease when increasing amounts of the drug are added to the system under equilibrium conditions.

Figure 3.16A-D shows the ITC profile of the experiment that was conducted. All the measurements were done at 298 K in buffer F with additionally 150 mM NaCl and 3% DMSO. The affinity between $KRas^{G12D}$ and Raf-RBD was initially measured alone (Figure 3.16A). In this case, a total of 19 injections of Raf-RBD (679 μM, located in the syringe) with a volume of 2 μl each were added to $KRas^{G12D}$•Mg^{2+}•GppNHp (60 μM, located in the cell). The thermodynamic parameters were calculated by nonlinear regression analysis using an iterative routine (eqn. nº5, experimental section 2.2.4). During the optimization process all the parameters were allowed to vary freely and are presented here as the final unchanged output from the program. The results indicate a 1:1 binding (N=1) and an obtained apparent K_D= 0.38 μM. Compared to the obtained values for $KRas^{WT}$ (K_D= 0.72 μM, section 3.1.1) one can find that the affinity of $KRas^{G12D}$ towards Raf is 2-fold higher than $KRas^{WT}$.

The ability to disrupt the Ras-Raf interaction in the presence of the compound #755 was tested using the same experimental conditions as described above for Ras-Raf (same temperature, buffer and pH). $KRas^{G12D}$ (35 μM) was placed in the adiabatic cell of the calorimeter. Raf (always at a concentration of 450 μM) was mixed beforehand with compound #755, the mixture was placed in the syringe and the Ras protein was titrated by performing 31 injections of 1.3 μl each, with an interval time of 150 s. Three consecutive measurements, with increasing concentrations of #755 were tested (Figure 3.16B-150 μM, C-300 μM and D-500 μM).

The first feature observed from the titration conducted in the presence of the drug is related to differences in the baseline (Figure 3.16B-D) when compared to the titration of Ras-Raf alone (Figure 3.16A): for all the three concentrations tested the differential power plot shows strong baseline perturbations over the complete duration of the experiment. These seem to be accentuated as the concentration of the drug increases and are not observed in the isotherm of Ras-Raf alone, nor for any control experiments performed (buffer-in-buffer, buffer-in-Ras, Raf-in-buffer, #755-in-Raf). They are therefore due to the presence of the compound. A possible explanation can be related with the existence of microscopically precipitated or aggregated Ras or Raf proteins by its presence (although no precipitation

was observed when the solutions were being mixed nor during NMR experiments). Nevertheless, an initially high heat of injection was obtained in all measurements, which still allowed the obtention of a well-defined binding curve. The inhibitory effect of #755 in complex formation can be clearly observed: the K_D of the Ras-Raf interaction increases by a 5-fold factor with increasing concentrations of the drug, from 0.41 μM at 150 mM to 1.94 μM at 500 mM. The affinity between the two proteins is indeed disrupted by the action of #755.

It is noteworthy the fact that all the four interaction experiments proceed with a very similar variation in the Gibbs energy. The presence of the compound has no interference in the degree of spontaneity of the association reaction. The Ras-Raf interaction alone has a slightly greater enthalpic contribution (ΔH= -23.4 kJ mol^{-1}) as compared to the entropy variation (-TΔS= -13.3 kJ mol^{-1}). However, upon addition of #755, the profile changes and the entropic contribution is now greater than the enthalpic one. This is observed at all concentrations of #755 tested.

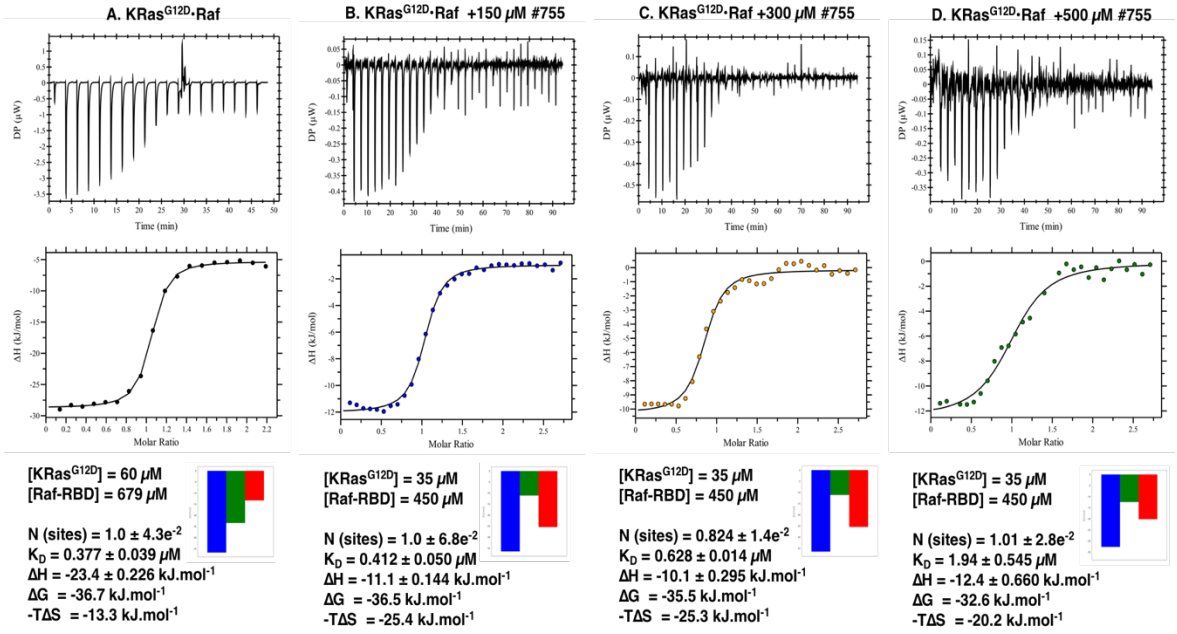

Figure 3.16. Titration of KRas^{G12D}•Mg^{2+}•GppNHp with the effector Raf-RBD in the presence of the compound #755 followed by ITC. All the experiments were done at 298 K and in the same buffer F (40 mM Tris/HCl pH 7.5, 10 mM $MgCl_2$, 2 mM DTE) with additionally 150 mM NaCl and 3% DMSO. **A.** The Ras-Raf interaction was firstly tested alone. The effect of #755 in the affinity of the complex was tested for three different concentrations of the drug: 150 μM **(B)**, 300 μM **(C)**, and 500 μM **(D)**. In all the cases Ras was placed in the cell and Raf, previously mixed with #755 in the desired concentration, was placed in the syringe of the calorimeter. The concentration of both proteins was kept constant while testing the effect of #755. For each experiment, the thermogram is represented as heat per unit of time (upper plot) and as the integrated heat for each injection per ratio of the Ras-Raf complex (lower plot). The signature plot is also shown along with the obtained thermodynamic values. Blue: ΔG, green: ΔH, red: -TΔS.

3.2.10 Compound #35129757

#757 is an amino acid analogue consisting of a proline linked to an indole-benzimidazole moiety that was also developed through derivatization of the same parental compound by the Fesik group [145]. Structural studies have shown that #757 binds to $KRas^{G12V}$•Mg^{2+}•GDP with a K_D= 340 μM. The indole moiety binds to the primary binding cleft, similarly to #727 described in section 3.2.4 and the bezimidazole moiety, being positive in nature, binds to a nearby secondary electronegative cleft, with the proline nitrogen of #757 interacting with the carboxylic side chain of Asp38 (similarly to #755 described above) [145].

Figure 3.17 shows the X-ray structure of #757 bound to $KRas^{G12V}$•Mg^{2+}•GDP (pdb: 4epy) along with the ^{31}P NMR titration on $KRas^{G12D}$•Mg^{2+}•GppNHp. Similarly to compound #755, dramatic spectral changes are observed in the equilibrium between states 1(T) and 2(T) by the action of #757: at 1.5 mM, K_{12} is reduced by 45% and at 3.0 mM it decreased by 69% (from 0.64 to 0.20, Table 3.3). Only state 1(T) undergoes a significant downfield shift of $\Delta\delta$= 0.1 ppm (from δ= -2.56 to δ= -2.47 ppm) upon addition of 3.0 mM of the drug, with the other resonances remaining unperturbed.

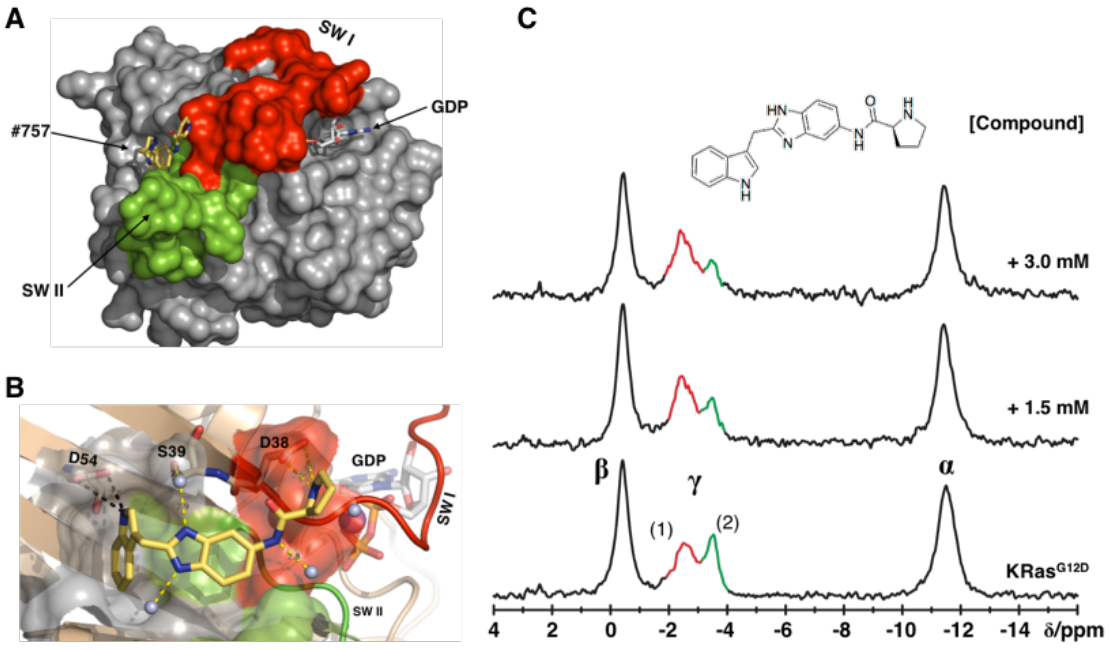

Figure 3.17. A. Molecular surface representation of $KRas^{G12V}$•Mg^{2+}•GDP complexed to the compound #757 (pdb: 4epy, [145]). The relative orientation of #757 and GDP is depicted. The surface of the protein is coloured in grey except for the residues comprising switch 1 and switch 2, which are coloured in red and green, respectively. **B.** Detail around the binding site of #757. The indol moiety of the drug is buried in the first cleft and contacting the carboxylic chain of Asp54. The benzimidazole moiety is located in the second binding cleft and stabilised by polar contacts to Glu38, Ser39 and H_2O molecules. **C.** Titration of $KRas^{G12D}$•Mg^{2+}•GppNHp with #757 followed by ^{31}P NMR spectroscopy.

The disruption of the Ras-Raf complex was tested by ITC using the same experimental design as described above. Figure 3.18 shows the obtained results for the interaction in the presence of 150 μM (B) and 300 μM (C) of #757. From the recorded differential power it can be inferred that each injection yields large peaks, even at the end of the titration, when all the Ras protein is virtually saturated with an excess of Raf and the heat variation should be minimal. As an injection is made into the sample cell, friction force of the ligand being injected, slight temperature mismatches between both solutions, and/or any mismatch of the Ras and Raf buffers will lead to a heat known as the heat of dilution. In this case, as for all the ITC measurements performed within the work of this thesis, all proteins were dialyzed against the same buffer prior the experiment. Control tests involving only the injection of buffer into buffer yielded a residual heat of mixture below 0.1 μcal s^{-1}. However, it was not possible dialyze the drug alone due to its small size and lyophilization was impractical due to the presence of DMSO. Therefore, the large peaks from the heat of mixture can be ascribed to discrepancies in the composition of the buffer in the syringe caused by its presence. Nevertheless, it was still possible to detect binding events as observed by the

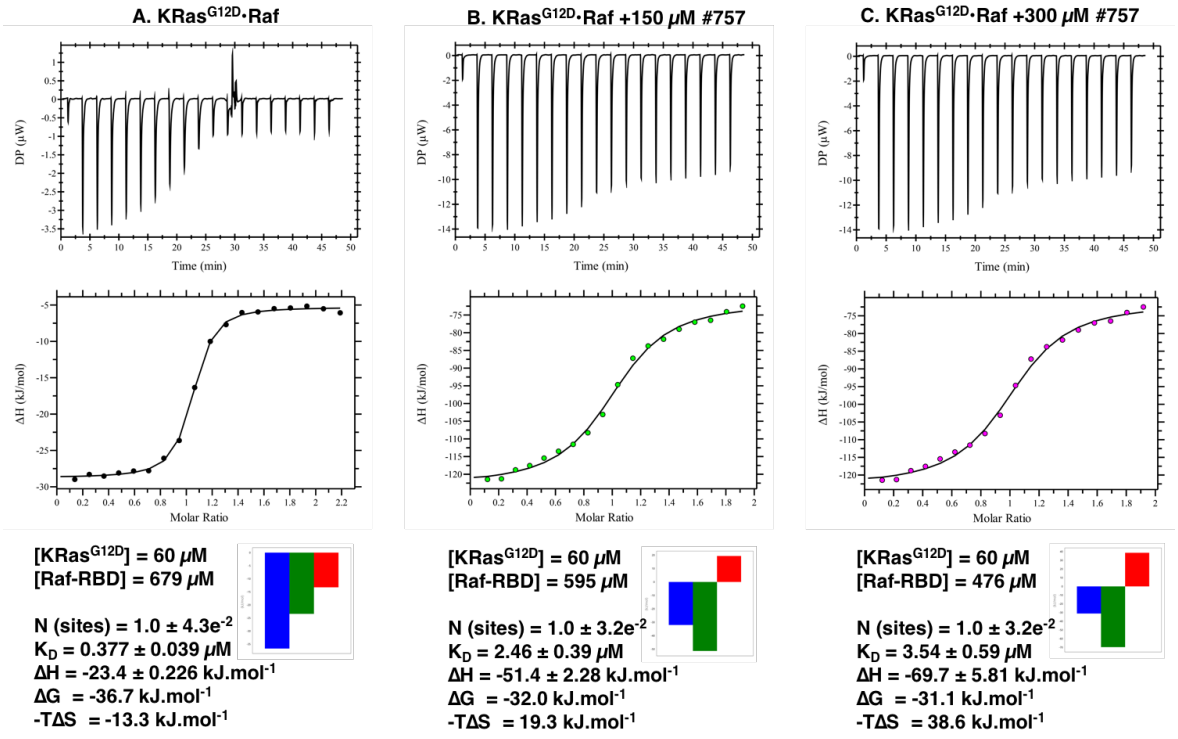

Figure 3.18. Titration of KRas^{G12D}•Mg^{2+}•GppNHp with Raf-RBD in the presence of the compound #757 followed by ITC. All the experiments were done at 298 K in the same buffer F (40 mM Tris/HCl pH 7.5, 10 mM $MgCl_2$, 2 mM DTE) with additionally 150 mM NaCl and 3% DMSO. **A.** The Ras-Raf interaction was firstly tested alone. The effect of compound #757 was subsequently studied at two different concentrations: 150 μM **(B)** and 300 μM **(C)**. Tests with higher concentrations rendered impossible the determination of a binding curve due to excessive drifts detected in the baseline.
In all experiments, Ras was placed in the cell and Raf, previously mixed with #757 in the desired concentration, was placed in the syringe. Note that the Raf concentration is not constant. The raw heat of the reaction is plotted in the upper graph and the integrated heat *per* Ras:Raf ratio is shown in the lower graph. The signature plot is also shown with the following colour code: blue: ΔG, green: ΔH, red: -TΔS.

typical sigmoidal behaviour of the integrated heats on Figure 3.18B and C. The presence of the compound #757 has a remarkable inhibitory effect on the interaction between the two proteins. The K_D of the interaction changes from 0.39 μM to 3.54 μM at 300 μM of #757, corresponding to a 9-fold decrease on the affinity of the protein complex.

3.2.11 Compound #35131307

Compound #307 is an analogue of the inhibitor Sulindac sulphide [147] whose structure and mechanism of action towards KRas have not yet been disclosed to the scientific community. Figure 3.19 shows its influence in the equilibrium of the conformational states detected by ^{31}P NMR. At a concentration of 3.0 mM, the equilibrium constant is 0.41, a value that compared to the Ras sample in 6% DMSO, corresponds to a clearly significant reduction of 36%.

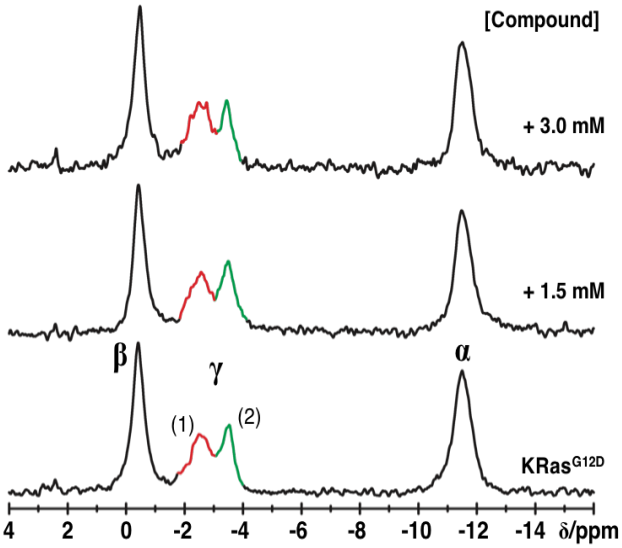

Figure 3.19. Titration of Ras^{G12D}•Mg^{2+}•GppNHp with compound #307.

3.2.12 Compound #35131308

Compound #308 is another analogue of Sulindac sulphide developed in parallel with the compound #307. Titration of KRas^{G12D} showed that significant spectral changes are observed for the conformational states at the γ-phosphate. These changes have the same order of magnitude as the ones induced by compound #307, indicating that they are most likely structurally related. At a 3.0 mM concentration, the equilibrium constant is 0.46, corresponding to a reduction of 28% compared to Ras in 6% DMSO. Also, a downfield shift by a $\Delta\delta$=

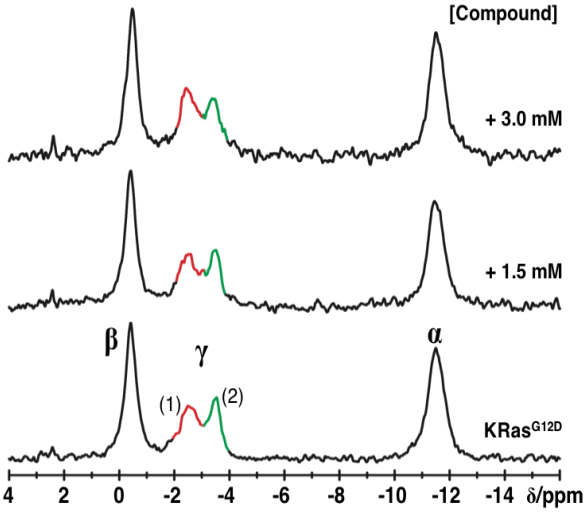

Figure 3.20. Titration of Ras^{G12D}•Mg^{2+}•GppNHp with compound #308.

0.08 and $\Delta\delta$= 0.1 ppm is observed for states 1(T) and 2(T), respectively. The β-phosphate, usually unperturbed, also shifts upfield in this case, with a $\Delta\delta$= -0.07 ppm.

3.2.13 Compound #35135612

#612 is another indol-based molecule containing a methylpentanamide functional group synthesized by Fesik and co-workers [145]. The functional derivatised moiety is highlighted by the red circle in Figure 3.21A and the titration series is presented in Figure 3.21B. Addition of #612 to Ras led to one of the greatest modifications in the equilibrium in terms of states 1(T) and 2(T) from all the investigated drugs. At 1.5 mM K_{12} is reduced by 38% and at 3.0 mM it decreases further to 70% (from 0.64 to 0.19, Table 3.3). The observed spectral changes are similar to the ones measured for the compound #755.

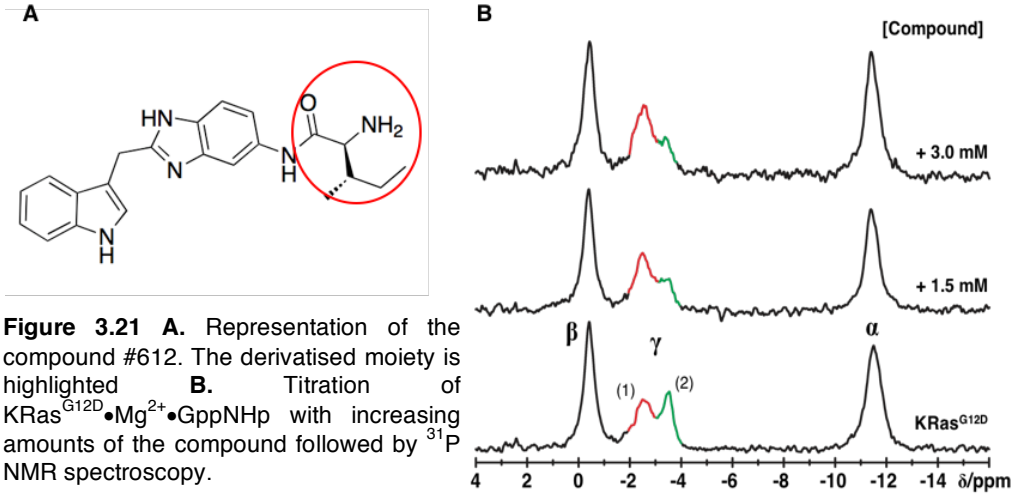

Figure 3.21 A. Representation of the compound #612. The derivatised moiety is highlighted **B.** Titration of $KRas^{G12D}$•Mg^{2+}•GppNHp with increasing amounts of the compound followed by ^{31}P NMR spectroscopy.

3.2.14 Compound #35135613

#613 is the parental indole-benzimidazole molecule that was used for the initial derivatization performed by Fesik and co-workers [145]. Several amino acid-linked analogues containing positively charged amine groups were synthesized using this scaffold. The point where #613 was derivatised is represented by the red circle on Figure 3.22A. The above tested compounds #755 #757 and #612 are its direct analogues obtained by this method. Studies conducted by the same group had shown that it binds $KRas^{G12D}$•Mg^{2+}•GDP with the lowest affinity of the series (K_D= 1.3 mM) and has no inhibitory effect in SOS-catalysed nucleotide exchange assays. Unfortunately, due to the limitations in the amount of $KRas^{G12D}$ available it was not possible to perform calorimetric measurements with #613. Figure 3.22B shows the ^{31}P NMR titration series and the effect

on the conformational equilibrium of KRas^{G12D}. Similarly to its derivatives, #613 promotes a drastic decrease in the equilibrium constant from 0.64 to 0.31 at a concentration of 3.0 mM. Significant chemical shift changes are also observed, especially for state 1(T) that moves downfield by a $\Delta\delta$ of 0.17 ppm, accompanied by a decrease in line broadening of ca. 40 Hz.

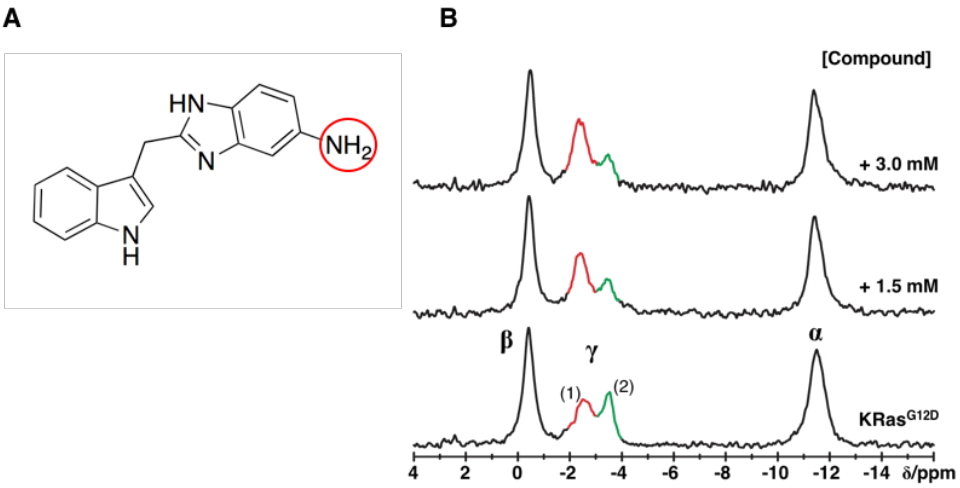

Figure 3.22. A. Representation of the compound #613. This is the parental molecule whose derivatization lead to the synthesis of compounds #755, #757 and #612 through an amide coupling process at the amine group of the benzoimidazol moiety (red circle).
B. Titration of KRas^{G12D}•Mg^{2+}•GppNHp with increasing amounts of the compound followed by ^{31}P NMR spectroscopy.

3.2.15 Compound #35135624

#624 is a sulfonamide containing an aminopyridin fluorbenzen moiety synthesized by the Fesik group [145]. The X-ray structure of the KRas^{G12D}•Mg^{2+}•GDP•#624 complex (pdb: 4epx) shows that the pyridine nitrogen atom is bound to the side chains of Asp54, Arg41 and Ser39 through mediated H_2O interactions (Figure 3.23A). The ^{31}P NMR experiments revealed that, as for all the Fesik compounds, the binding of #624 to KRas^{G12D} leads to significant spectral changes. The equilibrium constant at 3.0 mM is reduced to 0.28, corresponding to a 60% decrease compared to the Ras protein in 6% DMSO. At the same time, the most significant chemical shift changes from all the tested compounds are observed herein: the α- and β-phosphates shift downfield and upfield by $\Delta\delta = \pm 0.1$ ppm, respectively and state 2(T) undergoes a very large downfield shift, with a $\Delta\delta = 0.4$ ppm (from $\delta = -3.49$ to $\delta = -3.09$ ppm, Table 3.3). In parallel, a decrease in the linewidth of state 1(T) by 48 Hz and an increase in the one of state 2(T) by 58 Hz is detected, both indicating a modification in the rates of the conformational exchange between states 1(T)/2(T) induced by this drug.

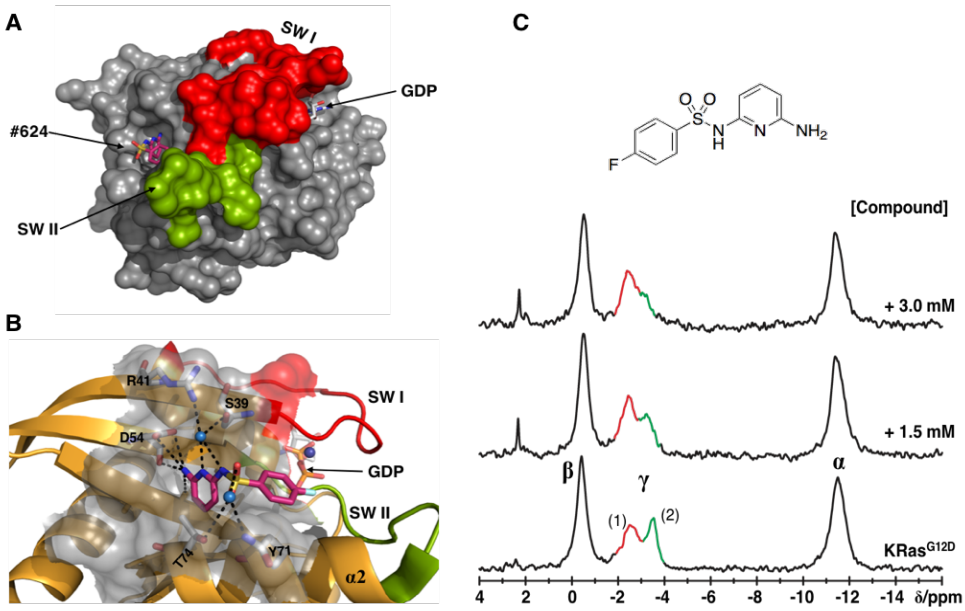

Figure 3.23. A. Molecular surface representation of $KRas^{G12V}$•Mg^{2+}•GDP complexed to the compound #624 (pdb: 4epx, [145]). The relative orientation of #624 and GDP is depicted. The surface of the protein is coloured in grey except for the residues comprising the switch 1 and switch 2, which are coloured in red and green, respectively. **B.** Detail around the binding site of #624.The blue spheres represent water molecules through which the pyridine NH_2, the ortho and the sulfonil nitrogen atoms bind. Note that this binding pocket is common for all the compounds tested from the Fesik group (#624, #755, #757, #613, #612). **C.** Titration of $KRas^{G12D}$•Mg^{2+}•GppNHp with #624 followed by ^{31}P NMR spectroscopy. The molecular structure of this drug is represented.

3.2.16 Compound #35135616

#616 is another indole derivative containing a dichloro aminoethyl moiety developed by Till Maurer and co-workers in collaboration with Genentech Inc. [18]. This small molecule was given the abbreviated designation of DCAI and it binds to $KRas^{G12D}$•Mg^{2+}•GMPCP in the same cleft that accommodates the compounds from the Fesik group (pdb: 4dst, Figure 3.24A and B). Studies had shown that the apparent K_D of the interaction with Ras is 1.1 mM. From the present ^{31}P NMR titration experiments, DCAI leads to a shift in the equilibrium constant in the opposite direction of all the other compounds tested, favouring an increase of the state 2(T) over state 1(T). At 3.0 mM, K_{12}= 1.05, which corresponds to an increase by 65%. At the same time both, the β-phosphate and state 2(T) shift downfield by a $\Delta\delta$ of 0.1 ppm. ITC binding studies performed here showed that the compound is indeed capable of inhibiting the formation of the Ras-Raf complex (Figure 3.25). At 300 μM of the drug, the affinity of the protein complex decreases 10-fold compared with the obtained values for Ras-Raf alone (K_D= 3.53 μM vs 0.38 μM). The titration was recorded with a very pronounced heat of mixture, which even with the best efforts, was impossible to minimize further. From the signature plot one can observe that the reaction proceeds with a negative entropic contribution in the presence of DCAI.

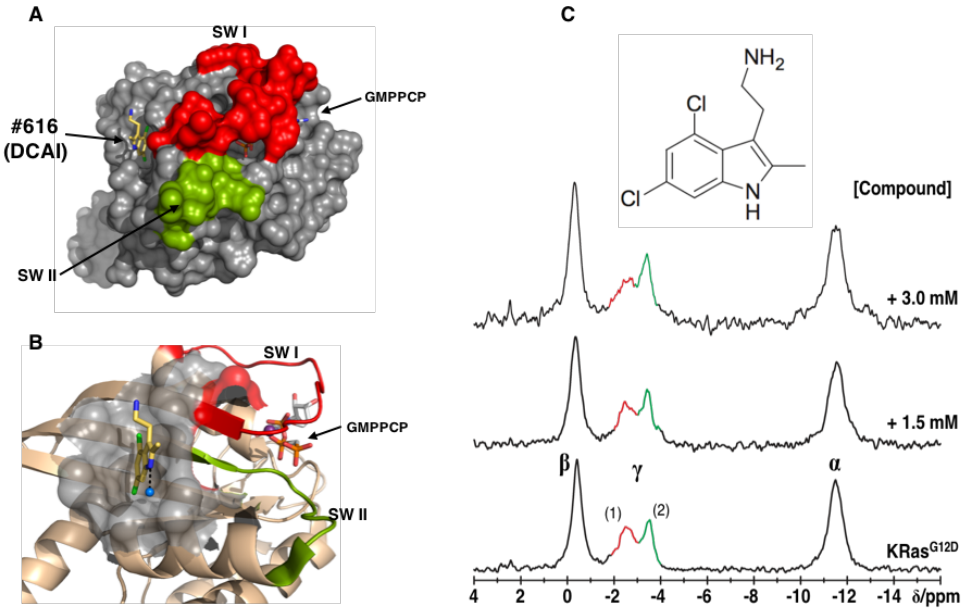

Figure 3.24 A. Molecular surface representation of $KRas^{G12d}$•Mg^{2+}•GMPPCP complexed to the compound #616 (DCAI, pdb: 4dst, [18]). The relative orientation with respect to the nucleotide is depicted. The surface of the protein is coloured in grey except for the residues comprising the switch 1 and switch 2, which are coloured in red and green, respectively. **B.** Detail around the binding site of DCAI. **C.** Titration of $KRas^{G12D}$•Mg^{2+}•GppNHp with DCAI followed by ^{31}P NMR spectroscopy. The molecular structure of this drug is represented.

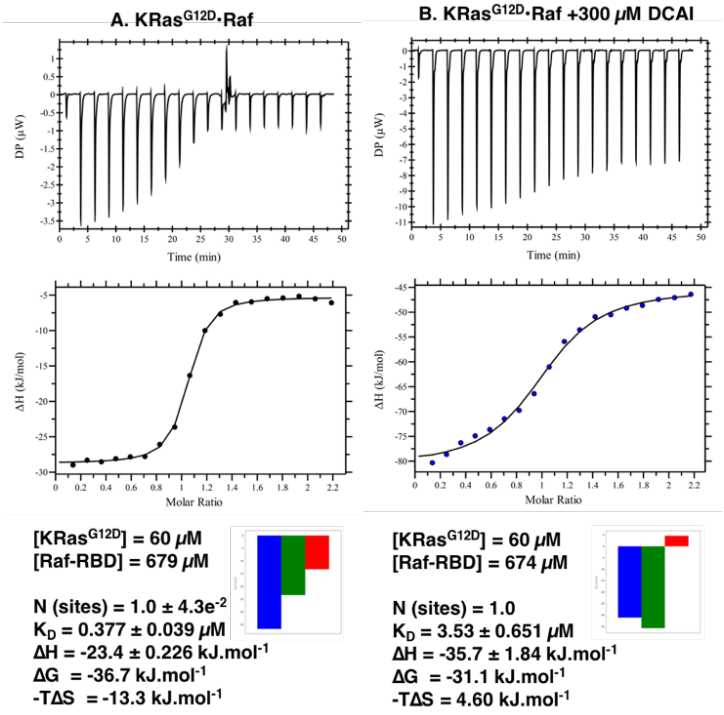

Figure 3.25. Binding between $KRas^{G12D}$•Mg^{2+}•GppNHp and Raf-RBD in the presence of the compound #616 (DCAI) followed by ITC. All the experiments were done in duplicate, at 298K and in the same buffer F (40 mM Tris/HCl pH 7.5, 10 mM $MgCl_2$, 2 mM DTE) with additionally 150 mM NaCl and 3% DMSO. The Ras-Raf interaction was firstly tested alone **(A)** and upon addition of 300 μM of the drug **(B)**. The raw heat of the reaction is plotted in the upper graph and the integrated heat *per* Ras:Raf ratio is shown in the lower graph. The signature plot is also shown with the following colour code: blue: ΔG, green: ΔH, red: $-T\Delta S$.

Table 3.3. ^{31}P NMR chemical shift values for KRas^{G12D}(1-188)•Mg^{2+}•GppNHp in 6% DMSO and in complex with a library of 15 different inhibitors.

Protein Complex	p:l	α-phosphate	β-phosphate	γ-phosphate		
		$\delta_{1(T)/2(T)}$ [a] [ppm]	$\delta_{1(T)/2(T)}$ [a] [ppm]	$\delta_{1(T)}$ [ppm]	$\delta_{2(T)}$ [ppm]	K_{12} [b]
KRas^{G12D}	--	-11.49	-0.37	-2.48	-3.53	0.70
+ 6% DMSO	--	-11.51	-0.40	-2.56	-3.49	0.64
+ #643	**1:1.5**	-11.55	-0.36	-2.50	-3.40	0.60
	1:3.0	-11.52	-0.42	-2.57	-3.48	0.57
+ #098	**1:1.5**	-11.54	-0.40	-2.46	-3.50	0.69
	1:3.0	-11.57	-0.45	-2.50	-3.49	0.72
+ #727	**1:1.5**	-11.47	-0.42	-2.47	-3.48	0.48
	1:3.0	-11.50	-0.47	-2.48	-3.48	0.41
+ #703	**1:1.5**	-11.56	-0.42	-2.50	-3.51	0.59
	1:3.0	-11.55	-0.42	-2.51	-3.48	0.68
+ #449	**1:1.5**	-11.56	-0.41	-2.56	-3.49	0.62
	1:3.0	-11.60	-0.46	-2.59	-3.53	0.68
+ #071	**1:1.5**	-11.45	-0.40	-2.46	-3.53	0.58
	1:3.0	--	--	--	--	--
+ #109	**1:1.5**	-11.51	-0.45	-2.53	-3.49	0.72
	1:3.0	--	--	--	--	--
+ #755	**1:1.5**	-11.44	-0.42	-2.54	-3.48	0.40
	1:3.0	-11.42	-0.43	-2.55	-3.44	0.19
+ #757	**1:1.5**	-11.45	-0.43	-2.49	-3.46	0.29
	1:3.0	-11.46	-0.44	-2.47	-3.48	0.20
+ #307	**1:1.5**	-11.54	-0.45	-2.51	-3.49	0.56
	1:3.0	-11.53	-0.45	-2.54	-3.45	0.41
+ #308	**1:1.5**	-11.50	-0.40	-2.49	-3.47	0.60
	1:3.0	-11.53	-0.47	-2.48	-3.40	0.46
+ #612	**1:1.5**	-11.43	-0.39	-2.51	-3.39	0.40
	1:3.0	-11.43	-0.41	-2.53	-3.41	0.24
+ #613	**1:1.5**	-11.45	-0.43	-2.40	-3.45	0.49
	1:3.0	-11.45	-0.47	-2.39	-3.45	0.31
+ #624	**1:1.5**	-11.47	-0.50	-2.44	-3.25	0.49
	1:3.0	-11.44	-0.50	-2.44	-3.09	0.28
+ #616	**1:1.5**	-11.55	-0.35	-2.53	-3.43	0.84
	1:3.0	-11.51	-0.30	-2.54	-3.40	1.02

All the values were derived from the experimental spectra recorded at 278 K in buffer F (40 mM Tris/HCl pH 7.5, 10 mM $MgCl_2$, 2 mM DTE), to which a total of 6% (v/v) DMSO was added. The obtained chemical shift values for Ras alone in the presence of DMSO are highlighted in light grey and were used as reference when comparing the effect of the different compounds. All the ^{31}P resonances were recorded in a magnetic field operating at a frequency of 202.456 MHz (500 MHz spectrometer). The estimated error for the fitted chemical shift values is ±0.002 ppm at the γ-phosphate. A EM function with LB= 15 Hz was applied during the processing of the FID.

[a] The α- and β-phosphates were fitted as a single resonance line.

[b] The estimated error for the calculated K_{12} values is ±0.2.

Table 3.4. ^{31}P NMR linewidths for KRas^{G12D}(1-188)•Mg^{2+}•GppNHp in 6% DMSO and in complex with a library of 15 different inhibitors.

Protein Complex	p:l	α-phosphate $\Delta\nu_{1/2\,(1),(2)}$ [a] [Hz]	β-phosphate $\Delta\nu_{1/2\,(1),(2)}$ [a] [Hz]	γ-phosphate $\Delta\nu_{1/2\,(1)}$ [Hz]	γ-phosphate $\Delta\nu_{1/2\,(2)}$ [Hz]
KRas^{G12D}	**--**	107.1[a]	69.0[a]	146.3	68.1
+ 6% DMSO	**--**	117.1	76.8	154.4	68.7
+ #643	**1:1.5**	120.1	78.0	150.8	82.3
	1:3.0	116.8	80.2	158.7	75.4
+ #098	**1:1.5**	104.0	75.7	131.7	65.9
	1:3.0	105.8	74.9	138.4	91.4
+ #727	**1:1.5**	112.2	77.0	135.6	79.0
	1:3.0	120.4	73.1	132.6	106.0
+ #703	**1:1.5**	123.0	77.0	140.3	103.9
	1:3.0	107.0	81.1	167.7	66.0
+ #449	**1:1.5**	117.9	72.8	178.2	83.8
	1:3.0	129.4	75.4	169.7	102.0
+ #071	**1:1.5**	140.6	130.0	259.0	104.9
	1:3.0	--	--	--	--
+ #109	**1:1.5**	129.2	76.16	151.3	97.2
	1:3.0	--	--	--	--
+ #755	**1:1.5**	106.0	78.9	143.9	101.4
	1:3.0	106.4	85.4	150.8	65.3
+ #757	**1:1.5**	111.7	73.0	150.0	86.7
	1:3.0	107.8	74.1	142.3	83.1
+ #307	**1:1.5**	117.3	71.9	153.5	97.6
	1:3.0	105.7	77.0	158.6	59.0
+ #308	**1:1.5**	112.6	75.8	142.9	76.0
	1:3.0	111.1	75.8	123.3	116.2
+ #612	**1:1.5**	103.9	80.2	125.5	102.9
	1:3.0	104.1	89.1	140.6	81.92
+ #613	**1:1.5**	106.2	73.5	113.5	113.5
	1:3.0	111.1	74.5	114.9	85.9
+ #624	**1:1.5**	112.8	75.7	126.3	100.2
	1:3.0	107.4	77.7	109.6	127.1
+ #616	**1:1.5**	135.3	85.1	143.0	90.9
	1:3.0	152.1	91.5	190.0	88.4

All the values were derived from the experimental spectra recorded at 278 K in buffer F (40 mM Tris/HCl pH 7.5, 10 mM $MgCl_2$, 2 mM DTE), to which a total of 6% (v/v) DMSO was added. The obtained linewidths for Ras alone in the presence of DMSO are highlighted in light grey and were used as reference when comparing the effect of the different compounds. All the ^{31}P resonances were recorded in a magnetic field operating at a frequency of 202.456 MHz (500 MHz spectrometer). The estimated error for the fitted linewidth values is ±0.02 ppm at the γ-phosphate. A EM function with LB= 15 Hz was applied during the processing of the FID and subtracted afterwards from the calculated linewidths
[a] The α- and β-phosphates were fitted as a single resonance line.

3.3 High Pressure ^{31}P NMR Spectroscopy.

3.3.1 Studies on GppNHp

^{31}P NMR spectroscopy is nowadays a very attractive method to study phosphate binding proteins and the behaviour of nucleotides in biological systems, especially when applied together with high pressure NMR methodologies. The effects of pressure on GTPases, particularly Ras, were elucidated in work pioneered at our department [125] but up to now, no high pressure data on the isolated nucleotides alone was available. In this section, a ^{31}P HP NMR investigation, up to 200 MPa, of the GTP analogue GppNHp is presented with the intent of having a reference system that can be applied from now on to virtually all GppNHp-bond proteins, helping in the distinction of trivial pressure effects occurring in the free nucleotides from the more relevant effects that are a consequence of pressure-induced conformational changes.

With the intent of shedding light on the influence of magnesium, which is a common co-factor of many GNBP's, the current study was conducted in the presence and in the absence of Mg^{2+} ions. The results presented here were published in the Journal of Biomolecular NMR, along with similar HP investigations on GMP, GDP, GTP, $GppCH_2P$ and GTPγS [226]. In order to avoid variations of pH with pressure, a pH that was 2-3 units above the apparent pK_a value for the last deprotonation step of the nucleotide was selected. This corresponds to a pH of 9.0 for the experiments performed in the presence of Mg^{2+} and to a pH of 11.5 for the experiments performed in its absence. Figure 3.26 shows the obtained HP ^{31}P pressure series. The experimental chemical shift values of the three phosphate groups were individually plotted against pressure and fitted with a second order polynomial from the Taylor expansion series (eqn. nº 15, section 2.2.5.4). The coefficients of this equation denoted as B_1 and B_2 correspond to the first order (linear) and second order (non-linear) pressure coefficients. The calculated coefficients for each phosphate group are given in Table 3.5. From the obtained data it can be observed that all phosphate groups shift upfield with pressure (towards more negative values of δ). This shift is rather small for the α-phosphate, with a $\Delta\delta$ of only -0.03 ppm between pamb and 200 MPa. However, larger effects are generally observed for the β- and γ-phosphates, with a $\Delta\delta$ of -0.25 and -0.2 ppm, respectively. Comparing both measurements, in the presence (A) and in the absence (B) of Mg^{2+}, it can be observed that the pressure-induced shift changes seem to be more pronounced in the second case, especially for the γ-phosphate, whose $\Delta\delta$ is -0.25 ppm and -0.4 ppm, in the presence and in the absence of the ion, respectively. The plots shown in Figure 3.26 represent the $\Delta\delta$, i.e. the variation of the chemical shift, ($\Delta\delta=\delta_{200MPa}-\delta_{0.1MPa}$). A similar plot with the absolute chemical shift values (δ) for each phosphate group is shown

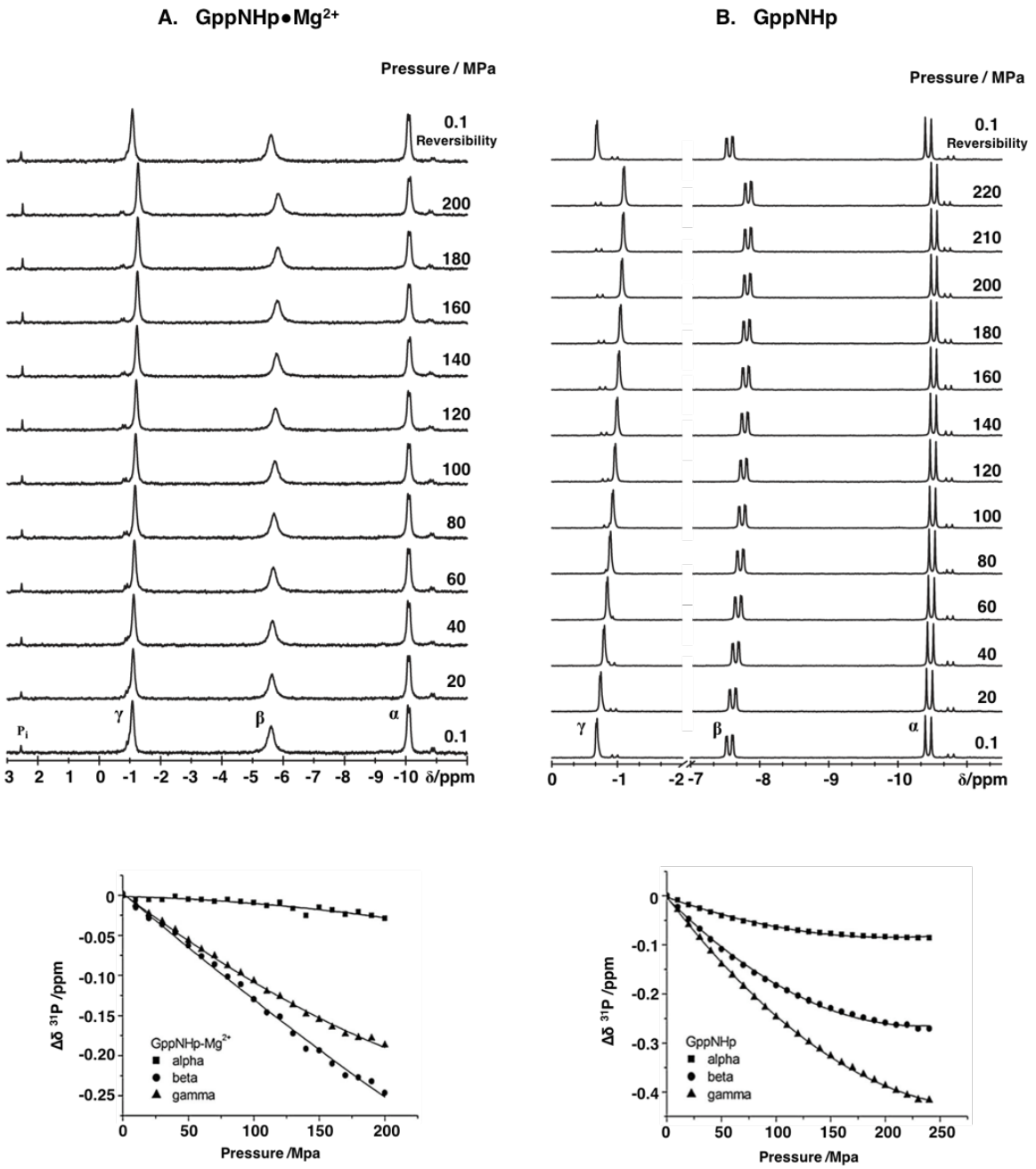

Figure 3.26. Pressure dependence of GppNHp in the presence **(A)** and in the absence **(B)** of Mg^{2+} followed by ^{31}P NMR spectroscopy. All measurements were done at 278 K, using a Bruker Avance 600 MHz spectrometer operating at a magnetic field of 242.896 MHz. The corresponding phosphate assignments are indicated, as well as the pressure values (in MPa) for each step. In all spectra, very small signals are observed, they shift continuously downfield, crossing their neighbors, the α- and γ-phosphates, as the pressure increases. These signals correspond to trace impurities in the sample such as $GppNH^+$. A splitting of the phosphorous resonances is observed in the absence of Mg^{2+} (B). They correspond to the $J_{31P,31P}$ homonuclear coupling. The same coupling also exists in the presence of Mg^{2+} (A) but is weakly recognizable due to the increase of the linewidths by the presence of the metal. The last step of the series is the test for reversibility. Samples were prepared by dissolving 5 mM of GppNHp in 40 mM Tris/HCl, 0.1 mM DSS, 10% D_2O, with pH 9.0 and 15 mM $MgCl_2$ **(A)** or pH 11.0 and 0.5 mM EDTA **(B)**. The observed pressure dependent chemical shift changes $(\Delta\delta=\delta(P)-\delta(P_0))$ for the α-, β- and γ-phosphates were plotted and the data fitted with a second order Taylor expansion (see experimental section 2.2.5.4, eqn. nº 15). The obtained pressure coefficients are listed in Table 3.5.

in Figure A of the appendix section, where the different magnitude of the shift changes for the two measurements can be better visualised (see also Tables D and E in the appendix). The pressure coefficients listed in Table 3.5 indicate that the non-linear pressure contribution is greater for GppNHp than Mg^{2+}•GppNHp. Indeed, all B_2 values are numerically higher in the first case. This portends the idea that Mg^{2+} has the effect of stabilising the ground-state conformation(s) of the nucleotide, rendering it more insensitive to a pressure-induced conformational transition. This is supported by a wealth of reported studies showing that guanine and adenine nucleotides when in presence of Mg^{2+} exist in solution as a mixture of different states, that is, tridentate complexes, with Mg^{2+} bound to the three phosphates, bidentate complexes with Mg^{2+} bound to α- and β-phosphates and monodentate complexes, with Mg^{2+} bound to one of the negatively charged oxygens of any phosphate group [27, 248].

Table 3.5. Pressure dependence of ^{31}P chemical shifts of GppNHp in the presence and in the absence of Mg^{2+} and respective pressure coefficients.

Nucleotide	^{31}P position	δ^{0a} /ppm	B_1 /ppm GPa^{-1}	B_2 /ppm GPa^{-2}
Mg^{2+}•GppNHp (pH 9)	α	-10.09	-0.032 ± 0.03	-0.493 ± 0.16
	β	-5.59	-1.380 ± 0.055	0.542 ± 0.275
	γ	-1.08	-1.250 ± 0.261	1.470 ± 0.131
	P_i	2.56	-0.490 ± 0.159	0.969 ± 0.078
GppNHp (pH 11.5)	α	-10.44	-0.797 ± 0.018	1.936 ± 0.074
	β	-7.57	-2.250 ± 0.034	4.843 ±0.141
	γ	-0.69	-2.920 ± 0.024	4.984 ± 0.100
	P_i	4.27	-0.442 ± 0.023	1.056 ± 0.094

B_1 and B_2 were obtained by fitting a second order Taylor expansion to the pressure-dependent chemical shifts (eqn. nº15, section 2.2.5.4). They are a numeric representation of the linear and non-linear pressure-induced conformational changes, respectively.

[a] δ^0 is the chemical shift value obtained from the fitting at ambient pressure at the corresponding pH.

3.3.2 ^{31}P HP NMR on HRas^{WT}(1-166)•Mg^{2+}•GppNHp

The results gathered from the studies on GppNHp constitute thereafter the basis for the analysis of the pressure-induced chemical shift changes on the Ras protein using ^{31}P NMR spectroscopy. The influence of pressure in the intrinsic equilibrium of HRas^{WT}(1-189) was previously studied in our department by ^{31}P NMR [125] but only in terms of intensity changes of states 1(T) and 2(T) and related equilibrium constants. Shift changes could not be evaluated at that time because the pressure effects originating from the nucleotide itself were missing. Therefore, in the light of the new data on the isolated nucleotide, a more complete description of the dynamics of Ras will be presented in this section. Since the ^{31}P NMR GDP, GTP and GppNHp spectra of HRas^{WT}(1-166) and HRas^{WT}(1-189) are almost identical, being the only detectable difference a small variation in the equilibrium populations (K_{12}=1.7 for HRas^{WT}(1-166)•GppNHp and K_{12}=1.9 for HRas^{WT}(1-189)•GppNHp) the HP experiments were performed using the truncated variant and because it was also previously studied in our department by HP 2D [^{1}H-^{15}N]-HSQC NMR methods, rendering a wealth of information that can now be compared with the present results [171]. The ^{31}P HP series were performed at two different temperatures that will be discussed in separate sections.

3.3.2.1 Measurements Conducted at 278 K

Figure 3.27 shows the ^{31}P NMR pressure series recorded at 278 K for HRas^{WT}(1-166). The measurements were carried in a Bruker Avance-600 spectrometer operating at a ^{31}P frequency of 242.896 MHz equipped with a prodigy cold probe. High hydrostatic pressure was transmitted to the sample with the aid of a manually operated compressor piston (for details see sections 1.3.1 and 2.2.5.2). The pressure was continuously increased from 0.1 MPa up to 250 MPa in 10 MPa steps. For sake of simplicity, only 20 MPa increments are depicted in Figure 3.27. The 3.0 mM protein loaded with GppNHp was dissolved in buffer F, with additionally 0.4 mM DSS and 20% D_2O. For each step, a ^{1}H and a ^{31}P spectra were recorded, comprised of 128 and 800 cumulative scans, respectively.

The interpretation of the pressure induced effects can be done separately in terms of chemical shift changes and peak areas for each one of the ^{31}P resonance lines recorded.

In order to determine the best window function, the HP series was processed separately with two different apodization functions: exponential multiplication (EM) and Gaussian multiplication (GM) and the obtained shift values were directly compared in Figure 3.28. From the analysis, the two functions lead to different degrees of accuracy on retrieving chemical shifts. This is especially notorious for state 2(T) on the γ-phosphate, to which $\Delta\delta=\delta_{250MPa}-\delta_{0.1MPa}$= 0.418 ppm, whilst the same variation for state 1(T) is only 0.015 ppm.

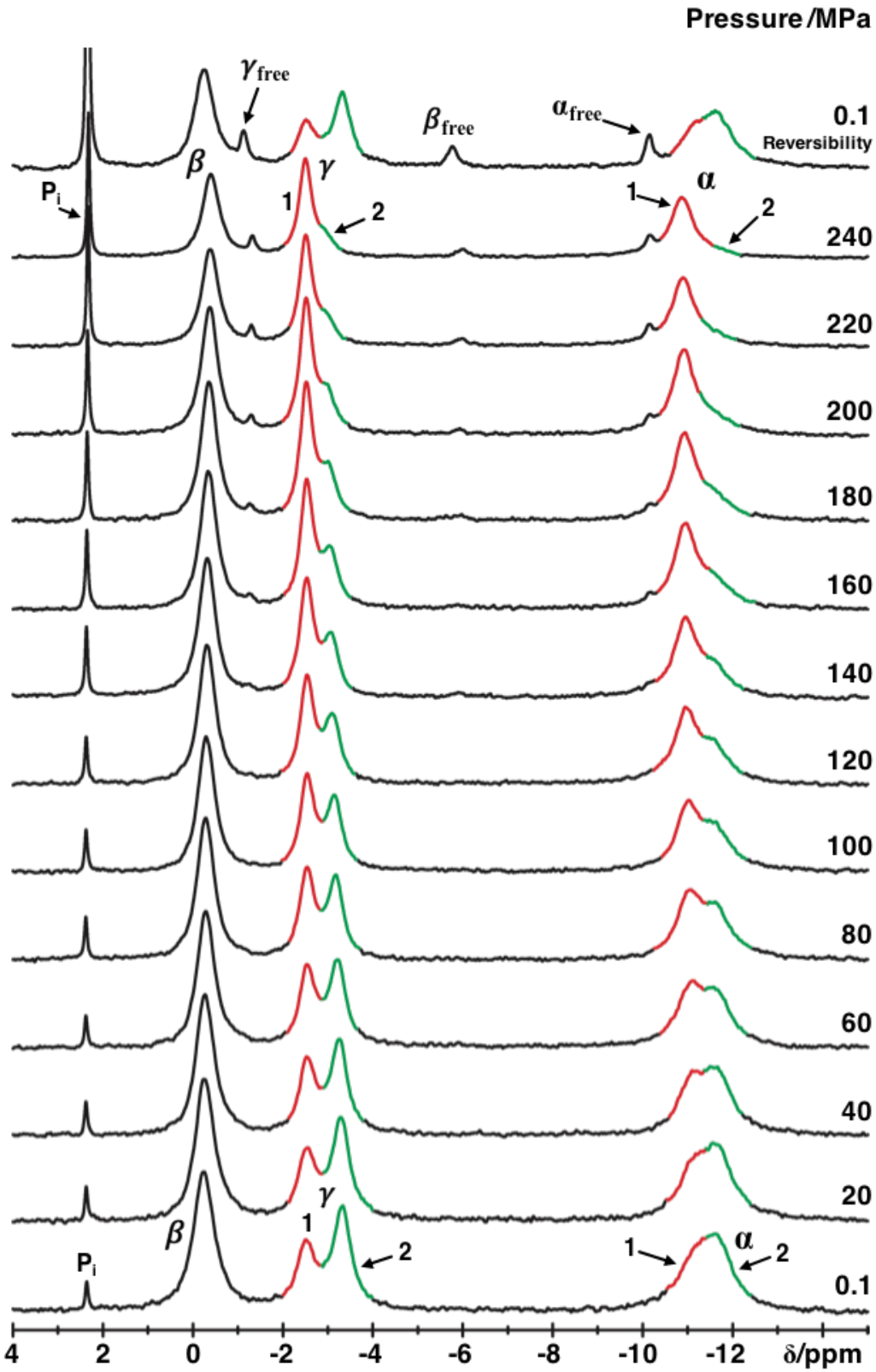

Figure 3.27. Conformational equilibria of $HRas^{WT}(1\text{-}166)\bullet Mg^{2+}\bullet GppNHp$ as a function of pressure determined by ^{31}P NMR. The 3.0 mM protein dissolved in buffer F (40 mM Tris/HCl pH 7.5, 10 mM $MgCl_2$, 2 mM DTE) with additionally 0.4 mM DSS and 20% D_2O was subjected to increasing step-variations of pressure, up to a maximum of 250 MPa. The pressure values are indicated near each step. The evolution of states 1(T) and 2(T) is represented by the red and green lines, respectively. The ^{31}P NMR resonances of the free nucleotide observed at higher pressures are also indicated. The last step corresponds to the reversibility test of the pressure-induced changes. The fitted chemical shift values for all the resonance lines are listed in Table F of the appendix section.

This very small variation of $\gamma_{1(T)}$ is within the limits of error of the fitting process and renders the accurate chemical shift determination a difficult task, especially when using the EM method. For state 2(T) on the α-phosphate, $\Delta\delta$= 0.061 ppm, corresponding to a 4-fold greater shift change compared to the $\gamma_{1(T)}$-phosphate. Nevertheless, the calculated Pearson correlation is much smaller for the $\alpha_{2(T)}$-phosphate (r= 0.752) than for the latter (r= 0.981). This is due to the greater overlap between states 1(T) and 2(T) on the α-phosphate as compared to the γ-phosphate. From the gathered data, it can be generalized that the GM filter used in the evaluation of the pressure-induced changes (and ultimately in the evaluation of the pressure coefficients) leads to a reduction in the absolute errors and was consequently chosen over the EM method. EM was also used in this pressure series to evaluate peak areas and linewidths, since GM typically destroys the Lorentzian shape of the signals and renders no information about such variables.

Using the GM method, the ^{31}P chemical shift values of each phosphate were plotted against pressure (Figure 3.29, black lines). They represent the uncorrected shift values, as obtained directly from the experimentally recorded spectra (Figure 3.27). The fitted pressure coefficients are listed on Table 3.6. Except for the β-phosphate, that shifts upfield, all the other signals shift downfield with pressure (contrary to the upfield shift of the free nucleotide). The largest shifts are observed for $\gamma_{2(T)}$ and $\alpha_{1(T)}$ with a $\Delta\delta$= 0.418 and 0.35

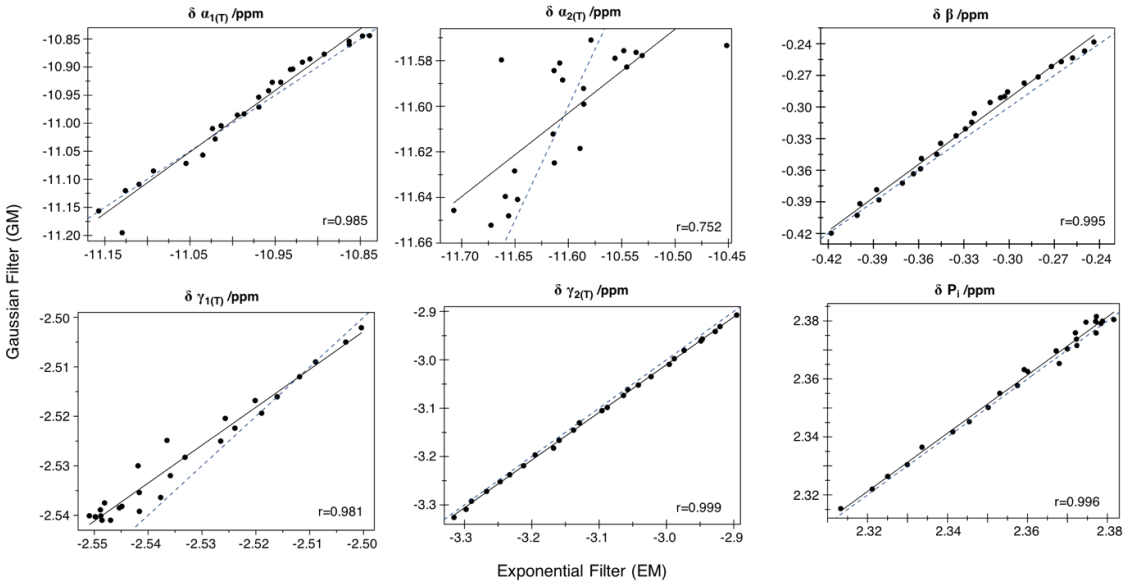

Figure 3.28. Correlation of the chemical shift values obtained upon fitting with an exponential filter (LB= 10 Hz) and with a Gaussian filter (selected LB and GB depending on the ^{31}P signals). The parameters were selected based in an optimal separation of the lines and/or an homogenous lineshape. For each plot, the Pearson correlation coefficient, r, is computed along with the linear regression of the data (straight line). In all cases except for the $\alpha_{2(T)}$-phosphate, there is a strong, positive correlation between the two methods used, with r close to 1. However, big discrepancies are observed for the $\alpha_{2(T)}$-phosphate, and to a smaller extent, for the $\gamma_{1(T)}$-phosphate, due not only to their partially overlapped signals in the ^{31}P NMR spectra, but also due to their very small chemical shift variation, $\Delta\delta=\delta_{250MPa}-\delta_{0.1MPa}$, leading to difficulties in the proper fitting of the data. The dashed line depicts the slope y=x.

ppm, respectively. Considerably smaller changes are observed for states $\gamma_{1(T)}$ and $\alpha_{2(T)}$, with $\Delta\delta$= 0.015 and 0.061 ppm, respectively. Qualitatively, the β and $\gamma_{2(T)}$-phosphates seem to show a more linear pressure dependence as compared to states $\alpha_{2(T)}$ and $\gamma_{1(T)}$, which are associated with a pronounced sigmoidal and parabolic behaviour. The use of a third order polynomial on these two phosphate lines led to a slightly better fit of the dispersion points as compared to the use of a second order fit.

The ^{31}P corrected chemical shift values are plotted against pressure for each phosphate group and are shown in Figure 3.29 (blue lines). The calculated B_1 and B_2 values are shown in Table 3.6. Since the free Mg^{2+}•GppNHp and uncorrected $HRas^{WT}$•Mg^{2+}•GppNHp shift in opposite directions (upfield and downfield, respectively) for all ^{31}P resonances except the β-phosphate, due to their opposite direction, the contributions from the free nucleotide add up to the uncorrected Ras and the final corrected values for the α and γ-phosphates shift downfield compared to the uncorrected case. The reasoning underlying the behaviour of β-phosphate is different but the correction process leads to the same final result (its downfield shift). For both cases (free nucleotide and uncorrected Ras), the β-phosphate shifts upfield with pressure. Since the direction is the same, this implies that the contribution from the free nucleotide in the original, uncorrected, values needs to be suppressed (subtracted). The final corrected values have now a reversed direction compared to the uncorrected ones, shifting therefore downfield. The reason for the reverse of the direction is only due to the magnitudes of the values involved (free Mg^{2+}•GppNHp: $\Delta\delta_\alpha$= 0.039 ppm, $\Delta\delta_\beta$= 0.31 ppm and $\Delta\delta_\gamma$= 0.22 ppm. For Ras•Mg^{2+}•GppNHp (uncorrected) $\Delta\delta\alpha_{1(T)}$= 0.35 ppm, $\Delta\delta\alpha_{2(T)}$= 0.06 ppm, $\Delta\delta_\beta$= 0.18 ppm, $\Delta\delta\gamma_{1(T)}$= 0.014 ppm and $\Delta\delta\gamma_{2(T)}$= 0.42 ppm).

The direction of the chemical shifts can also be inferred from the calculated pressure coefficients (Table 3.6). Both states $\alpha_{1(T)}$ and $\alpha_{2(T)}$ have positive first order coefficients, which are correlated with the downfield shift of their respective resonance lines. The small difference between their uncorrected B_1 and B_2 values compared to the corrected ones, respectively, is an indication that the local chemical environment surrounding the α-phosphate is not greatly modified as the pressure increases, at least not as much as the β and γ-phosphates.

It can be seen from Figure 3.29 that $\alpha_{2(T)corrected}$ shifts by a maximum of 0.09 ppm between 0.1 and 200 MPa, corresponding to a very small variation. State $\alpha_{1(T)corrected}$, on the other hand, has a more pronounced downfield shift by a $\Delta\delta$ of 0.39 ppm within the same pressure interval. State $\gamma_{2(T)corrected}$ shows the largest shift changes between 0.1 and 250 MPa ($\Delta\delta$= 0.642 ppm), followed by state $\alpha_{1(T)}$ ($\Delta\delta$= 0.389 ppm). It can also be observed from Figure 3.27 the release of the nucleotide at high pressures (above 200 MPa) from the presence of

additional small peaks at δ= -1.33, -6.0 and -10.15 ppm, corresponding to the α-, β- and γ-phosphates, respectively.

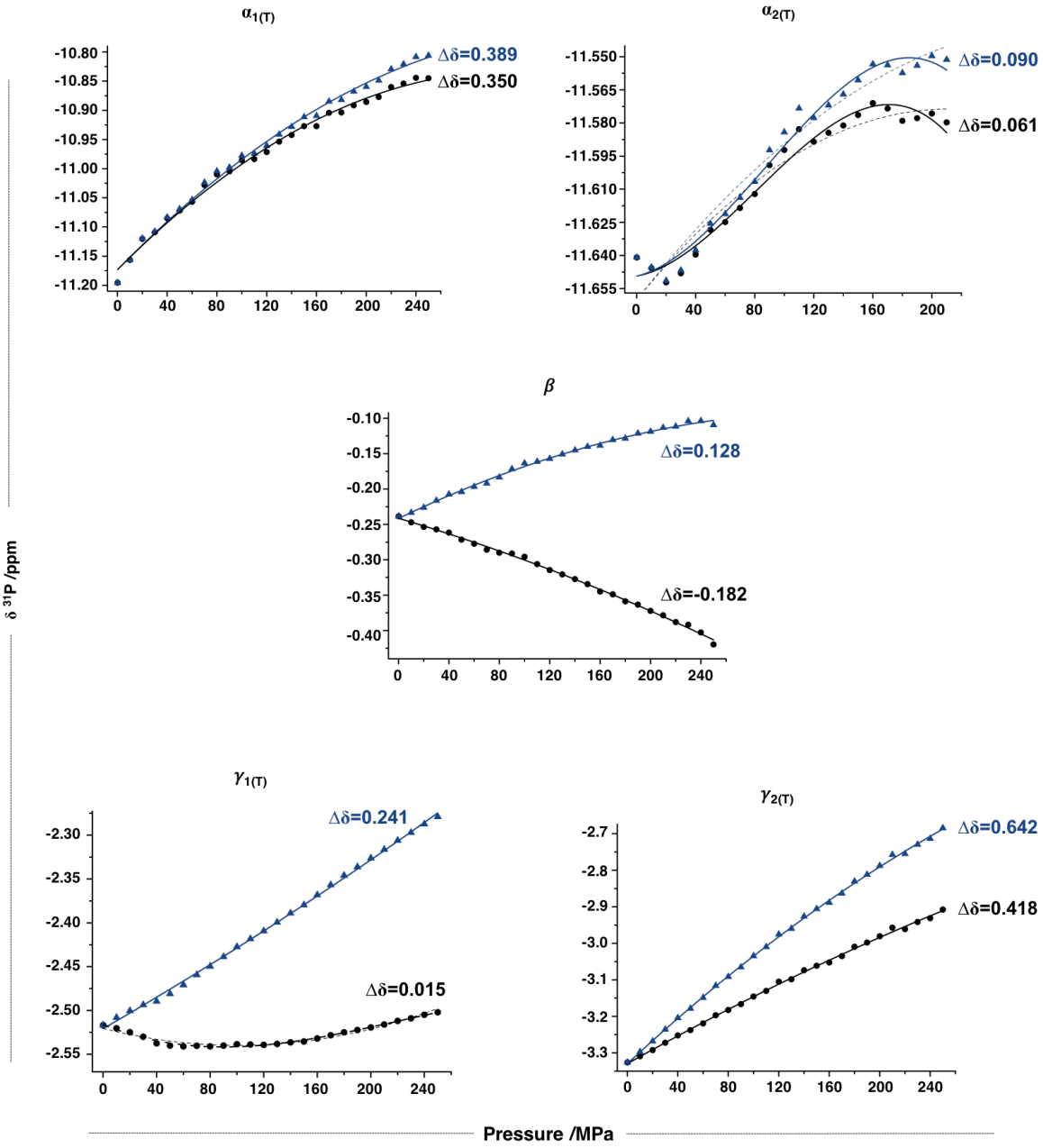

Figure 3.29. Corrected pressure dependence of ^{31}P NMR chemical shifts of HRas^{WT}(1-166)•Mg^{2+}•GppNHp recorded at 278 K. The $\Delta\delta_{freenuc\ fit}$ were applied as correction factors upon subtraction to $\delta_{Ras\ uncorrected}$, leading to the final $\delta_{corrected}$ values, represented here for each plot as blue triangles (-▲-). The uncorrected shift changes are also plotted again as black circles (-●-) for comparison. The second order polynomial fit of the Taylor expansion was applied for the determination of B_1 and B_2 as before. The obtained values are presented on Table 3.6. The calculated $\Delta\delta=\delta_{250MPa}-\delta_{0.1MPa}$ shift differences are shown near the respective curve. Note that the vertical scaling is different for each plot due to the different magnitudes of the Δδ values.

Table 3.6. Fitted pressure coefficients and thermodynamic molar free energies, ΔG, and volumes, ΔV, for $HRas^{WT}$(1-166)•Mg^{2+}•GppNHp at 278 K and pH 7.5.

^{31}P position	δ^{0a} /ppm	B_1 /ppm GPa^{-1}	B_2 /ppm GPa^{-2}	--	--
		Uncorrected			
$\alpha_{1(T)}$	-11.17	2.15 ± 0.08	-3.40 ± 0.32		
$\alpha_{2(T)}$	-11.66	0.82 ± 0.10	-1.95 ± 0.46		
β	-0.24	-0.53 ± 0.03	-0.64 ± 0.11		
$\gamma_{1(T)}$	-2.52	-0.38 ± 0.03	1.90 ± 0.11		
$\gamma_{2(T)}$	-3.33	1.94 ± 0.05	-1.06 ± 0.17		
P_i	2.37	0.26 ± 0.03	-1.99 ± 0.10		
		Corrected			
$\alpha_{1(T)}$	-11.17	2.18 ± 0.08	-2.90 ± 0.32		
$\alpha_{2(T)}$	-11.66	0.85 ± 0.10	-1.46 ± 0.46		
β	-0.24	0.85 ± 0.03	-1.20 ± 0.11		
$\gamma_{1(T)}$	-2.52	-0.88 ± 0.03	0.43 ± 0.11		
$\gamma_{2(T)}$	-3.33	3.20 ± 0.05	-2.53 ± 0.18		
	$\delta_1{}^b$ /ppm	$\delta_2{}^b$ /ppm	ΔG /kJ mol^{-1}	ΔV /mL mol^{-1}	Transition
		Uncorrected			
$\alpha_{1(T)}$	-11.38	-10.82	1.17 ± 1.26	-29.89 ± 7.12	1-to-0
$\alpha_{2(T)}$	-11.65	-11.58	9.31 ± 0.92	-121.67 ± 12.39	2-to-3
β	-0.23	-0.46	5.50 ± 0.14	-34.03 ± 2.17	
$\gamma_{1(T)}$	-2.53	-2.50	2.55 ± 1.39	-125.85 ± 74.71	1-to-0
$\gamma_{2(T)}$	-3.38	-2.86	4.0 ± 0.09	-34.68 ± 1.53	2-to-3
P_i	2.38	2.301	15.0 ± 2.73	-77.33 ± 17.18	
		Corrected			
$\alpha_{1(T)}$	-11.34	-10.77	1.81 ± 0.08	-29.21 ± 1.86	1-to-0
$\alpha_{2(T)}$	-11.64	-11.56	8.17 ± 1.25	-85.19 ± 12.3	2-to-3
β	-0.27	-0.10	3.12 ± 0.51	-42.44 ± 2.60	
$\gamma_{1(T)}$	-2.53	-2.25	5.54 ± 0.12	-39.34 ± 1.58	1-to-0
$\gamma_{2(T)}$	-3.45	-2.68	3.44 ± 0.41	-37.31 ± 1.89	2-to-3

[a] δ^0 is the chemical shift value obtained at ambient pressure at the corresponding pH.
[b] δ_1 and δ_2 are the chemical shift values obtained for the first and last pressure steps, respectively. Due to the linear tendency of the fitted curves, the obtained values constitute a coarse approximation.

The pressure coefficients B_1 and B_2 are a useful mathematical concept to quantify the magnitude of the observed pressure-induced changes. However, another kind of analysis that can be performed is based on the thermodynamic laws that govern the system under pressure: the Gibbs free energy (ΔG) and partial molar volumes (ΔV). Given two conformations in fast exchange, the experimental chemical shift changes can be fitted with eqn. nº 17 (section 2.2.5.4), to obtain the corresponding parameters. The only condition needed for a proper fitting of the data is that the dispersion plot of the chemical shifts must display a clear two-state transition (or higher) characterized by a sigmoidal shape This is not the always the case for all the plotted ^{31}P chemical shifts in Figure 3.29 (except for state $\gamma_{2(T)}$) as they show a more linear tendency, which renders the fitting inaccurate and largely

dependent on the starting values given for δ_1 and δ_2 for the initialization of the iteration process. The calculated ΔG and ΔV values are listed in Table 3.6, although the reader is advised for the large intrinsic error of the fitting of ΔG and ΔV.

Under slow exchange conditions, the pressure-induced conformational transition from state 2(T) to state 1(T) is associated with the relative population of both states, that in turn can be quantified by their respective areas. Taking K_{12} at each pressure and using it subsequently in eqn. nº 2 (section 2.2.4), the corresponding ΔG and ΔV values for the 2(T)-to-1(T) transition were calculated as shown in Figure 3.30. The obtained free energy difference between the two states is 1.53 kJ mol^{-1} and the associated volume change is -18.60 mL mol^{-1}. Identical values were previously reported for HRas^{WT}(1-189)•Mg^{2+}•GppNHp (ΔG_{12}= 1.42 kJ mol^{-1} and ΔV_{12}= -17.2 mL mol^{-1}) [125].

P /MPa	K_{12}	P /MPa	K_{12}
0.1	1.70	140	0.63
10	1.61	150	0.61
20	1.57	160	0.56
30	1.48	170	0.53
40	1.40	180	0.48
50	1.25	190	0.40
60	1.23	200	0.37
70	1.19	210	0.45
80	1.04	220	0.26
90	1.01	230	0.28
100	0.92	240	0.26
110	0.87	250	0.24
120	0.75		
130	0.71		

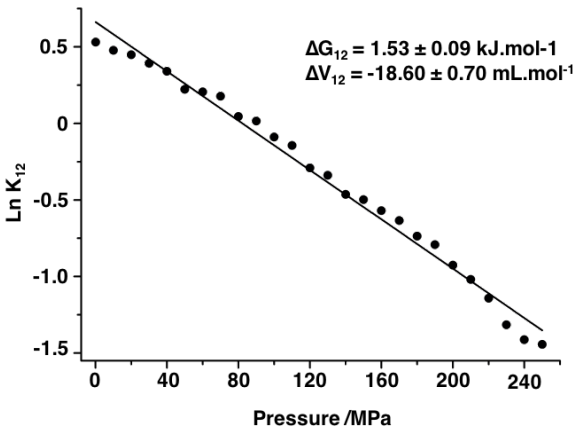

Figure 3.30. Plot of $LnK_{12}=A_{state2(T)}/A_{state1(T)}$ as a function of pressure. The calculated difference of the free energy, ΔG_{12} and partial molar volume, ΔV_{12} is 1.53 kJ mol^{-1} and -18.60 mL mol^{-1}, respectively. The calculated K_{12} values at each measured pressure point are given in the table. Comparable results are given in ref. [125].

3.3.2.2 Measurements Conducted at 303 K

A similar set of ^{31}P HP NMR experiments was conducted at 303 K for HRas^{WT}(1-166)•Mg^{2+}•GppNHp. The complete pressure series is shown in Figure 3.31. The increase of the temperature has a direct influence in the dynamics of the chemical exchange between states 1(T) and 2(T) mostly noticeable for the γ-phosphate where the interconversion between states at 278 K is slow in the NMR time scale and the corresponding resonances are well separated. As the temperature increases the rate of exchange becomes numerically similar to the chemical shift difference between states 1(T) and 2(T) (i.e, $\tau_{ex} \approx |\delta_{1(T)} - \delta_{2(T)}|$), leading to severe line broadening that culminates with their coalescence into a single sharp line at high temperature. The exchange rate constants determined in previous studies for the 1(T)-2(T) interconversion at 278 and 298 K are 42 s^{-1} and 387 s^{-1}, respectively [67].

The chemical shift variations for each one of the phosphate groups measured at 303 K follows the same general trends as the ones measured at 278 K, with the α- and γ-phosphate shifting downfield (dishielding) and β-phosphate shifting upfield (shielding) with pressure. The release of GppNHp is observed again at high pressures, especially above 175 MPa (Figure 3.31). Free GppNHp itself seems to be rapidly hydrolysed into its by-products, namely P_i and free GMP, located at δ~ 2.50

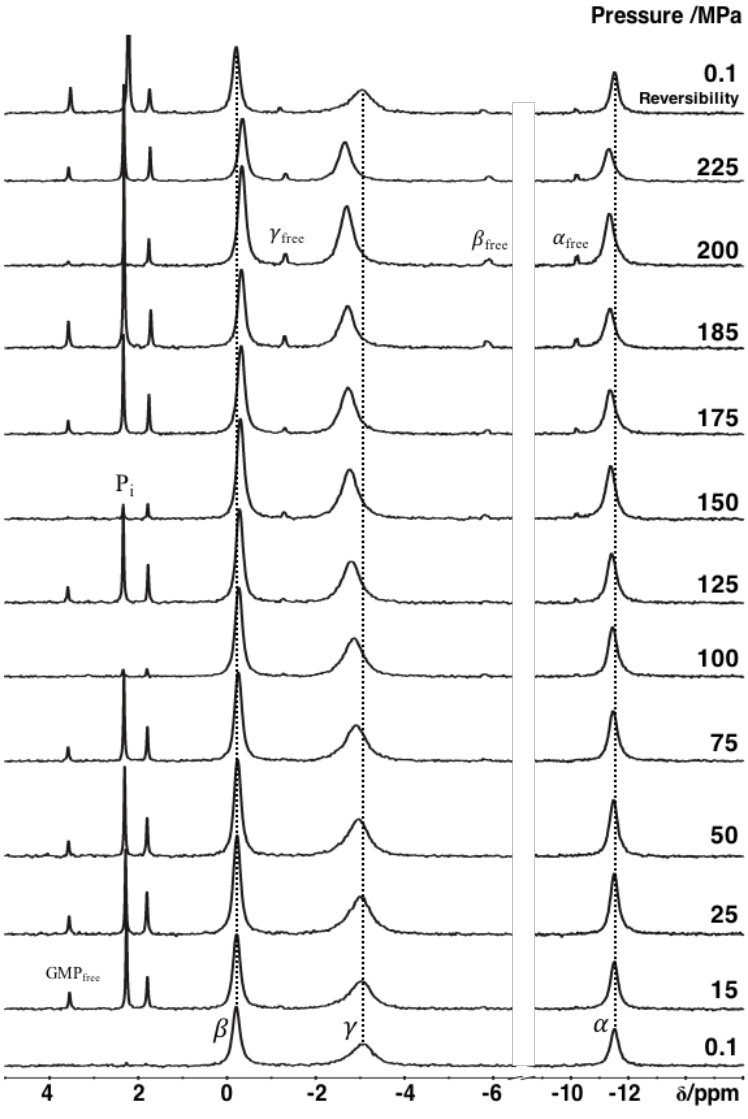

Figure 3.31. Conformational equilibria of HRas^{WT}(1-166)•Mg^{2+}•GppNHp as a function of pressure determined by ^{31}P NMR at 303 K. The 5.0 mM protein dissolved in buffer F (40 mM Tris/HCl pH 7.5, 10 mM $MgCl_2$, 2 mM DTE) with additionally 0.4 mM DSS and 20% D_2O was subjected to increasing step-variations of pressure, up to a maximum of 225 MPa. The chemical shift evolution of the α-, β- and γ-phosphates is represented by the dashed lines. The ^{31}P resonances of free GppNHp observed at higher pressures are also indicated.

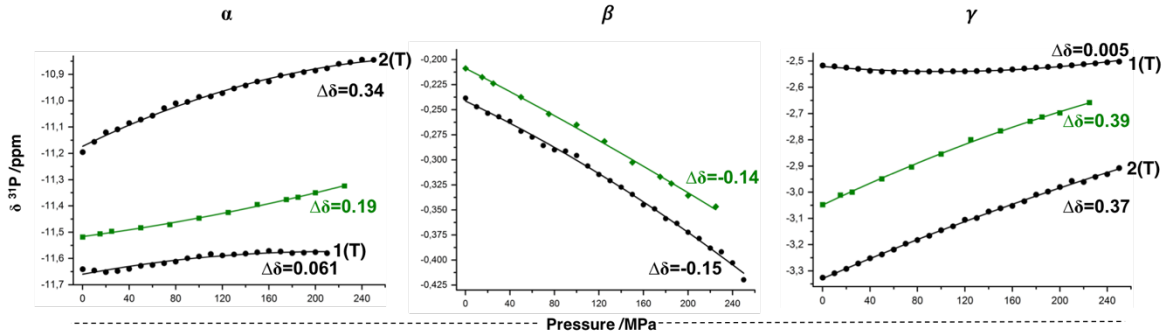

Figure 3.32. ^{31}P NMR chemical shift changes of HRas^{WT}(1-166)•Mg^{2+}•GppNHp as a function of pressure. The observed chemical shift dependence is plotted individually for the α-, β- and γ-phosphates. Measurements were performed at 303 K (coloured in green -■-) and are compared here with the corresponding ones performed at 278 K (coloured in black, -●-, see Figure 3.29 and corresponding text). Only the uncorrected shift changes are shown and presently discussed due to the lack of data at 303 K for the isolated Mg^{2+}•GppNHp molecule. Note that considerably less pressure points were collected at 303 K as compared to the 278 K series. The obtained values for the chemical shift variations, defined as $\Delta\delta=\delta_{225MPa}-\delta_{0.1MPa}$, (225 MPa being the highest pressure point recorded for the 303 K series), are shown near each curve for comparison. The second order polynomial fit of the Taylor expansion was applied for the determination of B_1 and B_2 as before. The obtained values are presented on Table 3.7. Note that the vertical scaling is different for each plot.

Table 3.7. Fitted pressure coefficients and thermodynamic molar free energies, ΔG, and volumes, ΔV, for HRas^{WT}(1-166)•Mg^{2+}•GppNHp at 303 K and pH 7.5.

^{31}P position	δ^{0a} /ppm	B_1 /ppm GPa^{-1}	B_2 /ppm GPa^{-2}	--
		Uncorrected		
α	-11.52	0.59 ± 0.01	1.22 ± 0.22	
β	-0.21	-0.57 ± 0.03	-0.25 ± 0.15	
γ	-3.05	2.15 ± 0.07	-1.86 ± 0.33	
P_i	2.23	1.15 ± 0.19	-3.80 ± 0.49	

	$\delta_1{}^b$ /ppm	$\delta_2{}^b$ /ppm	ΔG /kJ mol^{-1}	ΔV /mL mol^{-1}
		Uncorrected		
α	-11.52	-11.29	6.39 ± 0.27	-43.92 ± 1.74
β	-0.20	-0.37	5.50 ± 0.23	-43.17 ± 3.48
γ	-3.05^c	-2.66^c	5.65 ± 0.37	-54.78 ± 0.82
P_i	2.22	2.34	2.42 ± 4.69	-107.3 ± 48.0

a δ^0 is the chemical shift value obtained at ambient pressure at the corresponding pH.
b δ_1 and δ_2 are the chemical shift values obtained for the first and last pressure steps, respectively. Due to the linear tendency of the fitted curves, the obtained values constitute a coarse approximation.
c These values were fixed during the iteration routine.

ppm and δ~3.35 ppm, respectively. Another resonance line located at δ= 1.79 ppm can be ascribed to another by-product from the GppNHp hydrolysis, possibly, PO_3-NH_2 or a related species.

The polynomial fit of the uncorrected chemical shift changes is shown in Figure 3.32 for each phosphate group (coloured in green), alongside with the uncorrected data recorded at 278 K for comparison (coloured in black). The highest pressure point recorded for the 303

K series is 225 MPa, therefore the $\Delta\delta=\delta_{250MPa}-\delta_{0.1MPa}$ values are shown near each respective plot. The pressure-dependent chemical shift changes of the free Mg^{2+}•GppNHp were obtained only at 278 K (section 3.3.1). Due to the lack of data at 303 K, the corrections for this pressure series are not available. Nevertheless, from the uncorrected values several inferences can be made: the α-phosphate shows positive B_1 and B_2 values (left plot on Figure 3.32), which are correlated with a downfield change of the chemical shifts and with a positive curvature. The chemical shift changes were also fitted with the equation for a two-state transition model and the calculated Gibbs energies and partial molar values are given in Table 3.7.

3.3.3 ^{31}P HP NMR on HRas^{T35S}(1-166)•Mg^{2+}•GppNHp

The pressure-dependent ^{31}P NMR chemical shift changes of HRas^{T35S}•Mg^{2+}•GppNHp were investigated using the same experimental guidelines described for Ras^{WT} in section 3.3.2.1). A 4.37 mM protein sample dissolved in buffer F was increasingly subjected to high hydrostatic pressure, from 0.1 up to 190 MPa. A total of 19 pressure steps were performed and for each one a ^{1}H and a ^{31}P spectrum, comprised of 128 and 500 scans, respectively were recorded. Figure 3.33 shows 10 representative spectra of the series. The fitted values are presented in Table 3.8. The corrected (coloured in purple) and the uncorrected (coloured in black) pressure-dependent shift changes are compared in Figure 3.34. As it can be directly observed from the uncorrected values and the stacked spectra (dashed lines on Figure 3.33), the effect of pressurizing the protein leads to an upfield shift of the β- and γ-phosphates and to a downfield shift of the α-phosphate. The same shift directions are observed in the case of Ras^{WT}, except for the γ-phosphate, which moves downfield in the later (Figures 3.27 and 3.29). In the course of the experiment, the ^{31}P resonance signal corresponding to free P_i (δ= 2.38 ppm at 0.1 MPa, 2.35 ppm at 190 MPa) increases, especially at high pressures where the dissociation of GppNHp from the protein usually takes place. Rather surprisingly, and contrary to the observations for the *wild type* protein, the presence of free nucleotide is not detected in the last pressure steps in Ras^{T35S}. All the spectra recorded during this pressure series have an interesting feature arising from the presence of a very broad peak observed at $\delta\sim$ 3.34 ppm. GMP is observed around this value (typically δ_{GMP}= 3.83 ppm [226, 249]). However, due to its very large linewidth (124 Hz at 0.1 MPa, 120 Hz at 190 MPa) its chemical nature is unknown. A close analysis shows that Its chemical shift variation seems to be independent of pressure, as well as its linewidth and integrated area. The measured properties for the peak remain constant during the

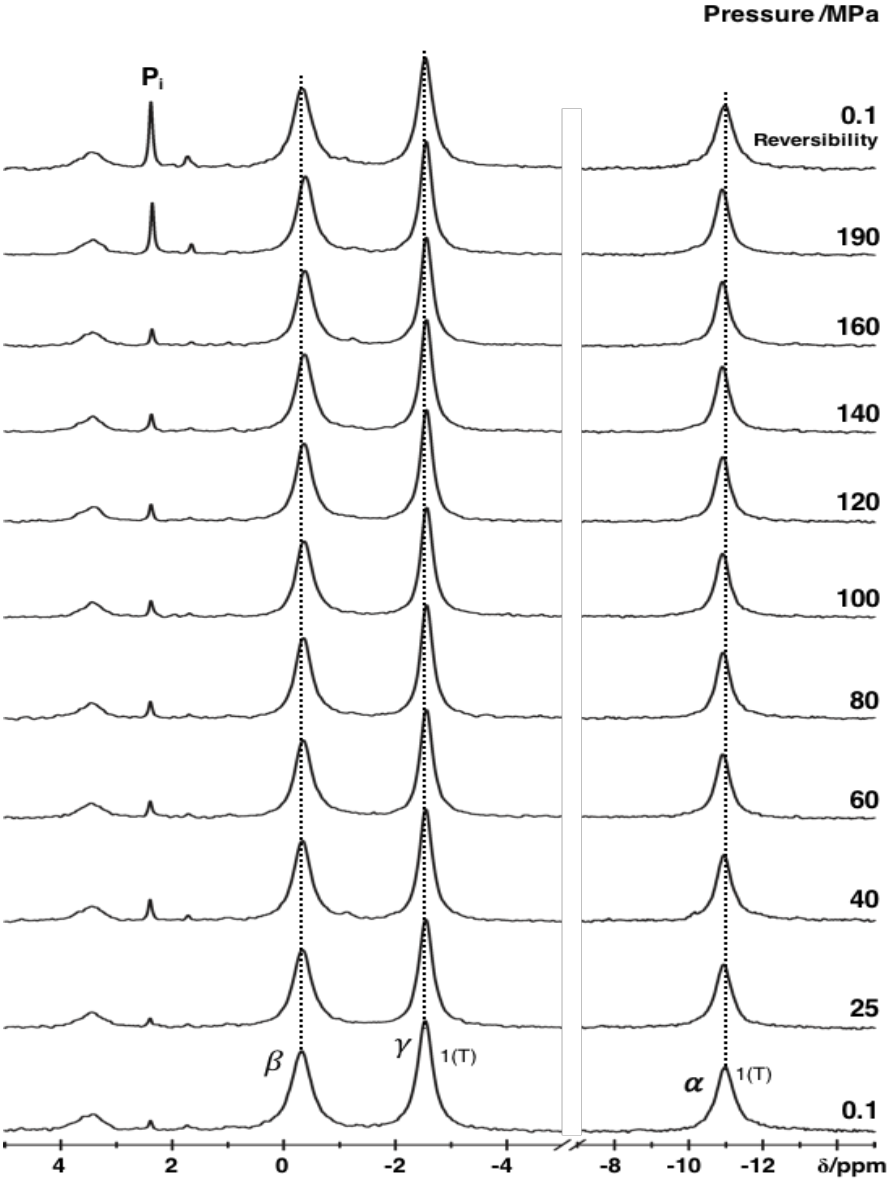

Figure 3.33. Conformational equilibria of HRas^{T35S}(1-166)•Mg^{2+}•GppNHp as a function of pressure determined by ^{31}P NMR at 278 K. The 4.37 mM protein dissolved in buffer F (40 mM Tris/HCl pH 7.5, 10 mM $MgCl_2$, 2 mM DTE) with additionally 0.4 mM DSS and 20% D_2O was subjected to increasing step-variations of pressure, up to a maximum of 190 MPa. The chemical shift evolution of the α-, β- and γ-phosphates is represented by the dashed lines. The fitted chemical shift values for all the resonance lines are listed in Table G of the appendix section. An EM function with LB= 4 Hz was applied to the processed FID.

complete course of the experiment. From its very broad shape it seems reasonable to assume that the phosphorous resonance(s) that encompasses is (are) associated with the Ras protein and are not due to the presence of a small molecule (impurity) or nucleotide by-product in solution (for which the linewidth would be only 10-20 Hz maximum). The possibility of being a contaminant from a large macromolecule (another protein) is also very

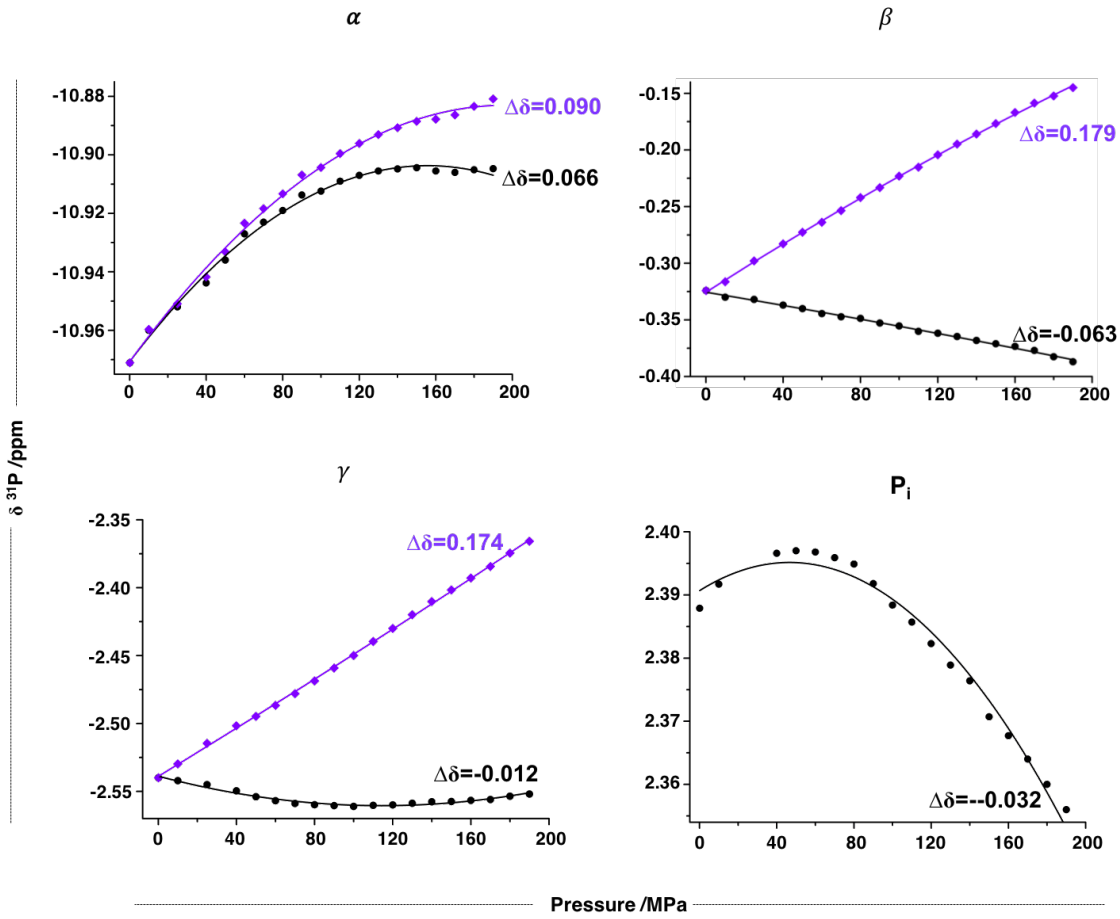

Figure 3.34. ^{31}P NMR chemical shift changes of HRas^{T35S}(1-166)•Mg^{2+}•GppNHp as a function of pressure recorded at 278 K. The observed chemical shift dependence is plotted individually for the α-, β- and γ-phosphates. The $\Delta\delta_{freenuc\ fit}$ were applied as correction factors to $\delta_{Ras\ uncorrected}$, leading to the final $\delta_{corrected}$ values, represented here for each plot as purple lozenges (-◆-). The uncorrected shift changes are also plotted as black circles (-●-) for comparison. The second order polynomial fit of the Taylor expansion was applied for the determination of B_1 and B_2. The obtained values are presented on Table 3.8. The calculated shift differences ($\Delta\delta=\delta_{190MPa}-\delta_{0.1MPa}$) are shown near the respective curve. Note that the vertical scaling is different for each plot to allow a better visualisation of the details from the different curves.

unlikely since previous biochemical methods such as PAGE and SEC, performed during protein purification, and HPLC, performed on the sample after the HP NMR series (a standard procedure done with the intent of quantifying the protein concentration and how much precipitation occurred during the NMR experiment) revealed no trace of impurities or other protein contaminants. Within the available data, the nature of this peak remains unclear. Assumptions accounting for possible phosphorylated Ras can be done. In fact, recent studies had shown that HRas can undergo phosphorylation at Thr144 and Thr148 by the enzyme GSK3b that targets the protein for proteasome-mediated degradation [250]. In principle, the same regulation mechanism can take place in *E. coli*. The only other known site of phosphorylation in Ras is specific for full length KRas4b and involves Ser181, located at the HVR [5]. Without further experimental evidence using NMR, LCMS or antibody-based

methods, the nature of the broad ^{31}P NMR signal cannot be clarified.

It is interesting to note that although no free nucleotide could be detected in the course of the pressure series, the resonance line of P_i is clearly observed even at the beginning of the experiment, in the low pressure range. There is no direct explanation for this phenomenon so far, despite being also often observed during titration experiments between Ras and its effectors and other regulators such as NF1 (Figures. 3.39 and 3.50). Interestingly, this peak cannot be found in any of the isolated proteins and is residual in Ras^{T35S} at ambient pressure (Figure 3.33, δ= 2.38 ppm), becoming only detectable when they are mixed, or in the present case, subjected to pressure [156]. It is possible that the Ras protein carries an additional phosphate molecule which is not detectable due to intermediate exchange between the protein-free and the protein-bound states but released by the presence of certain regulators or by pressure effects.

Regarding the uncorrected data (Figure 3.34, black circles), it can be inferred that all phosphate groups show a shift in the same direction as the corresponding ones in Ras^{WT} (Figure 3.30), however the magnitude of the changes is much smaller for the former than for the latter. For example, the β- and the $\gamma_{1(T)}$-phosphates on Ras^{WT} have a $\Delta\delta=\delta_{190\ MPa}-\delta_{0.1\ MPa}$ equal to -0.125 and 0.304 ppm, respectively. The corresponding values for Ras^{T35S} are -0.063 and 0.066 ppm. Qualitatively, and within the information retrieved from HP ^{31}P NMR, Ras^{T35S} seems less prone to undergo pressure-induced conformational changes between different states or more precisely between different sub*ensembles* of the same state when compared to Ras^{WT}. Upon correcting for unspecific pressure effects of the free nucleotide, the pressure dependencies (purple colour in Figure 3.34) follow the same trends described for Ras^{WT}, with all phosphates shifting downfield (just as observed for *wild type* β-, $\alpha_{1(T)}$- and $\gamma_{1(T)}$-phosphates in Figure 3.30). Concomitantly, both proteins follow a rather linear pressure dependence of the ^{31}P resonances either for the corrected and uncorrected cases, at least in the tested pressure range. One exception to this is for example the α-phosphate of Ras^{T35S} that shows large second order coefficients ($B_{2(corrected)}$= -2.27 ppm GPa^{-2}, the negative sign indicates that the α-phosphate shifts downfield with pressure, as observed in Figure 3.34).

Table 3.8. Fitted pressure coefficients and thermodynamic molar free energies, ΔG, and volumes, ΔV, for $HRas^{T35S}(1\text{-}166)\bullet Mg^{2+}\bullet$GppNHp at 278 K and pH 7.5.

^{31}P position	δ^{0a} /ppm	B_1 /ppm GPa^{-1}	B_2 /ppm GPa^{-2}	
		Uncorrected		
α	-10.971	0.86 ± 0.03	-2.77 ± 0.12	
β	-0.33	-0.29 ± 0.01	-0.14 ± 0.01	
γ	-2.54	-0.38 ± 0.02	1.67 ± 0.01	
P_i	2.39	0.19 ± 0.01	-2.05 ± 0.15	
		Corrected		
α	-10.97	0.89 ± 0.02	-2.27 ± 0.12	
β	-0.33	1.09 ± 0.01	-0.70 ± 0.01	
γ	-2.54	0.88 ± 0.01	0.20 ± 0.01	
	$\delta_1{}^b$/ppm	$\delta_2{}^b$/ppm	ΔG /kJ mol^{-1}	ΔV /mL mol^{-1}
		Uncorrected		
α	-10.98	-10.90	3.20 ± 0.14	-85.18 ± 3.18
β	-0.31	-0.39	3.74 ± 0.21	-46.20 ± 2.11
γ	-2.54[c]	-2.55[c]	9.55 ± 16.16	-36.17 ± 5.98
P_i	2.40	2.35	14.97 ± 1.46	-105.0 ± 10.1
		Corrected		
α	-10.98	-10.89	3.49 ± 0.65	-70.69 ± 5.53
β	-0.34	-0.13	4.55 ± 0.15	-50.97 ± 1.46
γ	-2.55	-2.37[c]	5.15 ± 0.23	-57.19 ± 2.32

[a] δ^0 is the chemical shift value obtained at ambient pressure at the corresponding pH.
[b] δ_1 and δ_2 are the chemical shift values obtained for the first and last pressure steps, respectively. Due to the linear tendency of the fitted curves, the obtained values constitute a coarse approximation.
[c] These values were fixed during the iteration routine.

3.3.4 ^{31}P HP NMR on KRas^{G12V}(1-189)•Mg^{2+}•GTP

The body of work performed so far for Ras^{WT} and Ras^{T35S} was also applied to the oncogenic mutant KRas^{G12V}(1-188) bound to its natural ligand, GTP.

Contrary to HRas^{WT} and HRas^{T35S}, the HP series conducted on KRas^{G12V}•Mg^{2+}•GTP was performed in a Bruker Avance 500 MHz spectrometer operating at a ^{31}P frequency of 202.456 MHz and using a selective ^{31}P 10 mm probe. When this series was recorded, the more sensitive Prodigy cold probe was not yet a member at our department. The use of a much less sensitive probe intrinsically limited the spectral quality as it can be observed from Figure 3.35. Even at a protein concentration of 3.23 mM and 3000 cumulative scans *per* step, the overall spectra are rather noisy, which rendered the proper fitting of low-populated states a difficult task. A total of 11 steps were recorded from 1.0 MPa up to 195 MPa are shown. Measurements above this value were unfruitful due to severe water leaking and consequently instability of the high-pressure line. Contrary to Ras^{WT} (and other mutants), the GDP-to-GTP nucleotide exchange reaction on Ras^{G12V} can be accomplished almost completely (i.e. the protein was 100% exchanged to GTP, with no Ras-GTP/Ras-GDP mixture). This can be observed from the spectrum at 1.0 MPa, where there are no visible ^{31}P NMR lines corresponding to the α- and β-phosphate of GDP-bound Ras.

In the course of the experiment, hydrolysis at the γ-phosphate occurs and hence the ^{31}P NMR signals from the GDP-bound protein become visible around δ= -10.1 ppm (α_{GDP}) and δ= -2.0 ppm (β_{GDP}). The α_{GDP} resonance shifts downfield with pressure (δ_{70MPa}= -10.31 ppm; δ_{195MPa}= -9.99 ppm) and the β_{GDP} shifts upfield (δ_{70MPa}= -1.92 ppm; δ_{195MPa}= -2.07 ppm, Figure 3.36 and Table 3.9). It is worth mention that the increase in the integral area for these two signals during the pressure series is dependent of time (as the hydrolysis occurs) and not on pressure. The recorded series shown in Figure 3.35 do not correspond to the sequential order by which the spectra were recorded (for example, after recording the 50 MPa step, the next measurement was performed at 150 MPa, the third one at 100 MPa, and so forth. This is valid only for the present HP series. All the others shown in this thesis were recorded by the sequential order of pressure in which they are presented). The appearance of the α_{GDP} and β_{GDP} signals is concomitant with the increase of P_i, which leads to the sharp line located at δ= 2.5 ppm. Just as detected before for Ras^{WT} and Ras^{T35S}, the effect of increasing pressure promotes a shift of the equilibrium towards state 1(T), directly observed by the decrease of the integrals representing state 2(T) (green lines) and respective increase of the integrals representing state 1(T) (red lines), following the slow exchange condition. One of the most interesting findings in the series is related with the partial splitting of the initial β-phosphate into two lines at high pressures, corresponding to states 1(T) and

2(T), respectively.

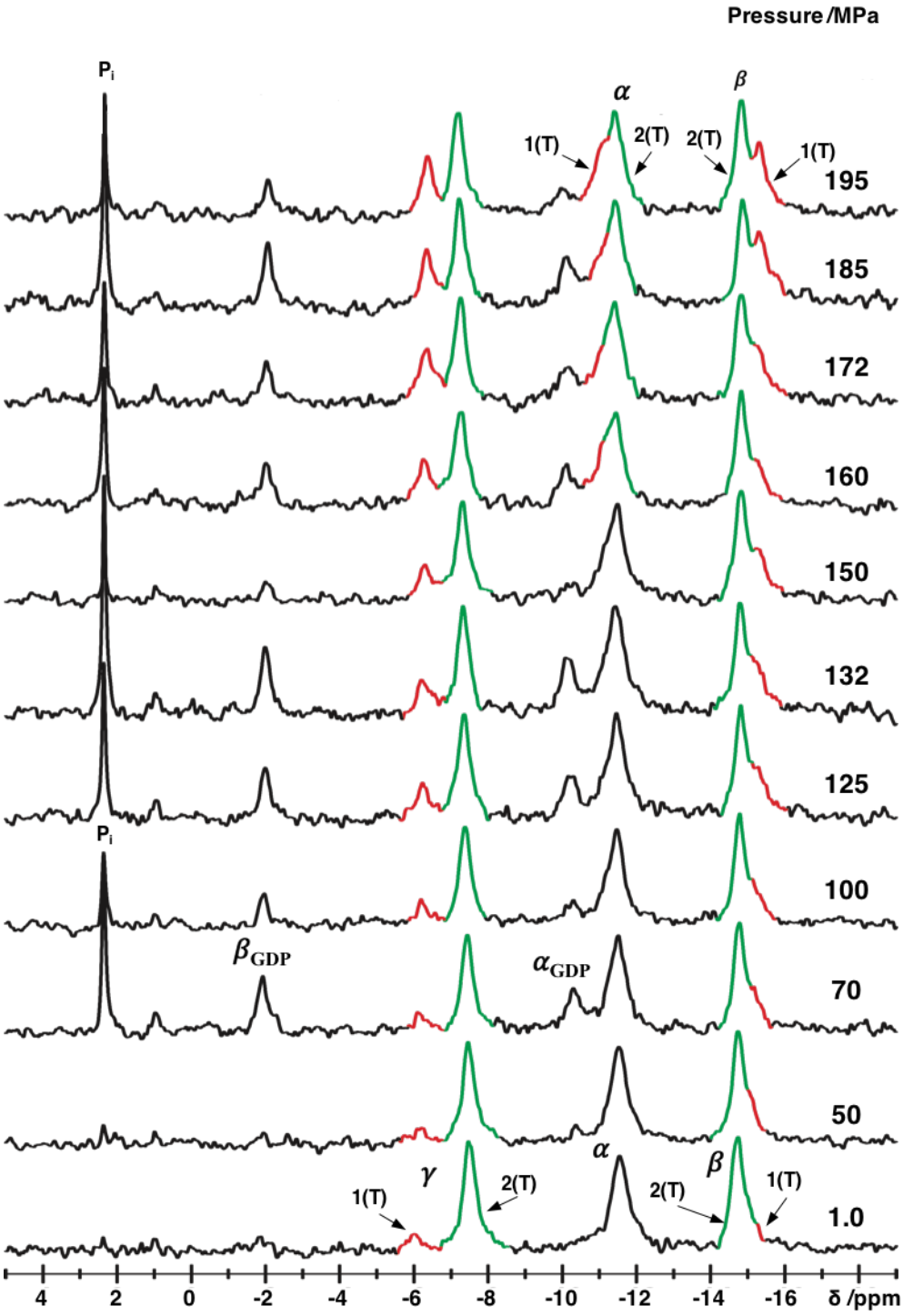

Figure 3.35. Conformational equilibria of $KRas^{G12V}(1\text{-}188)\bullet Mg^{2+}\bullet GTP$ as a function of pressure determined by ^{31}P NMR at 278 K. The 3.23 mM protein dissolved in buffer F (40 mM Tris/HCl pH 7.5, 10 mM $MgCl_2$, 2 mM DTE) with additionally 0.4 mM DSS and 20% D_2O was subjected to increasing step-variations of pressure, up to a maximum of 195 MPa. The pressure value for each step is indicated together with the evolution of states 1(T) and 2(T), represented by the red and green lines, respectively. The resonance lines corresponding to the phosphate groups of the protein bound to GDP are also indicated as α_{GDP} and β_{GDP}. Note that in this series the order of acquisition of the spectra does not coincide with the sequential increase of pressure. For example, after the 50 MPa, the next step recorded was the 150 MPa, and so on. The fitted chemical shift values for all the phosphate groups (corrected and uncorrected) are shown in Table H of the appendix section.

The two states are too close together to be resolved at 1.0 MPa but, as the pressure increases, the initial resonance becomes splitted to a point where the centre of $\beta_{1(T)}$ can be properly defined above 150 MPa. The two states on α-phosphate, on the other hand, become only resolved at very high pressures (above 195 MPa), contrary to the corresponding α-phosphate of Ras bound to GppNHp. The pressure-dependent chemical shift changes are shown in Figure 3.36. The uncorrected values, obtained directly upon application of a Gaussian filter to the FID, are coloured in black and the corresponding corrected values are coloured in red. For the correction of the data the intrinsic pressure dependence of the free Mg^{2+}•GTP nucleotide was subtracted to the uncorrected values. The pressure-dependence of free GTP was investigated in our department under similar conditions as the ones reported in this thesis for GppNHp (section 3.3.1), with appropriate adjustments for the physico-chemical properties of GTP [226].

From the Ras^{G12V} series, both states 1(T) and 2(T) on the α-phosphate shift downfield with pressure. Since the α-phosphate on the free nucleotide shifts on the opposite direction, the correction of the data was done by adding the absolute $\Delta\delta$ values from free Mg^{2+}•GTP to the $\delta_{uncorrected}$ values from Ras^{G12V}. The corrected chemical shifts show the same tendency as the uncorrected ones, moving even further downfield. Due to the low signal-to-noise ratio and to the asymmetry of the peaks, the fitted pressure coefficients have generally large associated errors, as in the case of the $\alpha_{1(T)}$-phosphate, with B_2= 16.5 $\pm$ 20.0 ppm GPa^{-2}. The uncorrected $\beta_{1(T)}$ and $\beta_{2(T)}$ phosphates move upfield as the pressure increases. Upon correction, their direction is reversed, following the same trend as observed previously for Ras^{WT} and Ras^{T35S}. Qualitatively, $\beta_{1(T)}$ shows a more linear pressure dependence than $\beta_{2(T)}$, with both developing a negative curvature. The calculated $B_{2(corrected)}$. values are -0.027 $\pm$ 1.90 ppm GPa^{-2} for the former and -7.428 $\pm$ 4.257 ppm GPa^{-2} for the latter. A proper fitting of the $\beta_{1(T)}$-phosphate could only be done above 50 MPa and only by using the GM method. It would be interesting to repeat this series up to 250-300 MPa in order to study the behaviour of this signal at higher pressures.

In GppNHp-bound Ras, states 1(T) and 2(T) are best separated for the γ-phosphate. The same is observed for Ras^{G12V}•Mg^{2+}•GTP but their pressure-dependent shifts are much less pronounced in the second case. The $\gamma_{1(T)}$-phosphate shows a negative first order dependence (B_1= -2.02 ppm GPa^{-1}), which becomes largely compensated upon correction (B_1= 0.158 $\pm$ 0.109 ppm GPa^{-1}) and the $\gamma_{2(T)}$-phosphate, on the other hand, shows a large second order dependency, with B_2 values of 7.541 ppm GP^{-2} and 10.741 ppm GPa^{-2} for the uncorrected and corrected cases, respectively.

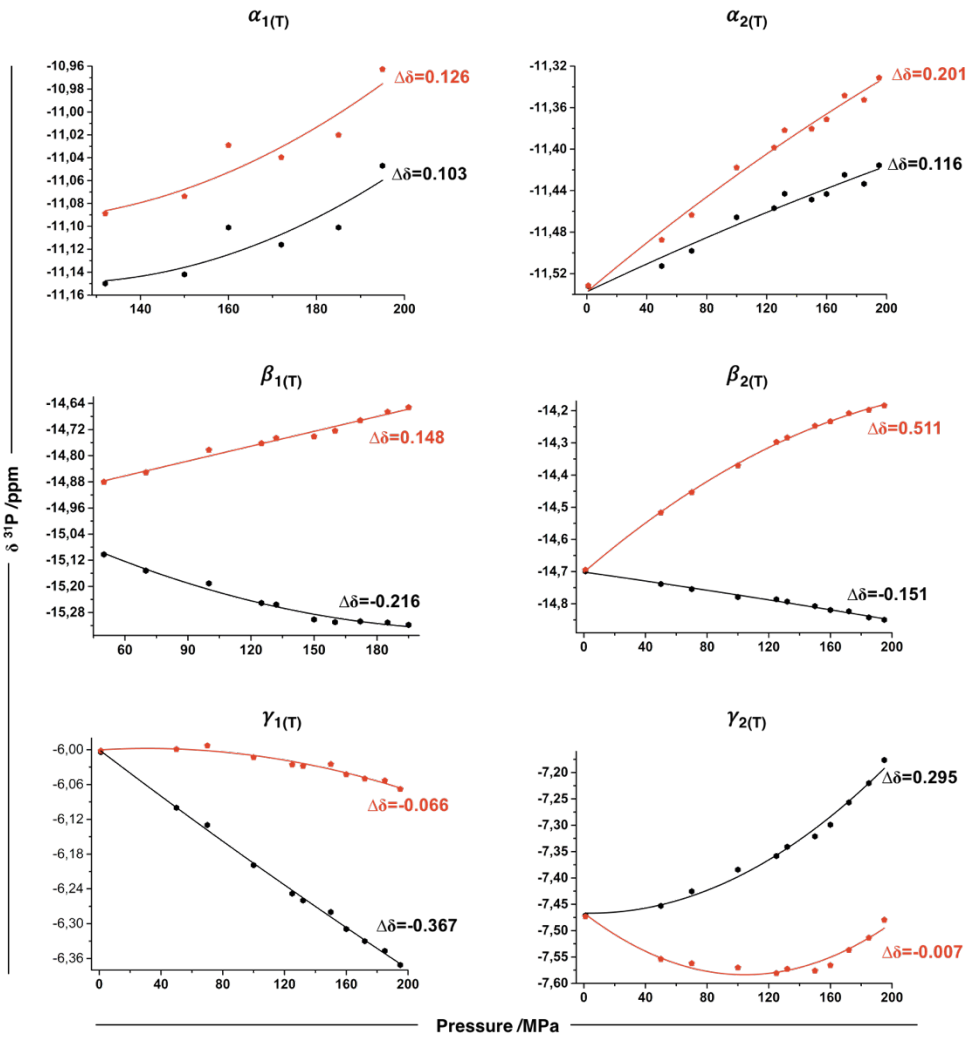

Figure 3.36. Corrected and uncorrected pressure dependence of ^{31}P chemical shifts for KRas^{G12V}(1-188)•Mg^{2+}•GTP recorded at 278 K. The $\Delta\delta_{freenuc\ fit}$ values of free Mg^{2+}•GTP [226] were applied as correction factors to $\delta_{Ras\ uncorrected}$, leading to the final $\delta_{corrected}$ values, represented here for each plot as red pentagons (-⬟-). The uncorrected shift changes are also plotted as black hexagons (-⬣-) for comparison. The second order polynomial fit of the Taylor expansion was applied for the determination of B_1 and B_2 as before. The obtained values are presented on Table 3.9 and the calculated $\Delta\delta=\delta_{195MPa}-\delta_{1.0MPa}$ values are shown near the respective curve. Note that the vertical scaling is different for each plot to allow a better visualisation of the details from the different curves.

Indeed, the overall second order coefficients presented in Table 3.9 for this pressure series are generally higher than the ones obtained either for Ras^{WT} or the T35S mutant, portending the idea that KRas^{G12V}•GTP is more responsive to pressure, at least in the vicinity of the nucleotide, than the other two GppNHp-bound proteins.

The slow exchange interconversion between states 1(T) and 2(T) was also analysed based on the integrated area of each peak. Ln K_{12} as a function of pressure is plotted in Figure 3.37 using the β- and γ-phosphates. From the fitting routine, a Gibbs energy ΔG_{12}= 5.865 ± 0.455 kJ mol^{-1} for the β-phosphate and ΔG_{12}= -6.524 ± 0.295 kJ mol^{-1} for the γ-phosphate

was obtained. The difference in the specific volumes for the two states $\Delta V_{12}=V_2-V_1$ is -31.11 ± 3.07 and 26.10 ± 2.19 mL mol^{-1}, respectively. Within the limits of error, the obtained values from the two phosphate groups are numerically similar. They have opposite signs due to the different directions of the 1(T)-2(T) transition. Their similarity is to be expected since they are a measure of a conformational transition that affects in principle the chemical environment of both α- and β-phosphates in a similar way.

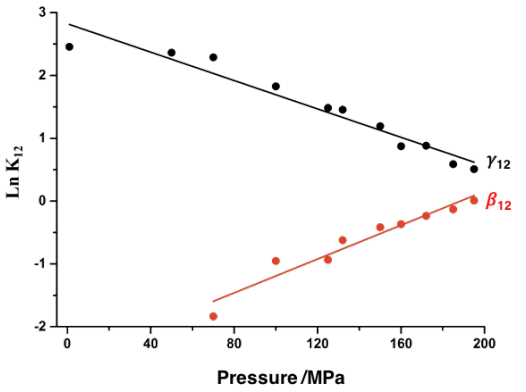

Figure 3.37. Plot of LnK_{12} as a function of pressure for $KRas^{G12V}(1\text{-}188)\bullet Mg^{2+}\bullet GTP$. The transition was analysed for the γ- and β-phosphates (coloured in black and red, respectively). The obtained free energy difference, ΔG_{12} and partial molar volume, ΔV_{12} for the γ-phosphate is -6.524 ± 0.295 kJ mol^{-1} and 26.10 ± 2.19 mL mol^{-1}, respectively. For the β-phosphate, ΔG_{12} = 5.865 ± 0.455 kJ mol^{-1} and ΔV_{12} = -31.11 ± 3.07 mL mol^{-1}, respectively.

Table 3.9. Fitted pressure coefficients and thermodynamic molar free energies, ΔG, and volumes, ΔV, for KRas^{G12V}(1-188)•Mg^{2+}•GTP at 278 K and pH 7.5.

^{31}P position	δ^{0a} /ppm	B_1 /ppm GPa^{-1}	B_2 /ppm GPa^{-2}	--	--
		Uncorrected			
$\alpha_{1(T)}$	-10.91	-4.01 ± 6.57	16.5 ± 20.0		
$\alpha_{2(T)}$	-11.54	0.68 ± 0.15	-0.39± 0.72		
$\beta_{1(T)}$	-14.95	-3.28 ± 0.48	7.07 ± 1.90		
$\beta_{2(T)}$	-14.70	-0.68 ± 0.10	-0.33 ± 0.43		
$\gamma_{1(T)}$	-6.00	-2.02 ± 0.11	0.64 ± 0.51		
$\gamma_{2(T)}$	-7,47	-0.06 ± 0.22	7.54 ± 1.02		
P_i	2.34	0.50 ± 0.20	-2.93 ± 0.73		
		Corrected			
$\alpha_{1(T)}$	-10.91	-3.48 ± 6.57	16.40 ± 20.0		
$\alpha_{2(T)}$	-11.54	1.21 ± 0.15	-0.89 ± 0.72		
$\beta_{1(T)}$	-14.95	1.52 ± 0.48	-0.03 ± 1.90		
$\beta_{2(T)}$	-14.70	4.12 ± 0.09	-7.43 ± 4.26		
$\gamma_{1(T)}$	-6.00	0.16 ± 0.11	-2.54 ± 0.51		
$\gamma_{2(T)}$	-7.47	-2.24 ± 0.02	10.74 ± 1.02		

	$\delta_1{}^b$ /ppm	$\delta_2{}^b$ /ppm	ΔG /kJ mol^{-1}	ΔV /mL mol^{-1}	Transition
		Uncorrected			
$\alpha_{1(T)}$	-11.15	-11.04c	27.42 ± 1.20	-156.66 ± 68.9	1-to-0
$\alpha_{2(T)}$	-11.53[c]	-11.42	6.77 ± 0.93	-70.00 ± 8.12	2-to-3
$\beta_{1(T)}$	-15.10	-15.32[c]	10.57 ± 2.19	-101.18 ± 15.70	1-to-0
$\beta_{2(T)}$	-14.70[c]	-14.85[c]	5.74 ± 0.75	-56.05 ± 6.04	2-to-3
$\gamma_{1(T)}$	-6.00[c]	-6.37[c]	5.97 ± 0.52	-61.42 ± 4.44	1-to-0
$\gamma_{2(T)}$	-7.47[c]	-7.18[c]	10.05 ± 1.36	-72.32 ± 9.26	2-to-3
P_i	2.36	2.33[c]	23.19 ± 7.06	-137.50 ± 40.0	--
		Corrected			
$\alpha_{1(T)}$	-11.09[c]	-10.96[c]	27.42 ± 9.98	-157.82 ± 57.44	1-to-0
$\alpha_{2(T)}$	-11.53	-11.33	6.04 ± 0.57	-62.63 ± 4.93	2-to3
$\beta_{1(T)}$	-14.90	-14.63	9.18 ± 1.32	-73.88 ± 10.17	1-to-0
$\beta_{2(T)}$	-14.69[c]	-14.18	5.32 ± 0.63	-66.18 ± 9.05	2-to3
$\gamma_{1(T)}$	-6.00	-6.11	9.96 ± 3.51	-55.23 ± 39.50	1-to-0
$\gamma_{2(T)}$[d]	--	--	--	--	2-to-3

[a] δ^0 is the chemical shift value obtained at ambient pressure at the corresponding pH.
[b] δ_1 and δ_2 are the chemical shift values obtained for the first and last pressure steps, respectively. Due to the linear tendency of the fitted curves, the obtained values constitute a coarse approximation.
[c] The value was fixed during the fitting routine.
[d] No convergence was attained from the fitting routine.

- This page was deliberately left blank -

3.4 Mutational Analysis of HRas^{WT}(1-166) Studied by ^{31}P NMR and ITC

The identification of non-conventional binding sites in the surface of Ras can be done by analysing the response of its individual amino acids to pressure. In fact specific residues of the protein (located either at the surface or at the core) could be identified in previous HP NMR experiments as being predominantly influenced by a given conformational transition and were colour-coded at the surface of the protein (Figure 1.13, section 1.3.2, [171]). These investigations constitute a mapping of the pressure-dependent conformational transitions of Ras and were taken in the present thesis as background information necessary to select specific amino acids and to perform site directed-mutagenesis on them with the expectation that the mutation would shit the conformational equilibrium towards one of the two conformational states in which the selected amino acids are involved. The correlation between the amino acids and their corresponding conformational transition as detected by HP is shown in Table 3.10. The ones selected for site-directed mutagenesis and their respective replacement are highlighted in orange colour. The next sections describe the results gathered from this mutational study on truncated HRas. An attempt to correlate the effect of the mutation with the any observed conformational transition is made herein. All mutants were created *de novo*, by designing the primers with the mutation at the centre and using standard PCR techniques (experimental sections 2.2.1.9 and 2.2.1.11).

Table 3.10. List of amino acids according to the associated conformational transition as determined by HP NMR and the ones chosen for SDM.

2(T)-to-3(T)		2(T)-to-1(T)		2(T)-to-1(0)	
Surface	**Core**	**Surface**	**Core**	**Surface**	**Core**
His27 Glu	Leu56	Asn26 Lys	Val9	Ser39 Leu	Phe82
Asp33 Lys	Gly115	His94 Asp	Val14	Glu3 Val	Met111
Ile46 Thr	Thr20	Ala66 Thr		Lys42	
Val44	Leu79	Gly138		Glu49	
Gly48	Val112 Arg	Ile139		Arg161	
Leu23				Val45	
His166				Arg135	
Ser127				Tyr137	
Asp132				Tyr141	
Thr124				Glu143	
Asp107				Ala130	
Ala121				Ala134	
Asn85 Ala				Ser136	
Asn86				Ile84	

1(0), 1(T), 2(T) and 3(T) represent the nucleotide free, the GEF recognition, the effector recognition and the GAP recognition states, respectively. The listed residues have also generally high B_1 and B_2 pressure coefficients, according to [171]. The ones chosen for site-directed mutagenesis are coloured in orange, together with the respective amino acid replacement. Mutagenesis was also attempted in the residues coloured in blue but with no success. Only residues involved in a two-state transition were considered.

3.4.1 Preliminary Considerations About Ras^{WT}(1-166)

Several ^{31}P NMR spectroscopy studies were firstly conducted on Ras^{WT} and used afterwards as a qualitative and quantitative resource for the assessment and comparison of similar studies conducted on the different mutants.

3.4.1.1 Conformational equilibria of H, K and NRas^{WT}(1-166)•Mg^{2+}•GppNHp

The dynamics of the full-length H and KRas^{WT}(1-188/189) were studied by ^{31}P NMR in section 3.1. Similar studies were also conducted herein for the *wild type* truncated variants (1-166), including NRas in terms of ^{31}P chemical shifts and equilibrium constants. The obtained spectra are shown in Figure 3.38 and the fitted values are listed in Table 3.11. There are obvious differences between the different isoforms: state 2(T) on γ-phosphate is shifted downfield in K and NRas as compared to HRas. The $\Delta\delta$ differences are ca. 0.06 ppm and 0.09 ppm, respectively. The chemical shift values of the other phosphate groups are very similar and their corresponding $\Delta\delta$ values are always within $\pm$ 0.05 ppm in the three proteins, a value close to the limits of the error for the measurements. The most striking difference however, arises from the equilibrium populations. The obtained K_{12} for NRas is 2.57, about 1.7-fold higher than HRas (K_{12}=1.57). The difference is rather surprising, considering that the degree of homology between the three isoforms is more than 90% and that their catalytic domain differs only in four residues (aa 151, 153, 165 and 166), none of them located at the switch regions [251]. The obtained linewidths on γ-phosphate for K and NRas are in average numerically larger than the corresponding ones for HRas. The obtained K_D values for the dissociation of the Ras-Raf complex are 0.42 $\pm$ 0.1, 0.60 $\pm$ 0.06 and 0.18 $\pm$ 0.05 μM for H-, K- and NRas, respectively. From these interaction studies it follows that the affinity of NRas towards Raf is 2.42-fold higher than the one of HRas and 3.45-fold higher than the one of KRas. These results are in agreement with the equilibrium distribution observed for the different isoforms in the ^{31}P NMR spectra, with NRas having the highest K_{12}, that is, being more populated in terms of state 2(T) (the effector recognition state), followed by KRas and HRas in this respective order.

The signature plot for the three proteins is very similar (similar ΔG and ΔH and -TΔS), with the NRas-Raf association being slightly more entropically favourable than the other two isoforms (-TΔS = -38.6 kJ mol^{-1} vs -28.3 kJ mol^{-1} (HRas) and -22.3 kJ mol^{-1} (KRas)). The enthalpies of binding, explicitly obtained from the measurements, are also identical (ΔH= -8.10, -13.2 and -10.8 kJ mol^{-1} for H, K and NRas, respectively).

It is worth mentioning the comparison between the equilibrium distribution of the full length (section 3.1.1, Figure 3.1) and the respective truncated H and KRas variants.

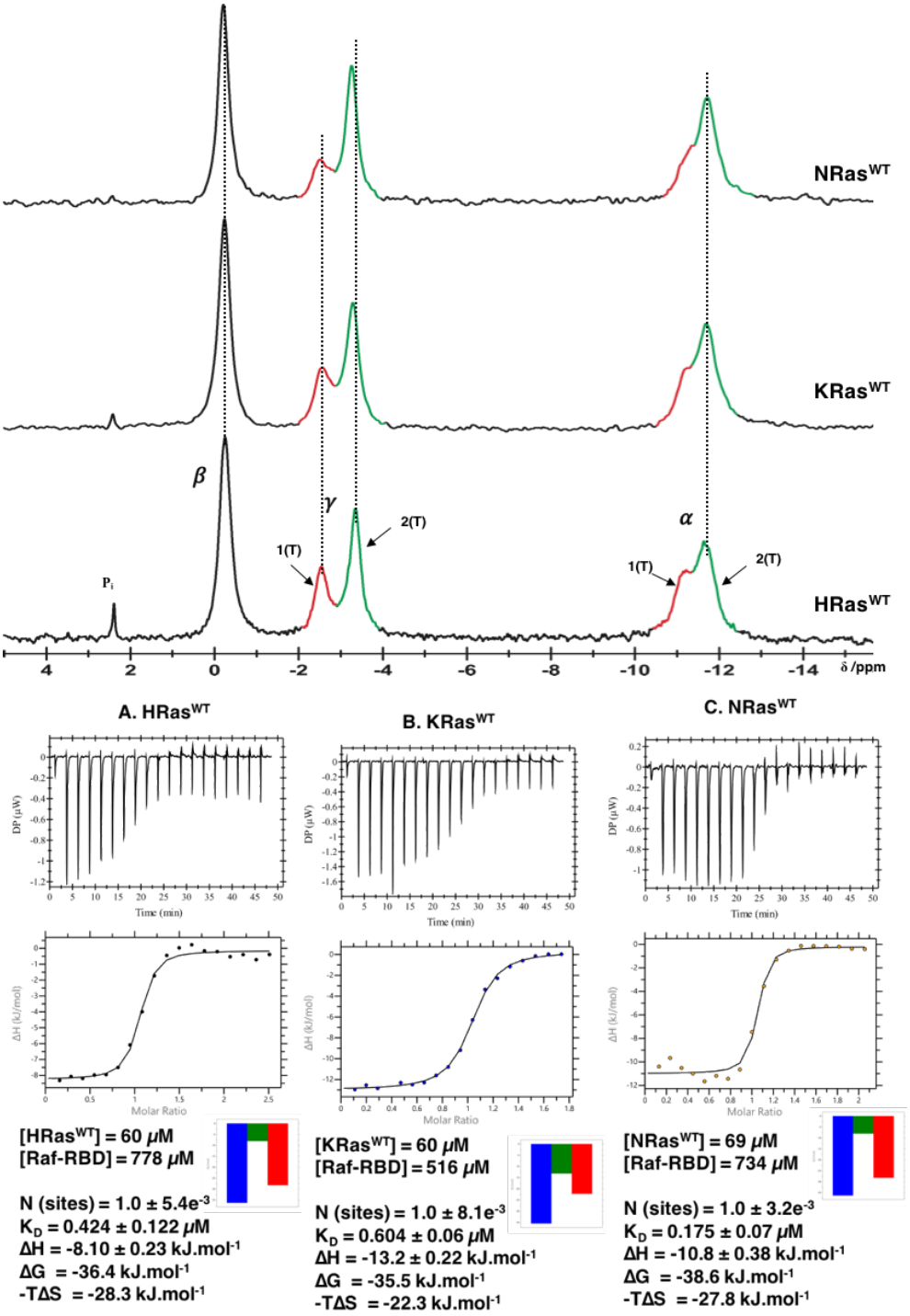

Figure 3.38. Conformational equilibrium of Ras^{WT}(1-166)•Mg^{2+}•GppNHp detected by ^{31}P NMR spectroscopy and thermodynamics of association with Raf-RBD detected by ITC. The equilibrium between states 1(T) and 2(T) for the truncated H, K and NRas isoforms was compared in terms of ^{31}P chemical shifts and equilibrium constants, K_{12}, on γ-phosphate. The three proteins with concentrations of 1.78, 1.10 and 0.62 mM, respectively were dissolved in buffer F (40 mM Tris/HCl pH 7.5, 10 mM $MgCl_2$, 2 mM DTE) with additionally 0.2 mM DSS and 5 or 10% D_2O. All the NMR measurements were performed at 278 K at 202.456 MHz (KRas (6000 scans, LB=15Hz), NRas (7000 scans, LB=15Hz)) or at 242.89 MHz (HRas, 1000 scans, LB= 8 Hz). The fitted chemical shift values, linewidths and K_{12} are listed in Table 3.11. The interaction with Raf-RBD was measured at 298 K. All the proteins were dissolved in the same buffer F with additionally 150 mM NaCl. The signature plots are presented alongside with the fitted thermodynamic values (blue: ΔG, green: ΔH, red: $-T\Delta S$) and the respective isotherms.

The former ones are slightly shifted towards state 2(T) as compared with the truncated forms (K_{12}= 1.9 vs 1.6 for FLHRas and cHRas, respectively and K_{12}=2.0 vs 1.8 for FLKRas vs cKRas, respectively). The observed differences, even if small, portend the importance of the HVR in the modulation of the conformational equilibrium detected in the vicinity of the nucleotide by ^{31}P NMR.

Table 3.11. ^{31}P NMR chemical shift values and linewidths for the truncated wild type isoforms of H, K and NRas in complex with Mg^{2+}•GppNHp.

Protein	α-phosphate		β-phosphate	γ-phosphate		K_{12} [b]
	$\delta_{1(T)}$ [ppm]	$\delta_{2(T)}$ [ppm]	$\delta_{1(T),2(T)}$ [a] [ppm]	$\delta_{1(T)}$ [ppm]	$\delta_{2(T)}$ [ppm]	
HRas^{WT}	-11.16	-11.68	-0.25	-2.56	-3.34	1.57
KRas^{WT}	-11.18	-11.70	-0.23	-2.58	-3.28	1.83
NRas^{WT}	-11.21	-11.72	-0.21	-2.53	-3.26	2.57
	$\Delta\nu_{1/2\ 1(T)}$ [Hz]	$\Delta\nu_{1/2\ 2(T)}$ [Hz]	$\Delta\nu_{1/2\ 1(T),2(T)}$ [Hz]	$\Delta\nu_{1/2\ 1(T)}$ [Hz]	$\Delta\nu_{1/2\ 2(T)}$ [Hz]	--
HRas^{WT}	92.74	84.34	47.06	64.76	51.43	
KRas^{WT}	57.29	102.28	48.19	69.04	55.30	
NRas^{WT}	66.52	94.29	43.15	72.76	47.80	

All the values are fitted from the experimental spectra recorded at 278 K, pH 7.5. The estimated errors from the fitting procedure are less than ± 0.01 ppm in chemical shift values and ± 0.15 Hz in linewidths at the γ-phosphate. An LB= 8 Hz was applied to the FID and subtracted afterwards from the final fitted linewidth values.

[a] The β-phosphate was fitted as a single Lorentzian line because states 1(T) and 2(T) cannot be separated at the magnetic field used

[b] The equilibrium constant, K_{12}, was calculated using the population distribution on the γ-phosphate. The associated error is ± 0.2.

3.4.1.2 Titration of HRas^{WT}(1-166)•Mg^{2+}•GppNHp with NF1 Followed by ^{31}P NMR

The catalytic domain of the GAP protein NF1 (aa 1198-1531, 35 kDa) was added to HRas^{WT}(1-166) in a titration experiment followed by ^{31}P NMR. The obtained data is shown graphically in Figure 3.39 and numerically in Table 3.12. The results gathered herein can be taken afterwards for a comparative analysis with similar titrations performed in different Ras mutants. In the presence of NF1, the chemical environment of all the three phosphate groups is affected, as it can be directly observed from their respective lineshapes on Figure 3.39. As usual, the most striking modifications are observed for the γ-phosphate. The interpretation can be done as follows: as NF1 is stepwise added to Ras the integrals of the resonance lines corresponding to states 1(T) (red colour) and 2(T) (green colour) decrease without any appreciable modification of their corresponding chemical shift values (Table 3.12), indicating that no major or dramatic structural rearrangements in the vicinity of the nucleotide occur upon binding to NF1. At the same time, another resonance line located in between states 1(T) and 2(T) becomes visible and its integral increases as the concentration of NF1 increases. In the light of the proposed model, this line is ascribed to

the conformational state that selectively recognizes GAP proteins and is named 3(T). The fitted lines for the three states and their interplay during the titration can be observed in Figure 3.39 for the γ-phosphate in the third, fourth and fifth steps of the titration. As the titration proceeds, the linewidths of states 1(T) and 2(T) (corresponding to unbound Ras) do not change appreciable and the linewidth of state 3(T) increases concomitantly with the increase of the molecular mass of the complex. Between the first spectrum and the last titration step the theoretical size of the complex increases by a factor of 3.0, from 18 kDa (Ras alone) to 54 kDa (note that state 3(T) seems to be only saturated in the last step, thus the 1:2 ratio was taken as the most representative of a 1:1 binding). The experimentally determined increase on the linewidth values for state 3(T) is also of the same magnitude (from ca. 65 Hz to 206 Hz, Table 3.12). Note that the line broadening of 65 Hz measured for state 2(T) in Ras alone (Table 3.12) is assumed to be also representative of state 3(T). A very similar value is obtained when considering the linewidth of state 3(T) in the first titration step (1:0.25 ratio, $\Delta\nu_{1/2\ 3(T)}$= 105.44 Hz) to which the natural line broadening of 45 Hz for state 2(T) is subtracted (105.44-45= 61 Hz, Table 3.12). The natural line broadening of Ras alone can be estimated from previous transverse relaxation experiments given the relationship $\Delta\nu_{1/2}=1/T_2.\pi$ (T_2= 4.1 and 7.1 ms for states 1(T) and 2(T), respectively [116]). Thus, the obtained linewidth at 1:1 binding matches nicely the increase in the theoretical size of the complex, which is also indicative that there are no additional contributions from exchange broadening process in the present titration. The interaction between Ras and NF1 follows a slow exchange mechanism, i.e. $|\Delta\omega\tau_c| >> 1$. From the peak separation, $\Delta\omega$, between state 3(T) and the other states, one obtains a lower limit of the lifetime of the Ras-NF1 complex equal to 8.93 ms in state 1(T) and 11.47 ms in state 2(T). Equivalent results were previously obtained on the titration of Ras with the protein GAP334 by ^{31}P NMR [117]. In principle, the α-phosphate should have a similar response to the presence of NF1 as the one observed for the γ-phosphate. However, the greater superposition of the NMR lines associated with the rapidly decreasing spectral quality due to dilution of Ras rendered impossible the proper fitting of the data in this case. Different approaches were attempted, including fixing the chemical shift values and linewidths for states 1(T) and 2(T) but with no success. Nevertheless, from the fitting of the last titration step, the obtained chemical shift value for state 3(T) at the α-phosphate is -11.124 ± 0.07 ppm.

The analysis of the β-phosphate, on the other hand, shows that as the titration proceeds, an additional signal arises at the left side of the original β-phosphate in the unbound Ras. This new signal lies at ca. δ= 0.07 ppm (Table 3.12) and its relative area increases with increasing concentrations of the titrant.

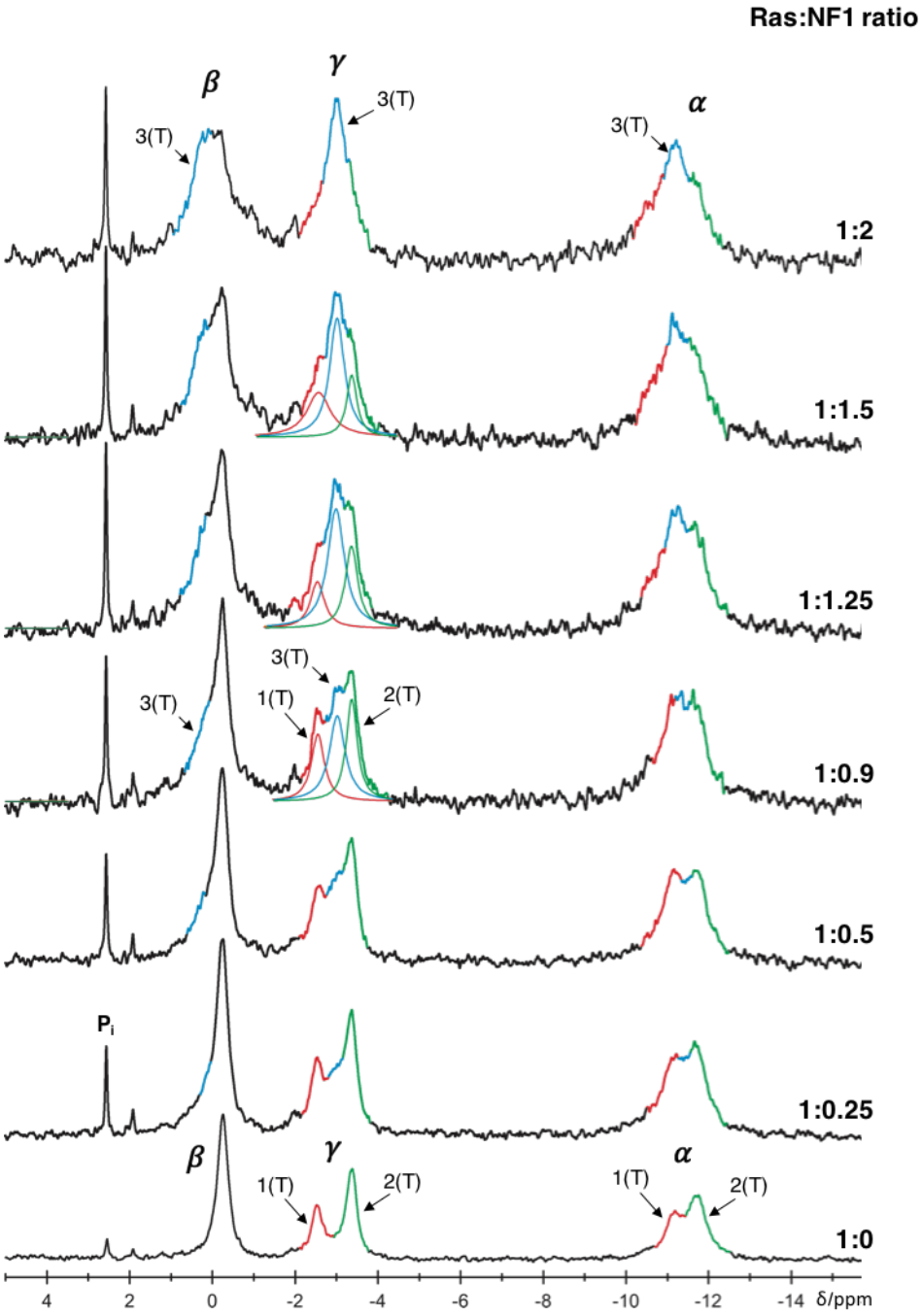

Figure 3.39. Protein complex formation between $HRas^{WT}(1\text{-}166)\bullet Mg^{2+}\bullet$GppNHp and NF1 followed by ^{31}P NMR spectroscopy at 278 K. To an initial 1.3 mM of Ras dissolved in buffer F (40 mM Tris/HCl pH 7.5; 10 mM $MgCl_2$; 2 mM DTE) with additionally 150 mM NaCl, 0.2 mM DSS in 10% D_2O, increasing amounts of the GAP protein NF1 (from a 0.65 mM stock solution) were added (the corresponding molar ratios for each step are presented). The concentration of Ras and NF1 in the final step (1:2 ratio) was 0.26 mM and 0.52 mM, respectively. An exponential filter with LB= 10 Hz was applied to the processed FID. Each spectra was obtained by accumulation of approximately 15000 scans. The resonance lines corresponding to the α-, β- and γ-phosphates are indicated as well as the states 1(T), 2(T) and 3(T), represented by the red, green and blue colours, respectively. As an example, the deconvolution into separated Lorentzian lines is shown for three different titration steps on the γ-phosphate. The most obvious effect that arises from adding NF1 to Ras is the appearance of the third resonance line (coloured in blue), corresponding to the Ras-GAP recognizing state 3(T). The obtained chemical shift values for this state at the 1:2 ratio for the α-, β- and γ-phosphates are -11.12 ppm, 0.07 ppm and -3.00 ppm, respectively (Table 3.12).

In the Ras-NF1 complex, the β-phosphate NMR signal is formed by these two lines that lie very close to each other. A remarkable finding can be observed at a ratio of 1:2, were the α- and γ-phosphates appear saturated, with the equilibria shifted almost completely towards state 3(T) and, by contrast, the β-phosphate becomes a very broad peak with an ill-defined centre that seems to feature two distinct conformational states that lie very close to each other. As result, It can be hypothesized that in the Ras-NF1 complex the β-phosphate is characterized by two distinct conformational states and constitute the reason why saturation was not achieved, even at a ratio of 1:2.

Table 3.12. ^{31}P NMR chemical shift values and linewidths for the protein-protein complex HRas^{WT}(1-166)•Mg^{2+}•GppNHp•NF1.

Protein complex	Ras:NF1 ratio	α-phosphate			β-phosphate		γ-phosphate		
		$\delta_{1(T)}$ [ppm]	$\delta_{3(T)}$ [ppm]	$\delta_{2(T)}$ [ppm]	$\delta_{1(T),2(T)}$ [ppm]	$\delta_{3(T)}$ [ppm]	$\delta_{1(T)}$ [ppm]	$\delta_{3(T)}$ [ppm]	$\delta_{2(T)}$ [ppm]
HRas^{WT}	**--**	-11.16	--	-11.72	-0.25	--	-2.54	--	-3.36
+NF1	**1:0.25**	-11.15	--[b]	-11.71	-0.25	--	-2.53	-3.00	-3.36
	1:0.5	-11.15	--[b]	-11.73	-0.25[d]	0.17	-2.54	-3.03	-3.36
	1:0.9	--[c]	--[c]	--[c]	-0.25[d]	0.06	-2.54	-3.02	-3.37
	1:1.25	--[c]	--[c]	--[c]	-0.25[d]	0.07	-2.54	-3.01	-3.36
	1:1.50	--[e]	-11.12	--[e]	-0.25[d]	0.05	-2.55	-3.02	-3.37
	1:2.0	--[e]	-11.12	--[e]	-0.25[d]	0.07	-2.58	-3.00	-3.37
		α-phosphate			**β-phosphate**		**γ-phosphate**		
		$\Delta\nu_{1/2\ 1(T)}$ [Hz]	$\Delta\nu_{1/2\ 3(T)}$ [Hz]	$\Delta\nu_{1/2\ 2(T)}$ [Hz]	$\Delta\nu_{1/2}$[a] [Hz]	$\Delta\nu_{1/2\ 3(T)}$ [Hz]	$\Delta\nu_{1/2\ 1(T)}$ [Hz]	$\Delta\nu_{1/2\ 3(T)}$ [Hz]	$\Delta\nu_{1/2\ 2(T)}$ [Hz]
HRas^{WT}	**--**	116.74	--	114.72	66.3	--	81.47	--	64.60
+NF1	**1:0.25**	--	--[b]	--	66.3	--	80.71	105.44	60.01
	1:0.5	--[c]	--[b]	--[c]	65.2[d]	172.0	96.57	113.3	58.47
	1:0.9	--[c]	--[c]	--[c]	65.5[d]	227.6	82.24	111.44	68.55
	1:1.25	--[c]	--[c]	--[c]	65.5[d]	213.7	89.32	109.22	78.70
	1:1.50	--[c]	--[c]	--[c]	--[c]	--[c]	98.65	158.45	68.00
	1:2.0	--[c]	--[c]	--[c]	--[c]	--[c]	91.98	206.19	91.98

All the values are fitted from the experimental spectra recorded at 278 K, pH 7.5. The estimated errors from the fitting procedure are ± 0.02 ppm in chemical shift values and ± 0.25 Hz in linewidths for the γ-phosphate. An LB= 10 Hz was applied to the processed FID and subtracted afterwards from the final fitted linewidth values.

[a] States 1(T) and 2(T) of the β-phosphate in cannot be separated at the magnetic field used and were therefore fitted as a single Lorentzian line.

[b] State 3(T) could not be appropriately fitted for the indicated titration step.

[c] Fitting of the resonance lines with independent Lorentzian functions was not possible due to their extreme overlapping at the magnetic field used.

[d] These values were fixed during the iteration routine.

[e] The α-phosphate was fitted with a single resonance line centred in state 3(T).

- This page was deliberately left blank -

3.4.2 Site-Directed Mutagenesis

3.4.2.1 2(T)-to-1(T) Transition: N26K, H94D and A66T

Following the guidelines presented in section 3.4, the effect of mutating amino acid residues involved in the conformational transition to the GEF recognizing state 1(T), was investigated. For the purpose, three residues from the list presented in Table 3.10 were selected. The amino acid chosen for the replacement was based in opposite physico-chemical properties relative to the one being replaced. Thus, the uncharged Asn26 was replaced by the positively charged Lys, the non-polar Ala66 was replaced by the polar Thr, a bulky by a small, a positive by a negative, and so on. The effect of each mutation cannot be truly predicted without a computational approach, but as the original amino acid residues are involved in the 2(T)-to-1(T) transition, it is expected that their modification would affect the population distribution of at least one of these states.

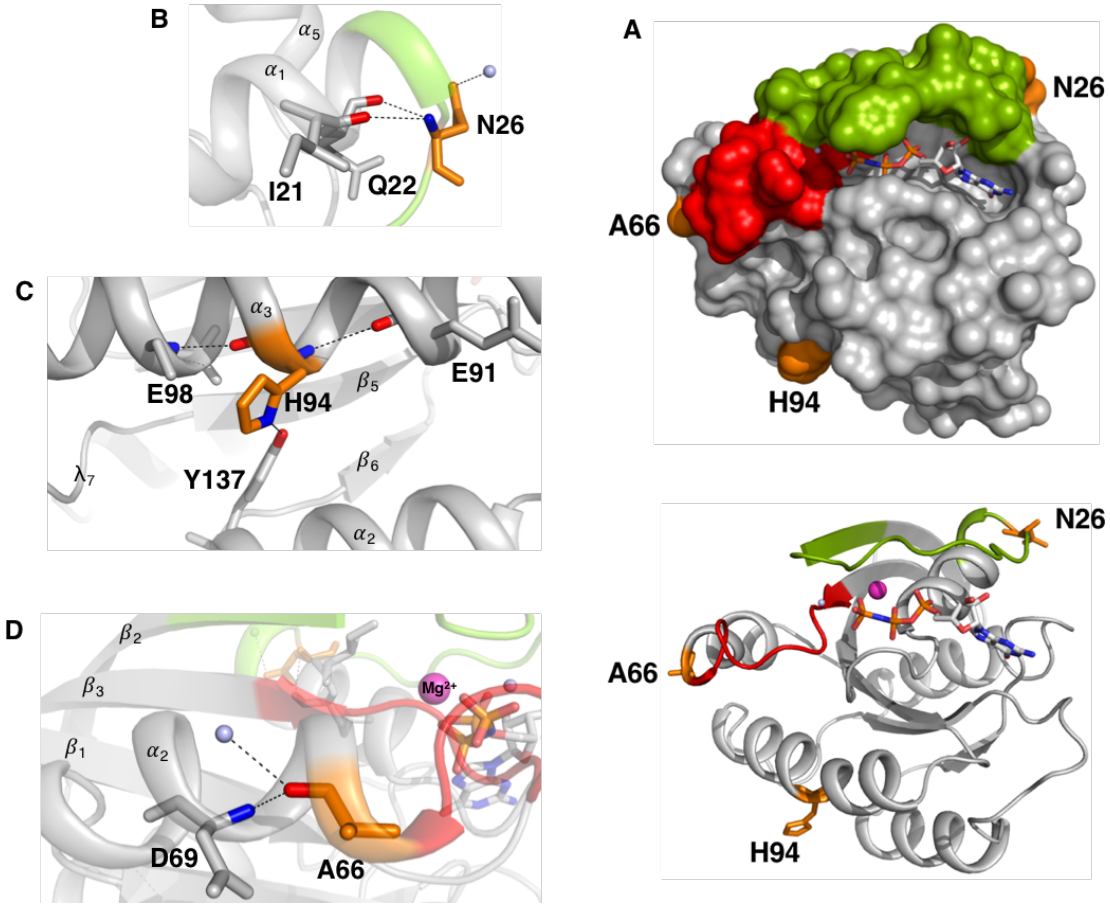

Figure 3.40. Localization on the Ras^{WT}•Mg^{2+}•GppNHp surface of the amino acid residues Asn26, His94 and Ala66 that were subjected to SDM (experimental section 2.2.1.11). These residues sense the 2(T)-to-1(T) transition upon pressure perturbation and were mutated with the prospect of shifting the equilibrium between one of these states. **A.** Localization of the three residues (coloured in orange) in the structure with a surface and a cartoon representation. Switch 1 is coloured in green, switch 2 is coloured in red and the Mg^{2+} ion is coloured in magenta. Key features near each residue, including polar contacts, are shown for Asn26, **B.**, His94, **C.** and Ala66, **D.** Important –NH and –OH moieties are coloured in blue and red, respectively. H_2O molecules are coloured in light blue. pdb: 5p21.

The localisation of the three residues on the surface of Ras^{WT}•Mg^{2+}•GppNHp is depicted in Figure 3.40. Asn26 belongs to the loop λ_2 that connects the helix α_1 to the β_2 strand, just at the beginning of switch 1. This residue is involved in two polar contacts between its main chain NH group to the carboxyl groups of Ile21 and Gln22, both located in the α_1 helix (Figure 3.40B). His94 is in the middle of the helix α_3, with the side chain protruding towards helix α_2 and establishing a polar contact with the side chain of Tyr137, Glu91 and Glu98 (C). Mutation to Asp would disrupt the H-bond with Tyr137 which could lead to an increase of the distance between α_2 and α_3. Ala66 is located in the helix α_2, at the end of the switch 2 and establishes a polar contact with Asp69 on the same helix and a H_2O molecule (D). Replacement to a Thr would introduce an additional polar group that would become oriented towards the outward surface of the protein, which could induce in principle significant structural modifications. From the three residues under investigation, only Asn26 is reported to be an “hot spot” for being involved in a disease of the central nervous system when mutated to Gly [252].

3.4.2.1.1 ^{31}P NMR GppNHp and GTP Spectra. Raf Interaction and GTPase Activity

Figures 3.41 and 3.42 show respectively the ^{31}P NMR spectra of the GppNHp and the GTP-bound protein complexes. The numerical values for the fitted chemical shifts and linewidths are shown in Table 3.13 and the corresponding GDP-bound spectra are shown in Figure B of the appendix section. From the obtained data it can be inferred that there are no significant differences in terms of shift values and linewidths between the three mutants and *wild type* Ras. The only exception to this statement is state 1(T) on γ-phosphate of Ras^{H94D}, whose linewidth is 20% smaller than the corresponding one in Ras^{WT} ($\Delta\nu_{1/2}$ = 59 vs 74 Hz). Ras^{N26K} shows an additional signal at δ= 0.98 ppm, with a linewidth of $\Delta\nu_{1/2}$= 19.2 Hz. The signal is most likely due to a contamination during the nucleotide exchange reaction. This is corroborated by the ^{1}H spectrum that also shows additional unknown peaks.

The GTP-bound spectra of the three mutants are also identical to the one of *wild type* Ras (Figure 3.42). The calculated equilibrium constants for Ras^{N26K} and Ras^{A66T} are respectively 9.30 and 10.4, somewhat smaller than K_{12}= 11.3 obtained for Ras^{WT}. However, the difference is not meaningful due to the large associated error (for all cases, including Ras^{WT} the integration of state 1(T) lies within the baseline noise and is therefore very inaccurate). The most interesting feature can be ascribed to the very broad peak ($\Delta\nu_{1/2}$ = 67 Hz) located at δ= 3.36 ppm in the spectrum of Ras^{H94D}•Mg^{2+}•GTP. This chemical shift usually corresponds to the NMR line of free GMP (this was confirmed by spiking experiments using the same protein sample). However, the peak is too broad to be associated with the free

nucleotide in the present case. Furthermore, it is also present in Ras^{H94D}•Mg^{2+}•GDP (δ= 3.39 ppm, $\Delta\nu_{1/2}$ = 73 Hz, Figure B, appendix section), but absent in the Ras^{H94D}•Mg^{2+}•GppNHp spectra, which indicates that alkaline phosphatase (AP) is capable of hydrolysing any phosphate group(s) associated with the signal. Within the available data, it is unclear if this peak corresponds to phosphorylated Ras. Although it is a possibility since neither the ^{1}H NMR spectra nor SDS-PAGE showed sign of potential contaminants on the sample.

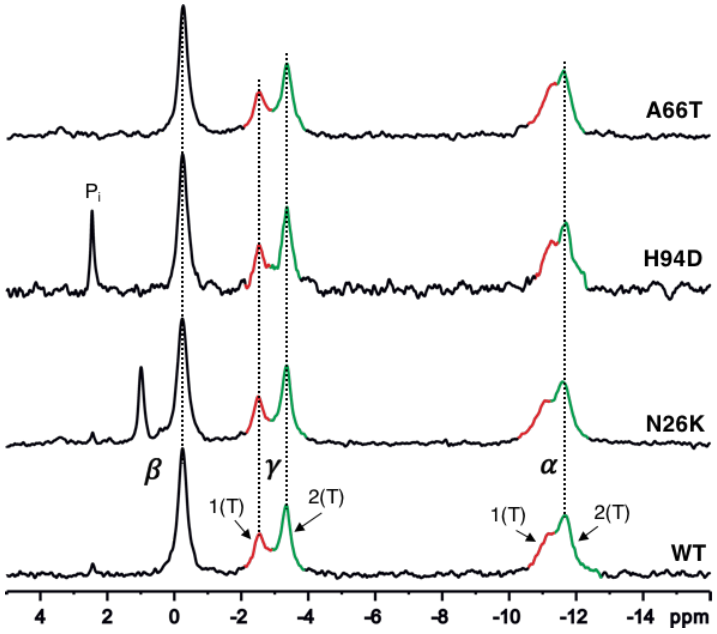

Figure 3.41. Conformational equilibria of the Ras•Mg^{2+}•GppNHp selected mutants detected by ^{31}P NMR. The mutants were created by SDM upon choosing specific residues associated with the 2(T)-to-1(T) conformational transition. All the measurements were done at 278 K in a 202.4 MHz magnetic field (500 MHz spectrometer). The proteins were dissolved in buffer F (40 mM Tris/HCl pH 7.5, 10 mM $MgCl_2$, 2 mM DTE) with additionally 0.2 mM DSS and 5% D_2O at concentrations of 1.5 mM (WT, 1700 scans), 1.60 mM (N26K, 3000 scans), 0.9 mM (H94D, 1000 scans) and 1.44 mM (A66T, 3000 scans). An EM filter with LB=15 Hz was used in all spectra.

From the obtained results, it can be generally concluded that the direct expectation of observing a conformational transition towards state 1(T) upon mutating the specific sensitive residues was not achieved.

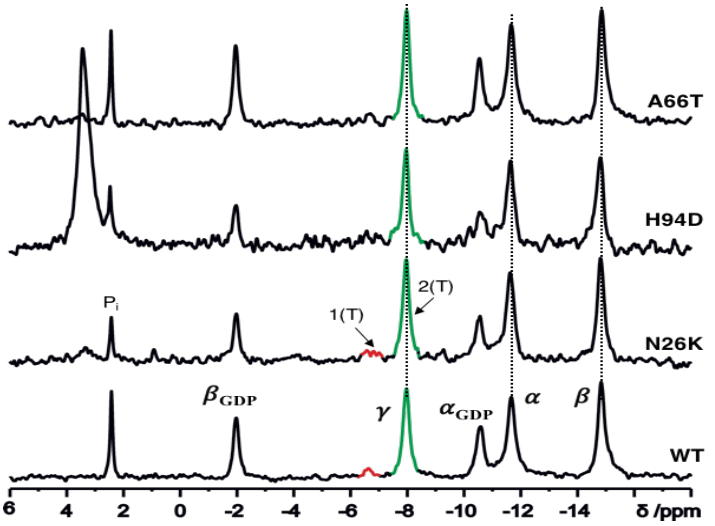

Figure 3.42. Conformational equilibria of the Ras•Mg^{2+}•GTP selected mutants detected by ^{31}P NMR at 278 K, 202.4 MHz and pH 7.5. The mutants were created by SDM upon choosing specific residues associated with the 2(T)-to-1(T) conformational transition. All proteins were dissolved in buffer F (see above) at a concentration of 1.7 mM (WT, 1200 scans), 0.95 mM (N26K, 2000 scans), 1.96 mM (H94 D, 700 scans) and 1.00 mM (A66T, 2000 scans). An EM filter with LB= 15Hz was used in all spectra.

However, the same ^{31}P chemical shifts and population distributions do not necessarily mean that the mutants have the same biochemical behaviour. In an attempt to elucidate if this is the case, the time-dependent intrinsic hydrolysis rate of each mutant was evaluated using HPLC. In parallel, their affinity towards Raf-RBD was also investigated by ITC. The results are shown in Figure 3.43 and

Table 3.13. ^{31}P NMR chemical shift values and linewidths obtained for the different mutants of HRas(1-166). The mutated residues are involved in the conformational transition 2(T)-to-1(T).

Protein complex	α-phosphate $\delta_{1(T)}$ [ppm]	α-phosphate $\delta_{2(T)}$ [ppm]	β-phosphate $\delta_{1(T),2(T)}$ [a] [ppm]	γ-phosphate $\delta_{1(T)}$ [ppm]	γ-phosphate $\delta_{2(T)}$ [ppm]	K_{12} [b]
			Mg^{2+}•GDP			
WT	-10.50		-1.97	--		--
N26K	-10.15		-1.99	--		--
H94D	-10.59		-1.99	--		--
A66T	-10.51		-2.00	--		--
			Mg^{2+}•GppNHp			
WT	-11.17	-11.68	-0.25	-2.57	-3.33	1.7
N26K	-11.07	-11.63	-0.25	-2.53	-3.35	1.5
H94D	-11.23	-11.68	-0.25	-2.55	-3.36	1.8
A66T	-11.14	-11.67	-0.28	-2.56	-3.37	1.8
			Mg^{2+}•GTP			
WT	-11.68		-14.87	-6.63	-7.98	11.3
N26K	-11.63		-14.83	-6.64	-7.97	10.4
H94D	-11.67		-14.83	--	-7.98	--
A66T	-11.65		-14.83	-6.65	-7.96	9.30
	α-phosphate $\Delta\nu_{1/2\ 1(T)}$ [Hz]	α-phosphate $\Delta\nu_{1/2\ 2(T)}$ [Hz]	β-phosphate $\Delta\nu_{1/2\ 1(T),2(T)}$ [a] [Hz]	γ-phosphate $\Delta\nu_{1/2\ 1(T)}$ [Hz]	γ-phosphate $\Delta\nu_{1/2\ 2(T)}$ [Hz]	--
			Mg^{2+}•GDP			
WT	46.89		30.02	--		
N26K	46.77		29.87	--		
H94D	48.71		30.15	--		
A66T	55.57		30.00	--		
			Mg^{2+}•GppNHp			
WT	105.39	75.15	45.84	74.47	55.07	
N26K	120.31	87.69	55.00	75.04	57.00	
H94D	121.21	58.26	46.23	59.05	57.04	
A66T	104.00	82.01	46.12	74.03	55.11	
			Mg^{2+}•GTP			
WT	54.74		45.66	20.33	35.44	
N26K	49.46		39.31	78.87		
H94D	43.66		36.54	--	29.74	
A66T	55.00		43.89	48.00	37.00	

All the values are fitted from the experimental spectra recorded at 278 K and pH 7.5. The maximum estimated errors are ± 0.07 ppm in chemical shift values and ± 0.4 Hz in linewidths for the γ-phosphate. An LB= 15 Hz was applied to the FID and subtracted afterwards from the fitted linewidths.
[a] States 1(T) and 2(T) of the β-phosphate in cannot be separated at the magnetic field used and were therefore fitted as a single Lorentzian line.
[b] The equilibrium constant, K_{12}, was calculated using the population distribution on the γ-phosphate. The associated error is ± 0.2.

Table 3.14. In principle, if a mutation promotes a shift towards state 1(T), even if this shift remains undetected by ^{31}P NMR, biochemical properties such as the GTPase activity should reflect the modification. In fact, it is known that state 2(T) (and probably also 3(T)) is associated with faster hydrolysis rates compared with for example, partial loss-of-function and oncogenic variants, that exist predominantly in state 1(T) such as Ras^{T35S} [67]. Figure

3.43A shows that under single turnover conditions all the three mutants have an identical hydrolysis rate, close to the one obtained for Ras^{WT} (k_{cat}= 0.026 min^{-1}) and similar half-life's (τ= 27-30 min., Table 3.14). Using the same experimental conditions, the GTPase activity was also tested for N26K, H94D and A66T in the presence of Raf-RBD. Since Ras^{WT}•Mg^{2+}•GTP already exists mainly in state 2(T), its intrinsic hydrolysis is not (or it is only very slightly) accelerated by addition of effector (k_{cat}= 0.029 min^{-1}), contrary for example to the state 1(T) Ras^{T35S} whose GTPase activity becomes accelerated more than 2.5-fold when Raf-RBD is added [67]. The situation of Ras^{A66T} and Ras^{N26K} is again similar to the one observed for *wild type*: addition of Raf-RBD does not change their hydrolysis rates and the calculated k_{cat} values are virtually identical in the presence and absence of the effector. In the case of Ras^{H94D}, however, addition of effector leads to a 1.7-fold increase in its GTPase activity, which is significant (k_{cat}= 0.035 min^{-1} and τ= 19.56 min., Figure 3.43B). Most likely, state 2(T) is further stabilised by Raf binding in H94D comparably to N26K or A66T, which accounts for the observed difference.

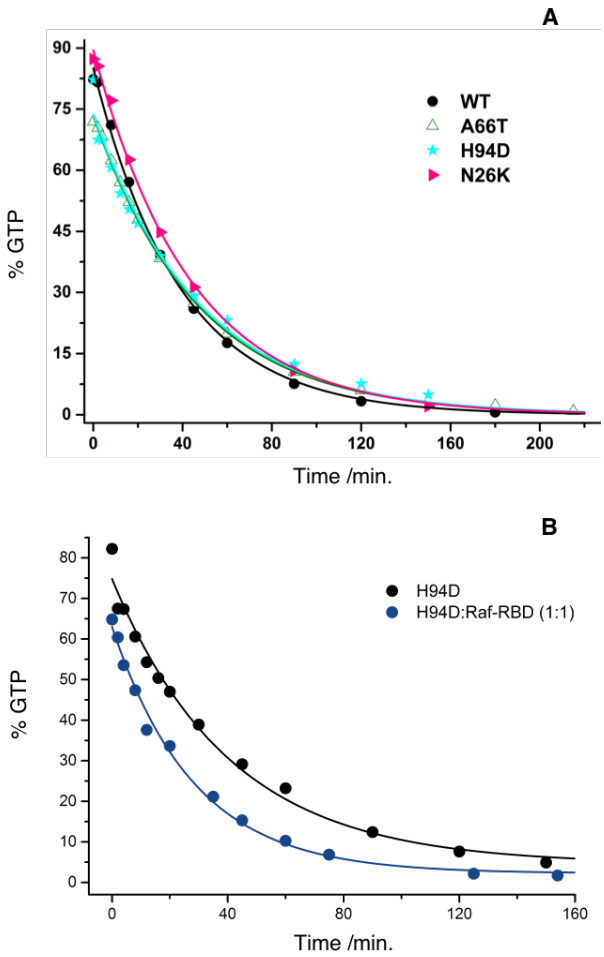

Figure 3.43. Determination of the intrinsic GTPase activity of HRas(1-166)•Mg^{2+}•GTP by HPLC at 310 K. Typically 100 μM of protein were dissolved in buffer F. At specific time intervals, 50 μl were snap-frozen in liquid N_2 to prevent a continuous hydrolysis reaction. The nucleotide concentration equals the protein concentration in absence of free nucleotide because Ras binds nucleotides in a ratio of 1:1. The HPLC system contains a pre-column, a C18 reversed phase column and a UV-detector measuring the nucleotide absorbance at λ= 254 nm. The protein precipitates in the mobile phase and is retained by the pre-column. At the same time the nucleotide is released and separated through the C18 column. Upon integration of the fluorescence signal from GTP, the percentage of Ras-GTP was plotted against time and the data fitted with a first order exponential decaying function. **A.** The measurements were conducted for the three mutants under study, N26K, H94D and A66T. **B.** The GTPase activity was also measured in the presence of Raf-RBD. From the three mutants, only H94D shows significant differences upon addition of two-fold excess of effector (k_{cat}=0.035 min^{-1}, τ= 19.56 min.).

The obtained affinities of binding between *wild type,* N26K, H94D, A66T and Raf-RBD are all very similar. They proceed with the same averaged ΔG of -36.5 kJ mol^{-1} and with similar enthalpic and entropic contributions. The formation of the complex between Ras^{WT} and Raf

is only ever so slightly enthropically favourable ($-T\Delta S$= -28.3 kJ mol^{-1}) than the one observed for the three mutants. The corresponding dissociation constant, K_D, in the case of *wild* type is 0.424 ± 0.12 μM. A similar value was obtained for Ras^{H94D}-Raf complex (K_D= 0.436 ± 0.07 kJ mol^{-1}) but a 1.75-fold lower value was obtained in the case of Ras^{N26K} and Ras^{A66T}, which is *per se* indicative of their slightly higher affinity towards Raf (their K_D is numerically more similar to the one obtained for the full length Ras^{WT}-Raf complex than the one obtained in the corresponding truncated Ras variant, Figure 3.2).

Table 3.14. Thermodynamics of interaction between HRas•Mg^{2+}•GppNHp and Raf-RBD measured by ITC and intrinsic GTPase activities measured by HPLC on the HRas•Mg^{2+}•GTP protein.

Protein	T K	[Ras] μM	[Raf] μM	ΔG kJ mol^{-1}	ΔH kJ mol^{-1}	$-T\Delta S$ kJ mol^{-1}	K_D μM	T K	k_{cat} min^{-1}	τ min.
HRas^{WT}	298	60	778	-36.4	-8.10 ± 0.23	-28.3	0.424 ± 0.12	310	0.026	26.85
HRas^{N26K}	298	40	454	-37.7	-16.10 ± 0.17	-21.7	0.248 ± 0.03	310	0.023	30.27
HRas^{H94D}	298	45	627	-36.3	-11.8 ± 0.19	-24.5	0.436 ± 0.07	310	0.021	32.92
HRas^{A66T}	298	52	546	-37.8	-14.0 ± 0.29	-23.9	0.239 ± 0.05	310	0.021	32.33

k_{cat} represents the hydrolysis rate constant and is calculated as 1/t. τ represents the half-life for the GTP hydrolysis (τ=t*ln2). ITC experiments were done according to the experimental section 2.2.4. The experimentally obtained thermograms and signature plots are shown in Figure F of the appendix section. The *N* parameter (binding sites) was allowed to vary during the fitting procedure. The greatest deviation from a 1:1 ratio was obtained for Ras^{H94D} with *N*= 1.0 ± 0.22. The error on all the other measurements was always smaller than ± 0.2.

3.4.2.2 2(T)-to-1(0) Transition: S39L and E3V

Ser39 and Glu3 are associated with the 2(T)-to-1(0) transition and show relatively high pressure coefficients, with $B_{1,2} \geq \sigma_0$ (σ_0 being the standard deviation) [171]. They are not involved with any known rasopathy but both constitute the binding site of the small compound Zn^{2+}-BPA, as determined previously by paramagnetic relaxation enhancements in ^{31}P NMR and [^{1}H-^{15}N]-HSQC experiments [158]. Their location on the surface of $HRas^{WT}$ is shown in Figure 3.44. Ser39 lies at the end of the switch 1 in the strand β_2 and is involved in the interaction with GAP-334 (H-bond to Glu950 [83]), Raf-RBD (H-bond to Arg67 and Arg89, [64]) and RalGDS (H-bond to Met30 and Tyr31, [253]). Exchange towards the non-polar amino acid leucine directly hinders some of these polar contacts due to the absence of the side chain hydroxyl group on the mutant. Glu3 is located in the β_1 strand and is not involved in any interaction with GAP's, GEF's or effectors. In the protein, Glu3 establishes solvent-mediated polar contacts with Glu76 from helix α_2 (Figure 3.44B). Mutation towards the non-polar valine very likely interrupts this interaction. Contrary to the other mutants investigated so far, E3V is located far away from the catalytic centre. Any shift of the equilibrium at the nucleotide-bound level would preclude an interesting result.

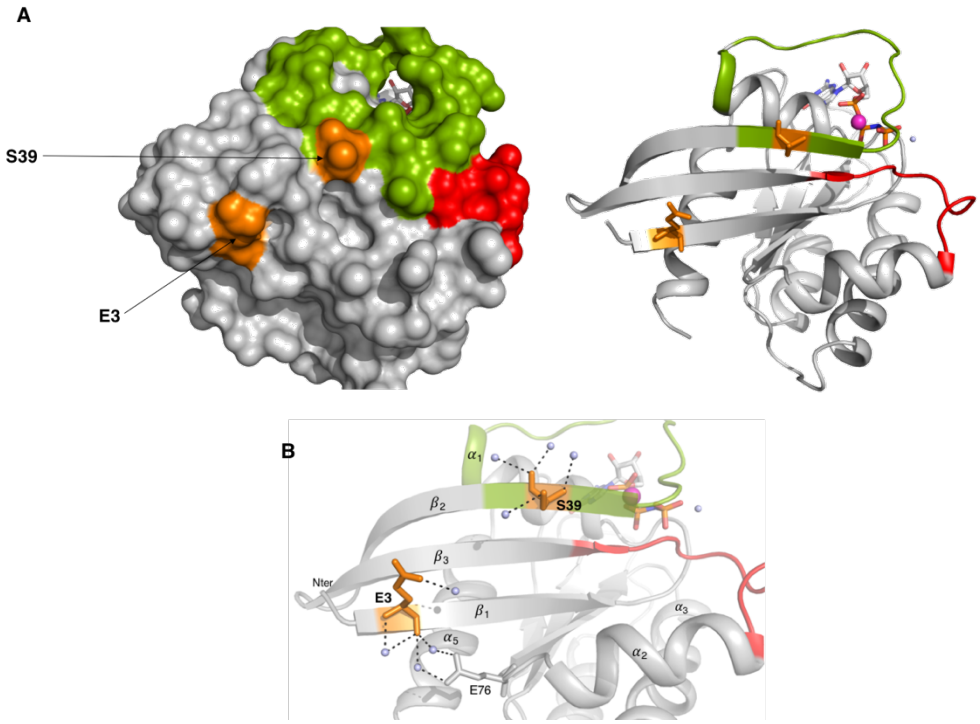

Figure 3.44. Localization on the $HRas^{WT}$•Mg^{2+}•GppNHp surface the amino acid residues Ser39 and Glu3 that were subjected to SDM. They are sensitive to the 2(T)-to-1(0) transition upon pressure perturbation and were mutated with the prospect of shifting the equilibrium in the same direction. **A.** The localization of both residues is shown in orange. Switch 1 is coloured in green, switch 2 is coloured in red and the Mg^{2+} ion is coloured in magenta. **B.** Key features near each residue, including polar contacts, are highlighted. pdb: 5p21.

3.4.2.2.1 ^{31}P NMR GppNHp and GTP Spectra. Raf Interaction and GTPase Activity

Both mutants show notable differences when compared with Ras^{WT} in terms of their equilibrium between states 1(T) and 2(T). This is directly observed from the GppNHp-bound ^{31}P NMR spectra shown in Figure 3.45A. The equilibrium constants calculated at the γ-phosphate are 1.5 and 2.0 for Ras^{S39L} and Ras^{E3V}, respectively. Compared to Ras^{WT} (K_{12}= 1.7), the first mutant is slightly shifted towards state 1(T) and the second one is significantly shifted towards state 2(T).

The increased state 1(T) on Ras^{S39L} can be observed not only for the γ- but also for the α-phosphate and the averaged peak linewidths are smaller than the corresponding ones in Ras^{WT} (Table 3.15). There are no changes in the positions of state 2(T), however when compared with Ras^{WT}, state 1(T) is downfield shifted by a Δδ of 0.1 and 0.07 ppm at the α- and γ-phosphates, respectively. A strong upfield shift of ca. -0.1 ppm of the α-phosphate is also observed in the ^{31}P NMR spectra of the GDP-bound complex (Figure B, appendix). The ^{31}P NMR spectra of Ras^{S39L} bound to GTP is identical to the *wild type* one (Figure 3.45B) in terms of chemical shifts, linewidths and equilibrium constants (K_{12}= 11.8 and 11.3, respectively).

Pronounced effects are observed in the case of Ras^{E3V} if one has in consideration the

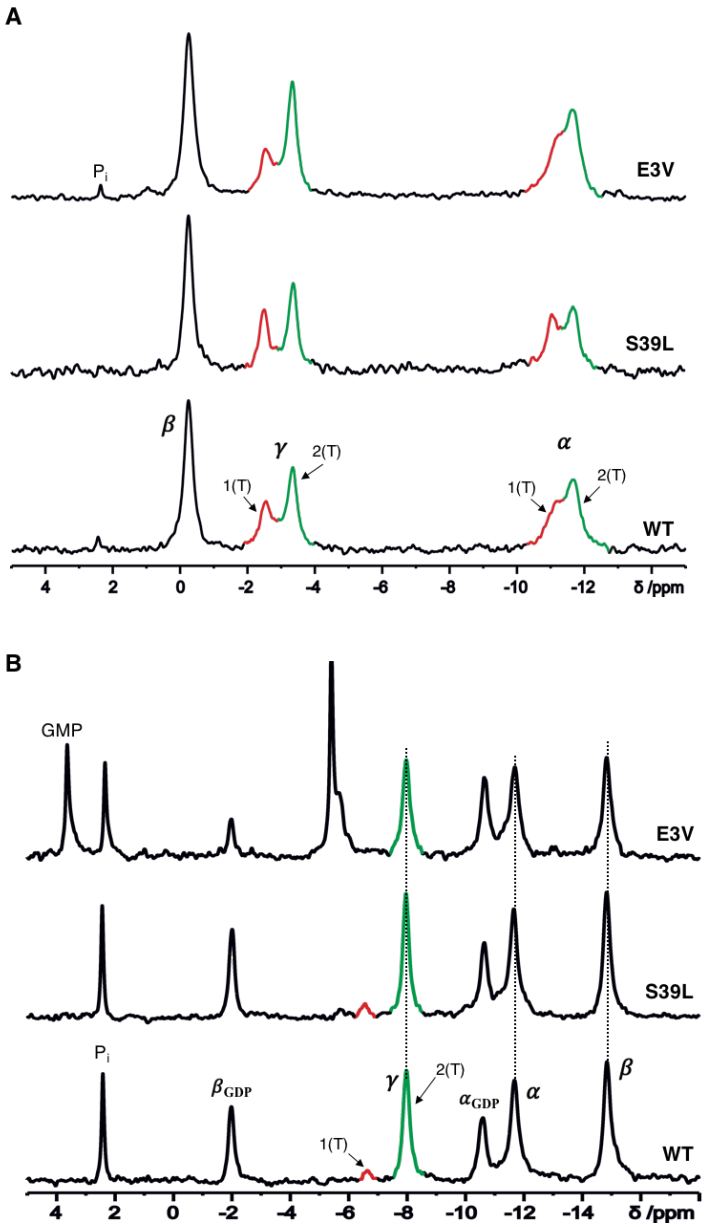

Figure 3.45. Effect of the mutated residues sensing the conformational transition 2(T)-to-1(0) in the equilibrium dynamics of the bound nucleotide **A.** Ras•Mg^{2+}•GppNHp (S39L 1.0 mM, 3000 scans; E3V 1.8 mM, 3000 scans) and **B.** Ras•Mg^{2+}•GTP (S39L 1.0 mM, 3000 scans; E3V 1.5 mM, 2000 scans).
All the measurements were done at 278 K in a 202.4 MHz magnetic field (500MHz spectrometer). The proteins were dissolved in buffer F (40 mM Tris/HCl pH 7.5, 10 mM $MgCl_2$, 2 mM DTE) with additionally 0.2 mM DSS and 5% D_2O. A Lorentzian line broadening of 15 Hz was applied to the FID. The calculated shift values, linewidths and equilibrium constants are given in Table 3.15.

distant localization of this residue with respect to the nucleotide. The mutation leads to a 18% increase in the population of state 2(T) of γ-phosphate but has no effect on the α-phosphate (Figure 3.45A). These effects are observed only in the GppNHp spectrum, with the GTP-bound nucleotide being again virtually identical to the one of Ras^{WT}. The only additional feature is an intense peak located at δ= -5.5 ppm that can be ascribed most likely to the presence of impurities during sample preparation (Figure 3.45B). Within the limits of error the obtained chemical shifts and linewidths remain unperturbed by the mutation in both cases.

Table 3.15. ^{31}P NMR chemical shift values and linewidths obtained for the different mutants of HRas(1-166). The mutated residues were selectively chosen according to their involvement in the pressure modulated 2(T)-to-1(0) conformational transition.

Protein complex	α-phosphate $\delta_{1(T)}$ [ppm]	α-phosphate $\delta_{2(T)}$ [ppm]	β-phosphate $\delta_{1(T),2(T)}$ [a] [ppm]	γ-phosphate $\delta_{1(T)}$ [ppm]	γ-phosphate $\delta_{2(T)}$ [ppm]	K_{12} [b]
			Mg^{2+}•GDP			
WT	-10.50		-1.97	--		--
S39L	-10.60		-2.03	--		--
E3V	-10.47		-1.99	--		--
			Mg^{2+}•GppNHp			
WT	-11.17	-11.68	-0.25	-2.57	-3.33	1.7
S39L	-11.08	-11.67	-0.25	-2.50	-3.35	1.5
E3V	-11.23	-11.68	-0.27	-2.59	-3.33	2.0
			Mg^{2+}•GTP			
WT	-11.68		-14.87	-6.63	-7.98	11.3
S39L	-11.65		-14.84	-6.54	-7.97	11.8
E3V	-11.68		-14.85	--	-7.98	--
	α-phosphate $\Delta\nu_{1/2\ 1(T)}$ [Hz]	**α-phosphate** $\Delta\nu_{1/2\ 2(T)}$ [Hz]	**β-phosphate** $\Delta\nu_{1/2\ 1(T),2(T)}$ [a] [Hz]	**γ-phosphate** $\Delta\nu_{1/2\ 1(T)}$ [Hz]	**γ-phosphate** $\Delta\nu_{1/2\ 2(T)}$ [Hz]	**--**
			Mg^{2+}•GDP			
WT	46.89		30.02	--		
S39L	51.39		35.00	--		
E3V	29.54		33.00	--		
			Mg^{2+}•GppNHp			
WT	105.39	75.15	45.84	74.47	55.07	
S39L	98.05	62.88	42.55	48.95	50.82	
E3V	122.22	67.33	54.39	78.74	53.00	
			Mg^{2+}•GTP			
WT	54.74		45.66	20.33	35.44	
S39L	53.36		37.95	41.55	32.43	
E3V	61.71		47.12	--	43.18	

All the values are fitted from the experimental spectra recorded at 278 K and pH 7.5. The maximum estimated errors are ± 0.07 ppm in chemical shift values and ± 0.4 Hz in linewidths for the γ-phosphate. An LB=15 Hz was applied to the FID and subtracted afterwards from the final fitted linewidths.
[a] States 1(T) and 2(T) of the β-phosphate in cannot be separated at the magnetic field used and were therefore fitted as a single Lorentzian line.
[b] The equilibrium constant, K_{12}, was calculated using the population distribution on the γ-phosphate. The associated error is ± 0.2.

The calculated k_{cat} values (Table 3.16), as well as the associated half-lifes are virtually identical. ITC measurements showed that Ras^{S39L} binds Raf-RBD with a 5.7-fold higher affinity than Ras^{WT} (K_D= 0.074 vs 0.424 μM). The interaction proceeds with a great enthalpic contribution in the case of the mutant (ΔH= -24.0 vs -8.10 kJ mol^{-1}). Regarding Ras^{E3V}, the affinity towards Raf is identical to the one measured for *wild type.*

In the light of the present results, Ras^{S39L} and Ras^{E3V} have different and somewhat opposite population distributions, despite the mutated residues being involved in the same conformational transition (the former stabilises state 1(T) but shows an enhanced binding affinity to Raf, the later stabilises state 2(T) and shows an unperturbed affinity to Raf).

A last set of experiments was conducted using the GppNHp-bound nucleotide Ras^{S39L} and Ras^{E3V} with the aim of further characterise state 1(T). It was hypothesised that both could have a hidden contribution from state 1(0), obscured by the overall similarity (same chemical shifts, same linewidths) between the ^{31}P NMR spectra of the mutants and the *wild type* protein. To test if this was the case, they were titrated with the small compound Cu^{2+}-cyclen that binds near the γ-phosphate only when Ras exists in state 1(T) and acts as a selective sensor for its identification [254]. The results are shown graphically and numerically in Figure C and Table I of the appendix section. The effect of Cu^{2+}-cyclen in the spectra Ras^{S39L} and Ras^{E3V} was the same: with increasing amounts of the drug the line broadening of state 1(T) increases dramatically up to a point where it disappears beyond detection. The effect is due to the paramagnetic influence of the Cu^{2+} ion that selectively collapses the line of state 1(T). Since paramagnetic relaxation is a localized effect, the other peaks of the spectra remain unperturbed. If the equilibrium was shifted in the 2(T)-to-1(0) direction by the mutations, a close-by, small resonance line corresponding to state 1(0) should be visible in the spectrum after collapsing state 1(T). However, the titration with Cu^{2+}-cyclen reveals no further spectral features.

Figure 3.16. Thermodynamics of interaction between HRas•Mg^{2+}•GppNHp and Raf-RBD measured by ITC and intrinsic GTPase activities measured by HPLC in the HRas•Mg^{2+}•GTP complex.

Protein	T K	[Ras] μM	[Raf] μM	ΔG kJ mol^{-1}	ΔH kJ mol^{-1}	$-T\Delta S$ kJ mol^{-1}	K_D μM	T K	k_{cat} min^{-1}	T min.
$HRas^{WT}$	298	60	778	-36.4	-8.10 ± 0.23	-28.3	0.424 ± 0.12	310	0.026	26.85
$HRas^{S39L}$	298	30	258	-40.8	-24.0 ± 0.33	-16.8	0.074 ± 0.01	310	0.029	24.04
$HRas^{E3V}$	298	28	486	-35.6	-19.4 ± 0.43	-16.2	0.603 ± 0.01	310	0.027	27.12

k_{cat} represents the hydrolysis rate constant and is calculated as 1/t. τ represents the half-life for the GTP hydrolysis (τ=t*ln2). ITC experiments were done according to the experimental section 2.2.4. The experimentally obtained thermograms and signature plots are shown in Figure F of the appendix section. The *N* parameter (binding sites) was allowed to vary during the fitting procedure. The greatest deviation from a 1:1 ratio was obtained for Ras^{E3V} with *N*= 1.0 ± 0.22. The error on all the other measurements was always smaller than ± 0.2.

The greatest deviation from a 1:1 ratio was obtained for Ras^{S39L} with *N*= 0.89 ± 0.12. The error on all the other measurements was always smaller.

3.4.2.3 2(T)-to-3(T) Transition: H27E and D33K

Stabilising state 3(T) is a very attractive idea from a pharmaceutical point of view, especially in the case of oncogenic Ras because promoting the transition would have two immediate and assisted effects: the change in conformation would drive away the protein from the permanently active state 2(T) and at the same time the high intrinsic GTPase activity of state 3(T) would account for an unprecedented re-cycling of Ras towards the guanine diphosphate state (from "(T)" to "(D)"). Contrary to the mutants studied above, the two residues are located in the switch 1 region and account for the stabilisation of the H_2O bonding network around the active site. Their localisation on the surface of the protein is shown in Figure 3.46, together with the structural details in their vicinity.

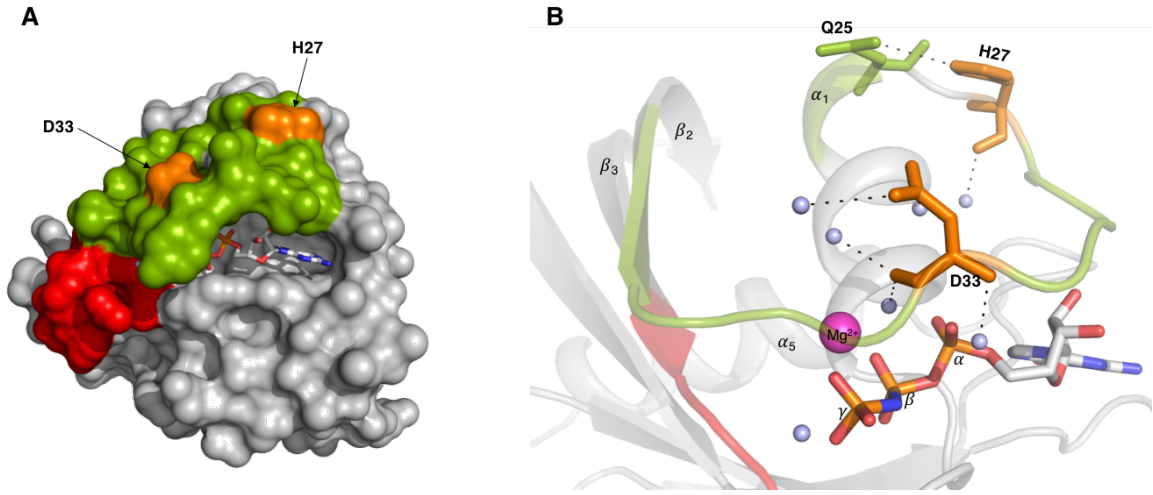

Figure 3.46. Localization on the $HRas^{WT}$•Mg^{2+}•GppNHp surface the amino acid residues His27 and Asp33 that were subjected to SDM. They are sensitive to the 2(T)-to-3(T) transition upon pressure perturbation and were mutated with the prospect of shifting the equilibrium in the same direction. **A.** The localization of both residues is shown in orange. switch 1 is coloured in green, switch 2 is coloured in red and the Mg^{2+} ion is coloured in magenta. **B.** Key features such as polar contacts are highlighted near each residue. pdb: 5p21.

3.4.2.3.1 ^{31}P NMR GppNHp and GTP Spectra. Raf Interaction and GTPase Activity

The GppNHp spectrum of the mutant Ras^{H27E} has a significantly lower equilibrium constant (K_{12}=1.0) than the *wild type* counterpart (K_{12}=1.7, Figure 3.47A and Table 3.17). The mutation promotes a clear effect by increasing the population of state 1(T), which becomes downfield shifted by δ= 0.07 and δ=0.34 ppm at the γ- and α-phosphates, respectively, when compared to Ras^{WT} A similar downfield shift of δ= 0.06 ppm is also observed for the β-phosphate alongside with a 55% broadening of its resonance line. The corresponding Ras^{H27E}•GTP spectrum on the other hand, shows no significant differences from Ras^{WT} (Figure 3.47B), albeit the K_{12} values are slightly different (10.0 vs 11.3). The GDP spectrum

of Ras^{H27E} (Figure B, appendix) shows a large downfield shift of the α-phosphate, with a Δδ= 0.36 ppm (δ= -10.50 ppm in Ras^{WT} and δ= -10.14 ppm in Ras^{H27E}, Table 3.17).

The differences observed between Ras^{D33K} and Ras^{WT} regarding the GppNHp-bound nucleotide are remarkable: the population distribution at the γ- and α-phosphates is collapsed and almost completely shifted towards state 2(T). State 1(T) exists as a residual line located within the noise level. The equilibrium constant is 11.3 and closely resembles the one of Ras^{WT}•Mg^{2+}•GTP (Table 3.17). At the α-phosphate, state 1(T), if present, is not clearly separated from the main resonance line. Additional differences between D33K and *wild* type are observed in terms of chemical shifts: the calculated values for the $\gamma_{1(T)}$- and $\gamma_{2(T)}$-phosphates in the former are δ= -2.47 and δ= -3.40 ppm, respectively and the corresponding ones in the latter are δ= -2.57 and δ= -3.33 ppm, respectively. The difference accounts for a Δδ of 0.1 ppm for state 1(T) and 0.07 ppm for state 2(T). The single resonance line of the α-phosphate lies at δ= -11.46 ppm, exactly in between the two states observed in Ras^{WT}. Contrary to the downfield shift of the α- and γ-lines, the β-phosphate is shifted upfield by a Δδ of -0.06 ppm. The spectra of the state 1(T) mutant Ras^{T35S}•Mg^{2+}•GppNHp is also shown in Figure 3.47A for comparison of the relative

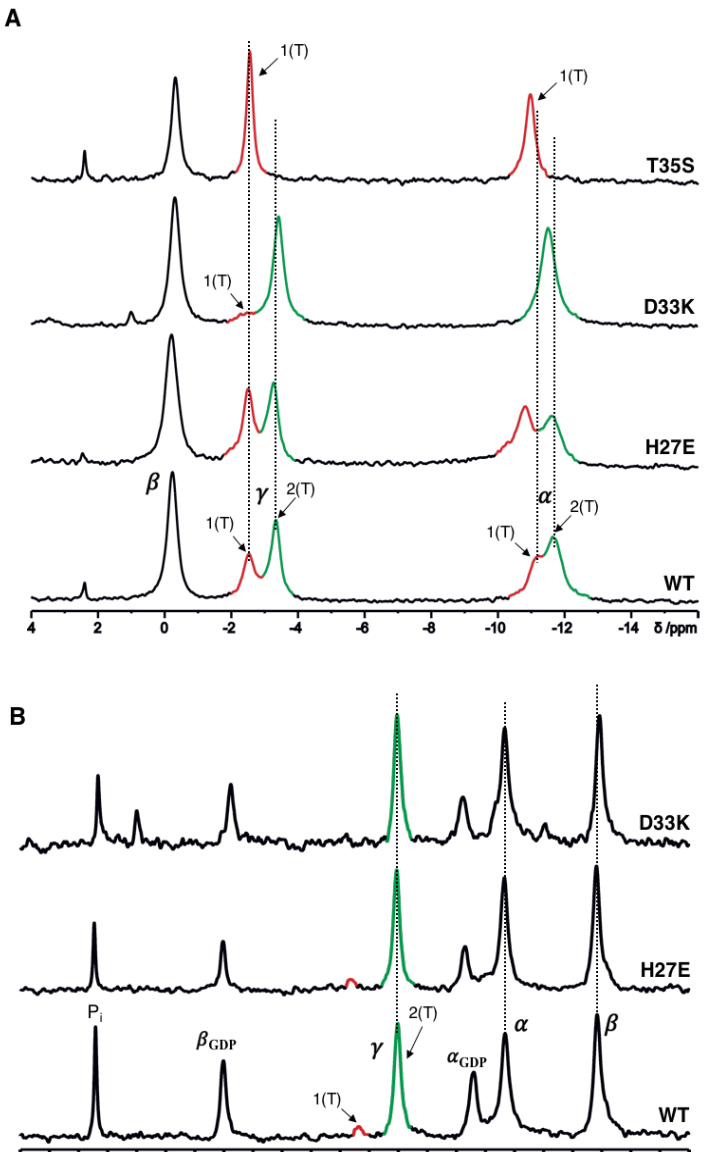

Figure 3.47. Effect of the mutated residues sensing the conformational transition 2(T)-to-3(T) in the equilibrium dynamics of the bound nucleotide **A.** Ras•Mg^{2+}•GppNHp (H27E 1.57 mM, 2600 scans; D33K 3.0 mM, 800 scans, T35S 0.75 mM 2000 scans) and **B.** Ras•Mg^{2+}•GTP (H27E 0.8 mM, 3000 scans; D33K 2.94 mM, 3000 scans).
All the measurements were done at 278 K in a 202.456 MHz magnetic field (500 MHz spectrometer). The proteins were dissolved in buffer F (40 mM Tris/HCl pH 7.5, 10 mM $MgCl_2$, 2 mM DTE) with additionally 0.2 mM DSS and 5% D_2O. A Lorentzian line broadening of 15 Hz was applied to the FID. The calculated shift values, linewidths and equilibrium constants are given in Table 3.17.

positions of the signals. No significant differences are observed between the GTP-bound mutants and Ras^{WT}. Based on the GppNHp-bound spectra, Ras^{D33K} seems to be shifted towards state 2(T). However, a significant contribution from state 3(T), which is coupled and indistinguishable from state 2(T) by ^{31}P NMR, can also be assumed at this point.

Table 3.17. ^{31}P NMR chemical shift values and linewidths obtained for the different mutants of HRas(1-166). The mutated residues were selectively chosen according to their involvement in the pressure modulated 2(T)-to-3(T) conformational transition.

Protein	α-phosphate $\delta_{1(T)}$ [ppm]	α-phosphate $\delta_{2(T)}$ [ppm]	β-phosphate $\delta_{1(T),2(T)}$ [a] [ppm]	γ-phosphate $\delta_{1(T)}$ [ppm]	γ-phosphate $\delta_{2(T)}$ [ppm]	K_{12} [b]
			Mg^{2+}•GDP			
WT	-10.50		-1.97	--		--
H27E	-10.14		-1.91	--		--
D33K	-10.22		-2.20	--		--
			Mg^{2+}•GppNHp			
WT	-11.17	-11.68	-0.25	-2.57	-3.33	1.7
H27E	-10.83	-11.67	-0.19	-2.50	-3.25	1.0
D33K	-11.46 [c]		-0.31	-2.47	-3.40	11.3
			Mg^{2+}•GTP			
WT	-11.68		-14.87	-6.63	-7.98	11.3
H27E	-11.65		-14.83	-6.35	-7.94	10.0
D33K	-11.66		-14.92	--	-7.97	--
	α-phosphate $\Delta\nu_{1/2\ 1(T)}$ [Hz]	**α-phosphate** $\Delta\nu_{1/2\ 2(T)}$ [Hz]	**β-phosphate** $\Delta\nu_{1/2\ 1(T),2(T)}$ [a] [Hz]	**γ-phosphate** $\Delta\nu_{1/2\ 1(T)}$ [Hz]	**γ-phosphate** $\Delta\nu_{1/2\ 2(T)}$ [Hz]	--
			Mg^{2+}•GDP			
WT	46.89		30.02	--		
H27E	50.32		32.00	--		
D33K	65.55		31.03	--		
			Mg^{2+}•GppNHp			
WT	105.39	75.15	45.84	74.47	55.07	
H27E	91.12	120.31	70.00	61.82	56.72	
D33K	77.31 [c]		41.92	73.40	55.07	
			Mg^{2+}•GTP			
WT	54.74		45.66	20.33	35.44	
H27E	49.73		42.91	45.12	36.57	
D33K	78.05		55.51	--	49.79	

All the values are fitted from the experimental spectra recorded at 278 K and pH 7.5. The maximum estimated errors are ± 0.07 ppm in chemical shift values and ± 0.4 Hz in linewidths for the γ-phosphate. An EM function with LB=15 Hz was used for processing the FID and subtracted afterwards.

[a] States 1(T) and 2(T) of the β-phosphate in cannot be separated at the magnetic field used and were therefore fitted as a single Lorentzian line.

[b] The equilibrium constant, K_{12}, was calculated using the population distribution on the γ-phosphate. The associated error is ± 0.2.

[c] α-phosphate on Ras^{D33K} was fitted with a single Lorentzian line.

The measurement of the intrinsic GTPase activity shows that Ras^{H27E} hydrolyses GTP at the same rate as Ras^{WT} (k_{cat}= 0.025 min^{-1}, τ= 28.20 min., Figure 3.48, Table 3.18), despite being considerably shifted towards state 1(T). Ras^{D33K} is surprisingly 1.5 times slower than Ras^{WT} (k_{cat}= 0.017 vs 0.026 min^{-1}, Table 3.18) yet the conformational equilibria of this mutant is almost completely shifted towards a state closely resembling 2(T) in Ras^{WT}, which is normally associated with a faster GTP hydrolysis. Addition of Raf-RBD has no influence in the catalytic activity of Ras^{H27E} (k_{cat}= 0.025 min^{-1}, τ= 27.39 min.), but induces a slightly faster hydrolysis in the case of Ras^{D33K} (k_{cat}= 0.019 min^{-1}, τ=36.37 min.), which is yet considerably slower than the typical rate of conversion for Ras^{WT} alone.

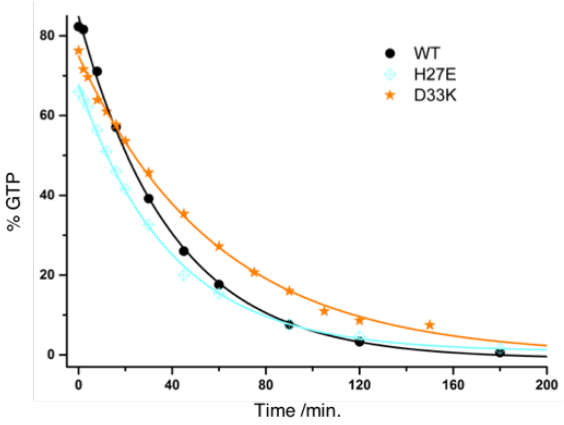

Figure 3.48. Determination of the intrinsic GTPase activity of the GTP-bound mutants Ras^{H27E} and Ras^{D33K} by HPLC at 310K. Upon integration of the fluorescence signal, the percentage of Ras-GTP was plotted against time and the data fitted with a first order exponential decaying function (see Figure 3.43 for details on the description of the method). The obtained rate constants are 0.026, 0.025 and 0.016 min^{-1} for WT, H27E and D33K, respectively (see also Table 3.18).

Ras^{H27E} has a slightly higher affinity to the effector (K_D= 0.225 ± 0.05 μM) than Ras^{WT} (K_D= 0.424 ± 0.12 μM), although the difference is attenuated by the experimental errors of each measurement. The associated enthalpy of binding is twice of the recorded for *wild type* (ΔH= -16.9 ± 0.18 vs -8.10 ± 0.23 kJ mol^{-1}), but both proceed with a similar Gibbs energy. The strength of the interaction between Ras^{D33K} and Raf is remarkably 26–fold lower than Ras^{WT} (K_D= 10.4 μM). The binding proceeds still with positive enthalpic and entropic contributions but the enthalpy variation is much lower than the one of Ras^{WT} (ΔH= -4.24 ± 0.25 kJ mol^{-1}).

Table 3.18. Thermodynamics of interaction between HRas•Mg^{2+}•GppNHp and Raf-RBD measured by ITC and intrinsic GTPase activities measured by HPLC in the HRas•Mg^{2+}•GTP complex.

Protein	T K	[Ras] mM	[Raf] mM	ΔG kJ mol^{-1}	ΔH kJ mol^{-1}	$-T\Delta S$ kJ mol^{-1}	K_D μM	T K	k_{cat} min^{-1}	τ min.
$HRas^{WT}$	298	60	778	-36.4	-8.10 ± 0.23	-28.3	0.424 ± 0.12	310	0.026	26.85
$HRas^{H27E}$	298	39.8	637	-38.0	-16.9 ± 0.18	-21.1	0.225 ± 0.05	310	0.025	28.20
$HRas^{D33K}$	298	145	1680	-28.5	-4.24 ± 0.25	-24.2	10.4 ± 1.93	310	0.016	41.46

k_{cat} represents the hydrolysis rate constant and is calculated as 1/t. τ represents the half-life for the GTP hydrolysis (τ=t*ln2). ITC experiments were done according to the experimental section 2.2.4. The experimentally obtained thermograms and signature plots are shown in Figure F of the appendix section. The *N* parameter (binding sites) was allowed to vary during the fitting procedure. The greatest deviation from a 1:1 ratio was obtained for Ras^{H27E} with *N*= 1.0 ± 0.18.

3.4.3 Interaction Between HRas^{H27E}•Mg^{2+}•GppNHp and Raf-RBD

A 1.5 mM solution of Ras^{H27E} was titrated with increasing amounts of Raf as shown in Figure 3.49. The experiment shows that for an equimolar concentration of the two proteins, the conformational equilibrium is completely shifted towards state 2*(T), characteristic of this particular interaction and closely related with state 2(T) (see sections 3.1.1-3 for additional details regarding the dynamics of state 2*(T)). This modification is also accompanied by the typical upfield shift of the corresponding line by a $\Delta\delta$= -0.27 ppm and with state 2*(T) located at δ= -3.54 ppm. Similar shifts were found upon titration of *wild type* HRas and KRas ($\delta_{2^*(T)}$= -3.6 and -3.51 ppm, respectively; Table 3.1 and [117]). The resonances of α- and β-phosphates remain virtually unperturbed during the titration (Table 3.19). The molecular mass of the Ras-Raf complex is 1.5-fold higher than Ras alone. This increase of size is directly related with the increase of the spectral linewidths as it can be seen from the β-phosphate, from $\Delta\nu_{1/2}$= 67.5 Hz in Ras alone to $\Delta\nu_{1/2}$ =102 Hz (1.5-fold) at a 1:1 ratio. This direct relationship is however not valid in the case of the α- and the γ-phosphates because they are exchange broadened by the presence of the distinct conformational states 1(T) and 2(T). The apparent dissociation constant can also be estimated from the ^{31}P NMR spectra given the existence of the two distinct resonance lines in a slow exchange regime located at the β-phosphate (blue coloured line in Figure 3.49). Their integrals were considered to be proportional to the concentration of free Ras ([Ras]$_{free}$) and to the concentration of the Ras-Ras complex ([RR]) for a given molar ratio. The value of [RR] is given by the ratio of the areas multiplied by [Ras]$_{free}$. From this assessment, an apparent K_D of

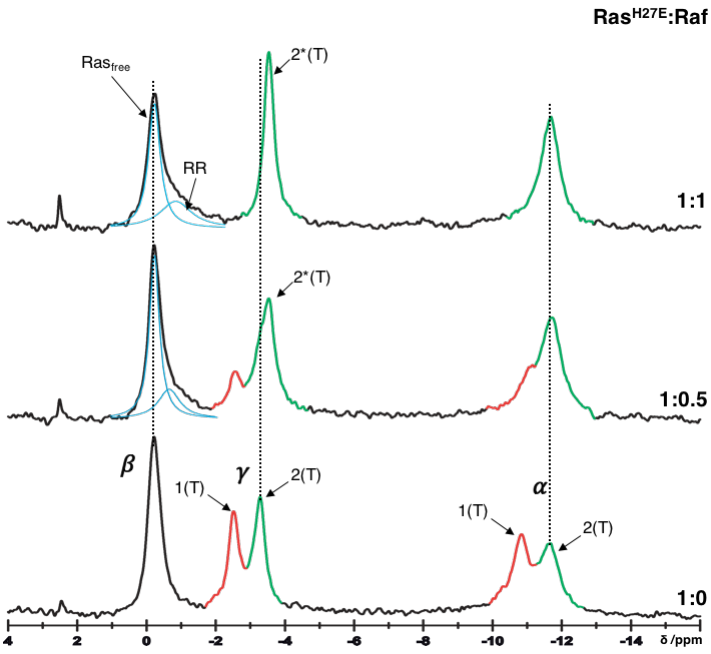

Figure 3.49. ^{31}P NMR spectroscopy on the titration of HRas^{H27E}•Mg^{2+}•GppNHp with the effector Raf-RBD measured at 278 K and pH 7.5. To an initial 1.5 mM solution of Ras^{H27E} dissolved in buffer F (40 mM Tris/HCl pH 7.5, 10 mM $MgCl_2$, 2 mM DTE) with additionally 0.2 mM DSS, 150 mM NaCl and 5% D_2O, increasing amounts of Raf-RBD from a highly concentrated 6.5 mM stock solution were added, up to a final ratio of 1:1. The evolution of state 2(T) into 2*(T) upon Raf binding is indicated. The integrated areas of the fitted Lorentzian lines at the β-phosphate, coloured in blue, are assumed to be directly proportional to the concentration of free Ras (Ras$_{free}$) and Ras-Raf (RR) complex and were used to calculate the apparent K_D of the interaction. An EM function with LB= 15Hz was applied to the FID during the processing of the data. The chemical shifts and linewidths are shown in Table 3.19.

ca. 100 μM was obtained which does not agree with the ITC measurements. It should be mentioned that this method is intrinsically inaccurate because relies on concentrations in the order of the mM range required in ^{31}P NMR but typically considered too high for a realistic determination of μM or sub-μM binding affinities.

$$K_D = \frac{[Ras]_{free}.[Raf]_{free}}{[RR]} \qquad [Ras]_{total} = [Ras]_{free} + [RR]$$

Table 3.19. ^{31}P NMR chemical shift values and linewidths for the protein-protein complex HRas^{H27E}(1-166)•Mg^{2+}•GppNHp•Raf-RBD.

Protein complex	Ras: Raf	α-phosphate $\delta_{1(T)}$ [ppm]	α-phosphate $\delta_{2(T)}$ [ppm]	β-phosphate $\delta_{1(T),2(T)}$[a] [ppm]	γ-phosphate $\delta_{1(T)}$ [ppm]	γ-phosphate $\delta_{2(T)}$ [ppm]
Ras^{H27E}	--	-10.83	-11.67	-0.22	-2.52	-3.27
+ Raf-RBD	1:0.6	-11.09	-11.72	-0.25	-2.55	-3.47
	1:1	--	-11.65	-0.26	--	-3.54
		α-phosphate $\Delta\nu_{1/2\ 1(T)}$ [Hz]	α-phosphate $\Delta\nu_{1/2\ 2(T)}$ [Hz]	β-phosphate $\Delta\nu_{1/2\ 1(T),2(T)}$[a] [Hz]	γ-phosphate $\Delta\nu_{1/2\ 1(T)}$ [Hz]	γ-phosphate $\Delta\nu_{1/2\ 2(T)}$ [Hz]
Ras^{H27E}	--	122	103.8	67.5	61.5	66.5
+ Raf-RBD	1:0.6	194	112	74.6	86.5	106.1
	1:1	--	122.8	102	--	60.5

All the values are fitted from the experimental spectra recorded at 278 K, pH 7.5. The maximum estimated errors from the fitting procedure are ± 0.02 ppm in chemical shift values and ± 0.12 Hz in linewidths for the γ-phosphate. An LB= 15 Hz was applied to the FID and subtracted afterwards from the final fitted linewidths.

[a] States 1(T) and 2(T) of the β-phosphate cannot be separated at the magnetic field used.

3.4.4 Interaction Between HRas^{D33K}•Mg^{2+}•GppNHp and Raf-RBD

Due to its intriguing properties, Ras^{D33K} was subjected to an additional series of biophysical studies, including the interaction with Raf-RBD. The results from the titration indicate that the residual population of state 1(T) (red coloured line in Figure 3.50) rapidly disappears upon addition of 0.5 molar equivalents of Raf. There is a direct response to the presence of effector as this population is converted into state 2(T). The typical upfield shift of state 2(T) is also observed as before upon titration of Ras^{WT} with the same protein (from δ= -3.40 ppm to δ= -3.63 ppm at 1:2 ratio, Table 3.20). This indicates that the changes in the chemical environment of the γ-phosphate that accompany the process of binding are identical to the ones observed for Ras^{WT}. However, the situation is different for the α- and β-phosphates: the initial resonance observed at the α-phosphate in Ras^{D33K} alone (δ= -11.46 ppm) seems to split into another component as soon as Raf is added and remains with the same configuration in all the subsequent steps of the titration (i.e. there is no additional change in chemical shifts or linewidths as the concentration of Raf is increased). This behaviour is markedly different from the titration of Ras^{WT}, where the α-phosphate is also converted into state 2*(T) shifting upfield by a $\Delta\delta$ of -0.15 ppm (Figure 3.1 and [117]. The formation of state 2*(T) is thus impaired in Ras^{D33K} for the α-phosphate, which might explain the low affinity of binding for the protein-protein complex (Table 3.18). The response of the β-phosphate is characterised by a severe increase of its line broadening and by the appearance of an additional component that protrudes from its right-side as a broad shoulder. This shoulder seems to be, in fact, formed by multiple resonances that cannot be resolved separately. An unknown peak at ca. 1.04 ppm can be found in all the spectra of the series and increases in

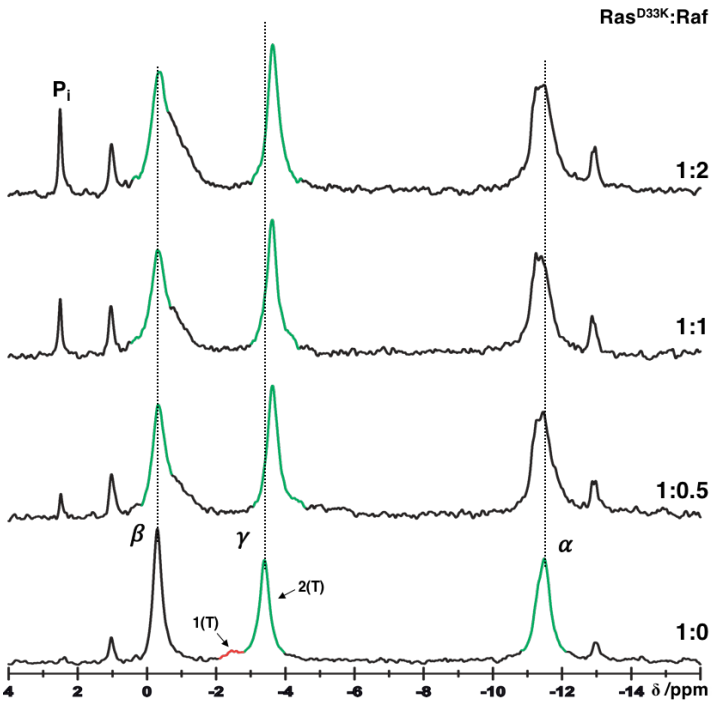

Figure 3.50. ^{31}P NMR spectroscopy on the titration of HRas^{D33K}•Mg^{2+}•GppNHp with the effector Raf-RBD measured at 278 K and pH 7.5. To an initial 2.94 mM solution of Ras^{D33K} dissolved in buffer F (40 mM Tris/HCl pH 7.5, 10 mM $MgCl_2$, 2 mM DTE) with additionally 0.2 mM DSS, 150 mM NaCl and 5% D_2O, increasing amounts of Raf-RBD from a highly concentrated 6.5 mM stock solution were added, up to a final ratio of 1:2. An EM function with LB= 15 Hz was applied to the FID during the processing of the data. The chemical shifts and linewidths are shown in Table 3.20.

intensity as the concentration of Raf-RBD is increased (note that this peak is already present in the spectrum of Ras alone). Within the available data It is not possible to ascertain if this peak is just an impurity or a new feature characteristic of the mutant Ras^{D33K}.

In the light of these results, the previous classification of Ras^{D33K} as a state 2(T)/3(T) fits its spectroscopic properties observed by ^{31}P NMR but is not in line with the typical biochemical characteristics of state 2(T) (higher affinity towards effectors, faster intrinsic and/or GAP-mediated hydrolysis, affinity towards GAP's).

Table 3.20. ^{31}P NMR chemical shift values and linewidths for the protein-protein complex $HRas^{D33K}(1\text{-}166)\bullet Mg^{2+}\bullet GppNHp\bullet Raf\text{-}RBD$.

Protein complex	Ras: Raf	α-phosphate		β-phosphate		γ-phosphate	
		$\delta_{1(T)}$ [ppm]	$\delta_{2(T)}$ [ppm]	$\delta_{1(T)}$ [ppm]	$\delta_{2(T)}$ [ppm]	$\delta_{1(T)}$ [ppm]	$\delta_{2(T)}$ [ppm]
Ras^{D33K}	--	-11.46		-0.31		-2.47	-3.40
+ Raf-RBD	1:0.5	--	-11.42	--	-0.34	--	-3.64
	1:1	--	-11.37	--	-0.32	--	-3.62
	1:2	--	-11.41	--	-0.33	--	-3.63
		α-phosphate		β-phosphate		γ-phosphate	
		$\Delta\nu_{1/2\ 1(T)}$ [Hz]	$\Delta\nu_{1/2\ 2(T)}$ [Hz]	$\Delta\nu_{1/2\ 1(T)}$ [Hz]	$\Delta\nu_{1/2\ 2(T)}$ [Hz]	$\Delta\nu_{1/2\ 1(T)}$ [Hz]	$\Delta\nu_{1/2\ 2(T)}$ [Hz]
Ras^{D33K}	--	77.31		41.92		73.40	55.48
+ Raf-RBD	1:0.5	--	106.37		63.65	--	60.95
	1:1	--	106.45		81.00	--	60.25
	1:2	--	120.31		84.15	--	63.85

All the values are fitted from the experimental spectra recorded at 278 K, pH 7.5. The maximum estimated errors from the fitting procedure are ± 0.02 ppm in chemical shift values and ± 0.12 Hz in linewidths for the γ-phosphate. An LB= 15 Hz was used in the processing of the FID and subtracted afterwards from the final fitted linewidth values.

3.4.5 Interaction Between HRas^{D33K}•Mg^{2+}•GppNHp and NF1

The features of the Ras^{D33K}•NF1 complex were also investigated herein and revealed to be very distinct from the ones of its counterpart Ras^{WT}•NF1. The most obvious difference lies in the fact that a resonance that unequivocally corresponds to state 3(T) cannot be identified in the ^{31}P NMR spectra. As seen in Figure 3.51, addition of NF1 leads to the appearance of an extremely broad line at the γ-phosphate that consists of multiple unresolved resonances (the fitted component is shown in Figure 3.51 for the ratios 1:0.75 and 1:1 on the γ-phosphate). Even at a molar ratio of 1:2 its centre cannot be accurately located as in the case of Ras^{WT}•NF1 (Figure 3.39). Furthermore, its centre lies around δ= -2.80 ppm (Table 3.21), which differs by a Δδ of 0.2 ppm from the typical state 3(T) located at δ= -3.0 ppm in the Ras^{WT}•NF1 complex (Table 3.12). The relative area of state 2(T) on the γ-phosphate (green line) does not decrease as the titration proceeds. In fact, its relative area in Ras^{D33K} alone and in the 1:1.75 Ras-NF1 complex is 1.73 ± 0.17 and 1.83 ± 0.32, respectively (the numbers have arbitrary units and were obtained as the integrals of the fitted lines). This constitutes an indication that state 2(T) remains unperturbed and cannot effectively be converted into state 3(T) by the presence of NF1.

The β-phosphate is also markedly different from the one in the *wild type* complex: with addition of NF1 it moves upfield, from δ= -0.35 ppm up to a maximum of δ= -0.17 ppm (Δδ= -0.18 ppm). More importantly, the saturation behaviour observed in Ras^{WT}•NF1 (section 3.4.1.2) is not observed in the present case (even at a ratio of 1:2 its main component is the original line found in Ras^{D33K} alone). Similar findings can be found at the α-phosphate: at complex ratios of 1:1.75 and 1:2 its main component is still the one of Ras^{D33K} alone. The resonance arising from the protein complex is again extremely broad and not well-defined. As result, the chemical shift values given in Table 3.21 for the $\alpha_{3(T)}$-phosphate are only a rough estimation since a proper fitting of the line is not possible. This result agrees with the observations found for the γ-phosphate and together they show that Ras^{D33K} cannot undergo the necessary conformational modifications to achieve state 3(T) which renders it incapable of binding NF1 either completely or partially.

The overall results indicate so far that Ras^{D33K} has an impaired affinity towards both, Raf-RBD and NF1. Based on these data, Ras^{D33K} does not follow the characteristics of a typical state 2(T) mutant, despite the apparent indications given by the shift of the equilibrium at the γ-phosphate of at the GppNHp-bound spectra level.

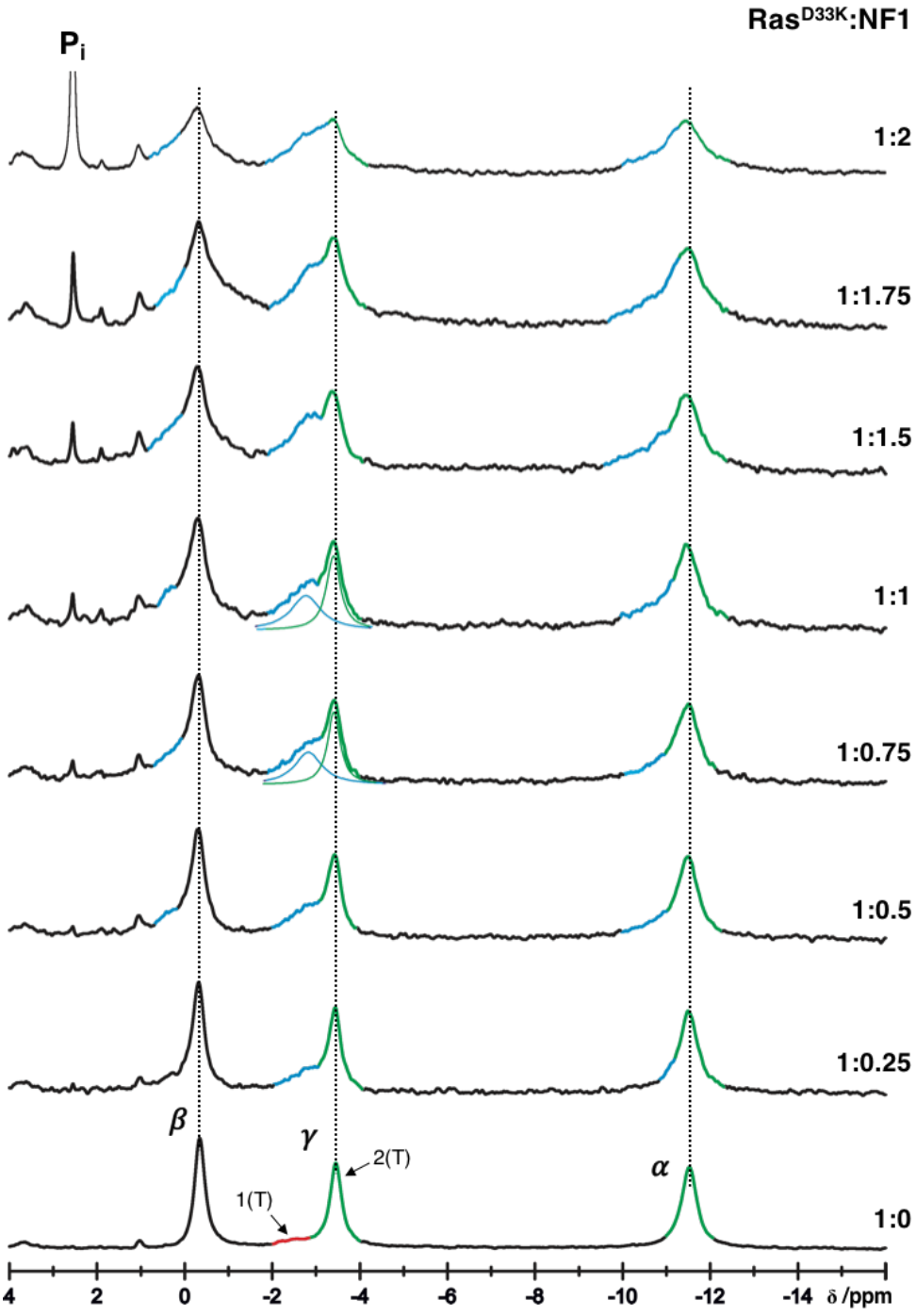

Figure 3.51. Protein complex formation between Ras^{D33K}•Mg^{2+}•GppNHp and NF1 followed by ^{31}P NMR spectroscopy at 278 K. To an initial 1.3 mM of Ras dissolved in buffer F (40 mM Tris/HCl pH 7.5; 10 mM $MgCl_2$; 2 mM DTE) with additionally 150 mM NaCl, 0.2 mM DSS in 10% D_2O, increasing amounts of the GAP protein NF1 (from a 0.74 mM stock solution) were added (the corresponding molar ratios for each step are presented). The concentration of Ras and NF1 in the final step (1:2 ratio) was 0.35 mM and 0.7 mM, respectively. An exponential filter with LB=15 Hz was applied to the processed FID. Each spectra was obtained by accumulation of approximately 10000 scans. The resonance lines corresponding to the α-, β- and γ-phosphates are indicated as well as the states 1(T) and 2(T), represented by the red and green colours, respectively. The dashed vertical lines mark the chemical shift position of the initial phosphate resonances observed in Ras^{D33K} alone. The new spectral features observed from the addition of NF1 to Ras are coloured in blue. As an example, the deconvolution into separated Lorentzian lines is shown for two different titration steps (1:0.75 and 1:1) on the γ-phosphate.

These results constitute perhaps the first evidence that the common correlation between the different structural states 1(T) and 2(T) and their correspondingly different functional and biochemical properties should be used with caution, especially when investigating atypical mutants, as the correlations might be true for Ras^{WT}, partial loss-of-function or oncogenic variants but might not apply in other cases [123]. Ras^{D33K} can undergo a conformational change towards state 2(T)/2*(T) at the γ-phosphate in the presence of effector. However, the impaired Raf binding observed from ITC can be in part explained by the inability of the β- and mostly the α-phosphate to undergo the necessary conformational modifications. The interaction with NF1 is also disrupted comparatively to Ras^{WT} as the binding seems to be severely impaired for all the three phosphate groups.

Table 3.21 ^{31}P NMR chemical shift values and linewidths for the protein-protein complex $HRas^{WT}(1\text{-}166)\bullet Mg^{2+}\bullet GppNHp\bullet NF1$.

Protein complex	Ras:NF1 ratio	α-phosphate		β-phosphate		γ-phosphate		
		$\delta_{3(T)}$ [ppm]	$\delta_{2(T)}$ [ppm]	$\delta_{1(T)2(T)}$ [ppm][b]	$\delta_{3(T)}$ [ppm]	$\delta_{1(T)}$ [ppm]	$\delta_{3(T)}$ [ppm]	$\delta_{2(T)}$ [ppm]
Ras^{D33K}	--	--	-11.52	-0.35	--	-2.67	--	-3.45
+NF1	1:0.25	-11.17	-11.52	-0.31	0.46	--	-2.80	-3.43
	1:0.5	-10.84	-11.49	-0.28	--[a]	--	-2.78	-3.41
	1:0.75	-10.92	-11.49	-0.27	--[a]	--	-2.82	-3.41
	1:1.0	-10.70	-11.46	-0.25	--[a]	--	-2.76	-3.40
	1:1.5	-10.79	-11.46	-0.21	--[a]	--	-2.80	-3.39
	1:1.75	-10.54	-11.45	-0.20	--[a]	--	-2.82[c]	-3.43[c]
	1:2.0	-11.09	-11.51	-0.17	--[a]	--	-2.80[c]	-3.37[c]
		α-phosphate		**β-phosphate**		**γ-phosphate**		
		$\Delta\nu_{1/2\ 3(T)}$ [Hz]	$\Delta\nu_{1/2\ 2(T)}$ [Hz]	$\Delta\nu_{1/2}$ [Hz]	$\Delta\nu_{1/2\ 3(T)}$ [Hz]	$\Delta\nu_{1/2\ 1(T)}$ [Hz]	$\Delta\nu_{1/2\ 3(T}$ [Hz])	$\Delta\nu_{1/2\ 2(T)}$ [Hz]
Ras^{D33K}	--	--	87.38	51.50	--	397	--	59.86
+NF1	1:0.25	202.4	99.16	61.08	559	--	176.8	62.42
	1:0.5	162.0	105.7	104.1	--[a]	--	183.4	67.29
	1:0.75	184.6	118.6	136.9	--[a]	--	177.5	67.76
	1:1.0	184.9	131.9	167.4	--[a]	--	187.2	77.03
	1:1.5	187.6	135.9	256.6	--[a]	--	172.2	81.02
	1:1.75	174.6	197.4	237.4	--[a]	--	194.5[c]	67.05[c]
	1:2.0	164.8	159.5	268.9	--[a]	--	151.7[c]	113.3[c]

All the values are fitted from the experimental spectra recorded at 278 K, pH 7.5. The estimated errors from the fitting procedure are ± 0.02 ppm in chemical shift values and ± 0.20 Hz in linewidths for the γ-phosphate. An LB= 15 Hz was applied to the FID and subtracted afterwards to the final fitted linewidth values.

[a] The resonance line could not be properly fitted

[b] States 1(T) and 2(T) of the β-phosphate cannot be separated at the magnetic field used and were therefore fitted as a single Lorentzian line.

[c] The given values are an approximation (error ±0.1 ppm and ±5.0 Hz) due to the very broad shape of the peaks.

3.4.6 ^{31}P Longitudinal Relaxation Times of Ras^{WT}, Ras^{T35A} and Ras^{D33K}

The goal of this study was to evaluate the T_1 spin-lattice relaxation for the GppNHp-bound Ras^{D33K} and to assess how the values compare with Ras^{WT} and Ras^{T35A}. The experiments were carried at 278 K in a spectrometer operating at a ^{31}P frequency of 242.896 MHz (600 MHz spectrometer). The magnitude of the recorded transverse magnetisation is dependent on the time given for the recovery after the initial 180º pulse. The plot of the relative signal areas as a function of the τ time is given in Figure 3.52 and the corresponding fitted T_1 values are shown in Table 3.22. Phosphorous relaxation times of nucleotides bound to proteins are rarely described in literature. Due to the fact that the ^{31}P atoms are isolated by their shell of oxygen atoms from other spins of the lattice, rather long T_1 times are to be expected. Indeed, the shortest T_1 presently recorded is within the range of 3 seconds. The values show that for all the three proteins, the relaxation rate of the α-phosphate is in average 1.5 times faster than the β- and γ-phosphates. If one compares the three proteins in terms of each phosphate group separately, the relaxation rates are very similar, i.e. the state 1(T) Ras^{T35A} and the state 2(T) Ras^{D33K} are similar to each other and also similar to Ras^{WT} whose 1(T)/2(T) T_1 times were averaged. The only major difference is observed in terms of M_0: the amount of longitudinal relaxation when the nuclear spins are fully relaxed is much lower in the case of Ras^{D33K} than in the other two proteins. The reason for this difference is simply related with the use of relative units for the calculation of the integrated areas and has no intrinsic biochemical meaning (in other words, all the plotted areas in the *y* axis should have been divided by the area of the signals obtained at M_0, in order to normalise the *y* scale from -1 to +1). Comparable T_1 measurements for Ras^{WT} and Ras^{T35A} are available from previous work performed at our department [116], where a magnetic field operating at a ^{31}P frequency of 202.456 MHz (500 MHz spectrometer) was used. The rate of relaxation depends on the magnetic field strength and therefore the two measurements have different T_1 times. Generally T_1 tends to decrease as the field strength increases. However, the comparison between the published data with the present one shows an opposite effect: the ^{31}P NMR T_1 times of Ras^{WT} and Ras^{T35A} decrease as the magnetic field increases from 202.4 to 242.8 MHz.

Normally T_1 is the shortest when the correlation time τ_c is approximately equal to the Larmor frequency. Molecules tumbling faster or slower are less efficient at spin-lattice relaxation, having therefore longer T_1 values. For atoms in highly mobile molecules (such as free water), changing field strength (and hence the Larmor frequency) will not appreciably alter the fraction of protons moving at this frequency. Thus, T_1 is generally not much affected. For atoms in molecules with intermediate or low mobility, however, shifting the magnetic

field to a higher value may significantly decrease the fraction of these nuclei that are able to interact at the new (higher) Larmor frequency.

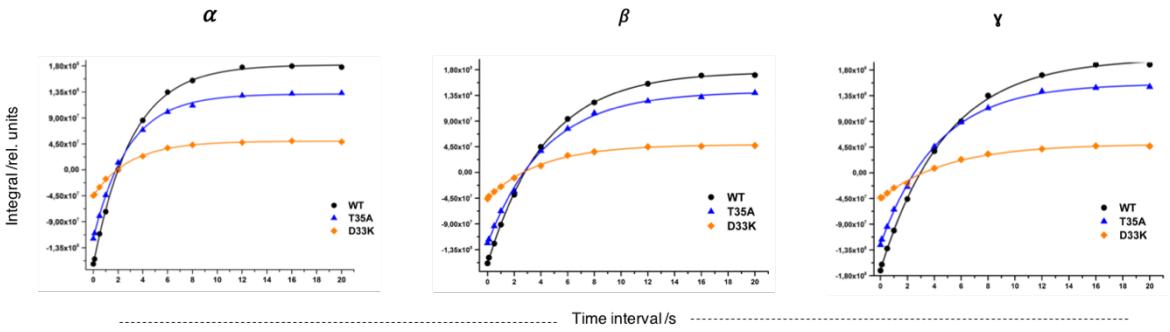

Figure 3.52. T_1 relaxation times in HRas(1-166)•Mg^{2+}•GppNHp. The integrals of the resonance lines of the α-, β- and γ-phosphates were plotted as a function of time, *t*, in an inversion recovery experiment (eqn. 10, experimental section 2.2.5.4). The lines corresponding to the two conformational states were averaged and the time allowed for the recovery of the magnetization was varied between 0.01 and 21.0 s. Measurements were performed for Ras^{WT} (-●-), Ras^{T35A} (-▲-) and Ras^{D33K} (-◆-) at 278 K in a spectrometer operating at a frequency of 242.896 MHz. All the protein samples were used at the same concentration of 1.0 mM and dissolved in buffer F (40 mM Tris/HCl pH 7.5; 10 mM $MgCl_2$; 2 mM DTE) with additionally 0.2 mM DSS in 10% D_2O. The relaxation times obtained from the fitting routine are shown in table 3.22.

Table 3.22. Phosphorous T_1 relaxation times in the HRas(1-166)•Mg^{2+}•GppNHp proteins.

Protein	T /K	α-phosphate	β-phosphate	γ-phosphate
Ras^{WT}	278	3.10 ± 0.05	4.35 ± 0.07	4.81 ± 0.11
Ras^{T35A}	278	2.83 ± 0.07	4.32 ± 0.14	4.25 ± 0.10
Ras^{D33K}	278	2.98 ± 0.1	4.02 ± 0.15	4.93 ± 0.31

T_1 is given in seconds. The data was obtained from a proton-decoupled inversion recovery experiment at 242.896 MHz.

Based on the multiple studies conducted so far on Ras^{D33K}, this mutant is considerably different from Ras^{WT}. The present analysis is relevant since T_1 times affect directly signal sensitivity and integration accuracy in NMR experiments. However, they do not provide additional clues about the biochemical nature of the protein. Nevertheless, the titration experiments conducted in the above sections 3.4.4 and 3.4.5 for the interaction with Raf-RBD and NF1 unequivocally elucidate important biochemical aspects.

Since the primary goal for investigating Ras^{D33K} was to promote a state 2(T)-to-3(T) transition (section 3.4.2.3), one question remains: was the equilibrium shifted in the expected direction? From the ^{31}P NMR titration measurements it does not seem to be the case. Nevertheless, a true binding affinity assay involving a GAP protein such as NF1 (not only for Ras^{D33K} but for all other mutants studied herein) remains to be done. Several attempts were made using ITC but in all the cases no obvious binding curves could be

obtained due to severe artefacts in the heat signatures, supporting the idea that Ras-GAP complex formation does not obey to a single step and/or to steady-state conditions [255, 256].

The assignment of Ras^{D33K} as being either predominantly shifted towards 1(T) or 2(T) is not straightforward: this mutant is biochemically similar to a typical state 1(T) (such as T35S or Y32R/W [123]) but its conformational equilibria is almost completely shifted towards state 2(T) from an NMR point of view. More importantly, it gives the first evidence that the common correlation between the different structural states 1(T) and 2(T) and their correspondingly different functional and biochemical properties should be used with caution.

Indeed, not all known state 1(T) mutants show a decreased affinity to effector or GAP proteins and/or a decreased GTPase activity (although being generally the case, there are exceptions [51, 123]). As result, and based in the ^{31}P NMR spectra of the GppNHp-bound nucleotide (Figure 3.47), Ras^{D33K} is hereafter classified as a state 2(T) mutant. Additional preliminary results from [^{1}H-^{15}N]-HSQC NMR (see section 3.4.9) support this conclusion: just as the typical state 1(T) Ras^{T35S} shows additional cross-peaks (relative to *wild* type) that are representative of state 1(T), also Ras^{D33K} shows additional cross-peaks that seem to be representative of state 2(T) and that are not observable in Ras^{T35S}. A detailed investigation of peak volumes between the three proteins (WT, T35S, D33K) is detrimental to understand the exchange mechanisms between states 1(T) and 2(T). The analysis is being presently conducted at our department. The importance of residue 33 in the modulation of the dynamics of the equilibrium between the two states can also be further investigated in the future by exploring the effect of replacement to other amino acids.

3.4.7 ^{31}P HP NMR on HRas(1-166)^{D33K}•Mg^{2+}•GppNHp

Ras^{D33K} opens the possibility for investigating the equilibria starting from the point of view of states 2(T) for the first time. In fact, to the best of the authors knowledge, this is the only known mutant whose equilibria at ambient pressure almost does not contemplate the contribution of state 1(T). Its conformational dynamics and unusual functionality constitutes one of the most surprising findings among the body of work performed within this thesis.

A total of 21 steps were performed in the ^{31}P HP NMR series of Ras^{D33K}, ranging from 0.1 up to 200 MPa. Figure 3.53 shows the ^{31}P HP NMR series of 11 of these steps with intervals of 20 MPa. The dependence of the chemical shifts as a function of pressure is shown graphically in Figure 3.54 and numerically in Table 3.23.

The most obvious pressure-induced change is the repopulation of state 1(T) at the γ-phosphate given by the increase of its corresponding integrated area (red line Figure 3.53). At the same time its resonance line shifts downfield by a $\Delta\delta$ of 0.054 ppm, (between 80 and 200 MPa. Below 80 MPa this resonance could not be properly fitted due to its only residual population). The downfield shift is accentuated upon correction ($\Delta\delta$= 0.156 ppm, from δ= -2.406 to δ= -2.250, Figure 3.54, and Table J appendix section) because the γ-phosphate of free Mg^{2+}•GppNHp moves in the opposite direction (i.e. upfield, Figure 3.26) than the γ-phosphate of the protein. The same behaviour is also observed for state 2(T). This signal (represented by the orange coloured lines in Figure 3.54) shows a very large downfield shift by a $\Delta\delta$= 0.47 ppm, from δ= -3.40 ppm at 0.1 MPa to δ= -2.93 MPa at 200 MPa.

The pressure dependence of the α-phosphate indicates that the re-population of state 1(T) is not possible in this case. Between the first and the last pressure steps the signal broadens slightly (ca. 8%) and moves downfield by $\Delta\delta$= 0.460 ppm ($\Delta\delta$= 0.480 ppm upon correction); the signal seems to consist of at least two components at high pressures (180-220 MPa) and has an ill-defined centre and a non-Lorentzian shape, with the components being too close together to allow an independent fit. Regarding the β-phosphate, its pressure dependency is similar to the one observed for Ras^{WT} and Ras^{T35S}, shifting upfield ($\Delta\delta$= -0.09 ppm) for the uncorrected shift values and downfield ($\Delta\delta$= 0.168 ppm) upon correction.

The fitting of a Taylor polynomial (eqn. nº15, experimental section 2.2.5.4) yielded again small and mostly negative second order B_2 coefficients which indicate a rather linear pressure dependence of the bound nucleotide. Although some exceptions occur such as the β-phosphate that shows a B_2 value markedly higher than B_1 (1.25 ppm GPa^{-2} vs -0.68 ppm GPa^{-1}, Table 3.23). In most curves, the fitting of the ΔG and ΔV parameters was only accomplished when fixing the initial and final chemical shift values, δ_1 and δ_2.

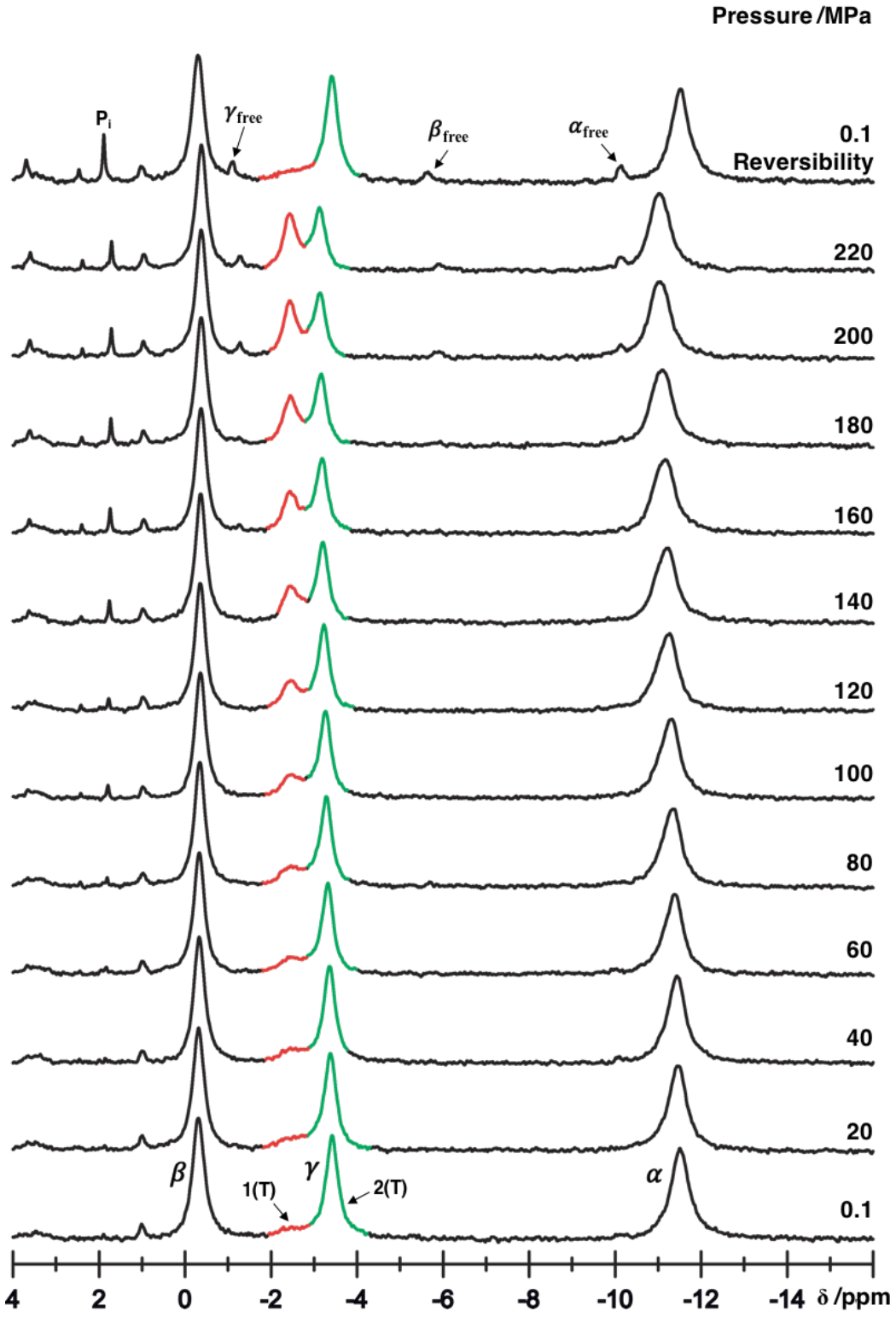

Figure 3.53. Conformational equilibria of HRas^{D33K}(1-166)•Mg^{2+}•GppNHp as a function of pressure determined by ^{31}P NMR at 278 K. The 4.45 mM protein dissolved in buffer F (40 mM Tris/HCl pH 7.5, 10 mM $MgCl_2$, 2 mM DTE) with additionally 0.4 mM DSS and 20% D_2O was subjected to increasing step-variations of pressure, up to a maximum of 200 MPa. Each spectrum was obtained by accumulation of 800 scans. The evolution of states 1(T) and 2(T) is represented by the red and green lines, respectively. The ^{31}P resonances of the free nucleotide observed at higher pressures are also indicated. The last step corresponds to the reversibility test of the pressure-induced changes. The fitted chemical shift values for all the resonance lines are listed in Table J of the appendix section.

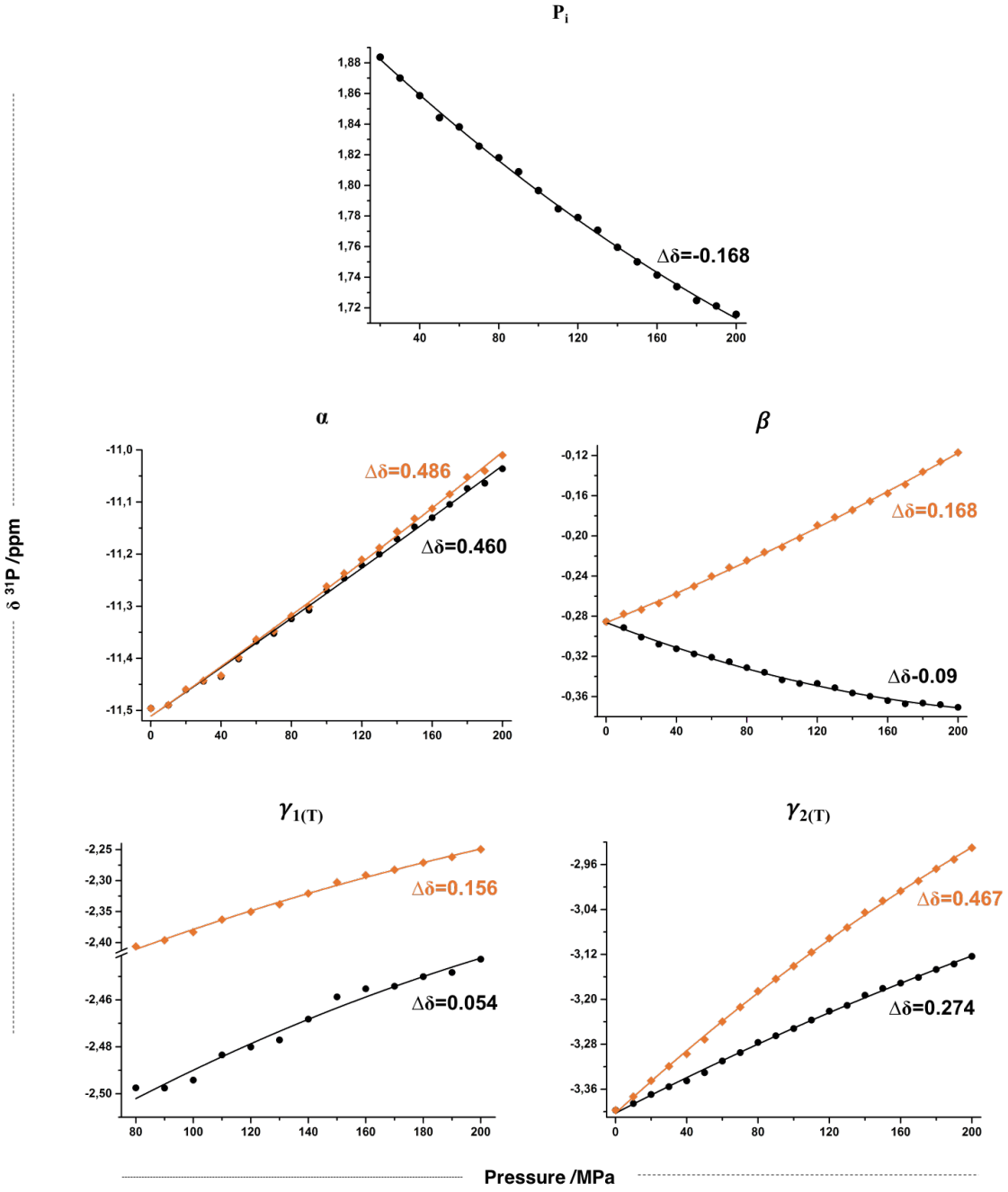

Figure 3.54. Corrected pressure dependence of ^{31}P chemical shifts of HRas^{D33K}(1-166)•Mg^{2+}•GppNHp recorded at 278 K. The $\Delta\delta_{freenuc\ fit}$ values were applied as correction factors upon addition or subtraction to the $\delta_{Ras\ uncorrected}$ values, depending on the direction of the observed shifts, leading to the final $\delta_{corrected}$ values, represented here for each plot as orange lozenges (-◆-). The uncorrected shift values are also plotted as black circles (-●-). The second order polynomial fit of a Taylor expansion was applied for the determination of B_1 and B_2 and the values are presented on Table 3.23. The calculated chemical shift differences, $\Delta\delta=\delta_{200MPa}-\delta_{0.1MPa}$, are shown near each curve. In the case of the γ1(T)-phosphate $\Delta\delta=\delta_{200MPa}-\delta_{80MPa}$. Note that the vertical scaling is different for each plot to allow a better visualisation of the details from the different curves.

Within the limits of error the values obtained for the α-, β- and $\gamma_{2(T)}$-phosphates are very similar, leading to a similar pressure-dependent similar type of transition for the three phosphate groups. Their averaged ΔG and ΔV values are 5.62 kJ mol^{-1} and 59.87 mL mol^{-1}, respectively for Ras uncorrected, and 5.93 kJ mol^{-1} and 59.2 mL mol^{-1} for Ras corrected. The application of the correction does not change significantly the thermodynamics, contrary to the observations for Ras^{WT}, where the correction seems to exert a greater influence (Table 3.23). In the case of the $\gamma_{1(T)}$-phosphate, considerably higher molar free energies and volumes were obtained when compared with the other three phosphate groups, and again within similar values between the corrected and uncorrected cases ($\Delta G_{corrected}$= 14.3 ± 0.8 kJ mol^{-1} and $\Delta V_{corrected}$= -105 mL mol^{-1}), which is indicative that state 1(T) is most likely related to a conformational modification that is different than the one sensed by the other phosphates.

P /MPa	K_{12}
80	2.50
90	2.28
100	2.07
110	1.92
120	1.96
130	1.68
140	1.60
150	1.46
160	1.39
170	1.34
180	1.09
190	1.07
200	0.97

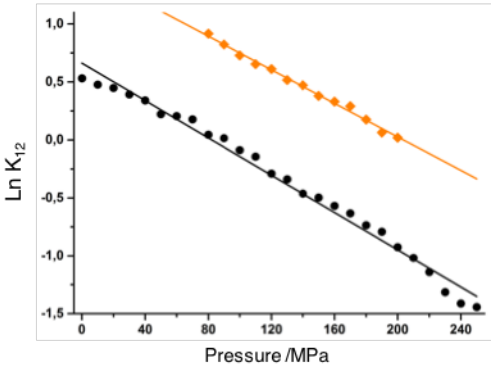

Figure 3.55. Plot of LnK_{12} as a function of pressure in Ras^{D33K}•Mg^{2+}•GppNHp (-◆-). The fit of the data gives a specific molar volume and Gibbs energy of ΔV= -16.72 ± 0.4 mL mol^{-1} and ΔG= 3.40 ± 0.01 kJ mol^{-1}, respectively. The K_{12} values for each pressure point are shown in the table. The plot of Ras^{WT} (-●-). is also shown for comparison (ΔG= 1.53 kJ mol^{-1} and ΔV= -18.63 mL mol^{-1}, see also Figure 3.30.

The fit of LnK_{12} as a function of pressure (Figure 3.55) leads to a ΔG_{12} of 3.40 kJ mol^{-1} and ΔV_{12} of -16.72 mL mol^{-1}, respectively. An identical volume variation was found in the case of Ras^{WT} (ΔV= -18.63 mL mol^{-1}, Figure 3.30), although the energy required for the conformational transition to take place is two-fold higher in Ras^{D33K}. In practical terms the mutant seems to be less pressure-responsive than the *wild type* (a higher energetic input is necessary to shift the equilibria in the same pressure interval).

The conformational aspects that define the γ-phosphate in Ras^{D33K} can be modulated by pressure, and the initial population defined by a K_{12}= 11.3 at 0.1 MPa can be brought back to the original ratio observed for Ras^{WT} (K_{12}= 1.7) around 150 MPa. One can envisage that given enough pressure, the equilibria could be shifted even further. On the other hand, the conformational aspects that define the α-phosphate are not as easily modulated and a direct shift from state 2(T) towards state 1(T) is not possible in this case. Indeed, Ras^{D33K} can be defined as being a state 2(T) mutant at the γ-phosphate. There is no direct or obvious indication from the present HP data that state 3(T) can be significantly populated.

Table 3.23. Fitted pressure coefficients and thermodynamic molar free energies, ΔG, and volumes, ΔV, for HRas^{D33K}(1-166)•Mg^{2+}•GppNHp at 278 K and pH 7.5.

^{31}P position	δ^{0a} /ppm	B_1 /ppm GPa^{-1}	B_2 /ppm GPa^{-2}	--	--
		Uncorrected			
α	-11.51	2.31 ± 0.11	0.45 ± 0.51		
β	-0.29	-0.68 ± 0.03	1.25 ± 0.11		
$\gamma_{1(T)}$	-2.56	0.80 ± 0.20	-1.06 ± 0.70		
$\gamma_{2(T)}$	-3.40	1.63 ± 0.04	-1.13 ± 0.20		
P_i	1.91	-1.25 ± 0.04	1.42 ± 0.18		
		Corrected			
α	-11.51	2.35 ± 0.11	0.94 ± 0.51		
β	-0.29	0.70 ± 0.03	0.70 ± 0.11		
$\gamma_{1(T)}$	-2.56	2.06 ± 0.20	-2.54 ± 0.70		
$\gamma_{2(T)}$	-3.40	2.89 ± 0.04	-2.60 ± 0.20		
	$\delta_1{}^b$ /ppm	$\delta_2{}^b$ /ppm	ΔG /kJ mol^{-1}	ΔV /mL mol^{-1}	Transition
		Uncorrected			
α	-11.49^c	-11.01	6.39 ± 0.28	-58.69 ± 4.0	--
β	-0.29^c	-0.37	4.76 ± 0.28	-62.40 ± 3.2	--
$\gamma_{1(T)}$	-2.50	-2.44	12.95 ± 1.05	-98.66 ± 9.3	1-to-0 (?)
$\gamma_{2(T)}$	-3.40^c	-3.12	5.72 ± 0.24	-58.55 ± 2.23	2-to-3 (?)
P_i	1.91	1.72	4.98 ± 0.21	-57.64 ± 2.10	--
		Corrected			
α	-11.50^c	-11.01^c	6.61 ± 0.28	-63.03 ± 2.51	--
β	-0.29	-0.12^c	5.63 ± 0.25	-54.86 ± 2.27	--
$\gamma_{1(T)}$	-2.41^c	-2.25	14.32 ± 0.83	-104.9 ± 5.97	1-to-0 (?)
$\gamma_{2(T)}$	-3.40a	-2.93^c	5.55 ± 0.25	-60.19 ± 2.45	2-to-3 (?)

[a] δ^0 is the chemical shift value obtained at ambient pressure at the corresponding pH.
[b] δ_1 and δ_2 are the chemical shift values obtained for the first and last pressure steps, respectively. Due to the linear tendency of the fitted curves, the obtained values constitute a coarse approximation.
[c] The value was fixed during the fitting routine.

3.4.8 Thermal Unfolding of HRas Proteins Investigated by nanoDSF

Thermal and chemical unfolding experiments are highly appreciated methods to quantify protein stability. With the intent of further characterise different mutants, with especial emphasis in Ras^{D33K}, the thermal unfolding of *wild type* Ras, together with four different mutants was investigated by nanoDSF. The work presented here was part of a two-day workshop conducted at our department and therefore the study could not be extended to all the proteins involved in this doctoral project.

The obtained results are presented graphically in Figure 3.56 and numerically in Table 3.24. They show that the thermal unfolding of Ras^{WT} is a biphasic process characterized by two melting temperatures, T_{m1}= 50.15 ºC and T_{m2}= 58.63 ºC. The same is observed for the mutants Ras^{H27E} and Ras^{T35S}, whose unfolding profiles and T_m values are almost identical. Contrary to Ras^{T35S}, the melting profile of the closely related mutant Ras^{T35A} proceeds in a

single step with only one T_m of 59.11 ºC, numerically close to the T_{m2} of the three proteins above mentioned. Biochemically, Ras^{T35A} exists predominantly in state 1(T), just like Ras^{T35S}. However, contrary to Ras^{T35S} that can still adopt a state 2(T) conformation in the presence of effectors, Ras^{T35A} remains locked in state 1(T) [156]. These structural differences might account for the strikingly different unfolding profiles. The case of Ras^{D33K} is also interesting since only one T_m was observed for a mutant that exists predominantly in the conformational state 2(T) (T_{m2}= 61.84 ºC, being 3.2 ºC higher than T_{m2} of Ras^{WT}).

It is worth mentioning the robustness of nanoDSF as a technique: despite Ras having no Trp amino acids in its sequence (there are only seven Tyr residues at positions 4, 32, 64, 71, 96, 137, 141), the melting profile of the protein could be measured within seconds, with a good intensity fluorescent signal and with high degree of accuracy (StdDev ≤ 0.11, Table 3.24).

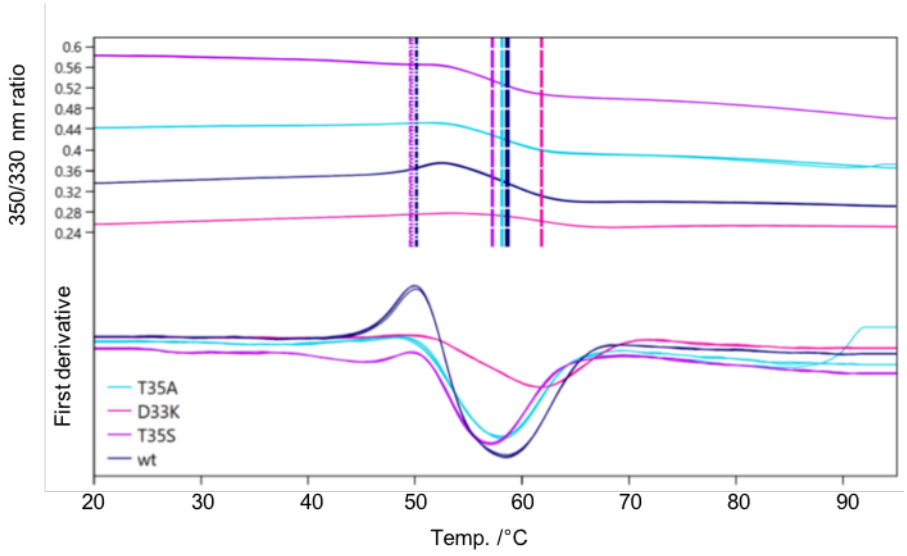

Figure 3.56. nanoDSF performed for the *wild type* Ras•Mg^{2+}•GppNHp protein and three selected mutants: D33K, T35A and T35S. All the proteins were dissolved in buffer F (40 mM Tris/HCl pH 7.5, 10 mM $MgCl_2$ and 2 mM DTE) in concentrations ranging between 1.0 and 1.3 mM and measured directly. The melting scan is shown in the upper panel as a fluorescence ratio plotted over the recorded temperature interval (20-95 ºC). The vertical lines are placed at the transition point of each curve and correspond to their peak maxima. In the lower panel the first derivatives of the fluorescence traces are shown for each protein. This represents a more convenient way to directly discriminate between the obtained T_m values for the different proteins.

Table 3.24. Melting temperatures experimentally obtained for HRas(1-166)•Mg^{2+}•GppNHp by nanoDSF.

Protein	T_{m1} /ºC	StdDev (n=3)	T_{m2} /ºC	StdDev (n=3)
WT	50.15	0.07	58.63	0.11
H27E	50.23	0.06	59.25	0.13
T35S	49.61	0.07	57.19	0.03
T35A	--	--	58.11	0.04
D33K	--	--	61.84	0.03

3.4.9 [^{1}H-^{15}N]-HSQC Spectra of HRas^{WT} and HRas^{D33K} Bound to Mg^{2+}•GppNHp

The differences in the conformational equilibrium detected at the α- and γ-phosphates between the ^{31}P NMR spectra of Ras^{WT} and Ras^{D33K} prompted a more detailed investigation of both proteins using high resolution 2D NMR techniques.

The [^{1}H-^{15}N]-HSQC spectrum of Ras^{WT} bound to GppNHp was previously published and assigned at 303 K by Ito and co-workers [94]. From this and subsequent studies [171, 257] it was found that 22 non-proline residues give no detectable ^{1}H-^{15}N cross-peaks (10-13, 21, 31-39, 57-64 and 71), contrary to the GDP-bound form, where all the residues can be assigned. These peaks belonging to the P-loop and both switch regions, become broadened beyond detection due to intermediate chemical exchange processes correlated with the existence of the conformational states 1(T) and 2(T) [122]. In contrast, the state 1(T) mutant Ras^{T35S}•Mg^{2+}•GppNHp is able to eradicate the exchange since state 2(T) is not present at ambient pressure. Its HSQC spectrum is therefore a fingerprint for state 1(T) (pdb: 2lcf) [95]. Likewise, Ras^{D33K} being the only known state 2(T) could be used to better understand the dynamics of this state.

Based on these premises, the first concern was to obtain a correct and detailed assignment of the ^{1}H-^{15}N cross-peaks for both proteins. This was accomplished by performing a HSQC temperature series from 278 to 303 K. The overall spectra are shown in Figure 3.57. The published assignment at 303 K [94] was automatically transferred to the Ras^{WT} spectra at the same temperature and adjusted for the slight differences in pH and buffer. The assignment at 278 K (shown in Figure 3.57) was obtained by following the temperature dependence of the chemical shifts. The assignment for Ras^{D33K} was done based in the one of Ras^{WT}.

It is important to note that the peak intensities and volumes of each protein are not directly comparable. The series on Ras^{WT} was recorded using the sofast methodology based on the Ernst angle [258], which allows for fast acquisition. The series on Ras^{D33K} were recorded using a standard Bruker HSQC pulse sequence.

A preliminary analysis of the series shows a temperature-dependence for most cross peaks, although some of them remain mostly unperturbed (G138, A146 in Ras^{WT} and G138, G15 in Ras$_{D33K}$). Several peaks are only visible at high temperatures (E99, Q153, H94) most likely because they are in slow exchange at low temperatures, remaining undetectable. It is worth mention that a few residues show double assignments in the spectra due to distinct conformational reorientation of their side chains (A11*, D47* in Ras^{D33K}). With the assignment obtained herein, the accurate comparison of the different peak intensities, volumes and chemical shifts between the two proteins is now presently being investigated

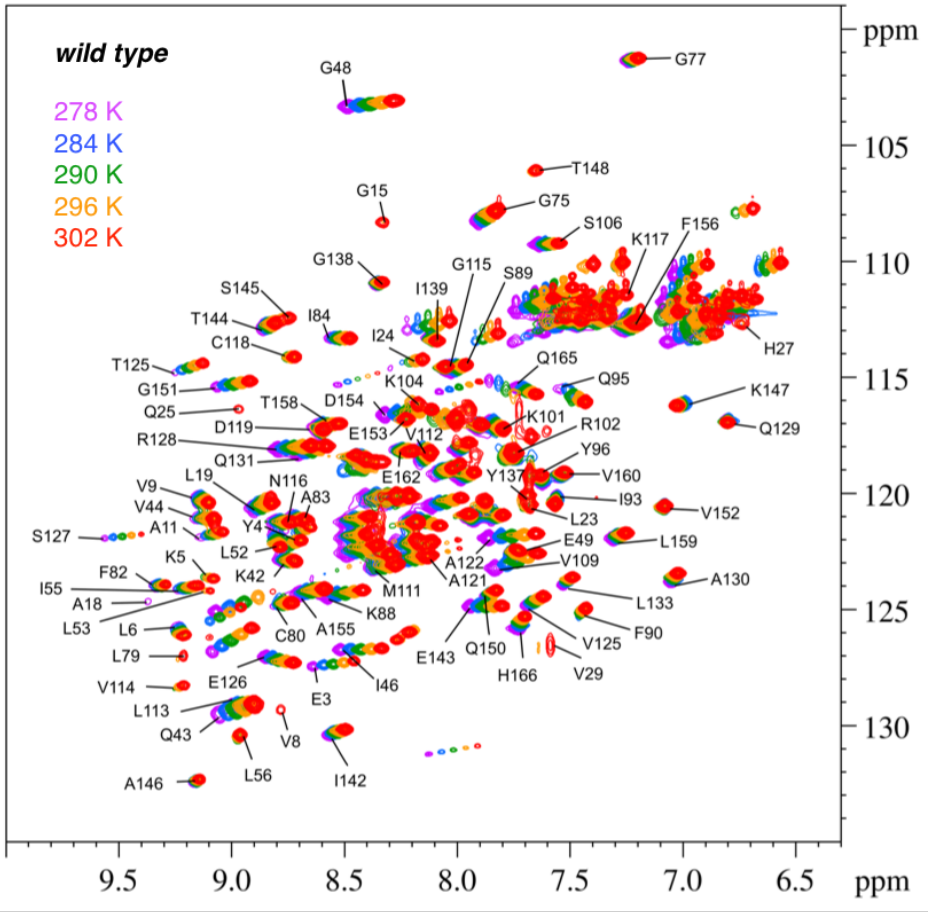
wild type
278 K
284 K
290 K
296 K
302 K
ppm
105
110
115
120
125
130
9.5
9.0
8.5
8.0
7.5
7.0
6.5
ppm

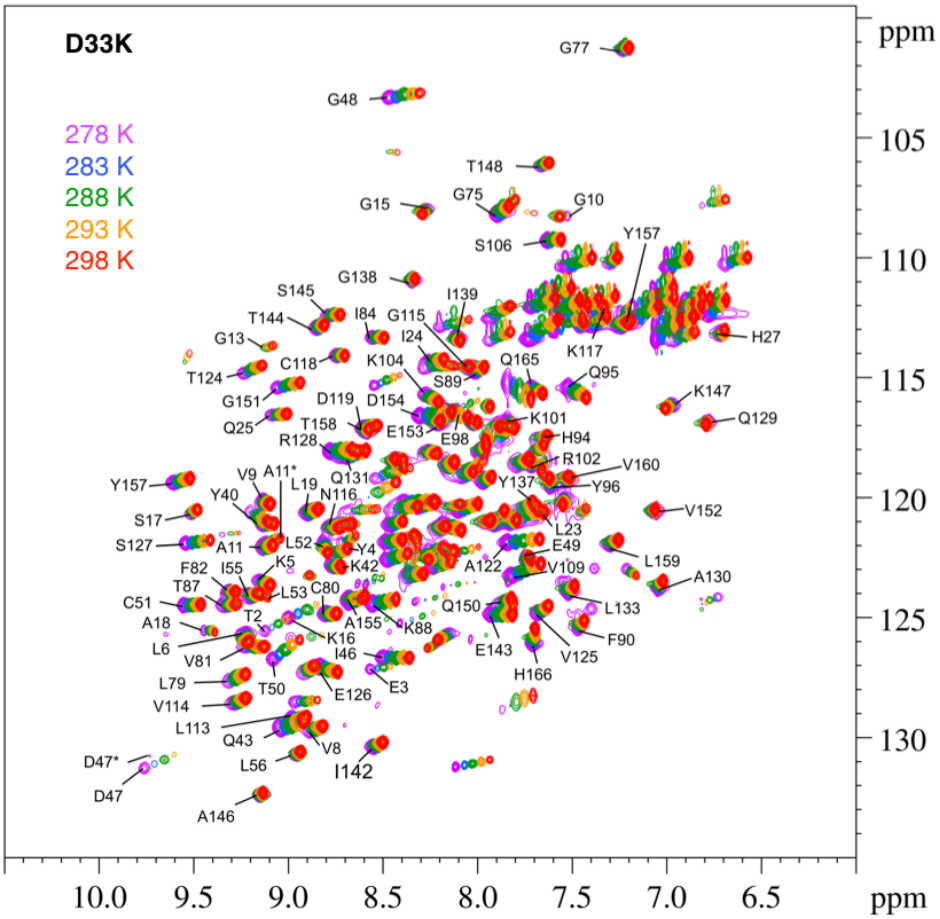
D33K
278 K
283 K
288 K
293 K
298 K
ppm
105
110
115
120
125
130
10.0
9.5
9.0
8.5
8.0
7.5
7.0
6.5
ppm

at our department. The help of Dr. Markus Bech Erlach and Sebastian on the processing of the spectra presented here is gratefully acknowledged.

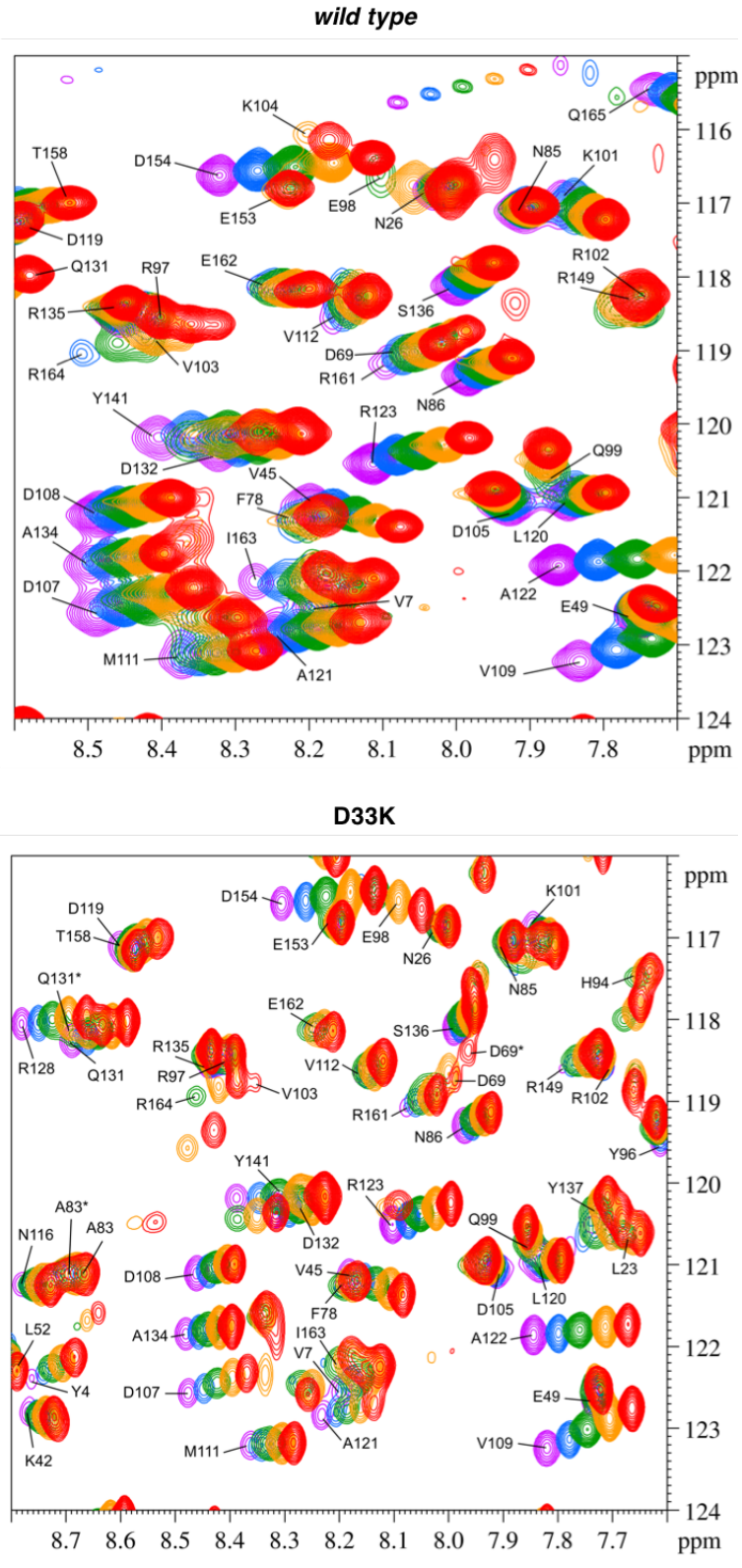

Figure 3.57. [^{1}H-^{15}N]-HSQC NMR spectra of HRas(1-166)•Mg^{2+}•GppNHp proteins.

Left page: a temperature series was recorded between 278 and 303 K for the *wild type* protein (on the top) and the D33K mutant (on the bottom). Both proteins ranging between 1.0 and 1.3 mM were dissolved in buffer F (40 mM Tris/HCl pH 7.5, 10 mM $MgCl_2$, 2 mM DTE) with additionally 10% D_2O and 0.1 mM DSS. Five HSQC spectra were recorded for each protein in a spectrometer operating at a proton frequency of 800 MHz. Both proteins were extensively dialyzed against the same buffer before acquisition. The assignment for Ras^{WT} at 303 K was directly transferred from the one published by Ito et al [94] and manually adjusted to the present conditions (pH, type of buffer). The assignment shown herein refers to 278 K and was obtained by analysing the temperature-dependent chemical shift changes of each peak. Note that the peak volumes or intensities between both proteins are not directly comparable: in the case of Ras^{WT} a sofast HMQC pulse sequence was used while Ras^{D33K} was measured using a standard HSQC method.

Right page: detail of the central region where several cross-peaks overlap. Some of these residues show a marked difference in terms of peak volumes between the HP series of Ras^{WT} and Ras^{D33K} (currently under analysis at our department), portending their involvement in conformational transitions that are specific for each protein.

3.4.10 ^{31}P NMR investigations of HRas(1-166)^{G12P} and HRas(1-166)$^{T35S/G12V}$

The reasons underlying the investigations on these two last mutants are not directly related with the mutational analysis of Ras derived from the HP investigations, described in the above sections. In fact, both mutants are already known by the scientific community and have been characterised over the past years. Particularly, the crystal structure of Ras^{G12P} was obtained under collaborative work pioneered by our department already in 1993 [259]. Both mutants are revisited within the framework of this thesis because their interesting properties: Ras^{G12P} was found to be the only mutant from G12 with non-transforming properties and Ras$^{G12V/T35S}$ was found to be a partial gain-of-function mutant, capable of activating some signal transduction pathways by interacting with specific effectors such as Raf-RBD but not with others, such as Ral-GDF.

Contrary to the mutational studies presented in section 3.4.2, the two mutants were not created *de novo* at our department, instead, the vectors containing the sequences were kindly provided by the research group of Prof. Dr. Alfred Wittinghofer from Max-Planck Institute for Molecular Physiology, Dortmund. Their conformational equilibria was never investigated in terms of ^{31}P NMR spectroscopy rendering them an interesting case of study, especially Ras$^{G12V/T35S}$, which has a contribution of two opposing mutants (G12V, a gain-of-function and T35S, a partial loss-of-function).

3.4.10.1 ^{31}P NMR GppNHp and GTP Spectra. Raf Interaction and GTPase Activity

The spectral features of Ras^{G12P}•Mg^{2+}•GppNHp are very distinct from the *wild* type protein as one can infer from Figure 3.58A: with exception of $\alpha_{2(T)}$-phosphate that remains unaltered, all other resonances become upfield shifted by an average of δ= -0.17 ppm, the highest deviation being observed for the $\gamma_{2(T)}$-phosphate with a $\Delta\delta$= -0.35 ppm. A concomitant overall line broadening is also observed, especially in the case of state 2(T), (Table 3.25). The ^{31}P NMR spectra of Ras^{G12V} was also investigated for comparison (the mutation was created *de novo* by SDM. Note that this corresponds to the truncated variant (aa 1-166). Again, pronounced shift differences are observed between the two proteins: with exception of the $\gamma_{2(T)}$-phosphate, all the resonances in Ras^{G12V} become downfield shifted by an average of $\Delta\delta$= 0.22 ppm compared with Ras^{G12P}. In this respect, the biggest change is observed for the β-phosphate, with a $\Delta\delta$= 0.43 ppm. On the other hand, the $\gamma_{2(T)}$-phosphate shifts upfield by a $\Delta\delta$ of -0.41 ppm. Together, these differences constitute one of the largest spectral modifications observed so far between two any point mutants and *wild type* variant in the ^{31}P NMR spectra of Ras proteins. Replacing Gly12 by a Pro leads to a modification of the equilibrium constant, K_{12}, from 1.70 to 1.16, respectively. Substitution to

Val leads to a further decrease to K_{12}= 0.84, as the population ratio is inverted and state 1(T) surpasses the population of state 2(T) (Table 3.25).

The ^{31}P NMR spectra of the respective GTP-bound proteins is shown in Figure 3.58B. State 1(T) at the γ-phosphate of Ras^{G12P} cannot be unequivocally identified, although it seems to appear as a very broad shoulder very close to state 2(T) and slightly upfield shifted when compared with Ras^{WT} ($\Delta\delta$= -0.05 ppm, from δ= -2.57 to δ= -2.62 ppm). However, the most striking differences between Ras^{G12P} and Ras^{WT} are in terms of chemical shifts of the β- and $\gamma_{2(T)}$-phosphate groups, the former being upfield shifted and the latter being downfield shifted by $\Delta\delta$= -0.13 (from δ= -0.25 ppm to δ= -0.38 ppm) and a $\Delta\delta$= 0.12 ppm (from δ= -7.98 ppm to δ= -7.86 ppm), respectively, Table 3.25. The GTP spectrum of Ras^{G12V} has also distinct features from those of Ras^{G12P}: a general line broadening is again observed for all resonance lines of the oncogenic mutant and all its three phosphate signals, α-, β- and $\gamma_{2(T)}$ become downfield shifted by a $\Delta\delta$= 0.13, 0.3 and 0.28 ppm, respectively, when compared to Ras^{G12P}. This difference is particularly remarkable for the $\gamma_{2(T)}$-phosphate, assigned at δ= -7.58 ppm in Ras^{G12V} and δ= -7.86 ppm in Ras^{G12P}. In addition, both $\gamma_{2(T)}$-phosphates are downfield shifted when compared with Ras^{WT} (δ= -7.98 ppm). It is also worth mention that the yield of the nucleotide exchange reaction (calculated from the ratio of the areas between GTP-bound and GDP-bound Ras choosing either the α- or β-phosphates) is much higher in the case of Ras^{G12V} (ca. 92%) than in the case of Ras^{G12P} (ca. 65%), which asserts for the different nature of these mutants. It is indeed common for oncogenic variants such as G12V, G12D or G13R to undergo an almost complete (over 90%) exchange to GTP, contrary to non-oncogenic ones, whose degree of exchange is normally much lower (70-75%). This observation precludes the assessment that Ras^{G12P}, contrary to the other, has characteristics of a non-transforming mutation.

To better characterise $Ras^{G12V/T35S}$, the point-mutant Ras^{T35S} was also investigated separately. As it can be directly observed from Figure 3.58A, the GppNHp spectrum of the double mutant resembles directly the one of Ras^{T35S} for whom state 2(T) is completely abolished, in contrast to Ras^{G12V}, where the equilibria between states is still maintained (K_{12}= 0.84). Rather surprisingly, the chemical shift values of the double mutant are numerically closer to the ones of Ras^{G12V} than Ras^{T35S}. For example, the β-phosphate in $Ras^{G12V/T35S}$ lies at δ= 0.08 ppm. The same resonance is observed in Ras^{G12V} at δ= 0.05 ppm and in Ras^{T35S} at δ= -0.33 ppm. This corresponds to a $\Delta\delta$ of 0.05 ppm in the first case and -0.25 ppm in the second case. Based on the fitted values of Table 3.25 similar considerations can be done for the α- and γ-phosphates (both are closer to Ras^{G12V} than Ras^{T35S}.

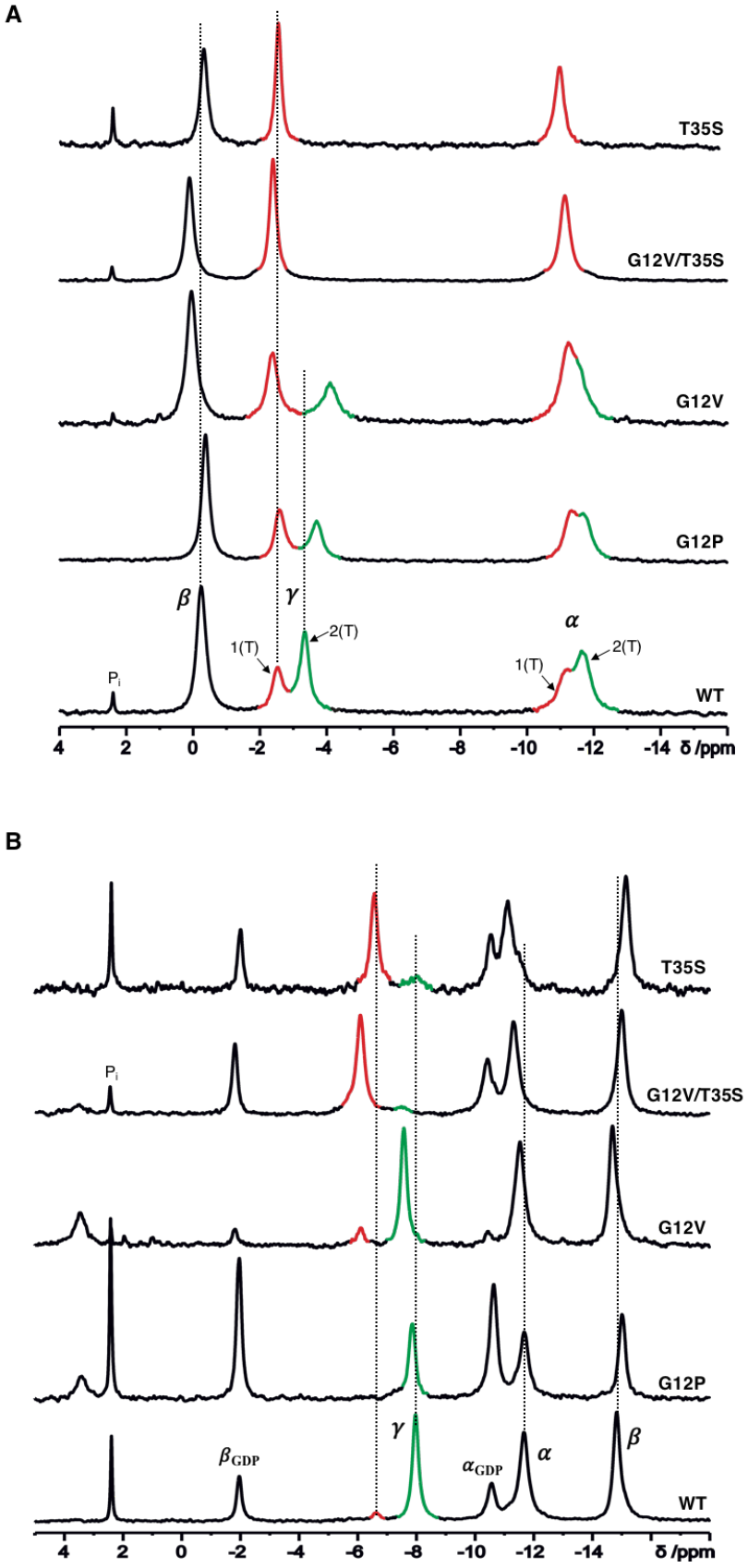

Figure 3.58. Conformational dynamics of Ras^{G12P}, Ras^{G12V}, Ras^{T35S} and $Ras^{G12V/T35S}$ investigated by ^{31}P NMR spectroscopy at 278 K. The proteins were dissolved in buffer F (40 mM Tris/HCl pH 7.5, 10 mM $MgCl_2$, 2 mM DTE) with additionally 0.2 mM DSS and 10% D_2O, at a final concentration ranging between 0.92 and 1.63 mM. The measurements were done for **A.** Ras•Mg^{2+}•GppNHp and **B.** Ras•Mg^{2+}•GTP. All the spectra except Ras^{G12P} were obtained in a magnetic field operating at a ^{31}P resonance of 242.896 MHz (600 MHz spectrometer). Ras^{G21P} was measured at a ^{31}P frequency of 202.456 MHz (500 MHz spectrometer). An EM function with LB= 10 Hz was used during the processing of the FID's. α_{GDP} and β_{GDP} represent the chemical shift of α- and β-phosphate groups of GDP-bound Ras, respectively.

For example, the $\gamma_{1(T)}$-phosphate is located at δ= -2.56 ppm in the serine mutant, δ= -2.38 ppm in the oncogenic mutant and δ= -2.40 ppm in G12V/T35S). The averaged linewidths in $Ras^{G12V/T35S}$ are numerically more similar to Ras^{T35S} due to the lack of exchange broadening processes between states 1(T) and 2(T) in these two mutants, contrary to Ras^{G12V} (Table 3.25).

Similar results can be found when comparing the GTP-bound spectra (Figure 3.58B): $Ras^{G12V/T35S}$ is state 1(T)-driven, just like Ras^{T35S} and in opposition to Ras^{G12V}, which exists predominantly in state 2(T). The respective equilibrium constants are 0.05, 0.13 and 9.38 (Table 3.23). Again, the chemical shift values for the double mutant are closer to the ones of Ras^{G12V} than Ras^{T35S}. For example, the $\gamma_{1(T)}$-phosphate lies at δ= -6.10 ppm in both, G12V/T35S and in G12V and at δ= -6.57 ppm in T35S. An interesting feature can be observed in the spectrum of Ras^{T35S} located at δ= -11.47 ppm as a shoulder on the α-phosphate. The ^{31}P NMR spectra of each protein in complex with Mg^{2+}•GDP is shown in Figure D of the appendix section. Typical chemical shift differences between α- and β-phosphates of different proteins are observed and are in line with the above results for the GppNHp and GTP-bound spectra.

Although biochemical properties of different Ras mutants can be presumed at some extent from the spectral characteristics, general or unanimous correlations cannot be made since conformation is not necessarily linked to a particular function (as seen in the previous case of Ras^{D33K}, a state 2(T) mutant with impaired Raf affinity). In detriment of this idea, Ras^{G12P} and $Ras^{G12V/T35S}$ were investigated in terms of their affinity to Raf-RBD by ITC and in terms of their ability to hydrolyse their natural ligand, GTP, by HPLC.

The obtained results show that Ras^{G12P} has a slightly higher rate of hydrolysis relative to Ras^{WT} (k_{cat}= 0.035 min^{-1} vs 0.026 min^{-1}, respectively, Figure 3.59 and Table 3.26). Two somewhat higher values (k_{cat}= 0.043 and 0.055 min^{-1}) were previously reported in the literature [260, 261], although both values are in agreement within the limits of the error for the present measurement. Addition of effector Raf-RBD does not change significantly the obtained values (k_{cat}= 0.039 min^{-1}, τ= 17.78 min., data not shown). The intrinsic GTPase activity of Ras^{G12P} remains unchanged compared with the *wild type* protein and contrary to a typical oncogenic variant where the same reaction is severely impaired. The three dimensional structure of Ras^{G12P} was found to be very similar to that of *wild type* (pdb entry: 1ago [259]), especially in the vicinity of the catalytic residue Gln61, which accounts for a possible explanation of their similar rate constants. The thermodynamics of binding to Raf shows that the association proceeds as usual with a greater entropic contribution ($-T\Delta S$= -21.2 kJ mol^{-1}, ΔH= -14.4 $\pm$ 0.56 kJ mol^{-1}, Table 3.26). The free energies of binding for Ras^{WT}

and Ras^{G12P} re respectively ΔG= -36.4 and ΔG= -35.6 kJ mol^{-1} and the corresponding dissociation constants are 0.42 ± 0.12 and 0.59 ± 0.12 μM (Table 3.26).

Table 3.25. ^{31}P NMR chemical shift values and linewidths obtained for the different mutants of HRas(1-166).

Protein	α-phosphate $\delta_{1(T)}$ [ppm]	α-phosphate $\delta_{2(T)}$ [ppm]	β-phosphate $\delta_{1(T),2(T)}$ [a] [ppm]	γ-phosphate $\delta_{1(T)}$ [ppm]	γ-phosphate $\delta_{2(T)}$ [ppm]	K_{12} [b]
			Mg^{2+}•GDP			
WT	-10.50		-1.97	--		--
G12P	-10.55		-1.95	--		--
G12V	-10.61		-1.97	--		--
G12V/T35S	-10.40		-1.82	--		--
T35S	-10.53		-2.01	--		--
			Mg^{2+}•GppNHp			
WT	-11.17	-11.68	-0.25	-2.57	-3.33	1.70
G12P	-11.31	-11.69	-0.38	-2.62	-3.68	1.16
G12V	-11.22	-11.57	0.05	-2.38	-4.09	0.84
G12V/T35S	-11.19	--	0.08	-2.40	--	--
T35S	-10.97	--	-0.33	-2.56	--	--
			Mg^{2+}•GTP			
WT	-11.68		-14.87	-6.63	-7.98	11.3
G12P	-11.66		-15.00	--	-7.86	--
G12V	-11.43		-14.70	-6.10	-7.58	9.38
G12V/T35S	-11.33		-15.00	-6.10	-7.48	0.05
T35S	-11.11		-15.14	-6.57	-8.0	0.13
	α-phosphate $\Delta\nu_{1/2\ 1(T)}$ [Hz]	α-phosphate $\Delta\nu_{1/2\ 2(T)}$ [Hz]	β-phosphate $\Delta\nu_{1/2\ 1(T)/2(T)}$ [a] [Hz]	γ-phosphate $\Delta\nu_{1/2\ 1(T)}$ [Hz]	γ-phosphate $\Delta\nu_{1/2\ 2(T)}$ [Hz]	
			Mg^{2+}•GDP			
WT	46.89		30.02	--		
G12P	47.21		35.13	--		
G12V	58.08		32.73	--		
G12V/T35S	89.62		40.84	--		
T35S	69.52		43.70	--		
			Mg^{2+}•GppNHp			
WT	105.39	75.15	45.84	74.47	55.07	
G12P	71.44	88.43	35.66	62.54	91.96	
G12V	122.2	98.84	75.66	91.70	143.3	
G12V/T35S	81.94	--	56.68	51.84	--	
T35S	66.72	--	53.55	40.94	--	
			Mg^{2+}•GTP			
WT	54.74		45.66	20.33	35.44	
G12P	58.04		38.70	--	46.32	
G12V	76.52		62.31	34.79	46.81	
G12V/T35S	78.83		62.02	65.00	58.01	
T35S	50.41		60.66	59.54	67.68	

All the values are fitted from the experimental spectra recorded at 278 K and pH 7.5. The maximum estimated errors are ± 0.02 ppm in chemical shift values and ± 0.15 Hz in linewidths for the γ-phosphate. An EM function with LB= 10 Hz was used for processing the FID.

[a] States 1(T) and 2(T) of the β-phosphate in cannot be separated at the magnetic field used and were therefore fitted as a single Lorentzian line.

[b] The equilibrium constant, K_{12}, was calculated using the population distribution on the γ-phosphate. The associated error is ± 0.2.

From the obtained values it can be hypothesised that the Pro12 mutation does not greatly affect the structural configuration of the effector loop region (aa 32-40) involved in the binding of Raf-RBD since the binding proceeds with the same energetics and affinity as the one observed for Ras^{WT}.

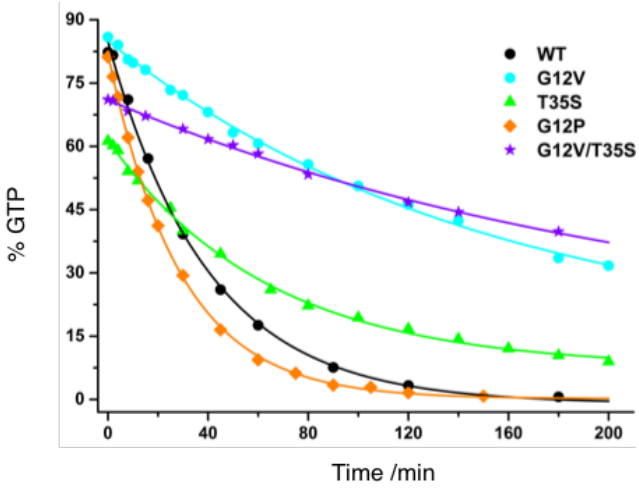

Figure 3.59. Determination of the intrinsic GTPase activity of Ras^{G12P}, Ras^{G12V}, $Ras^{G12V/T35S}$ and Ras^{T35S} by HPLC at 310 K. Upon integration of the fluorescence signal, the percentage of Ras-GTP was plotted against time and the data fitted with a first order exponential decaying function. The fitted rate constants and half-life times are shown in Table 3.26 (see Figure 3.43 for details on the description of the method).

The GTPase activity of the double mutant is extremely slow, proceeding with a k_{cat}= 0.003 min^{-1} and a surprising slow half-life of 208.5 min. (ca. 3 hours). For a better characterisation, the same measurements were conducted in the single mutants Ras^{G12V} and Ras^{T35S} (Table 3.26). By comparison it becomes evident that $Ras^{G12V/T35S}$ follows closely the properties of the oncogenic variant (k_{cat}= 0.005 min^{-1}, τ=136.1 min.), with Ras^{T35S} having a more than 2-fold faster hydrolysis rate (k_{cat}= 0.011 min^{-1}, τ= 61.64 min.). k_{cat} and k_{12} values have been reported elsewhere in the literature for full length (1-188/189) Ras^{G12V} and Ras^{T35S} and are comparable to the ones presently obtained for the truncated (1-166) forms [67, 262].

The affinity of $Ras^{G12VT35S}$ towards Raf-RBD is more than 15 times lower than Ras^{WT} (k_D= 13.52 ± 2.7 μM vs 0.42 ± 0.1 μM) and more than 2 times lower than Ras^{T35S} (K_D= 6.45 ± 1.2 μM, Table 3.26). Both point-mutants separately have a lower affinity than the *wild type* protein. However, their combination into the double mutant seems to have a synergistic effect that leads to a further decreased affinity for the effector. The enthalpy variation, ΔH, is -4.38 ± 0.2 kJ mol^{-1}, a value three times lower than the one obtained for Ras^{T35S} and Ras^{G12V} separately. The binding proceeds with a similar free energy variation for all proteins, possibly due to an entropic compensation (the reader is advised for the fact that only ΔH is explicitly calculated form the experimental data, therefore, the global ΔG values might not reflect the energetic reality of the binding process; experimental section 2.2.4).

Table 3.26. Thermodynamics of interaction between HRas•Mg^{2+}•GppNHp and Raf-RBD measured by ITC and intrinsic GTPase activities measured by HPLC for HRas•Mg^{2+}•GTP.

Protein	T K	[Ras] mM	[Raf] mM	ΔG kJ mol^{-1}	ΔH kJ mol^{-1}]	$-T\Delta S$ kJ mol^{-1}	K_D μM	T K	k_{cat} min^{-1}	τ min.
$HRas^{WT}$	298	60	778	-36.4	-8.10 ± 0.23	-28.3	0.424 ± 0.12	310	0.026	26.85
$HRas^{G12P}$	298	31	312	-35.6	-14.4 ± 0.56	-21.2	0.591 ± 0.12	310	0.035	20.01
$HRas^{G12V/T35S}$	298	107	1730	-27.8	-4.38 ± 0.24	-23.4	13.52 ± 2.69	310	0.003	208.5
$HRas^{T35S}$	298	51	850	-29.7	-13.3 ± 0.66	-16.3	6.45 ± 1.20	310	0.011	61.64
$HRas^{G12V}$	298	85	836	-35.3	-13.5 ± 0.41	-21.9	0.66 ± 0.15	310	0.005	136.1

k_{cat} represents the hydrolysis rate constant and is calculated as 1/t. τ represents the half-life for the GTP hydrolysis (τ=t*ln2). ITC experiments were done according to the experimental section 2.2.4. The experimentally obtained thermograms and signature plots are shown in Figure F of the appendix section. The *N* parameter (binding sites) was allowed to vary during the fitting procedure. The greatest deviation from a 1:1 ratio was obtained for $Ras^{G12V/T35S}$ with *N*= 1 ± 0.14. The error on all the other measurements was always smaller than ± 0.2.

3.4.10.2 Interaction Between $HRas^{G12P}$•Mg^{2+}•GppNHp and Raf-RBD

As already revealed by ITC, the thermodynamics of binding between Ras^{G12P} and Raf-RBD was found to be very similar to the *wild type* protein. The same interaction was investigated by ^{31}P NMR. As usual, addition of increasing amounts of effector leads to the modification of the initial equilibria by promoting a conformational transition of the initial population defined by the state 1(T) (red coloured lines) into state 2(T) (green coloured lines) and subsequent formation of the Ras-Raf complex indicated by the typical upfield shift of state 2(T) that culminates with the formation of state 2*(T) at the γ-phosphate (Figure 3.60). The concomitant shift change is from δ= -3.68 ppm (1:0 ratio) up to δ= -3.90 ppm (Δδ= -0.22 ppm, Table 3.27). The same spectral features and evolution of chemical shifts were found during the titration of $KRas^{WT}$ and $HRas^{H27E}$, (Figures 3.1 and 3.49) but not $HRas^{D33K}$ (Figure 3.50), whose association with the effector is lower than *wild type*. The β-phosphate was fitted with a single Lorentzian line across the titration series although it would be probably best characterised by a two-line fitting, as previously performed for Ras^{H27E} (Figure 3.49, Table 3.19).

The linewidth of the β-phosphate increases from $\nu_{1/2}$= 36.51 Hz to $\nu_{1/2}$= 81.68 Hz at a protein ratio of 1:1. This corresponds to a to a 2.25-fold increase, which is somewhat larger than expected, according to the molecular mass of the protein-protein complex (from 1:0 to 1:1 ratio the increase of the molecular mass should be only 1.52-fold). Therefore, the β-phosphate is further broadened by exchange processes which makes it difficult to distinguish between the free and the bound Ras protein.

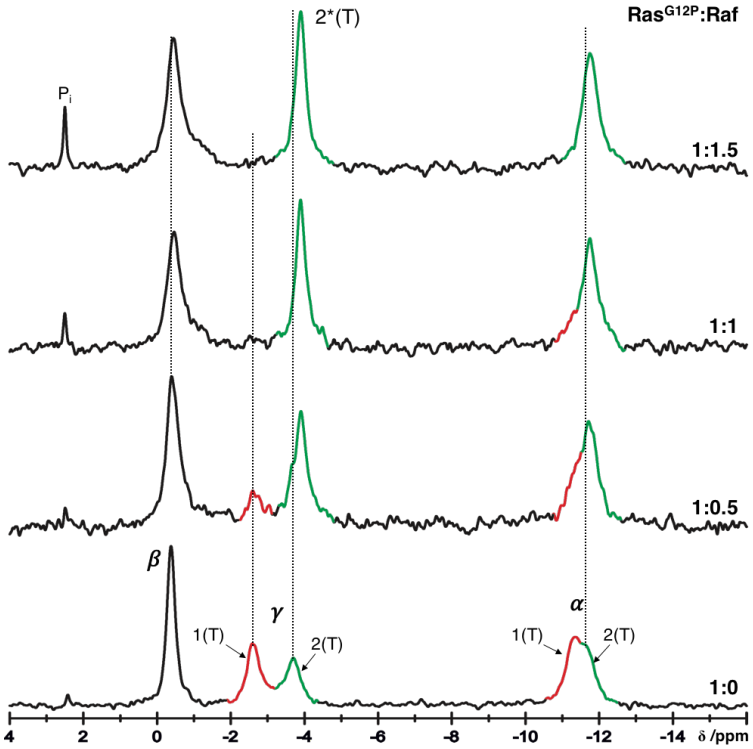

Figure 3.60. ^{31}P NMR spectroscopy on the titration of HRas^{G12P}•Mg^{2+}•GppNHp with the effector Raf-RBD measured at 278 K. To an initial 0.74 mM solution of Ras^{G12P} dissolved in buffer F (40 mM Tris/HCl pH 7.5, 10 mM $MgCl_2$, 2 mM DTE) with additionally 0.2 mM DSS, 150 mM NaCl and 5% D_2O, increasing amounts of Raf-RBD were added. The molar ratio is indicated for each titration step. The final concentrations of Ras and Raf (1:1.5 ratio) are 0.58 mM and 0.92 mM, respectively. All ^{31}P resonances were recorded at a frequency of 202.456 MHz (500 MHz spectrometer). An EM function with LB= 15 Hz was applied during the processing of the FID.

Table 3.27. ^{31}P NMR chemical shift values and linewidths for the protein-protein complex HRas^{G12P}(1-166)•Mg^{2+}•GppNHp•Raf-RBD.

Protein Complex	ratio	α-phosphate		β-phosphate[a]	γ-phosphate	
		$\delta_{1(T)}$ [ppm]	$\delta_{2(T)}$ [ppm]	$\delta_{1(T)/2(T)}$ [ppm]	$\delta_{1(T)}$ [ppm]	$\delta_{2(T)}$ [ppm]
Ras^{G12P}	--	-11.31	-11.69	-0.37	-2.62	-3.68
+ Raf-RBD	1:0.5	-11.45	-11.77	-0.43	-2.64	-3.90
	1:1	-11.55	-11.77	-0.47	--	-3.90
	1:1.5	--	-11.77	-0.47	--	-3.90
		α-phosphate		**β-phosphate[a]**	**γ-phosphate**	
		$\Delta\nu_{1/2\ 1(T)}$ [Hz]	$\Delta\nu_{1/2\ 2(T)}$ [Hz]	$\Delta\nu_{1/21(T),2(T)}$ [Hz]	$\Delta\nu_{1/2\ 1(T)}$ [Hz]	$\Delta\nu_{1/2\ 2(T)}$ [Hz]
Ras^{G12P}	--	80.46	73.60	36.51	67.12	81.58
+ Raf-RBD	1:0.5	141.0	70.97	68.19	96.70	76.54
	1:1	96.35	77.04	81.68	--	52.13
	1:1.5	--	87.45	88.24	--	53.51

All the values are fitted from the experimental spectra recorded at 278 K, pH 7.5. The maximum estimated errors from the fitting procedure are ± 0.02 ppm in chemical shift values and ± 0.16 Hz in linewidths for the γ-phosphate. An EM function with LB=15 Hz was used in the processing of the FID and subtracted from the final linewidths.

3.4.10.3 Interaction Between HRas^{G12P}•Mg^{2+}•GppNHp and NF1

The lack of oncogenicity of Ras^{G12P} is likely related to its normal GTPase activity. Kinetic parameters reported in literature are very similar to Ras^{WT} in terms of k_{on}, k_{off} nucleotide rate constants and effector and GAP association affinities [259]. The interaction of this mutant with NF1 was investigated here by ^{31}P NMR. Due to the larger chemical shift separation between states 1(T) and 2(T) at the γ-phosphate in Ras^{G12P} compared to Ras^{WT} (the distance between both states, $\Delta\delta = \delta_{2(T)} - \delta_{1(T)}$, is 2.52 ppm and 1.63 ppm, respectively, Figure 3.61 and Table 3.28), the characterization of state 3(T) by deconvolution of the partially superimposed ^{31}P NMR lines was easier to perform.

As expected, the overall titration series shown in Figure 3.61 is very similar to the one obtained for the *wild type* protein: the new resonance line of state 3(T) appears as soon as NF1 is added to the NMR tube and its integrated area increases as the Ras:NF1 ratio increases. Its chemical shift position is independent of the concentration of NF1 and is slightly upfield shifted ($\Delta\delta$= 0.22 ppm) when compared to the same state 3(T) in the titration series of Ras^{WT} ($\delta_{3(T)\ /G12P}$= -3.22 ppm vs $\delta_{3(T)\ /WT}$= -3.00 ppm, section 3.4.1.2, Figure 3.39), possibly due to the intrinsically different chemical environment of the γ-phosphate prompted by the presence of the P12 mutation. Between Ras^{G12P} free and the last titration step at 1:1 ratio, the increase of linewidth is only of 1.7-fold as measured at the γ-phosphate (from a $\Delta\nu_{1/2}$= 92.32 to 117.8 Hz), which is only half of the expected increase in linewidth since the molecular mass of the protein complex is 3-fold higher than Ras alone. Since the dynamics of the γ-phosphate in Ras^{G12P} is different than Ras^{WT} (different K_{12} and $\Delta\nu_{1/2}$ values), it is likely that state 3(T) in the Ras^{G12P}•NF1 is exchange broadened by states 1(T) and 2(T). It is also observed that the chemical shift value of these states remains unperturbed over the course of the titration ($\delta_{1(T)} \approx$ -2.62 ppm and $\delta_{2(T)} \approx$ -3.72 ppm, Table 3.28), indicating that the interaction still follows a slow exchange mechanism in the NMR time scale.

The same dynamic features are observed in the case of the α-phosphate, although the deconvolution of the third state is more difficult due to the closer proximity of the NMR lines. Again, states 1(T) and 2(T) do not seem to shift significantly during the titration (Table 3.28, note that the error in the chemical shift determination of sates 1(T) and 2(T) for the α-phosphate is much larger than the one obtained for the γ-phosphate, ±0.08 ppm vs ±0.01 ppm, respectively). The chemical shift position of state 3(T) could only be unequivocally determined at the molar ratio of 1:1 and was found to be δ= -11.15 ppm. A similar value of δ= -11.12 ppm was found in the titration of Ras^{WT} (Table 3.12). The binding of Ras to NF1 originates a severe perturbation in the chemical environment of the β-phosphate: as the

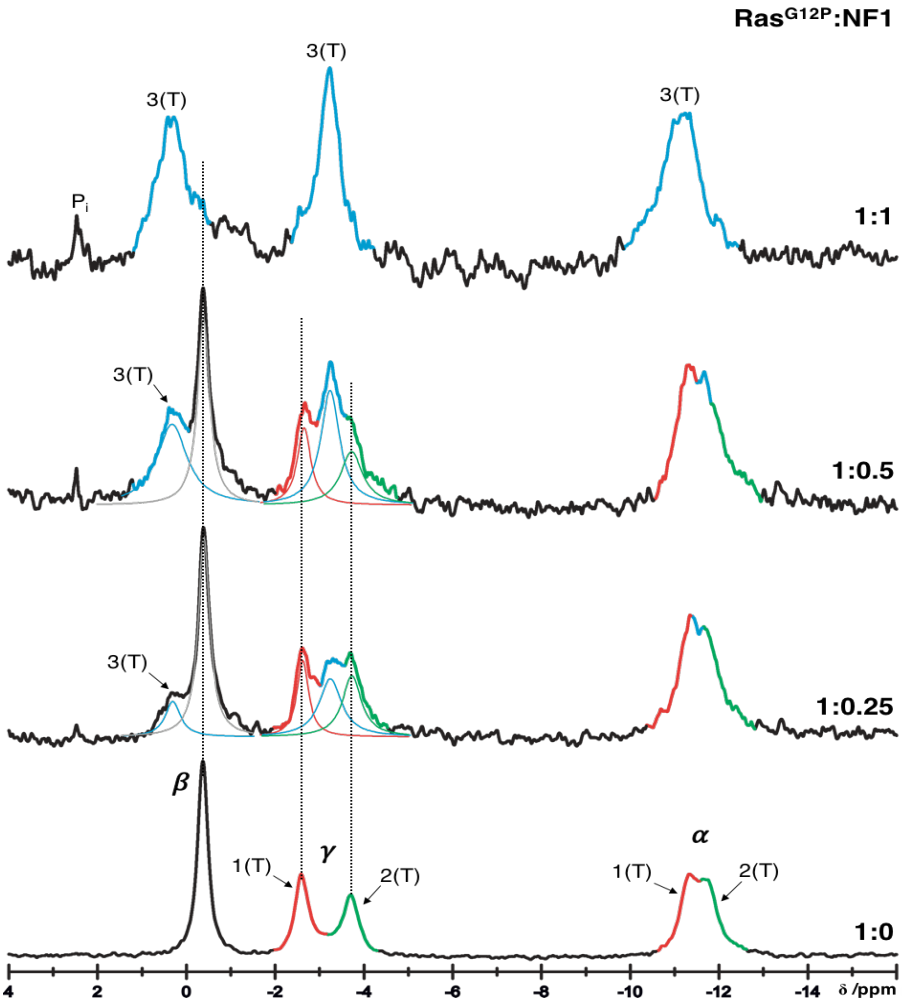

Figure 3.61. Protein complex formation between Ras^{G12P}•Mg^{2+}•GppNHp and NF1 followed by ^{31}P NMR spectroscopy at 278 K. To an initial 0.82 mM of Ras dissolved in buffer F (40 mM Tris/HCl pH 7.5; 10 mM $MgCl_2$; 2 mM DTE) with additionally 150 mM NaCl, 0.2 mM DSS in 10% D_2O, increasing amounts of the GAP protein NF1 (from a 0.71 mM stock solution) were added (the corresponding molar ratios for each step are presented). The concentrations of Ras and NF1 in the final step (1:1 ratio) are 0.30 mM and 0.29 mM, respectively. An EM filter with LB=15 Hz was applied to the processed FID. The number of scans was increased over the course of the titration, from 3000 in the first step, to 11000 in the last step. The resonance lines corresponding to the α-, β- and γ-phosphates are indicated as well as the states 1(T) and 2(T), represented by the red and green coloured lines, respectively. The new spectral features observed from the addition of NF1 to Ras are coloured in blue. As an example, the deconvolution into separated Lorentzian lines is shown for two different titration steps (1:0.25 and 1:0.5) on the γ-phosphate.

main line (corresponding to $[Ras]_{free}$) decreases, a new very broad line appears at the left side, whose area increases as the concentration of NF1 increases (Figure 3.61). This new line could be ascribed to the Ras-NF1 ([RNF1]) complex, although additional contributions might be lying underneath its broad shape.

At a protein ratio of 1:1 almost completely saturation is achieved (Figure 3.61). This is marked by three single broad peaks at the α- , β- and γ-phosphates, respectively, and by the disappearance of the former states 1(T) and 2(T). The very broad nature of the β-

phosphate ($\Delta\nu_{1/2}$= 196.7 Hz) indicates that at least two different conformations with distinct chemical environments in its vicinity might be present when the Ras-NF1 complex is formed, as already observed in the case of the Ras^{WT}-NF1 complex.

Table 3.28. ^{31}P NMR chemical shift values and linewidths for the protein-protein complex $HRas^{G12P}$(1-166)•Mg^{2+}•GppNHp•NF1.

Protein complex	Ras:NF1 ratio	α-phosphate			β-phosphate		γ-phosphate		
		$\delta_{1(T)}$ [ppm]	$\delta_{3(T)}$ [ppm]	$\delta_{2(T)}$ [ppm]	δ^a [ppm]	$\delta_{3(T)}$ [ppm]	$\delta_{1(T)}$ [ppm]	$\delta_{3(T)}$ [ppm]	$\delta_{2(T)}$ [ppm]
$HRas^{G12P}$	--	-11.32	--	-11.73	-0.37	--	-2.60	--	-3.70
+NF1	1:0.25	-11.31	--[b]	-11.73	-0.39	0.31	-2.62	-3.24	-3.73
	1:0.5	-11.25	--[b]	-11.71	-0.39	0.31	-2.64	-3.24	-3.72
	1:1	--	-11.15	--	-0.40	0.31	--	-3.22	
		α-phosphate			β-phosphate		γ-phosphate		
		$\Delta\nu_{1/2,1(T)}$ [Hz]	$\Delta\nu_{1/2,3(T)}$ [Hz]	$\Delta\nu_{1/2\ 2(T)}$ [Hz]	$\Delta\nu_{1/2}{}^a$ [Hz]	$\Delta\nu_{1/2,3(T)}$ [Hz]	$\Delta\nu_{1/2\ 1(T)}$ [Hz]	$\Delta\nu_{1/2,3(T)}$ [Hz]	$\Delta\nu_{1/2,2(T)}$ [Hz]
$HRas^{G12P}$	--	76.80	--	115.0	50.20	--	76.22	--	92.32
+NF1	1:0.25	101.3	--[b]	164.4	61.32	87.47	61.80	133.4	110.7
	1:0.5	79.11	--[b]	183.1	65.64	186.1	74.81	109.8	131.0
	1:1	--	204.5	--	--	196.7	--	117.8	--

All the values are fitted from the experimental spectra recorded at 278 K, pH 7.5. The maximum estimated errors from the fitting procedure are ± 0.02 ppm in chemical shift values and ± 0.11 Hz in linewidths for the γ-phosphate. ^{31}P data were recorded at a frequency of 242.896 MHz. An EM function with LB= 15 Hz was used in the processing of the FID and subtracted afterwards from the final fitted linewidth values.

[a] States 1(T) and 2(T) of the β-phosphate cannot be separated at the magnetic field used and were therefore fitted as a single Lorentzian line.

[b] State 3(T) of α-phosphate could not be fitted independently of states 1(T) and 2(T) at the indicated molar ratio.

3.4.10.4 Interaction Between $HRas^{G12V/T35S}$•Mg^{2+}•GppNHp and Raf-RBD

The interaction between $Ras^{G12V/T35S}$ and Raf-RBD was already surveyed by ITC within the framework of this thesis. The obtained K_D value of 13.52 μM (Table 3.26) led to the conclusion that this mutant binds the effector with much lower affinity than the *wild type* protein. Due to its interesting nature, a ^{31}P NMR titration using the same effector was envisaged. The spectral series are shown in Figure 3.62 and can be interpreted as follows: as Raf is added to Ras, the population of the initially predominant state 1(T) is converted into the effector recognizing state 2(T). The process can be identified by the decrease of the integrated area of state 1(T) and concomitant increase in the area of the new state 2(T), both being directly dependent of the concentration of Raf added at each step. An upfield shift of state 1(T) is observed from, δ= -2.37 ppm to ca. δ= -2.60 ppm ($\Delta\delta$= -0.23 ppm, note that in the final titration steps, its centre is not well defined due to its broad nature and the chemical shift values listed in Table 3.29 are just an approximation). A shift in the same

direction is also observed for the $\alpha_{1(T)}$ and $\beta_{1(T)}$-phosphates, albeit less pronounced ($\Delta\delta \approx$ -0.05 ppm). The chemical shift of state 2(T) at the γ-phosphate is δ= -4.18 ppm and independent of the concentration of Raf added.The corresponding chemical shift values in the titration of Ras^{WT} and Ras^{H27E} are δ= -3.60 ppm [117] and δ= -3.54 ppm (Table 3.19), respectively. In the case of $Ras^{G12V/T35S}$ the initial state 2(T) is not defined and therefore it is assumed that the observed state 2(T) represented by the green coloured line that rises along the titration in Figure 3.62 is in fact state 2*(T). Based on this assumption, both, the red and green coloured resonance lines at the γ-phosphate represent respectively the Ras-free and the Ras-bound complexes. From their integrated areas it is possible to obtain the dissociation constant for the complex at any given ratio. The calculations led to an averaged apparent K_D of 0.1 mM, which is one order of magnitude higher than the value obtained from ITC (13.52 μM). The mismatch in the obtained values between both techniques is expected as the concentrations used in NMR are much higher than the typical K_D interval for the interaction (low hundreds in the nM range).

Table 3.29. ^{31}P NMR chemical shift values and linewidths for the protein-protein complex $HRas^{G12V/T35S}$(1-166)•Mg^{2+}•GppNHp•Raf-RBD.

Protein complex	ratio	α-phosphate		β-phosphate		γ-phosphate	
		$\delta_{1(T)}$ [ppm]	$\delta_{2(T)}$ [ppm]	$\delta_{1(T)}$ [ppm]	$\delta_{2(T)}$ [ppm]	$\delta_{1(T)}$ [ppm]	$\delta_{2(T)}$ [ppm]
$Ras^{G12V/T35S}$		-11.13	--	0.12		-2.37	--
+ Raf-RBD	1:0.25	-11.12	-11.72	0.12[a]		-2.36	-4.17
	1:0.5	-11.12	-11.58	0.12	-0.20	-2.40	-4.17
	1:1	-11.14	-11.57	0.07	-0.26	-2.50	-4.17
	1:1.25	-11.16[b]	-11.58	0.08	-0.23	-2.60[b]	-4.17
	1:1.5	-11.16[b]	-11.58	0.08	-0.23	-2.66[b]	-4.18
		α-phosphate		**β-phosphate**		**γ-phosphate**	
		$\Delta\nu_{1/2\ 1(T)}$ [Hz]	$\Delta\nu_{1/2\ 2(T)}$ [Hz]	$\Delta\nu_{1/2\ 1(T)}$ [Hz]	$\Delta\nu_{1/2\ 2(T)}$ [Hz]	$\Delta\nu_{1/2\ 1(T)}$ [Hz]	$\Delta\nu_{1/2\ 2(T)}$ [Hz]
$Ras^{G12V/T35S}$		73.82	--	53.44		47.49	--
+ Raf-RBD	1:0.25	90.46	111.5	67.23[a]		53.00	113.6
	1:0.5	117.4	109.0	67.29	109.0	57.43	121.1
	1:1	169.5	179.4	91.82	152.7	131.3	126.2
	1:1.25	128.2	129.8	91.55	107.2	198.0	118.9
	1:1.5	115.9	149.1	73.07	123.3	253.1	138.6

All the values are fitted from the experimental spectra recorded at 278 K, pH 7.5. The maximum estimated errors from the fitting procedure are ± 0.02 ppm in chemical shift values and ± 0.16 Hz in linewidths for the γ-phosphate. An EM function with LB= 10 Hz was used in the processing of the FID. Data were recorded at 242.896 MHz.

[a] States 1(T) and 2(T) of the β-phosphate cannot be separated at the magnetic field used and were therefore fitted as a single Lorentzian line.

[b] The centre of the peak is not well defined enough to allow an accurate fitting. The listed value is a very rough estimation.

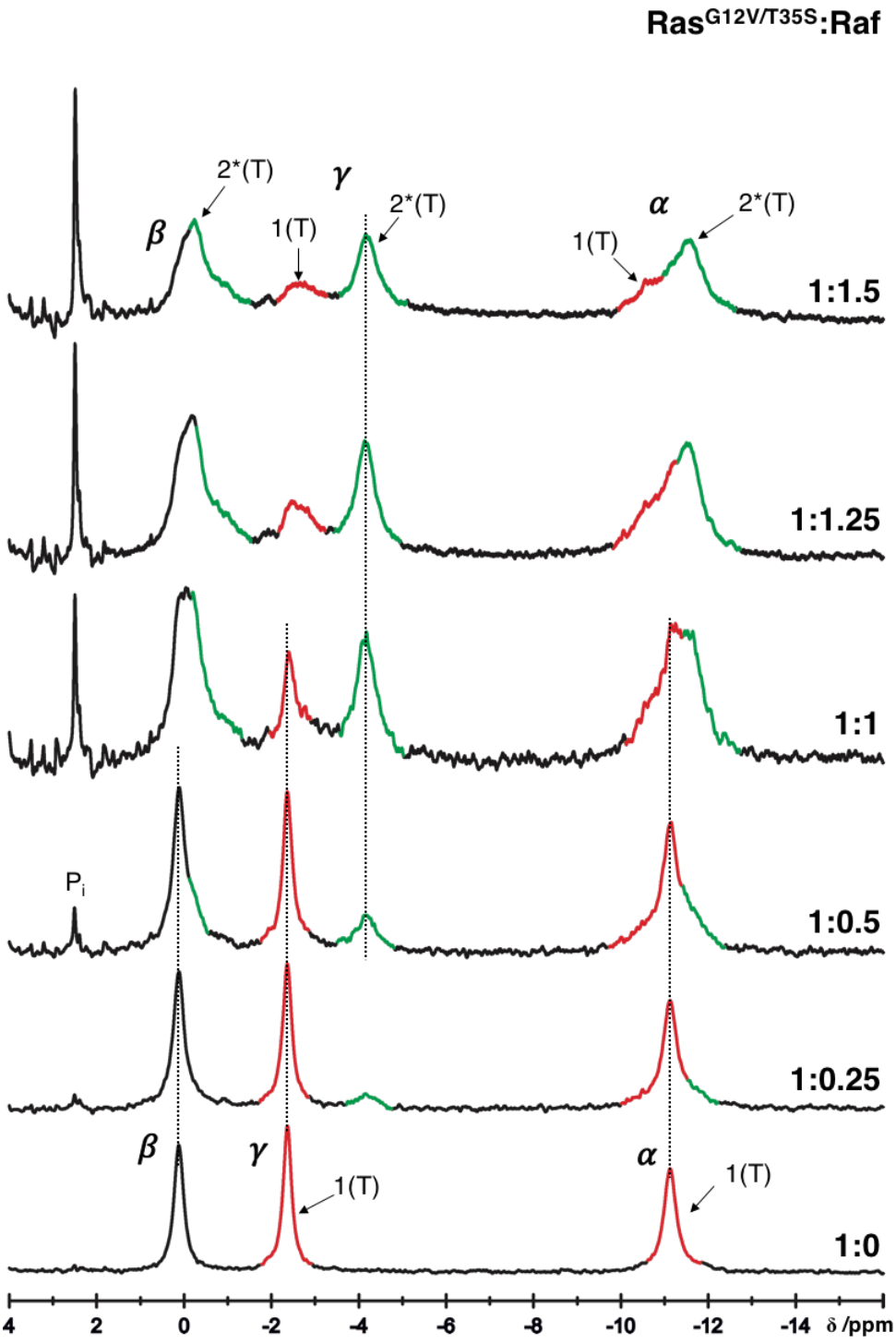

Figure 3.62. ^{31}P NMR spectroscopy on the titration of HRas$^{G12V/T35S}$•Mg^{2+}•GppNHp with the effector Raf-RBD measured at 278 K. To an initial 1.09 mM solution of Ras$^{G12V/T35S}$ dissolved in buffer F (40 mM Tris/HCl pH 7.5, 10 mM $MgCl_2$, 2 mM DTE) with additionally 0.2 mM DSS, 150 mM NaCl and 10% D_2O, increasing amounts of Raf-RBD were added. The molar ratio is indicated for each titration step. The final concentrations of Ras and Raf (1:1.5 ratio) are 0.75 mM and 1.5 mM, respectively. All ^{31}P resonances were recorded at a frequency of 242.896 MHz (600 MHz spectrometer). The number of scans was increased from 2000 (first step) up to 16000 (last step). An EM window with LB= 10 Hz was applied during the processing of the FID.

3.5 High Pressure Macromolecular Crystallography (HPMX)

The crystallographic work presented herein is a collaboration with Nathalie Colloc'h, Eric Girard, Anne-Claire Dhaussy and Thierry Prangé. The individual contribution from the author of the present thesis to the project relied in protein crystallisation and data acquisition. All structure refinements, b-factor calculations and compressibility curves that originated the final results were kindly provided and analysed according to the expertise of the team of crystallographers.

3.5.1 Crystal Structure of Ras^{WT}(1-166)•Mg^{2+}•GppNHp at Ambient Pressure

There are many crystal structures of Ras^{WT} deposited on the pdb database solved at low (~ 278 K) or at cryogenic temperatures (most of them at 100 K or bellow). However, since all the HPMX data were collected at RT, the structure of Ras^{WT} was firstly determined in the same conditions and sample environment (loading into the DAC, beam alignment, etc.). The final refined structure was obtained at a resolution of 1.8 Å and serves as a control experiment necessary to provide meaningful relationships and to minimise any instrumental discrepancies between conventional and HP crystallography.

The ambient pressure (corresponding to 0.1 MPa, abbreviated as pamb), RT structure is shown in Figure 3.63 (coloured in cyan), and a comparison with the representative structure of GppNHp-bound Ras from Pai et al. is made (coloured in grey, pdb: 5p21, [12]). 5p21 was obtained at 277 K, whereas this one was obtained in the 293-298 K interval. Both crystallise under the same trigonal space group $P3_221$ and are essentially identical, with a perfect superposition for all the helixes and β-sheets that are in a distal position relative to the nucleotide (α_5, β_1, β_2, β_3). Some residues shown at the surface and nearby the C-terminal region have slightly different rotation angles (Figure 3.63A, R128, R135 and H166). The only noticeable differences occur always in loops and at the helix α_2 (aa 66-74). As can be seen from Figure 3.63B and C (left side), helix α_2 from 5p21 is spatially closer to helix α_3 than the corresponding one in the structure obtained at RT. In the latter, the helix α_2 is pushed upward (indicated by the arrow in Figure 3.63C) and becomes slightly displaced away from helix α_3. The maximum separation between the two α_2 helixes on the two structures measured at any two corresponding Cα's is ca. 2.0 Å.

The remaining residues that comprise switch 2 and switch 1 align very well respective to their counterparts, with only minor deviations that can be assigned to a different spatial orientation of specific residues resulting from their multiple rotational degrees of freedom.

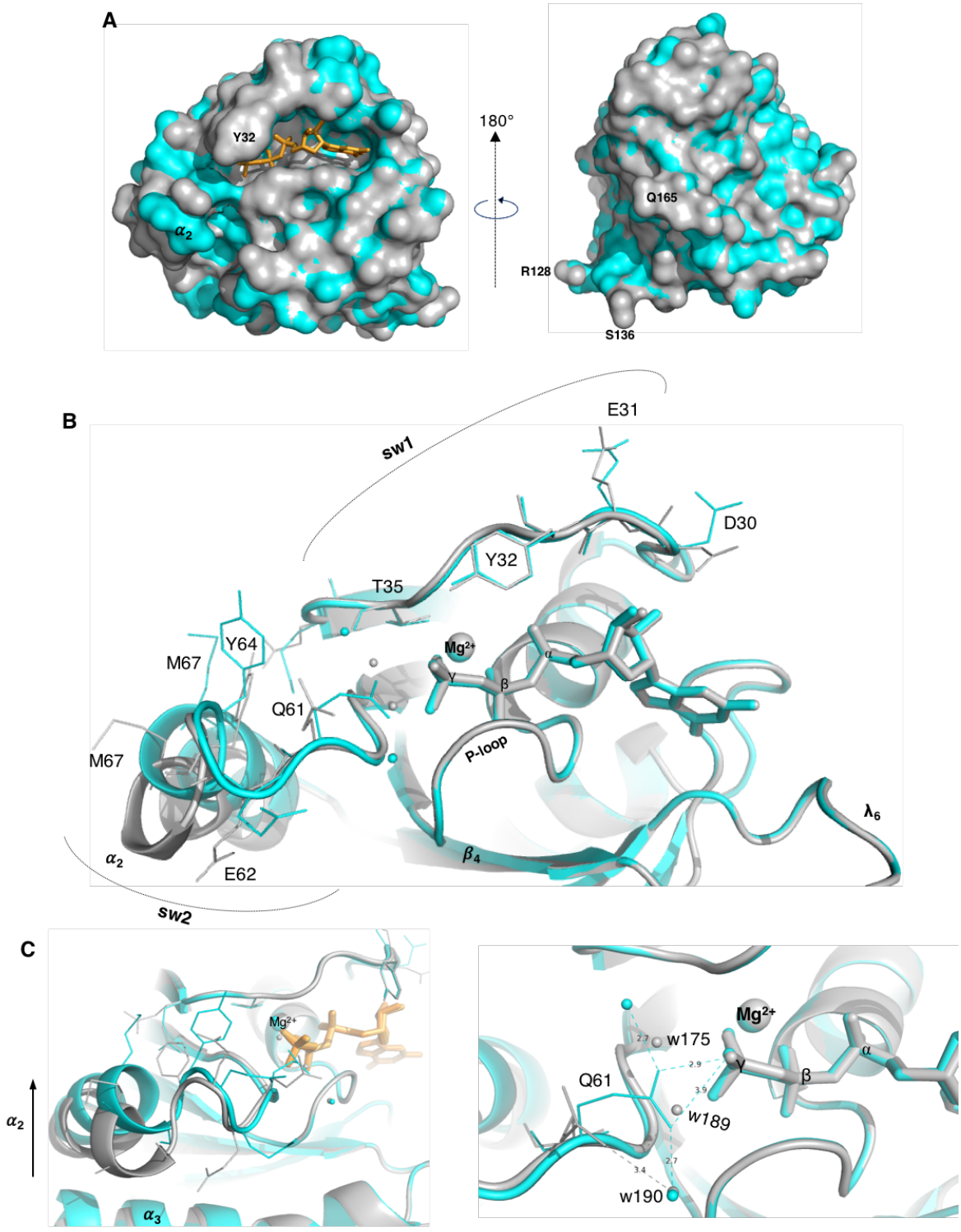

Figure 3.63. Refined crystal structure of $HRas^{WT}$(1-166)•Mg^{2+}•GppNHp obtained at ambient pressure and room temperature (coloured in cyan) and comparison with one of the representative structures from Pai et al [12], pdb: 5p21, recorded at 277 K (coloured in grey). Both structures are superimposed. **A.** Surface representation evidencing some residues at the C-terminal that show different orientations due to rotational movement (R128, S136, Q165). **B.** Structural details around the nucleotide binding site. The residues that show a significantly different degree of rotation between both structures are represented as thin lines (D30, E31, Y32 in switch 1 and Q61, E62, E63, Y64, M67 in switch 2). **C.** The small but significant upward movement of the helix α_2 of switch 2 in the RT structure obtained in this work compared to 5p21 is evidenced (left side). At the right side, details of the catalytic waters are evidenced: the catalytic water (w175) and the nearby w189, from 5p21 are shown as small spheres. In comparison, no equivalent waters could be found in the electron density map of the RT structure. Instead, their role is replaced by the terminal extremity of Q61 that moves closer to the γ-phosphate. As consequence, the H-bonding network between both structures is slightly different.

This effect can be observed for D30 and E31 in switch 1 and for Q61, E62, E63, Y64 and M67 in switch 2.

The two structures show also differences in terms of trapped waters at the catalytic centre: the catalytic water, known for initiating the nucleophilic attack to the γ-phosphate during the GTPase reaction is named w175 in the 5p21 structure and is coordinated to the γ-phosphate, T35, G60 and to another nearby water named w189 in a tetragonal geometry (Figure 3.63C right side). None of them could be found in the RT structure. As result, the H-bond network is slightly different and leads to the movement of Q61 closer to the γ-phosphate, allowing the NH side chain of this residue to be at a distance of 3.0 Å from the γ-phosphate (the corresponding residue is more than 8 Å away in 5p21), establishing therefore a direct contact with it. An identical orientation of Q61 is observed in both, the Ras-GAP (pdb: 1wq1 [83]) and the Ras-SOS (pdb: 1nvw, [45]) complexes, where none of the two crucial waters (w175 and w189) can be found. These differences in the number of waters can also be extended to the complete unit cell: the RT crystal has much less crystallographic waters than 5p21. A possible reason can be related with different degrees of hydration due to different contents of PEG in the crystals (32% in the present work. The PEG content of 5p21 is not expressly mentioned in the published paper).

- This page was deliberately left blank -

3.5.2 Crystal Structure of $Ras^{WT}(1\text{-}166)\bullet Mg^{2+}\bullet$GppNHp at High Pressure

A total of four datasets were obtained:

- 200 MPa, resolution of 1.9 Å
- 270 MPa, resolution of 2.0 Å
- 490 MPa, resolution of 1.85 Å
- 650 MPa, resolution of 1.70 Å

During the experimental elaboration of this work it was directly verified that an important factor regarding the pressure response of the crystals was the incubation time at certain pressure values. When a continuously ramping was performed from 0.1 MPa up to above 270 MPa, with no waiting time for the accommodation of the crystal to high pressures, diffraction was completely lost. In fact, good Bragg reflections at the two last recorded points (490 MPa and 650 MPa) could only be gathered upon an overnight incubation around 200 MPa. From these results, it was possible to conclude that a slow adaptation to high pressure was necessary, suggesting the existence of a slow conformational modification taking place in the range of 200-270 MPa.

3.5.2.1 Analysis of the Compressibility Curve

A transition to a new conformation was also verified by the analysis of the compressibility curve (the metric dependency of the crystal cell parameters with the applied thrust) [180] and indicated that the unit cell volume decreases linearly with pressure, down to 3.6%, measured at 270 MPa relative to ambient pressure (Figure 3.64). Above this point an unusual expansion of 0.6% was observed, from 270 MPa to 490 MPa. At the maximum pressure recorded of 650 MPa, for which a complete crystallographic dataset was obtained, the calculated increase in volume relative to 270 MPa was 0.75%. At even higher pressures, the volume of the cell was reduced again and diffraction degraded rapidly (resolution of 3.6 Å at 850 MPa), rendering impossible the obtention of a full dataset. At low pressure (between 20 and 150 MPa) it was decided to collect only a few reflections,

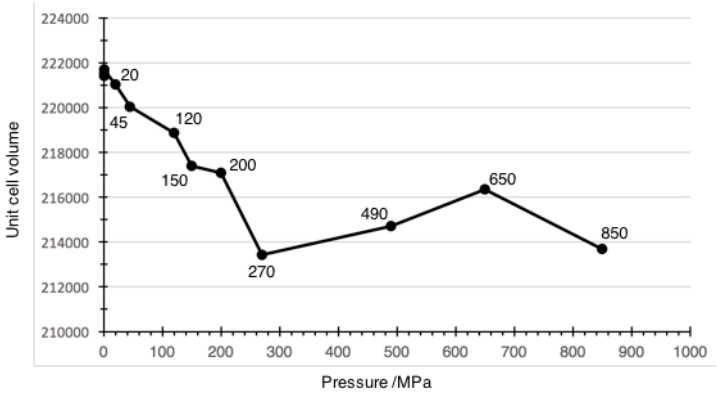

Figure 3.64. Compressibility curve obtained for the HP series on $HRas^{WT}(1\text{-}166)\bullet Mg^{2+}\bullet$GppNHp at RT. The volume of the unit cell (shown in $Å^3$) is plotted as a function of pressure. Only four complete data sets were recorded at 200, 270, 490 and 650 MPa. For the lower pressure points it was chosen to collect only a few frames. At 850 MPa the crystal degraded very rapidly.

enough to characterise the unit cell, but not complete datasets due to user time limitations at the synchrotron beamlines. Data acquisition in this range was also avoided because the accurate measurement of the pressure in the DAC is difficult at low pressures (between a few tens of MPa, up to ca. 120 MPa). The pressure uncertainty of a crystal mounted at 100 MPa is ± 20 MPa. Pressure increases in the DAC as the thickness of the metallic gasket (a thin foil) decreases. For an increase of 100 MPa, this reduction is typically less than 10 μm and difficult to measure precisely by the separation of the Fluoresceence emission lines of a Ruby chip [178, 240]. The movement of the piston located on the DAC through which thrust is transmitted is also non-linear due to mechanical constrains and aggravates further this uncertainty [178, 229]. The problem is alleviated at higher pressures, especially above 200 MPa, where the thrust can be steadily maintained with minimal oscillations (after overnight incubation at 250 MPa, the oscillation was typically ±15 MPa).

From Figure 3.64 it can be taken that the transition zone for the conformational modification occurs slightly above 270 MPa, probably around 300-400 MPa. This is also concluded by the increase in the quality of the diffraction, as revealed by the resolution limits which are 1.75 Å at 0.1 MPa, 1.9 Å at 200 MPa, 2.0 Å at 270 MPa and increase afterwards to 1.85 Å and 1.70 Å at 490 and 650 MPa, respectively. The number of visible waters in the electron density maps follows the same trend, with 112, 85, 58, 108 and 167 molecules at 0.1, 200, 270, 490 and 650 MPa, respectively.

3.5.2.2 Analysis of rmsd and b-factor Values

Global Differences

The crystal structures refined at HP are shown in Figure 3.65. Additional details of the Mg^{2+} ion coordination environment are shown in Figure G of the appendix section. By doing a sequence alignment followed by a structural superposition using the Pymol® software, it was found that only minor changes are observed in terms of reorientation of the protein backbone at different pressures. The helixes α_1, α_3 and α_4 are perfectly aligned. The most noticeable differences occur at the loops λ_5 and λ_7, at the switch regions, including the helix α_2 and at the β_2 and β_3 strands for which the highest deviation (relative to the pamb structure, coloured in grey) is seen at 490 MPa (coloured in orange) and 650 MPa (coloured in blue, Figure 3.65A left). The residues of all five structural motifs are presented in Figure 3.65B. It is noticeable that the switch 1 (aa 30-40) is less affected by pressure effects comparatively with switch 2 (aa 60-76), given by the higher disorder of the latter relative to the former (shown by different torsional and rotational orientation of almost all residues from the helix α_2 at different pressures, compared with the more structured switch 1). The three

other motifs (P-loop, G4 and G5) remain almost unperturbed in the tested pressure range. This result is expected given that they are detrimental for the tight binding of the α- and β-phosphate groups and confer specificity for the guanine nucleotide. The switch regions are shown in more detail in Figure 3.65C (switch 1) and D (switch 2). Again, with exception of some residues such as E31, D30 and E37, there are no pronounced modifications at switch 1, contrary to switch 2.

A more quantitative analysis of the data can be given by looking to the b-factors (determined at the alpha carbons to avoid the problem of multiple positions of the side chains), whose interpretation can provide an insight into the functional relevance of possible excited states existing at high pressure [179]. The averaged factors increase from 20.0 $Å^2$ at 0.1 MPa to 29.2 $Å^2$ at 200 MPa and to 33.6 $Å^2$ at 270 MPa. However, they decrease significantly to 17.0 $Å^2$ at 490 MPa and to 13.5 $Å^2$ at 650 MPa, leading to the reasoning that that the two last structures are further stabilised comparatively to the 200 and 270 MPa ones.
The rmsd values between the different HP structures were calculated and shown in Figures 3.65-3.67. A rather small averaged deviation of 0.17 ± 0.12 Å was obtained between the 0.1 and the 200 MPa structures. A similar value of 0.23 ± 0.15 Å was obtained for the pair pamb-p270 (Figure 3.66A). However, after the transition state, a deviation of 0.47 ± 0.23 Å was obtained for p270-p490 (Figure 3.67A). A smaller rmsd of 0.28 Å was obtained for the pair pamb-p650 (Figure 3.68A). Together these values indicate again the existence of a relevant structural rearrangement around 490 MPa.

Specific Differences

3.5.2.2.1 Structure at 270 MPa

Since the 200 MPa structure is quite similar to the 270 MPa one (average rmsd of 0.13 Å, Figure 3.66A black line), only the comparison between pamb and p270 will be presented (Figure 3.66A yellow line). The two structures are very similar in the switch 1 region, with only slight differences in the orientation of E37, E31 and D30. The most pronounced ones are observed in the middle of the helix α_2 for R68 and D69 (Figure 3.66C). The b-factors increase in average 13 $Å^2$ and more than 20 $Å^2$ around switch 2 (Q61-Q70, M72, R73) and in the loop λ_7, comprised between the helix α_3 and the sheet β_5 (residues K105-D108, Figure 3.66B). A similar averaged value of 10 $Å^2$ was found between pamb-p200 and almost no isotropic displacement was found between p200 and p270. The latter structure seems to be less stable than the one at ambient pressure, given the observed increase of the b-factors. Overall, the most noticeable pressure-induced modification between 270 and 0.1

MPa was the destabilisation of switch 2, especially the α_2 helix that became slightly pushed towards the loop λ_7. Since no considerable differences are observed between the p200 and the p270, they are assumed to represent the same high-energy sub-state.

3.5.2.2.2 Structure at 490 MPa

The collection of high completeness data at 490 MPa was only possible when the crystal as left at 250 MPa overnight and subsequently ramped up to 450 MPa prior to data acquisition. The mean rmsd between p490 and 0.1 MPa is 0.56 $\pm$ 0.40 Å, with several local values being higher than 0.7 Å (Figure 3.67A, orange line). The most pronounced effects were detected at the beginning of the N-terminal extremity (M1, T2), at the β_2 and β_3 strands, comprising the residues from Q43 to L52 and at the switch 2, especially in the S65-M72 sequence (Figure 3.67C). A concerted shift is observed for the β_2-β_3 strands and the first N-terminal residues, all moving towards the helix α_5 comparatively to the 0.1 MPa structure. The switch 2 becomes also largely shifted towards the helix α_3 and the loop λ_7 located close to the C-terminal. Concomitantly, the segment that precedes switch 1 (T20-E31) becomes slightly shifted towards the nucleotide (Figure 3.67D). Remarkably, the average main chain b-factors from the structure at 490 MPa are 16 Å^2 smaller than the corresponding ones at 270 MPa (Figure 3.67B). They are also 3.5 Å^2 lower than the obtained ones at 0.1 MPa. However, different areas on the protein are affected differently. For example, switch 2 becomes destabilised by pressure (having higher b-factors than the corresponding region at ambient pressure). At the same time, the β_2-β_3 region becomes greatly stabilised, with all the local b-factors differing by more than -6 Å^2 relative to pamb.

3.5.2.2.3 Structure at 650 MPa

The refined structure at 650 MPa closely resembles the one obtained at 490 MPa but it seems to be further stabilised (less disordered) by pressure as indicated by the temperature factors. The averaged rmsd between both is small and equal to 0.28 $\pm$ 0.39 Å (Figure 3.68A, blue line. A higher value of 0.61 $\pm$ 0.45 Å was obtained relative to 0.1 MPa, black line). The structural differences between p650 and pamb are similar to the ones already reported between p490 and pamb, with most of them involving the residues at the beginning of switch 1 (I24-N26), the N-terminal (M1-Y4), and the Q43-D54 sequence, comprising the strands β_2 and β_3 (Figures. 3.67C and D).

The comparison of p650 with p490 shows that all main chain b-factors are lower in the former structure relatively to the latter, with exception of the sequence E62-A66 (Figure 3.68B). The beginning and the end of the switch 2 is further stabilised at 650 MPa, as

observed again by the large decrease of the b-factors (more than -5 Å^2 relative to p490) for the T58-Q61 and R68-Y71 regions. A similar decrease is observed for some areas comprising switch 1 (F28-D33, D33, I36-S39), the helix α_3 (E91, Q99-V103) and the loop λ_{10} that connects the β_6 strand to the helix α_5 (T148-G151). The calculated b-factors for the nucleotide and for the Mg^{2+} ion are also significantly decreased.

Despite the structural similarity between the p650 and p490 structures, several local differences can be found (rmsd < 0.8 Å) comprising the residues Q61-A66, R68, Q70-M72. Their different reorientation comparatively to p490 leads to a simultaneous displacement of the helix α_2 towards of the loop λ_4 and towards the bulk (Figure 3.68E, bottom). One of the most dramatic displacements is observed for Gln61. This residue is normally positioned almost in-plane with the γ-phosphate as it establishes an H-bond with it in all the refined structures except at 650 MPa, where it assumes a perpendicular position and points upwards and towards the bulk. In this new position, Gln61 becomes stabilised by an H-bond between its side chain and one of the oxygen atoms of the γ-phosphate from the adjacent molecule in the unit cell. The b-factor of the nitrogen atom engaged in the H-bond shows a large decrease when compared with the other structures (37 Å^2 at pamb, 46 Å^2 at p490 and 25 Å^2 at p650), indicating that the new position for Gln61 at 650 MPa is a very stable one (Figure 3.68E, top).

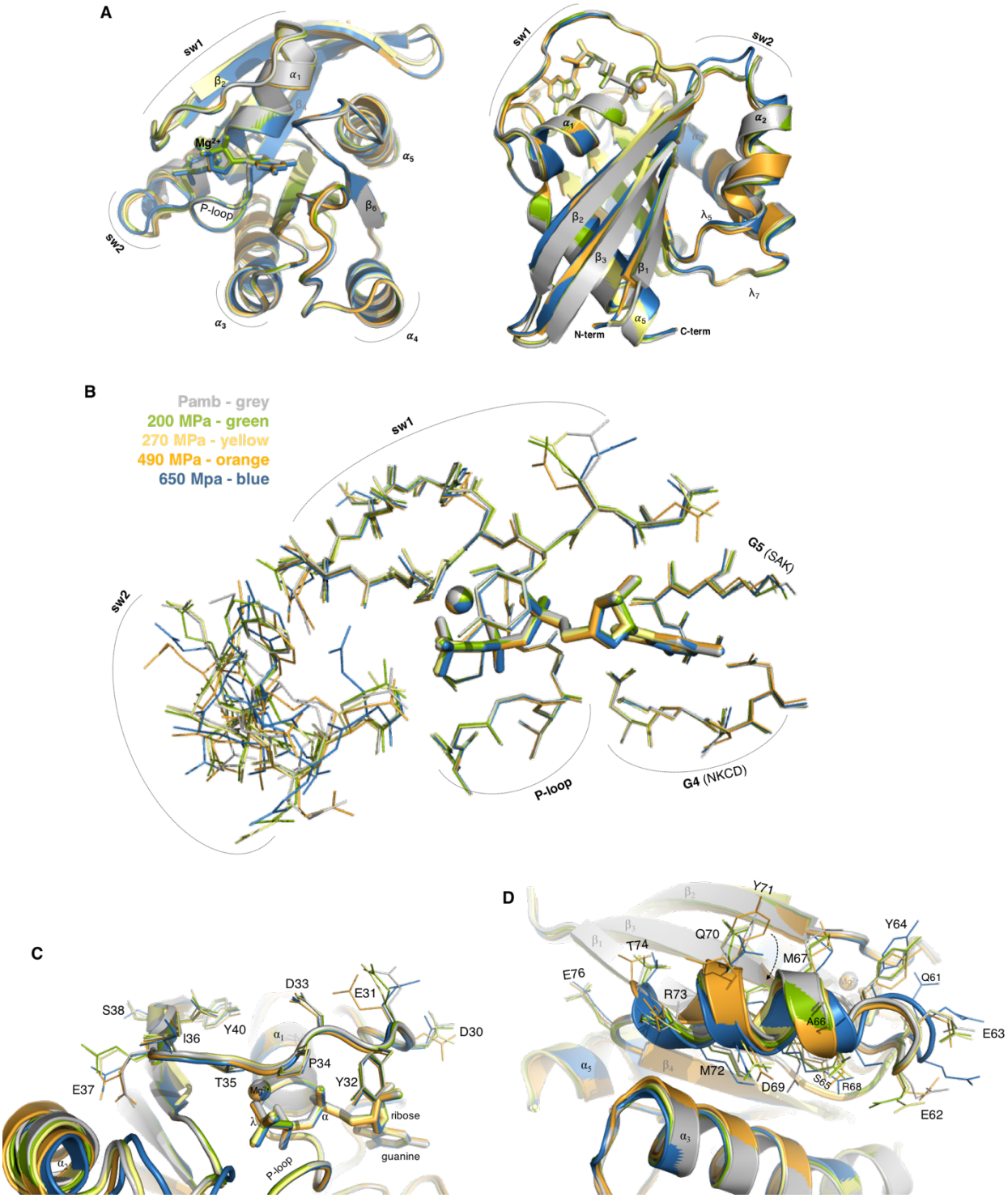

Figure 3.65. HP series on HRas^{WT}(1-166)•Mg^{2+}•GppNHp at RT. **A.** General overview of the superimposed structures evidencing differences in the relative orientation of the α-helixes and β-sheets. **B.** An overview of the pressure-induced effects on the motifs of the G domain surrounding the catalytic centre is given (switch 1, aa 30-40; switch 2, aa 60-76; P-loop, aa 10-17; G4, aa 116-119; G5, aa 145-147). The Mg^{2+} ion is represented as a sphere located nearby the γ-phosphate **C.** Details at switch 1 evidencing the re-orientation of the side chains for some residues. **D.** Details at switch 2.

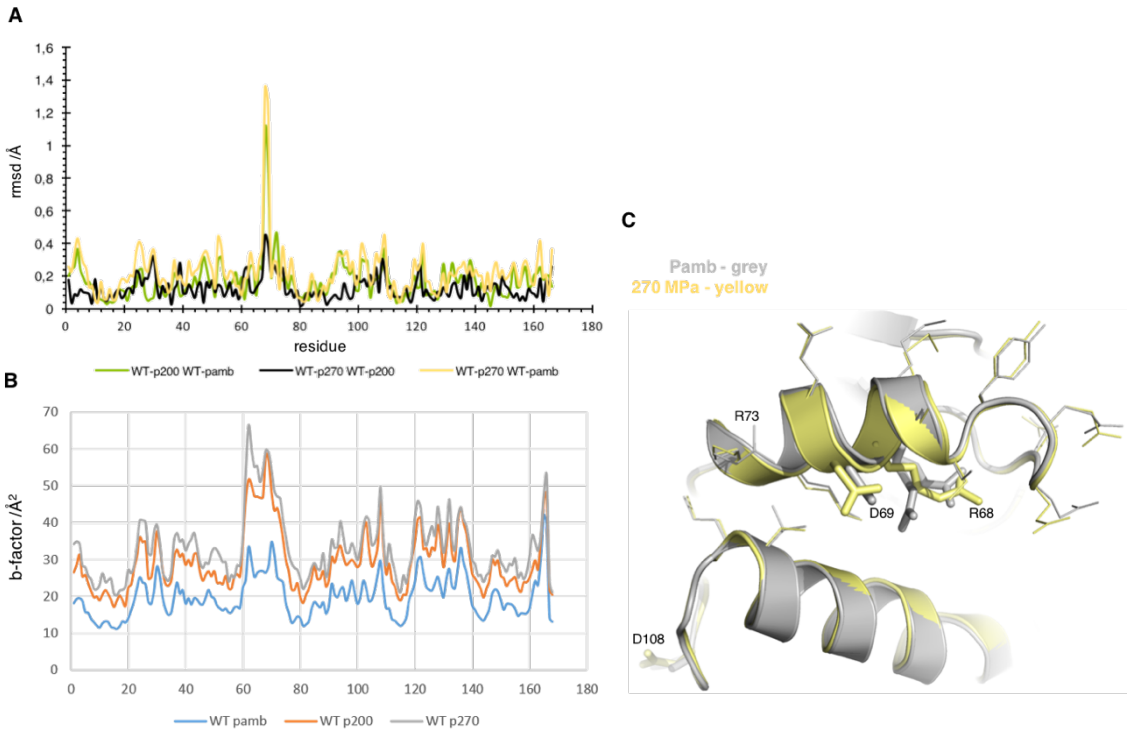

Figure 3.66. Structural details of Ras^{WT}(1-166)•Mg^{2+}•GppNHp obtained at 270 MPa (coloured in yellow) and comparison with pamb (coloured in grey) and the 200 MPa structure (coloured in green). **A.** Rmsd plot of p200 against pamb (green line), p270 against p200 (black line) and p260 against pamb (yellow line). **B.** Plot of the b-factors for pamb, p200 and p270. **C.** Local details evidencing the regions where the most pronounced structural differences between p270 and pamb were detected (around helix α_2 and loop λ_7).

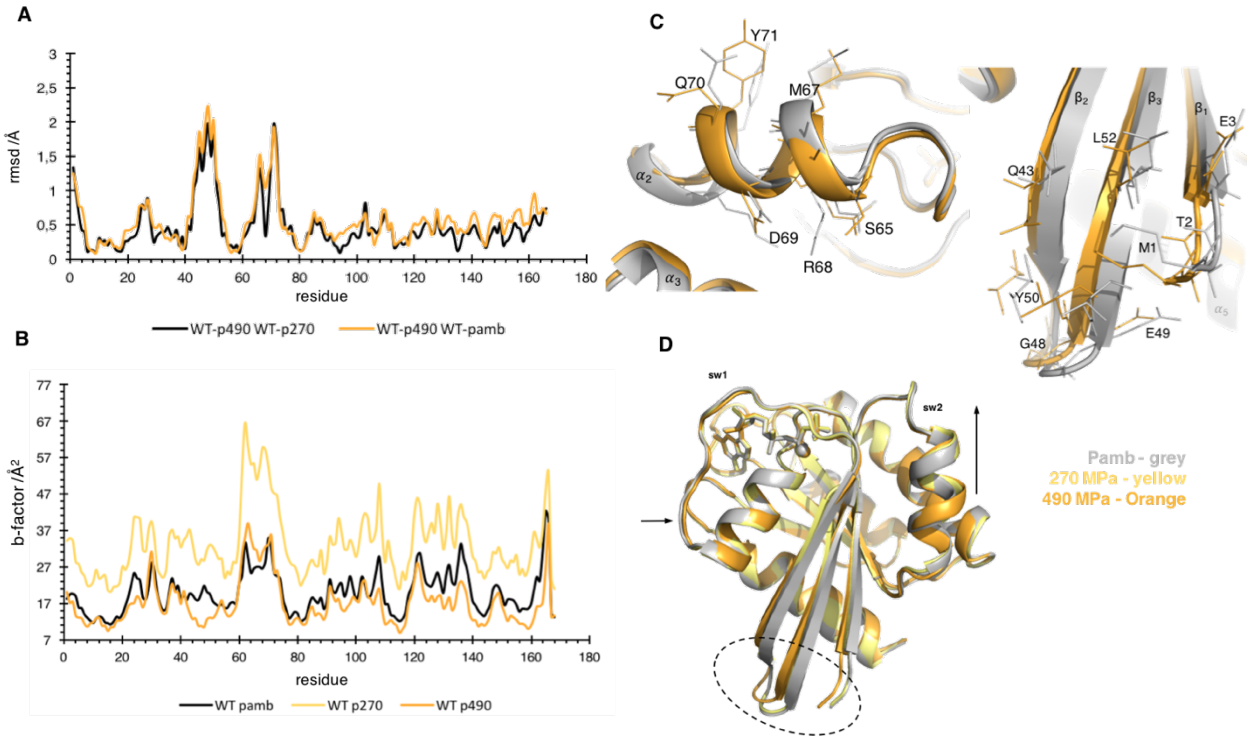

Figure 3.67. Structural details of Ras^{WT}(1-166)•Mg^{2+}•GppNHp obtained at 490 MPa (coloured in orange) and comparison with pamb (coloured in grey) and the 270 MPa structure (coloured in yellow). **A.** rmsd plot of p490 against p270 (black line) and p490 against pamb (orange line). **B.** Plot of the b-factors for pamb, p270 and p490. **C.** Local details evidencing the regions where the most pronounced structural differences between p490 and pamb were detected (at helix α_2, Y64-M72 and at the N-terminal, including M1-Y4 and β_2-β_3 strands, Q43-L52. Additional modifications were detected at the helix α_5 (rmsd > 0.7 Å) involving F146, Y157, R161, E162 and Q165. **D.** General overview of the structural changes observed between pamb, p270 and p490 at the N-terminal (dashed circle) and at the switch 2 region, marked by the upward arrow and by the movement of α_2 towards α_3, located behind it.

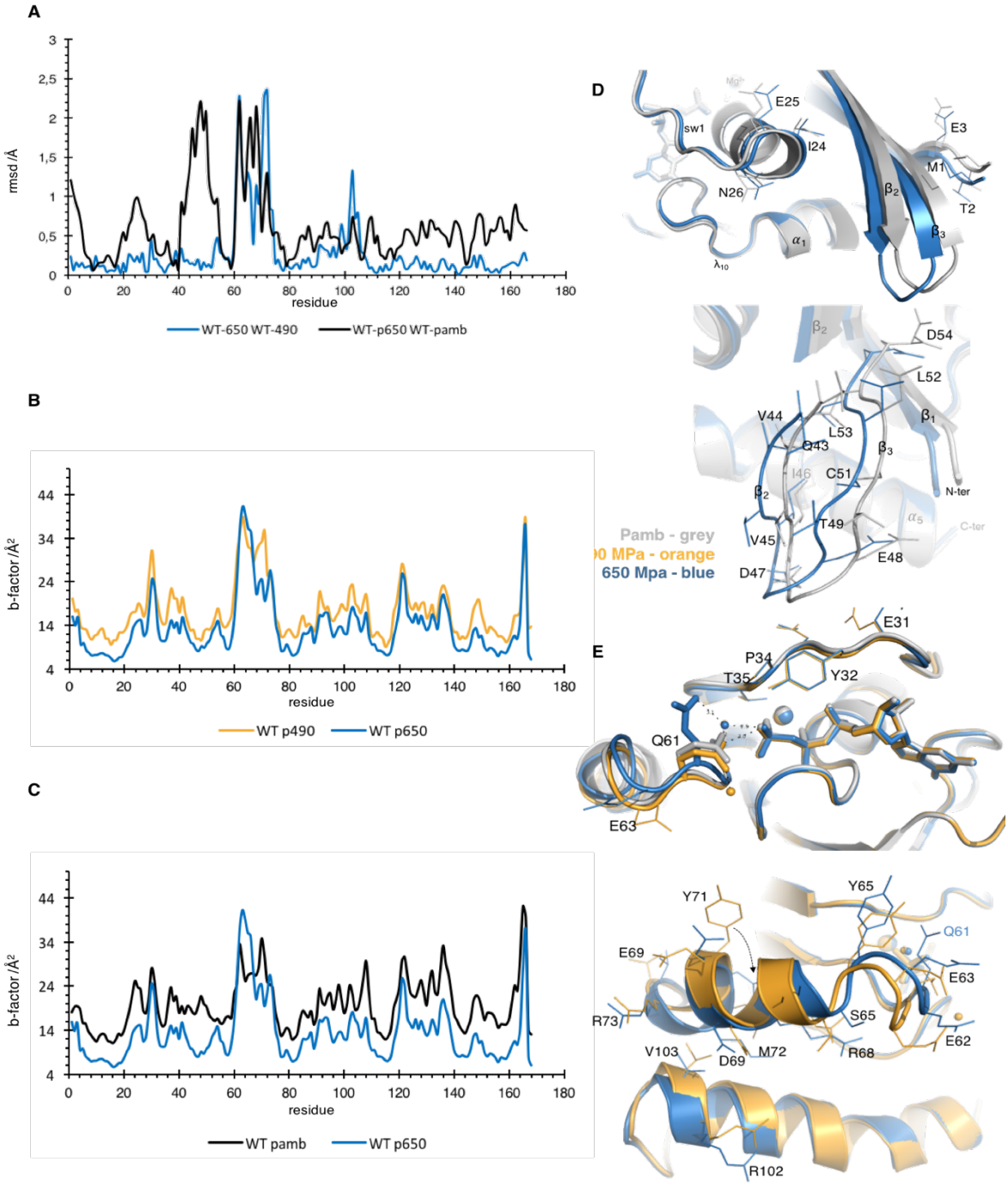

Figure 3.68. Structural details of Ras^{WT}(1-166)•Mg^{2+}•GppNHp obtained at 650 MPa (coloured in blue) and comparison with pamb (coloured in grey) and with the 490 MPa structure (coloured in orange). **A.** rmsd plot of p650 against p490 (blue line) and p650 against pamb (black line). **B.** Plot of the b-factors for p490 and p650. **C.** Plot of the b-factors for p650 and pamb. **D.** Local details evidencing the structural differences for which the rmsd values are higher than 1.0 Å, between p650 (blue) and pamb (grey). In the upper Figure the N-terminal region is highlighted (M1-Y4) together with the residues comprising the beginning of the helix α_1 (I24-N26). The observed differences in the strands β_2 and β_3 are highlighted in the lower Figure for the residues Q43-D54. Other significant changes, not depicted here, were also found again at the helix α_2 (Q62-D69, Y71, M72) and for E162 located at the helix helix α_5. **E.** Details of the structural modifications (rmsd > 1.0 Å) between p490 (blue and p650 (orange). The pamb structure is also shown (grey). In the upper Figure, the different orientation of Q61 in p650 is evidenced. The switch 1 is almost identical for all the three proteins but remarkable differences are observed again at the switch 2, namely at the helix α_2, represented in the lower picture.

3.5.3 Crystal Structure of Ras^{D33K}(1-166)•Mg^{2+}•GppNHp at Ambient Pressure

Ras^{D33K} was solved with a resolution of 1.95 Å at RT and ambient pressure. The structure is very similar to Ras^{WT}, with the total averaged rmsd value between both being only 0.13 Å. Their similarity can be inferred from the perfect superposition of their crystal structures, shown in Figure 3.69A (Ras^{WT} is coloured in grey and Ras^{D33K} is coloured in green). The refined electron density in the vicinity of Lys33 is shown in Figure 3.69B. The side chains of Lys33 and Asp33 point in the same outward direction, towards the surface of the proteins, and the switch 1 is almost identical for both. The only noticeable differences are the distinct rotational orientations of Asp30 and Glu37, together with the formation of an H-bond between Lys33 and Glu31. The switch 2 is only slightly different for residues Q61-Y64 and R68-Q70, with an rmsd > 0.3 Å. The obtained b-factors are also very similar in the two structures (20 $Å^2$ for Ras^{WT} and 21 $Å^2$ for Ras^{D33K}).

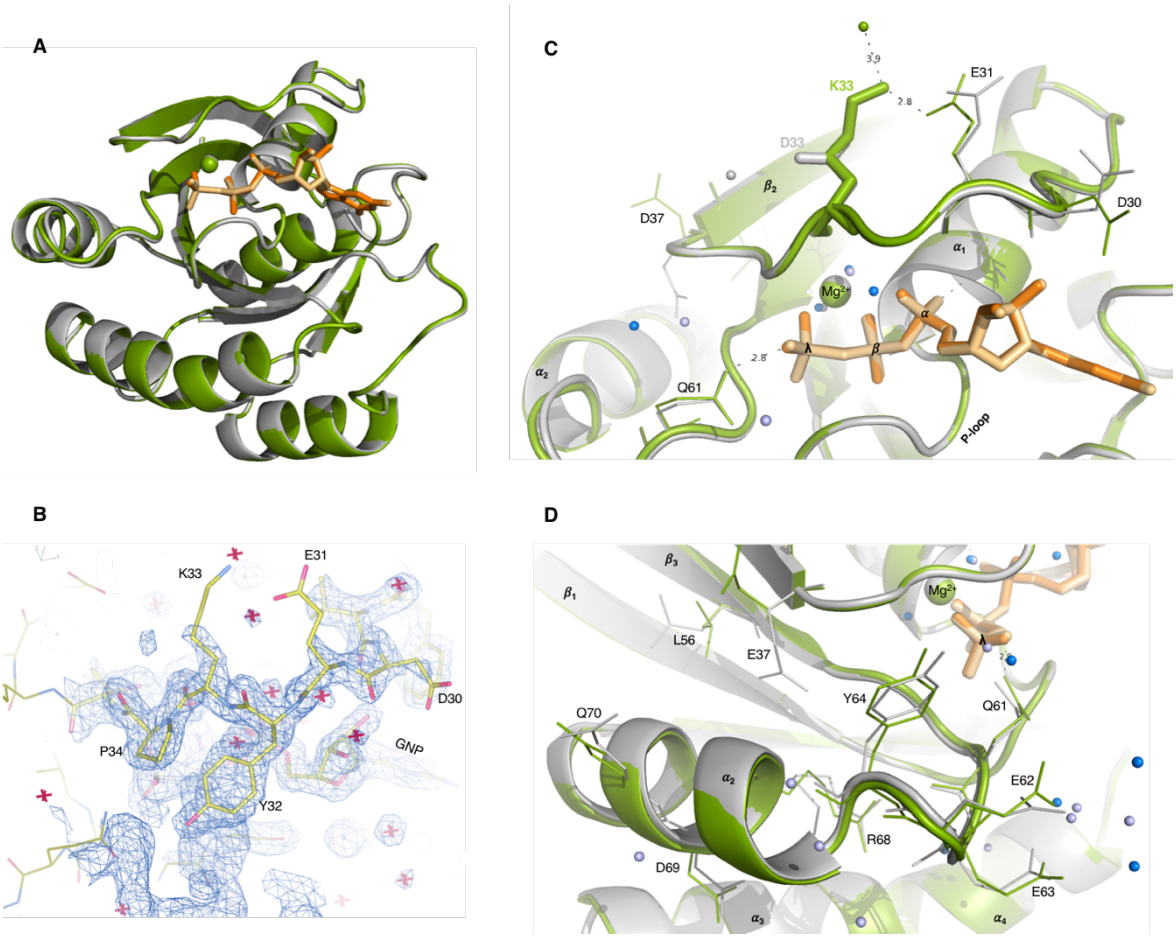

Figure 3.68. Refined crystal structure of HRas^{D33K}(1-166)•Mg^{2+}•GppNHp obtained at ambient pressure and RT (coloured in green) and comparison with the *wild type* protein obtained in the same conditions (coloured in grey). **A.** Cartoon representation of the superimposed structures. The nucleotide from Ras^{WT} is coloured in dark orange and the nucleotide from Ras^{D33K} is coloured in light orange. **B.** View of the electron density map of Ras^{D33K} around the mutated residue. The neighboring amino acids are also shown. **C.** Comparison of the structural details between both proteins at the switch 1 region. **D.** Comparison at the switch 2 region. The residues showing different degrees of rotation are represented as thin lines. The small dark blue coloured spheres refer to the solvent waters of Ras^{D33K} and the light blue coloured ones refer to those of Ras^{WT}.

- This page was deliberately left blank -

3.5.4 Crystal Structure of $Ras^{D33K}(1\text{-}166)\bullet Mg^{2+}\bullet$GppNHp Under High Pressure

3.5.4.1 Analysis of the Compressibility Curve

Two complete HP datasets were collected for Ras^{D33K} under pressure

- 200 MPa, resolution of 2.1 Å
- 880 MPa, resolution of 1.65 Å

In the first one, pressure was continuously ramped from 0.1 MPa with no waiting period for pressure accommodation. In the second one, again an overnight incubation at 550 MPa revealed to be necessary to achieve very high pressure, otherwise diffraction was completely lost. A third dataset was recorded at 500 MPa after previous incubation at 200 MPa for ca. 2 hours. Although, perhaps due to the short incubation period, diffraction was quickly lost, rendering impossible the acquisition of a full-refined structure. Figure 3.70 shows that the unit cell volume decreases 1.7% from 0.1 to 500 MPa and 4.6% from 0.1 to 880 MPa. The decrease between 200 and 880 MPa is of 2.9%. These results indicate that the transition zone for Ras^{D33K} occurs at a higher pressure (ca. 500 MPa) comparatively to Ras^{WT} (300-400 MPa).

The quality of the diffraction also improves with pressure, as observed from the obtained resolution limits (1.95 Å at 0.1 MPa, 2,1 Å at 200 MPa, 1,65 Å at 500 MPa and 1.8 Å at 880 MPa). The same trend can be observed by the number of crystallographic waters which increases from 80 (pamb) to 82 (p200) and 237 (p880). The same assessment can be followed by considering the averaged values of the b-factors, which decrease from 21 $Å^2$ at 0.1 MPa to 16.8 $Å^2$ at 880 MPa. The rmsd value between ambient pressure and 200 MPa is 0.17 Å and 0,64 Å between 200 and 880 MPa. Together these results suggest again a

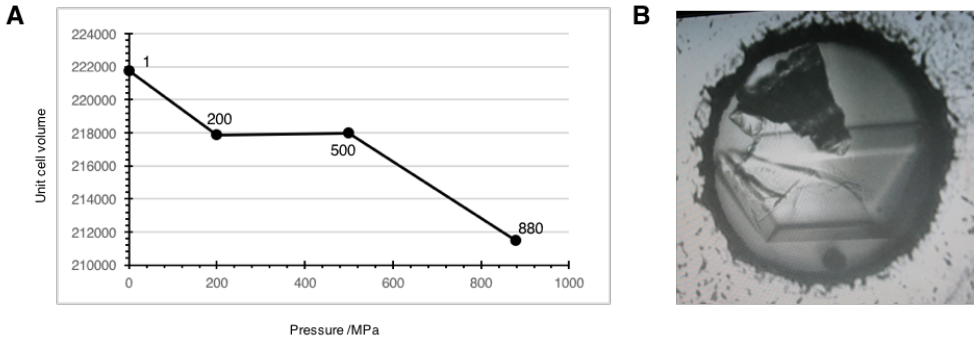

Figure 3.70. A. Compressibility curve obtained for the HP series on $HRas^{D33K}(1\text{-}166)\bullet Mg^{2+}\bullet$GppNHp at RT. The volume of the unit cell (shown in $Å^3$) is plotted as a function of pressure. **B.** Photography of a Ras^{D33K} crystal at 880 MPa. The crystal occupies the full length of the DAC (400 nm). Several cracks are noticeable at one of the edges due to the extreme pressure. The tiny circle in the bottom of the cavity is a ruby sphere used for an online measurement of the pressure. Due to its rather flat shape, the crystal needed to be reoriented using a diamond splinter (dark figure on the top). This process helps the acquisition of high completeness data. Surrounding the cavity is the metallic gasket that was carefully machined and positioned between the culets of the two diamond anvils.

structural rearrangement between 200 and 880 MPa and possibly the existence of a new conformation at very high pressure.

3.5.4.2. Analysis of rmsd and b-factor Values

Global Differences

A general overview of the Ras^{D33K} HP series is given in Figure 3.71. As already observed in the case of Ras^{WT}, there are no dramatic changes on the protein structure such as a complete unwinding of an helix or a broad displacement of a loop comparatively the 0.1 MPa structure. The superimposed structures shown in Figure 3.71A indicate that the helixes α_3, α_4 and α_5 remain unaltered, being the only affected regions switch 1, the helix α_2 and the C-terminal of the protein. A closer look to the five fingerprint motifs of the G domain (Figure 3.71B) evidences again the greater mobility of switch 2 with pressure relative to switch 1 and an almost unperturbed behaviour for the P-loop, G4 and G5.

Specific Differences

3.5.4.2.1 Structure at 200 MPa

The 200 MPa structure is quite similar to the one solved at ambient pressure, with an averaged rmsd of 0.17 $\pm$ 0.09 Å (Figure 3.72A). The switch 1 is virtually identical in both proteins and only significant changes are observed in switch 2, for which an rmsd > 0.5 Å was obtained at Glu63 and Arg68 (Figure 3.72A). The global behaviour of Ras^{D33K} between these two pressure points seems to be similar to the one of Ras^{WT} between ambient pressure and 270 MPa. However, there is almost no change in the b-factors in the case of the mutant (ca. 1.2 $Å^2$, Figure 3.72B vs 13 $Å^2$, Figure 3.66B, respectively). High local b-factors (> 6 $Å^2$) could only be found in the switch 2 (Q62, E63-D69, Y71) and for S39 in switch 1, G151 in the helix α_5 along with the Mg^{2+} ion. Given these results it can be inferred that Ras^{D33K} seems to be less prone to pressure-induced conformational rearrangements comparatively to Ras^{WT} (both show a small difference in the rmsd values and almost no difference in the temperature factors).

3.5.4.2.2 Structure at 880 MPa

The 880 MPa structure, however, is remarkably different from the other two. The obtained average rmsd values are 0.71 ± 0.5 Å and 0,64 ± 0.5 Å relatively to 0.1 MPa and 200 MPa (Figure 3.73A). Furthermore, the closest pressure point in the *wild type* series is 650 MPa. Comparing both, a relatively high rmsd is also obtained (0.32 Å).

The main differences between Ras^{D33K} at 0.1 MPa and at 880 MPa (rmsd >1.0 Å) lie at the very beginning of the N terminal (M1, T2), at the helix α_1 (I24-H27) at the beginning of switch 1 (V29-Y32), the β_2 and β_3 strands (R41-D54), the switch 2 (Q61 – M67, Y71 – T74), and residues A122 ,R128 (helix α_4), and E162 (helix α_5). At 880 MPa, the segment I24-Y32 becomes shifted by more than 1.0 Å towards the nucleotide and the residues E31, E37, S39 and R41 point in different directions. Furthermore, in the switch 2, the loop λ_4 (Q61 – Y64) becomes shifted by more than 2.0 Å towards helix α_5. Finally, the α_2 helix (S65 – T74) becomes shifted by 1.0 Å towards the loop λ_4, with all residues pointing in different directions (Figure 3.73C). Particularly, the crucial Gln61 becomes H-bonded to NH side chain of Tyr64, pointing away from the nucleotide γ-phosphate, as already observed in Ras^{WT} at 650 MPa (Figure 3.73D, top). The b-factors decrease in average 4.5 Å between p880 and pamb (Figure 3.73B). However, a local increase is observed at the end of P-loop (K16-L19), switch 1 (Y32-I36), switch 2 (A59-M67, Y71), at the Mg^{2+} ion together with two H_2O molecules coordinating it.

3.5.4.2.3 Ras^{D33K} at 880 MPa vs Ras^{WT} at 650 MPa

When comparing the p880 Ras^{D33K} with p650 Ras^{WT} significant differences can be found in switch 1 (V29-Y32) and the switch 2 (Q61-T74, Figure 3.72C). The obtained rmsd values in these regions are always higher than 0.7 Å. In Ras^{D33K} at 880 MPa switch 1 shifts more with pressure than the corresponding region in Ras^{WT} at 650 MPa (increased b-factors in the segment Y32-I36). It is not possible to conclude if this happens because of the presence of the mutation or because of a higher pressure (880 MPa instead of 650 MPa).

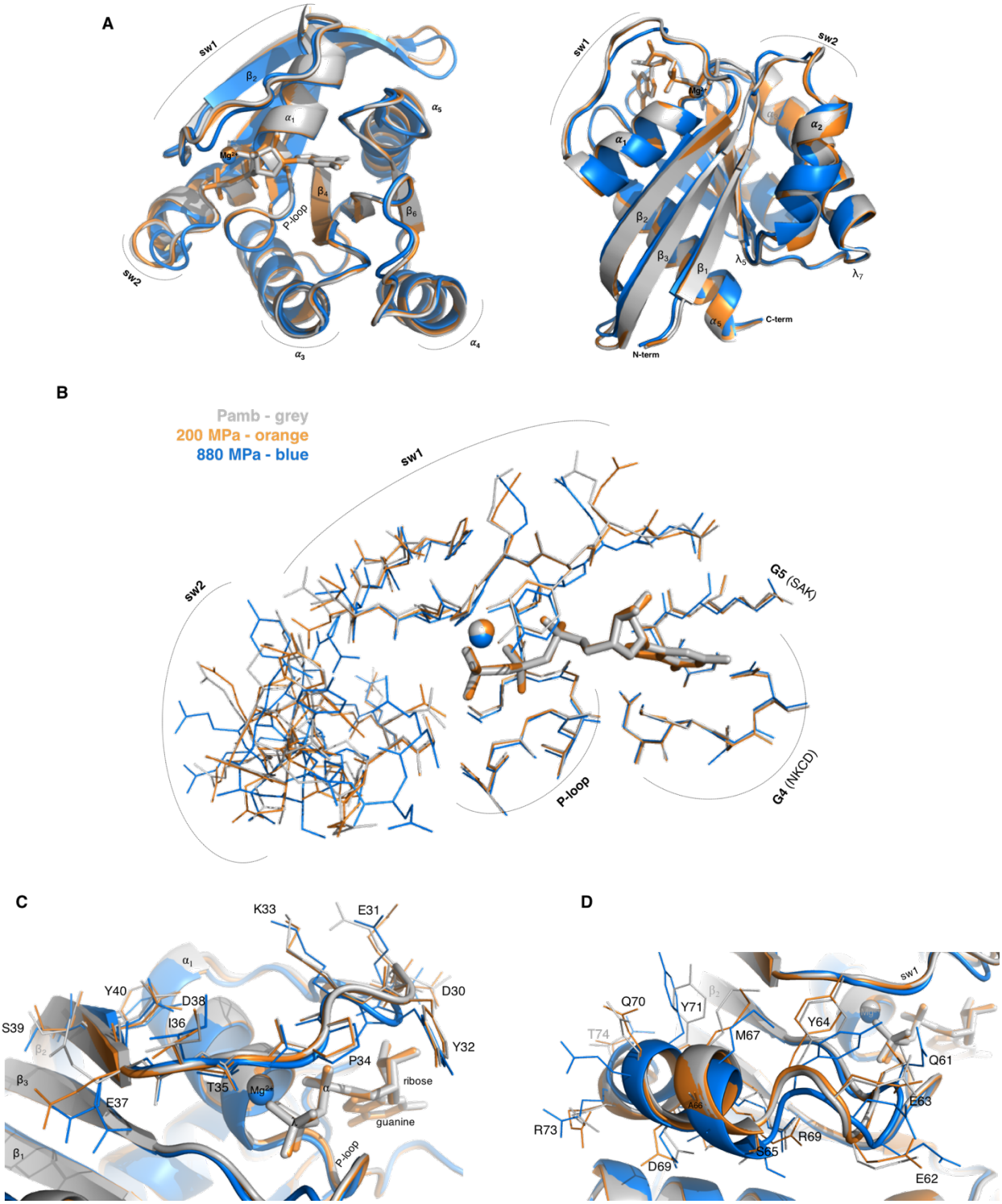

Figure 3.71. HPMX on HRas^{D33K}(1-166)•Mg^{2+}•GppNHp at RT. **A.** General overview of the superimposed structures evidencing differences in the relative orientation of the α-helixes and β-sheets. **B.** An overview of the pressure-induced effects on the residues surrounding the catalytic centre is given (switch 1, aa 30-40; switch 2, aa 60-76; P-loop, aa 10-17; G4, aa 116-119; G5, aa 145-147). **C.** Details at the switch 1. **D.** Details at the switch 2.

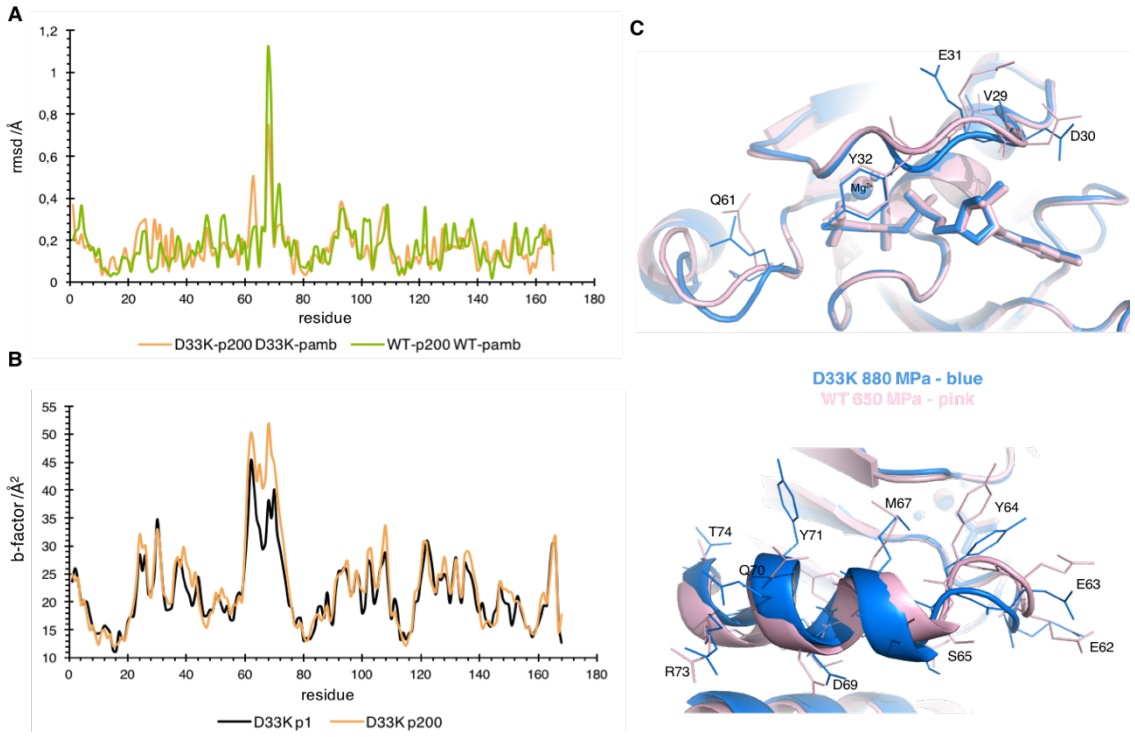

Figure 3.72. HP X-ray crystallography on $Ras^{D33K}(1\text{-}166)\bullet Mg^{2+}\bullet$GppNHp. **A.** Rmsd plot of p200 against pamb (orange line) and comparison with Ras^{WT} p200 against Ras^{WT} pamb (green line). **B.** Plot of the b-factors for D33K pamb and D33K p200 **C.** Structural details evidencing the detected differences (rmsd > 1 Å) at switch 1 (top) and switch 2 (bottom) between Ras^{D33K} at 880 MPa (blue coloured) and Ras^{WT} at 650 MPa (pink coloured).

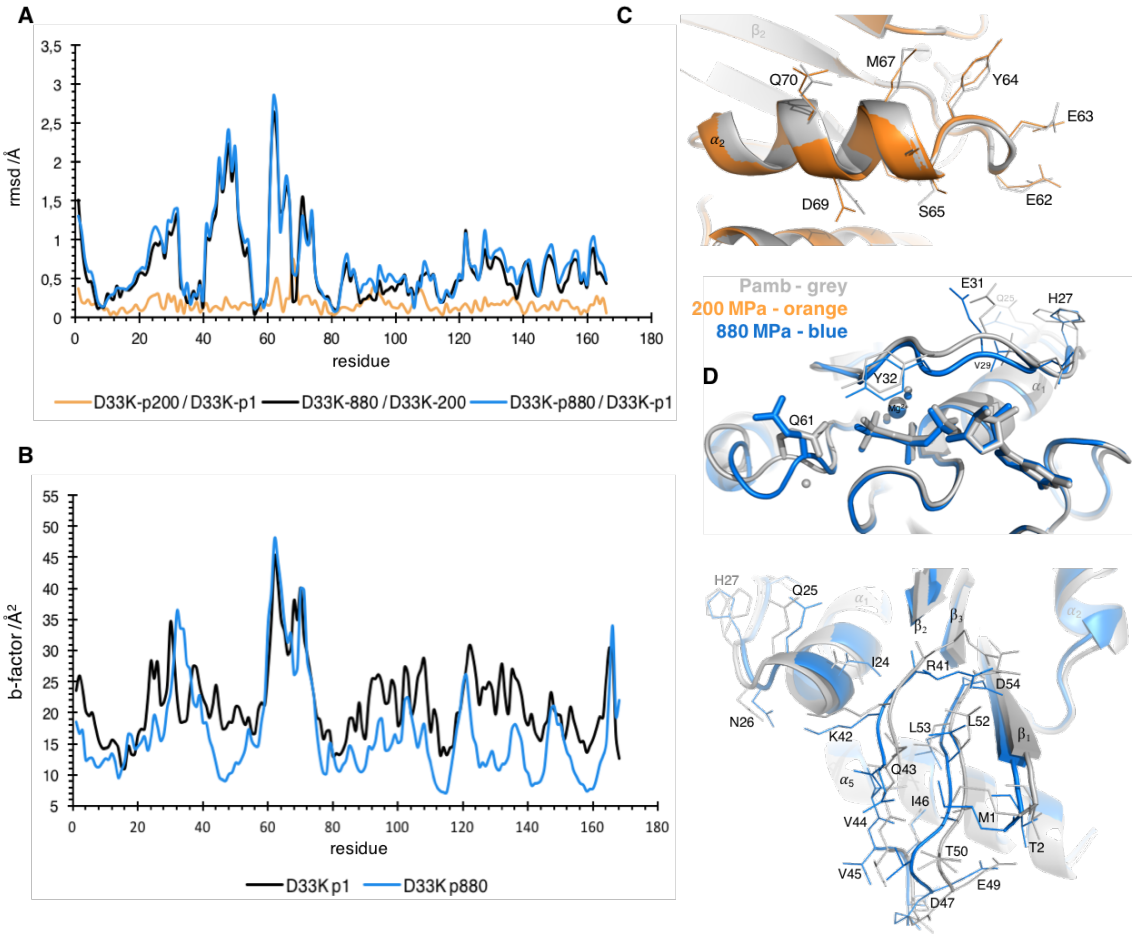

Figure 3.73. HP X-ray crystallography on $Ras^{D33K}(1\text{-}166)\bullet Mg^{2+}\bullet$GppNHp. **A.** rmsd plot of p200 against pamb (orange line), p880 against p200 (black line) and p880 against pamb (blue line). **B.** Plot of the b-factors for pamb and p880. **C.** Structural details evidencing the observed small deviations (rmsd > 0.5 Å) at switch 2 between Ras^{D33K} at pamb and at 200 MPa. **D.** Similar comparison between pamb and p880. Significant differences were found at the beginning of switch 1 (top) and especially at the N-terminal region (rmsd > 1.0 Å), involving the residues from the β2 and β3 sheets (bottom).

- This page was deliberately left blank -

3.5.5 Crystal Structure of $HRas^{WT}(1\text{-}166)\bullet Mg^{2+}\bullet GppNHp$ Soaked with Zn^{2+}-cyclen

3.5.5.1 Analysis of the Compressibility Curve

For the purpose of these investigations, the previously grown Ras crystals were soaked with 10-12 mM of Zn^{2+}-cyclen from a highly concentrated stock solution (> 20 mM) at least 10 hours before data acquisition. Four complete datasets were obtained, all within the same trigonal $P3_221$ space group:

- 0.1 MPa, resolution 1.8 Å
- 180 MPa, resolution 2.05 Å
- 240 MPa, resolution 2.80 Å
- 520 MPa, resolution 2.70 Å

The analysis of the compressibility curve shows that the unit cell volume decreases linearly with pressure, down to 5% at 520 MPa (Figure 3.74, orange line; only a few frames were collected at 100 MPa). The decreasing is continuous, contrary to the behaviour of the Apo structure (black line), whose volume increases between 270 and 490 MPa. It can be observed that at any given pressure the cell volume of the protein soaked with the drug is always smaller than the Apo structure, indicating that the inhibitor is diffusing and interacting with Ras in the crystal (either specifically or unspecifically). In this series, incubation was only performed for the last point at 200 MPa overnight. Afterwards, thrust was continuously applied up to 520 MPa followed by data acquisition. Contrary to the observations for the Apo structure, the quality of the diffraction does not improve with the increase of pressure. The resolution limits are around 2.0 Å at low pressures and 2.8 Å at high pressures. The number of visible waters also decreases with pressure, again as opposed to the Apo protein, from 95 at pamb to 62, 69, 10 and 34 at p100, p180, p240 and p520 MPa, respectively.

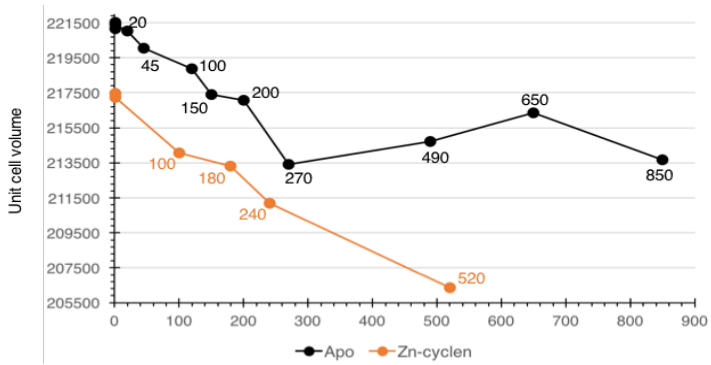

Figure 3.74. Compressibility curve obtained for the HP series on $HRas^{WT}(1\text{-}166)\bullet Mg^{2+}\bullet GppNHp$ crystals soaked with 10-12 mM Zn^{2+}-cyclen at RT (orange coloured line). The compressibility of Ras^{WT} alone, named here as Apo, is also shown for comparison (black coloured line).

3.5.5.2. Analysis of rmsd and b-factor Values

The averaged main chain b-factors increased with pressure, from 22 $Å^2$ at ambient pressure to 31 $Å^2$ at 100 MPa, 29 $Å^2$ at 180 MPa, 43 $Å^2$ at 240 MPa, decreasing subsequently to 30 $Å^2$ at 520 MPa. It is worth mention that the structure at 240 MPa was collected on the same crystal used at 100 MPa. This can partially explain the degradation of the diffraction at 240 MPa (very small number of crystallographic waters, high b-factors). The averaged rmsd values between Ras^{WT}•Zn^{2+}-cyclen at ambient pressure and p100, p180, p240 and p520 MPa are 0.17, 0.19, 0.36 and 0.87 Å, respectively.

Rather surprisingly, no Zn^{2+}-cyclen molecules are visible in the electron density maps of the crystal structures at 100, 180 and 240 MPa.

3.5.5.2.1 Ras Apo vs Ras•Zn^{2+}-cyclen at Ambient Pressure

No significant differences were observed between Ras^{WT} Apo and in complex with Zn^{2+}-cyclen at 0.1 MPa. The average rmsd between both is 0.13 Å. The highest local deviations (rmsd > 0.3 Å) were found for D110 and V111 at the loop λ_7. No differences were detected near the C-terminal H166 or at Q61. Both the Mg^{2+} ion and GppNHp lie at the exact same position. Similar results were found when comparing Ras•Zn^{2+}-cyclen at ambient pressure with the structures resolved at 100 and 180 MPa.

3.5.5.2.2 Structure at 240 MPa

The structure obtained at 240 MPa is not drastically different from the one at 0.1 MPa, however high local main-chain rmsd values were found between both involving the helix α_1 and the remaining switch 1 region (rmsd > 0.5 Å for L23, N26, H27, D30-T35 and D38). Particularly, T35, D33 and G48 showed an rmsd > 1.0 Å. These overall modifications led to the shift of switch 1 away from the nucleotide and from the Mg^{2+} ion comparatively with its corresponding position at 0.1 MPa. Additional differences were found in switch 2 that also shifts away from the nucleotide: L56, D57-E63, R68, D69 were all found to have a rmsd > 0.5 Å relative to 0.1 MPa. For Q61-Q63 the deviation is greater than 1.0 Å. The Mg^{2+} ion is itself shifted by 0.71 Å towards the bulk relative to the ambient pressure structure. More importantly, Zn^{2+} is observed in the electron density map between the O1 of the γ-phosphate (distance of 2.5 Å), the side chain of Y32 (distance of 2.6 Å) and the side chain of P34 from the adjacent molecule in the unit cell (distance of 2.9 Å). However, the cyclen moiety that should surround the metal is not visible. Given these results alone, it is difficult to conclude whether if cyclen is too disordered to be localized or not present at all.

3.5.5.2.3 Structure at 520 MPa

The 520 MPa structure is considerably different from the one at ambient pressure. Both are superimposed in Figure 3.75. The average rmsd value is 0.8 Å with localised differences accounting for a rmsd > 1.5 Å (Figure 3.76A). These occur mainly in switch 1 and in the loop λ_7 that connects the strands β_2 and β_3 (rmsd of 1.6 Å for V44-C51). This last region shifts towards the bulk relative to the ambient pressure structure (Figure 3.75B).

Structural differences were also found at switch 2, particularly for Q61, E63 and the segment S65-Y71, all with an rmsd > 1.0 Å relative to the 0.1 MPa structure (Figure 3.75C). It is also worth mention that switch 2 in the Ras•Zn^{2+}-cyclen at 520 MPa is structurally more similar to Ras Apo at p490 than Ras Apo at p650. With the exception of switch 1, both structures (Ras•Zn^{2+}-cyclen p520 and Apo p490) can be considered identical. The analysis of the temperature factors shows that these are increased by pressure in average 8.0 $Å^2$ and more than 20 $Å^2$ in both switch regions (D33-D38, E62-Y64, D69-Y71, Figure 3.76B) at 520 MPa.

Similarly to the p280 structure, a Zn^{2+} ion has been visualized in the electron density map of p520, located close to the nucleotide and at a distance of 2.0 Å from O1 of the γ-phosphate. This ion lies very close to its symmetrical counterpart, with the distance between them being 4.2 Å (Figure 3.76D); it shows a full occupancy, a high temperature factor (ca. 70 $Å^2$) and is further coordinated by three H_2O molecules (at a distance of 2.01, 2.56 and 2.78 Å). However, as for p280, no cyclen was detected around it.

The most important difference between the structure solved at 520 MPa and the one at ambient pressure lies in the switch 1 (Figures 3.75B and 3.76C): at 520 MPa the segment comprising S17-S39 shows a rmsd > 0.5 Å, with I24-H27 having a deviation higher than 1.0 Å. At the same time, D30-D38 became shifted towards the bulk by almost 5.0 Å. Due to such a large movement, the side chain of T35, that normally coordinates the Mg^{2+} ion, is now more than 4.0 Å away from it, as shown in Figure 3.76C. At the otherwise normal position of the side chain OH group from T35 lies now a water molecule coordinating the Mg^{2+} ion.

The 520 MPa structure is considerably different than he one at 240 MPa. The average rmsd between both is 0.79 Å, with the residues E31-E37 showing a deviation higher than 5.0 Å. Marked differences are also found at the segment β_2-β_3 (V44-T50, rmsd > 1.0 Å) and at switch 2 (Q61-Q63, S65-M67, Q70, Y71, rmsd > 1.0 Å). Other major differences involve the position of both metal ions, with Mg^{2+} and Zn^{2+} being displaced towards switch 2 in p520 by 1.69 and 2.26 Å, respectively.

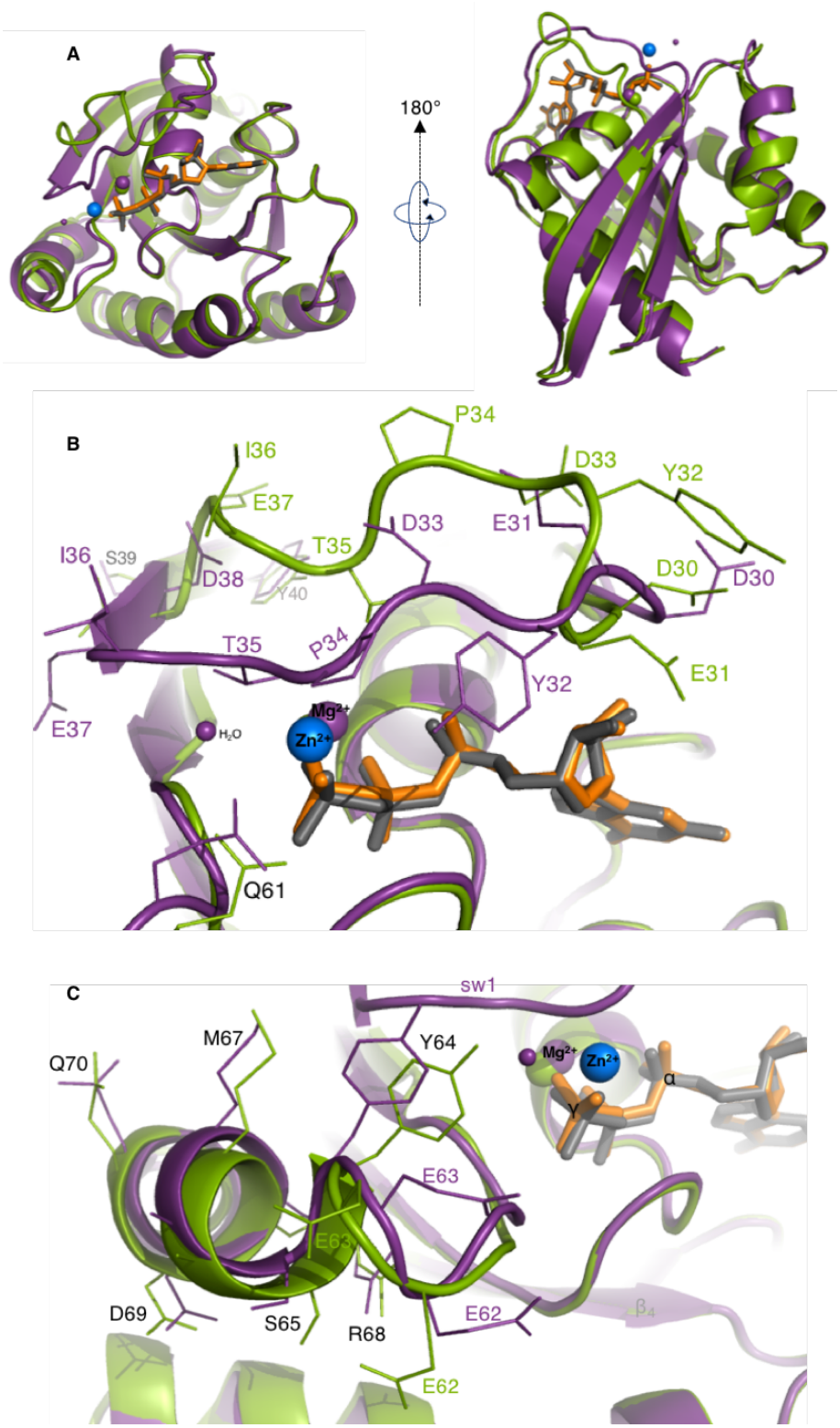

Figure 3.75. HPMX on HRas^{WT}(1-166)•Mg^{2+}•GppNHp at RT complexed with the small inhibitor Zn^{2+}-cyclen. The refined structure at 520 MPa (coloured in green with the nucleotide in dark grey) is shown superimposed with the one at ambient pressure (coloured in violet with the nucleotide in orange). Both crystals were soaked for at least 10 hours with 12 mM Zn^{2+}-cyclen **A.** General overview evidencing the overall differences between both. **B.** Structural details of switch 1 (aa 30-40). **C.** Structural details of switch 2 (aa 60-70). For both structures, no Zn^{2+}-cyclen was detected in the electron density maps. However, Zn^{2+} alone (coloured in blue) was detected in the 520 MPa structure close to the γ-phosphate. The cyclen group could not be found, although due to the large movement of switch 1 there is enough space to accommodate it.

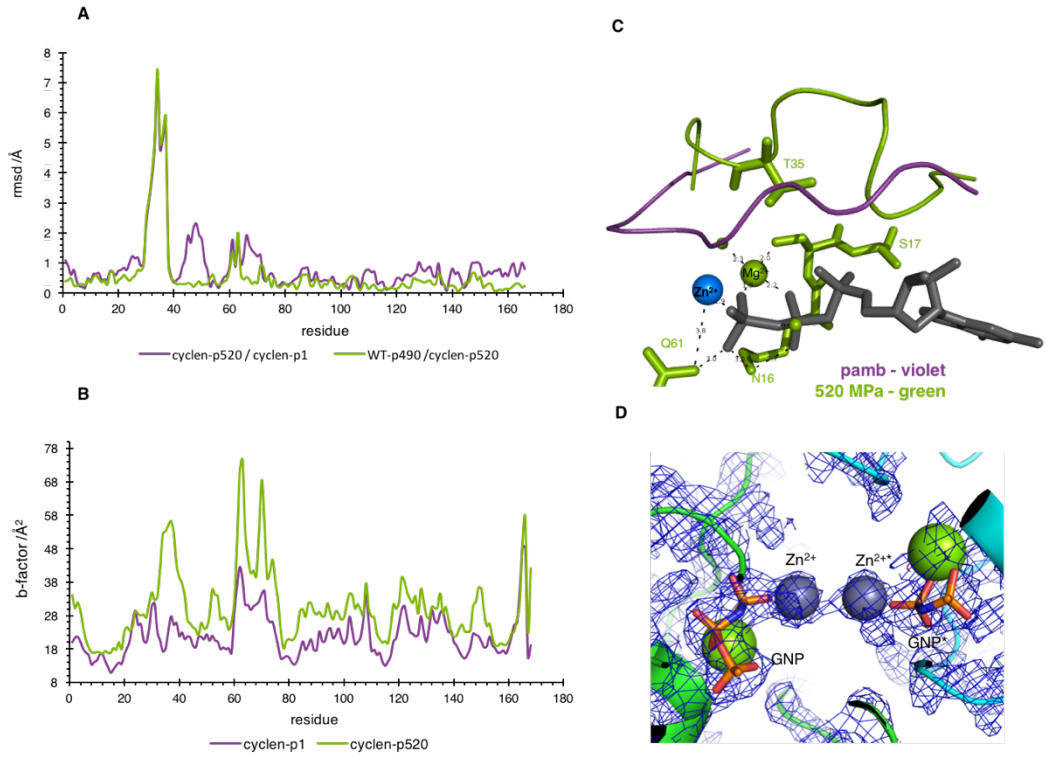

Figure 3.76. HP X-ray crystallography on Ras^{WT}(1-166)•Mg^{2+}•GppNHp complexed with Zn^{2+}-cyclen. **A.** rmsd plot of p520 against pamb (violet line) and Ras^{WT} Apo p490 against Ras•Zn^{2+}-cyclen p520. **B.** Plot of the b-factors for Ras•Zn^{2+}-cyclen at pamb (violet line) and p520 (green line). **C.** Details around the Zn^{2+} coordination site. This ion is stabilised by contacting the γ-phosphate and the side chain of Q61. The movement of switch 2 relative to the original position at pamb (violet ribbon) leads to the displacement of T35 and Y32 outwards. At 520 MPa these residues can no longer establish polar contacts with the nucleotide. D. Details evidencing the spatial symmetry of the Zn^{2+} ion. The distance between its symmetric counterpart is 4.2 Å.

- This page was deliberately left blank -

4. Discussion

“If you’re not part of the solution, you’re part of the precipitate”

Henry J. Tillman

4.1 Full-Length H and KRas. Conformational Equilibria and Inhibition by Zn^{2+}-cyclen

Due to the renovated interest in KRas it was presently investigated if the body of work previously conducted in HRas in terms of ^{31}P NMR could be transferred to KRas [67, 116, 155].

4.1.1 Interaction of $KRas^{WT}(1-188)•Mg^{2+}•GppNHp$ with Raf-RBD

The results showed that the equilibrium population distribution is almost identical in $HRas^{WT}$ and $KRas4b^{WT}$: two conformational states dominate the GppNHp spectrum with a K_{12}= 2.0 in both proteins (section 3.1.1, Figure 3.1). The interaction of $KRas^{WT}$ with the effector Raf-RBD was tested by ^{31}P NMR and showed that complex formation is characterised by a significant upfield shift of state 2(T) ($\Delta\delta$= -0.21 ppm, from δ= -3.30 ppm to δ= -3.51 ppm, Table 3.1). The difference indicates the state 2(T) is modified in the Ras-Raf complex by small conformational changes that are generally termed as an induced fit model of binding [263]. In order to distinguish these small but significant differences the notion of state 2*(T) was presently introduced. Additional studies reported by our department, involving the partial-loss-of-function mutants Ras^{T35A} and Ras^{T35S} led to the same conclusion regarding the weak-effector bound state 1(T): also in this case, state 1(T) isomerises into state 1*(T) upon effector binding [156] The upfield shift resulting from the general isomerisation process observed in the ^{31}P NMR spectra can be used in other studies as a fingerprint to discriminate between Ras mutants that can bind to Raf from non-binding ones.

The affinity of full length $HRas^{WT}$ and $KRas^{WT}$ towards Raf was also tested by ITC. The obtained K_D values of 0.24 μM and 0.72 μM, respectively, indicate that the former binds with a 3-fold greater affinity to the effector than the latter (Figure 3.2). Previous measurements reported in the literature indicate a K_D= 0.084 μM for the $HRas^{WT}$-Raf complex (measured at the same temperature and in 50 mM Tris/HCl pH 7.4, 5 mM $MgCl_2$ with 100 mM NaCl) [33, 244, 264], which corresponds to a 3-fold higher affinity compared with the presently obtained value. This difference can be due to the differences in buffer composition. No affinity data measured by ITC was found in the literature for the KRas•Raf complex.

The experimental ΔH, ΔG and $-T\Delta S$ values obtained here for $HRas^{WT}$•Raf are -13.1, -37.7 and -24.6 kJ mol^{-1}, respectively, and the corresponding published ones from the same study are -21.7, -40.6 and -18.8 kJ mol^{-1}, respectively [33]. The interaction has a very similar associated Gibbs free energy in both cases. The main difference lies on the different contributions: the published data has a greater enthalpic contribution and the present measurements show a greater entropic contribution.

In the case of the four Ras isoforms, all known effectors contact the protein surface in a similar way by establishing an intermolecular β-strand comprised of Ras-β_2 and β_3, and RBD-β_1 and β_2 elements [243]. Based on these structural similarities the 3-fold difference in the measured affinity might be due to the simple uncertainty of the measurements but can also be due to the influence of the hypervariable region (HVR) which is structurally different in both, H- and KRas isoforms.

4.1.2 Stabilization of State 1(T) by Zn^{2+}-cyclen Studied by ^{31}P NMR

The direct modulation of the conformational equilibrium by stabilising state 1(T) upon interaction with Zn^{2+}-cyclen was also addressed in this work in section 3.1.2. The obtained titration curves (Figure 3.3) show that this small compound binds to both isoforms in a cooperative manner (n=2) and their sigmoidal behaviour is indicative of at least two binding sites. The same conclusion was obtained when previous ^{31}P NMR spectroscopic studies conducted by our group revealed that $HRas^{WT}•Mg^{2+}•GppNHp$ shifts towards the weak binding state 1(T) upon binding of Zn^{2+} or Cu^{2+}-cyclens [157, 254]. This result also corroborates the finding of two different binding sites for Zn^{2+}-cyclen on the surface of the protein [157].

By fitting the plot of the chemical shift difference ($\Delta\delta$) of state 1(T) over the course of the titration as a function of Zn^{2+}-cyclen concentration to the Hill equation, a numerical value for the dissociation constant was found to be equal to 9.9 ± 0.2 mM (Figure 3.3), for both Ras isoforms. In parallel with this data, additional experiments reported by our group involving the titration of Ras^{T35S} led to the calculation of an IC_{50} =18 mM for this drug [156].Taken together, these values clearly show that the affinity of Zn^{2+}-cyclen for Ras is too low for *in vivo* investigations. However, its mode of action on Ras, and possibly on other GTPases renders it a lead compound for the allosteric inhibition of effector interaction. Its direct localization at the active centre of Ras can be exploited to derive more selective compounds, especially for oncogenic variants. Despite its low affinity, studies performed by stopped-flow kinetics were able to show that it has a clear inhibitory effect on the Ras-Raf interaction.

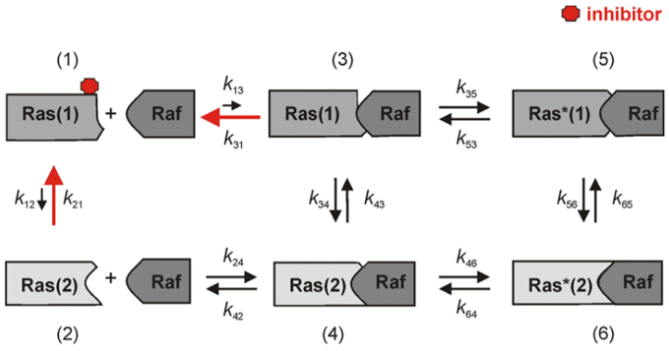

Figure 4.1. Typical mode of action of Zn^{2+}-cyclen and other state 1(T) inhibitors. Upon interaction with Raf, state 2(T) of Ras isomerises into state 2*(T). Zn^{2+} cyclen perturbs this process by stabilising state 1(T), decreasing the population of state 2(T) and preventing the transition into state 2*(T). Taken from [156].

The reported association rate constant, k_{on}, for the complex formation in its absence and in its presence is 19.0 μM^{-1} s^{-1} and 2.2 μM^{-1} s^{-1}, respectively [156]. Figure 4.1 shows schematically its mode of action.

The studies on the inhibition of Ras by Zn^{2+}-cyclen were further complemented by investigating the displacement of this drug from full-length $HRas^{WT}$ and $KRas^{G12D}$ upon addition of increasing amounts of Raf-RBD (Figures 3.4 and 3.6, respectively). It was demonstrated that both, Raf and Zn^{2+}-cyclen compete for binding to Ras and that the original equilibrium observed at the γ-phosphate for the Ras-Raf complex can be fully restored when a 2-fold excess of effector is added to the original Ras•Zn^{2+}-cyclen complex. These results were further complemented by fluorescence titration experiments reported in the published paper [156]. They further indicated that the interaction between the conformational state 1(T) and Zn^{2+}-cyclen prevents the formation of a trimeric complex Ras•Zn^{2+}-cyclen•Raf in significant concentrations.

4.1.3 Conformational Equilibria of $KRas^{G12D}$•GTP and $KRas^{G12V}$•GTP

The conformational equilibria for the full-length oncogenic variants $KRas^{G12D}$ and $KRas^{G12V}$ bound to Mg^{2+}•GTP was also investigated by ^{31}P NMR (section 3.1.4, Figure 3.5 and Table 3.6). From the obtained spectra, state 1(T) at the γ-phosphate can be directly observed for G12V but not for G12D or the *wild type* proteins. This indicates that the P-loop mutation form Gly12 to Val12 leads to a significant perturbation of the chemical environment on the γ-phosphate. However, the mutation to Asp has virtually no significant influence based on the spectra of $KRas^{WT}$. Structural relationships that might explain these differences are difficult to assess, especially because there are no crystal structures of the GTP-bound mutants. The observation of the corresponding crystal structures of $HRas^{G12D}$(1-166)•Mg^{2+}•GppNHp (pdb: 1agp) and $HRas^{G12V}$(1-166)•Mg^{2+}•GppNHp (pdb: 4efm) shows that the arrangement of Gln61, Tyr32 and Pro34 differs markedly between the two mutants. In the case of $HRas^{G12D}$ the Asp12 side chain establishes an H-bond to the side chains of Gln61 and Tyr32, that becomes very close (2.65 Å) to the γ-phosphate and pulled towards the interior of the molecule. Gln61 is also pulled towards the γ-phosphate and Pro34 is fully exposed at the surface. In the case of $HRas^{G12V}$ Tyr32 points away from the molecular surface, being more than 4 Å distant the γ-phosphate [265]. These differences account for the different ^{31}P NMR spectral features of the GTP-bound proteins, especially the different movement of Tyr32, and for their different GTPase activity (G12D being 70% faster than G12V) [266, 267].

- This page was deliberately left blank -

4.2 Modulation of the Conformational Equilibrium of KRas^{G12D}(1-188)•Mg^{2+}•GppNHp by Small Compounds

4.2.1 General Considerations

The effect of different 15 small compounds in the conformational equilibrium of KRas^{G12D} bound to Mg^{2+}•GppNHp was investigated by ^{31}P NMR (section 3.2). Six of them (#643, #098, #703, #449, #071, #109) have no pronounced effects, contrary to the remaining nine (#727, #755, #757, #612, #613, #624, #307, #308, #616) that lead to a decrease of the K_{12} values relative to Ras alone. The highest effects are observed for the Fesik compounds #755 and #757 [145] as well as (but at a smaller extent) the Sulindac analogues #307 and #308 [147, 148]. A global overview is given in Figure 4.2 were the equilibrium constants are plotted for the tested concentrations of 1.5 mM (grey) and 3.0 mM (orange). Under the present conditions, the equilibrium could not be shifted completely. This may be due to an inherent property of these inhibitors or simply because the 3.0 mM maximum concentration is not sufficient.

Most of the compounds are intrinsic allosteric inhibitors of Ras that act by stabilising state 1(T) leading to a decreased SOS-mediated exchange activity; although their main function is assumed to focus on the GDP-bound state (as state 1(D) stabilisers), their action can be extended to GppNHp-bound Ras as proven here, and most certainly also to GTP-bound

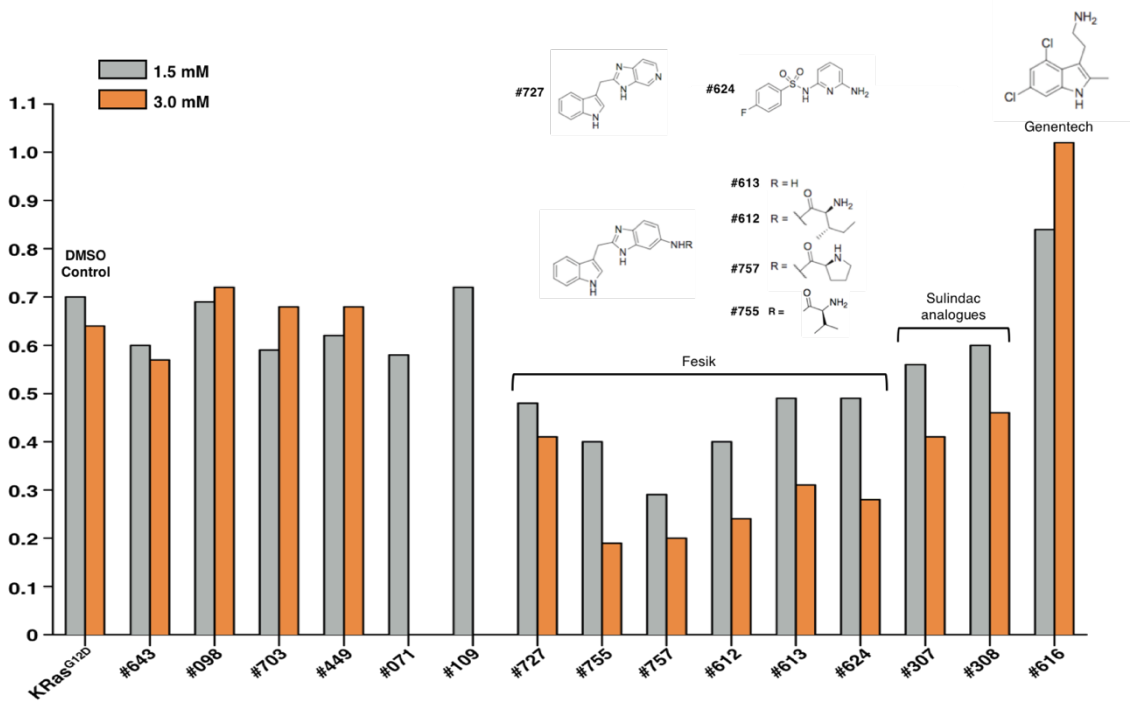

Figure 4.2. Comparative plot of the obtained equilibrium constants, $K_{12}=A_{state2(T)}/A_{state1(T)}$, for the γ-phosphate of KRas^{G12D}•Mg^{2+}•GppNHp in the presence of the tested compounds at 1.5 mM (grey colour) and 3.0 mM (orange colour). The first bar, noted as, 'KRas^{G12D}, refers to the control experiment were the influence on K_{12} was measured in the absence (grey) and in the presence (orange) of 6% DMSO. The six compounds published by the Fesik group and their structural differences are indicated together with DCAI from Genentech.

Ras. This series of experiments also shows that ^{31}P NMR spectroscopy can be used to quickly select and score potential drug candidates from large libraries. This is extremely useful in the field of Ras inhibition and can be potentially extended to any other GNBP from the Ras superfamily.

The inhibitory effect of the two Fesik compounds and DCAI is discussed in more detail in the following sections.

4.2.2 Inhibition of Ras-Raf Interaction by #755 and #757 Followed by ITC

Both compounds impair the protein complex formation, with #757 having the highest inhibitory effect (sections 3.2.9 and 3.2.10). The measured K_D for the Ras-Raf binding increases from 0.37 μM to 0.62 μM in the presence of 300 μM of #755 and from 0.37 μM to 3.54 μM in the presence of an equal concentration of #757. Both differ only in the substituents at their benzimidazole group, with #755 having an methylbuthanamide moiety and #757 having a bulkier, proline-like, moiety (Figures 3.15 and 3.17) [133, 145]. The bigger size of the proline substituent of #757 allows the molecule to expand further into the binding cleft (Figure 3.17) and accounts for the enhanced disruption of Ras-Raf mediated interaction [145]. As #757 is bulkier, its binding on the Ras surface leads to a more pronounced rigidity of the protein around the binding site compared to #755, which implies a greater effort in performing a conformational modification to achieve Raf binding. This interpretation explains the negative entropic contribution (positive $-T\Delta S$, Figure 3.18) of the process in the presence of #757, contrary to #755, where the more hydrophilic methylbuthanamide would favour an extended water network in the vicinity of the binding cleft, responsible for the positive enthalpic and entropic contributions (Figure 3.16).

The positive increase in entropy from the Ras-Raf complex alone comparatively with the same complex in the presence of #755 ($-T\Delta S$= -13.3 kJ mol^{-1} vs -25 kJ mol^{-1}, Figure 3.16) could be unrelated with the characteristics of complex formation but instead due only to unspecific effects (such as decreased solubility of the ligand in solution). A direct contribution for the increase in entropy can be related with the binding of #755 to Ras and the associated release of hydration waters from the contact surface of the protein [268]. The true contributions, however, are difficult to rationalize due to the likely existence of enthalpy-entropy compensation mechanisms where a ligand modification that results in a change in the enthalpic contribution to binding $\Delta\Delta H \equiv \Delta H_{\text{Ras/drug-Raf}} - \Delta H_{\text{Ras-Raf}}$ can be partially or fully offset by a similar change in the entropic component of binding, $\Delta\Delta TS \equiv \Delta TS_{\text{Ras/drug-Raf}} - \Delta TS_{\text{Ras-Raf}}$ [244, 269]. When enthalpy-entropy compensation occurs, normally $\Delta\Delta H$ and $\Delta\Delta TS$ share the same and that $\Delta\Delta G \approx 0$. This is presently the case for #757: comparing the

titration in the presence of 150 μM of #757 (Figure 3.18B) with the Ras-Raf interaction alone (Figure 3.18A) it follows that $\Delta\Delta H$= -28 kJ mol^{-1} and $\Delta\Delta TS$= -32 kJ mol^{-1}. The changes in the Gibbs energy, $\Delta\Delta G$, are only 4 kJ mol^{-1}. Similar values are obtained for the binding of the two proteins measured in the presence of 300 μM of the drug [270, 271].

4.2.3 Inhibition of Ras-Raf Interaction by #616 (DCAI) Followed by ITC

DCAI from Genentech [18] represents an interesting case since it inhibits Raf binding by a factor of 10 (K_D= 3.53 μM at 300 μM of #616 vs 0.37 μM in Ras alone) but shifts the equilibrium in the opposite direction, favouring state 2(T) (K_{12} increases from 0.7 in Ras in 6% DMSO to 1.02 at 3.0 mM, section 3.2.16, Table 3.3). *In vivo* Ras-Raf inhibition in its presence was also reported and further supports the present ITC data [18]. How can a compound stabilise the effector recognising state and at the same time inhibit the interaction with Raf? Within the conformational model of Ras it can be speculated that #616 stabilises state 3(T) that is adjacent to state 2(T) in the ^{31}P NMR spectrum (see [171] and section 3.4.1.2). The chemical shift of state 2(T) shifts downfield, from δ= -3.49 ppm in Ras in 6% DMSO to δ= -3.40 ppm at 3.0 mM of the drug (Table 3.2) and the chemical shift of state 3(T) in the Ras-NF1 complex is δ= -3.0 ppm. A $\Delta\delta$ of 0.4 ppm is observed. It is not possible to unequivocally ascertain if the drug stabilises indeed state 3(T) despite leading to the same downfield shift of state 2(T) and to an increase of its relative area. If this is the case, DCAI would have a double effect as an inhibitory drug, since it could also stimulate the GTPase reaction. A straightforward way to prove this hypothesis would rely in the comparison of the intrinsic and GAP stimulated GTPase reaction in its absence and in its presence.

- This page was deliberately left blank -

4.3 High Pressure ^{31}P NMR Spectroscopy

4.3.1 High Pressure ^{31}P NMR on GppNHp

Reported studies have shown that pressure coefficients of model peptides are significantly influenced by pH when the side chain pK_a value is close to the pH value at which the experiment is being performed [272]. Assuming that this finding is applicable to other molecules, including nucleotides, the pH-dependent chemical shift changes of GppNHp were presently avoided by working at a pH value of 2-3 units above the pK_a for the deprotonation of the third phosphate group [116]. This corresponds to a pH of 9.0 and 11.5 in the presence and in the absence of Mg^{2+}, respectively.

Following the pressure-dependent resonance lines in Figure 3.26, section 3.3.1, it is possible to observe that all the chemical shifts decrease with pressure (they become more negative, corresponding to an upfield shift in the spectra, see also Figure A, appendix). If this would be due to a pressure induced pH-change (and not to a pressure effect), then the pH of the sample would drop by more than 2 units (or the intrinsic pKa should increase). This possible variation in pH was followed by measuring any shift changes of the ^{1}H resonance spectra from the Tris buffer, which works as a pH sensor. A maximum shift of -0.006 ppm at pH 9.0 (in the presence of Mg^{2+}) and -0.0012 ppm (in the absence of Mg^{2+}) was found [226]. This corresponds to a slight increase in the pH smaller than 0.2 units (which is on itself difficult to detect by NMR) and would lead to a small downfield shift of the phosphate resonances, partially compensating the pressure-induced upfield shifts. The pK_a value of the nucleotide should decrease since pressure usually leads to a dissociation of protons. Therefore, the obtained pressure shifts cannot be explained by a pH or a pK_a effect and are therefore a true consequence of intrinsic pressure-induced structural modifications on GppNHp [226, 249].

4.3.1.1 Pressure Effects in the Presence and in the Absence of Mg^{2+}

All calculated second order coefficients are higher for GppNHp than Mg^{2+}•GppNHp (Table 3.5), indicating that Mg^{2+} has the effect of stabilising the ground-state conformation(s) of the nucleotide, rendering it more insensitive modulation by pressure.

In the presence of this ion (Figure 3.26A), the α-phosphate shows the smallest pressure dependence, with a $\Delta\delta$ of -0.028 ppm between 0.1 and 200 MPa. The β- and γ-phosphates are prone to considerably larger effects, with $\Delta\delta$ values of -0.25 and -0.2 ppm, respectively. The same behaviour is also observed in the absence of Mg^{2+} (Figure 3.26B): the α-phosphate is always the least pressure dependent. Comparing the intensity of the shift changes with and without Mg^{2+}, it becomes clear that the $\Delta\delta$ values are considerably higher

in the latter case. Considering γ-phosphate as an example, $\Delta\delta$= -0.2 ppm in the presence and $\Delta\delta$=-0.40 in the absence of Mg^{2+}.

All phosphorous resonances, including inorganic phosphate (P_i), are characterized by negative B_1 values. This is indicative of an initial upfield shift of the resonance lines, as the pressure is increased. The conclusion is valid for both, with and without Mg^{2+}.

Analysing now the differences between the two separately, in the absence of Mg^{2+} all phosphate resonances are characterized by positive B_2 coefficients, indicating a "saturation" like behaviour at high pressures (i.e. the pressure induced chemical shift changes become smaller at higher pressures, which is noticeable by the plateau-like shape of the curves in Figure 3.27, and this can be associated with $B_2 > 0$). The same is observed, in fact, in the presence of Mg^{2+}, except for the α-phosphate that has a negative B_2. Published results by our group have shown that at higher pressures there is a general tendency for the adenine and guanine nucleotides to dissociate from the metal ion. This is generally accompanied by a downfield shift of the resonance lines [226, 249]. Although, no downfield shift is presently observed for any of the Mg^{2+}•GppNHp phosphates. The same effect could also be used in a tentative way to explain the "saturation"-like behaviour of the curves. However, the same behaviour is observed for GppNHp in the absence of Mg^{2+} (Figure 3.26) which leads to the conclusion that the small chemical shift changes at higher pressure are not a specific effect arising from the release of Mg^{2+} but due to a true pressure-dependent mechanism that is correlated with the structural dynamics of GppNHp in solution [226, 249].

Although HP NMR in nucleotide binding proteins is not a widely pursued topic by the scientific community, the knowledge gathered about the behaviour of isolated GppNHp and other nucleotides under pressure is detrimental to understand the true mechanistic pressure effects on the conformation and equilibrium of Ras and other nucleotide binding proteins [273].

The ^{31}P NMR chemical shifts of nucleotides can be mainly ascribed to two factors: conformational strain of bonds and electric field effects that lead to the polarization of the oxygens in the phosphate groups. Bond polarization by hydrogen bonding or nearby electric charges that can cause small shifts in the protonation/deprotonation equilibrium may be the dominant factors [274]. Additional effects might be caused by magnetic anisotropy of the guanine ring that assumes different averaged positions relative to the phosphate groups in a syn/anti equilibrium [275]. The average position and average orientation of the ring is influenced by pressure, which leads to the observed chemical shift dependencies at the phosphate groups.

4.3.2 High Pressure ^{31}P NMR on Ras Proteins

4.3.2.1 HP ^{31}P NMR on HRas^{WT}(1-166)•Mg^{2+}•GppNHp

Measurements at 278 K

For all proteins investigated, the processing of the experimental data with an appropriate Gaussian function revealed to be better than a Lorentzian function in retrieving accurate chemical shift values (section 3.3.2.1, Figure 3.28).

As the pressure increases, the integrals corresponding to state 2(T) decrease, concomitantly with the increase of the integrals corresponding to state 1(T) (Figure 3.27, green line). At 250 MPa, state 1(T) dominates over 2(T), given by the decrease in the equilibrium constant from 1.7 at 0.1 MPa to 0.24 at 250 MPa. This entails a direct evidence for the pressure-induced 2(T)-to-1(T) transition. The calculated difference of the free energy, ΔG_{12} and partial molar volume, ΔV_{12}, is 1.53 kJ mol^{-1} and -18.60 mL mol^{-1}, respectively (Figure 3.30). Similar values were found in previous studies on the full-length variant [125]. it is thus possible to conclude that the dependence of LnK_{12} with pressure is not linear. A closer look to the distribution plot indicates a slight but continuous deviation from linearity over the tested pressure interval. This is a direct evidence for the fact that 1(T) and 2(T) do not represent pure states but have additional (or 'hidden') contributions from states 3(T) and 1(0) [171, 276].

Since in state 1(0) the affinity of Ras towards the nucleotide is much lower comparatively with state 1(T), the release of nucleotide from the protein should be observed at high pressures [67]. This is indeed detected, especially at 220 and 240 MPa by the presence of the small additional peaks at δ= -1.33, -6.0 and -10.15 ppm, corresponding to the free α, β and γ-phosphates, respectively (Figure 3.27). This finding, together with previous denaturing studies involving GdmCl [125] leads to the conclusion that state 1(0) is coupled with state 1(T) and by application of pressure, the equilibrium can be shifted in the 1(T)-to-1(0) direction. It is expected that such a conformational transition involves a great readjustment of the Ras surface and should be therefore governed by a slow exchange mechanism, which is marked by a change in the ^{31}P NMR peak areas of the $\gamma_{1(T)}$-phosphate but not in chemical shifts. This is verified when considering the uncorrected values for the $\gamma_{1(T)}$-phosphate: the variation of the pressure-induced shift, $\Delta\delta$, is only 0.015 ppm (Figure 3.29 and Table F, appendix section) corresponding to a very small change that lies in the limits of the error of the measurement. However, the corrected value shifts downfield by a $\Delta\delta$ of 0.241 ppm (blue line in Figure 3.29). In this case the transition 1(T)-to-1(0) becomes governed by a fast exchange process.

If the transition to the nucleotide free state 1(0) is coupled with state 1(T), then by exclusion, the transition towards the GAP recognition state is coupled with state 2(T). This is directly observed from the Ras-GAP titration experiments (Figure 3.39 and [117]). Following the ^{31}P pressure dependence of the $\gamma_{2(T)}$-phosphate (Figure 3.27 and Table F appendix section) one can observe that this signal shifts from δ= -3.33 ppm at 0.1 MPa, to δ= -3.00 ppm at 110 MPa, down to δ= -2.68 ppm at 250 MPa (these refer to the corrected pressure values). Such continuous downfield shift is indicative that this state is in fast exchange with another state, namely 3(T), that becomes prominent at high pressures. Previous HP [^{1}H-^{15}N]-HSQC NMR investigations have shown that 3(T) is most populated around 110-130 MPa (Figure 1.13, section 1.3.2 [171]) and the presently obtained HP ^{31}P chemical shifts nicely agree with this result (the corrected δ values obtained at 110 and 130 MPa are -3.0 and -2.96 ppm, respectively).

4.3.2.1.1 Analysis of Pressure Coefficients, Energy and Volume Changes

The necessity for subtracting the pressure-dependent chemical shifts of free Mg^{2+}•GppNHp from the chemical shifts of the protein is supported by the observation that the ^{31}P NMR signals of the free nucleotide and the nucleotide-bound protein shift in opposite directions (the α- and γ-phosphates shift upfield in the former and downfield in the latter. The β-phosphate shifts in the same direction, Figures 3.26 and 3.29). Upon correction, all phosphate groups of the nucleotide-bound protein shift further downfield relative to the uncorrected case, as indicated by the absolute increase of the B_1 values. The most linear pressure-dependence was found for the $\gamma_{1(T)}$-phosphate, whose B_2 decreases from 1.90 to 0.4 ppm GPa^{-1} upon correction and the most non-linear dependence was found for $\alpha_{1(T)}$ and $\alpha_{2(T)}$-phosphates, with a $B_{2(\text{corrected})}$= -2.40 and -1.46 ppm GPa^{-1}, respectively (Table 3.6).

The obtained ΔG and ΔV values are largely dependent of the initial values given as input for the iteration process (experimental section 2.2.5.4, eqn. nº17). Nevertheless, the fitting led to some interesting results: It is valid to assume in a first approach that state 2(T) on both, the α- and γ-phosphates is prone to the same type of transition. However, the obtained ΔG and ΔV values are considerable different (Table 3.6). For example, $\Delta G\alpha_{2(T)\text{corrected}}$= 8.17 kJ mol^{-1} and $\Delta G\gamma_{2(T)\text{corrected}}$= 3.44 kJ mol^{-1}. The corresponding ΔV values are -85.19 and -37.31 mL mol^{-1}. The difference can be due to the intrinsic difficulty of the fitting routine or due to a more complex profile of the conformational equilibria, with the $\alpha_{2(T)}$- and $\gamma_{2(T)}$-phosphates effectively sensing different transitions. The same kind of assessment can be made regarding state 1(T). The averaged $\Delta G_{\text{corrected}}$ value for the 2(T)-to-3(T) transition is 5.81 kJ mol^{-1} which is in good agreement with the reported value of 5.2 kJ mol^{-1} from

previous experiments [171]. A slightly greater difference is found in terms of ΔV values (-61.25 vs -81.0 mL mol^{-1}, respectively). Regarding the 1(T)-to-1(0) transition greater discrepancies between both measurements were found with the averaged $\Delta G_{corrected.}$= 3.68 kJ mol^{-1} obtained from the present ^{31}P HP data and the reported one being 12.4 kJ mol^{-1}.

Measurements at 303 K

When the temperature is increased from 278 to 303 K (Figures 3.31 and 3.32), the two conformational states coalesce into a single resonance line. The ^{31}P NMR series becomes represented by the chemical shift evolution of the three phosphate groups, with their populations being a weighted average of the ones detected at 278 K. The obtained ΔG and ΔV values for the α-, β- and γ-phosphates are numerically very similar to each other (ΔG= 6.39, 5.50 and 5.65 kJ mol^{-1}, respectively and ΔV= -43.92, -43.17 -54.78 mL mol^{-1}, respectively, Table 3.7), Their similarity is a direct indication that the three phosphate groups are experiencing the same type of transition at this temperature.

In summary, the ^{31}P HP NMR series presently investigated provide a much more comprehensive survey for the dynamics of the protein at the nucleotide bound level than the previously published HP series (Figure 1.12A, [125]).

4.3.2.2 HP ^{31}P NMR on Ras^{T35S}(1-166)•Mg^{2+}•GppNHp

From the series shown in Figure 3.33 (section 3.3.3), increasing the pressure has no effect on the dynamics of state 2(T). This means that this state cannot be repopulated, even at high pressures. For such reason, the only possible conformational transition that can be assigned to the system is the 1(T)-to-1(0).

The response of Ras^{T35S} to pressure is generally smaller and more linear than Ras_{WT} (Figure 3.33). One exception is the α-phosphate of the mutant that shows a large second order coefficient ($B_{2(corrected)}$= -2.27 ppm GPa^{-2}, Table 3.8).

The obtained thermodynamic values for each phosphate group are numerically similar, indicating that all are involved in the same transition even at 278 K (ΔG= 3.49, 4.55, and 5.15 kJ mol^{-1} and ΔV= -70.7, -51.0 and -57.0 mL mol^{-1} for the α-, β- and γ-phosphates, respectively, Table 3.8). One would expect that at high pressure a large amount of bound nucleotide would be released by the protein, as state 1(0) becomes populated. However, no free Mg^{2+}•GppNHp can be observed in this series (Figure 3.33), contrary to Ras^{WT} (Figure 3.27). This apparent contradiction has no straightforward explanation. One can argue that most likely the 'true' nucleotide-releasing state occurs at much higher pressures than 200 MPa and that the population distribution of state 1(0) obtained from a

thermodynamic model previously reported in other studies is greatly overestimated (i.e. at ca. 200 MPa, the population of state 1(0) is probably much lower than predicted) [171]). Another explanation can be related with the existence of residual amounts of alkaline phosphatase (AP) inside the NMR tube. The presence of this enzyme would exert a sequential hydrolytic activity in the nucleotide that would be released, and given enough time, all of it would be converted to P_i. Indeed the P_i resonance line, located at δ= 3.37 ppm (Figure 3.33) increases in its relative area over time. Nucleotide exchange using an immobilised AP column procedure instead of the 'classical' approach (experimental section 2.2.2.4) was precisely devised and performed for all Ras samples used in HP experiments in order to alleviate this problem.

Two obtained crystal isoforms of Ras^{T35S}•Mg^{2+}•GppNHp (pdb: 3kkn, form 1 and 3kkm form 2) constituted the first evidence for the occurrence of regional polysterism on state 1(T): both forms are a structural manifestation of this state [242]. From an NMR point-of-view, this type of polysterism would be characterised by the existence of more than one signal for a specific phosphate group(s), just like in the *wild type* case. However, no additional signals are detectable during the pressure series close to state 1(T), probably due to the too small modifications of the chemical environment around the nucleotide and to an intermediate or fast exchange regime for the interconversion between such conformations.

4.3.2.3 HP ^{31}P NMR on $KRas^{G12V}$(1-188)•Mg^{2+}•GTP

There are two remarkable features that deserve to be addressed: the first one is the direct observation of two distinct conformational states, 1(T) and 2(T), on the β-phosphate and their interplay as the pressure is increased from 0.1 up to 195 MPa (section 3.3.4, Figure 3.35. These states cannot be separated at the corresponding β-phosphate on the HP series of Ras^{WT} bound to GppNHp as they lie very close to each other (Figure 3.27 and [125]). The second feature is related with the different response to pressure of GTP and GppNHp-bound Ras. From the higher B_2 values and the more pronounced curvature of the chemical shift dependencies (Figure 3.36 and Table 3.9) it can be concluded that GTP-bound Ras is more sensitive to pressure than GppNHp-bound Ras. This is a reasonable finding since one can envisage that the additional imido group from GppNHp is capable of establishing additional polar contacts with the protein backbone (Figure 1.2), leading to a more conformational stiffing in its vicinity [124]. The considerations for the specific transitions made for Ras^{WT} and Ras^{T35S} are the same in the case of Ras^{G12V}, with state 2(T) being directly coupled to state 3(T) and state 1(T) being coupled with 1(0). The obtained ΔG and

ΔV values are in this case is particularly inaccurate due to the small number of pressure points collected and the high signal-to-noise ratio of the experimental data.

4.3.2.4 HP ^{31}P NMR on HRas^{D33K}(1-166)•Mg^{2+}•GppNHp

The ^{31}P pressure-dependence of a novel mutant Ras^{D33K}•Mg^{2+}•GppNHp was also investigated in this thesis in section 3.4.7. Contrary to Ras^{T35S} that exists in state 1(T), Ras^{D33K} is almost completely shifted towards state 2(T) and shows only a residual population of state 1(T) at 0.1 MPa (Figure 3.53). Pressure leads to the direct effect of repopulating state 1(T) at the γ-phosphate but not at the α-phosphate which remains locked in the initial conformation and shifts only by a $\Delta\delta$ of 0.054 ppm (Figure 3.54, Table 3.23). Although the characteristic downfield shift of the chemical shift values is observed for all the phosphate groups, the calculated thermodynamic parameters are rather different from Ras^{WT}. For example, $\Delta G\gamma_{1(T)corrected}$ is equal to 14.32 kJ mol^{-1} and 5.54 kJ mol^{-1} in Ras^{D33K} and Ras^{WT}, respectively. This envisages the conclusion that the conformational transitions induced by pressure on Ras^{D33K} are not identical to the ones observed for Ras^{WT}.

4.3.2.5 General Considerations

The HP investigations on the different Ras proteins revealed that the observed conformational transitions have a more complex thermodynamics than the initial model proposed by us [125, 171]. The experiments prove unequivocally the existence of several discrete conformations that can be assessed by pressure perturbation [159, 165], with almost all phosphate groups showing indeed a non-linear response. Nevertheless, the accurate characterization of high energy states revealed to be difficult because the conformational readjustments can be easily missed when the associated chemical shift changes are not very strong as in the case of ^{31}P NMR. The fitting of the broad Lorentzian lines with very often ill-defined centres is difficult and subtle but important aspects are impossible to detect, accounting for the also rather linear pressure dependency of most phosphate groups. Additional pH-dependent shift changes can obscure the true effects of pressure

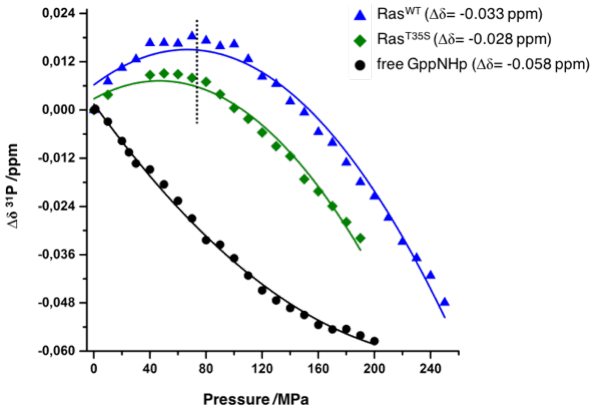

Figure 4.3. ^{31}P chemical shift variation of P_i plotted as a function of pressure for Mg^{2+}•GppNHp (black), Ras^{WT} (blue) and Ras^{T35S} (green). The dashed line indicates the pressure point of 70 MPa, for which the direction of the chemical shifts are reversed (from upfield to downfield).

[226]. To test if this is the case the analysis of the shift changes of free inorganic phosphate (P_i) was performed. Its resonance moves initially downfield by a $\Delta\delta$ of 0.023 ppm (between 0.1 and 80 MPa) in Ras^{WT} and Ras^{T35S} (Figure 4.3) and then upfield, with a $\Delta\delta$ of -0.054 ppm between 80 and 250 MPa. The total variation in the complete interval is only -0.033 ppm to which corresponds an insignificant change in pH over the course of the pressure series. Similar results were obtained by the analysis of the Tris signal in the ^{1}H NMR spectra (data not shown) [116, 249, 273], proving that the pH does not change considerably.

The ^{31}P chemical shift changes of Ras^{WT}, Ras^{T35S} and Ras^{D33K} are plotted together in Figure 4.4, allowing a general overview of the results: at the α-phosphate (top graph), the highest variation is observed for Ras^{D33K}, where the range of the $\Delta\delta$ values (from -11.49 to -11.0 ppm) occurs somewhere in between the values determined for states 1(T) and 2(T) of Ras^{WT}. The α-phosphate of Ras^{T35S} shows the less pronounced pressure dependence, with a $\Delta\delta$ of 0.090 ppm between 0.1 and 190 MPa. In all cases, the corrected and uncorrected shifts are close related and follow the same downfield direction.

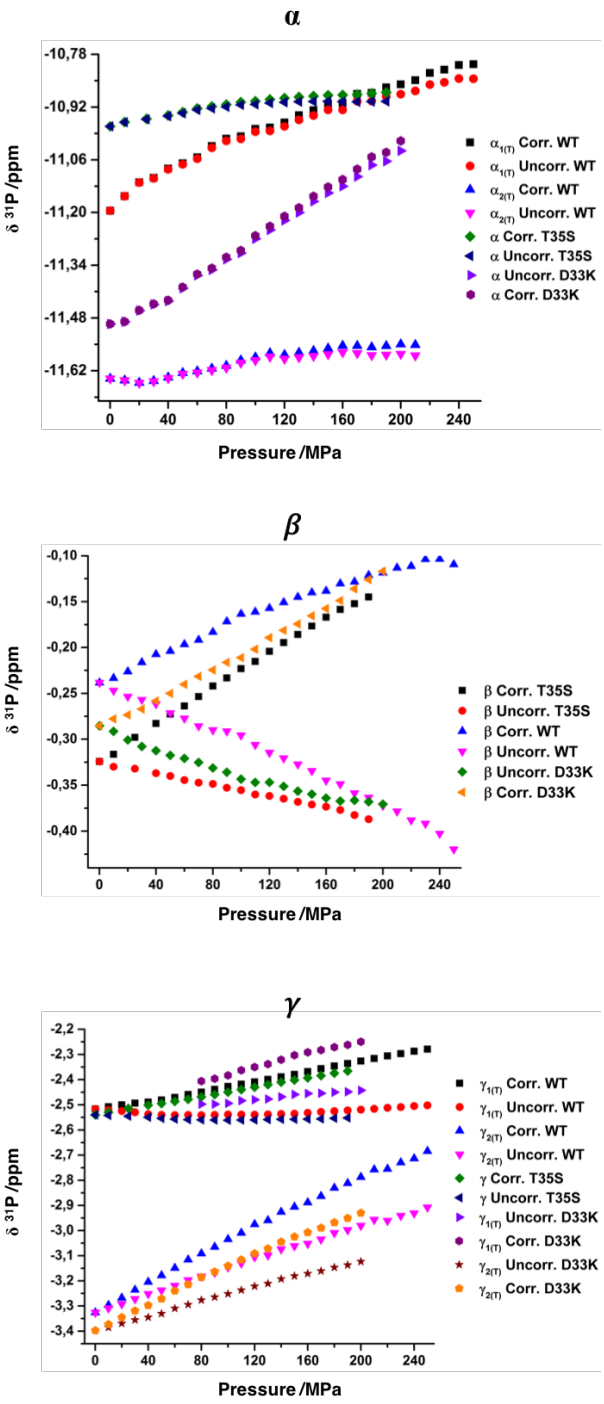

Figure 4.4. ^{31}P pressure-dependent chemical shift changes of Ras^{WT} and Ras^{T35S} and Ras^{D33K} in complex with Mg^{2+}•GppNHp recorded at 278 K, pH 7.5. Each plot shows the uncorrected and corrected changes for the α- (top), β- (middle) and γ-phosphates (bottom). Another version of this plot is shown in Figure E of the appendix where, instead the absolute chemical shifts, δ, shown here, the $\Delta\delta$'s= $\delta_{\text{last pressure point}}$-$\delta_{0.1\text{MPa}}$ are plotted as a function of pressure.

The chemical shift of the β-phosphate on Ras^{D33K} at 0.1 MPa lies somewhere in between

the one of Ras^{WT} and Ras^{T35S}. The magnitude of its pressure-induced shift is more or less identical for the three proteins (middle graph). In the case of γ-phosphate (bottom graph), the chemical shifts can be separated into two groups corresponding to state 1(T) and state 2(T), with the magnitude the former being smaller than the latter.

4.4 ^{31}P NMR Spectra of H, K and $NRas^{WT}(1\text{-}166)\bullet Mg^{2+}\bullet$GppNHp

It was shown herein that NRas, is the isoform with the highest K_{12} value (2.57 vs 1,57 for HRas and 1.83 for KRas) and with the lowest apparent K_D for Raf binding (0.18 μM vs 0.60 μM for KRas and 0.42 μM for HRas, section 3.4.1.1, Figure 3.38, Table 3.11). These results are in good agreement with each other as NRas is the variant with a higher state 2(T) population and concomitantly higher Raf-affinity.In this respect, contradictory results are published in a recent study reporting the first crystal structure of $NRas^{WT}$, where it is shown that the affinity of NRas to Raf is lower than the two other isoforms (the measured K_D values at 308 K for H, K and NRas are 0.094, 0.098 and 0.206 μM, respectively) [277].

4.5 Interaction of Ras^{WT}, Ras^{G12P} and Ras^{D33K} with NF1 Followed by ^{31}P NMR

4.5.1 $Ras^{WT}(1\text{-}166)\bullet Mg^{2+}\bullet$GppNHp$\bullet$NF1

The titration allowed the unequivocal assignment of state 3(T) for the α-, β- and γ-phosphates at -11.12, 0.07 and -3.00 ppm, respectively (Section 3.4.1.2, Table 3.12). A similar value was found in previous studies published by our group for the Ras-GAP333 complex [117]. In saturating amounts of NF1 (ratio 1:2, Figure 3.39), the α- and γ-phosphates are defined by a single resonance whose linewidth at half-height increases by a 3-fold factor (from 64 to 205 Hz), nicely reflecting 3-fold increase in size on the molecular mass of the complex (from 18 to 54 kDa).

The ill-defined, asymmetric centre of the β-phosphate above a 1:1 ratio is indicative of the existence of at least two different local conformational states. Keeping in mind the functional cycle of Ras, they can be explained on the basis that the GAP mechanism involves not only the isomerisation process, where Ras changes conformation to bind GAP, but also a transition state conformation that becomes stabilised by the arginine finger provided from GAP and is spatially oriented close to the β-phosphate (Figure 1.4) [23, 83]. The existence of different conformations at the nucleotide level in the Ras-GAP complex was also proved in recent studies involving FTIR spectroscopy and QM simulations [84]. The authors have shown that the geometry of $Mg^{2+}\bullet$GTP changes from a staggered position of the non-

bridging oxygen atoms of the β- and γ-phosphates to an eclipsed conformation, defined by different torsional and dihedral angles. This is caused by a change in the coordination to the Mg^{2+} ion from tridentate to bidentate forced by Ras and helped by the Arg finger from the GAP protein. These observations are in agreement with the profile of the present ^{31}P NMR titration.

4.5.2 Ras^{G12P}(1-166)•Mg^{2+}•GppNHp•NF1

Due to the greater separation between states 1(T) and 2(T) ($\Delta\delta$= 2.52 ppm, section 3.4.10.3, Figure 3.61 vs $\Delta\delta$= 1.63 ppm in Ras^{WT}) at the γ-phosphate, state 3(T) is better defined in this complex. Its resonance becomes upfield shifted by a $\Delta\delta$ of 0.22 ppm relative to its counterpart in the *wild type* protein (section 3.4.1.2, Figure 3.39 and [259]). Similar features are observed at the β-phosphate (at a 1:1 ratio, $\delta_{3(T)}$= 0.31 ppm and $\delta_{2(T),1(T)}$= 0.40 ppm, Table 3.28). Due to the identical profile of the titration relative to Ras^{WT}, the binding affinity of both proteins can be assumed as identical. Previous studies showed that this is indeed the case by using Ras^{G12P} to inhibit the GAP-mediated GTPase reaction of Ras^{Y32W}, whose GAP affinity is equal to Ras^{WT} but shows a large fluorescent change upon GTP hydrolysis that can be easily quantified [259]. The measurements have shown that the affinity of Ras^{G12P} to p120-GAP is slightly decreased (ca. 2.8-fold lower) compared to Ras^{WT}. A similar decrease was found in the case of Ras^{G12V} but not for Ras^{G12D}, which still retains the affinity to GAP [265, 278].

4.5.3 Ras^{D33K}(1-166)•Mg^{2+}•GppNHp•NF1

Ras^{D33K} has a lower affinity towards NF1 (section 3.4.5, Figure 3.51 and Table 3.21). Even at a Ras:NF1 ratio of 1:2, the line corresponding to state 3(T) could not be detected, indicating that complex formation is impaired, although a quantitative measurement for the interaction is not possible to obtain directly from the ^{31}P NMR titration.

The structural basis for the loss of affinity is so not clear since the contact surface with GAP is much more extensive than Raf and not only subjected to the effector-loop region [31, 38]. From the published Ras-GAP complex (pdb: 1wq1 [83]), D33 interacts with the positively charged N942 and K949 residues. Since both are also present in the structure of NF1, the lower affinity of Ras^{D33K} to NF1 can be explained by the same reasoning used for the Ras^{D33K}-Raf complex, based on the steric and electrostatic clashes between the two Lys residues (K33 and K949, see discussion section 4.7).

The measurement of the affinity between Ras and NF1 was attempted by ITC but in all cases no obvious binding curves could be obtained due to severe artefacts in the heat

signatures, corroborating the idea that the Ras-GAP complex formation does not obey to a single step and/or to steady-state conditions [255, 256]. Other methods such as fluorescence spectroscopy and thermophoresis could be used in the future to measure the affinity, complementing the present ^{31}P NMR data [77, 108, 255].

4.6 Mutational Studies on HRas^{WT}(1-166)

4.6.4 General Considerations

Figure 4.5 summarises the features of the GppNHp-bound ^{31}P NMR spectra obtained upon site-directed mutagenesis on Ras. From the seven investigated mutants, four of them (H27E, S39L, E3V and D33K) show novel structural properties, with Ras^{E3V} and Ras^{D33K}, being the most notable ones by dramatically affecting the dynamics of the bound nucleotide (D33K) and by exerting a clear allosteric interference that can be propagated from a distant localisation in the surface of the protein (E3V) and still affect the catalytic centre. This mutational investigation was performed with the expectation of shifting the conformational equilibrium at the nucleotide-bound level in the same direction previously predicted by HP NMR [125, 171]. The overall results show that in the light of the proposed 4-state model, the absence of a direct

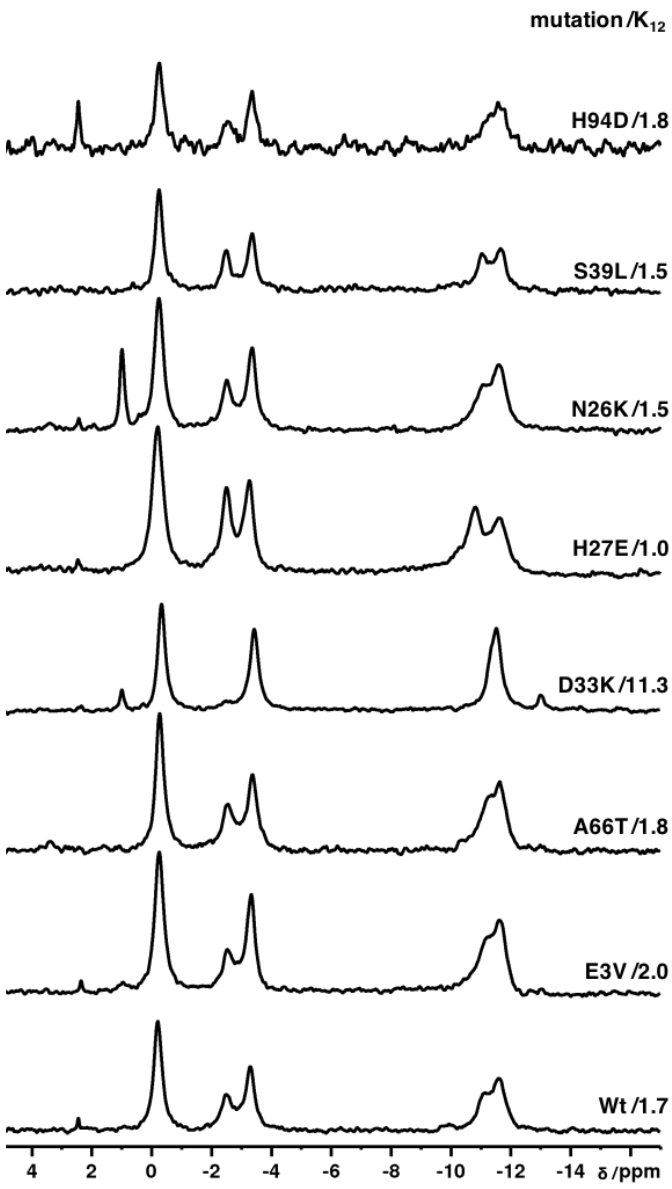

Figure 4.5. ^{31}P NMR spectra of the different Ras mutants bound to Mg^{2+}•GppNHp, created by SDM for the study of the conformational dynamics of Ras. The respective mutation, together with the calculated equilibrium constant, K12=Area2(T)/Area1(T) at the γ-phosphate is indicated. All the spectra were recorded at 278 K, pH 7.5 in a magnetic field operating at a ^{31}P frequency of 202.456 MHz (500 MHz spectrometer).

modification in the chemical shifts or integrated areas on the phosphate resonances of states 1(T) and 2(T) does not necessarily mean that the global equilibria is not affected. Any mutation can change both parameters for the conformational states 1(0) and/or 3(T) that are intrinsically hidden in the ^{31}P NMR spectra since they are low populated at ambient pressure (0.4 and 7.7%, respectively [166, 171]). To this respect, the directly observable ^{31}P NMR spectral lines can remain inalterable relative to Ras^{WT} but the equilibria can still be shifted by the mutation. For example, if state 1(T) increases at expense of state 2(T) but if this is compensated by an increase of state 3(T) at expense of state 1(0), the equilibrium would still be shifted towards state 1(T) and there would be no noticeably modification relative to Ras^{WT} (K_{12}= 1.7). This could be the case of Ras^{N26K}, Ras^{H94D} and Ras^{A66T}, all with a K_{12} value close to 1.7.

Figure 4.6 is a schematic representation of how the equilibrium can be modulated by the interplay of the four conformational states. Ras^{WT}, Ras^{T35S}, Ras^{H27E} and Ras^{D33K} are given as examples. For each one, the four states are indicated and arranged by their increasing order of energy. Possible conformational transitions from the most populated, lowest energy states 1(T) and 2(T) are indicated by the dashed arrows. Note that additional transitions exist and that different arrangements of the four states for the same protein are also possible. For example, state 1(T) on Ras^{T35S} can become populated by decreasing the energy for this state and/or by increasing the energy of state 2(T). State 1(T) in Ras^{H27E} can become populated by decreasing the energy of state 1(0) and state 2(T) in Ras^{D33K} can become populated by decreasing the energy of state 3(T) or increasing the energy of state

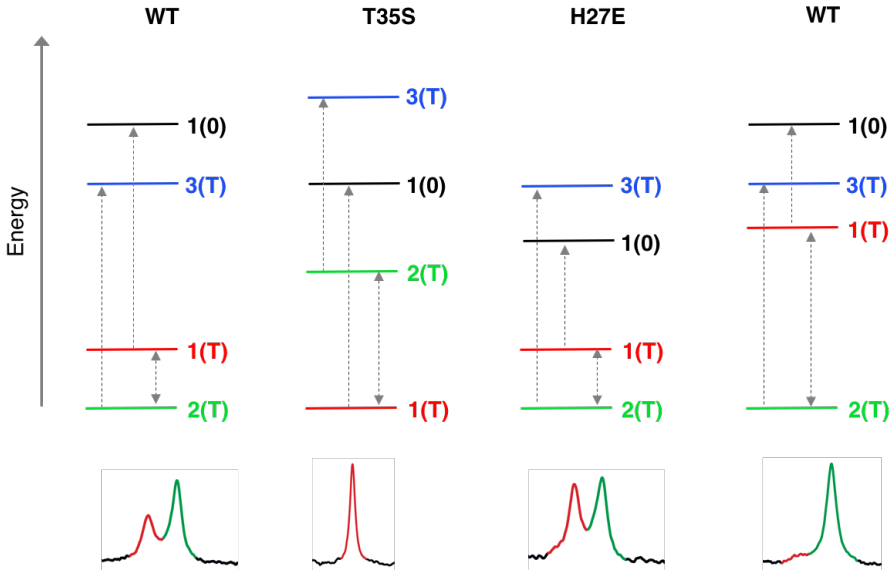

Figure 4.6. Interplay between the four different conformational states of Ras proteins. States 1(T) to 4(T) are coloured in red, green, blue and black, respectively and shown by their increasing order of energy Ras *wild type*, T35S, H27E and D33K are given as examples. The respective ^{31}P NMR resonance at the γ-phosphate is also shown. The dashed lines represent conformational transitions starting from states 1(T) and 2(T). Note that other possibilities exist.

1(T)/1(0). The energy difference between them can be modulated by pressure, as discussed in section 4.3.2 [123, 125, 171].

In summary, the study of the different Ras mutants shows the complex dynamics of this protein but also the limitations of ^{31}P NMR in uncovering all of its conformational states [16, 123, 125, 163]. A discussion of the spectroscopic and biochemical properties of each mutant is given in the following sections.

4.6.2 2(T)-to-1(T) Transition: N26K, A66T and H94D

In the light of the results obtained none of the three individual mutants led to a directly observable shift of the conformational equilibria in the direction of state 1(T). Their investigated properties are not different from the *wild type* protein. No chemical shift or linewidth differences were detected between them and Ras^{WT} (section 3.4.2.1, Figures 3.41 and 3.42, Table 3.13) despite N26K and A66T being located in the vicinity of the nucleotide at the beginning of switch 1 and middle of switch 2, respectively (Figure 3.40, [16]). A 1.7-fold increase in of the intrinsic hydrolysis rate for Ras^{H94D} in presence of Raf-RBD was however detected (k_{cat}= 0.035 min^{-1} vs 0.021 min^{-1} in Ras^{H94D} alone, Figure 3.43B and Table 3.14). The dissociation constant for the Raf binding obtained for the three mutants is also similar to Ras^{WT}. An averaged increase of -8 kJ mol^{-1} in the enthalpy of binding was however found for all of them relatively to Ras^{WT}. With exception of D94, the other two mutants are involved in polar contacts with the surface of Raf [33].

4.6.3 2(T)-to-1(0) Transition: E3V and S39L

Larger effects were found in the case of Ras^{E3V} and Ras^{S39L}. Both mutations led to a meaningful modification of the conformational dynamics, independent of the expected direction of the underlying transition (section 3.4.2.2).

Ras^{S39L} shows a significant perturbation of state 1(T) at the α- and γ-phosphates, both becoming downfield shifted by 0.1 ppm relative to Ras^{WT} (δ= -11.08 and -2.50 ppm, respectively vs δ= -11.17 and -2.57 ppm in Ras^{WT}, Table 3.15), and with a decrease in the equilibrium constant from 1.7 to 1.5 favouring state 1(T). The rates of exchange for this state are also slightly faster comparatively to Ras^{WT} as given the average 1.4-fold decrease of their line broadening. Rather interestingly, the affinity of Ras^{S39L} to Raf increases by more than 5-fold, despite the shift towards the weak effector interacting state (K_D= 0.0074 vs 0.424 μM, Table 3.16).

Ras^{E3V}, on the other hand, shifts in the opposite direction, showing a 20% increase in the integrated area of state 2(T) at the γ-phosphate (Figure 3.45). The equilibrium constant

increases from 1.7 to 2.0. However, the affinity to Raf remains unperturbed (K_D= 0.603 μM), as well as the GTPase activity (k_{cat}= 0.027 min^{-1}, τ= 27.12 min.). The effects of the mutation are remarkable considering that it lies at the beginning of the N-terminal, more than 20 Å away from the γ-phosphate. The modulation of the dynamics of the nucleotide happens by a true allosteric mechanism in this case. It is possible that the same mechanism is responsible by the action of the state 1(T) inhibitor Zn^{2+}-BPA whose binding site is located in the same region [158].

The two mutants investigated herein show antagonistic effects as both shift the equilibrium in different directions, with S39L affecting state 1(T) and E3V affecting state 2(T), but both residues were found to be involved in the same type of transition, towards state 1(0). In this respect it is worth mention that effect of a specific mutation on the dynamics of a protein depends on many factors including the amino acid that is chosen for replacement and it is only predictable at some extent by computational methods [279]. Furthermore, as discussed above in section 4.6.1, the ^{31}P NMR chemical shifts and peak areas are only surrogate markers for changes in the dynamics of the protein because states 3(T) and 1(0) are not immediately accessible for scrutiny. For example, the mutation E3V can still promote an increase on the population of state 1(0) at expense of state 1(T). In this case, the equilibrium would still be shifted towards state 2(T) as observed in Figure 3.45.

4.6.4 2(T)-to-3(T) Transition: H27E and D33K

Only D33K is located in the effector-loop region of the protein (aa 30-40), although both mutations affect pronouncedly the dynamics of the GppNHp-bound nucleotide (section 3.4.2.3).

Replacement of His27 to Glu changed the population towards state 1(T), leading to a decrease of the equilibrium constant from 1.7 to 1.0. The three phosphate groups become downfield shifted by an average $\Delta\delta$ of 0.07 ppm for the β- and γ-phosphates and more than 0.3 ppm for the α-phosphate (Figure 3.47, Table 3.17). His27 is located at the beginning of switch 1 and more than 14 Å away from the γ-phosphate, indicating that the interference detected at the phosphate groups has an allosteric basis. It is likely that its substitution to a negatively charged Glu causes a reorientation of the neighbouring Phe28 that lies perpendicular to the centre of the nitrogen base in the *wild type* structure [14, 117, 242]. The reorientation of the aromatic ring due to the presence of the negative charge would alter the magnetic anisotropy at the guanine base (for example, if the Phe ring moves from a perpendicular to a more parallel position relative to guanine, the nuclei from the guanine base would become more shielded to the external field B_0), which would be transmitted

through the nucleotide system and lead ultimately to a modification of the magnetic susceptibility at the phosphate groups [116, 275]. Biochemically it was verified that the intrinsic GTPase reaction of Ras^{H27E} is no different than Ras^{WT} (k_{cat}= 0.025 min^{-1}, τ= 27.39 min. vs k_{cat}= 0.026 min^{-1}, τ= 26.85 min., Figure 3.48) and that its affinity towards Raf-RBD is increased by a 2-fold factor (K_D= 0.23 for Ras^{H27E} and K_D= 0.42 for Ras^{WT}), leading to the idea that the mutation could have endorsed not only a conformational shift towards state 1(T) but also a functional modification on the remaining state 2(T) population by slightly increasing their affinity towards effectors. The energetics of the binding proceeds with a greater enthalpic contribution in the case of Ras^{H27E} comparatively to the *wild type* protein (ΔH= -16.9 vs -8.10 kJ mol^{-1}, respectively, Table 3.18), meaning that the mechanism of the interaction is essentially different in terms of network of H-bonding at the binding interface of the two proteins.

Mutation of the negatively charged Asp33 to a positively charged Lys in Ras^{D33K} led to a drastic increase in the equilibrium constant, from 1.7 to 11.3, with state 2(T) being the most preponderant and state 1(T) collapsing to the level of the baseline noise (Figure 3.47 and Table 3.17). An upfield shift of -0.07 ppm was observed for state 2(T), with the new resonance line located at δ= -3.40 ppm (vs δ= -3.33 in Ras^{WT}). The resonance of state 2*(T) in the Ras-Raf complex is located at δ= -3.51 ppm for full-length $KRas^{WT}$ (Table 3.1), δ= -3.60 ppm for the truncated variant [117] and at δ= -3.54 ppm for Ras^{H27E} (Table 3.17), all values being slightly upfield shifted relatively to γ2(T) in Ras^{D33K} alone, excluding the assignment of the $\gamma_{2(T)}$-phosphate as a 2*(T) state. It was in fact verified that the $\gamma_{2(T)}$-phosphate of Ras^{D33K} can still undergo a further upfield shift, towards state 2*(T), in the presence of Raf-RBD ($\delta_{2^*(T)}$= -3.63 ppm, Figure 3.50, Table 3.20), leading to the conclusion that this mutant can still isomerise into the Raf-recognition state as in the case of Ras^{WT} (Figure 3.1), although with a much lower affinity (see section 4.7).

To the best of our knowledge, Ras^{D33K} is the only known Ras mutant that is almost completely shifted towards state 2(T). This finding is particularly interesting if one considers that other known mutants from the switch 1 region such as T35A, T35S, Y40C, Y32W, Y40C, among others, are all typically state 1(T)-driven, whose state 2(T) is either residual or completely undetectable as in the case of T35S (Figure 3.47A) or T35A [123]. Direct experimental evidence also indicates that typically all switch 1 mutants have impaired affinity to Raf-RBD and impaired intrinsic GTPase activity [67, 123]. These biochemical properties correlate well with Ras^{D33K}, which also shows impaired affinity to Raf (K_D= 10.4 μM vs 0.42 μM relative to Ras^{WT}) and a slightly lowered GTPase activity (k_{cat}= 0.016 min^{-1} vs 0.026 min^{-1}, Table 3.18).

- This page was deliberately left blank -

4.7 Interaction Between Ras^{D33K} and Raf-RBD Followed by ^{31}P NMR. Structural Basis for the Loss of Affinity

The binding of Ras^{D33K} to Raf was investigated by ITC and ^{31}P NMR in section 3.4.4 (Figure 3.50, Tables 3.18 and 3.20). The apparent K_D of 10.4 μM taken from the ITC measurements shows that this point mutation located in the middle of the effector-loop region drastically reduces the affinity towards Raf. A lower affinity was previously reported in the only available study, where it was shown that the binding of Raf to Ras^{D33A} was greatly reduced and completely abolished in the case of Ras^{D33K} [63]. it is possible that the presently obtained K_D of 10.4 μM might be slightly underestimated. From the data retrieved by ITC, it is clear that the binding to Raf still proceeds with favourable enthalpic and entropic contributions but the enthalpy variation is much lower comparatively to Ras^{WT} (ΔH= -4.24 $\pm$ 0.25 kJ mol^{-1} for Ras^{D33K} vs -8.10 $\pm$ 0.23 kJ mol^{-1} for Ras^{WT}). This enthalpy decrease correlates very well with the disruption of an important H-bonding network that can be found in the Ras^{WT}-Raf complex but that is most likely abolished in the case of the Ras^{D33K}-Raf complex.

The crystal structure of the Ras^{WT}•Mg^{2+}•GppNHp•Raf-RBD complex is shown in Figure 4.7, with Ras^{WT} coloured in light brown and Raf coloured in light purple (pdb: 1g0n [64]). The contact interface between the two proteins involves mainly the antiparallel arrangement between a β-sheet from Raf and β_3 from Ras and the effector-loop region comprising mainly switch 1 and an α-helix from Raf (Figure 4.7B). The negatively charged residues E31 and D33 from Ras^{WT} are crucial for establishing polar contacts with the positive ones, K84 and R73, from Raf, each pair acting like a clamp, holding the proteins together. The disruption of this clamping effect can be seen when the crystal structure of Ras^{D33K} obtained in the present work (section 3.5.3) is superimposed (coloured in light green in Figure 4.7): there is an obvious clash between K33 from Ras^{D33K} and K84 from Raf, which in fact is not only a steric clash but also an electrostatic one, as both residues have the same charge and repel each other.

This local hindrance has more profound consequences evidenced in Figure 4.7C: as K84 is held tightly by D33 and E81 in Ras^{WT}, its side chain -NH group becomes perfectly aligned to initiate a series of long-range H-bonding networks, that culminate with the establishment of polar contacts between crystallographic waters (represented as light purple spheres in Figure 4.7C) and the α-phosphate of the bound GppNHp. The same effect cannot happen in the case of Ras^{D33K} because K84 cannot approach the effector-loop region and initiate the process. It is likely that disruption of the water network leads to a more profound effect in the modification of the chemical environment in the vicinity of the nucleotide (by changing

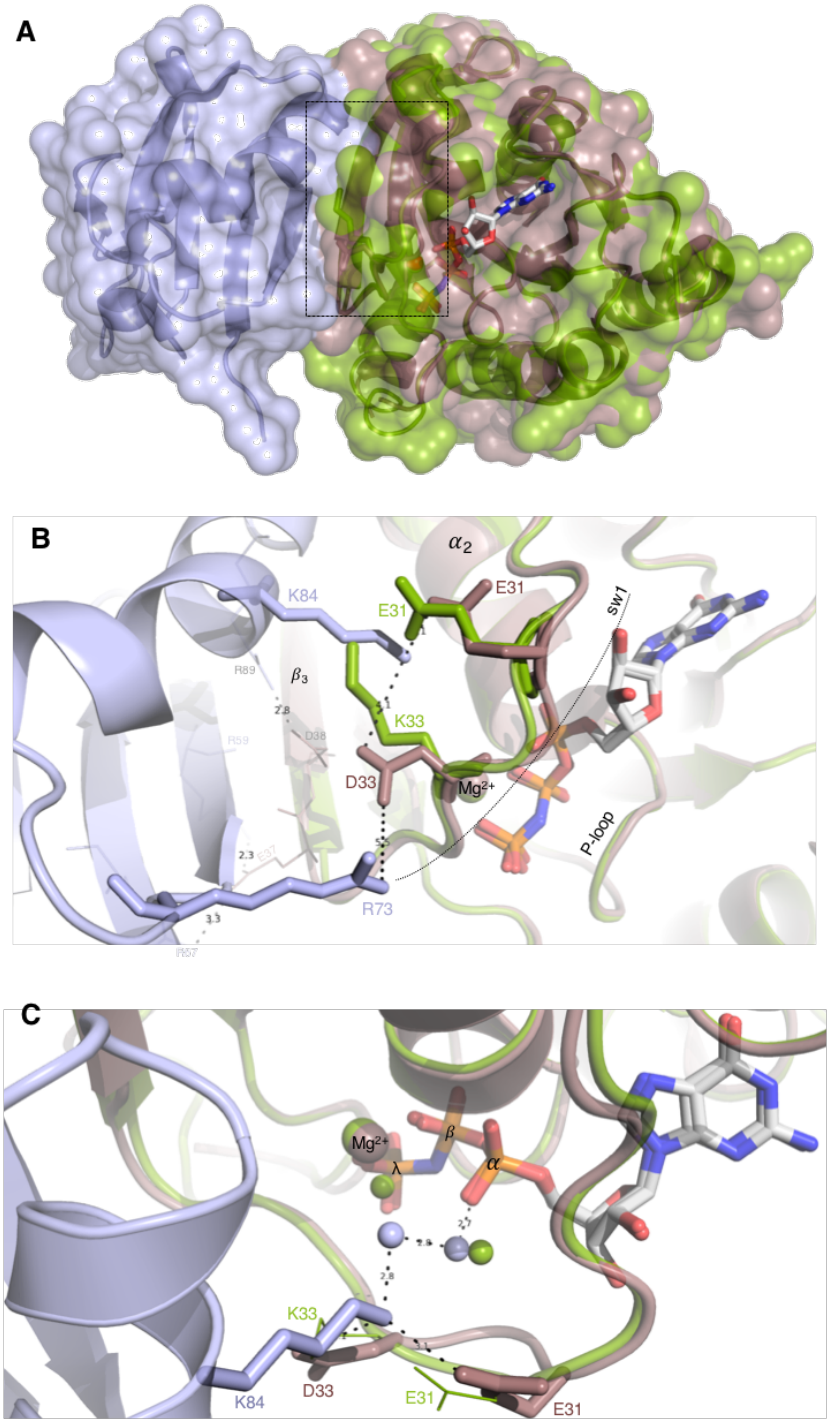

Figure 4.7. Structural basis for the interaction of Ras^{WT} and Ras^{D33K} with Raf-RBD. **A.** The surface of the crystal structure of the protein-protein complex $HRas^{WT}$(1-166)•Mg^{2+}•GppNHp•Raf-RBD is shown (pdb: 4g0n). Ras^{WT} is coloured in light brown and the RBD domain of Raf is coloured in light purple. Into this structure, the presently obtained x-ray structure of $HRas^{D33K}$•Mg^{2+}•GppNHp at pamb was superimposed (coloured in light green). The Ras-Raf interface region marked by the dashed rectangle is shown in detail in **B.** Important residues at the interface are represented as sticks and polar contacts between Ras^{WT} and Raf are represented by the dashed lines. Note how K33 from the superimposed Ras^{D33K} structure clashes in space with K84 from Raf and also in terms of electronic charge (both being positive). The disruption of the interface in Ras^{D33K} has more profound consequences evidenced in **C.** In the *wild type* complex, K84 from Raf is held in place by E31 and D33 (both light brown coloured) and establishes long range polar contacts mediated by crystallographic waters (represented by the small light purple spheres) that culminate with the direct stabilisation of the α-phosphate. In the case of Ras^{D33K}, K84 is unable to take part in these interactions. Note that the GppNHp nucleotide from both structures is superimposed. Additional important polar contacts between Ras^{WT} and Raf are evidenced in the background.

the polarisation of the P-O bonds, for example) than the point mutation on itself. In fact, Ras^{D33K} shows a lower content of crystallographic waters at the nucleotide binding site compared to Ras^{WT} (pdb: 5p21), with Gln61 assuming the same position as in the Ras-GAP complex (pdb: 1wq1, [83]) by binding directly to the γ-phosphate (see section 4.10.2).

4.8 Thermal Unfolding of Ras Followed by nanoDSF

A series of interesting conclusions can be taken directly from the thermal unfolding studies (section 3.4.8). From the obtained values (Figure 3.56, Table 3.24) It can be concluded that Ras has two sequential melting temperatures (T_m), the first one around 50 ºC, that corresponds to the melting of state 1(T), and the second one around 58 ºC, that corresponds to the melting of state 2(T). The latter being slightly more energetically stable than the former is the last to unfold. This was observed for Ras^{WT} and Ras^{H27E}, for whom K_{12}= 1.7 and 1.0, respectively. Rather surprisingly, two T_m values were also found for the state 1(T) mutant Ras^{T35S}, but only one for Ras^{T35A} (T_m= 58.11 ºC). This apparent contradiction can be explained considering that although being both state 1(T)-driven, the former, contrary to the latter, can readily isomerise into state 2(T) in the presence of effectors [156]. As the thermal unfolding is a sequential process, Ras^{T35S} can undergo the two thermal transitions, but not Ras^{T35A} for which a direct conversion from state 1(T) to 2(T) is not possible. A different unfolding pathway needs to occur in this case. This result is in good agreement with previous experiments where GdmCl was used to induce the chemical denaturation of Ras^{WT} and Ras^{T35S}, followed by ^{31}P NMR [125].

Ras^{D33K} shows a single T_m of 61.84 ºC (Table 3.24). In this case, state 2(T) has a higher population than its counterpart in Ras^{WT} (K_{12}= 11.3 vs 1.7), being more energetically stable, which accounts for the 3ºC higher T_m than the averaged T_{m2} values. As state 1(T) is not significantly populated, its thermal unfolding remains undetected.

4.9 Conformational Dynamics of Ras^{G12P} and $Ras^{G12V/T35S}$ Followed by ^{31}P NMR

4.9.1 Considerations About Ras^{G12P}

Ras^{G12P} was previously found to be the only mutant of Gly12 that has non-transforming properties in cells and leads to a normal phenotype [280], although there are no relevant structural and/or thermodynamic studies available in the literature and the exact mechanism that renders it non-transforming is still unknown. In terms of equilibrium populations, the ^{31}P NMR spectrum of Ras^{G12P}•Mg^{2+}•GppNHp is more similar to Ras^{G12V} than to Ras^{WT} (Figure

3.58A). However, the biochemical properties of the former are in fact more similar to the ones of Ras^{WT}: both show similar rates of GTP hydrolysis (k_{cat}= 0.035 min^{-1} and k_{cat}= 0.026 min^{-1}, respectively) and similar affinities towards Raf-RBD (K_D= 0.59 μM vs K_D= 0.42 μM, respectively, Table 3.26). Such findings further support the classification of Ras^{G12P} as non-transforming [259, 261]. On the other hand, the typical oncogene Ras^{G12V} has a normal affinity to Raf but an extremely slow hydrolysis rate (k_{cat}= 0.005 $min^{-1,}$ Table 3.26). The *wild type*-like affinity of Ras^{G12P} to effectors was further confirmed by following its titration with Raf-RBD by ^{31}P NMR (section 3.4.10.2). The structural basis for the non-transforming properties of Ras^{G12P} is most likely related with differences in the orientation of Gln61 located in switch 2: in the case of Ras^{WT} and Ras^{G12P}, this residue is positioned in its catalytic conformation by making an H-bond with the catalytic water, ready to initiate the nucleophilic attack. In the case of Ras^{G12V} the corresponding water molecule is not present in the crystal structure and Gln61 points towards the helix α_3, in the opposite direction of the γ-phosphate, due to the steric hindrance promoted by the presence of Val12 [259, 281]. In other cases as in Ras^{G12D}, Gln61 is oriented in the right direction but involved in a H-bond with D12 and unable to coordinate the catalytic water.

4.9.2 Considerations About $Ras^{G12V/T35S}$

The mutant has been used extensively in a wide range of cellular-based assays after it was found that it could retain the interaction with the effectors Raf and CDC25, among others but not with PiK3 or Ral-GDS, leading to the activation of only specific signalling cascades such as Ras/Raf/MEK/ERK but not EGF/EGFR or the Pi3K/AKT/mTOR pathways [110]. Although there is substantial evidence that it can activate the ERK pathway through Raf recognition and binding, the exact mechanism is also not known. Furthermore, the extent and duration of the activation seems to be largely dependent on the type of cell line [282].

In the scope of the work presented herein, the main question was if the nature of the double-mutant could be governed by one of the mutants alone, and if so, what would be the preponderant contribution. From the ^{31}P NMR investigations it was demonstrated that $Ras^{G12V/T35S}$ has a greater contribution from Ras^{T35S}, whose properties dominate the GppNHp and the GTP spectra, with both being a state 1(T) mutant, contrary to Ras^{G12V} for which a K_{12}= 1.16 (at the γ-phosphate of bound-GppNHp) was obtained (section 3.4.10, Table 3.25). Although spectroscopically similar to Ras^{T35S}, the intrinsic GTPase and the affinity to Raf-RBD of $Ras^{G12V/T35S}$ is much lower than the corresponding values obtained for the isolated mutants (Ras^{G12V} and Ras^{T35S}, Figure 3.62). Thus, the apparent K_D for

dissociation from Raf was found to be 13.52 μM against 0.66 μM and 6.45 μM, respectively. In summary, the low affinity measured between $Ras^{G12V/T35S}$ and Raf-RBD is in slight disagreement with the idea that the mutant can readily activate the Ras/Raf/MEK/ERK pathway upon association with Raf-RBD in living cells. It is plausible that the pathway can still be activated but the extent of and the potency of the downstream relayed signals is certainly much lower than the one observed in the case of Ras^{WT} or Ras^{G12V} alone. The experimental evidence for such difference reported in the literature is not unanimous: some investigations suggest that $Ras^{G12V/T35S}$ retains a full-fledged binding activity, just like Ras^{G12V} [61, 111] while others suggest, in line with the presently obtained data, that the activation occurs but is greatly decreased [110]. One can envisage the activation of Raf-dependent pathways taking place through a bypass mechanism that does not necessarily require Raf as initiator. Nevertheless, in the light of the present data that the double mutant does not have the same degree of affinity to the effector as the oncogene Ras^{G12V}. This fact should be taken into consideration when devising cell-based assays.

4.10 High Pressure Macromolecular Crystallography (HPMX)

4.10.1 $HRas^{WT}(1\text{-}166)\bullet Mg^{2+}\bullet$GppNHp

Crystal structure at Ambient Pressure

The presently obtained RT crystal structure of Ras^{WT} is similar to the representative 5p21 one, obtained at 277 K (section 3.5.1, Figure 3.63). There are however several local distinctions comprising the switch 2, all marked by the different re-orientation of the side chains of specific residues relative to the protein backbone. These differences are more related with the commonly known intrinsic disorder of switch 2 than with the actual difference in temperature of the two structures [28, 94, 95]. The absence of the nucleophilic waters at RT is responsible for the different orientation of Gln61 relative to the same residue in 5p21 [12], envisaging the delicate balance between the spatial arrangement of these highly mobile regions and the nature of the macromolecular crystal (type of symmetry, degree of hydration, type of buffer, etc.).

Crystal Structures at High Pressure

The compressibility of the unit cell shows unequivocally the existence of a transition sate around 300 MPa (section 3.5.2.1, Figure 3.64). Two high energy conformers were solved above this point, the first at 490 and the second one at 650 MPa. Both differ from the structure at 0.1 MPa by an averaged rmsd value of 0.47 and 0.28 Å, respectively.

The overall observed structural changes indicate that a new conformation of the protein was trapped at 490 MPa given by the direct increase in resolution from 2.0 Å before the transition zone to 1.8 Å at 490 MPa and 1.7 Å at 650 MPa (Figure 3.67). The regions where the highest rmsd values between p650 and p490 are obtained correspond simultaneously to the regions in the p650 structure with the lowest thermal b-factors (Figure 3.68A and B). This interesting correlation indicates that the conformational state trapped at 650 MPa could either correspond to a further stabilization of the same excited state observed at 490 MPa or could correspond to a new state. In one hand, their very similar structures might indicate that the conformer is only further stabilised at 650 MPa. On the other hand, the observed differences at switch 2, especially at Q61 (Figure 3.68E), could indicate a glimpse of a new high energy conformer, whose structural features cannot be completely uncovered at his pressure and therefore would require a jump to higher pressures. The results obtained from Ras^{D33K} at 880 MPa (section 3.5.4.2) indicate that this structure represents a new conformer relative to the 650 MPa one of Ras^{WT} (Figure 3.72C), supporting the first assumption.

Attempting to correlate the HPMX features with the HP NMR data is difficult. At 250 MPa in solution, states 1(T)/1(0) prevail. and are marked by an open conformation in which the entire switch 1 moves away from the nucleotide assuming a position similar to the one found in the nucleotide-free Ras•SOS complex (Figure 1.5) [44, 95, 242]. However, such large rearrangement could not be found in any of the presently solved structures, not even at 650 MPa. The overall changes in the crystal are therefore less pronounced.

It is known from NMR and X-ray studies that not only switch 2 but also switch 1 is highly mobile due to the transient binding of Tyr32 to the γ-phosphate [51, 123]. However, many crystal structures of Ras^{WT}•Mg^{2+}•GppNHp show a very well defined electron density for switch 1, with Tyr32 always contacting the γ-phosphate. When this residue is found to be distant from it (especially in structures crystallised under the $P3_221$ space group, as 5p21), it seems to be only because of the crystal packing constrains that force it to interact with the γ-phosphate of a symmetry-related molecule (Figure G, appendix). The same constrains are probably also responsible for the well defined electron density of the whole switch 1, that has therefore no spatial freedom to fluctuate. The analysis of all the refined HP structures obtained in the present work either for Ras^{WT} and Ras^{D33K} also show the existence of these forces between the molecules that constitute the unit cell of the crystal (Figure G). Since hydrostatic pressure is transmitted homogeneously to the whole, infinite and three-dimensional, crystalline system [175, 183], even a pressure as high as 650 MPa is not enough to overcome them. The only possibility to alleviate their influence would be the transition of the $P3_221$ symmetry into another space group. This can indeed occur given

that the crystal is kept under pressure during a long enough time. This relationship is an interesting topic worth pursuing on its own in the future. Another, and perhaps easier, possibility of approaching the problem is to attempt the direct crystallisation of Ras into a space group different than $P3_221$. As example, several structures were reported to crystallise under the R32 space group, for which the movement of Tyr32 is not hindered by the crystal packing (neither the rest of the switch regions) [60, 283]. In one of these studies [241] the obtained crystals, still representative of a typical state 2(T) (pdb: 5b2z), were subsequently subjected to the Humid Air and Glue-coating (HAG) crystallisation method [284] which induced a direct transition of the lattice from state 2(T) to state 1(T) (pdb: 5b30). In 5b30, the loss of the Thr35 and Tyr32 interaction with the γ-phosphate caused a marked deviation of switch 1 away from GppNHp which resulted in the expansion of the accessible surface area comparatively with 5b2z. Neither the 490 nor the 650 MPa structures presently obtained show such large movement for their switch regions.

It is important to clarify that, independent of the possible hindrances caused by crystal packing, only subtle pressure-induced conformational changes are indeed expected in the crystal or at least they are considered to be within our model, the true representation for behaviour of the protein in solution. This observation is in agreement with previous studies where a slight change in the O-P-O dihedral and torsional angles of the bound nucleotide is sufficient to promote a conformational shift of the equilibrium given by the transient binding of Y32 and T35 to the γ-phosphate [84, 117]. To this respect, the 5b2z and 5b30 structures are very likely an extreme example for the conformational transition between states 1(T) and 2(T) represented by a dramatic movement of the switch regions. In solution, the protein needs to rapidly discriminate between the different partners (GEF's, GAP's, effectors) and therefore both states need to be closer to each other in the conformational landscape. In the light of this model and given the present HPMX results, the structures refined at 490 and 650 MPa are considered to be a representation of state 1(T), contrary to the ambient and low pressure (< 200 MPa) ones. This conclusion is obviously not definitive and needs further evidence by solving structures at even higher pressures or by using complementary techniques such as cryo-EM that allow the possibility of trapping the multiple conformational states of Ras.

it is worth mention the inherent difficulties of retrieving meaningful real space refined diffraction data of low populated conformational states. Almost all crystal structures are built by interpreting density maps at 1σ greater than the mean electron density of the unit cell, which is the approximate boundary between the signal from the molecule and the noise

from the density map. The temperature factors represent a Gaussian decay of the electron density of the modelled atoms and because they combine contributions from motions, static disorder and model errors, their interpretation can disguise discretely disordered alternative side-chain and main-chain conformations [285, 286]. This is especially pertinent for systems like Ras, where rare conformational states can be easily missed. Several recently developed methods seem to be able to tackle the problem by building many structural models simultaneously into the electron density [99, 287, 288]. They are certainly worth to explore in future investigations coupled to HPMX on Ras.

4.10.2 $HRas^{D33K}$ (1-166)•Mg^{2+}•GppNHp

Crystal structure at Ambient Pressure

The crystal structure of Ras^{D33K} at 0.1 MPa and RT is almost identical to Ras^{WT} (section 3.5.3, Figure 3.69). The result is not altogether surprising given that the 2-state equilibria observed in solution for Ras^{WT} is abolished in the crystal, being the typical X-ray structure also exclusively representative of state 2(T) [28, 241, 281]. The substitution of Asp33 to Lys did not led to drastic modifications of switch 1, which still overlays perfectly with its counterpart in Ras^{WT}. As expected, the only significant differences lie at the intrinsically disordered switch 2 moiety, for which the calculated b-factors are around 20 $Å^2$ in both proteins.

Crystal structures at High Pressure

The major features discussed in the above section 4.10.1 for Ras^{WT} are also representative of the series on Ras^{D33K}. Unequivocal structural modifications were observed at high pressure, especially above 500 MPa, for which a transition state of Ras^{D33K} takes place (section 3.5.4.1). The decrease in temperature factors at 880 MPa relative to 200 and 0.1 MPa supports the conclusion that the obtained structure is indeed a higher energy conformational and functional state of Ras (Figure 3.71). This structure could represent Ras in state 1(T) or a transition structure through a conformational pathway that culminates with the stabilisation of this state.

There is no direct evidence for a strict correlation between the crystal and the solution structures [119, 120, 183]. Therefore, the 880 MPa structure could represent state 1(T) on its own right. Additional experiments at higher pressures and the careful investigation of the compressibility of the unit cell using short pressure intervals around the 880 MPa value would provide an unequivocal answer about the nature of this state.

The fact that the transition point for Ras^{D33K} occurs at higher pressures (around 500 MPa) than Ras^{WT} (around 350 MPa) indicates that the mutant is more resistant to pressure-modulation than the *wild type* variant (Figure 3.70). Indeed, the nucleotide binding pocket of Ras^{D33K} seems to be more closed than the *wild type* counterpart, which might account for the difference.

The 880 MPa structure of Ras^{D33K} also helps to further understand the functional aspects of the conformation detected at 650 MPa for Ras^{WT}: both represent most likely the same high energy conformer that is structurally different than the one detected at 490 MPa for the *wild type* protein (Figure 3.72C). Although possible, it is very unlikely that the difference between Ras^{WT} at p650 and Ras^{D33K} at p880 is due to the presence of the K33 mutation, but instead due to the 230 MPa difference in pressure between both (if the mutation alone would account for the different structural changes, these would have been also observed at intermediate and low pressures, which is not the case).

In summary, the use of a novel Ras mutant coupled to state-of-the-art HPMX technologies represents an unprecedented approach to tackle the rather complex dynamics of a protein that is of capital importance to both, normal and the aberrant cellular functions. Its unique biochemical properties and structural topography were glimpsed herein and will hopefully help the scientific community to derive meaningful relationships and to better understand its role as a master switch of the cell.

4.10.3 $HRas^{WT}(1\text{-}166)\bullet Mg^{2+}\bullet$GppNHp in Complex with Zn^{2+}-cyclen

The volume of the unit cell at 0.1 MPa of Ras^{WT} soaked with 10 mM Zn^{2+}-cyclen is similar to the Apo protein at ~200-300 MPa (section 3.5.5.1, Figure 3.74). A similar relationship can be inferred from ^{31}P NMR since Zn^{2+}-cyclen leads to the stabilisation of state 1(T) (Figure 3.3) at expense of state 2(T). A shift in the same direction is obtained by ^{31}P HP NMR, with an associated decrease in the partial molar volume of the protein in solution (ΔV= -18.60 mL mol^{-1}, section 3.3.2.1, Figure 3.27). These relationships are only qualitative but they are nevertheless in line with the mode of action of this drug.

Furthermore, the HP studies performed for Ras^{WT} in the presence of Zn^{2+}-cyclen are able to corroborate the results gathered from the HP series on the Apo protein. They show that pressure leads unequivocally to a modification of switch 2 and the segment β_2-β_3 comprising loop λ_7, both being independent of the presence of Zn^{2+}-cyclen (Figure 3.75). On the other hand, the effect of pressure alone is not capable of inducing relevant modifications on switch 1. The same is true for Zn^{2+}-cyclen alone, since the structures at ambient pressure in both

series are almost identical. However, a synergistic effect seems to be achieved when both are used at the same time: at 520 MPa a large shift of switch 1 is indeed observed and despite cyclen not being detected, there is enough space for it around the Zn^{2+} ion in the electron density map (Figure 3.76). In the light of these data, it can be assumed that the Ras•Zn^{2+}-cyclen complex at 520 MPa is indeed a representative structure of the conformational state 1(T) observed in solution [125, 171].

The absence of assignable electron density for the cyclen moiety can be due to different reasons: it can be highly mobile and therefore disordered, it can be partially obscured by the intense scattering of the metal ion or, under very high pressures, it can dissociate from it. In principle, the coordination to Zn^{2+} is very stable at ambient pressure [289]. The stability under pressure was also confirmed by HP ^{31}P NMR up to 200 MPa (unpublished results), although no studies are available in the 500 MPa pressure range.

It is worth mention that no Zn^{2+}-cyclen was observed at the second binding site coordinated to H166 near the C-terminal region, contrary to the previous structure reported by us at ambient pressure (pdb: 3l8y, Figure 1.10 [157]). This 2.05 Å structure was crystallised in the H32 space group and contained 142 water molecules. The different space group ($P3_221$ in the present case) can account for an additional difficulty for the drug to diffuse through the crystal and bind specifically to Ras. The lower number of waters has also a direct influence in the degree of hydration and thus in the number of solvent-accessible channels, essential for the communication with the surrounding environment in which the crystal is grown and through which pressure is transmitted.

5. Appendix

“The important thing in science is not so much to obtain new facts as to discover new ways of thinking about them”

William Laurence Bragg

5.1 Figures

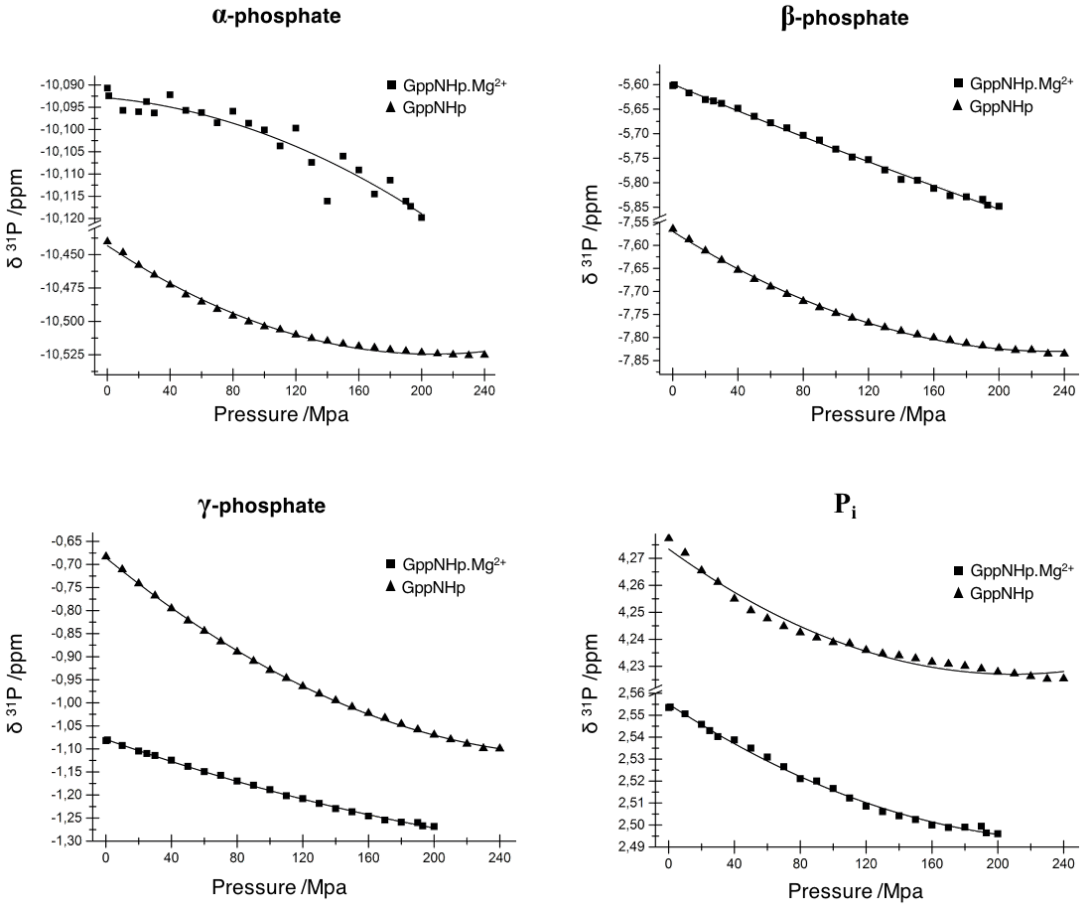

Figure A. Pressure dependence of GppNHp followed by ^{31}P NMR spectroscopy. All measurements were done at 278 K, using a Bruker Avance 600 MHz spectrometer operating at a magnetic field of 242.9 MHz. The pressure-induced chemical shift changes for α-, β- and γ-phosphates, together with inorganic phosphate (Pi) were plotted as a function of pressure. In each plot the dependence for the same phosphate signal in the presence (squares) and in the absence (triangles) of Mg^{2+} is shown. A general trend arises from the comparison of the two situations: the magnitude of the chemical shift changes, i.e. the $\Delta\delta$, is always larger for the experiments done in the absence of the metal ion (see Figure 3.26 and Tables D and E). Samples were prepared by dissolving 5 mM of GppNHp in 40 mM Tris/HCl, 0.1 mM DSS, 10% D_2O, with pH 9.0 and 15 mM $MgCl_2$ (in the presence of Mg^{2+}) or pH 11.5 and 0.5 mM EDTA (in the absence). The data points were fitted with a second order Taylor expansion.

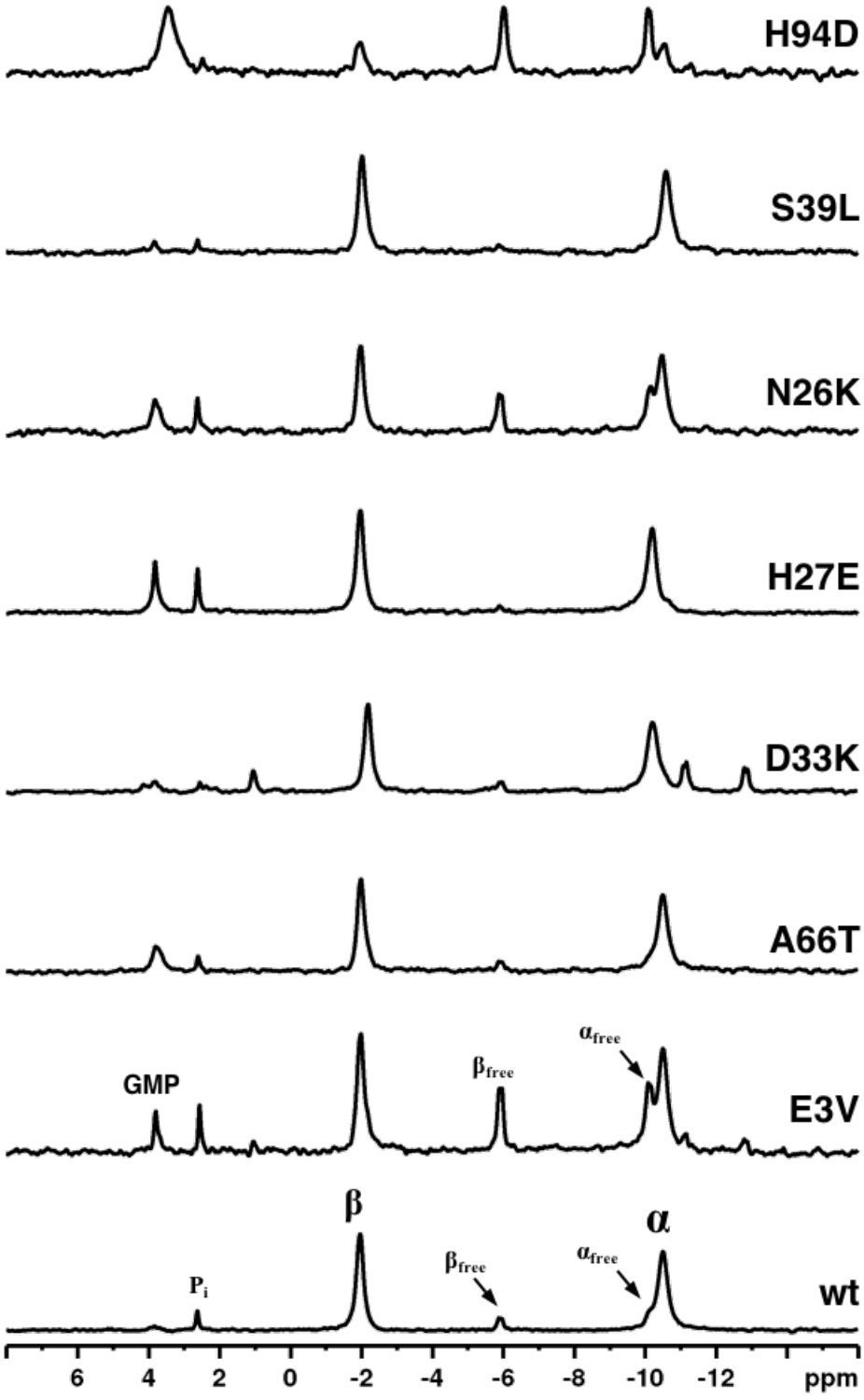

Figure B. Conformational equilibria of the Ras(1-166)•Mg^{2+}•GDP selected mutants detected by ^{31}P NMR. The mutants were created by SDM upon choosing specific residues associated with the conformational transitions derived from HP investigations. All the measurements were done at 278 K in a 202.4 MHz magnetic field (500 MHz spectrometer). The proteins were dissolved in buffer F (40 mM Tris/HCl pH 7.5, 10 mM $MgCl_2$, 2 mM DTE) with additionally 0.2 mM DSS and 5% D_2O at concentrations ranging between 0.6 and 1.5 mM.

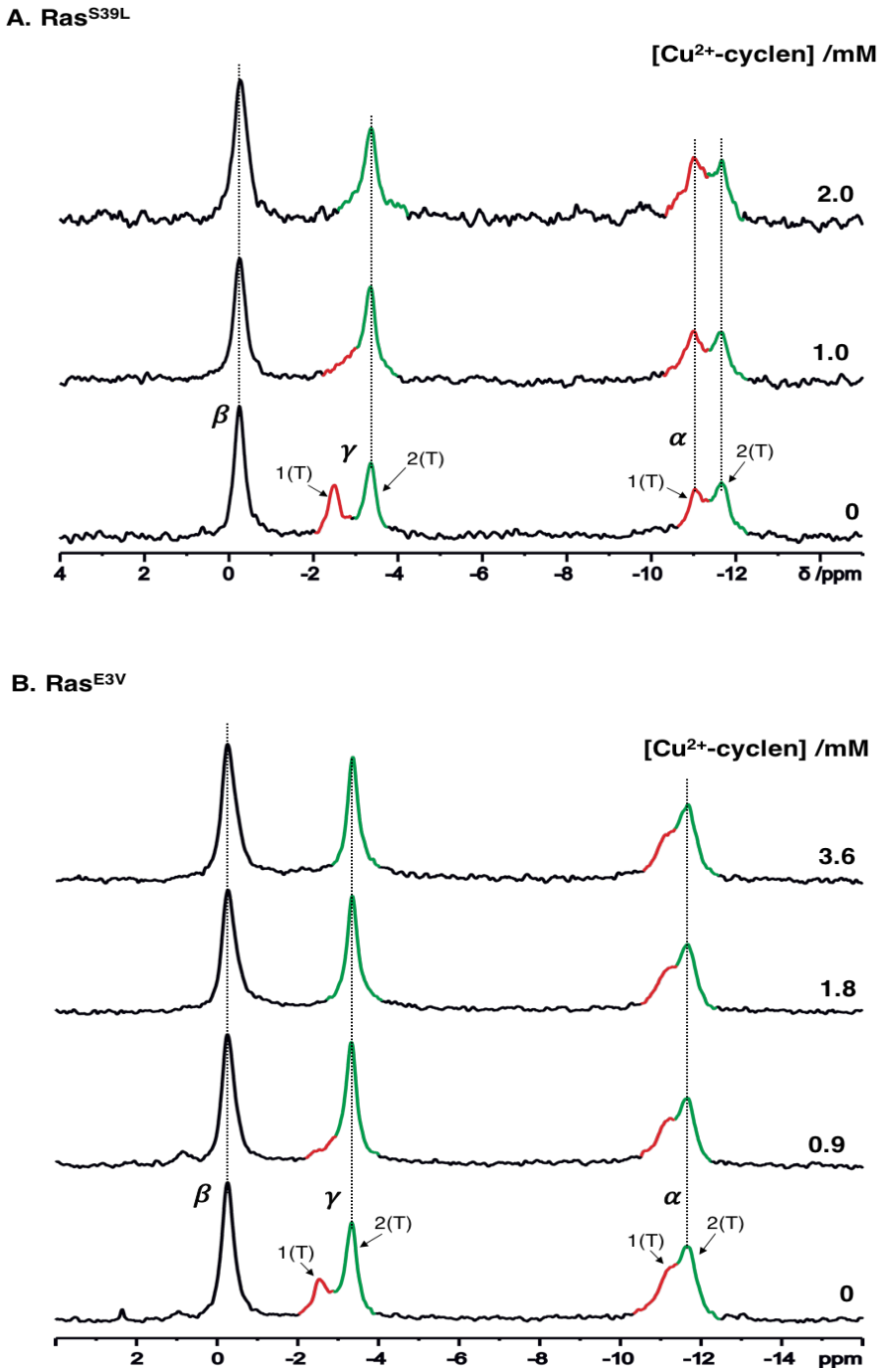

Figure C. Impact of Cu^{2+}-cyclen binding to HRas(1-166)•Mg^{2+}•GppNHp followed by ^{31}P NMR spectroscopy. Two mutants, **A.** Ras^{S39L} and **B.** Ras^{E3V} were titrated with increasing amounts of the drug. The measurements were performed at 278 K in a 202.456 MHz magnetic field (500 MHz spectrometer) and in buffer F at pH 7.5. The initial concentrations of Ras^{S39L} and Ras^{E3V} were 1.0 and 1.86 mM, respectively. To each protein Cu^{2+}-cyclen was added from a highly concentrated stock solution. The concentration of the drug for each step is indicated.
Cu^{2+}-cyclen binds near the γ-phosphate when Ras exists only in the conformational state 1(T) and can be used as a probe to recognize this specific state, being especially useful in novel mutants where the assignment of specific states from the chemical shifts can be difficult. The state 1(T) resonance on γ-phosphate becomes broadened beyond detection upon addition of low milimolar concentrations (1-4 mM), which proves its unequivocally assignment. This method is independent of mutations or the nature of the GTP analogue used. The fitted chemical shift values and linewidths are given in Table I.

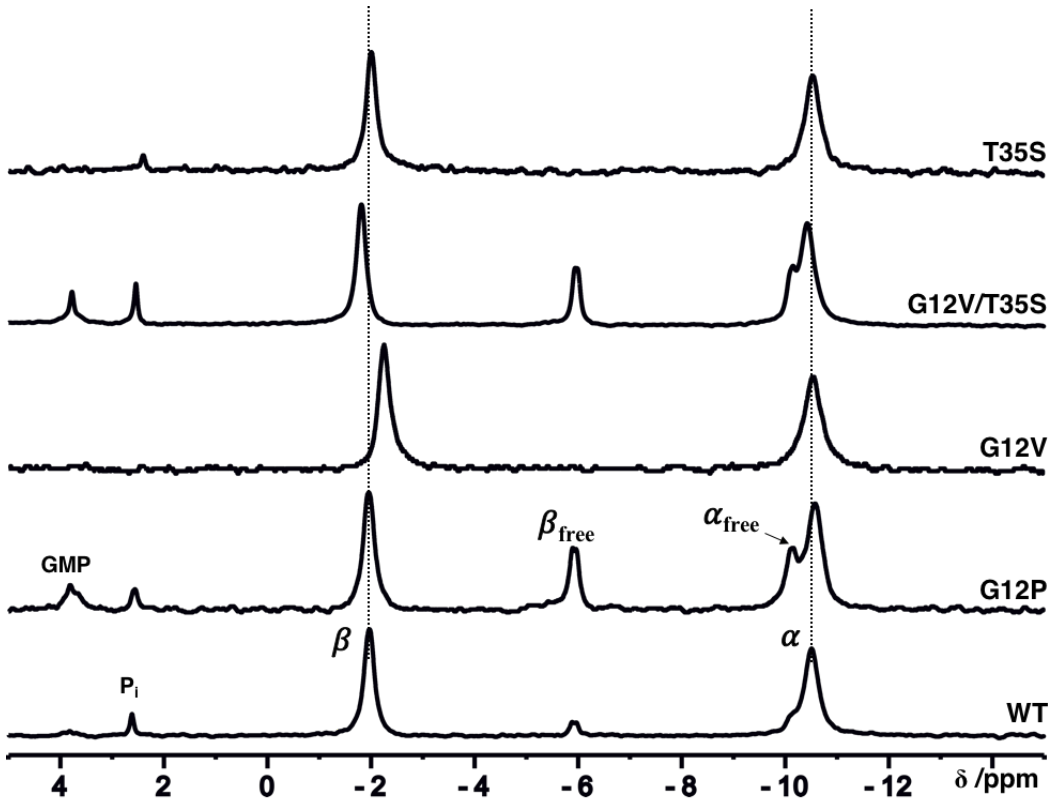

Figure D. Conformational equilibria of HRas(1-166)•Mg^{2+}•GDP detected by ^{31}P NMR at 278 K. All protein complexes were dissolved in buffer F (40 mM Tris/HCl pH 7.5, 10 mM $MgCl_2$, 2 mM DTE) with additionally 0.2 mM DSS and 5-10% D_2O. The final concentrations were in the range of 0.4 and 1.9 mM. ^{31}P resonances were recorded in a magnetic field operating at a frequency of 242.896 MHz (600 MHz spectrometer) except for Ras^{G12P}, where a 202.456 MHz (500 MHz spectrometer) was used. The chemical shifts corresponding to the α- and β-phosphates of bound GDP are indicated, as well as the unbound or free (α_{free} , β_{free}) nucleotide. The presence of free nucleotide results from practical aspects of the purification process, were free GDP is added to buffer D, used during last step of the purification. The presence of Pi and GMP is observed in some cases and results most likely from the time-dependent degradation of free GDP. An exponential lorentizan line broadening of 15 Hz was applied to the FID during data processing. The obtained shift values and linewidths are shown in Table 3.25, section 3.4.10.1.

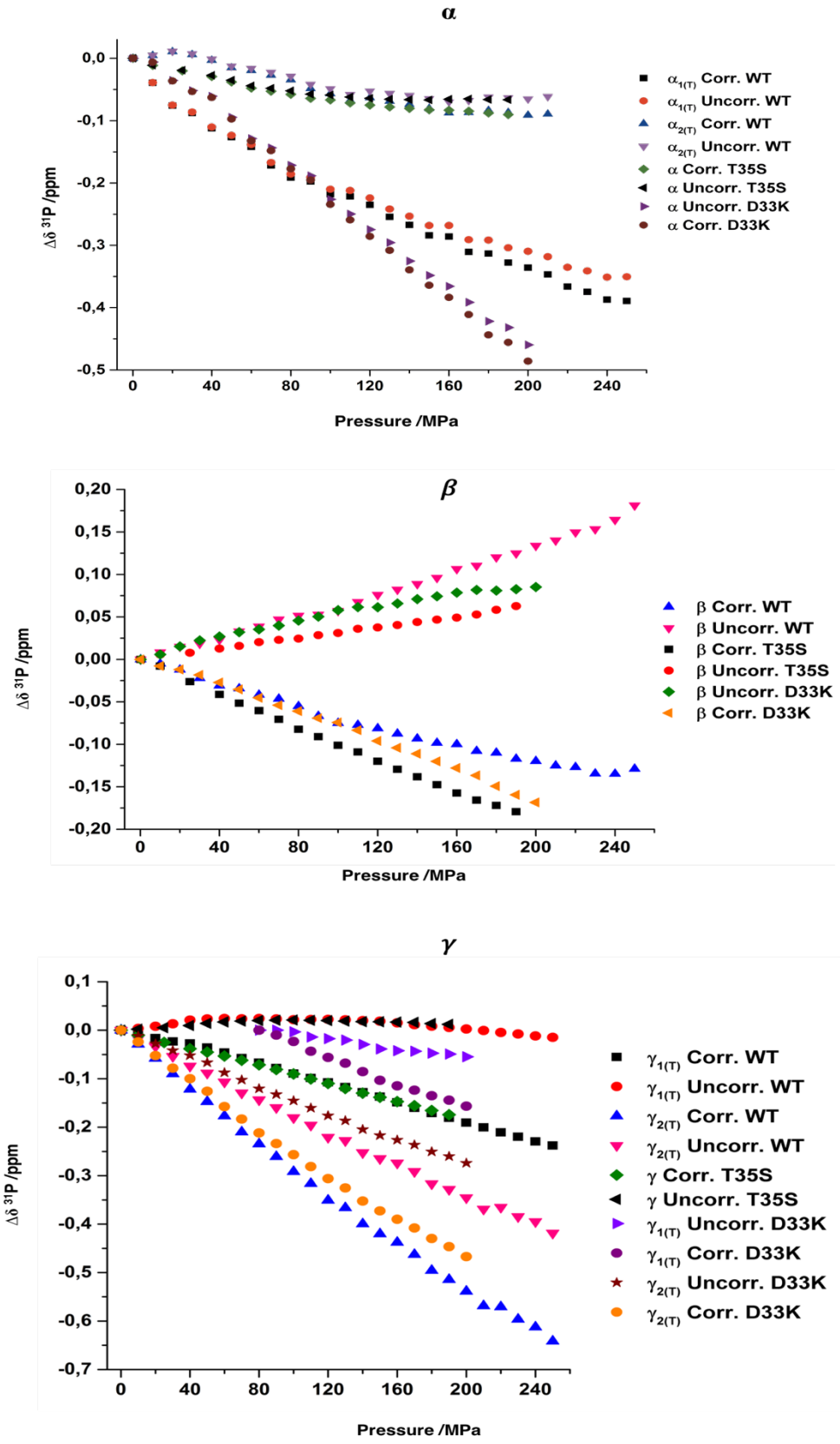

Figure E. Plot of the variation of the pressure-dependent chemical shift changes, $\Delta\delta=\delta_{\text{last pressure point}}-\delta_{0.1MPa}$ of Ras^{WT}, Ras^{T35S} and Ras^{D33K} in complex with Mg^{2+}•GppNHp at 278 K and pH 7.5. Each plot shows the uncorrected and corrected changes for the α- (top), β- (middle) and γ-phosphates (bottom).

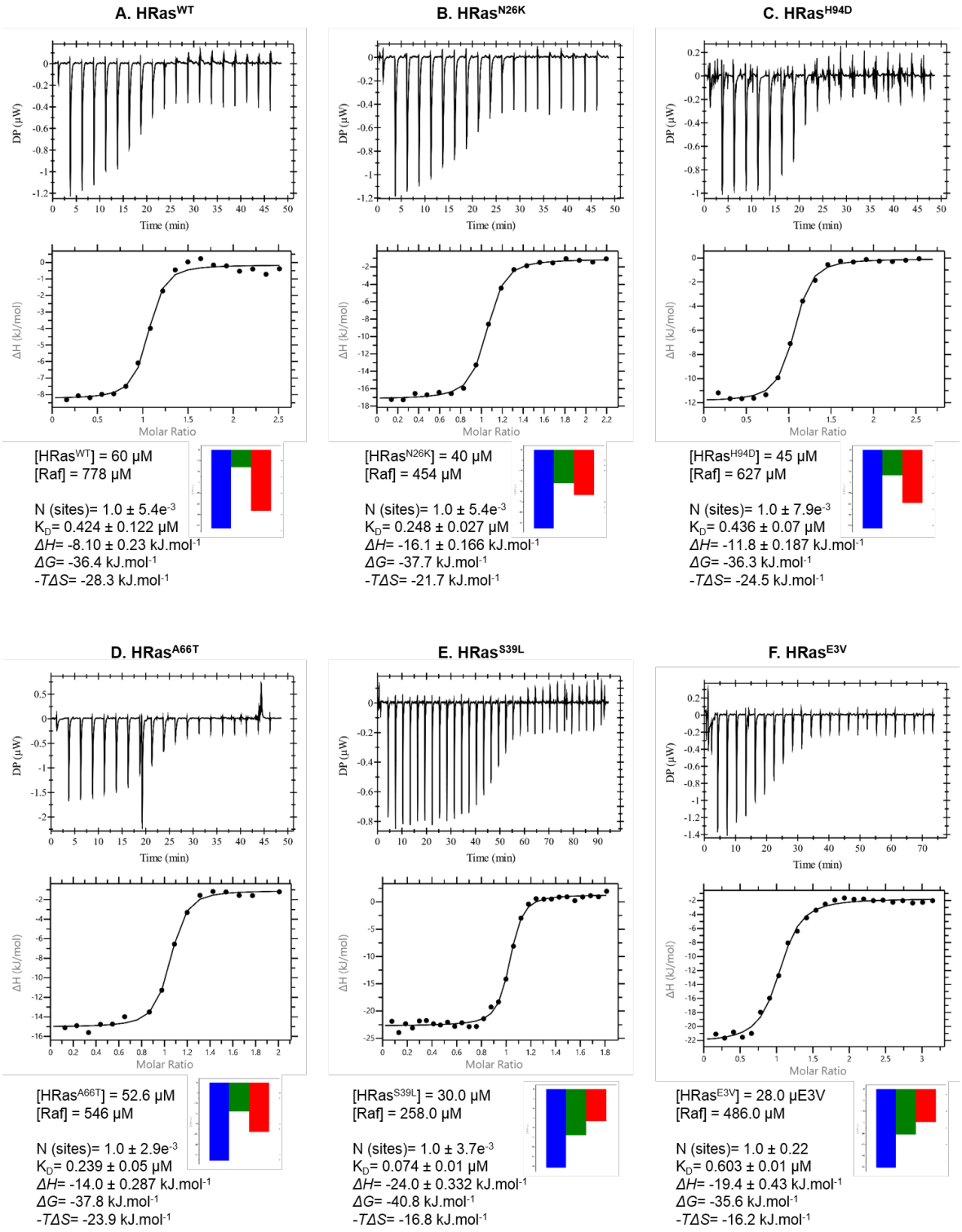

Figure F. Thermodynamics of the interaction between different mutants of HRas(1-166)•Mg^{2+}•GppNHp and the Ras binding domain of the effector protein Raf measured by ITC. All experiments were performed at 298 K in buffer F (40 mM Tris/HCl pH 7.5, 10 mM $MgCl_2$, 2 mM DTE) with additionally 150 mM NaCl. All proteins were extensively dialyzed against this buffer. Ras was always placed in the cell of the calorimeter and Raf was always placed in the syringe. All the experiments were performed according to the default setting of the device used with a referential power of 10 μcal s^{-1} and a spacing between injections of 150 s or longer with a injection time of 2 s and stirring speed of 750 rpm. A total of either 19 or 31 injections of 2 μl each were applied in the determination of K_D values. For each mutant tested, the raw heat of the reaction is plotted in the upper graph and the integrated heat *per* Ras:Raf ratio is shown in the lower graph. The signature plot is also shown with the following colour code: blue: ΔG, green: ΔH, red: -TΔS. The thermograms shown here correspond to the best fitted data from a duplicate or sometimes a triplicate series of experiments, conducted for each mutant. All the data was corrected for the intrinsic heat of mixing given by buffer-in-buffer and buffer-in-protein injections (in the case of the different Ras mutants, the calibration used was relative to the heat of buffer-in-Ras^{WT}). For details see 2.2.4

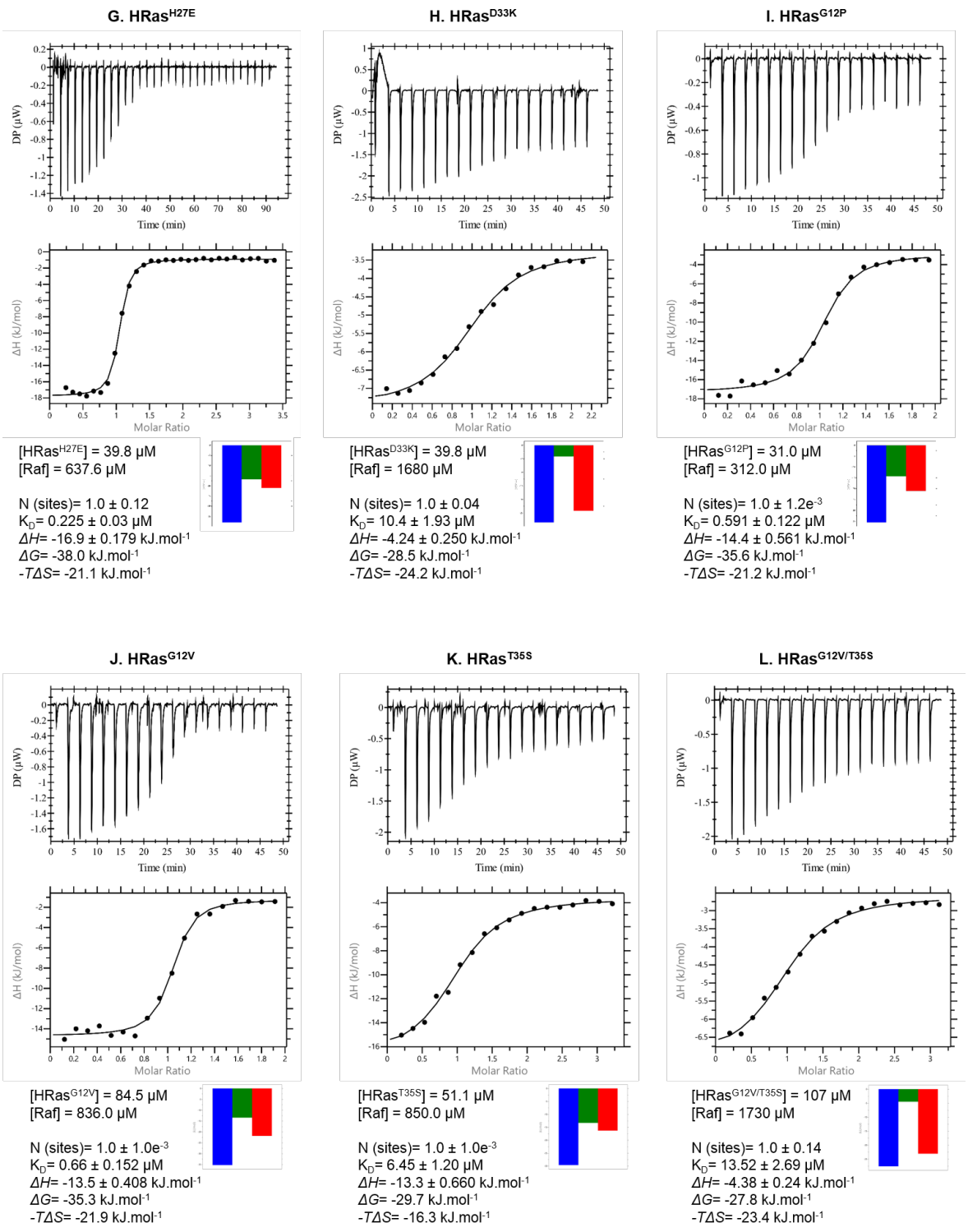

Figure F - Continuation from the previous page. Thermodynamics of the interaction between different mutants of HRas(1-166)•Mg^{2+}•GppNHp and the Ras binding domain of the effector protein Raf measured by ITC. All experiments were performed at 298 K in buffer F (40 mM Tris/HCl pH 7.5, 10 mM $MgCl_2$, 2 mM DTE) with additionally 150 mM NaCl. All proteins were extensively dialyzed against this buffer. Ras was always placed in the cell of the calorimeter and Raf was always placed in the syringe. All the experiments were performed according to the default setting of the device used with a referential power of 10 μcal s^{-1} and a spacing between injections of 150 s or longer with a injection time of 2 s and stirring speed of 750 rpm. A total of either 19 or 31 injections of 2 μl each were applied in the determination of K_D values. For each mutant tested, the raw heat of the reaction is plotted in the upper graph and the integrated heat *per* Ras:Raf ratio is shown in the lower graph. The signature plot is also shown with the following colour code: blue: ΔG, green: ΔH, red: -TΔS. The thermograms shown here correspond to the best fitted data from a duplicate or sometimes a triplicate series of experiments, conducted for each mutant. All the data was corrected for the intrinsic heat of mixing given by buffer-in-buffer and buffer-in-protein injections (in the case of the different Ras mutants, the calibration used was relative to the heat of buffer-in-Ras^{WT}). For details see experimental section 2.2.4.

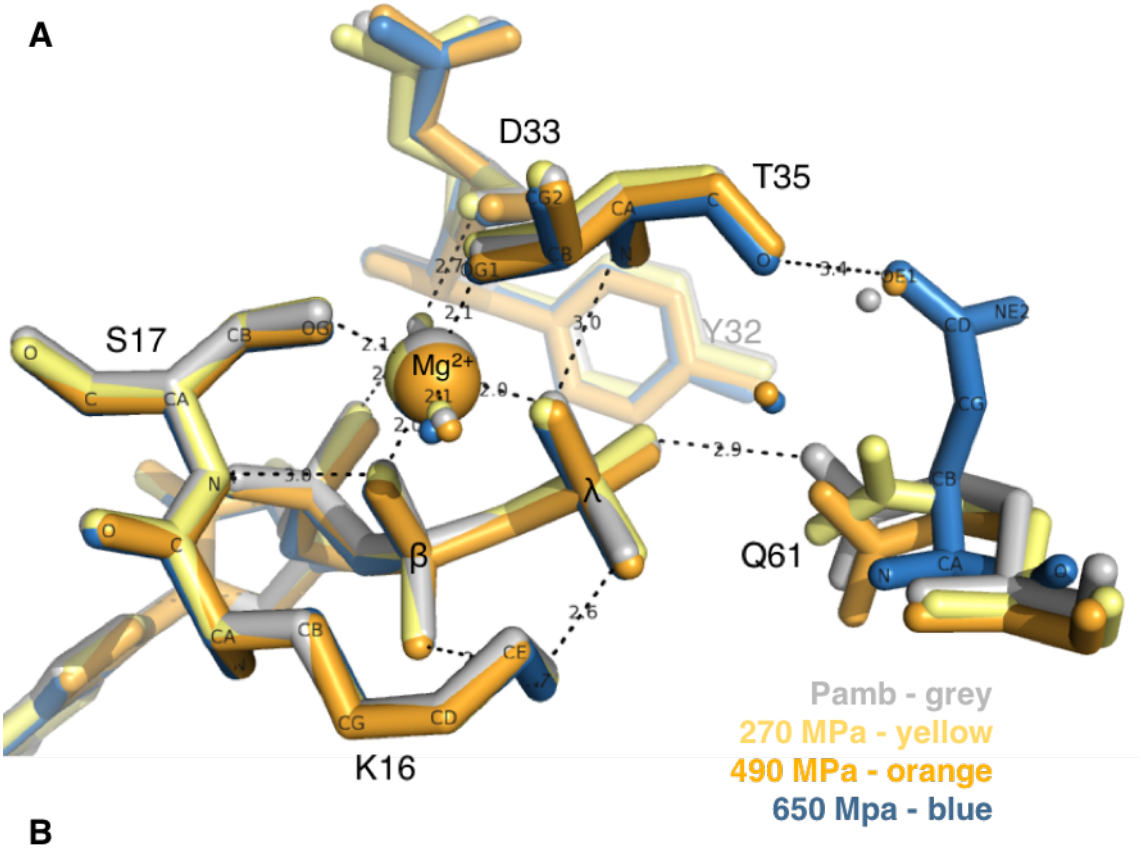

Figure G. High pressure macromolecular crystallography on HRas^{WT}(1-166)•Mg^{2+}•GppNHp. **A.** Details evidencing the coordination to the Mg^{2+} ion. The structures refined at pamb, 270, 490 and 650 MPa are superimposed and coloured in grey, yellow, orange and blue, respectively. The Mg^{2+} ion is coordinated by six atoms: S17, O1γ, T35, O1β, w200 and w201. The coordination profile is virtually identical for all the recorded pressure points. The same coordination is also found in the case of the HPMX series of Ras^{D33K}. w200 is surrounded by six atoms: Mg^{2+}, S17-OH, Oγ, T35-OH, D33-OH, Oα and w201 is surrounded by five atoms: Mg^{2+}, D33-NH, Y32-OH, Oβ and Oγ. Note that Y32, shown in the background, is establishing a polar contact with one oxygen atom from the γ-phosphate of an adjacent nucleotide molecule. **B.** In fact, not only Y32 but most residues from the switch regions (particularly switch 1) are packed in the asymmetric unit against the neighbouring molecules. This tight packing seems to be a fundamental property of the crystallisation under the $P3_221$ space group and is observed at all investigated pressure points. Within the obtained data, it is considered that the tight packing hinders the pressure-induced movement of the switch regions, preventing the observation of a 'true' open conformation, even at 650 MPa.

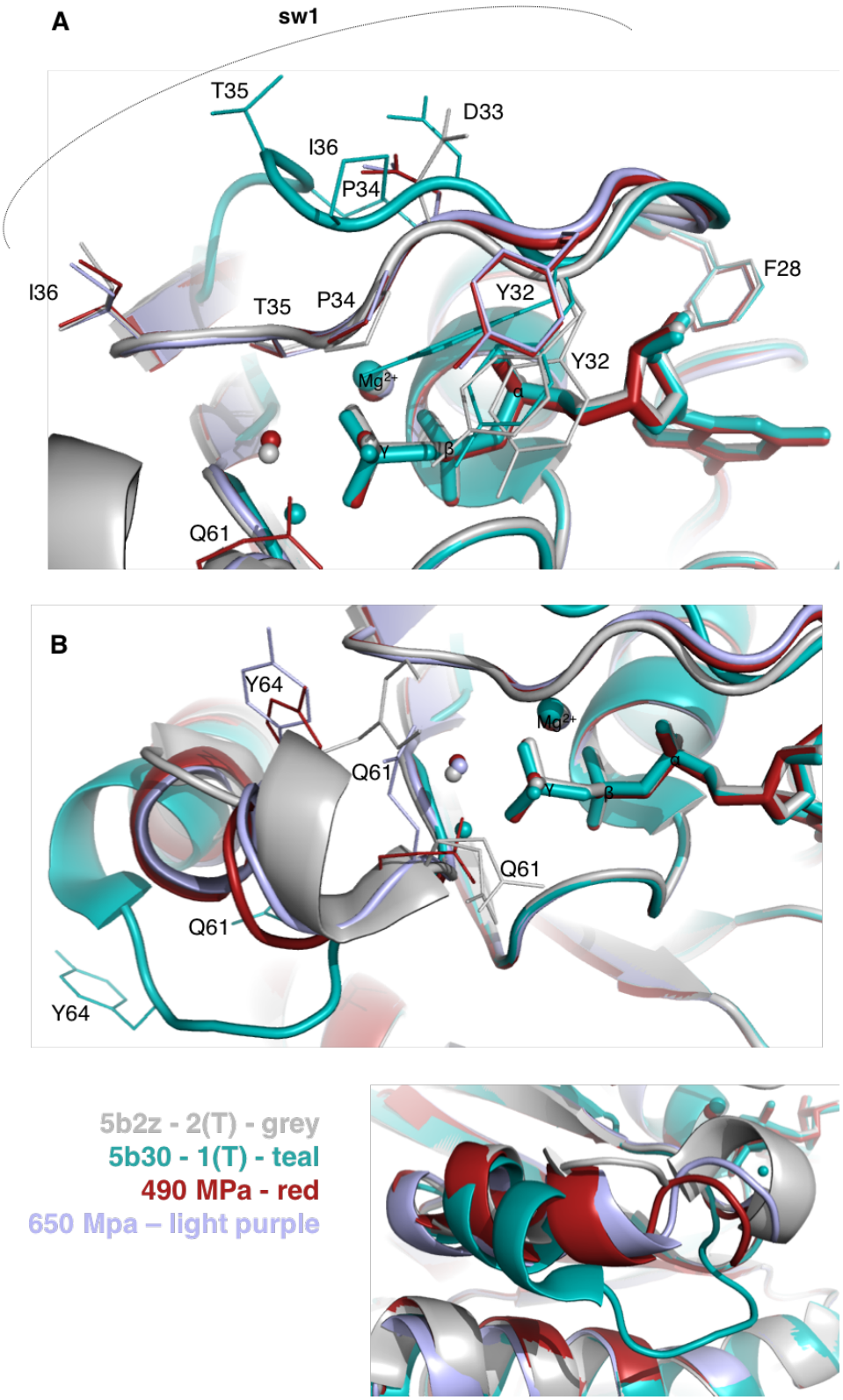

Figure H. Structural comparison between crystal forms of $HRas^{WT}$(1-166)•Mg^{2+}•GppNHp obtained by conventional X-ray at 77 K obtained for states 2(T) (coloured in grey, pdb: 5b2z) and 1(T) (coloured in teal, pdb: 5b30) seemingly obtained by Shima et al. [238] with the presently refined structures at 490 MPa (red coloured) and 650 MPa)light purple). All the proteins are aligned and superimposed **A.** Details of the switch 1 region. Note how both HP structures are better related to 5b2z than 5b30. The specific orientation in space of important residues is evidenced (F28,Y32, D33, P34, T35, I36). **B.** Details of the intrinsically disordered switch 2 region, showing the different orientation of Q61 and Y64 (top). A global overview is given in the bottom (aa 60-70).

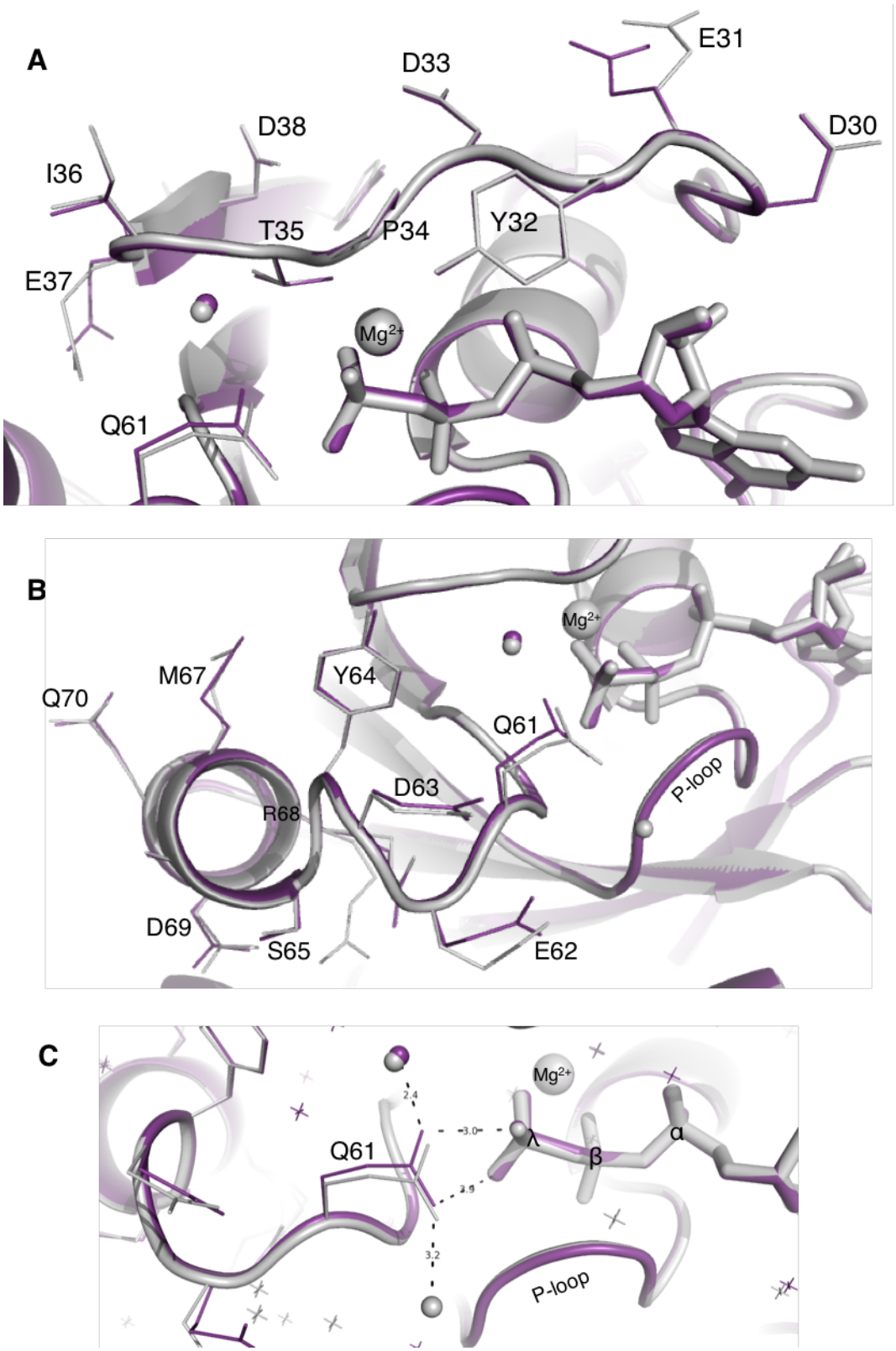

Figure I. Structural comparison between the refined crystal structure of Ras^{WT} in the Apo form, obtained at pamb and RT (grey colour) with the one obtained from the crystals soaked with 12 mM Zn^{2+}-cyclen (violet colour). No Zn^{2+} ions or the Zn^{2+}-cyclen were observed in the electron density map of the latter structure. Details regarding the orientation of the residues comprising switch 1 and switch 2 are given in A. and B., respectively. Note how the two structures superimpose perfectly, even at the highly mobile switch 2 region. C. Structural details of Q61 and the surrounding trapped waters. In both cases Q61 binds directly to the nucleotide and no equivalent nucleophilic waters, with respect to 5p21 (w175 and w189), could be found in the density maps.

5.2 Tables

Table A. ^{31}P NMR chemical shift values for HRas and KRas4b•Mg^{2+}•GppNHp proteins and their titration with the state 1(T) inhibitor Zn^{2+}-cyclen[a]

Protein complex	p:l	α-phosphate		β-phosphate		γ-phosphate		K_{12}[c]
		$\delta_{1(T)}$ [ppm]	$\delta_{2(T)}$ [ppm]	$\delta_{1(T)}$ [ppm]	$\delta_{2(T)}$ [ppm]	$\delta_{1(T)}$ [ppm]	$\delta_{2(T)}$ [ppm]	
FLHRas^{WT}[d]	--	-11.25	-11.71	-0.26	-0.16	-2.54	-3.24	1.90
+ Zn^{2+}-cyc	1:1.7	-11.18	-11.68	-0.23[b]		-2.55	-3.30	2.23
	1:3.4	-11.17	-11.67	-0.25[b]		-2.47	-3.35	2.02
	1:7	-11.18	-11.65	-0.46	-0.22	-2.18	-3.38	1.42
	1:11	-11.08	-11.63	-0.64	-0.23	-2.00	-3.48	1.17
	1:15	-10.96	-11.49	-0.77	-0.22	-1.88	-3.52	0.74
	1:23	-10.92	-11.58	-0.94	-0.19	-1.71	-3.56	0.42
	1:30	-10.81	-11.51	-1.04	-0.05	-1.64	-3.58	0.17
FLKRas^{WT}	--	-11.27	-11.73	-0.32	-0.21	-2.58	-3.30	2.01
+ Zn^{2+}-cyc	1:1.7	-11.21	-11.72	-0.21[b]		-2.53	-3.29	2.28
	1:3.4	-11.17	-11.67	-0.25[b]		-2.44	-3.30	1.55
	1:7	-11.08	-11.63	-0.32[b]		-2.18	-3.35	1.09
	1:11	-11.00	-11.64	-0.66	-0.22	-1.98	-3.39	0.78
	1:15	-10.93	-11.59	-0.79	-0.21	-1.83	-3.43	0.57
	1:23	-10.84	-11.56	-0.97	-0.23	-1.69	-3.47	0.25
	1:30	-10.74	-11.46	-1.06	-0.29	-1.61	-3.51	0.21

[a]All the values are presented in ppm and fitted from the experimental spectra recorded at 278 K, pH 7.5 with 10 mM $MgCl_2$ and 2 mM DTE. The protein:ligand (p:l) equivalents from the titration steps are shown. The estimated errors from the fitting procedure are less than ± 0.05 ppm in chemical shift values. An LB= 15 Hz was applied to the FID and subtracted afterwards to the calculated linewidth values.
[b]The β-phosphate was fitted as a single Lorentzian line because states 1 and 2 cannot be separated.
[c]The equilibrium constant, K_{12}, calculated using the population distribution on the γ-phosphate, is defined as the ratio between the relative areas of state 2 and state 1: $K_{12}=[A_{state\ 2}]/[A_{state\ 1}]$. The error associated with this calculation is ± 0.2 due to the partial overlapping of the resonance lines.

Table B. ^{31}P NMR chemical shift values and linewidths for the protein-drug complex $HRas^{WT}$(1-189)•Mg^{2+}•GppNHp•Zn^{2+}-cyclen and the displacement upon Raf-RBD titration.

Protein complex	p:l	α-phosphate		β-phosphate		γ-phosphate	
		$\delta_{1(T)}$	$\delta_{2(T)}$	$\delta_{1(T)}$	$\delta_{2(T)}$	$\delta_{1(T)}$	$\delta_{2(T)}$
$HRas^{WT}$		-11.27	-11.73	-0.26	-0.16	-2.60	-3.30
+ Zn^{2+}-cyc	1:32	-10.92	-11.56	-1.01	-0.03	-1.64	-3.59
+ Raf-RBD	1:0.4	-10.92	-11.60	-0.86	-0.16	-1.79	-3.54
	1:0.8	-10.93	-11.61	-0.89	-0.19	-1.80	-3.57
	1:1.2	-10.96	-11.62	-0.89	-0.17	-1.76	-3.56
	1:1.5	--	-11.61	--	-0.19	--	-3.56
		α-phosphate		β-phosphate		γ-phosphate	
		$\Delta\nu_{1/2}$ (1)	$\Delta\nu_{1/2}$ (2)	$\Delta\nu_{1/2}$ (1)	$\Delta\nu_{1/2}$ (2)	$\Delta\nu_{1/2}$ (1)	$\Delta\nu_{1/2}$ (2)
$HRas^{WT}$		136.4	80.5	40.9	56.2	94.6	58.5
+ Zn^{2+}-cyc	1:32	107.1	105.2	71.4	75.3	54.5	73.3
+ Raf-RBD	1:0.4	105.4	81.6	72.4	83.7	56.4	65.5
	1:0.8	121.0	114.3	69.3	79.8	57.2	64.2
	1:1.2	112.4	110.0	78.0	89.3	51.8	60.8
	1:1.5	--	127.3	--	62.5	--	43.4

All values are determined from the spectra recorded at 278 K and pH 7.5 upon proper deconvolution of the spectral lines. The estimated error for the chemical shifts and linewidths is is ± 0.015 ppm and 0.18 Hz, respectively.

Table C. ^{31}P NMR chemical shift values and linewidths for the protein-drug complex KRas^{G12D}•Mg^{2+}•GppNHp•Zn^{2+}-cyclen and the displacement upon Raf-RBD titration.

Protein Complex	p:l	α-phosphate		β-phosphate		γ-phosphate		K_{12}
		$\delta_{1(T)}$ [ppm]	$\delta_{2(T)}$ [ppm]	$\delta_{1(T)}$ [ppm]	$\delta_{2(T)}$ [ppm]	$\delta_{1(T)}$ [ppm]	$\delta_{2(T)}$ [ppm]	
KRas^{G12D}		-11.41	-11.71	-0.38		-2.48	-3.54	0.70
+ Zn^{2+}-cyc	1:0.5	-11.37	-11.65	-0.39		-2.45	-3.53	0.71
	1:1.5	-11.37	-11.68	-0.37		-2.40	-3.51	0.69
	1:5.0	-11.22	-11.50	-0.44		-2.12	-3.60	0.51
	1:9.0	-11.24	-11.62	-0.45		-1.70	-3.62	0.36
		α-phosphate		β-phosphate		γ-phosphate		
		$\Delta\nu_{1/2\ 1(T)}$ [Hz]	$\Delta\nu_{1/2\ 2(T)}$ [Hz]	$\Delta\nu_{1/2\ 1(T)}$ [Hz]	$\Delta\nu_{1/2\ 2(T)}$ [Hz]	$\Delta\nu_{1/2\ 1(T)}$ [Hz]	$\Delta\nu_{1/2\ 2(T)}$ [Hz]	
KRas^{G12D}		82.6	87.1	72.6		160.3	78.0	
+ Zn^{2+}-cyc	1:0.5	92.2	89.7	67.8		145.9	68.6	
	1:1.5	72.8	86.8	74.8		158.5	77.1	
	1:5.0	60.5	127.6	66.4		196.0	88.7	
	1:9.0	86.4	80.0	82.6		190.2	79.0	

All values are determined from the spectra recorded at 278 K and pH 7.5 upon proper deconvolution of the spectral lines. The estimated error for the chemical shifts and linewidths is is ± 0.015 ppm and 0.18 Hz, respectively. An LB= 15 Hz was applied to the FID and subtracted afterwards to the calculated linewidth values.

Table D. ^{31}P pressure-dependent chemical shift values and linewidths of the Mg^{2+}•GppNHp nucleotide.

Pressure [MPa]	α-phosphate		β-phosphate		γ-phosphate		P_i	
	δ [ppm]	$\Delta\nu_{1/2}$ [Hz]	δ [ppm]	$\Delta\nu_{1/2}$ [Hz]	δ [ppm]	$\Delta\nu_{1/2}$ [Hz]	δ [ppm]	$\Delta\nu_{1/2}$ [Hz]
0.1	-10.091	29.63	-5.602	54.25	-1.082	24.56	2.554	6.16
10	-10.096	29.97	-5.617	53.52	-1.093	24.87	2.551	9.35
20	-10.096	29.98	-5.631	53.05	-1.105	24.94	2.546	6.98
30	-10.096	29.78	-5.638	55.19	-1.114	25.10	2.540	4.60
40	-10.092	30.06	-5.648	54.11	-1.125	24.78	2.539	4.83
50	-10.096	30.11	-5.665	55.36	-1.138	24.82	2.535	5.25
60	-10.096	30.47	-5.678	55.25	-1.149	24.57	2.531	4.46
70	-10.098	30.31	-5.688	54.48	-1.157	23.83	2.527	5.95
80	-10.097	30.39	-5.703	57.59	-1.170	24.58	2.521	6.55
90	-10.099	30.55	-5.713	54.15	-1.179	24.14	2.520	4.48
100	-10.100	30.64	-5.732	55.57	-1.189	24.17	2.517	6.09
110	-10.104	30.71	-5.748	54.53	-1.202	23.36	2.512	4.57
120	-10.099	30.68	-5.753	55.81	-1.208	22.93	2.509	3.42
130	-10.107	30.86	-5.774	56.08	-1.218	22.90	2.506	3.59
140	-10.116	30.85	-5.793	53.89	-1.230	22.84	2.504	4.19
150	-10.106	30.85	-5.795	54.71	-1.236	22.92	2.502	3.74
160	-10.109	30.61	-5.811	56.57	-1.246	22.37	2.500	4.95
170	-10.114	31.02	-5.826	54.66	-1.255	22.32	2.499	3.46
180	-10.111	31.50	-5.829	56.60	-1.260	22.30	2.499	4.33
190	-10.116	31.22	-5.834	56.86	-1.260	22.04	2.500	3.95
200	-10.119	31.50	-5.848	56.86	-1.268	21.91	2.496	3.38
0.1	-10.090	29.52	-5.600	54.28	-1.081	25.79	2.551	7.97

All values are determined from the spectra recorded at 278 K and pH 9.0. The artificial Lorentzian broadening of 4 Hz applied to the FID was subtracted from the final linewidth values presented here. An LB= 4 Hz was applied to the FID and subtracted afterwards to the calculated linewidth values.

Table E. ^{31}P pressure-dependent chemical shift values of the GppNHp nucleotide in the absence of Mg^{2+}.

Pressure [MPa]	α-phosphate δ /ppm	β-phosphate δ /ppm	γ-phosphate δ /ppm	Pi δ
0.1	-10.44	-7.56	-0.68	4.28
10	-10.45	-7.59	-0.71	4.27
20	-10.46	-7.61	-0.74	4.27
30	-10.47	-7.63	-0.77	4.26
40	-10.47	-7.65	-0.80	4.26
50	-10.48	-7.67	-0.82	4.25
60	-10.49	-7.69	-0.84	4.25
70	-10.49	-7.71	-0.87	4.24
80	-10.50	-7.72	-0.89	4.24
90	-10.50	-7.73	-0.91	4.24
100	-10.50	-7.75	-0.93	4.24
110	-10.51	-7.76	-0.95	4.24
120	-10.51	-7.77	-0.96	4.24
130	-10.51	-7.78	-0.98	4.23
140	-10.51	-7.79	-0.99	4.23
150	-10.52	-7.79	-1.01	4.23
160	-10.52	-7.80	-1.02	4.23
170	-10.52	-7.81	-1.03	4.23
180	-10.52	-7.81	-1.05	4.23
190	-10.52	-7.82	-1.06	4.23
200	-10.52	-7.82	-1.07	4.23
210	-10.52	-7.83	-1.08	4.23
0.1	-10.44	-7.56	-0.68	4.28

All values are determined from the spectra recorded at 278 K and pH 11.5.

Table G. Uncorrected and corrected ^{31}P NMR pressure-dependent chemical shift values of $HRas^{T35S}$(1-166)•Mg^{2+}•GppNHp recorded at 278 K and pH 7.5.

Pressure [MPa]	α-phosphate		β-phosphate		γ-phosphate		P_i
	δ [ppm] **uncorrected**	δ [ppm] **corrected**	δ [ppm] **uncorrected**	δ [ppm] **corrected**	δ [ppm] **uncorrected**	δ [ppm] **corrected**	δ [ppm]
0.1	-10,971	-10,971	-0,324	-0,324	-2,540	-2,540	2,388
10	-10,960	-10,960	-0,330	-0,316	-2,542	-2,530	2,392
25	-10,952	-10,951	-0,332	-0,298	-2,545	-2,515	--
40	-10,944	-10,942	-0,337	-0,283	-2,550	-2,502	2,397
50	-10,936	-10,933	-0,340	-0,273	-2,554	-2,495	2,397
60	-10,927	-10,923	-0,345	-0,264	-2,557	-2,487	2,397
70	-10,923	-10,918	-0,347	-0,254	-2,559	-2,478	2,395
80	-10,919	-10,913	-0,349	-0,242	-2,560	-2,469	2,395
90	-10,914	-10,907	-0,353	-0,233	-2,561	-2,459	2,392
100	-10,912	-10,904	-0,355	-0,223	-2,561	-2,450	2,388
110	-10,909	-10,900	-0,360	-0,215	-2,560	-2,440	2,386
120	-10,907	-10,896	-0,362	-0,204	-2,560	-2,430	2,382
130	-10,906	-10,893	-0,365	-0,195	-2,559	-2,420	2,379
140	-10,905	-10,891	-0,368	-0,186	-2,558	-2,410	2,376
150	-10,904	-10,889	-0,371	-0,177	-2,558	-2,402	2,371
160	-10,906	-10,888	-0,373	-0,167	-2,557	-2,393	2,368
170	-10,906	-10,886	-0,377	-0,159	-2,556	-2,384	2,364
180	-10,905	-10,883	-0,383	-0,152	-2,554	-2,375	2,360
190	-10,905	-10,881	-0,387	-0,145	-2,552	-2,366	2,356
0.1	-10.969	-10.969	-0.317	-0.3224	-2.536	-2.540	2.305

All the uncorrected values were determined by processing the FID with a proper Gaussian function. The corrected values were obtained by simple addition or subtraction of $\Delta\delta_{freenuc\ fit}$ to the $\delta_{uncorrected}$ from the protein.

Table F. Uncorrected and corrected ^{31}P NMR pressure-dependent chemical shift values of HRas^{WT}(1-166)•Mg^{2+}•GppNHp recorded at 278 K and pH 7.5.

Pressure [MPa]	α-phosphate $\delta_{1(T)}$ [ppm]	α-phosphate $\delta_{2(T)}$ [ppm]	β-phosphate δ [ppm]	γ-phosphate $\delta_{1(T)}$ [ppm]	γ-phosphate $\delta_{2(T}$ [ppm]$_{)}$	P_i [ppm]
			Uncorrected			
0.1	-11.195	-11.641	-0.238	-2.517	-3.326	2.359
10	-11.157	-11.646	-0.247	-2.520	-3.309	2.370
20	-11.120	-11.652	-0.254	-2.525	-3.292	2.363
30	-11.109	-11.648	-0.257	-2.530	-3.272	2.370
40	-11.085	-11.640	-0.262	-2.538	-3.252	2.374
50	-11.072	-11.628	-0.272	-2.540	-3.238	2.376
60	-11.057	-11.625	-0.277	-2.541	-3.219	2.380
70	-11.028	-11.619	-0.286	-2.540	-3.197	2.380
80	-11.010	-11.612	-0.290	-2.541	-3.183	2.380
90	-11.005	-11.599	-0.291	-2.540	-3.167	2.382
100	-10.986	-11.592	-0.296	-2.539	-3.146	2.380
110	-10.984	-11.583	-0.306	-2.539	-3.130	2.379
120	-10.971	-11.589	-0.315	-2.539	-3.105	2.380
130	-10.954	-11.584	-0.321	-2.538	-3.099	2.376
140	-10.942	-11.581	-0.327	-2.536	-3.074	2.372
150	-10.927	-11.576	-0.335	-2.535	-3.061	2.370
160	-10.927	-11.571	-0.345	-2.532	-3.052	2.365
170	-10.904	-11.573	-0.349	-2.528	-3.035	2.363
180	-10.904	-11.579	-0.359	-2.525	-3.009	2.358
190	-10.891	-11.578	-0.363	-2.522	-2.998	2.355
200	-10.886	-11.576	-0.372	-2.519	-2.981	2.350
210	-10.877	-11.580	-0.379	-2.516	-2.957	2.345
220	-10.860	--	-0.388	-2.512	-2.961	2.342
230	-10.854	--	-0.392	-2.509	-2.942	2.336
240	-10.844	--	-0.403	-2.505	-2.931	2.330
250	-10.845	--	-0.420	-2.502	-2.908	2.326
0.1	-11.142	-11.638	-0.248	-2.514	-3.325	2.322
Pressure MPa	**α-phosphate** $\delta_{1(T)}$ [ppm]	**α-phosphate** $\delta_{2(T)}$ [ppm]	**β-phosphate** δ [ppm]	**γ-phosphate** $\delta_{1(T)}$ [ppm]	**γ-phosphate** $\delta_{2(T)}$ [ppm]	--
			Corrected			
0.1	-11,195	-11,641	-0,238	-2,517	-3,326	
10	-11,156	-11,645	-0,233	-2,508	-3,297	
20	-11,119	-11,651	-0,226	-2,500	-3,268	
30	-11,108	-11,647	-0,216	-2,494	-3,236	
40	-11,083	-11,638	-0,207	-2,490	-3,204	
50	-11,069	-11,626	-0,204	-2,481	-3,179	
60	-11,053	-11,621	-0,197	-2,471	-3,149	
70	-11,024	-11,614	-0,192	-2,459	-3,116	
80	-11,004	-11,607	-0,183	-2,450	-3,091	
90	-10,998	-11,592	-0,172	-2,439	-3,065	
100	-10,977	-11,584	-0,163	-2,427	-3,034	
110	-10,974	-11,573	-0,161	-2,418	-3,010	
120	-10,961	-11,578	-0,157	-2,409	-2,975	
130	-10,941	-11,572	-0,151	-2,399	-2,960	
140	-10,928	-11,567	-0,145	-2,389	-2,926	
150	-10,911	-11,561	-0,140	-2,380	-2,906	
160	-10,909	-11,553	-0,138	-2,368	-2,888	
170	-10,885	-11,554	-0,130	-2,357	-2,863	
180	-10,882	-11,557	-0,128	-2,346	-2,830	
190	-10,868	-11,554	-0,121	-2,336	-2,812	
200	-10,860	-11,550	-0,119	-2,326	-2,787	
210	-10,849	-11,551	-0,113	-2,316	-2,757	
220	-10,829		-0,111	-2,306	-2,755	
230	-10,821		-0,104	-2,297	-2,730	
240	-10,808		-0,104	-2,287	-2,713	
250	-10,806		-0,110	-2,279	-2,684	
0.1	-11,195		-0,238	-2,517	-3,326	

All the uncorrected values were determined by processing the FID with a proper Gaussian function. The corrected values were obtained by simple addition or subtraction of $\Delta\delta_{freenuc\ fit}$ to the $\delta_{uncorrected}$ from the protein.

Table H. Uncorrected and corrected ^{31}P NMR pressure-dependent chemical shift values of KRas^{G12V}(1-189)•Mg^{2+}•GTP recorded at 278 K and pH 7.5.

Pressure [MPa]	α-phosphate		β-phosphate		γ-phosphate		P_i
	$\delta_{1(T)}$ [ppm]	$\delta_{2(T)}$ [ppm]	$\delta_{1(T)}$ [ppm]	$\delta_{2(T)}$ [ppm]	$\delta_{1(T)}$ [ppm]	$\delta_{2(T)}$ [ppm]	[ppm]
			Uncorrected				
1.0	--	-11,532	--	-14,699	-6,004	-7,471	--
50	--	-11,513	-15,102	-14,739	-6,100	-7,453	2,365
70	--	-11,498	-15,152	-14,754	-6,130	-7,426	2,374
100	--	-11,466	-15,191	-14,779	-6,199	-7,384	2,354
125	--	-11,457	-15,251	-14,786	-6,248	-7,358	2,350
132	-11,150	-11,443	-15,256	-14,793	-6,260	-7,341	2,355
150	-11,142	-11,449	-15,301	-14,807	-6,280	-7,321	2,347
160	-11,101	-11,443	-15,310	-14,819	-6,309	-7,299	2,347
172	-11,116	-11,425	-15,307	-14,823	-6,330	-7,257	2,337
185	-11,101	-11,433	-15,311	-14,842	-6,347	-7,220	2,325
195	-11,047	-11,416	-15,318	-14,850	-6,371	-7,176	--
1.0	--	-11.539	--	-14.712	-5.989	-7.422	--
	α-phosphate		**β-phosphate**		**γ-phosphate**		--
	$\delta_{1(T)}$ [ppm]	$\delta_{2(T)}$ [ppm]	$\delta_{1(T)}$ [ppm]	$\delta_{2(T)}$ [ppm]	$\delta_{1(T)}$ [ppm]	$\delta_{2(T)}$ [ppm]	
			Corrected				
1.0	--	-11,532	--	-14,695	-6,002	-7,473	
50	--	-11,488	-14,880	-14,517	-5,999	-7,554	
70	--	-11,464	-14,851	-14,454	-5,993	-7,562	
100	--	-11,418	-14,782	-14,370	-6,013	-7,570	
125	--	-11,399	-14,762	-14,297	-6,026	-7,581	
132	-11,089	-11,382	-14,746	-14,284	-6,028	-7,573	
150	-11,074	-11,380	-14,741	-14,247	-6,025	-7,576	
160	-11,029	-11,371	-14,724	-14,233	-6,043	-7,566	
172	-11,040	-11,348	-14,692	-14,208	-6,050	-7,537	
185	-11,020	-11,353	-14,666	-14,198	-6,053	-7,514	
195	-10,963	-11,331	-14,652	-14,184	-6,068	-7,480	
1.0	--	-11.532	--	-14.695	-6.068	-7.480	

All the uncorrected values were determined by processing the FID with a proper Gaussian function. The corrected values were obtained by simple addition or subtraction of $\Delta\delta_{freenuc\ fit}$ to the $\delta_{uncorrected}$ from the protein.

Table I. ^{31}P NMR chemical shift values and linewidths for the protein-drug interaction HRas^{S39L}•Mg^{2+}•GppNHp and HRas^{E3V}•Mg^{2+}•GppNHp with Cu^{2+}-cyclen[a].

Protein complex	p:l	α-phosphate		β-phosphate	γ-phosphate		K_{12}[c]
		$\delta_{1(T)}$ [ppm]	$\delta_{2(T)}$ [ppm]	$\delta_{1(T),2(T)}$ [ppm]	$\delta_{1(T)}$ [ppm]	$\delta_{2(T)}$ [ppm]	
HRas^{S39L}	--	-11.08	-11.67	-0.25	-2.50	-3.35	1.5
+ Cu^{2+}-cyc	1:2	-11.01	-11.66	-0.27	-2.94	-3.36	1.9
	1:4	-11.07	-11.67	-0.28	--	-3.35	--
HRas^{E3V}	--	-11.23	-11.68	-0.27	-2.59	-3.33	2.0
+ Cu^{2+}-cyc	1:0.5	-11.18	-11.66	-0.28	-3.01	-3.33	--
	1:1	-11.18	-11.67	-0.29	--	-3.36	--
	1.2	-11.17	-11.67	-0.29	--	-3.37	--
		α-phosphate		β-phosphate	γ-phosphate		--
		$\Delta\nu_{1/2\ 1(T)}$ [Hz]	$\Delta\nu_{1/2\ 2(T)}$ [Hz]	$\Delta\nu_{1/2\ 1(T),2(T)}$ [Hz]	$\Delta\nu_{1/2\ 1(T)}$ [Hz]	$\Delta\nu_{1/2\ 2(T)}$ [Hz]	
HRas^{S39L}	--	98.05	62.88	42.55	48.95	50.82	
+ Cu^{2+}-cyc	1:2	87.36	61.37	48.47	163.72	47.21	
	1:4	122.88	45.45	58.38	--	78.83	
HRas^{E3V}	--	122.22	67.33	54.39	78.74	53.00	
+ Cu^{2+}-cyc	1:0.5	122.82	60.23	56.97	250	44.95	
	1:1	118.73	67.05	61.55	--	61.55	
	1:2	117.31	74.55	70.00	--	62.18	

[a]All the values fitted from the experimental spectra recorded at 278 K, with 40 mM Tris/HCl pH 7.5, 10 mM $MgCl_2$, 2 mM DTE, 0.2 mM DSS and 5% D_2O. The protein:ligand (p:l) equivalents from the titration steps are shown. The estimated errors from the fitting procedure are less than ± 0.02 ppm in chemical shift values for the γ-phosphate.
[b]The β-phosphate was fitted as a single Lorentzian line because states 1 and 2 cannot be separated. An LB= 15 Hz was applied to the FID and subtracted afterwards from the final fitted linewidth values.
[c]The equilibrium constant, K_{12}, calculated using the population distribution on the γ-phosphate, is defined as the ratio between the relative areas of state 2 and state 1: $K_{12}=[A_{state\ 2}]/[A_{state\ 1}]$. The error associated with this calculation is ± 0.2 due to the partial overlapping of the resonance lines.

Table J. Uncorrected and corrected ^{31}P NMR pressure-dependent chemical shift values (in ppm) of HRas^{D33K}(1-166)•Mg^{2+}•GppNHp recorded at 278 K and pH 7.5.

Pressure [MPa]	α-phosphate $\delta_{1(T)/2(T)}$ [ppm]	β-phosphate $\delta_{1(T),2(T)}$ [ppm]	γ-phosphate $\delta_{1(T)}$ [ppm]	γ-phosphate $\delta_{2(T)}$ [ppm]	P_i [ppm]
		Uncorrected			
0.1	-11.496	-0.285	--	-3.397	--
10	-11.490	-0.291	--	-3.386	--
20	-11.460	-0.301	--	-3.369	1.884
30	-11.444	-0.308	--	-3.356	1.870
40	-11.435	-0.312	--	-3.345	1.859
50	-11.401	-0.318	--	-3.331	1.844
60	-11.367	-0.321	--	-3.310	1.838
70	-11.352	-0.325	--	-3.295	1.826
80	-11.324	-0.331	-2.497	-3.277	1.818
90	-11.308	-0.336	-2.498	-3.265	1.809
100	-11.270	-0.343	-2.494	-3.252	1.797
110	-11.246	-0.347	-2.484	-3.237	1.785
120	-11.221	-0.347	-2.480	-3.221	1.779
130	-11.200	-0.351	-2.477	-3.211	1.771
140	-11.171	-0.356	-2.468	-3.193	1.759
150	-11.148	-0.360	-2.459	-3.180	1.750
160	-11.130	-0.364	-2.455	-3.171	1.741
170	-11.104	-0.367	-2.454	-3.161	1.734
180	-11.074	-0.366	-2.450	-3.147	1.725
190	-11.064	-0.368	-2.448	-3.137	1.724
200	-11.036	-0.371	-2.443	-3.123	1.716
0.1	-11.498	-0.285	--	-3.396	--

Pressure [MPa]	α-phosphate $\delta_{1(T)}$ [ppm]	α-phosphate $\delta_{2(T)}$ [ppm]	β-phosphate δ [ppm]	γ-phosphate $\delta_{1(T)}$ [ppm]	γ-phosphate $\delta_{2(T)}$ [ppm]	--
			Corrected			
0.1	-11.496		-0.285	--	-3.397	
10	-11.490		-0.278	--	-3.373	
20	-11.460		-0.274	--	-3.345	
30	-11.443		-0.267	--	-3.319	
40	-11.433		-0.258	--	-3.297	
50	-11.398		-0.250	--	-3.271	
60	-11.364		-0.240	--	-3.240	
70	-11.348		-0.231	--	-3.214	
80	-11.319		-0.224	-2.406	-3.186	
90	-11.301		-0.216	-2.396	-3.164	
100	-11.262		-0.211	-2.383	-3.141	
110	-11.237		-0.202	-2.363	-3.116	
120	-11.210		-0.189	-2.350	-3.091	
130	-11.188		-0.181	-2.338	-3.072	
140	-11.156		-0.174	-2.321	-3.045	
150	-11.132		-0.165	-2.303	-3.025	
160	-11.112		-0.158	-2.291	-3.007	
170	-11.085		-0.149	-2.283	-2.989	
180	-11.052		-0.136	-2.271	-2.968	
190	-11.040		-0.126	-2.262	-2.951	
200	-11.010		-0.117	-2.250	-2.930	
0.1	-11.496		-0.285	--	-3.397	

All the uncorrected values were determined by processing the FID with a proper Gaussian function. The corrected values were obtained by simple addition or subtraction of $\Delta\delta_{freenuc\ fit}$ to the $\delta_{uncorrected}$ from the protein.

5.3 List of Figures

1. Introduction

2. Methods

3. Results

5. Appendix

6.4 List of Tables

2. Methods

3. Results

5. Appendix

5.5 List of Abbreviations

AP	alkaline phosphatase
APS	ammonium persulfate
Arf	ADP ribosilation factor
bp	base pair
BSA	bovine serum albumin
c	truncated
ca.	circa
CCD	charge coupled device
Cdc25	cell division cycle 25
CFC	cardio-facio-cutaneous
CM	carboxymethyl
CS	costello syndrome
Cu^{2+}-cyclen	copper cyclen
CV	column volume
DAC	diamond anvil cell
DEAE	diethylaminoethanol
DACH	diacylglycerol
DFT	density Functional Theory
DMSO	dimethyl Sulfoxide
DNA	desoxyribonucleic acid
DTE	dithioerithrol
DSS	4,4-dimethyl-4-silapentane-1-sulfonic acid
E. coli.	*Escherichia coli*
EDTA	ethylenediaminetetracetic acid
e.g.	*exempli gratia*
EM	exponential Multiplication
ERK	extracellular signal-regulated kinase
ESRF	European Synchrotron Radiation Facility
EtBr	ethidium bromide
EtOH	ethanol
eV	electron volt
FID	free induction decay
FL	full length
FPLC	fast protein liquid chromatography
FTI	farnesyl transferase inhibitor
G	Gibbs free Energy (the variation is denoted ΔG)
GAP	GTPase Activating Protein
GB	Gaussian broadening
GDP	guanosine diphosphate
GdmCl	guanidinium hydrochloride
GEF	guanine Exchange Factor
GM	Gaussian multiplication
GNBP	guanine nucleotide binding protein
GPa	giga pascal
GppNHp	5'-Guanylyl imidodiphosphate
Grb2	growth factor receptor-bound protein 2
GSK3β	glycogen synthase kinase 3β
GSH	reduced glutathione
GST	glutathione S-transferase
GTP	guanosine triphosphate
H	enthalpy (the variation is denoted ΔH)
HP	high pressure
HPLC	high performance liquid chromatography
HPMX	high pressure macromolecular crystallography
HSQC	heteronuclear single quantum coherence
HVR	hypervariable region

IC	inhibitory concentration
ie.	*id est*
IEX	ion exchange chromatography
IPTG	isopropyl β-d-1-thiogalactopyranoside
ITC	isothermal titration calorimetry
J	joule
K	kelvin
kcal	kilocalorie
kDa	kilo Dalton
kJ	kilo joule
L	litre
LB	lysogeny Broth
LCMS	liquid chromatography Mass spectrometry
M	molar
MAPK	mitogen activated protein kinase
MD	molecular dynamics
MeOH	methanol
MHz	mega Hertz
min	minute
MLV	murine leukemia virus
mM	milimolar
MM	minimal medium
MPa	mega pascal
MR	molecular replacement
MST	microscale thermophoresis
NAG	N-acetyl glucosamine
NAM	N-acetyl muramic acid
NF1	neurofibromatin 1
ng	nanogram
NMM	new minimal medium
NMR	nuclear Magnetic Resonance
NTA	nitrilotriacetic acid
OD	optical density
Pa	pascal
pamb	ambient pressure
PCR	polymerase chain reaction
Pdb	protein data bank
PEG	polyethylene glycol
PET	polyethylene terephthalate
P_i	inorganic phosphate
PI3K	phosphoinositide 3 kinase
pM	picomolar
PMSF	phenylmethanesulphonylfluoride
ppm	parts per million
QCM	quartz crystal microbalance
QM	quantum mechanics
Rab	ras in the brain
Raf-RBD	rapidly accelerated fibrosarcoma Ras binding domain
RalGDF	ras-like protein
Ran	ras in the nucleus
Rap	receptor associated protein
Rho	ras homologous
Rmsd	root mean square deviation
RPLC	reversed phase liquid chromatography
rpm	rotations per minute
RT	room temperature
RTK	receptor tyrosine kinase
S	entropy (the variation is denoted ΔS)

s	second
SAM	S-adenosyl methionine
SDM	site directed mutagenesis
SDS-PAGE	sodium dodecyl sulphate Polyacrylamide Gel Electrophoresis
SEC	size exclusion chromatography
Shc	src homology
SOC	super optimal broth with catabolite repression
SOS	Son of Sevenless
SP	sulphopropyl
SPR	surface Plasmon Resonance
sw1	switch 1
sw2	switch 2
T	temperature (the variation is denoted ΔT)
T_1	longitudinal relaxation
TAE	tris-acetate-EDTA
TB	terrific broth
TBE	tris-borate-EDTA
TEMED	tetramethylethylinediamine
TFB	transformation buffer
Tris	tris(hydroxymethil)aminomethane
TROSY	transverse relaxation optimized spectroscopy
μM	micromolar
WT	*wild type*
Zn^{2+}-BPA	zinc-bisphenol acid
Zn^{2+}-cyclen	zinc-cyclen

Conventions:
throughout this thesis, all the amino acid names are abbreviated either by their three letter code (e.g. Asp33) or by their single letter (D33). Both are often used interchangeably. The commonly used abbreviation for the switch 1 and switch 2 regions is switch 1 and switch 2, respectively. However, the equivalent abbreviations SW I and SW II were sometimes used in the captions of several Figures.

5.6 List of Publications

M Spoerner, M Karl, **P Lopes**, M Hoering, K Loeffel, A Nuehs, J Adelsberger, W Kremer and H Kalbitzer. High pressure ^{31}P NMR spectroscopy on guanine nucleotides. J Biomol NMR. 2017 61(1), pp 1-13.

M Marques, D Gianolio, G Cibin, J Tomkinson, S Parker, R. Valero, **P Lopes** and L. Carvalho. A molecular view of cisplatin's mode of action: interplay with DNA bases and acquired resistance. Phys Chem Chem Phys. 2015 17(14), pp 5155-5171.

I Rosnizeck, D Filchtinski, **P Lopes**, B Kieninger, C Herrmann, H Kalbitzer and M Spoerner. Elucidating the Mode of Action of a Typical Ras State 1(T) Inhibitor. Biochem. 2014 53(24), pp 3867-3878.

P Lopes, M Marques, R Valero, J Tomkinson and L. Carvalho. Guanine: A Combined Study Using Vibrational Spectroscopy and Theoretical Methods. Spectrosc-INT J. 2012 5(27), pp 273-292.

C. Matos, L. Carvalho, **P. Lopes** and M Marques. New Strategies Against Prostate Cancer – Pt(II)-Based Chemotherapy. Curr Med Chem. 2012 19(27), pp 4678-4687.

P Lopes, R Valero, J Tomkinson, M Marques and L Batista de Carvalho. Applying vibrational spectroscopy to the study of nucleobases – adenine as a case study. New J Chem. 2013 37(9), pp 2691-2699.

6. References

“It takes a long time to understand nothiing”

Edward Dahlberg

1. Harvey, J.J., *An Unidentified Virus which causes the Rapid Production of Tumours in Mice.* Nature, 1964. **204**(4963): p. 1104-1105.

2. Kirsten, W.H. and L.A. Mayer, *Morphologic Responses to a Murine Erythroblastosis Virus2.* JNCI: Journal of the National Cancer Institute, 1967. **39**(2): p. 311-335.

3. Shimizu, K., et al., *Isolation and Preliminary Characterization of the Transforming Gene of a Human Neuroblastoma Cell Line.* Proceedings of the National Academy of Sciences of the United States of America, 1983. **80**(2): p. 383-387.

4. Milroy, L.-G. and C. Ottmann, *The Renaissance of Ras.* ACS Chemical Biology, 2014. **9**(11): p. 2447-2458.

5. Wittinghofer, A., *Ras Superfamily Small G Proteins: Biology and Mechanisms 1: General Features, Signaling*. 2014: Springer Vienna.

6. Willumsen, B.M., et al., *The p21 ras C-terminus is required for transformation and membrane association.* Nature, 1984. **310**(5978): p. 583-586.

7. Ahearn, I.M., et al., *Regulating the regulator: post-translational modification of RAS.* Nat Rev Mol Cell Biol, 2012. **13**(1): p. 39-51.

8. Wang, M. and P.J. Casey, *Protein prenylation: unique fats make their mark on biology.* Nat Rev Mol Cell Biol, 2016. **17**(2): p. 110-122.

9. Shen, M., et al., *Farnesyltransferase and geranylgeranyltransferase I: structures, mechanism, inhibitors and molecular modeling.* Drug Discovery Today, 2015. **20**(2): p. 267-276.

10. de Vos, A.M., et al., *Three-dimensional structure of an oncogene protein: catalytic domain of human c-H-ras p21.* Science, 1988. **239**(4842): p. 888.

11. Pai, E.F., et al., *Structure of the guanine-nucleotide-binding domain of the Ha-ras oncogene product p21 in the triphosphate conformation.* Nature, 1989. **341**(6239): p. 209-214.

12. Pai, E., et al., *Refined crystal structure of the triphosphate conformation of H-ras p21 at 1.35 A resolution: implications for the mechanism of GTP hydrolysis*. Vol. 8. 1990.

13. Saraste, M., P.R. Sibbald, and A. Wittinghofer, *The P-loop: a common motif in ATP- and GTP-binding proteins.* Trends in Biochemical Sciences, 1990. **15**(11): p. 430-434.

14. Vetter, I.R. and A. Wittinghofer, *The Guanine Nucleotide-Binding Switch in Three Dimensions.* Science, 2001. **294**(5545): p. 1299.

15. Wittinghofer, A. and H. Waldmann, *Ras—A Molecular Switch Involved in Tumor Formation.* Angewandte Chemie International Edition, 2000. **39**(23): p. 4192-4214.

16. Wittinghofer, A. and I.R. Vetter, *Structure-Function Relationships of the G Domain, a Canonical Switch Motif.* Annual Review of Biochemistry, 2011. **80**(1): p. 943-971.

17. Lu, S., et al., *Drugging Ras GTPase: a comprehensive mechanistic and signaling structural view.* Chemical Society Reviews, 2016. **45**(18): p. 4929-4952.

18. Maurer, T., et al., *Small-molecule ligands bind to a distinct pocket in Ras and inhibit SOS-mediated nucleotide exchange activity.* Proceedings of the National Academy of Sciences, 2012. **109**(14): p. 5299-5304.

19. Banerjee, A., et al., *The disordered hypervariable region and the folded catalytic domain of oncogenic K-Ras4B partner in phospholipid binding.* Current Opinion in Structural Biology, 2016. **36**(Supplement C): p. 10-17.

20. Chavan, Tanmay S., et al., *High-Affinity Interaction of the K-Ras4B Hypervariable Region with the Ras Active Site.* Biophysical Journal. **109**(12): p. 2602-2613.

21. Castellano, E. and E. Santos, *Functional Specificity of Ras Isoforms: So Similar but So Different.* Genes & Cancer, 2011. **2**(3): p. 216-231.

22. Hu, J.-S. and A.G. Redfield, *Conformational and Dynamic Differences between N-ras P21 Bound to GTPγS and to GMPPNP as Studied by NMR.* Biochemistry, 1997. **36**(16): p. 5045-5052.

23. Scheidig, A.J., C. Burmester, and R.S. Goody, *The pre-hydrolysis state of p21ras in complex with GTP: new insights into the role of water molecules in the GTP hydrolysis reaction of ras-like proteins.* Structure, 1999. **7**(11): p. 1311-S2.

24. Farnsworth, C.L. and L.A. Feig, *Dominant inhibitory mutations in the Mg(2+)-binding site of RasH prevent its activation by GTP.* Molecular and Cellular Biology, 1991. **11**(10): p. 4822-4829.

25. Farrar, C.T., C.J. Halkides, and D.J. Singel, *The frozen solution structure of p21 ras determined by ESEEM spectroscopy reveals weak coordination of Thr35 to the active site metal ion.* Structure, 1997. **5**(8): p. 1055-1066.

26. Schweins, T., et al., *The role of the metal ion in the p21ras catalysed GTP-hydrolysis: Mn2+ versus Mg2+11Edited by K. Nagai.* Journal of Molecular Biology, 1997. **266**(4): p. 847-856.

27. Rudack, T., et al., *The Role of Magnesium for Geometry and Charge in GTP Hydrolysis, Revealed by Quantum Mechanics/Molecular Mechanics Simulations.* Biophysical Journal, 2011. **103**(2): p. 293-302.

28. Lu, S., et al., *Ras Conformational Ensembles, Allostery, and Signaling.* Chemical Reviews, 2016. **116**(11): p. 6607-6665.

29. Wittinghofer, A. and E.F. Pal, *The structure of Ras protein: a model for a universal molecular switch.* Trends in Biochemical Sciences, 1991. **16**(Supplement C): p. 382-387.

30. Milburn, M.V., et al., *Molecular switch for signal transduction: structural differences between active and inactive forms of protooncogenic ras proteins.* Science, 1990. **247**(4945): p. 939.

31. Bos, J.L., H. Rehmann, and A. Wittinghofer, *GEFs and GAPs: Critical Elements in the Control of Small G Proteins.* Cell, 2007. **129**(5): p. 865-877.

32. Rajalingam, K., et al., *Ras oncogenes and their downstream targets.* Biochimica et Biophysica Acta (BBA) - Molecular Cell Research, 2007. **1773**(8): p. 1177-1195.

33. Nakhaeizadeh, H., et al., *The RAS-Effector Interface: Isoform-Specific Differences in the Effector Binding Regions.* PLOS ONE, 2016. **11**(12): p. e0167145.

34. Takashima, A. and D.V. Faller, *Targeting the RAS oncogene.* Expert Opinion on Therapeutic Targets, 2013. **17**(5): p. 507-531.

35. Kolch, W., *Meaningful relationships: the regulation of the Ras/Raf/MEK/ERK pathway by protein interactions.* Biochemical Journal, 2000. **351**(2): p. 289.

36. Lenzen, C., et al., *Kinetic Analysis by Fluorescence of the Interaction between Ras and the Catalytic Domain of the Guanine Nucleotide Exchange Factor Cdc25Mm* Biochemistry, 1998. **37**(20): p. 7420-7430.

37. Cherfils, J. and M. Zeghouf, *Regulation of Small GTPases by GEFs, GAPs, and GDIs.* Physiological Reviews, 2013. **93**(1): p. 269.

38. Hennig, A., et al., *Ras activation revisited: role of GEF and GAP systems*, in *Biological Chemistry*. 2015. p. 831.

39. Cherfils, J. and P. Chardin, *GEFs: structural basis for their activation of small GTP-binding proteins.* Trends in Biochemical Sciences, 1999. **24**(8): p. 306-311.

40. Chardin, P., et al., *Human Sos1: a guanine nucleotide exchange factor for Ras that binds to GRB2.* Science, 1993. **260**(5112): p. 1338.

41. Vo, U., et al., *Monitoring Ras Interactions with the Nucleotide Exchange Factor Son of Sevenless (Sos) Using Site-specific NMR Reporter Signals and Intrinsic Fluorescence.* Journal of Biological Chemistry, 2016. **291**(4): p. 1703-1718.

42. Li, N., et al., *Guanine-nucleotide-releasing factor hSos1 binds to Grb2 and links receptor tyrosine kinases to Ras signalling.* Nature, 1993. **363**(6424): p. 85-88.

43. Fam, N.P., et al., *Cloning and characterization of Ras-GRF2, a novel guanine nucleotide exchange factor for Ras.* Molecular and Cellular Biology, 1997. **17**(3): p. 1396-1406.

44. Boriack-Sjodin, P.A., et al., *The structural basis of the activation of Ras by Sos.* Nature, 1998. **394**(6691): p. 337-343.

45. Margarit, S.M., et al., *Structural Evidence for Feedback Activation by Ras·GTP of the Ras-Specific Nucleotide Exchange Factor SOS.* Cell, 2003. **112**(5): p. 685-695.

46. Hall, B.E., et al., *Structure-based Mutagenesis Reveals Distinct Functions for Ras Switch 1 and Switch 2 in Sos-catalyzed Guanine Nucleotide Exchange.* Journal of Biological Chemistry, 2001. **276**(29): p. 27629-27637.

47. Marshall, C.J., *Ras effectors.* Current Opinion in Cell Biology, 1996. **8**(2): p. 197-204.

48. McCormick, F. and A. Wittinghofer, *Interactions between Ras proteins and their effectors.* Current Opinion in Biotechnology, 1996. **7**(4): p. 449-456.

49. Vigil, D., et al., *Ras superfamily GEFs and GAPs: validated and tractable targets for cancer therapy?* Nat Rev Cancer, 2010. **10**(12): p. 842-857.

50. Koide, H., et al., *GTP-dependent association of Raf-1 with Ha-Ras: identification of Raf as a target downstream of Ras in mammalian cells.* Proceedings of the National Academy of Sciences, 1993. **90**(18): p. 8683-8686.

51. Spoerner, M., et al., *Dynamic properties of the Ras switch I region and its importance for binding to effectors.* Proceedings of the National Academy of Sciences, 2001. **98**(9): p. 4944-4949.

52. Herrmann, C., G.A. Martin, and A. Wittinghofer, *Quantitative Analysis of the Complex between p21 and the Ras-binding Domain of the Human Raf-1 Protein Kinase.* Journal of Biological Chemistry, 1995. **270**(7): p. 2901-2905.

53. Cutler, R.E., et al., *Autoregulation of the Raf-1 serine/threonine kinase.* Proceedings of the National Academy of Sciences of the United States of America, 1998. **95**(16): p. 9214-9219.

54. Hmitou, I., et al., *Differential Regulation of B-Raf Isoforms by Phosphorylation and Autoinhibitory Mechanisms.* Molecular and Cellular Biology, 2007. **27**(1): p. 31-43.

55. Roskoski, R., *RAF protein-serine/threonine kinases: Structure and regulation.* Biochemical and Biophysical Research Communications, 2010. **399**(3): p. 313-317.

56. Fischer, A., et al., B- and C-RAF Display Essential Differences in Their Binding to Ras: The Isotope Specific N Terminus OF B-RAF Facilitates Ras Binding. Journal of Biological Chemistry, 2007. **282**(36): p. 26503-26516.

57. Matallanas, D., et al., *Raf Family Kinases: Old Dogs Have Learned New Tricks.* Genes & Cancer, 2011. **2**(3): p. 232-260.

58. Filchtinski, D., et al., *What Makes Ras an Efficient Molecular Switch: A Computational, Biophysical, and Structural Study of Ras-GDP Interactions with Mutants of Raf.* Journal of Molecular Biology, 2010. **399**(3): p. 422-435.

59. Huang, L., et al., *Three-dimensional structure of the Ras-interacting domain of RalGDS.* Nat Struct Mol Biol, 1997. **4**(8): p. 609-615.

60. Nassar, N., et al., *The 2.2 A crystal structure of the Ras-binding domain of the serine/threonine kinase c-Raf1 in complex with RaplA and a GTP analogue.* Nature, 1995. **375**(6532): p. 554-560.

61. Akasaka, K., et al., *Differential Structural Requirements for Interaction of Ras Protein with Its Distinct Downstream Effectors.* Journal of Biological Chemistry, 1996. **271**(10): p. 5353-5360.

62. Winkler, D.G., et al., *Identification and Characterization of Mutations in Ha-Ras That Selectively Decrease Binding to cRaf-1.* Journal of Biological Chemistry, 1997. **272**(39): p. 24402-24409.

63. Terada, T., et al., *Nuclear magnetic resonance and molecular dynamics studies on the interactions of the ras-binding domain of raf-1 with wild-type and mutant ras*

proteins 11Edited by A. R. Fersht. Journal of Molecular Biology, 1999. **286**(1): p. 219-232.

64. Fetics, Susan K., et al., *Allosteric Effects of the Oncogenic RasQ61L Mutant on Raf-RBD.* Structure, 2015. **23**(3): p. 505-516.

65. Gohlke, H., L.A. Kuhn, and D.A. Case, *Change in protein flexibility upon complex formation: Analysis of Ras-Raf using molecular dynamics and a molecular framework approach.* Proteins: Structure, Function, and Bioinformatics, 2004. **56**(2): p. 322-337.

66. Gohlke, H., C. Kiel, and D.A. Case, *Insights into Protein–Protein Binding by Binding Free Energy Calculation and Free Energy Decomposition for the Ras–Raf and Ras–RalGDS Complexes.* Journal of Molecular Biology, 2003. **330**(4): p. 891-913.

67. Spoerner, M., et al., *Conformational States of Human Rat Sarcoma (Ras) Protein Complexed with Its Natural Ligand GTP and Their Role for Effector Interaction and GTP Hydrolysis.* Journal of Biological Chemistry, 2010. **285**(51): p. 39768-39778.

68. Gorman, C., et al., *Equilibrium and Kinetic Measurements Reveal Rapidly Reversible Binding of Ras to Raf.* Journal of Biological Chemistry, 1996. **271**(12): p. 6713-6719.

69. Sydor, J.R., et al., *Transient Kinetic Studies on the Interaction of Ras and the Ras-Binding Domain of c-Raf-1 Reveal Rapid Equilibration of the Complex.* Biochemistry, 1998. **37**(40): p. 14292-14299.

70. Goldfinger, L.E., *Choose your own path: specificity in Ras GTPase signaling.* Molecular BioSystems, 2008. **4**(4): p. 293-299.

71. Hekman, M., et al., *Novel C-Raf phosphorylation sites: serine 296 and 301 participate in Raf regulation.* FEBS Letters, 2005. **579**(2): p. 464-468.

72. Schweins, T., et al., *Substrate-assisted catalysis as a mechanism for GTP hydrolysis of p21ras and other GTP-binding proteins.* Nat Struct Mol Biol, 1995. **2**(1): p. 36-44.

73. Wittinghofer, A., K. Scheffzek, and M.R. Ahmadian, *The interaction of Ras with GTPase-activating proteins.* FEBS Letters, 1997. **410**(1): p. 63-67.

74. Matte, A., L.W. Tari, and L.T.J. Delbaere, *How do kinases transfer phosphoryl groups?* Structure, 1998. **6**(4): p. 413-419.

75. Wittinghofer, A., *Phosphoryl transfer in Ras proteins, conclusive or elusive?* Trends in Biochemical Sciences, 2006. **31**(1): p. 20-23.

76. Lassila, J.K., J.G. Zalatan, and D. Herschlag, *Biological Phosphoryl-Transfer Reactions: Understanding Mechanism and Catalysis.* Annual Review of Biochemistry, 2011. **80**(1): p. 669-702.

77. Maegley, K.A., S.J. Admiraal, and D. Herschlag, *Ras-catalyzed hydrolysis of GTP: a new perspective from model studies.* Proceedings of the National Academy of Sciences of the United States of America, 1996. **93**(16): p. 8160-8166.

78. Shutes, A. and C.J. Der, *Real-Time In Vitro Measurement of Intrinsic and Ras GAP-Mediated GTP Hydrolysis*, in *Methods in Enzymology*. 2006, Academic Press. p. 9-22.

79. Rensland, H., et al., *Is there a rate-limiting step before GTP cleavage by H-ras p21?* Biochemistry, 1991. **30**(46): p. 11181-11185.

80. Wittinghofer, A., *Signaling mechanistics: Aluminum fluoride for molecule of the year.* Current Biology, 1997. **7**(11): p. R682-R685.

81. Sternweis, P.C. and A.G. Gilman, *Aluminum: a requirement for activation of the regulatory component of adenylate cyclase by fluoride.* Proceedings of the National Academy of Sciences of the United States of America, 1982. **79**(16): p. 4888-4891.

82. Graham, D.L., et al., *MgF3– as a Transition State Analog of Phosphoryl Transfer.* Chemistry & Biology, 2002. **9**(3): p. 375-381.

83. Scheffzek, K., et al., *The Ras-RasGAP Complex: Structural Basis for GTPase Activation and Its Loss in Oncogenic Ras Mutants.* Science, 1997. **277**(5324): p. 333.

84. Rudack, T., et al., *Ras and GTPase-activating protein (GAP) drive GTP into a precatalytic state as revealed by combining FTIR and biomolecular simulations.* Proceedings of the National Academy of Sciences, 2012. **109**(38): p. 15295-15300.

85. Kötting, C., et al., *The GAP arginine finger movement into the catalytic site of Ras increases the activation entropy.* Proceedings of the National Academy of Sciences of the United States of America, 2008. **105**(17): p. 6260-6265.

86. Miao, W., et al., *p120 Ras GTPase-activating Protein Interacts with Ras-GTP through Specific Conserved Residues.* Journal of Biological Chemistry, 1996. **271**(26): p. 15322-15329.

87. Glennon, T.M., J. Villà, and A. Warshel, *How Does GAP Catalyze the GTPase Reaction of Ras?: A Computer Simulation Study.* Biochemistry, 2000. **39**(32): p. 9641-9651.

88. Sharma, N., U. Sonavane, and R. Joshi, *Probing the wild-type HRas activation mechanism using steered molecular dynamics, understanding the energy barrier and role of water in the activation.* European Biophysics Journal, 2014. **43**(2): p. 81-95.

89. Lu, S., et al., *The Structural Basis of Oncogenic Mutations G12, G13 and Q61 in Small GTPase K-Ras4B.* 2016. **6**: p. 21949.

90. Scrima, A., et al., *The Rap–RapGAP complex: GTP hydrolysis without catalytic glutamine and arginine residues.* The EMBO Journal, 2008. **27**(7): p. 1145-1153.

91. Seewald, M.J., et al., *RanGAP mediates GTP hydrolysis without an arginine finger.* Nature, 2002. **415**(6872): p. 662-666.

92. Kraulis, P.J., et al., *Solution Structure and Dynamics of Ras p21.cntdot.GDP Determined by Heteronuclear Three- and Four-Dimensional NMR Spectroscopy.* Biochemistry, 1994. **33**(12): p. 3515-3531.

93. Trahey, M. and F. McCormick, *A cytoplasmic protein stimulates normal N-ras p21 GTPase, but does not affect oncogenic mutants.* Science, 1987. **238**(4826): p. 542.

94. Ito, Y., et al., *Regional Polysterism in the GTP-Bound Form of the Human c-Ha-Ras Protein.* Biochemistry, 1997. **36**(30): p. 9109-9119.

95. Araki, M., et al., *Solution Structure of the State 1 Conformer of GTP-bound H-Ras Protein and Distinct Dynamic Properties between the State 1 and State 2 Conformers.* Journal of Biological Chemistry, 2011. **286**(45): p. 39644-39653.

96. Acharya, K.R. and M.D. Lloyd, *The advantages and limitations of protein crystal structures.* Trends in Pharmacological Sciences, 2005. **26**(1): p. 10-14.

97. Kigawa, T., et al., *Selenomethionine incorporation into a protein by cell-free synthesis.* Journal of Structural and Functional Genomics, 2002. **2**(1): p. 29-35.

98. Wenye, Z., et al., *Direct Targeting of the Ras GTPase Superfamily Through Structure- Based Design.* Current Topics in Medicinal Chemistry, 2017. **17**(1): p. 16-29.

99. Lang, P.T., et al., *Automated electron-density sampling reveals widespread conformational polymorphism in proteins.* Protein Science, 2010. **19**(7): p. 1420-1431.

100. Prior, I.A., P.D. Lewis, and C. Mattos, *A comprehensive survey of Ras mutations in cancer.* Cancer Research, 2012. **72**(10): p. 2457-2467.

101. Forbes, S.A., et al., *COSMIC: mining complete cancer genomes in the Catalogue of Somatic Mutations in Cancer.* Nucleic Acids Research, 2011. **39**(suppl_1): p. D945-D950.

102. Karnoub, A.E. and R.A. Weinberg, *Ras oncogenes: split personalities.* Nat Rev Mol Cell Biol, 2008. **9**(7): p. 517-531.

103. Almoguera, C., et al., *Most human carcinomas of the exocrine pancreas contain mutant c-K-RAS genes*. Vol. 53. 1988. 549-54.

104. Burmer, G.C. and L.A. Loeb, *Mutations in the KRAS2 oncogene during progressive stages of human colon carcinoma.* Proceedings of the National Academy of Sciences, 1989. **86**(7): p. 2403-2407.

105. Enomoto, T., et al., *K-ras activation in neoplasms of the human female reproductive Tract.* Cancer Research, 1990. **50**(19): p. 6139.

106. Zhou, B., C.J. Der, and A.D. Cox, *The role of wild type RAS isoforms in cancer.* Seminars in Cell & Developmental Biology, 2016. **58**(Supplement C): p. 60-69.

107. Kiel, C. and L. Serrano, *Structure-energy-based predictions and network modelling of RASopathy and cancer missense mutations.* Molecular Systems Biology, 2014. **10**(5): p. 727.

108. Eccleston, J.F., et al., *Kinetics of interaction between normal and proline 12 Ras and the GTPase-activating proteins, p120-GAP and neurofibromin. The significance*

of the intrinsic GTPase rate in determining the transforming ability of ras. Journal of Biological Chemistry, 1993. **268**(36): p. 27012-27019.

109. Gremer, L., et al., *Fluoride complexes of oncogenic Ras mutants to study the Ras-RasGAP interaction*, in *Biological Chemistry*. 2008. p. 1163.

110. White, M.A., et al., *Multiple ras functions can contribute to mammalian cell transformation.* Cell, 1995. **80**(4): p. 533-541.

111. Khosravi-Far, R., et al., *Oncogenic Ras activation of Raf/mitogen-activated protein kinase-independent pathways is sufficient to cause tumorigenic transformation.* Molecular and Cellular Biology, 1996. **16**(7): p. 3923-3933.

112. Joneson, T., et al., *Stimulation of Membrane Ruffling and MAP Kinase Activation by Distinct Effectors of RAS.* Science, 1996. **271**(5250): p. 810.

113. Fiordalisi, J.J., et al., *A distinct class of dominant negative Ras mutants: cytosolic GTP-bound Ras effector domain mutants that inhibit Ras signaling and transformation and enhance cell adhesion.* Journal of Biological Chemistry, 2002. **277**(13): p. 10813-10823.

114. Jacobsen, N.E., *Interpretation of Proton (1H) NMR Spectra*, in *NMR Spectroscopy Explained*. 2007, John Wiley & Sons, Inc. p. 39-73.

115. Jacobsen, N.E., *Fundamentals of NMR Spectroscopy in Liquids*, in *NMR Spectroscopy Explained*. 2007, John Wiley & Sons, Inc. p. 1-38.

116. Spoerner, M., et al., *Conformational States of Ras Complexed with the GTP Analogue GppNHp or GppCH2p: Implications for the Interaction with Effector Proteins.* Biochemistry, 2005. **44**(6): p. 2225-2236.

117. Geyer, M., et al., *Conformational Transitions in p21ras and in Its Complexes with the Effector Protein Raf-RBD and the GTPase Activating Protein GAP.* Biochemistry, 1996. **35**(32): p. 10308-10320.

118. Stumber, M., et al., *Observation of Slow Dynamic Exchange Processes in Ras Protein Crystals by 31P Solid State NMR Spectroscopy.* Journal of Molecular Biology, 2002. **323**(5): p. 899-907.

119. Iuga, A., et al., *Solid-state 31P NMR Spectroscopy of Microcrystals of the Ras Protein and its Effector Loop Mutants: Comparison Between Crystalline and Solution State.* Journal of Molecular Biology, 2004. **342**(3): p. 1033-1040.

120. Ader, C., et al., *Solid-State 31P NMR Spectroscopy of Precipitated Guanine Nucleotide-Binding Protein Ras in Complexes with Its Effector Molecules Raf Kinase and RalGDS.* The Journal of Physical Chemistry B, 2007. **111**(10): p. 2752-2757.

121. Geyer, M., et al., *Structure of the Ras-binding domain of RalGEF and implications for Ras binding and signalling.* Nat Struct Mol Biol, 1997. **4**(9): p. 694-699.

122. Spoerner, M., et al., *Conformational states of human H-Ras detected by high-field EPR, ENDOR, and 31P NMR spectroscopy.* Magnetic Resonance in Chemistry, 2005. **43**(S1): p. S74-S83.

123. Spoerner, M., A. Wittinghofer, and H.R. Kalbitzer, *Perturbation of the conformational equilibria in Ras by selective mutations as studied by 31P NMR spectroscopy.* FEBS Letters, 2004. **578**(3): p. 305-310.

124. Spoerner, M., et al., *Slow conformational dynamics of the guanine nucleotide-binding protein Ras complexed with the GTP analogue GTPγS.* FEBS Journal, 2007. **274**(6): p. 1419-1433.

125. Kalbitzer, H.R., et al., *Fundamental Link between Folding States and Functional States of Proteins.* Journal of the American Chemical Society, 2009. **131**(46): p. 16714-16719.

126. Digilio, M.C., et al., *RASopathies: Clinical Diagnosis in the First Year of Life.* Molecular Syndromology, 2011. **1**(6): p. 282-289.

127. Gremer, L., et al., *Germline KRAS Mutations Cause Aberrant Biochemical and Physical Properties Leading to Developmental Disorders.* Human mutation, 2011. **32**(1): p. 33-43.

128. Tartaglia, M., G. Zampino, and B.D. Gelb, *Noonan Syndrome: Clinical Aspects and Molecular Pathogenesis.* Molecular Syndromology, 2010. **1**(1): p. 2-26.

129. Tidyman, W.E. and K.A. Rauen, *The RASopathies: developmental syndromes of Ras/MAPK pathway dysregulation.* Current Opinion in Genetics & Development, 2009. **19**(3): p. 230-236.

130. Tidyman, W.E. and K.A. Rauen, *Noonan, Costello and cardio–facio–cutaneous syndromes: dysregulation of the Ras–MAPK pathway.* Expert Reviews in Molecular Medicine, 2008. **10**.

131. Fernández-Medarde, A. and E. Santos, *Ras in Cancer and Developmental Diseases.* Genes & Cancer, 2011. **2**(3): p. 344-358.

132. Schubbert, S., K. Shannon, and G. Bollag, *Hyperactive Ras in developmental disorders and cancer.* 2007. **7**: p. 295.

133. Cox, A.D., et al., *Drugging the undruggable RAS: Mission Possible?* 2014. **13**: p. 828.

134. Zhang, F. and J.K. Cheong, *The renewed battle against RAS-mutant cancers.* Cellular and Molecular Life Sciences, 2016. **73**(9): p. 1845-1858.

135. Brock, E.J., et al., *How to Target Activated Ras Proteins: Direct Inhibition vs. Induced Mislocalization.* Mini reviews in medicinal chemistry, 2016. **16**(5): p. 358-369.

136. Wang, W., G. Fang, and J. Rudolph, *Ras inhibition via direct Ras binding—is there a path forward?* Bioorganic & Medicinal Chemistry Letters, 2012. **22**(18): p. 5766-5776.

137. Cromm, P.M., et al., *Direct Modulation of Small GTPase Activity and Function.* Angewandte Chemie International Edition, 2015. **54**(46): p. 13516-13537.

138. Liu, M., et al., *Antitumor Activity of SCH 66336, an Orally Bioavailable Tricyclic Inhibitor of Farnesyl Protein Transferase, in Human Tumor Xenograft Models and Transgenic Mice.* Cancer Research, 1998. **58**(21): p. 4947.

139. End, D.W., et al., *Characterization of the Antitumor Effects of the Selective Farnesyl Protein Transferase Inhibitor R115777 in Vivo and <em>in Vitro</em&gt.* Cancer Research, 2001. **61**(1): p. 131.

140. Rotblat, B., et al., *The Ras Inhibitor Farnesylthiosalicylic Acid (Salirasib) Disrupts The Spatiotemporal Localization Of Active Ras: A Potential Treatment For Cancer*, in *Methods in Enzymology*. 2008, Academic Press. p. 467-489.

141. Laheru, D., et al., *Integrated preclinical and clinical development of S-trans, trans-farnesylthiosalicylic acid (FTS, Salirasib) in pancreatic cancer.* Investigational New Drugs, 2012. **30**(6): p. 2391-2399.

142. Berndt, N., A.D. Hamilton, and S.M. Sebti, *Targeting protein prenylation for cancer therapy.* 2011. **11**: p. 775.

143. James, G.L., J.L. Goldstein, and M.S. Brown, *Polylysine and CVIM Sequences of K-RasB Dictate Specificity of Prenylation and Confer Resistance to Benzodiazepine Peptidomimetic in Vitro.* Journal of Biological Chemistry, 1995. **270**(11): p. 6221-6226.

144. Patgiri, A., et al., *An Orthosteric Inhibitor of the Ras-Sos Interaction.* Nature chemical biology, 2011. **7**(9): p. 585-587.

145. Sun, Q., et al., *Discovery of Small Molecules that Bind to K-Ras and Inhibit Sos-Mediated Activation.* Angewandte Chemie, 2012. **124**(25): p. 6244-6247.

146. Herrmann, C., et al., *Sulindac Sulfide inhibits Ras signaling*. Vol. 17. 1998. 1769-76.

147. Waldmann, H., et al., *Sulindac-Derived Ras Pathway Inhibitors Target the Ras–Raf Interaction and Downstream Effectors in the Ras Pathway.* Angewandte Chemie International Edition, 2004. **43**(4): p. 454-458.

148. Karaguni, I.-M., et al., *The New Sulindac Derivative IND 12 Reverses Ras-induced Cell Transformation.* Cancer Research, 2002. **62**(6): p. 1718.

149. Ostrem, J.M., et al., *K-Ras(G12C) inhibitors allosterically control GTP affinity and effector interactions.* Nature, 2013. **503**(7477): p. 548-551.

150. Lim, S.M., et al., *Therapeutic Targeting of Oncogenic K-Ras by a Covalent Catalytic Site Inhibitor.* Angewandte Chemie (International ed. in English), 2014. **53**(1): p. 199-204.

151. Hunter, J.C., et al., *In situ selectivity profiling and crystal structure of SML-8-73-1, an active site inhibitor of oncogenic K-Ras G12C.* Proceedings of the National Academy of Sciences, 2014. **111**(24): p. 8895-8900.

152. Herrero, A., et al., *Small Molecule Inhibition of ERK Dimerization Prevents Tumorigenesis by RAS-ERK Pathway Oncogenes.* Cancer Cell, 2015. **28**(2): p. 170-182.

153. Freeman, Alyson K., Daniel A. Ritt, and Deborah K. Morrison, *Effects of Raf Dimerization and Its Inhibition on Normal and Disease-Associated Raf Signaling.* Molecular Cell. **49**(4): p. 751-758.

154. Yao, Z., et al., *BRAF Mutants Evade ERK-Dependent Feedback by Different Mechanisms that Determine Their Sensitivity to Pharmacologic Inhibition.* Cancer Cell, 2015. **28**(3): p. 370-383.

155. Spoerner, M., et al., *A novel mechanism for the modulation of the Ras-effector interaction by small molecules.* Biochemical and Biophysical Research Communications, 2005. **334**(2): p. 709-713.

156. Rosnizeck, I.C., et al., *Elucidating the Mode of Action of a Typical Ras State 1(T) Inhibitor.* Biochemistry, 2014. **53**(24): p. 3867-3878.

157. Rosnizeck, I.C., et al., *Stabilizing a Weak Binding State for Effectors in the Human Ras Protein by Cyclen Complexes.* Angewandte Chemie International Edition, 2010. **49**(22): p. 3830-3833.

158. Rosnizeck, I.C., et al., *Metal–Bis(2-picolyl)amine Complexes as State 1(T) Inhibitors of Activated Ras Protein.* Angewandte Chemie International Edition, 2012. **51**(42): p. 10647-10651.

159. Silva, J.L., et al., *High-Pressure Chemical Biology and Biotechnology.* Chemical Reviews, 2014. **114**(14): p. 7239-7267.

160. Onuchic, J.N., Z. Luthey-Schulten, and P.G. Wolynes, *Theory of Protein Folding: The Energy Landscape Perspective.* Annual Review of Physical Chemistry, 1997. **48**(1): p. 545-600.

161. Frauenfelder, H. and P.G. Wolynes, *Rate theories and puzzles of hemeprotein kinetics.* Science, 1985. **229**(4711): p. 337.

162. Monod, J., J. Wyman, and J.-P. Changeux, *On the nature of allosteric transitions: A plausible model.* Journal of Molecular Biology, 1965. **12**(1): p. 88-118.

163. Akasaka, K., *Probing Conformational Fluctuation of Proteins by Pressure Perturbation.* Chemical Reviews, 2006. **106**(5): p. 1814-1835.

164. de Oliveira, G.A.P. and J.L. Silva, *A hypothesis to reconcile the physical and chemical unfolding of proteins.* Proceedings of the National Academy of Sciences, 2015. **112**(21): p. E2775-E2784.

165. Kitahara, R., et al., *Pressure-induced chemical shifts as probes for conformational fluctuations in proteins.* Progress in Nuclear Magnetic Resonance Spectroscopy, 2013. **71**(Supplement C): p. 35-58.

166. Akasaka, K., *High Pressure Bioscience – Basic Concepts, Applications and Frontiers*. 2015.

167. Akasaka, K., *Exploring the entire conformational space of proteins by high-pressure NMR*, in *Pure and Applied Chemistry*. 2003. p. 927.

168. Munte, C.E., et al., *Distinct Conformational States of the Alzheimer β-Amyloid Peptide Can Be Detected by High-Pressure NMR Spectroscopy.* Angewandte Chemie International Edition, 2013. **52**(34): p. 8943-8947.

169. Kalbitzer, H.R., et al., *15N and 1H NMR study of histidine containing protein (HPr) from Staphylococcus carnosus at high pressure.* Protein Science : A Publication of the Protein Society, 2000. **9**(4): p. 693-703.

170. Kachel, N., et al., *Observation of intermediate states of the human prion protein by high pressure NMR spectroscopy.* BMC Structural Biology, 2006. **6**(1): p. 16.

171. Kalbitzer, H.R., et al., *Intrinsic Allosteric Inhibition of Signaling Proteins by Targeting Rare Interaction States Detected by High-Pressure NMR Spectroscopy.* Angewandte Chemie International Edition, 2013. **52**(52): p. 14242-14246.

172. Kremer, W., et al., *Pulsed Pressure Perturbations, an Extra Dimension in NMR Spectroscopy of Proteins.* Journal of the American Chemical Society, 2011. **133**(34): p. 13646-13651.

173. Itié, J.P., et al., *Crystallography under high pressure using synchrotron radiation.* Journal of Physics D: Applied Physics, 2015. **48**(50): p. 504007.

174. Jannasch, H.W. and C.D. Taylor, *Deep-Sea Microbiology.* Annual Review of Microbiology, 1984. **38**(1): p. 487-487.

175. Fourme, R., et al., *Advances in High-Pressure Biophysics: Status and Prospects of Macromolecular Crystallography.* Annual Review of Biophysics, 2009. **38**(1): p. 153-171.

176. Kundrot, C.E. and F.M. Richards, *Collection and processing of X-ray diffraction data from protein crystals at high pressure.* Journal of Applied Crystallography, 1986. **19**(4): p. 208-213.

177. Katrusiak, A. and Z. Dauter, *Compressibility of lysozyme protein crystals by X-ray diffraction.* Acta Crystallographica Section D, 1996. **52**(3): p. 607-608.

178. Girard, E., et al., *Macromolecular crystallography at high pressure with pneumatic diamond anvil cells handled by a six-axis robotic arm.* Journal of Applied Crystallography, 2010. **43**(4): p. 762-768.

179. Girard, E., et al., *The First Crystal Structure of a Macromolecular Assembly under High Pressure: CpMV at 330 MPa.* Biophysical Journal, 2005. **88**(5): p. 3562-3571.

180. Girard, E., et al., *Structure-Function Perturbation and Dissociation of Tetrameric Urate Oxidase by High Hydrostatic Pressure.* Biophysical Journal, 2010. **98**(10): p. 2365-2373.

181. Kurpiewska, K., et al., *Structural investigation of ribonuclease A conformational preferences using high pressure protein crystallography.* Chemical Physics, 2016. **468**(Supplement C): p. 53-62.

182. Girard, E., et al., *Toward fully fledged high-pressure macromolecular crystallography.* Journal of Applied Crystallography, 2007. **40**(5): p. 912-918.

183. Collins, M.D., C.U. Kim, and S.M. Gruner, *High-Pressure Protein Crystallography and NMR to Explore Protein Conformations.* Annual Review of Biophysics, 2011. **40**(1): p. 81-98.

184. Fourme, R., et al., *Using a quasi-parallel X-ray beam of ultrashort wavelength for high-pressure virus crystallography: implications for standard macromolecular crystallography.* Acta Crystallographica Section D, 2003. **59**(10): p. 1767-1772.

185. Fourme, R., et al., *High-Pressure Macromolecular Crystallography (HPMX): Status and prospects.* Biochimica et Biophysica Acta (BBA) - Proteins and Proteomics, 2006. **1764**(3): p. 384-390.

186. Losen, M., et al., *Effect of Oxygen Limitation and Medium Composition on Escherichia coli Fermentation in Shake-Flask Cultures.* Biotechnology Progress, 2004. **20**(4): p. 1062-1068.

187. Ehrenberg, M., H. Bremer, and P.P. Dennis, *Medium-dependent control of the bacterial growth rate.* Biochimie, 2013. **95**(4): p. 643-658.

188. Egli, T., *Microbial growth and physiology: a call for better craftsmanship.* Frontiers in Microbiology, 2015. **6**: p. 287.

189. Tao, H., et al., *Functional Genomics: Expression Analysis of Escherichia coli Growing on Minimal and Rich Media.* Journal of Bacteriology, 1999. **181**(20): p. 6425-6440.

190. Madigan, M.T., *Brock biology of microorganisms*. 2012.

191. Dagert, M. and S.D. Ehrlich, *Prolonged incubation in calcium chloride improves the competence of Escherichia coli cells.* Gene, 1979. **6**(1): p. 23-28.

192. Hanahan, D., *Studies on transformation of Escherichia coli with plasmids.* Journal of Molecular Biology, 1983. **166**(4): p. 557-580.

193. *Promega Miniprep Quick Protocol*. 2017 [cited 2017 20 September]; Available from: https://www.promega.com/-/media/files/resources/protcards/pureyield-plasmid-miniprep-system-quick-protocol.pdf.

194. *Promega Midiprep Quick Protocol*. 2017 [cited 2017 20 June]; Available from: https://www.promega.com/-/media/files/resources/protcards/pureyield-plasmid-midiprep-system-quick-protocol.pdf.

195. Tucker, J., et al., *Expression of p21 proteins in Escherichia coli and stereochemistry of the nucleotide-binding site.* The EMBO Journal, 1986. **5**(6): p. 1351-1358.

196. McCracken, G.H., J.D. Nelson, and M.L. Thomas, *Discrepancy Between Carbenicillin and Ampicillin Activities Against Enterococci and Listeria.* Antimicrobial Agents and Chemotherapy, 1973. **3**(3): p. 343-349.

197. Jacobsen, N.E., *NMR spectroscopy explained : simplified theory, applications and examples for organic chemistry and structural biology*. 2007, Hoboken, N.J.: Wiley-Interscience.

198. Sivashanmugam, A., et al., *Practical protocols for production of very high yields of recombinant proteins using Escherichia coli.* Protein Science, 2009. **18**(5): p. 936-948.

199. Invitrogen. *GENEART Site-Directed Mutagenesis User Guide*. 2017 [cited 2017 2 Jully]; Available from: https://tools.thermofisher.com/content/sfs/manuals/geneart_site_directed_mutagenesis_man.pdf.

200. Alcalde, M., *Mutagenesis Protocols in Saccharomyces cerevisiae by In Vivo Overlap Extension*, in *In Vitro Mutagenesis Protocols: Third Edition*, J. Braman, Editor. 2010, Humana Press: Totowa, NJ. p. 3-14.

201. Singh, A., et al., *Protein recovery from inclusion bodies of Escherichia coli using mild solubilization process.* Microbial Cell Factories, 2015. **14**: p. 41.

202. James, G.T., *Inactivation of the protease inhibitor phenylmethylsulfonyl fluoride in buffers.* Analytical Biochemistry, 1978. **86**(2): p. 574-579.

203. Cleland, W.W., *Dithiothreitol, a New Protective Reagent for SH Groups*.* Biochemistry, 1964. **3**(4): p. 480-482.

204. Repaske, R., *Lysis of gram-negative bacteria by lysozyme.* Biochimica et Biophysica Acta, 1956. **22**(1): p. 189-191.

205. Linke, D., *Chapter 34 Detergents: An Overview.* Methods in Enzymology, 2009. **463**: p. 603-617.

206. Ninfa, A.J., D.P. Ballou, and M. Benore, *Fundamental Laboratory Approaches for Biochemistry and Biotechnology*. 2009: Wiley.

207. Arakawa, T. and S.N. Timasheff, *Mechanism of protein salting in and salting out by divalent cation salts: balance between hydration and salt binding.* Biochemistry, 1984. **23**(25): p. 5912-5923.

208. Wingfield, P.T., *Protein Precipitation Using Ammonium Sulfate.* Current protocols in protein science / editorial board, John E. Coligan ... [et al.], 2001. **APPENDIX 3**: p. Appendix-3F.

209. Zhang, Y. and P.S. Cremer, *Interactions between macromolecules and ions: the Hofmeister series.* Current Opinion in Chemical Biology, 2006. **10**(6): p. 658-663.

210. Nes, W.D., *Protein Purification: Principles, High-Resolution Methods, and Applications. Second Edition Edited by Jan-Christer Janson and Lars Rydén (Uppsala University). John Wiley & Sons: New York. 1988. 695 pp. ISBN 0-471-18626-0.* Journal of the American Chemical Society, 1999. **121**(7): p. 1625-1625.

211. Boardman, N.K. and S.M. Partridge, *Separation of neutral proteins on ion-exchange resins.* Biochemical Journal, 1955. **59**(4): p. 543.

212. Healthcare, G. 2017 [cited 2017 27 June]; Available from: http://www.gelifesciences.com/webapp/wcs/stores/servlet/catalog/en/GELifeSciences-de/products/AlternativeProductStructure_17442/.

213. Scheffzek, K., et al., *Crystal structure of the GTPase-activating domain of human p120GAP and implications for the interaction with Ras.* Nature, 1996. **384**(6609): p. 591-596.

214. Laemmli, U.K., *Cleavage of Structural Proteins during the Assembly of the Head of Bacteriophage T4.* Nature, 1970. **227**(5259): p. 680-685.

215. Schägger, H. and G. von Jagow, *Tricine-sodium dodecyl sulfate-polyacrylamide gel electrophoresis for the separation of proteins in the range from 1 to 100 kDa.* Analytical Biochemistry, 1987. **166**(2): p. 368-379.

216. Gasteiger, E., et al., *Protein Identification and Analysis Tools on the ExPASy Server*, in *The Proteomics Protocols Handbook*, J.M. Walker, Editor. 2005, Humana Press: Totowa, NJ. p. 571-607.

217. Hoffman, N.E. and J.C. Liao, *Reversed phase high performance liquid chromatographic separations of nucleotides in the presence of solvophobic ions.* Analytical Chemistry, 1977. **49**(14): p. 2231-2234.

218. Martin L, Schwarz S, and Breitsprecher D, *Analyzing Thermal Unfolding of Proteins: The Prometheus NT.48. Application Note NT-PR-001*, N. Technologies, Editor. 2014.

219. Martin, L., M. Maschberger, and D. Breitsprecher, *Thermal Unfolding of Antibodies with the Prometheus NT.48*, N. Technologies, Editor. 2015. p. 1.

220. Senisterra, G., I. Chau, and M. Vedadi, *Thermal Denaturation Assays in Chemical Biology.* ASSAY and Drug Development Technologies, 2011. **10**(2): p. 128-136.

221. Jerabek-Willemsen, M., et al., *Molecular Interaction Studies Using Microscale Thermophoresis.* Assay and Drug Development Technologies, 2011. **9**(4): p. 342-353.

222. Renaud, J.-P., et al., *Biophysics in drug discovery: impact, challenges and opportunities.* Nat Rev Drug Discov, 2016. **15**(10): p. 679-698.

223. Falconer, R.J., *Applications of isothermal titration calorimetry – the research and technical developments from 2011 to 2015.* Journal of Molecular Recognition, 2016. **29**(10): p. 504-515.

224. Khalef, N., O. Campanella, and A. Bakri, *Isothermal calorimetry: methods and applications in food and pharmaceutical fields.* Current Opinion in Food Science, 2016. **9**(Supplement C): p. 70-76.

225. Freyer, M.W. and E.A. Lewis, *Isothermal Titration Calorimetry: Experimental Design, Data Analysis, and Probing Macromolecule/Ligand Binding and Kinetic Interactions.* Methods in Cell Biology, 2008. **84**: p. 79-113.

226. Spoerner, M., et al., *High pressure 31P NMR spectroscopy on guanine nucleotides.* Journal of Biomolecular NMR, 2016: p. 1-13.

227. Raiford, D.S., C.L. Fisk, and E.D. Becker, *Calibration of methanol and ethylene glycol nuclear magnetic resonance thermometers.* Analytical Chemistry, 1979. **51**(12): p. 2050-2051.

228. Shaka, A.J., P.B. Barker, and R. Freeman, *Computer-optimized decoupling scheme for wideband applications and low-level operation.* Journal of Magnetic Resonance (1969), 1985. **64**(3): p. 547-552.

229. Erlach, M.B., et al., *Ceramic cells for high pressure NMR spectroscopy of proteins.* Journal of Magnetic Resonance, 2010. **204**(2): p. 196-199.

230. Wishart, D.S., et al., *1H, 13C and 15N chemical shift referencing in biomolecular NMR.* Journal of Biomolecular NMR, 1995. **6**(2): p. 135-140.

231. Baskaran, K., et al., *Chemical shift optimization in multidimensional NMR spectra by AUREMOL-SHIFTOPT.* Journal of Biomolecular NMR, 2009. **43**(4): p. 197-210.

232. Maurer, T. and H.R. Kalbitzer, *Indirect Referencing of31P and19F NMR Spectra.* Journal of Magnetic Resonance, Series B, 1996. **113**(2): p. 177-178.

233. Levenberg, K., *A method for the solution of certain non-linear problems in least squares.* Quarterly of Applied Mathematics, 1944. **2**(2): p. 164-168.

234. Marquardt, D., *An Algorithm for Least-Squares Estimation of Nonlinear Parameters.* Journal of the Society for Industrial and Applied Mathematics, 1963. **11**(2): p. 431-441.

235. Hausser, K.H. and H.R. Kalbitzer, *NMR in medicine and biology: structure determination, tomography, in vivo spectroscopy*. Physics in life sciences. 1991: Springer-Verlag.

236. Hill, A.V., *The possible effects of the aggregation of the molecules of hemoglobin on its dissociation curves.* The Journal of Physiology\, 1910. **40}**: p. i--vii\.

237. Goutelle, S., et al., *The Hill equation: a review of its capabilities in pharmacological modelling.* Fundamental & Clinical Pharmacology, 2008. **22**(6): p. 633-648.

238. Fourme, R., et al., *High-pressure protein crystallography (HPPX): instrumentation, methodology and results on lysozyme crystals.* Journal of Synchrotron Radiation, 2001. **8**(5): p. 1149-1156.

239. Katrusiak, A., *High-pressure crystallography.* Acta Crystallographica Section A, 2008. **64**(1): p. 135-148.

240. Forman, R.A., et al., *Pressure Measurement Made by the Utilization of Ruby Sharp-Line Luminescence.* Science, 1972. **176**(4032): p. 284.

241. Matsumoto, S., et al., *Molecular Mechanism for Conformational Dynamics of Ras·GTP Elucidated from In-Situ Structural Transition in Crystal.* Scientific Reports, 2016. **6**: p. 25931.

242. Shima, F., et al., *Structural Basis for Conformational Dynamics of GTP-bound Ras Protein.* Journal of Biological Chemistry, 2010. **285**(29): p. 22696-22705.

243. Kiel, C., L. Serrano, and C. Herrmann, *A Detailed Thermodynamic Analysis of Ras/Effector Complex Interfaces.* Journal of Molecular Biology, 2004. **340**(5): p. 1039-1058.

244. Wohlgemuth, S., et al., *Recognizing and Defining True Ras Binding Domains I: Biochemical Analysis.* Journal of Molecular Biology, 2005. **348**(3): p. 741-758.

245. Kiel, C., A. referee: Wittinghofer, and C. referee: Herrmann, *Untersuchung von Ras/Effektor-Komplexen mit gezielt veränderten elektrostatischen Eigenschaften*. 2003, Ruhr-Universität Bochum: Bochum. p. pp. 175.

246. Wu, X., et al., *Inhibition of Ras-effector interactions by cyclic peptides.* MedChemComm, 2013. **4**(2): p. 378-382.

247. Upadhyaya, P., et al., *Inhibition of Ras Signaling by Blocking Ras–Effector Interactions with Cyclic Peptides.* Angewandte Chemie International Edition, 2015. **54**(26): p. 7602-7606.

248. Szabó, Z., *Multinuclear NMR studies of the interaction of metal ions with adenine-nucleotides.* Coordination Chemistry Reviews, 2008. **252**(21): p. 2362-2380.

249. Karl, M., et al., *Pressure response of 31P chemical shifts of adenine nucleotides.* Biophysical Chemistry, 2017.

250. Ting, P.Y., et al., *Tyrosine phosphorylation of RAS by ABL allosterically enhances effector binding.* The FASEB Journal, 2015. **29**(9): p. 3750-3761.

251. Nussinov, R., et al., *K-Ras4B/calmodulin/PI3Kα: A promising new adenocarcinoma-specific drug target?* Expert Opinion on Therapeutic Targets, 2016. **20**(7): p. 831-842.

252. Song, C., et al., *Regulation of a Novel Human Phospholipase C, PLCε, through Membrane Targeting by Ras.* Journal of Biological Chemistry, 2001. **276**(4): p. 2752-2757.

253. Huang, L., et al., *Structural basis for the interaction of Ras with RalGDS.* Nat Struct Mol Biol, 1998. **5**(6): p. 422-426.

254. Meierhofer, T., et al., *Cu2+-cyclen as Probe to Identify Conformational States in Guanine Nucleotide Binding Proteins.* Journal of the American Chemical Society, 2011. **133**(7): p. 2048-2051.

255. Nixon, A.E., et al., *Kinetics of Inorganic Phosphate Release during the Interaction of p21ras with the GTPase-Activating Proteins, p120-GAP and Neurofibromin.* Biochemistry, 1995. **34**(47): p. 15592-15598.

256. Ahmadian, M.R., et al., *Individual Rate Constants for the Interaction of Ras Proteins with GTPase-Activating Proteins Determined by Fluorescence Spectroscopy.* Biochemistry, 1997. **36**(15): p. 4535-4541.

257. Liao, J., et al., *Two conformational states of Ras GTPase exhibit differential GTP-binding kinetics.* Biochemical and Biophysical Research Communications, 2008. **369**(2): p. 327-332.

258. Ernst, R.R. and W.A. Anderson, *Application of Fourier Transform Spectroscopy to Magnetic Resonance.* Review of Scientific Instruments, 1966. **37**(1): p. 93-102.

259. Franken, S.M., et al., *Three-dimensional structures and properties of a transforming and a nontransforming glycine-12 mutant of p21H-ras.* Biochemistry, 1993. **32**(33): p. 8411-8420.

260. Ahmadian, M.R., et al., *Guanosine triphosphatase stimulation of oncogenic Ras mutants.* Proceedings of the National Academy of Sciences, 1999. **96**(12): p. 7065-7070.

261. Frech, M., et al., *Role of Glutamine-61 in the Hydrolysis of GTP by p21H-ras: An Experimental and Theoretical Study.* Biochemistry, 1994. **33**(11): p. 3237-3244.

262. Kalbitzer, H.R. and M. Spoerner, *Chapter Four - State 1(T) Inhibitors of Activated Ras*, in *The Enzymes*, F. Tamanoi, Editor. 2013, Academic Press. p. 69-94.

263. Weikl, T.R. and C. von Deuster, *Selected-fit versus induced-fit protein binding: Kinetic differences and mutational analysis.* Proteins: Structure, Function, and Bioinformatics, 2009. **75**(1): p. 104-110.

264. Rudolph, M.G., et al., *Thermodynamics of Ras/Effector and Cdc42/Effector Interactions Probed by Isothermal Titration Calorimetry.* Journal of Biological Chemistry, 2001. **276**(26): p. 23914-23921.

265. Al-Mulla, F., et al., *Structural differences between valine-12 and aspartate-12 Ras proteins may modify carcinoma aggression.* The Journal of Pathology, 1999. **187**(4): p. 433-438.

266. John, J., et al., *C-terminal truncation of p21H preserves crucial kinetic and structural properties.* Journal of Biological Chemistry, 1989. **264**(22): p. 13086-13092.

267. John, J., M. Frech, and A. Wittinghofer, *Biochemical properties of Ha-ras encoded p21 mutants and mechanism of the autophosphorylation reaction.* Journal of Biological Chemistry, 1988. **263**(24): p. 11792-11799.

268. Klebe, G., *Applying thermodynamic profiling in lead finding and optimization.* Nat Rev Drug Discov, 2015. **14**(2): p. 95-110.

269. Kiel, C., et al., *Recognizing and Defining True Ras Binding Domains II: In Silico Prediction Based on Homology Modelling and Energy Calculations.* Journal of Molecular Biology, 2005. **348**(3): p. 759-775.

270. Jelesarov, I. and H.R. Bosshard, *Isothermal titration calorimetry and differential scanning calorimetry as complementary tools to investigate the energetics of biomolecular recognition.* Journal of Molecular Recognition, 1999. **12**(1): p. 3-18.

271. Chodera, J.D. and D.L. Mobley, *Entropy-enthalpy compensation: role and ramifications in biomolecular ligand recognition and design.* Annual review of biophysics, 2013. **42**: p. 121-142.

272. Koehler, J., et al., *Pressure Dependence of 15N Chemical Shifts in Model Peptides Ac-Gly-Gly-X-Ala-NH2.* Materials\, 2012. **5**: p. 1774-1786\.

273. Spoerner, M., et al., *High pressure 31P NMR spectroscopy on guanine nucleotides.* Journal of Biomolecular NMR, 2017. **67**(1): p. 1-13.

274. Moedritzer, K., *pH dependence of phosphorus-31 chemical shifts and coupling constants of some oxyacids of phosphorus.* Inorganic Chemistry, 1967. **6**(5): p. 936-939.

275. Cozzone, P.J. and O. Jardetzky, *Phosphorus-31 Fourier transform nuclear magnetic resonance study of mononucleotides and dinucleotides. 1. Chemical shifts.* Biochemistry, 1976. **15**(22): p. 4853-4859.

276. Ford, B., et al., *Structure of the G60A Mutant of Ras: Implications for the Dominant Negative Effect.* Journal of Biological Chemistry, 2005. **280**(27): p. 25697-25705.

277. Johnson, C.W., et al., *The small GTPases K-Ras, N-Ras, and H-Ras have distinct biochemical properties determined by allosteric effects.* Journal of Biological Chemistry, 2017. **292**(31): p. 12981-12993.

278. Krengel, U., et al., *Three-dimensional structures of H-ras p21 mutants: Molecular basis for their inability to function as signal switch molecules.* Cell. **62**(3): p. 539-548.

279. Betts, M.J. and R.B. Russell, *Amino Acid Properties and Consequences of Substitutions*, in *Bioinformatics for Geneticists*. 2003, John Wiley & Sons, Ltd. p. 289-316.

280. Seeburg, P.H., et al., *Biological properties of human c-Ha-ras1 genes mutated at codon 12.* Nature, 1984. **312**(5989): p. 71-75.

281. Muraoka, S., et al., *Crystal structures of the state 1 conformations of the GTP-bound H-Ras protein and its oncogenic G12V and Q61L mutants.* FEBS Letters, 2012. **586**(12): p. 1715-1718.

282. Kinoshita, T., et al., *Raf/MAPK and rapamycin-sensitive pathways mediate the anti-apoptotic function of p21Ras in IL-3-dependent hematopoietic cells.* Oncogene, 1997. **15**(6): p. 8.

283. Buhrman, G., G. Wink, and C. Mattos, *Transformation Efficiency of RasQ61 Mutants Linked to Structural Features of the Switch Regions in the Presence of Raf.* Structure, 2007. **15**(12): p. 1618-1629.

284. Baba, S., et al., *Humidity control and hydrophilic glue coating applied to mounted protein crystals improves X-ray diffraction experiments.* Acta Crystallographica Section D: Biological Crystallography, 2013. **69**(Pt 9): p. 1839-1849.

285. Davis, I.W., et al., *The Backrub Motion: How Protein Backbone Shrugs When a Sidechain Dances.* Structure. **14**(2): p. 265-274.

286. Shapovalov, M.V. and R.L. Dunbrack, *Statistical and conformational analysis of the electron density of protein side chains.* Proteins: Structure, Function, and Bioinformatics, 2007. **66**(2): p. 279-303.

287. Pearce, N.M., et al., *A multi-crystal method for extracting obscured crystallographic states from conventionally uninterpretable electron density.* Nature Communications, 2017. **8**: p. 15123.

288. Fraser, J.S., et al., *Hidden alternative structures of proline isomerase essential for catalysis.* Nature, 2009. **462**: p. 669.

289. Reichenbach-Klinke, R., M. Zabel, and B. Konig, *Synthesis and structure of cyclen hydroxylamine ligands and their zinc(ii) complexes.* Dalton Transactions, 2003(1): p. 141-145.